

Sustainable Materials for Next Generation Energy Devices

Sustainable Materials for Next Generation Energy Devices

Challenges and Opportunities

Edited by

Kuan Yew Cheong

Universiti Sains Malaysia, Malaysia

Lung-Chien Chen

National Taipei University of Technology, Taiwan



ELSEVIER

Elsevier

Radarweg 29, PO Box 211, 1000 AE Amsterdam, Netherlands
The Boulevard, Langford Lane, Kidlington, Oxford OX5 1GB, United Kingdom
50 Hampshire Street, 5th Floor, Cambridge, MA 02139, United States

© 2021 Elsevier Inc. All rights reserved

No part of this publication may be reproduced or transmitted in any form or by any means, electronic or mechanical, including photocopying, recording, or any information storage and retrieval system, without permission in writing from the publisher. Details on how to seek permission, further information about the Publisher's permissions policies and our arrangements with organizations such as the Copyright Clearance Center and the Copyright Licensing Agency, can be found at our website: www.elsevier.com/permissions.

This book and the individual contributions contained in it are protected under copyright by the Publisher (other than as may be noted herein).

Notices

Knowledge and best practice in this field are constantly changing. As new research and experience broaden our understanding, changes in research methods, professional practices, or medical treatment may become necessary.

Practitioners and researchers must always rely on their own experience and knowledge in evaluating and using any information, methods, compounds, or experiments described herein. In using such information or methods they should be mindful of their own safety and the safety of others, including parties for whom they have a professional responsibility.

To the fullest extent of the law, neither the Publisher nor the authors, contributors, or editors, assume any liability for any injury and/or damage to persons or property as a matter of products liability, negligence or otherwise, or from any use or operation of any methods, products, instructions, or ideas contained in the material herein.

Library of Congress Cataloguing-in-Publication Data

A catalog record for this book is available from the Library of Congress

British Library Cataloguing-in-Publication Data

A catalogue record for this book is available from the British Library

ISBN: 978-0-12-820628-7

For information on all Elsevier publications
visit our website at <https://www.elsevier.com/books-and-journals>

Publisher: Matthew Deans

Acquisitions Editor: Christina Gifford

Editorial Project Manager: Fernanda A. Oliveira

Production Project Manager: Sojan P. Pazhayattil

Cover Designer: Greg Harris



Working together
to grow libraries in
developing countries

Typeset by SPi Global, India

www.elsevier.com • www.bookaid.org

Contributors

Numbers in parentheses indicate the pages on which the authors' contributions begin.

- Seckin Akin** (181), Nanotechnology R&D Laboratory; Department of Metallurgical & Materials Engineering, Karamanoglu Mehmetbey University, Karaman, Turkey
- Nowshad Amin** (103), Institute of Sustainable Energy, Universiti Tenaga Nasional (@The Energy University), Kajang, Selangor, Malaysia
- Sambandam Anandan** (27), Nanomaterials & Solar Energy Conversion Lab, Department of Chemistry, National Institute of Technology, Tiruchirappalli, India
- A.K. Arof** (283), Centre for Ionics University of Malaya, Physics Department, Faculty of Science, University of Malaya, Kuala Lumpur, Malaysia
- Subramanian Arulmani** (27), Nanomaterials & Solar Energy Conversion Lab, Department of Chemistry, National Institute of Technology, Tiruchirappalli, India
- Roberto Baca-Arroyo** (359), Department of Electronics, School of Mechanical and Electrical Engineering, National Polytechnic Institute, Mexico City, Mexico
- M.H. Buraidah** (283), Centre for Ionics University of Malaya, Physics Department, Faculty of Science, University of Malaya, Kuala Lumpur, Malaysia
- Chien Fat Chau** (103), College of Engineering, Universiti Tenaga Nasional (@The Energy University), Kajang, Selangor, Malaysia
- Yoshitaka Fujimoto** (343), Department of Physics, Tokyo Institute of Technology, Oh-okayama, Meguro-ku, Tokyo, Japan
- Ajai Kumar Garg** (317), Ministry of Electronics and Information Technology (MeitY), New Delhi, India
- Su Mei Goh** (103), College of Engineering, Universiti Tenaga Nasional (@The Energy University), Kajang, Selangor, Malaysia
- Navneet Kumar Gupta** (317), CSIR-Central Institute of Mining and Fuel Research, Dhanbad, Jharkhand, India
- Sanjeev Kumar Gupta** (317), Ministry of Electronics and Information Technology (MeitY), New Delhi, India
- Hairul Hisham Hamzah** (221), School of Chemical Sciences, Universiti Sains Malaysia, Gelugor, Pulau Pinang, Malaysia
- Jinming Hu** (149), Beijing Key Lab of Nanophotonics and Ultrafine Optoelectronic Systems, School of Physics; Key Lab of Advanced Optoelectronic Quantum Design and Measurement, Ministry of Education, Beijing Institute of Technology, Beijing, PR China

Hieng Kiat Jun (133), Department of Mechanical and Material Engineering, Lee Kong Chian Faculty of Engineering and Science, Universiti Tunku Abdul Rahman, Sungai Long Campus, Kajang, Malaysia

Sumanta Kumar Karan (251), Materials Science Centre, Indian Institute of Technology Kharagpur, Kharagpur, India

Go Kawamura (59), Department of Electrical and Electronic Information Engineering, Toyohashi University of Technology, Toyohashi, Aichi, Japan

Ismail Cihan Kaya (181), Department of Metallurgical & Materials Engineering, Konya Technical University, Konya; Nanotechnology R&D Laboratory, Karamanoğlu Mehmetbey University, Karaman, Turkey

Bhanu Bhusan Khatua (251), Materials Science Centre, Indian Institute of Technology Kharagpur, Kharagpur, India

Jin Kon Kim (251), National Creative Research Initiative Center for Smart Block Copolymers, Department of Chemical Engineering, Pohang University of Science and Technology, Pohang, Kyungbuk, Republic of Korea

Chin Wei Lai (103), Nanotechnology & Catalysis Research Centre (NANOCAT), University of Malaya (UM), Kuala Lumpur, Malaysia

Dasheng Lee (85), Department of Energy and Refrigerating Air-Conditioning Engineering, National Taipei University of Technology, Taipei, Taiwan, ROC

Lu-Yin Lin (3), Department of Chemical Engineering and Biotechnology, National Taipei University of Technology, Taipei, Taiwan

Foo Wah Low (103), Institute of Sustainable Energy, Universiti Tenaga Nasional (@The Energy University), Kajang, Selangor, Malaysia

Sandip Maiti (251), National Creative Research Initiative Center for Smart Block Copolymers, Department of Chemical Engineering, Pohang University of Science and Technology, Pohang, Kyungbuk, Republic of Korea

Atsunori Matsuda (59), Department of Electrical and Electronic Information Engineering, Toyohashi University of Technology, Toyohashi, Aichi, Japan

Hiroyuki Muto (59), Institute of Liberal Arts and Sciences; Department of Electrical and Electronic Information Engineering, Toyohashi University of Technology, Toyohashi, Aichi, Japan

Noorhashimah Mohamad Nor (221), School of Materials & Mineral Resources Engineering, Engineering Campus, Universiti Sains Malaysia, Nibong Tebal; NanoBiotechnology Research and Innovation (NanoBRI), Institute for Research in Molecular Medicine, Universiti Sains Malaysia, Gelugor, Pulau Pinang, Malaysia

Khairunisak Abdul Razak (221, 251), School of Materials & Mineral Resources Engineering, Engineering Campus, Universiti Sains Malaysia, Nibong Tebal, Pulau Pinang; NanoBiotechnology Research and Innovation (NanoBRI), Institute for Research in Molecular Medicine, Universiti Sains Malaysia, Gelugor, Pulau Pinang, Malaysia

Nurul Asma Samsudin (103), Institute of Sustainable Energy, Universiti Tenaga Nasional (@The Energy University), Kajang, Selangor, Malaysia

Mohammad Shakeri (103), Institute of Sustainable Energy, Universiti Tenaga Nasional (@The Energy University), Kajang, Selangor, Malaysia

Savas Sonmezoglu (181), Nanotechnology R&D Laboratory; Department of Metallurgical & Materials Engineering, Karamanoglu Mehmetbey University, Karaman, Turkey

Andrea Sorrentino (27), Institute for Polymers, Composites, and Biomaterials (IPCB), National Research Council of Italy (CNR), Naples, Italy

Wai Kian Tan (59), Institute of Liberal Arts and Sciences, Toyohashi University of Technology, Toyohashi, Aichi, Japan

L.P. Teo (283), Centre for Ionics University of Malaya, Physics Department, Faculty of Science, University of Malaya, Kuala Lumpur, Malaysia

Sieh Kiong Tiong (103), Institute of Sustainable Energy, Universiti Tenaga Nasional (@The Energy University), Kajang, Selangor, Malaysia

Shengyi Yang (149), Beijing Key Lab of Nanophotonics and Ultrafine Optoelectronic Systems, School of Physics; Key Lab of Advanced Optoelectronic Quantum Design and Measurement, Ministry of Education, Beijing Institute of Technology, Beijing, PR China

Yulisa Yusoff (103), Institute of Sustainable Energy, Universiti Tenaga Nasional (@The Energy University), Kajang, Selangor, Malaysia

Zhenheng Zhang (149), Beijing Key Lab of Nanophotonics and Ultrafine Optoelectronic Systems, School of Physics; Key Lab of Advanced Optoelectronic Quantum Design and Measurement, Ministry of Education, Beijing Institute of Technology, Beijing, PR China

Preface

This book focuses on sustainable functional materials for the next generation of energy devices. This approach intends to mitigate the impact(s) of the consumption of nonrenewable energy sources, whose escalation over the past several centuries is due to the industrial revolution. This phenomenon is not expected to subside for the coming decades as dependence on energy production in various aspects in our current technologically dependent world is expected to dramatically increase. Internet-of-things (IoT), one of many disruptive technologies, being driven by artificial intelligence, will require significant energy to sustain the rapidly growing information needs of humankind. In the near future, as the global economy expands, energy devices both in static and mobile modes will become essential building blocks in IoT to sustain continuous global development. Devices that store and/or convert energy from renewable sources, not only must be available to address the issue of energy shortage but may create another global issue—electronic waste—when IoT devices, including energy devices, are not being disposed of properly. Therefore a potential energy shortage and electronic waste issues must be simultaneously and creatively addressed. Adopting green, sustainable, and renewable concepts to produce functional materials in fabricating energy devices may reduce the burden of electronic waste(s). The main aim of this book is to present some of the latest state-of-the-art knowledge and innovative know-how related to producing and utilizing environmentally friendly functional materials. Information on recent advances is described by experts in the fields of materials science and energy that can be further developed for and employed in producing a feasible next generation of energy storage and/or conversation devices. The book consists of 14 chapters divided into three parts that focus on sustainable materials for energy storage and conversion, and includes several advanced concepts.

Part I: Electrochemical systems and energy storage

There are four chapters in this initial part. [Chapter 1](#) provides an overview of synthesis methods, physical properties, and energy storage capabilities for three groups of sustainable functional materials (metal alloys and compounds, conducting polymers, and carbon) for next-generation supercapacitors. A related

application is addressed in [Chapter 2](#): a design concept of conducting polymers based on engineered nanoarchitectures. [Chapter 3](#) reports on the current development and operational principles of next-generation batteries mainly based on an Fe-air system. The last chapter of this part presents a literature survey on patent search using a ThemeScape map for the development of functional materials for fuel cells.

Part II: Energy conversion and harvesting

The second part consists of five chapters; the first four chapters ([Chapters 5–8](#)) focus on sustainable functional materials for solar cells. [Chapter 5](#) details synthesis strategies for graphene and its derivatives for photovoltaic (solar cell) applications. Solution processing and use of “green” nanoscale sensitizers, namely Sn-, Ag-, and Bi-based compounds, for quantum dot-sensitized solar cells is reviewed in [Chapter 6](#). Chemical synthesis methods and properties of bare and core–shell colloidal quantum dots and their applications in solar cells are presented in [Chapter 7](#). Future perspectives of metal oxide-based inorganic hole-transporting materials for perovskite solar cells are discussed in [Chapter 8](#). [Chapter 9](#) focuses on recent advances in piezoelectric materials and structures for sustainable energy harvesting.

Part III: Advanced sustainable energy, materials, and device concepts

A total of five chapters comprises the final part. [Chapter 10](#) compiles the latest developments, in particular novel design approaches, of bio-organic materials as a nanogenerator. In [Chapter 11](#), novel polysaccharide polymer matrices as polymer electrolytes for dye-sensitized and quantum dot-sensitized solar cells are presented. Recent progress in biomass-derived functional carbon nanomaterials as efficient metal-free catalysts for oxygen reduction reaction(s) at fuel cell cathodes is reviewed in [Chapter 12](#). A first-principles density-functional study of graphene layers for advanced toxic gas sensors is provided in [Chapter 13](#). In the final chapter of this part and book, electronic properties and applications of recycled silicon waste are described.

We would like to express our sincere thanks to all contributing authors for their commitment and dedication throughout the project. Their valuable knowledge and keen insights into future technological challenges have produced a book that should be a solid reference and valuable resource for readers who wish to explore this field. This high-quality edited book would not have been published without the close collaboration and support given by Fernanda Oliveira (Editorial Project Manager). Special thanks are due to Christina Gifford (Acquisitions Editor) for her constant support and Dr. Aloysius Hepp

(Advisory Editor—Functional (Energy) Materials) for contributing to the vision of this book and his continuous encouragement and valuable suggestions throughout the publication process.

Kuan Yew Cheong

Universiti Sains Malaysia, Penang, Malaysia

Lung-Chien Chen

National Taipei University of Technology, Taipei, Taiwan

Chapter 1

Sustainable functional materials for next-generation supercapacitors

Lu-Yin Lin

Department of Chemical Engineering and Biotechnology, National Taipei University of Technology, Taipei, Taiwan

1 Introduction

To reduce pollution generation and fossil fuel consumption, it is necessary to develop efficient energy storage devices. The Li-ion battery is one of the most efficient energy storage devices, which converts chemical energy to electricity via redox reactions at the electrolyte and active material interface. The Li-ion battery can achieve high energy density, but the complex chemical reaction for energy storage leads to relatively smaller power density. Also, the Li-ion battery is not recommended in large-scale applications due to possible explosion during operation, as seen in small devices. Fig. 1 shows the Ragone plot for commonly used energy storage devices [1]. The battery has high energy density due to the conversion of chemical energy into electricity, while the capacitor has high power density because of the ion adsorption/desorption energy storage feature. To pursue high power and energy densities, development of a combination of battery and supercapacitor, the so-called supercapabattery, is necessary. The supercapacitor does not replace the battery, but is incorporated with the battery to provide huge amounts of energy in a short period of time. Supercapacitors can be applied to many fields, such as transportation, consumer electronics, and green energy storage. For the transportation application such as automobiles, buses, planes, trains, hybrid electric vehicles, and elevators, the supercapacitor is mainly used for turning on/off the engine completely at start/stop moments, and for regenerative braking, short-term energy storage, and burst-mode power delivery. For consumer electronics like computers and communications applications, the supercapacitor is frequently applied for memory protection and as an internal back-up power. For green energy storage like wind energy and solar energy, the supercapacitor can store large amounts of energy

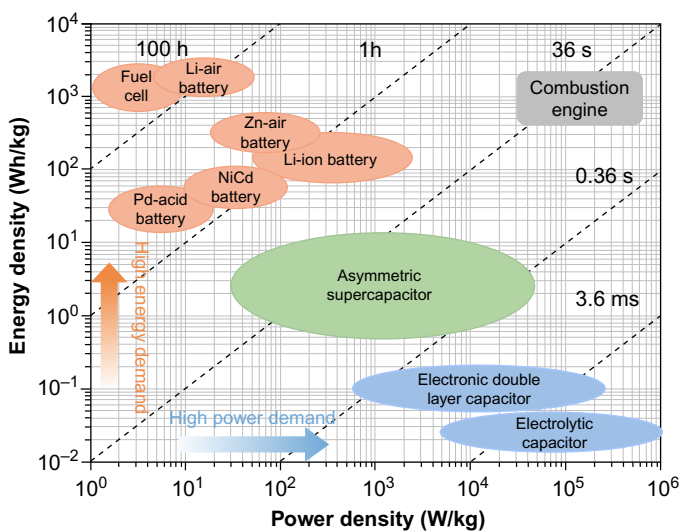


FIG. 1 Ragone plot for energy storage devices [1]. (Reprinted with permission from Y. Shao, M.F. El-Kady, J. Sun, Y. Li, Q. Zhang, M. Zhu, H. Wang, B. Dunn, R.B. Kaner, Design and mechanisms of asymmetric supercapacitors, *Chem. Rev.* 118 (2018) 9233–9280. Copyright (2018) American Chemical Society.)

in the form of strong winds and scorching sunshine. Table 1 shows the applications of supercapacitors and corresponding samples and functions.

The supercapacitor is also called an electrochemical capacitor. According to the energy storage mechanism, the supercapacitor can be classified into three sorts. The first is the electric double-layer capacitor (EDLC), which stores charges via Coulombic static charge adsorption/desorption, known as double layer. The second is the pseudocapacitor, which stores charges by using fast surface Faradaic redox reactions in a wide potential range at the active material and electrolyte interface. The third sort of supercapacitor is the hybrid supercapacitor or supercapabattery [2], which combines the EDLC electrode and the pseudocapacitor electrode to take advantage of both kinds of storage mechanism. The working mechanism for the hybrid supercapacitor is like a combination of battery and traditional supercapacitor. The supercapacitor can also be classified as symmetric supercapacitor and asymmetric supercapacitor according to the similarity of the positive and negative electrodes. On the other hand, the supercapacitor is composed of current collector, separator, active material, and electrolyte. The specific capacitance and potential window of the supercapacitor are mainly influenced by the active material and electrolyte, respectively. The active material should possess high surface area and be able to conduct effective reversible redox reactions for achieving high specific capacitance. The electrolyte is responsible for widening the potential window and attaining excellent cycling stability using suitable solvent and redox additives.

TABLE 1 Application of supercapacitors and corresponding samples and functions.

Application	Actual samples	Functions
Transportation	(1) Bus (2) Plane (3) Train (4) Automobile (5) Hybrid electric vehicle (6) Elevator	(1) Regenerative braking (2) Short-term energy storage (3) Burst power delivery
Customer electronics	(1) Computers (2) Communications	(1) Memory protection (2) Internal back-up power
Green energy storage	(1) Wind energy (2) Solar energy	Storage energy from strong winds and scorching sunshine conditions

This text first introduces the components of supercapacitors, including current collector, electrolyte, and active material. Subsequently, the properties and advantages of the active material are introduced to understand the effects of material selection and design on the energy storage ability of supercapacitors.

2 Components of supercapacitors

2.1 Current collectors

The current collectors of supercapacitors include Ni foams [3-8], Cu foils [9-11], Ti foils [12, 13], conductive glasses [14-16], and carbon clothes [17-19]. Among the substrates, carbon-based substrates such as carbon cloth and carbon fiber are more environmentally friendly and sustainable, since carbon is the basis of organisms and can release less pollution. On the other hand, due to the large developments of wearable devices nowadays, flexible substrates such as Ni foams and carbon clothes have become more and more popular. Since Ni foam has high porosity and high electrical conductivity, the active material can be deposited on the Ni foam easily using electrodeposition or hydrothermal synthesis. Carbon cloth has better flexibility than Ni foam to endure more bending and stretching environments, although porosity and electrical conductivity are smaller for carbon cloth. In addition, carbon cloth should usually be treated with acids to increase the hydrophilic property for depositing active materials more efficiently in aqueous conditions. Li and coworkers used a low-temperature chemical coprecipitation method to synthesize nickel cobalt-layered hydroxide on Ni foam, Cu foil, and carbon cloth, and compared the energy storage abilities of these electrodes based on different current collectors [20]. Our group investigated the electrochemical energy storage ability of

nickel cobalt oxide and nickel cobalt molybdenum oxide core-shell electrodes with Ni foam and carbon cloth substrates. Fig. 2A and B, and C and D, respectively, shows scanning electron microscopy images of the Ni foam and carbon cloth substrates. The results indicate that the electrode with the Ni foam substrate can attain a higher specific capacitance due to the extra formation of nickel hydroxide on the surface of the Ni foam and the higher electrical conductivity of the nickel metal [18]. There are still many details to be studied about the effects of current collectors on the growth of active materials. It is expected that by suitably selecting the current collector the high electrical conductivity and high specific surface area features can be simultaneously achieved for establishing excellent energy storage electrodes.

2.2 Electrolyte

The electrolyte for supercapacitors can be classified into liquid electrolyte [21-41] and quasi-solid-state electrolyte [42-44] according to the solvent used to prepare the electrolyte. For liquid electrolytes, based on the properties of the liquid solvents, the electrolyte can be classified into aqueous electrolyte [21-29], organic electrolyte [30-38], and ionic liquid electrolyte [39-41]. On the other hand, the redox additives can also be incorporated in the electrolyte to enhance the redox reactions and hence the energy storage abilities [45, 46].

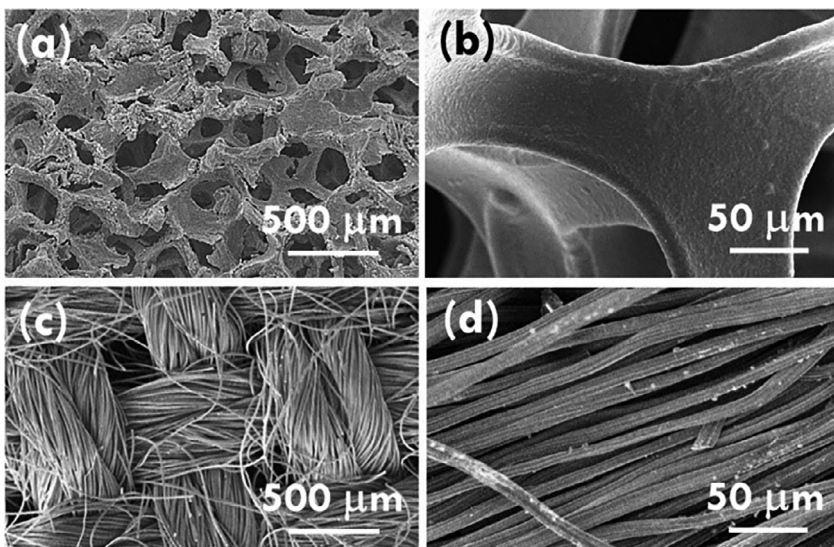


FIG. 2 (A and B) Ni foam and (C and D) carbon cloth [18]. (Reprinted with permission from Y.-H. Chiu, L.-Y. Lin, Effect of activating agents for producing activated carbon using a facile one-step synthesis with waste coffee grounds for symmetric supercapacitors, *J. Taiwan Inst. Chem. Eng.* 101 (2019) 177-185. Copyright (2019) Elsevier Ltd.)

The aqueous electrolyte is more environmentally friendly and sustainable, since there are almost no toxic organics and indecomposable polymers in this electrolyte.

2.2.1 *Liquid electrolyte*

Aqueous electrolyte

The aqueous electrolyte with nontoxic, low-cost, and high ionic conductivity advantages has been widely applied to supercapacitors, but the water decomposition voltage of 1.23 V versus reversible hydrogen electrode leads to a relatively smaller potential window and smaller energy and power densities of supercapacitors based on the aqueous system. To overcome the narrow potential window for the supercapacitor with the aqueous solution, some reports have applied unique ways, such as constructing highly porous structures to confine water molecules from decomposing to hydrogen and hydroxide ions and hence to broaden the potential window of the aqueous system [47]. The aqueous electrolyte can be classified into acid, alkaline, and neutral types, such as sulfuric acid [21-24], potassium hydroxide [25-27], and sodium sulfate [28, 29]. Among other types of electrolyte, the acid and alkaline types are corrosive but have higher ionic conductivity.

Organic electrolyte

The aqueous electrolyte was commonly used in supercapacitors for academic study, but the organic electrolyte has been applied in commercial supercapacitors because the potential window of 2.5-2.8 V can be attained in the organic system. However, the toxic organic solvent causes serious pollution to the environment. The commonly used organic solvents for the organic electrolyte include acetonitrile [33-35] and propylene carbonate [36-38].

Ionic electrolyte

The ionic electrolyte is a salt composed of anion and cation. The melting point of the ionic electrolyte is lower than 100°C. The ionic electrolyte has low vapor pressure and nonflammable features, which lead to good electrochemical stability and a wide potential window for supercapacitors in the ionic electrolyte system. However, high viscosity, low ionic conductivity, and high cost restrict the application of the ionic electrolyte. The commonly used ionic electrolytes include *N*-butylpyridinium chloride, 1-(carboxymethyl)-pyridinium chloride, and 1-ethyl-3-methylimidazolium chloride.

2.2.2 *Quasi-solid-state electrolyte*

The quasi-solid-state electrolyte can not only act as the ion transport medium, but also as the separator. The quasi-solid-state electrolyte has nonleakage and easy operational advantages, which make it suitable for applying to wearable

devices. The commonly used quasi-solid-state electrolytes include polyvinyl alcohol-KOH (PVA-KOH) and polyvinyl alcohol-H₃PO₄ (PVA-H₃PO₄). Yang et al. used PVA-KOH electrolyte and NiCo₂O₄ core-shell electrodes to assemble quasi-solid-state energy storage devices [42]. Chen and coworkers compared the energy storage ability of the quasi-solid-state supercapacitors with different quasi-solid-state electrolytes. The result indicates that the PVA-H₃PO₄ electrolyte-based supercapacitor showed the best electrochemical performance even under bending conditions [43]. It should be noted that when using the quasi-solid-state electrolytes to assemble the supercapacitors the ionic conductivity should be enhanced, and the thermal stability should also be controlled to improve the electrochemical stability of the supercapacitors for coping with repeated bending requirements [44]. Full wetting of the active material by the quasi-solid-state electrolyte is important. It should be noted that in most cases the quasi-solid state was attained by evaporating the liquid solvent in the electrolyte. Since the quasi-solid condition allows for fewer ions to diffuse and transfer in the electrolyte, fully soaking the active material in the liquid electrolyte, especially in the inner sides of active material before achieving the quasi-solid condition, is thus regarded to be the key step to attain good contact at the electrode/electrolyte interface.

2.2.3 Redox additives

The electrolyte plays the role of transporting ions in the supercapacitors. It has been verified that applying redox additives can efficiently enhance the Faradaic redox reactions during the charge/discharge process and hence improve the energy storage ability of the supercapacitors [45, 46]. The redox additive can be classified into organic and inorganic types. An inorganic redox additive such as the iodide/iodine system was proposed. Frackowiak et al. report the electrochemical behavior of supercapacitor carbon electrodes operating in different aqueous solutions modified by various redox-active species (hydroxybenzenes, bromine derivatives, and iodide) [48]. However, due to the more abundant resources and the wider operating potential window, organic redox additives have been applied intensively in the past. Our group applied hydroquinone (HQ) and *p*-phenylenediamine (PPD) as redox additives in acid, alkaline, and neutral electrolytes for assembling supercapacitors. The results indicate that by using sulfuric acid as the liquid electrolyte the best energy storage ability of supercapacitors with HQ and PPD redox additives can be achieved. Furthermore, our group investigated the effects of HQ and PPD ratios in the sulfuric acid electrolyte on the energy storage ability of supercapacitors. The energy storage ability of the activated carbon-based supercapacitors with the single redox additive-contained electrolyte and the two redox additives-contained electrolyte was also compared. As shown in Fig. 3A and B, a higher specific current charge can be achieved for supercapacitors with 10mM HQ and 10mM PPD in the sulfuric acid electrolyte (10+10), compared to those for

supercapacitors composed of electrolyte without redox additives (0+0) and with a single redox additive of HQ (10+0) and PPD (0+10). From the galvanostatic charge/discharge plot (Fig. 3C) the highest specific capacitance of 234.45 F/g corresponding to the specific current charge of 52.1 mAh/g was obtained for the supercapacitor with 10 mM HQ and 10 mM PPD in its sulfuric acid electrolyte [49].

2.3 Active materials

The active material plays significant roles in the specific capacitance of the supercapacitor. The active material can be classified into carbon materials, conducting polymers, and metal compounds. The most sustainable material for electrochemical capacitors is considered to be carbon materials. The reason why is similar to that for the carbon-based substrate as explained in Section 2.1. Different active materials store charges using different energy storage mechanisms. The energy storage mechanism can be classified into two types depending on the features of the active material. The physical energy storage mechanism involves ion adsorption and desorption, which commonly

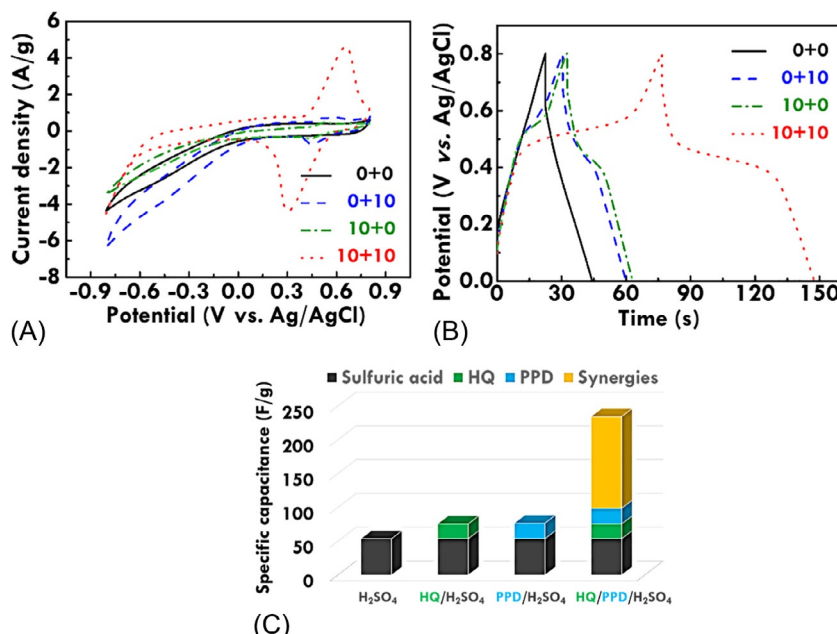


FIG. 3 (A) Cyclic voltammetry curves and (B) galvanostatic charge/discharge curves for AC-based supercapacitors with different HQ and PPD in the electrolytes; (C) bar plot for specific capacitance relating to AC-based supercapacitors with different electrolytes [49]. (Reprinted with permission from B. Akinwolemiwa, C. Peng, G.Z. Chen, Redox electrolyls in supercapacitors, *J. Electrochem. Soc.* 162 (2015) A5054-A5059. Copyright (2019) Elsevier Ltd.)

happens for carbon materials. This mechanism is for the so-called EDLCs. The charge/discharge rate is faster for this type due to the simple ion adsorption/desorption principle. The other one is the electrochemical energy storage mechanism, which is quick and highly reversible. The energy is stored by using the redox reactions occurring between the active material and the electrolyte. This type of energy storage mechanism commonly occurs for conducting polymers and metal compounds. It should also be noted that the energy can be stored by using the redox reactions for carbon materials with numerous functional groups attached. Hence, the energy storage mechanism is not simple and unique for a single type of active material. In the third part, the properties of active materials and previous literature regarding supercapacitors with different active materials are introduced in detail.

3 Active materials for supercapacitors

3.1 Carbon materials

Carbon materials with abundant sources, high electrical conductivity, high chemical stability, and environmentally friendly properties have been regarded as one of the most commonly used electrode active materials. The carbon material is regarded to be the most sustainable functional material for energy storage [50-52]. The commonly used carbon materials for supercapacitors include activated carbon (AC) [53-55], carbon nanotubes (CNTs) [56-59], and reduced graphene oxide (rGO) [60-63]. Carbon material can be singly applied as an active material or combined with other sorts of active material to fabricate the composites. Our group fabricated CNT and rGO nanobelt as the active material on the supercapacitor electrode and achieved a specific capacitance of 252.4 F/g, which is higher than those for supercapacitors with pure CNT (39.7 F/g) and pure rGO nanosheet (19.8 F/g) electrodes [64]. We also used coffee grounds as a biomaterial to produce AC as the active material for supercapacitors. Five-fold specific capacitance was achieved for supercapacitor with homemade AC compared to that for the supercapacitor with the commercial AC [17].

3.2 Conducting polymers

Conducting polymers are also called conducting plastics, which have low-cost, high electrical conductivity, and environmentally friendly properties. The commonly used conducting polymers contain polyaniline (PANI) [65-67], polypyrrole (PPY) [68-72], and polythiophene (PT) [73-76]. However, volume expansion during the charge/discharge process for the conducting polymer causes poor cycling stability. Therefore combining the conducting polymer with other sorts of active materials has been widely adopted to enhance the cycling stability of supercapacitors with conducting polymer active materials [77-80]. Laforgue and coworkers synthesized PT using the chemical route as

the active material for supercapacitors. A specific capacity of 40 mAh/g was obtained for the resulting supercapacitor at a scan rate of 20 mV/s [73]. Sivakkumar et al. used a chemical polymerization technique to synthesize PANI nanofibers for supercapacitors. At the current density of 1 A/g the supercapacitor can achieve a specific capacitance of 554 F/g [81]. Yang and coworkers used oil/water mixed solvent to fabricate a free-standing PPY membrane as the active material for supercapacitors, which showed a specific capacitance of 261 F/g at a scan rate of 25 mV/s [82].

3.3 Metal compounds

Metal compounds applied as active material for supercapacitors are classified into three sorts: metal hydroxides [83–86], metal oxides [87–92], and metal sulfides [93–97]. The metal hydroxides can be converted to metal oxides after annealing. Most of the previous literature first synthesized metal hydroxides with a unique structure and converted the metal hydroxides into metal oxides with the same unique structure. On the other hand, since sulfur has larger electronegativity than oxide, metal sulfides have higher theoretical capacitance than metal oxides, but metal oxides are more stable in air compared to metal sulfides. Since these three sorts of metal compounds have different pros and cons, a suitable combination of metal compounds is expected to achieve highly effective active materials.

Metal hydroxide with high theoretical capacitance, excellent electrochemical redox activity, and multiple crystalline structures was commonly applied as the active material to the positive electrode of supercapacitors [84]. Particular hydroxides of different metals such as Ni, Co, Fe, Ti, V, Mo, and Nb are emerging as promising materials for supercapabattery electrodes [98]. For example, $\text{Ni}(\text{OH})_2$ and $\text{Co}(\text{OH})_2$ are the intermediate products of NiO and Co_3O_4 [99]. By applying dewater and oxidation reactions, nickel and cobalt hydroxides can be converted to nickel and cobalt oxides. Nickel hydroxide has poor electrical conductivity and cycling stability, so the combination with carbon materials was usually adopted to improve the electrochemical performance of nickel hydroxides by enhancing the electrical conductivity and improving the cycling stability [85, 86].

Metal oxide has abundant redox states and small charge transfer resistances, which can promote multiple Faradaic reactions and display high energy and power densities [87]. The earliest metal oxides applied to supercapacitors were RuO_2 [88–90] and IrO_2 [91, 92]. Numerous sources have verified the high specific capacitance of RuO_2 as a pseudocapacitor material. However, the rare source of RuO_2 makes it expensive and limits its application. In recent years, researchers focused on low-cost transition metal oxides, such as MnO_2 , NiO , MoO_3 , TiO_2 , WO_3 , and Co_2O_3 . The energy storage ability of transition metal oxides can be improved by designing nanostructures with high surface area and fabricating composites with carbon materials and conducting polymers.

Nickel oxide with a high theoretical capacitance, low cost, and easily acquired properties has been widely designed as flower-like [100], sheet-like [101], and sphere-like [102] structures and applied as the active material for supercapacitors. Cobalt oxide with excellent reversible redox properties, high electrical conductivity, and high stability features has also been applied as active materials for supercapacitors [103]. Our group used different hydrothermal processes to synthesize cobalt oxide rhombic and nanobrush structures on the nickel foam substrate as the supercapacitor electrodes. Due to the different surface areas and electrical conductivities, the rhombic electrode and the nano-brush electrode, respectively, show the specific capacitance of 509 and 169 F/g [104]. We also applied a two-step hydrothermal process to fabricate multidimensional cobalt oxide active material for supercapacitors [105]. On the other hand, bimetallic oxides such as nickel cobalt oxide have also been widely applied as active materials for supercapacitors, due to the synergic effect from nickel and cobalt as well as the numerous redox reactions generated from the two metals [106, 107]. Nickel molybdenum oxide with high electrochemical activity from nickel and high electrical conductivity from molybdenum has also been intensively used as the active material for supercapacitors. Furthermore, the design of the core-shell structure is one of the efficient ways to increase the active surface area and electrical conductivity of the active material. Cheng et al. used a two-step hydrothermal process to fabricate the nickel cobalt oxide/nickel molybdenum oxide core-shell structure. Due to the high specific surface area and multiple redox reactions, the core-shell electrode shows excellent electrochemical performance [108]. Our group designed nickel cobalt oxide and nickel molybdenum oxide core-shell electrodes of supercapacitors and investigated the substrate effects [18] and structure-directing agent effects [109] on the morphology of the active materials and the energy storage ability of the supercapacitors. This active material was further used for assembling the flexible quasi-solid-state supercapacitors [110]. To further understand the core-shell structure design, we also investigated the effects of the growth sequence of core and shell on morphology and energy storage ability [111], the material effects of the nickel cobalt oxide core-based core-shell structure with the same morphology but different shell sorts [112], and the electrochemical performance of the nickel cobalt oxide/nickel molybdenum oxide core-shell electrodes with different core morphologies [113]. Our group fabricated the nickel cobalt sulfide nanorod and nickel molybdenum oxide nanosheet core-shell structure as the energy storage material for supercapacitors. Due to the one-dimensional charge transfer path of the nanorod core and the nanosheet structure of the nanosheet shell, this electrode achieved a specific capacity of 2.22 mAh/cm^2 at the current density of 10 mA/cm^2 [114]. In addition, to enhance the Faradaic redox reactions of the metal oxide electrode, we investigated the energy storage ability of ternary metallic oxides based on nickel and cobalt. The morphology and specific capacitance of the ternary metallic oxide electrodes are shown in Fig. 4. The result shows that the highest specific capacitance of 1.45 F/cm^2 can be

obtained for the nickel cobalt molybdenum oxide electrode, due to the extra molybdenum for providing higher electrical conductivity [115]. Furthermore, we incorporated nickel, cobalt, molybdenum, and copper in the quaternary metal oxide and applied it as an active material for supercapacitors. Fig. 5A and B is the cyclic voltammetry and the galvanostatic charge/discharge plots for the quaternary metallic oxide electrodes, respectively. The results show that the nickel cobalt molybdenum copper oxide electrode can attain the highest specific capacitance of 1.57 mAh/cm^2 because of the high electrical conductivity of copper and the sheet-like structure that provides the high surface area [4]. Our group further investigated the effects of the ratio for nickel, cobalt, molybdenum, and copper in the quaternary metal oxide on active material morphology and supercapacitor energy storage ability [6]. On the other hand, nickel foam with high electrical conductivity and high specific surface area has been widely applied as the current collector for supercapacitor electrodes. The nickel foam can release nickel ions in the acid solution, which broadens the application of nickel foam on synthesizing the nickel-based active materials. Our group further investigated the morphology and energy storage ability of the nickel-based active material based on synthesis with and without adding the nickel precursor to the hydrothermal solutions [116, 117].

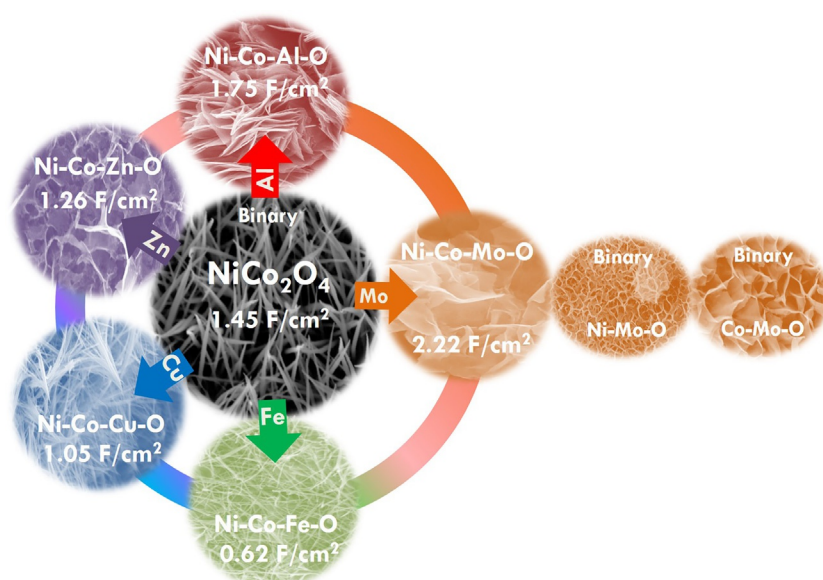


FIG. 4 Scheme for the morphology and specific capacitance of nickel cobalt-based ternary metal oxides [115]. (Reprinted with permission from Y.M. Chen, J.H. Cai, Y.S. Huang, K.Y. Lee, D.S. Tsai, A nanostructured electrode of IrO_x foil on the carbon nanotubes for supercapacitors, *Nanotechnology* 22 (2011) 115706. Copyright (2018) American Chemical Society.)

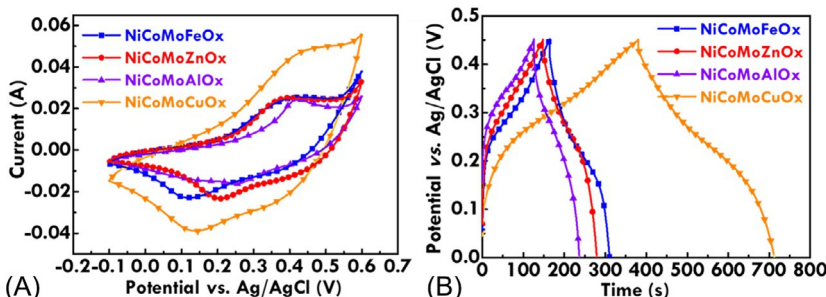


FIG. 5 (A) Cyclic voltammetry at 10 mV/s and (B) galvanostatic charge/discharge plots at 5 mA/cm² for quaternary metal oxide electrodes [4]. (Reprinted with permission from H.-X. Lai, L.-Y. Lin, J.-Y. Lin, Y.-K. Hsu, All binder-free electrophoresis deposition synthesis of nickel cobalt hydroxide/ultraphene and activated carbon electrodes for asymmetric supercapacitors, *Electrochim. Acta* 273 (2018) 115–126. Copyright (2019) Elsevier Ltd.)

Metal sulfide has high electrical conductivity and high stability. The main metal sulfides applied as the active material for supercapacitors include cobalt sulfide and nickel sulfide [93]. Cobalt sulfide utilized the Faradaic redox reactions between cobalt sulfide and hydroxide ions and the reversible redox reactions between Co²⁺/Co³⁺ to store and release energy. To enhance the electrochemical performance of the cobalt sulfide electrodes, a vast quantity of literature has focused on designing the well-defined structure of cobalt sulfides such as sheet-like [94, 95] and tube-like [96] structures. Our group synthesized a cobalt sulfide nanoflower structure as the active material for supercapacitors. The structure displayed excellent energy storage ability due to the high surface area [97]. On the other hand, nickel sulfide used the redox reactions between nickel sulfide and hydroxide ions as well as Ni²⁺/Ni³⁺ to conduct energy storage and release. With different nickel and sulfide ratios, numerous nickel sulfides such as Ni₃S₂, Ni₆S₅, Ni₇S₆, NiS, Ni₃S₄, and NiS₂ have been applied as the active materials for supercapacitors. There are also some sources that combine nickel sulfide with carbon materials to improve the electrochemical properties [118, 119]. Bimetallic sulfides such as nickel cobalt sulfide also have bimetallic properties, which can generate abundant redox reactions and display excellent energy storage ability. Our group designed nickel cobalt sulfide and cobalt sulfide core-shell structures for supercapacitors. The results show that the core-shell electrode shows a higher specific capacitance (8.47 F/cm²) than the electrodes with pure core and pure shell structures [8]. We also investigated the nickel and cobalt ratio effect on the morphology and energy storage ability of the nickel cobalt sulfide electrodes. The result shows that the highest specific capacitance of 258.2 mAh/g can be achieved for the nickel cobalt sulfide electrode with a nickel-to-cobalt ratio of 1 to 2 at the current density of 5 A/g [120]. On the other hand, the nickel metal feature for the nickel foam substrate to release nickel ions in the acid solution can also be applied

for synthesizing nickel cobalt sulfide electrodes [121, 122]. Our group used nickel precursor-free solutions with different pH values to fabricate nickel cobalt sulfides in the hydrothermal process and investigated the morphology and energy storage ability for the active materials prepared in the hydrothermal solutions with different pH values [122]. Other than nickel and cobalt sulfides with high theoretical capacitances, other metal sulfides such as molybdenum sulfide [68] and tungsten sulfide [123] have also been applied as active materials for supercapacitors.

To have a clearer comparison of the active materials, Table 2 lists the advantages and disadvantages of carbon material, conducting polymer, and metal compounds as the active materials for energy storage devices.

TABLE 2 List of advantages and disadvantages of carbon materials, conducting polymers, and metal compounds as the active material for supercapacitors.

Sort	Materials	Advantage	Disadvantage
Carbon	Activated carbon	(1) Excellent mechanical property (2) High cycling stability (3) Large surface area (4) High porosity (5) Low cost	(1) Small specific capacitance (2) Poor electrical conductivity
	Carbon nanotube	(1) Excellent mechanical property (2) High cycling stability (3) Excellent electrical property (4) Good electron transportation (5) Good electrolyte accessibility	(1) Small specific capacitance (2) High cost
	Reduced graphene oxide	(1) Excellent mechanical property (2) High cycling stability (3) Large surface area (4) Excellent electrical property	(1) Small specific capacitance (2) High cost

Continued

TABLE 2 List of advantages and disadvantages of carbon materials, conducting polymers, and metal compounds as the active material for supercapacitors—cont'd

Sort	Materials	Advantage	Disadvantage
Conducting polymer	Polyaniline	(1) Flexibility (2) Ease of synthesis (3) Ease of doping/dedoping (4) Controllable conductivity	(1) Poor cycling stability (2) Small specific capacitance
	Polypyrrole	(1) Flexibility (2) Ease of synthesis (3) Applicable to neutral electrolytes	(1) Poor cycling stability (2) Small specific capacitance (3) Difficulty of doping/dedoping
	Polythiophene	(1) Flexibility (2) Ease of synthesis (3) Favorable cycling stability (4) Environmental stability	(1) Poor cycling stability (2) Small specific capacitance (3) High cost (4) Poor electrical conductivity
Metal compound	Metal hydroxide	(1) Numerous redox states (2) High redox activity (3) High theoretical capacitance (4) Easy synthesis	(1) Poor cycling stability (2) Poor electrical conductivity
	Metal oxide	(1) Numerous redox states (2) High redox activity (3) High theoretical capacitance	(1) Poor cycling stability (2) Poor electrical conductivity
	Metal sulfide	(1) Numerous redox states (2) High redox activity (3) High theoretical capacitance (4) High electrical conductivity	(1) Poor cycling stability (2) Complex synthesis

3.4 Carbon, conducting polymer, and metal compound composites

Although carbon material has high electrical conductivity and high porosity properties, the specific capacitance is relatively smaller for supercapacitors with pure carbon materials due to EDLC energy storage behavior. To enhance the specific capacitance of the supercapacitors with carbon material, composites of the carbon material and other sorts of active materials have been widely developed. Chen et al. proposed a review to introduce hybrid materials between CNTs and redox active materials such as electronically conducting polymers and transition metal oxides [124]. Our group fabricated rGO and PANI nanotube composites as the active material for supercapacitors. Due to the unique tubular structure of PANI for providing one-dimensional straight electron transfer paths and high surface area, a specific capacitance of 437.8 F/g was obtained for supercapacitors with rGO/PANI active material [65]. Luo et al. fabricated PANI and rGO composite hydrogel as an active material for supercapacitors. At a current density of 2.6 A/g, a supercapacitor electrode can achieve a specific capacitance of 1120 F/g [125].

To reduce volume expansion of polymer during the charge/discharge process, composites of conducting polymer were fabricated. Our group synthesized the PPY and MoS₂ composite as the active material for supercapacitors. A higher specific capacitance of 182.28 F/g was obtained for the supercapacitor with the composite, compared to those for the supercapacitor with pure PPY (116.95 F/g) and pure MoS₂ (40.58 F/g) [68]. Our group also used the ultraviolet light-assisted electrodeposition method to deposit PPY on TiO₂ as active material for supercapacitors. The TiO₂ nanorod array can provide a suitable base for growing the PPY with high surface area. This electrode can achieve a specific capacitance of 200.45 F/g at a scan rate of 5 mV/s [69].

The composites of metal compounds and carbon were also proposed to take advantages of both EDLC and redox reactive charge storage mechanisms. Our group used the electrophoresis method to fabricate the nickel cobalt hydroxide and rGO composite as the active material for supercapacitors. Due to the abundant redox reactions generated by using the nickel cobalt hydroxides and the high electrical conductivity of the rGO, the asymmetric supercapacitor with this composite positive electrode shows a specific capacitance of 222 mF/g at the current density of 20 mA/cm². Our group also used different hydrothermal times to fabricate nickel cobalt hydroxide and rGO composites and investigated the effects of direct/indirect growth of active materials on the substrate on the morphology of active materials and energy storage ability of supercapacitors [126]. Our group fabricated tungsten sulfide and rGO composite as the composite active material for supercapacitors. Due to the high surface area of the tungsten sulfide nanosheet and the high electrical conductivity of the rGO, this supercapacitor electrode can achieve a specific capacitance of 1275 F/g at the current density of 2 A/g [123].

4 Future prospects

To pursue more comfortable and knowledgeable high-tech lives, wearable devices have been developed intensely in recent years. The establishment of flexible and stretchable energy storage devices has thus become one of the main trends for the future. The flexible conductive substrate, the hard-to-leak electrolyte under bendable and stretchable environments, and the active material with high maintenance under repeated bending conditions are the main points for the present studies. Carbon cloth and carbon fiber conductive substrates with high electrical conductivity and high flexibility properties have been considered as the most suitable soft conducting substrates for supercapacitors. However, carbon substrates should be pretreated, such as acid treatment to increase the hydrophilic properties and attain suitable active material growth environments. The quasi-solid and solid electrolytes with hard-to-leak properties under bending and stretching conditions have been regarded as the first choice for flexible energy storage devices. Furthermore, soft conducting polymer is the most useful active material for flexible supercapacitors. However, volume expansion during the charge/discharge process for the conducting polymer often leads to poor cycling stability of the supercapacitor, so it is necessary to combine other kinds of active materials to improve its cycling stability. In addition, choosing suitable processes to assemble supercapacitors with low electrical resistances is also one of the indispensable factors to achieve highly efficient supercapacitors. On the other hand, although the conducting substrate, electrolyte, and active materials have been widely developed at present, there is no rule for the suitable combination of each component. For example, fabricating nickel cobalt oxide as the active material on the substrates of nickel foam or carbon cloth may require different suitable synthesizing methods, and the most efficient active material morphology may also be varied. If rules for the suitable combination of a conducting substrate, electrolyte, and active material can be developed in the future, efficient supercapacitors that can fit numerous conditions are expected to be effectively and easily developed. On the other hand, there is no standard method to evaluate the energy storage ability of supercapacitors. Although it would be more reliable to compare energy and power densities of a supercapacitor with other devices for evaluating their energy storage abilities, the unit should take into account that the weight is for the pure active material or for the whole device. As another example, when evaluating cycling stability, the applied current density and charge/discharge cycles vary from literature to literature, which makes types of cycling stability hard to compare with each other.

References

- [1] Y. Shao, M.F. El-Kady, J. Sun, Y. Li, Q. Zhang, M. Zhu, H. Wang, B. Dunn, R.B. Kaner, Design and mechanisms of asymmetric supercapacitors, *Chem. Rev.* 118 (2018) 9233–9280.
- [2] G.Z. Chen, Supercapacitor and supercapattery as emerging electrochemical energy stores, *Int. Mater. Rev.* 62 (4) (2017) 173–202.

- [3] H.-X. Lai, L.-Y. Lin, J.-Y. Lin, Y.-K. Hsu, All binder-free electrophoresis deposition synthesis of nickel cobalt hydroxide/ultraphene and activated carbon electrodes for asymmetric supercapacitors, *Electrochim. Acta* 273 (2018) 115–126.
- [4] Y.-Y. Huang, L.-Y. Lin, X. Li, Efficient battery supercapacitor hybrid devices with quaternary metal oxide electrodes based on nickel and cobalt, *J. Energy Storage* 25 (2019) 100826.
- [5] P.-Y. Lee, L.-Y. Lin, Synthesizing nickel-based transition bimetallic oxide via nickel precursor-free hydrothermal synthesis for battery supercapacitor hybrid devices, *J. Colloid Interface Sci.* 538 (2019) 297–307.
- [6] T.-Y. Chen, L.-Y. Lin, Morphology variation for the nickel cobalt molybdenum copper oxide with different metal ratios and their application on energy storage, *Electrochim. Acta* 298 (2019) 745–755.
- [7] K.-L. Chiu, L.-Y. Lin, Applied potential-dependent performance of the nickel cobalt oxysulfide nanotube/nickel molybdenum oxide nanosheet core-shell structure in energy storage and oxygen evolution, *J. Mater. Chem. A* 7 (2019) 4626–4639.
- [8] J.-W. Cheng, L.-Y. Lin, W.-L. Hong, L.-Y. Lin, H.-Q. Chen, H.-X. Lai, Rational design of nickel cobalt sulfide/cobalt sulfide sheet-on-sheet structure for asymmetric supercapacitors, *Electrochim. Acta* 283 (2018) 1245–1252.
- [9] S.L. Chiam, H.N. Lim, S.M. Hafiz, A. Pandikumar, N.M. Huang, Electrochemical performance of supercapacitor with stacked copper foils coated with graphene nanoplatelets, *Sci. Rep.* 8 (2018) 3093.
- [10] R.S. Dey, H.A. Hjuler, Q. Chi, Approaching the theoretical capacitance of graphene through copper foam integrated three-dimensional graphene networks, *J. Mater. Chem. A* 3 (2015) 6324–6329.
- [11] P. Xu, K. Ye, M. Du, J. Liu, K. Cheng, J. Yin, G. Wang, D. Cao, One-step synthesis of copper compounds on copper foil and their supercapacitive performance, *RSC Adv.* 5 (2015) 36656–36664.
- [12] C. Wang, P. Zhou, Z. Wang, Y. Liu, P. Wang, X. Qin, X. Zhang, Y. Dai, M.-H. Whangbo, B. Huang, TiN nanosheet arrays on Ti foils for high-performance supercapacitance, *RSC Adv.* 8 (2018) 12841–12847.
- [13] F. Wang, X. Wu, X. Yuan, Z. Liu, Y. Zhang, L. Fu, Y. Zhu, Q. Zhou, Y. Wu, W. Huang, Latest advances in supercapacitors: from new electrode materials to novel device designs, *Chem. Soc. Rev.* 46 (2017) 6816–6854.
- [14] A. Scialia, A. Varzi, A. Lamberti, E. Tresso, S. Jeong, T. Jacob, S. Passerini, High energy and high voltage integrated photo-electrochemical double layer capacitor, *Sustain. Energy Fuels* 2 (2018) 968–977.
- [15] S. Korkmaz, F.M. Tezel, Ä°. A. Kariper, Synthesis and characterization of GO/V₂O₅ thin film supercapacitor, *Synth. Met.* 242 (2018) 37–48.
- [16] S. Kalasina, N. Phattharasupakun, T. Maihom, V. Promarak, T. Sudyoadsuk, J. Limtrakul, M. Sawangphruk, Novel hybrid energy conversion and storage cell with photovoltaic and supercapacitor effects in ionic liquid electrolyte, *Sci. Rep.* 8 (2018) 12192.
- [17] Y.-H. Chiu, L.-Y. Lin, Effect of activating agents for producing activated carbon using a facile one-step synthesis with waste coffee grounds for symmetric supercapacitors, *J. Taiwan Inst. Chem. Eng.* 101 (2019) 177–185.
- [18] W.-L. Hong, L.-Y. Lin, Studying the substrate effects on energy storage abilities of flexible battery supercapacitor hybrids based on nickel cobalt oxide and nickel cobalt oxide@nickel molybdenum oxide, *Electrochim. Acta* 308 (2019) 83–90.
- [19] Y. Wang, S. Tang, S. Vongehr, J. Ali Syed, X. Wang, X. Meng, High-performance flexible solid-state carbon cloth supercapacitors based on highly processible N-graphene doped poly-acrylic acid/polyaniline composites, *Sci. Rep.* 6 (2016) 12883.

20 PART | I Electrochemical systems and energy storage

- [20] T. Li, R. Li, H. Luo, Facile *in situ* growth of Ni/Co-LDH arrays by hypothermal chemical coprecipitation for all-solid-state asymmetric supercapacitors, *J. Mater. Chem. A* 4 (2016) 18922–18930.
- [21] M.F.Y.M. Hanappi, M. Deraman, M. Suleman, N.S.M. Nor, N.E.S. Sazali, E. Hamdan, N.S.M. Tajuddin, N.H. Basri, M.R.M. Jasni, M.A.R. Othman, Influence of aqueous KOH and H₂SO₄ electrolytes ionic parameters on the performance of carbon-based supercapacitor electrodes, *Funct. Mater. Lett.* 10 (2017) 1750013.
- [22] M. GaliÅ„ski, A. Lewandowski, I. StÅ™pníak, Ionic liquids as electrolytes, *Electrochim. Acta* 51 (2006) 5567–5580.
- [23] D. Jiménez-Cordero, F. Heras, M.A. Gilarranz, E. Raymundo-Piñero, Grape seed carbons for studying the influence of texture on supercapacitor behaviour in aqueous electrolytes, *Carbon* 71 (2014) 127–138.
- [24] H. Wu, X. Wang, L. Jiang, C. Wu, Q. Zhao, X. Liu, B.A. Hu, L. Yi, The effects of electrolyte on the supercapacitive performance of activated calcium carbide-derived carbon, *J. Power Sources* 226 (2013) 202–209.
- [25] B. Rajagopalan, J.S. Chung, Reduced chemically modified graphene oxide for supercapacitor electrode, *Nanoscale Res. Lett.* 9 (2014) 535.
- [26] X.-F. Wang, Z. You, D.-B. Ruan, A hybrid metal oxide supercapacitor in aqueous KOH electrolyte, *Chin. J. Chem.* 24 (2006) 1126–1132.
- [27] J. Huang, B.G. Sumpter, V. Meunier, A Universal model for nanoporous carbon supercapacitors applicable to diverse pore regimes, carbon materials, and electrolytes, *Chem. Eur. J.* 14 (2008) 6614–6626.
- [28] Q.T. Qu, B. Wang, L.C. Yang, Y. Shi, S. Tian, Y.P. Wu, Study on electrochemical performance of activated carbon in aqueous Li₂SO₄, Na₂SO₄ and K₂SO₄ electrolytes, *Electrochim. Commun.* 10 (2008) 1652–1655.
- [29] M.F. El-Kady, M. Ihns, M. Li, J.Y. Hwang, M.F. Mousavi, L. Chaney, A.T. Lech, R.B. Kaner, Engineering three-dimensional hybrid supercapacitors and microsupercapacitors for high-performance integrated energy storage, *Proc. Natl. Acad. Sci.* 112 (2015) 4233–4238.
- [30] X. Lin, H. Lou, W. Lu, F. Xu, R. Fu, D. Wu, High-performance organic electrolyte supercapacitors based on intrinsically powdery carbon aerogels, *Chin. Chem. Lett.* 29 (2018) 633–636.
- [31] X. Wang, Y. Li, F. Lou, M.E. Melandsø, Buan, E. Sheridan, D. Chen, Enhancing capacitance of supercapacitor with both organic electrolyte and ionic liquid electrolyte on a biomass-derived carbon, *RSC Adv.* 7 (2017) 23859–23865.
- [32] C. Song, J. Yun, H. Lee, H. Park, Y.R. Jeong, G. Lee, M.S. Kim, J.S. Ha, A shape memory high-voltage supercapacitor with asymmetric organic electrolytes for driving an integrated NO₂ gas sensor, *Adv. Funct. Mater.* 29 (2019) 1901996.
- [33] Q. Dou, S. Lei, D.-W. Wang, Q. Zhang, D. Xiao, H. Guo, A. Wang, H. Yang, Y. Li, S. Shi, X. Yan, Safe and high-rate supercapacitors based on an “acetonitrile/water in salt” hybrid electrolyte, *Energy Environ. Sci.* 11 (2018) 3212–3219.
- [34] Y. Yamada, K. Furukawa, K. Sodeyama, K. Kikuchi, M. Yaegashi, Y. Tateyama, A. Yamada, Unusual stability of acetonitrile-based superconcentrated electrolytes for fast-charging lithium-ion batteries, *J. Am. Chem. Soc.* 136 (2014) 5039–5046.
- [35] D.-E. Jiang, Z. Jin, D. Henderson, J. Wu, Solvent effect on the pore-size dependence of an organic electrolyte supercapacitor, *J. Phys. Chem. Lett.* 3 (2012) 1727–1731.
- [36] J. Eskusson, A. JÄRNE, T. Thomberg, E. Lust, Supercapacitors based on propylene carbonate with addition of sulfur containing organic solvents, in: *Meeting Abstracts 2014, MA2014-02*, 2014, p. 192.

- [37] Z.-A. Zhang, Y.-Q. Lai, J. Li, Y.-X. Liu, Electrochemical behavior of wound supercapacitors with propylene carbonate and acetonitrile based nonaqueous electrolytes, *J. Cent. South Univ. Technol.* 16 (2009) 247–252.
- [38] Y.W. Xu, S.H. Xu, M. Li, Y.P. Zhu, L.J. Zhou, L.W. Wang, P.K. Chu, Electronic double layer supercapacitor based on three-dimensional silicon microchannel plates in organic electrolyte, *Mater. Res. Innov.* 19 (2015) 303–309.
- [39] R. Thangavel, A.G. Kannan, R. Ponraj, V. Thangavel, D.-W. Kim, Y.-S. Lee, High-energy green supercapacitor driven by ionic liquid electrolytes as an ultra-high stable next-generation energy storage device, *J. Power Sources* 383 (2018) 102–109.
- [40] L. Yu, G.Z. Chen, Ionic liquid-based electrolytes for supercapacitor and supercapattery, *Front. Chem.* 7 (2019) 272.
- [41] M. Haque, Q. Li, V. Kuzmenko, A.D. Smith, P. Enoksson, Ionic liquid electrolyte for supercapacitor with high temperature compatibility, *J. Phys. Conf. Ser.* 922 (2017) 012011.
- [42] W. Yang, Z. Gao, J. Ma, X. Zhang, J. Wang, J. Liu, Hierarchical NiCo₂O₄@NiO core-shell hetero-structured nanowire arrays on carbon cloth for a high-performance flexible all-solid-state electrochemical capacitor, *J. Mater. Chem. A* 2 (2014) 1448–1457.
- [43] Q. Chen, X. Li, X. Zang, Y. Cao, Y. He, P. Li, K. Wang, J. Wei, D. Wu, H. Zhu, Effect of different gel electrolytes on graphene-based solid-state supercapacitors, *RSC Adv.* 4 (2014) 36253–36256.
- [44] C. Zhong, Y. Deng, W. Hu, J. Qiao, L. Zhang, J. Zhang, A review of electrolyte materials and compositions for electrochemical supercapacitors, *Chem. Soc. Rev.* 44 (2015) 7484–7539.
- [45] S.T. Senthilkumar, R.K. Selvan, J.S. Melo, Redox additive/active electrolytes: a novel approach to enhance the performance of supercapacitors, *J. Mater. Chem. A* 1 (2013) 12386–12394.
- [46] B. Akinwolemiwa, C. Peng, G.Z. Chen, Redox electrolyls in supercapacitors, *J. Electrochem. Soc.* 162 (2015) A5054–A5059.
- [47] H. Xia, C. Huo, Electrochemical properties of MnO₂/CNT nanocomposite in neutral aqueous electrolyte as cathode material for asymmetric supercapacitors, *Int. J. Smart Nano Mater.* 2 (4) (2011) 283–291.
- [48] E. Frackowiak, M. Meller, J. Menzel, D. Gastol, K. Fic, Redox-active electrolyte for supercapacitor application, *Faraday Discuss.* 172 (2014) 179–198.
- [49] Y.-C. Chen, L.-Y. Lin, Investigating the redox behavior of activated carbon supercapacitors with hydroquinone and p-phenylenediamine dual redox additives in the electrolyte, *J. Colloid Interface Sci.* 537 (2019) 295–305.
- [50] A. Ayala-Cortés, D.R. Lobato-Peralta, C.E. Arreola-Ramos, D.C. Martínez-Casillas, D.E. Pacheco-Catalán, A.K. Cuentas-Gallegos, C.A. Arancibia-Bulnes, H.I. Villafañe-Vidales, Exploring the influence of solar pyrolysis operation parameters on characteristics of carbon materials, *J. Anal. Appl. Pyrolysis* 140 (2019) 290–298.
- [51] D.C. Martínez-Casillas, I. Mascorro-Gutiérrez, C.E. Arreola-Ramos, H.I. Villafañe-Vidales, C.A. Arancibia-Bulnes, V.H. Ramos-Sánchez, A.K. Cuentas-Gallegos, A sustainable approach to produce activated carbons from pecan nutshell waste for environmentally friendly supercapacitors, *Carbon* 148 (2019) 403–412.
- [52] K. Fic, A. Platek, J. Piwek, E. Frackowiak, unsustainable materials for electrochemical capacitors, *Mater. Today* 21 (4) (2018) 437–454.
- [53] S. Ahmed, A. Ahmed, M. Rafat, Supercapacitor performance of activated carbon derived from rotten carrot in aqueous, organic and ionic liquid based electrolytes, *J. Saudi Chem. Soc.* 22 (2018) 993–1002.

- [54] R. Farzana, R. Rajarao, B.R. Bhat, V. Sahajwalla, Performance of an activated carbon supercapacitor electrode synthesised from waste Compact Discs (CDs), *J. Ind. Eng. Chem.* 65 (2018) 387–396.
- [55] V. Subramanian, C. Luo, A.M. Stephan, K.S. Nahm, S. Thomas, B. Wei, Supercapacitors from activated carbon derived from banana fibers, *J. Phys. Chem. C* 111 (2007) 7527–7531.
- [56] G. Wu, P. Tan, D. Wang, Z. Li, L. Peng, Y. Hu, C. Wang, W. Zhu, S. Chen, W. Chen, High-performance supercapacitors based on electrochemical-induced vertical-aligned carbon nanotubes and polyaniline nanocomposite electrodes, *Sci. Rep.* 7 (2017) 43676.
- [57] H. Pan, J. Li, Y. Feng, Carbon nanotubes for supercapacitor, *Nanoscale Res. Lett.* 5 (2010) 654–668.
- [58] S. Zhou, S. Zeng, S. Zhang, J. Qiao, J. Di, M. Chen, N. Liu, Q. Li, Hierarchical carbon nanotube hybrid films for high-performance all-solid-state supercapacitors, *RSC Adv.* 7 (2017) 52010–52016.
- [59] A. Dang, T. Li, C. Fang, C. Tang, T. Zhao, X. Chen, C. Xiong, Q. Zhuang, A novel hierarchically carbon foam templated carbon nanotubes/polyaniline electrode for efficient electrochemical supercapacitor, *Fuller. Nanotubes Carbon Nanostruct.* 27 (2019) 440–445.
- [60] T. Purkait, G. Singh, D. Kumar, M. Singh, R.S. Dey, High-performance flexible supercapacitors based on electrochemically tailored three-dimensional reduced graphene oxide networks, *Sci. Rep.* 8 (2018) 640.
- [61] B. Xu, H. Wang, Q. Zhu, N. Sun, B. Anasori, L. Hu, F. Wang, Y. Guan, Y. Gogotsi, Reduced graphene oxide as a multi-functional conductive binder for supercapacitor electrodes, *Energy Storage Mater.* 12 (2018) 128–136.
- [62] Y. Cao, M. Zhu, P. Li, R. Zhang, X. Li, Q. Gong, K. Wang, M. Zhong, D. Wu, F. Lin, H. Zhu, Boosting supercapacitor performance of carbon fibres using electrochemically reduced graphene oxide additives, *Phys. Chem. Chem. Phys.* 15 (2013) 19550–19556.
- [63] C. Wang, J. Zhou, F. Du, Synthesis of highly reduced graphene oxide for supercapacitor, *J. Nanomater.* 2016 (2016) 7.
- [64] L.-Y. Lin, M.-H. Yeh, J.-T. Tsai, Y.-H. Huang, C.-L. Sun, K.-C. Ho, A novel core-shell multi-walled carbon nanotube@graphene oxide nanoribbon heterostructure as a potential supercapacitor, *J. Mater. Chem. A* 1 (2013) 11237–11245.
- [65] T.-W. Chang, L.-Y. Lin, P.-W. Peng, Y.X. Zhang, Y.-Y. Huang, Enhanced electrocapacitive performance for the supercapacitor with tube-like polyaniline and graphene oxide composites, *Electrochim. Acta* 259 (2018) 348–354.
- [66] A. Eftekhari, L. Li, Y. Yang, Polyaniline supercapacitors, *J. Power Sources* 347 (2017) 86–107.
- [67] B. Rajender, S. Palaniappan, Simultaneous oxidation and doping of aniline to polyaniline by oxidative template: electrochemical performance in supercapacitor, *Int. J. Polym. Mater. Polym. Biomater.* 64 (2015) 939–945.
- [68] C.-C. Tu, P.-W. Peng, L.-Y. Lin, Weight ratio effects on morphology and electrocapacitive performance for the MoS₂/polypyrrole electrodes, *Appl. Surf. Sci.* 444 (2018) 789–799.
- [69] Z.-D. Ni, Y.-T. Song, H.-Q. Chen, L.-Y. Lin, UV light-assisted electropolymerization of pyrrole on TiO₂ for supercapacitors: investigating the role of TiO₂, *Electrochim. Acta* 190 (2016) 313–321.
- [70] A. Sardar, P.S. Gupta, Polypyrrole based nanocomposites for supercapacitor applications: a review, *AIP Conf. Proc.* 2018 (1953) 030020.
- [71] Y. Huang, H. Li, Z. Wang, M. Zhu, Z. Pei, Q. Xue, Y. Huang, C. Zhi, Nanostructured polypyrrole as a flexible electrode material of supercapacitor, *Nano Energy* 22 (2016) 422–438.

- [72] T. Jiayou, M. Wenzhen, L. Nishuang, R. Xiaoliang, S. Yuling, S. Jun, G. Yihua, High-performance solid-state supercapacitors fabricated by pencil drawing and polypyrrole depositing on paper substrate, *Nano-Micro Lett.* 7 (2015) 276–281.
- [73] A. Laforgue, P. Simon, C. Sarrazin, J.-F. Fauvarque, Polythiophene-based supercapacitors, *J. Power Sources* 80 (1999) 142–148.
- [74] H. Zhang, Z. Hu, M. Li, L. Hu, S. Jiao, A high-performance supercapacitor based on a polythiophene/multiwalled carbon nanotube composite by electropolymerization in an ionic liquid microemulsion, *J. Mater. Chem. A* 2 (2014) 17024–17030.
- [75] A.K. Thakur, M. Majumder, R.B. Choudhary, S.N. Pimpalkar, Supercapacitor based on electropolymerized polythiophene and multiwalled carbon nanotubes composites, *IOP Conf. Ser. Mater. Sci. Eng.* 149 (2016) 012166.
- [76] H. Vijeth, M. Niranjana, L. Yesappa, S.P. Ashokkumar, H. Devendrappa, Polythiophene nanocomposites as high performance electrode material for supercapacitor application, *AIP Conf. Proc.* 2018 (1942) 140017.
- [77] C.C. Chang, T. Imae, Synergistic performance of composite supercapacitors between carbon nanohorn and conducting polymer, *ACS Sustain. Chem. Eng.* 6 (2018) 5162–5172.
- [78] J. Yang, Y. Liu, S. Liu, L. Li, C. Zhang, T. Liu, Conducting polymer composites: material synthesis and applications in electrochemical capacitive energy storage, *Mater. Chem. Front.* 1 (2017) 251–268.
- [79] Y. Zhang, X. Zhang, K. Yang, X. Fan, Y. Tong, Z. Zhang, X. Lu, K. Mai, Q. Ni, M. Zhang, X. Chen, Ultrahigh energy fiber-shaped supercapacitors based on porous hollow conductive polymer composite fiber electrodes, *J. Mater. Chem. A* 6 (2018) 12250–12258.
- [80] T.O. Magu, A.U. Agobi, L. Hitler, P.M. Dass, A review on conducting polymers-based composites for energy storage application, *J. Chem. Rev.* 1 (2019) 19–34.
- [81] S.R. Sivakkumar, W.J. Kim, J.-A. Choi, D.R. MacFarlane, M. Forsyth, D.-W. Kim, Electrochemical performance of polyaniline nanofibres and polyaniline/multi-walled carbon nanotube composite as an electrode material for aqueous redox supercapacitors, *J. Power Sources* 171 (2007) 1062–1068.
- [82] Q. Yang, Z. Hou, T. Huang, Self-assembled polypyrrole film by interfacial polymerization for supercapacitor applications, *J. Appl. Polym. Sci.* 132 (2014) 41615.
- [83] X. Xiong, D. Ding, D. Chen, G. Waller, Y. Bu, Z. Wang, M. Liu, Three-dimensional ultrathin Ni(OH)_2 nanosheets grown on nickel foam for high-performance supercapacitors, *Nano Energy* 11 (2015) 154–161.
- [84] Y. Zhang, X. Xia, J. Kang, J. Tu, Hydrothermal synthesized porous Co(OH)_2 nanoflake film for supercapacitor application, *Chin. Sci. Bull.* 57 (2012) 4215–4219.
- [85] S. Min, C. Zhao, Z. Zhang, G. Chen, X. Qian, Z. Guo, Synthesis of $\text{Ni(OH)}_2/\text{RGO}$ pseudocomposite on nickel foam for supercapacitors with superior performance, *J. Mater. Chem. A* 3 (2015) 3641–3650.
- [86] R. Wang, A. Jayakumar, C. Xu, J.-M. Lee, Ni(OH)_2 nanoflowers/graphene hydrogels: a new assembly for supercapacitors, *ACS Sustain. Chem. Eng.* 4 (2016) 3736–3742.
- [87] C. Yuan, H.B. Wu, Y. Xie, X.W. Lou, Mixed transition-metal oxides: design, synthesis, and energy-related applications, *Angew. Chem.* 53 (2014) 1488–1504.
- [88] Z.-S. Wu, D.-W. Wang, W. Ren, J. Zhao, G. Zhou, F. Li, H.-M. Cheng, Anchoring hydrous RuO_2 on graphene sheets for high-performance electrochemical capacitors, *Adv. Funct. Mater.* 20 (2010) 3595–3602.
- [89] W. Wang, S. Guo, I. Lee, K. Ahmed, J. Zhong, Z. Favors, F. Zaera, M. Ozkan, C.S. Ozkan, Hydrous ruthenium oxide nanoparticles anchored to graphene and carbon nanotube hybrid foam for supercapacitors, *Sci. Rep.* 4 (2014) 4452.

- [90] J. Ye, H.-F. Cui, X. Liu, T. Lim, W.-D. Zhang, F.-S. Sheu, Preparation and characterization of aligned carbon nanotube-ruthenium oxide nanocomposites for supercapacitors, *Small* 1 (2005) 560–565.
- [91] D.-Q. Liu, S.-H. Yu, S.-W. Son, S.-K. Joo, Investigation and fabrication of AlGaN/GaN MOS-HEMTs with gate insulators grown by photoelectrochemical oxidation method, *ECS Trans.* 16 (2008) 103–109.
- [92] Y.M. Chen, J.H. Cai, Y.S. Huang, K.Y. Lee, D.S. Tsai, A nanostructured electrode of IrO_x foil on the carbon nanotubes for supercapacitors, *Nanotechnology* 22 (2011) 115706.
- [93] X. Rui, H. Tan, Q. Yan, Nanostructured metal sulfides for energy storage, *Nanoscale* 6 (2014) 9889–9924.
- [94] J.-Y. Lin, S.-W. Chou, Cathodic deposition of interlaced nanosheet-like cobalt sulfide films for high-performance supercapacitors, *RSC Adv.* 3 (2013) 2043–2048.
- [95] Z. Yang, C.-Y. Chen, H.-T. Chang, Supercapacitors incorporating hollow cobalt sulfide hexagonal nanosheets, *J. Power Sources* 196 (2011) 7874–7877.
- [96] J. Pu, Z. Wang, K. Wu, N. Yu, E. Sheng, Co_9S_8 nanotube arrays supported on nickel foam for high-performance supercapacitors, *Phys. Chem. Chem. Phys.* 16 (2014) 785–791.
- [97] J.-M. Chiu, L.-Y. Lin, C.-C. Tu, S.-S. Yang, Synthesis of the cobalt sulfide hydrangea macrophylla for the energy storage electrode, *J. Appl. Electrochem.* 47 (2017) 393–404.
- [98] T. Nguyen, M.F. Montemor, Redox active materials for metal compound based hybrid electrochemical energy storage: a perspective view, *Appl. Surf. Sci.* 422 (2017) 492–497.
- [99] W. Sun, X. Rui, J. Zhu, L. Yu, Y. Zhang, Z. Xu, S. Madhavi, Q. Yan, Ultrathin nickel oxide nanosheets for enhanced sodium and lithium storage, *J. Power Sources* 274 (2015) 755–761.
- [100] D. Du, Z. Hu, Y. Liu, Y. Deng, J. Liu, Preparation and characterization of flower-like microspheres of nano-NiO as electrode material for supercapacitor, *J. Alloys Compd.* 589 (2014) 82–87.
- [101] M. Huang, F. Li, J.Y. Ji, Y.X. Zhang, X.L. Zhao, X. Gao, Facile synthesis of single-crystalline NiO nanosheet arrays on Ni foam for high-performance supercapacitors, *CrystEngComm* 16 (2014) 2878–2884.
- [102] W. Yu, X. Jiang, S. Ding, B.Q. Li, Preparation and electrochemical characteristics of porous hollow spheres of NiO nanosheets as electrodes of supercapacitors, *J. Power Sources* 256 (2014) 440–448.
- [103] X.-H. Xia, J.-P. Tu, Y.-J. Mai, X.-L. Wang, C.-D. Gu, X.-B. Zhao, Self-supported hydrothermal synthesized hollow Co_3O_4 nanowire arrays with high supercapacitor capacitance, *J. Mater. Chem.* 21 (2011) 9319–9325.
- [104] Y.-B. Liu, L.-Y. Lin, Y.-Y. Huang, C.-C. Tu, Investigation of the electroactive capability for the supercapacitor electrode with cobalt oxide rhombus nanopillar and nanobrush arrays, *J. Power Sources* 315 (2016) 23–34.
- [105] W.-L. Hong, L.-Y. Lin, Y.-B. Liu, L.-Y. Lin, C.-C. Tu, Application of novel multiple-dimensional cobalt oxides as the electroactive material on supercapacitors, *RSC Adv.* 6 (2016) 72845–72851.
- [106] K. Wang, Z. Zhang, X. Shi, H. Wang, Y. Lu, X. Ma, Temperature-dependent self-assembly of NiO/ Co_3O_4 composites for supercapacitor electrodes with good cycling performance: from nanoparticles to nanorod arrays, *RSC Adv.* 5 (2015) 1943–1948.
- [107] J. Chang, J. Sun, C. Xu, H. Xu, L. Gao, Template-free approach to synthesize hierarchical porous nickel cobalt oxides for supercapacitors, *Nanoscale* 4 (2012) 6786–6791.

- [108] D. Cheng, Y. Yang, J. Xie, C. Fang, G. Zhang, J. Xiong, Hierarchical NiCo₂O₄@NiMoO₄ core-shell hybrid nanowire/nanosheet arrays for high-performance pseudocapacitors, *J. Mater. Chem. A* 3 (2015) 14348–14357.
- [109] W.-L. Hong, L.-Y. Lin, Influence of structure directing agents on synthesizing battery-type materials for flexible battery supercapacitor hybrids, *J. Taiwan Inst. Chem. Eng.* 100 (2019) 105–116.
- [110] W.-L. Hong, L.-Y. Lin, Design of nickel cobalt oxide and nickel cobalt oxide@nickel molybdenum oxide battery-type materials for flexible solid-state battery supercapacitor hybrids, *J. Power Sources* 435 (2019) 226797.
- [111] W.-L. Hong, L.-Y. Lin, L.-Y. Lin, Growing sequence effects of core-shell nanostructure on morphology and electrocapacitive ability for energy-storage electrodes, *Electrochim. Acta* 255 (2017) 309–322.
- [112] L.-Y. Lin, L.-Y. Lin, Material effects on the electrocapacitive performance for the energy-storage electrode with nickel cobalt oxide core/shell nanostructures, *Electrochim. Acta* 250 (2017) 335–347.
- [113] L.-Y. Lin, H.-Y. Lin, W.-L. Hong, L.-Y. Lin, Influences of core morphology on electrocapacitive performance of NiCo₂O₄-based core/shell electrodes, *Thin Solid Films* 667 (2018) 69–75.
- [114] K.-C. Ho, L.-Y. Lin, A review of electrode materials based on core-shell nanostructures for electrochemical supercapacitors, *J. Mater. Chem. A* 7 (2019) 3516–3530.
- [115] Y.-Y. Huang, L.-Y. Lin, Synthesis of ternary metal oxides for battery-supercapacitor hybrid devices: influences of metal species on redox reaction and electrical conductivity, *ACS Appl. Energ. Mater.* 1 (2018) 2979–2990.
- [116] H.-Y. Sun, L.-Y. Lin, Y.-Y. Huang, W.-L. Hong, Nickel precursor-free synthesis of nickel cobalt-based ternary metal oxides for asymmetric supercapacitors, *Electrochim. Acta* 281 (2018) 692–699.
- [117] L.-Y. Lin, X. Li, Y.-Y. Huang, H.-Y. Sun, Synthesizing Ni-based ternary metal compounds for battery-supercapacitor hybrid devices with and without using nickel precursors, *Mater. Sci. Semicond. Process.* 98 (2019) 81–89.
- [118] J. Yan, G. Lui, R. Tjandra, X. Wang, L. Rasenthiram, A. Yu, $\hat{\pm}$ -NiS grown on reduced graphene oxide and single-wall carbon nanotubes as electrode materials for high-power supercapacitors, *RSC Adv.* 5 (2015) 27940–27945.
- [119] J. Yang, X. Duan, W. Guo, D. Li, H. Zhang, W. Zheng, Electrochemical performances investigation of NiS/rGO composite as electrode material for supercapacitors, *Nano Energy* 5 (2014) 74–81.
- [120] C.-F. Yu, L.-Y. Lin, Effect of the bimetal ratio on the growth of nickel cobalt sulfide on the Ni foam for the battery-like electrode, *J. Colloid Interface Sci.* 482 (2016) 1–7.
- [121] J.-F. Yu, L.-Y. Lin, Structure variation of nickel cobalt sulfides using Ni foam and nickel salt as the nickel source and the application on the supercapacitor electrode, *J. Energy Storage* 7 (2016) 295–304.
- [122] Z.-H. Ye, L.-Y. Lin, C.-F. Yu, Nickel precursor-free synthesis of nickel cobalt sulfide on Ni foam: effects of the pH value on the morphology and the energy-storage ability, *J. Energy Storage* 8 (2016) 60–68.
- [123] C.-C. Tu, L.-Y. Lin, B.-C. Xiao, Y.-S. Chen, Highly efficient supercapacitor electrode with two-dimensional tungsten disulfide and reduced graphene oxide hybrid nanosheets, *J. Power Sources* 320 (2016) 78–85.

26 PART | I Electrochemical systems and energy storage

- [124] G.Z. Chen, Understanding supercapacitors based on nano-hybrid materials with interfacial conjugation, *Prog. Nat. Sci. Mater.* 23 (3) (2013) 245–255.
- [125] Y. Luo, Q.E. Zhang, W. Hong, Z. Xiao, H. Bai, A high-performance electrochemical supercapacitor based on a polyaniline/reduced graphene oxide electrode and a copper(II) ion active electrolyte, *Phys. Chem. Chem. Phys.* 20 (2018) 131–136.
- [126] S.-S. Yang, L.-Y. Lin, X. Li, C.-W. Ma, H.-X. Lai, L.-Y. Lin, Methodology for synthesizing the nickel cobalt hydroxide/oxide and reduced graphene oxide complex for energy storage electrodes, *J. Energy Storage* 14 (2017) 112–124.

Chapter 2

Nanoarchitected conducting polymers: Rational design and relative activity for next-generation supercapacitors

Subramanian Arulmani^a, Andrea Sorrentino^b, and Sambandam Anandan^a

^a*Nanomaterials & Solar Energy Conversion Lab, Department of Chemistry, National Institute of Technology, Tiruchirappalli, India,* ^b*Institute for Polymers, Composites, and Biomaterials (IPCB), National Research Council of Italy (CNR), Naples, Italy*

1 Introduction

An ever-growing population, environmental pollution, and global warming pose a severe problem concerning future energy demand, of which the energy crisis is topmost due to the exhaustion of fossil fuels and the lack of energy storage for the future [1]. However, the conversion of energy is more complicated through energy sector industries due to an increase in pollution along with significant CO₂ emissions (about 80 wt%) globally. Increasing the probability of realizing the conversion and conservation of energy by reducing carbon efficiency is the primary vision for future energy-associated requirements [2]. Therefore ongoing problems such as fuel cost and demand on fossil fuels are alarming and accelerating toward newer technological implementations. Many practices are available, but the need for new developments is ongoing. Hence, significant consideration is needed to develop high-energy/power-efficient devices to overcome societal and industrial challenges.

Many existing skills are dedicated to harvesting energy from renewable sources, but obstacles still need to be overcome for large-scale practice. Therefore the utilization of extensively achievable energy storage strategies is preferred. For a decade, developments and regulations for energy requirements through research on energy storage have continued. Electrochemical energy storage devices (EESDs) are the perfect alternatives for these issues. They

usually consist of batteries and supercapacitors, which have seen considerable development in recent years.

Of the two major constituents, batteries are devices that are a combination of one or more electrochemical cells where the flow of electrons is achieved through chemical reactions [3]. Nowadays, rechargeable Li-ion batteries are the widely used consumer-based battery, which provide high-energy density per weight/volume as well as higher efficiency. However, they have some disadvantages, like the high cost of production, fabrication, and maintenance. Technically, intercalation/deintercalation of cations such as H^+ or Li^+ is a progressive way to produce electricity. However, diffusion at the electrode surface during the cycling process limits their continuous usage. Furthermore, batteries require an enormous amount of time for charging, and provide only high-energy density instead of power. Consequently, the usage of these batteries is slightly reduced [4]. Conversely, supercapacitors require distinctly less charging time, offer more power density than batteries, and have a prolonged life cycle, extensive working temperature, and are commercially viable regarding maintenance.

The first supercapacitors were used in the middle of the 20th century when US companies General Electric and Standard Oil of Ohio (SOHIO) conducted the first experiments. The developed supercapacitors provided specific capacity of around 1 farad (F) and were patented by SOHIO in 1971. The Panasonic Company released the first commercial supercapacitor to the market in 1982 with the name “Gold Cap” but it had a limitation of high equivalent series resistance (ESR). At the same time, the Pinnacle Research Institute established the first electrical double-layer capacitance (EDLC) supercapacitor, especially for military purposes. However, these EDLC supercapacitors also had more ESR. After continued research for 10 years, Maxwell Laboratories announced an EDLC supercapacitor named “BoostCap” in 1992, which had a low ESR with an insignificant capacity of 1 kF. However, developments were made after 2007 with maximum voltage and enhanced volumetric/gravimetric energy density compared to conventional EDLC supercapacitors. The presently available supercapacitors provide over several thousand farads and around 10,000 charge/discharge cycles with the current density ranging from 10s to 100s of amperes (A). By considering these views in the field of supercapacitor application, supercapacitors can operate at high currents compared to batteries, and they fill the gap between batteries and capacitors [5].

Recently, thinking and working on supercapacitors are receiving more consideration due to the storage and consumption of energy through its functioning mechanisms. Thus performance is principally contingent with numerous features like EDLC, pseudocapacitance, and in some cases a combination of both [6]. The primary function of EDLC is the reaction on the surface of the electrode material and the attained capacitance because of the electrostatic charge accumulation process at the interface between the electrode and electrolyte. The main property of this group of materials

is their electrode surface area. Carbon-based materials like graphene, carbon nanotubes (CNTs), and activated carbons with different shapes, sizes, and structures are used as EDLC materials. Likewise, pseudocapacitance comes from the redox behavior of the materials during the interchange of ions/electrons.

Until 1971, pseudocapacitor materials stored the charge through the transference of charge between the electrode and electrolyte [7]. Pseudocapacitance is proportionate to the charge transferred during the process, which can be designated through the following equation [8]:

$$C_{Pc} = q \left(\frac{d\theta}{dV} \right) \quad (1)$$

where q =the faradic charge required for adsorption/desorption of ions, $d\theta$ =the change in fractional coverage of the surface, and dV =the change in potential. The value of $d\theta/dV$ is not a linear one, so the capacitance is not always constant and is called pseudocapacitance. The faradic process empowers pseudocapacitors to realize significantly higher energy density as well as specific capacitance (C_s) than EDLCs. According to Conway's investigation, the faradic process results from the following mechanisms: (1) underpotential deposition, (2) redox pseudocapacitance, and (3) intercalation pseudocapacitance [9, 10].

Underpotential deposition happens when the metal ions are arranged in an absorbed monolayer on a different metal surface at their redox potential, for example, H or Cu on Pt, Bi on Au, Bi on Ag, H on Rh or Pt. Then, the redox reaction is a process of "surface charge storage," which is realized through electrochemical adsorption of ions on/near the surface as well as the continuous electron transfer process at active redox sites. In this regard, metal oxides, sulfides, nitrides, hydroxides, and conducting polymers (CPs) are recognized examples of pseudocapacitive materials. The intercalation pseudocapacitance can be constructed through the intercalation of electroactive species without crystallographic phase change, for example, Li on MoS₂ or TiS₂ [8, 9].

For all the mechanisms, the relative charge storage depends on the electrode material, which is commonly determined through its physicochemical properties, such as chemical composition, crystal structure, surface area, and porosity. Among three crucial mechanisms, redox pseudocapacitance is more advantageous due to surface redox reactions. Specifically, CPs are better compared to metal oxides because of the facile synthesis (through chemical or electrochemical methods), low cost, high specific energy and power, excellent conductivity, light weight, and boosted flexibility compared to other pseudocapacitive materials. There is an almost endless selection of monomers, oligomers, and selective chemistries available for the tuning of polymer matrices. The controlled synthesis of CPs provides not only diverse structural and morphological variations but also exhibits the whole spectrum of physicochemical properties regarding energy storage systems.

The purpose of this section is to elucidate the accessible chemistries behind the diverse nanostructured CPs and their performance in advanced electrochemical energy storage technologies. Throughout this chapter, we outline the synthetic approaches toward diverse nanoarchitectures, the importance of configurations, and anticipated architectures, and emphasize their synergistic exchanges on enhanced electrochemical characteristics.

2 Chemistry of CPs

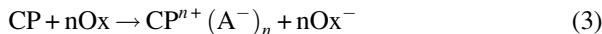
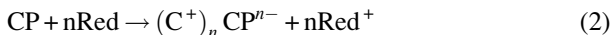
Conventional polymers such as plastics, rubbers, and resins always display resistance property, and they are either insulators or dielectric materials. McNeill and coworkers were the first to look at the conducting nature of polymers during the pyrolysis of tetraiodopyrrole to construct unexpectedly conductive materials in 1963 [11]. CPs are organic materials that are the constituent of conjugated chain structures. Most CPs are insulators in their neutral conditions. The presence of conjugation in their structures provides robust UV-visible absorption.

Furthermore, they possess fluorescence properties, can be quenched by chain aggregation, and have narrow and tunable bandgaps. Neutral state CPs have less conductivity compared to their ionic state. The average conductivity of neutral state CPs is in the range of 10^{-10} – 10^{-5} S cm $^{-1}$, which may be increased to 1 – 10^4 S cm $^{-1}$ by altering the chemical or electrochemical redox reaction, which occurs because of modification of either its semiconductive or conductive forms [12]. This type of conductive enhancement process is commonly called “doping,” which is responsible for the movement of ions through the skeleton. Doping can be done by using either positive or negative charge carriers. If doping is possible with positive charge bearers, it is called p-doping, and if it is done through negative charge bearers, it is called n-doping. Meantime, the oppositely charged counter ions will always be entrapped and released from the polymer to sustain its charge neutrality. The critical feature of a CP is the delocalization of π -electrons compared to a conventional polymer [13]. The skillful process of the synthesis and doping of a polymer will improve its usages in a variety of fields, including sensors, actuators, solar cells, memory-based devices, electrochromic devices, and EESDs. In this way, the preparation of supercapacitor electrodes or devices with CPs may display a variety of benefits like better conductivity, flexibility, comparative cheapness, and effortless synthetic procedures.

A CP delivers its capacitance performance during its redox process. During the oxidation process, ions are transported to the polymer backbone from the electrolyte, and the reverse of this takes place when reduction occurs. This kind of reversible reaction happens throughout the entire polymer chain, not only on the surface. The main advantage of this process is the charging/discharging phenomena, as well as doping/dedoping, which may not produce any structural

alterations such as phase variations and will provide a highly reversible process [14].

CPs offer a very high capacitance because of the occurrence of faradic processes that are not available in EDLCs. Availability of the highly conductive nature of CPs improves the charge transfer kinetics of the electrode similar to EDLC-based materials due to the presence of charge carriers, easy mobility of charges, superficial kinetics, and voluntarily accessible solvated counterions. Furthermore, the n-doping (reduction) nature, which allows the electron into the conduction band, and the p-doping (oxidation) nature, which removes the electron from the valence band, increase its charge carrier concentrations.



These two equations depict the general doping nature of a CP.

Eq. (2) shows the process of the n-doping reaction, and Eq. (3) shows p-doping, where CP is the general term for a CP chain, (Ox) and (Red) are the oxidant and reductant used, and (C^+) and (A^-) are the countercation and counteranion, respectively [15].

2.1 Types of CPs

Depending upon the presence of main chain constituents, the CPs are varying majorly as aromatic cycles, double bonds, or both. Classification of a CP is due to the absence or presence of heteroatoms in its polymer skeleton. Poly(fluorene)s, polyphenylenes, polypyrenes, polyazulenes, and polynaphthalenes are examples of the lack of heteroatom category. Poly(pyrrole)s (PPy), polycarbazoles, polyindoles, and polyazepines are examples of the nitrogen atom containing CPs, which are situated in the inside of the aromatic ring. The CP polyaniline (PANI), which also comes under this group, has the nitrogen atom positioned outside the aromatic ring. Likewise, sulfur-containing aromatic ring polymers are poly(thiophene)s (PTh) and poly(3,4-ethylene dioxythiophene) (PEDOT). Poly(*p*-phenylene sulfide) is the polymer that contains its sulfur on the outside of the aromatic ring. Above all, polymers are classified under aromatic cycles. Poly(acetylene) (PAC) is a polymer that has only double bonds. Poly(*p*-phenylene vinylene) (PPV) is a combination of both aromatic cycles and double bonds. PAC, PANI, PPy, PPV, PTh, and PEDOT are widely used for various applications (Fig. 1).

2.2 Electrochemical efficacy of CPs

Even though CPs were developed in the middle of the 19th century, they received increased consideration after 2000 due to the awarding of the Nobel Prize in Chemistry to Heeger, MacDiarmid, and Shirakawa for their

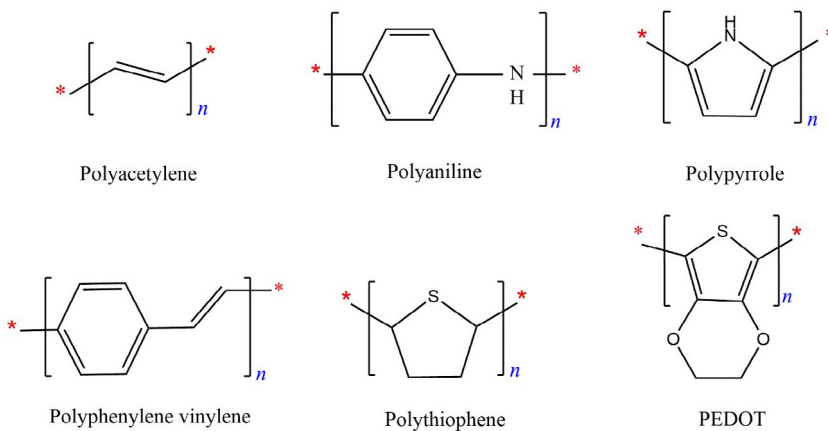


FIG. 1 Structures of commonly available and used CPs.

revolutionary effort on CPs. CPs are organic molecules containing conjugated double bonds that can combine and show they are the electrically conductive properties of metals or semiconductors. Advantages such as low cost, considerable structural diversity, high flexibility, and durability compared to traditional polymers make them ideal for electrode materials for supercapacitors. In CPs, initially, the high surface area that is in contact with the electrolyte experiences high charge/discharge rates. Furthermore, the availability of short path lengths for ionic transport allows for faster ionic diffusion within the CP network. To this end, they display tolerance of the stress and strain of an electrochemical reaction, henceforth improving the life cycle of the supercapacitor [16].

A supercapacitor device constructed using PANI shows a specific energy of 10 Wh kg^{-1} with a slightly lower specific power of 2 kW kg^{-1} , whereas carbon-based devices can only reach a specific power of $3\text{--}4\text{ kW kg}^{-1}$ and specific energy of $3\text{--}5\text{ Wh kg}^{-1}$ [17]. Besides, π -conjugated polymers have better gravimetric/volumetric pseudocapacitance in nonaqueous electrolytes with a wide working voltage of $\sim 3\text{--}4\text{ V}$. Therefore CPs are more beneficial when compared to carbon-based materials. Snook et al. reviewed the utilization of significant CP materials in supercapacitors together with PANI, PPy, and PTh alone and their derivatives, as well as their composites with CNTs and some of the inorganic materials that make improvements to their properties [18]. Eftekhari et al. [19] also discussed the considerable differences between CPs and inorganic substances that are used for supercapacitors. They summarized that the lattice structure of inorganic materials offers an appropriate space for the adsorption/intercalation of electroactive species. However, in the case of CPs, even though the polymer matrix has enough empty spaces, they are not able to fit and cause volume variations during continuous operations. The

designing of the materials should also offer an appropriate space for hosting CP dopants in the progression of the electrochemical reactions. Flexibility is attained through direct response with a variety of anions and cations (compared to the inorganic pseudocapacitors, which only accomplish the reaction with a restricted number of electroactive species) that provide an opportunity for the modification of future CP-based pseudocapacitors [19].

The availability of synergized properties from both traditional polymers and organic CPs always meets the necessities for flexible, lightweight, and environmentally friendly devices. Though the bulk counterpart of CPs shows the capability of providing a notable C_s , they suffer from restricted cycling stability because of structural alteration, which leads to fast decay during their electrochemical performance [20]. Therefore the designing of CPs at the nanoscale may provide numerous beneficial features, such as (1) they can undergo innovative reactions that are not possible with their bulk materials, (2) the pathways for the charge/mass transport through the ions can be shortened, and (3) improved holding of the strain within electrodes is possible by electrochemical reactions. Furthermore, CP nanoarchitectures are formed through the self-assembling process and designed as molecular building blocks by weaker intermolecular interactions (such as hydrogen bonding, π - π stacking, and hydrophobic interactions) among the adjacent molecules [21, 22]. The energy storage performance of these nanoarchitectures is anticipated to be better in comparison to their bulk counterpart. Meanwhile, the arrangement and availability of polymer nanostructures allow increased flexibility and lighter weight. Furthermore, it also promotes a high surface area, unique optoelectronic properties, higher conductivity, better stability, and ease of processability [23].

Nanoarchitected CP-based materials have proven to have excellent mobility, solubility, small bandgaps, massive absorption enrichment, and the opportunity to tailor suitable and novel morphology, which makes them an excellent candidate for countless uses in the energy field [24]. CPs can be produced either chemically or electrochemically through oxidative polymerization of the appropriate monomer in solution. Furthermore, these CPs have more than a few connected redox states that switch the electrical conductivity through the full range from insulator to metal [25]. So far, CPs in various forms (e.g., nanorods, nanosheets, and nanowalls) have been established and efficiently utilized as electrode material for energy storage options [26]. Additionally, CPs with diverse nanoarchitectures possess high surface area and high porosity, which provide good performance. Factors like intrinsic conduction, large surface-to-volume ratio, and surface interactions at the nanoscale architectures offer beneficial functions, which are much better than their bulk counterparts [27], because their polymerization methods mainly influence the nanoarchitected CPs. Therefore selecting appropriate polymerization approaches is significant to regulate their nanoarchitected morphologies. Standard polymerization methods include *in situ* polymerization, electrochemical polymerization, interfacial polymerization, dilute polymerization, emulsion

polymerization, and so on. Among these, *in situ* polymerization, electrochemical polymerization, and interfacial polymerization are extensively used for the preparation of different nanostructured materials [13, 28].

3 Pure CPs in supercapacitors

Among the CPs, PANI has attracted considerable attention due to its low cost, excellent mechanical and environmental stability, adjustable conductivity, and multiple redox states. PANI can be prepared by the oxidation of aniline, but the synthetic approaches will vary depending upon the medium and oxidant usages. PANI is significant in three different exchangeable arrangements: the oxidized form (leucoemeraldine), the reduced form (pernigraniline), and the emeraldine base (EB) form. The process of doping involves the conversion of nonconducting EB into the conducting emeraldine salt (ES) with the aid of acid treatment. The ionic materials/electrolytes that are associated with this process are called “dopants” [28]. They are exclusive electroactive materials with considerable π -conjugation length. Although the protonated form of PANI (ES) is described as poorly conductive, PANI is one of the most studied CPs in electrochemical applications because of its environmental stability and high doping level of 0.5 (i.e., two monomer units per dopant). The chemical structure of PANI controls its physical properties, including electrical conductivity and C_s . Doping the polymer chain through an oxidizing (p-type) or reducing (n-type) component changes the uniform charge distribution over the π -orbitals, which results in lattice distortion. Subsequently, the electrons are strongly coupled with the lattice. Consequently, the delocalization of electrons in the overlapping π -orbitals offers an opportunity for high electrical conductivity, which is a significant prerequisite for the electrochemical performance of PANI. The electrochemical interaction of the redox sites is also controlled by this strategy [29]. Hence, doping is more significant, whether during polymerization or postpolymerization, which is hugely responsible for its pseudocapacitive nature. The morphological structure directs the electrochemical accessibility of the redox sites all over the polymer matrix [30].

Furthermore, PANI shows a maximum C_s of up to 2000 F g^{-1} . Attaining theoretical capacitance is not straightforward [31]. Nanostructured morphology, process/degree of polymerization, type of dopant, concentration of dopant, and ionic diffusion length are the key parameters to achieve maximum C_s . The oxidation of (the process of polymerization) aniline and its substitutes may harvest diverse micro- and nanostructures of different sizes and shapes, which include nanofibers, nanowires, nanotubes, hollow spheres, helices, flowers, and so on. By adapting extensive diversity in synthetic situations through the change in reagent concentration, pH, or homogeneous or heterogeneous polymerization processes, addition rate/time of reagents can have a reflective impact on the ensuing polymer’s nanoarchitecture. Specific capacitance is exceptionally reliant on synthesis conditions and construction of nanoarchitectures with

diverse morphologies. The effect of manageable parameters such as concentration and temperature on the nucleation and growth mechanism is recognized, as there is direct competition between the nucleation inception and growth process resulting in the construction of further small particles or the growth of a few larger ones [19]. This is why PANI can sustain and substantially contribute to the field of nano/macrosceince. The structure, morphology, and electrochemical activities of nanomaterials may also be modified through precise surfactants/templates [32].

Although PANI can be synthesized in a low acid or aqueous solution, it has been recognized as only a regular nanostructure. The construction of these irregularities is important because free energy and kinetic barriers lead to difficulties in the ordering of the oligoanilines or polymer chains from their favorite coiled conformation to an ordered array. Besides, exploring the characteristics of PANI morphology, dimension and size of electrode materials is also noteworthy because they can assist with the connection between structures and performance. So far, diverse structured PANI materials have been synthesized and used for supercapacitors such as nanosized spheres, roses, cloud-like and rhombic plates, layered flowers, columns, blocks, and dendrites [33].

Nanoarchitected PANI-based electrodes provide easy accessibility of ions/electrons during their electrochemical reactions. Morphologically controlled PANI is also essential for better product applications and theoretical studies. To this point, morphology has been extensively considered through its strong impact on properties and applications [34]. Numerous strategies are available for the construction of various nanostructures with different morphologies [35–37]. Among “hard” or “soft” template synthesis, seeding polymerization, interfacial polymerization, rapid mixing reaction, electrochemical deposition, radiolytic polymerization, and dilute polymerization are the most feasible. Furthermore, the C_s of different nanostructured PANI electrodes is in the range of $200\text{--}1000\text{ F g}^{-1}$ using a three-electrode configuration and C_s values are higher than their bulk dimensions. The experimental results disclose that the transformation from bulk forms to nanoarchitectures for PANI is better for expanding their electrochemical performance as supercapacitor electrodes [38]. Grover et al. [39] developed PANI nanostructures with various morphologies (nanotube, nanorod, nanosphere, and nanosheet) through a soft-template process by triggering the amount of *N*-cetyl-*N,N,N*-trimethyl ammonium bromide (CTAB) surfactant (Fig. 2A). The formation of PANI structures is explained by looking at the possible mechanistic pathways of different growth patterns and the aggregation archetype of monomeric units in which they are assumed during polymerization. The as-prepared materials were analyzed in a solid-state supercapacitor cell, among others; the PANI nanotube shows the highest C_s of 367 F g^{-1} at 5 mV s^{-1} and its stability was retained up to 91.5% during continuous 1000 GCD cycles due to the availability of hollow structure, high porous nature with large surface area, and short diffusion path length that

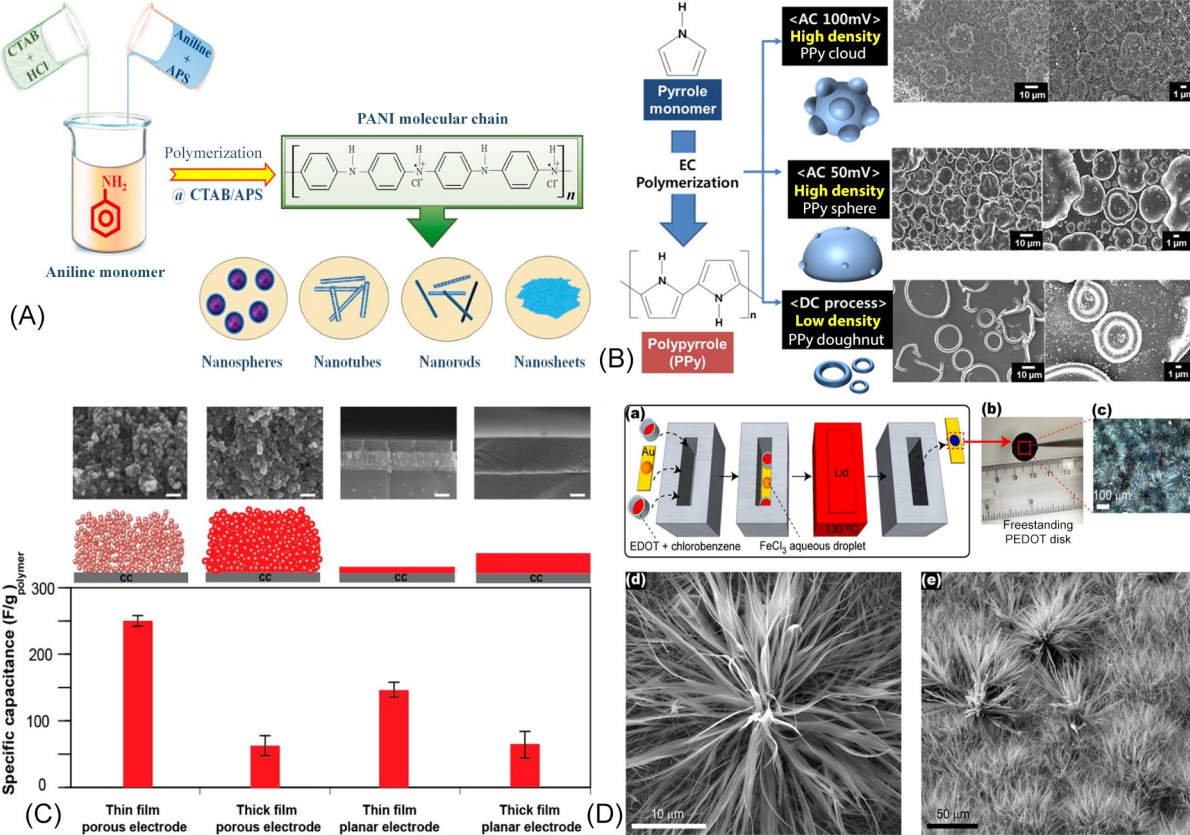


FIG. 2 Diverse structured pure CPs used in supercapacitors. (A) Illustration for the formation of PANI in different forms [39]. (B) Electropolymerization of pyrrole by applying direct current (DC) and alternating current (AC) power [40]. (C) Effect of polymer thickness and 3D nanostructures on the specific capacitance of oCVD polythiophene-SEM images (scale bar is 200 nm) and specific capacitance values of thin (250 nm) and thick (800 nm) films on planar FTO electrodes, and of thin (~ 4 nm) and thick (~ 6 nm) films inside mesoporous electrodes of TiO_2 ; specific capacitance is based on per mass of polymer and reported with 2 standard deviations [41]. (D) Evaporative vapor-phase polymerization (EVPP) leads to high aspect ratio PEDOT one-dimensional nanoribbons and nanofibers: (a) flow process diagram of EVPP-PEDOT nanofibers shows oxidant droplet's color change from orange to blue during polymerization; (b) mechanically robust freestanding disk-shaped film; (c) low-magnification optical microscopy shows that this blue-colored disk-shaped film is composed of highly textured, vertically directed, anisotropic, one-dimensional architectures; (d) top view scanning electron micrograph (SEM) indicates vertically directed high aspect ratio nanoribbons; (e) low-magnification tilted SEM image shows large-scale morphology composed of a high packing density of vertically directed high aspect ratio nanofibers and nanoribbons [42].

promotes the movement of electrolytic ions [39]. Developing a practical and straightforward method to prepare regular PANI with multidimensional nanoarchitectures remains a scientific challenge.

PPy is another CP that also takes part in supercapacitor applications due to its high-energy storage capacity, facile synthesis, eco-friendly nature, and flexibility during electrochemical processing. High conductivity ($1\text{--}100 \text{ S cm}^{-1}$), a fuller potential window, and high capacitance per unit volume ($400\text{--}500 \text{ F cm}^{-3}$) result in a high charge/discharge rate (doping/dedoping) with high charge density in supercapacitor performance similar to other CPs. These pseudocapacitors suffer due to their poor cyclability and reduced mass activity. The restrictions of dopant anions to the interior sites are due to the high-density PPy, mainly when and wherever thicker electrodes are used. However, to minimize the thickness of the PPy layers, Lee et al. [40] used an efficient one-step procedure to synthesize PPy using AC impedance spectroscopy by controlling frequency as well as amplitude (Fig. 2B). During this process, nano/microstructures with a definite morphology of PPy with thin film were obtained, which covered the Au current collector. The size, density, and morphology of PPy were controlled by a highly precise electrochemical process (AC electropolymerization) and utilized as electrodes in supercapacitor cells. The fabricated device showed a high C_s of 568 F g^{-1} , and around 77% of initial capacitance was retained after 10,000 continuous cycles [40].

Zhang et al. [43] reported that PPy with different morphologies (nanodots, vertically aligned nanorods, nanowires, and nanomats) were assembled through randomly fallen nanowires, which were synthesized through an electrodeposition technique on graphite rods (potentiostatic polymerization method) at various polymerization times. The effect of morphologies on the C_s was verified from the perspective of the mass transfer process [43]. Similarly, PTh has the property of a highly tunable, air-stable organic CP with better environmental stability. Among the all conjugated polyheterocycles, PTh is the most studied polymer [44]. Senthilkumar et al. [45] prepared PTh by a chemical oxidative polymerization approach in the presence and absence of three different (cationic—CTAB, anionic—SDS, and nonionic—Triton X-100) surfactants using FeCl_3 as oxidant and obtained different morphologies. The specific capacitance found for PTh prepared with Triton X-100 was 117 F g^{-1} , which was higher (up to 33%) compared to surfactant-free PTh (78 F g^{-1}) [45]. The direct vapor-to-solid oxidative polymerization (oxidative chemical vapor deposition [oCVD]) of the thiophene monomer was done with antimony pentachloride for a single-step polymerization. Moreover, the coating of PTh was done on porous nanostructures of anodized aluminum oxide, titanium dioxide, and activated carbon. The ultrathin conformal PTh coatings formed were reserved for high surface areas, which showed 1.6 times enhanced capacitance for planar films than that of open planar geometries (Fig. 2C) [41].

Another variety of CPs is PEDOT, which theoretically possesses the highest conductivity (4500 S cm^{-1}) among all CPs. Electrochemical charge storage in

PEDOT is afforded through its surface phenomenon, which is firmly contingent on its electrical conductivity as well as the surface area of the polymer electrode material. Three standard methods are used for the synthesis of PEDOT via solution-based oxidation, electrochemical synthesis, and vapor-phase deposition. It is easy to obtain maximum ability through vapor-phase deposition technology. This kind of synthetic method provides increased adhesion property among polymer and current collectors. Alternatively, the solution-based oxidation of PEDOT offers lower C_s , which is in the range of 150 F g^{-1} . In a few cases, it can reach 400 F g^{-1} . Even though exceptional capacitance was attained, it was unstable in water and when used as an electrode in supercapacitors [46].

Furthermore, vapor-phase deposition technology is suitable for the preparation of freestanding films of PEDOT nanofibers, which possess high electrical conductivity of 130 S cm^{-1} , and the availability of nanofibrillar morphology leads to highly efficient electrodes displaying a maximum C_s of 175 F g^{-1} (Fig. 2D). Deposition without using organic binders or conductive additives not only provides an adhesive property, but also results in low internal resistance to the electrode. The ensuing free, thin, mechanically robust film offers excellent cycling stability as well as high-capacity retention (92%) even after 10,000 continuous charge/discharge cycles [42]. Likewise, various nanostructures (nanodendrites and nanospheres) of PEDOT were produced through the hydrothermal process without the use of templates and afforded a highly crystalline nature. Nanodendrites are possibly more beneficial because of their high C_s (284 F g^{-1}) with a maximum energy density of 39.44 Wh kg^{-1} and outstanding cycling stability (5000 charges/discharge cycles) compared to nanospheres [47].

3.1 Nanohybrids of CPs with carbon in supercapacitors

Even though pure CPs act as a potential pseudocapacitive material, the nature and redox property of pure CPs are unable to survive during continuous charge/discharge cycling because of expansion and shrinkage of the polymer backbone. This is because of a number of limitations such as restricted cycling stability (brittle and weak mechanical strength), high and informal self-discharge rate with deprivation of electrodes, and deterioration of electrochemical performance. Furthermore, the formation of by-products during hydrolysis takes place. To minimize these problems, it is necessary to control the microstructures such as grain size, thickness, specific surface area, and pore character of the material through the formation of hybrids [48].

A hybrid material is a combination of diverse components as well as mechanisms of action, which are homogeneous when seen through macroscopic investigation and heterogeneous in microscopic examination. Additionally, improved physicochemical properties are observed compared to those of the specific components used alone. Therefore the formation of CPs as hybrids with

other nanomaterials may afford promising candidates, and their improved performance will be achieved in the energy storage sector. Until now, continuous growth in the expansion of nanohybrids of CPs is because of the combination of CPs with different types of materials, such as metals, carbonaceous materials, and inorganic compounds, such as layered materials. Furthermore, interactions are subclassified into two groups: weak interactions such as van der Waals, hydrogen bonding, electrostatic interaction, etc., and strong interactions such as chemical bonding among the two phases [49]. The hybrid materials of carbon and CPs display synergistic properties that combine the benefits of both materials in C_s and long-term cycling stability. At present, research into tuning the micro-/nanoarchitectures of the hybrid material, which effectively improves the interface between carbons and CPs, is intensive. Principally, to combine PANI polymers with carbon-based materials, three methods are widely used, namely electrochemical recombination, solution polymerization, and in situ polymerization.

Furthermore, hybrid formation directs the chemical structure of CPs for the enhancement of their electrochemical actions. CPs with diverse carbons with different chemical configurations, morphology, and phase structure are essential for fundamental consideration of their interface, which offers the foundation for future developments of their device performance [50]. Nanosized carbons (activated carbon, CNTs, and graphene) are more familiar as promising support materials for CPs for supercapacitors with better synergic effects [51]. This kind of electrode is not only useful for pseudocapacitive reactions because of the synergistic effects, but also improves rate capability due to the higher conductivity of the substrate and excellent cycle stability initiated from the outstanding mechanical possessions of the supportive carbon materials [19]. The choice of PANI with CNT as a hybrid may deliver improved outcomes because of the assortment of both pseudocapacitances with EDLC mechanisms. The synergism between CNT and PANI not only escalates their C_s but also expands cycling stability of the polymer during the charge/discharge evolution.

Regarding PANI-based hybrids, the chemical method could escalate the connection of PANI and carbon during the polymerization of aniline monomer and activated carbon powder. Subsequently, with the adding of oxidants, in situ polymerization results, and PANI/carbon composites will be formed. For instance, Wang et al. proposed a fast and straightforward electrochemical polymerization method (within 3 min at a constant current density of 60 mA cm^{-2}) for the fabrication of PANI nanofibers supported on carbon paper without the usage of any polymeric binders as well as conducting materials. The aligned polyaniline nanofiber array architecture delivered C_s , which reached 531 F g^{-1} at 3 mA cm^{-2} [52]. Likewise, the composites of CPs and CNTs displayed excessive potential as supercapacitor electrodes due to their conductivity, high surface area, and the ability to store energy via two charge storage mechanisms. Also, multiwalled carbon nanotubes (MWCNTs) can store roughly twice the energy density per mass unit than single-walled carbon

nanotubes [26]. Generally, strategies such as the dispersion of CNTs and the interfacial interaction between CNTs and PANI affect the performance of hybrid materials. Maximum research is currently being focused on improving the dispersion of MWCNTs in the polymer matrix over surface chemical modification of CNTs, which can generally be achieved through the oxidation of MWCNTs [53].

In the meantime, morphology also played a vital role in their specific capacitance. PANI/MWCNT thin films with 3D architectures on the surface were organized with the nanocasting technique (fresh plant leaves used as a template). The biomimetic surface morphology (multiscale papilla-like nano-scale texture) was effectively reproduced from *Xanthosoma sagittifolium* leaves. This 3D architecture provides a C_s of 535 F g^{-1} at 1 A g^{-1} for a 5 wt% MWCNT loading because of improvement in ion/electron transport. The mutual roughness and MWCNT loading of the designed 3D nanocomposite electrode expands the interface of PANI/electrolyte to confirm that enough redox reaction can produce increased electronic conductivity and connectivity to offer a fast electrochemical response [54].

PANI outcropping whiskers embraced on CNTs (PANI@CNT) were prepared through a simple in situ (chemical oxidative) polymerization method with the help of an amphiphilic triblock copolymer (P123) (Fig. 3A). This hybrid simplifies charge and ion transport at the electrode/electrolyte interface. The nanohybrid electrode reveals remarkable electrochemical properties with superior charge storage capacitance (348.9 F g^{-1} at 0.5 A g^{-1}), rapid rate responsiveness, and sustained cycling performance because of its chemistry and nanoarchitecture. Furthermore, this suggests that there is a simplistic pathway for tailoring insertion/deinsertion of ions through high roughness in the electrodes. In this nanohybrid, CNTs possibly act as a backbone material for facile electron transfer, and the porous PANI perform duties for capacitance enhancement. The enhanced performance is harmonized due to its electrode surface morphology and roughness with outcropping whiskers (V-type channels) at the edges of the PANI@CNT nanohybrid that offer an energetic pathway for speedy circulation of ions [55].

Among the carbon-based materials, graphene has attracted much consideration because of its exceptional electronic conductivity triggered via the π - π conjunction system. Typically, graphene is widely used as the transporter of pseudocapacitance materials as well as a current collector due to its high specific surface area. The combination of graphene/PANI has been widely used since 2011, and its synthesis in a 3D network was reported in 2012. Yu et al. developed a template-free preparation for vertically aligned PANI nanocone arrays on a 3D graphene network, which quickly and precisely controlled the length and shape (Fig. 3B). Both mass loading and length of nanocones rise with the increase in its deposition time. Furthermore, the length of PANI nanocones shows a noticeable impact on their properties and supercapacitance performance. The available space between nanocones offers an unblocked diffusion

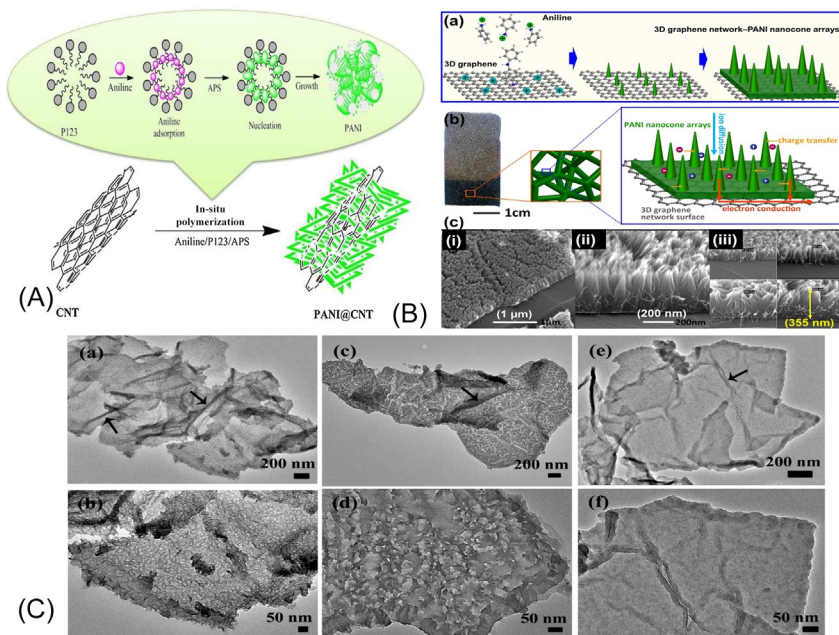


FIG. 3 (A) Graphic illustration of an amphiphilic triblock copolymer-guided polyaniline outcropping whiskers-embraced CNT nanohybrid formation [55]. (B) (a) Electrodeposition process of PANI on the surface of 3D graphene network; (b) structural schematic illustration of 3D graphene network-PANI nanocone arrays; (c) vertically aligned PANI nanocone arrays on the surface of 3D graphene (i and ii), and length of PANI nanocones on graphene (iii) [56]. (C) TEM images of rGO-PEDOT (a, b), rGO-PANI (c, d), and rGO-PPy (e, f) [57].

track for electrolyte ions, which simplifies the protonation and deprotonation progression. These features endorse capacitance performance through high C_s (751.3 F g^{-1} at 1 A g^{-1}), high-rate performance, and high cyclic stability [56, 58].

Regarding the high surface area, high electrical conductivity, and scalability, graphene nanoribbons (GNRs) have always been considered perfect carbon substrates for the holding of CPs. In this regard, Tour and coworkers applied a cost-effective *in situ* polymerization approach for the fabrication of GNR/PANI composites with highly ordered and vertically aligned PANI nanorods, which are grown on the GNRs. The result is a high C_s of 340 F g^{-1} and up to 90% capacitance retention during their cycling performance (4200 cycles) because of the synergistic effect of electrically conductive GNRs and high-capacitance PANI [59].

The combination of porous carbon with CPs is an appropriate method to make use of the plentiful pore structure of carbon and high C_s per unit area of CPs. Ordered mesoporous carbon (OMCx) with regular and highly interconnected channels is ideal for countering the difficulties of the quick passage of

electrolyte ions [60]. Zhang et al. described the dual practice of template SBA-15 through an equivalent volume impregnation and in situ polymerization approach to make use of the pores created in the carbonization process between SBA-15 and OMCx. In this method, PANI was well covered on the surface of the OMCx's nanorods and influenced the electrochemical performance. OMC8/PANI could reach 343 F g^{-1} at 0.2 A g^{-1} in a two-electrode system, and its cyclic performance was also excellent after 2000cycles, with only a 5% decrease in capacity [61].

Additionally, nanostructured PANI was produced on interconnected porous carbon (ICPC) through in situ electropolymerization. The available large surface area ($750 \text{ m}^2 \text{ g}^{-1}$) with interconnected pore construction conveys the penetration of aniline. Besides, it leads to the development of nanostructured PANI on its matrix. The results revealed that the fixing of PANI to ICPC improves the C_s (861 F g^{-1} at 0.5 A g^{-1}) compared to their counterparts. It was noted that ICPC performed as an EDLC and enhanced the redox or pseudocapacitive nature of nanostructured PANI. ICPC act as a suitable framework for accepting PANI and as a separator for the accumulation of PANI particles that aid volume peculiarity due to swelling and shrinking during continuous cycling. The composite displays excellent cycling stability because of the synergism between PANI and ICPC that signifies its usability in supercapacitors [62].

Besides the different approaches for each CP, Zhang et al. adopted a single synthetic approach as an in situ polymerization method for the preparation of reduced graphene oxide (rGO)-CP composite materials. In this approach, three CPs, namely PANI, PPy, and PEDOT and its graphene-based composites, were successfully prepared with various morphologies. Typically, the existence of an acid and the ensuing doping of the anion counterpart of the acid (e.g., SO_4^{2-} for acid H_2SO_4) on the CP matrix were significant in controlling the electrical properties. CPs such as PEDOT, PANI, and PPy were directly covered on rGO sheets at loadings up to 90 wt% via the in situ polymerization method. Also, the solvent ethanol was found to be crucial in the preparation system since it not only enhanced the dispersion of rGO sheets but also enabled the diffusion and growth of polymer monomers on the surface of the rGO sheets. Here, ethanol facilitates the distribution of monomers to the nucleation sites on rGO. Subsequent to oxidative polymerization, CPs were coated on the surface of rGO because of the strong π - π interactions between the CP and rGO sheets (Fig. 3C). The electrochemical characteristics showed superior capacitive performance of rGO-CPs, for example, the C_s of rGO-PANI was 361 F g^{-1} , which is higher than that of rGO-PPy (249 F g^{-1}) and rGO-PEDOT (108 F g^{-1}) at a current density of 0.3 A g . Likewise, the capacity retention of rGO-CP composites was increased when compared to their individual polymers [57].

4 Design and developmental configurations

Strategies are more significant for enhanced performance in pseudocapacitors than those constructed with CPs from both a chemical (morphological and

polymer structural) and device engineering perspective through their nanoarchitectures. It is well known that three-electrode cyclic voltammetry analyses are the only properties of electrode materials. By thermodynamical determination, given an inert electrode in an aqueous or pH-neutral electrolyte, water will be divided into oxygen at roughly 1 V versus Ag/AgCl. Likewise, hydrogen can be split at -0.3 V versus Ag/AgCl. To avoid these reactions, the working potential window is limited to around 0.6–0.8 V for symmetric configuration in an aqueous medium for the extreme lifetime of a device. In a few cases, it may be eliminated due to polarization at the material surfaces. For example, PANI is a habitually positively polarized molecule and PEDOT is negatively polarized versus Ag/AgCl. Therefore PANI can be stable and may be utilized at higher potential in an aqueous medium. Likewise, PEDOT can be polarized at lower potential also in the three-electrode system. In the meantime, the fabrication of a symmetric system with either PANI or PEDOT only provides its potential window. Therefore the device is limited to the three-electrode system. Conversely, the merging of PANI and PEDOT permits the extension of the voltage window up to 1.6 V through asymmetric configurations [15]. This asymmetric device will work by reversing the polarity, which allows the electrodes to work outside their potential window (Fig. 4). By exploiting the more positive potential window of p-type polymers with a moderately more negative potential window of n-type derivatives, the maximum voltage of the device can be achieved.

The progress of wearable electronics, including flexible smartphones and smart armbands, focuses on the requirement of new flexible and wearable energy storage devices. Among the other energy storage strategies, flexible and wearable supercapacitors have become a fascination due to prominent flexibility, compactness, light weight, speedy charge/discharge, extended life cycle, and the possibilities of integrating with other segments corresponding to batteries and fuel cells [63]. Typically, a bending test is essential to scrutinize the structural and electrical integrity of the flexible supercapacitor device through unique bending angles and cycles.

4.1 CP-based stretchable, flexible supercapacitors

Advanced materials should be designated to produce a maximum charge storage capacity and high-energy density. Subsequently, they must be crucial to regulate the electrode packing density for ideal volumetric performance. Furthermore, their interconnected porous structure with strong mechanical durability will offer maximum usability for energy storage performance. Various CPs have been extensively applied in supercapacitors due to their large capacitances, upright flexibility, and high conductivity. Typically, powder-like CPs have comparatively weak mechanical properties.

Consequently, virtually interconnected nanostructures have been considered to support the structure of CPs. Chemically converted graphene (CCG) and polyaniline nanofibers (PANI-NFs) were developed through simple vacuum filtration of the mixed dispersions of each component with the help of

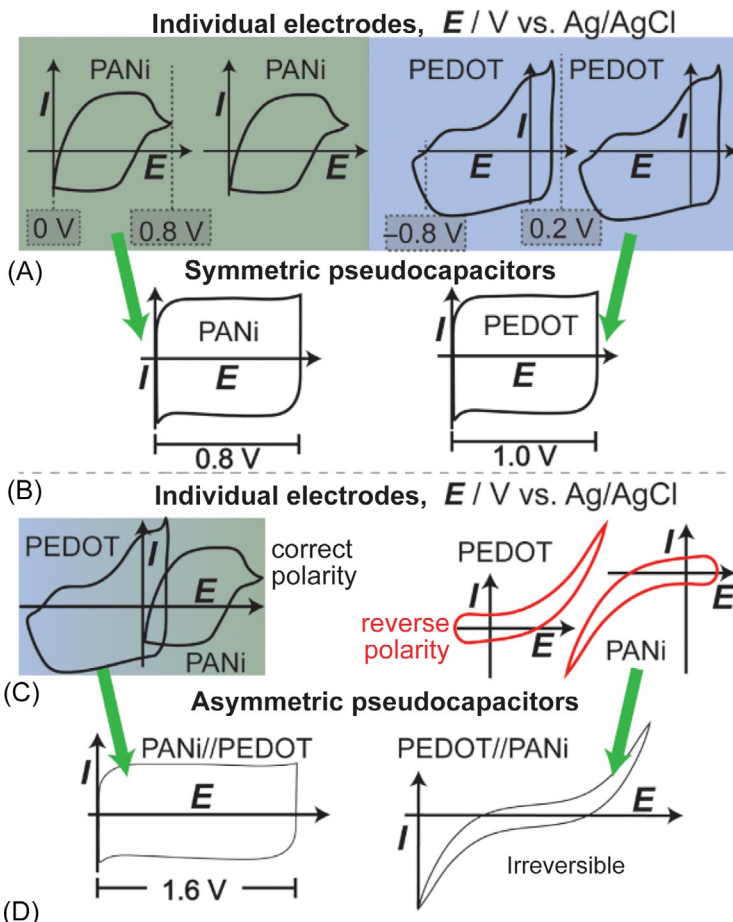


FIG. 4 (A) Three-electrode cyclic voltammograms of PANI (left) and PEDOT (right) in LiClO_4 versus Ag/AgCl. Note: PANI does not exhibit protonation peaks in neutral electrolytes. (B) Two-electrode cyclic voltammograms of electrochemical capacitors using symmetric electrodes of PANI (left) and PEDOT (right). (C) (Left) Three-electrode cyclic voltammetry of PANI and PEDOT superimposed. (Right) PEDOT and PANI cycled with opposite polarity versus Ag/AgCl shows irreversibility and water oxidation/reduction. (D) (Left) PANI as the positive electrode and PEDOT as the negative electrode in a two-electrode device shows an extended reversible voltage window. (Right) PEDOT as the positive electrode and PANI as the negative electrode gives an irreversible, nonideal device [15].

ultrasonication. The as-formed composite film has a layered structure, and the PANI-NFs are sandwiched between two CCG sheets. This configuration shows excellent mechanical stability, has high flexibility, and has the potential to be made into numerous desired structures. The conductivity of the film is $5.5 \times 10^2 \text{ S m}^{-1}$ (44% of CCG), which is around 10 times that of a PANI-NF film and displays the electrochemical capacitance of 210 F g^{-1} at 0.3 A g^{-1} [64].

Likewise, a single-step approach was developed for the fabrication of 3D flexible electrodes for supercapacitors. This process is more suitable for all kinds of CPs by the combination with graphene. The colloidal graphene oxide (GO) solution was mixed with PANI nanotubes (PANI-NT) or a PPy solution, and heating of the mixture offered a CP/graphene composite. In this case, the CP not only serves as an intense reducing agent for GO but also acts as a spacer that avoids graphene sheets from being restacked in the composite film and correspondingly delivering a 3D structure. The micrographs of the composites confirm that PANI-NT and PPy are decisively implanted among the graphene layers. This 3D structure, with the exfoliation of graphene sheets, offers more interspace for the high accessibility of electrolyte ions during its electrochemical cycling (Fig. 5A and B). This supercapacitor device offered 323.1 F g⁻¹

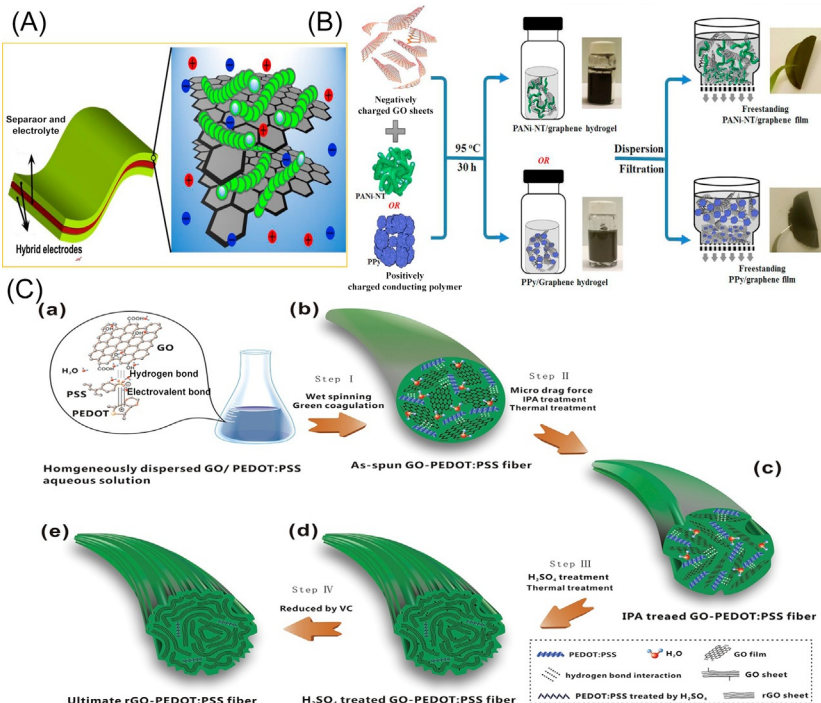


FIG. 5 (A) Schematic depiction of a flexible supercapacitor (high-density graphene and PANI nanotube composites). (B) Synthesis of PANI-NT/graphene and PPy/graphene composites [65]. (C) Schematic diagram of the fabrication processes of rGO-PEDOT:PSS fiber. (a) Homogeneously dispersed aqueous solution of GO-PEDOT:PSS for wet spinning; (b) as-spun GO-PEDOT:PSS fiber with a smooth surface and a relatively disordered inside structure; (c) IPA-treated GO-PEDOT:PSS fiber with a slightly wrinkled surface and a relatively ordered inside structure; (d) H₂SO₄-treated GO-PEDOT:PSS fiber with a highly wrinkled surface; (e) ultimate rGO-PEDOT:PSS fiber with reduced GO and a highly ordered inside structure [66].

(gravimetric) and 369.5 Fm^{-3} (volumetric) capacitance at 1 A g^{-1} in $1.0 \text{ M H}_2\text{SO}_4$ solution [65].

Typically, poly(3,4-ethylenedioxythiophene):poly(styrene sulfonate) (PEDOT:PSS) consumes numerous stimulating features such as excellent film-forming property, eminently visible light transmissivity, beneficial conductivity, and chemical stability. Due to these, they are frequently used as electrodes for supercapacitors. However, the conductivity and C_s of PEDOT:PSS fibers are lower, which limits their electrochemical performance. Therefore the formation of a hybrid/composite with graphene will be more helpful. Li et al. fabricated rGO-PEDOT:PSS composite fibers by wet spinning with an eco-friendly coagulation bath. The availability of maximum oxygen-rich functional groups of the GO and the hydrophilic property of PEDOT:PSS offers the homogeneous mixed aqueous solution of GO-PEDOT:PSS. The available PEDOT:PSS molecular chains and GO layers may transfer into small fixed areas, particularly in the core region, so the outer surface of the fibers will be of uniform thickness. Further, the fibers were treated with isopropanol (IPA), the PEDOT:PSS and GO may come closer and arrange as layer-by-layer in different directions. Treatment of H_2SO_4 and reduction with vitamin C provides ultimate rGO-PEDOT:PSS fibers with an extremely wrinkled structure on the surface and also having inside pores. By associating with IPA-treated fibers and H_2SO_4 , the definitive fibers with different rGO fillings show higher conductivity up to 590 S cm^{-1} and strain strength up to 18.4 MPa (Fig. 5C). Specific areal capacitance is as high as 131 mF cm^{-2} (53 F cm^{-3} calculated from cyclic voltammetry) at $20 \mu\text{A cm}^{-2}$ and the corresponding specific areal energy density is $4.55 \mu\text{Wh cm}^{-2}$ [66].

4.2 CP-based wearable supercapacitors

With rapid progression in stretchable and multifunctional wearable electronics, research has tended to move toward new power devices. These must possess lightness, transferability, and stretchability. Besides, the stretchable and wearable supercapacitor could be more useful as a ring or a wristband power device, or it may be unified into a stretchable and day-to-day wearable textile cloth. An all-solid-state supercapacitor is constructed through the in situ “growth and wrapping” technique, in which the electrode comprised of PANI deposited on carbon woven fabric (CWF) and wrapped with graphene (CWF/polyaniline/graphene composite). The hybrid electrode displays excellent mechanical and electrochemical properties through optimized few-layer graphene. It efficiently improves cycling stability up to 88.9% after 5000 continuous charge/discharge cycles. Also, the device has a high areal capacity of 790 F cm^{-2} at 1 A cm^{-2} with areal energy of $28.21 \mu\text{Wh cm}^{-2}$ at the power density of 0.12 mW cm^{-2} . The performance of the device with a bending angle of 180 degrees does not show any significant decrease in power density [67].

Wang and coworkers fabricated a supercapacitor device through extremely stretchable and washable all-yarn-based self-charging knitting power textile material, which progressed, together with biomechanical energy harvesting and concurrent energy storage, through a hybridizing triboelectric nanogenerator (TENG). The all-solid-state symmetric yarn supercapacitor is made up by dip coating carbon nanofiber (CNF) and PEDOT:PSS sequentially on a carbon fiber (CF) bundle. The as-devised yarn supercapacitor is then entwined into the TENG fabric to produce a self-charging power textile for wearable electronics. The yarn supercapacitor is symmetrically amassed from two parallelly organized PEDOT:PSS-CNF-CF electrodes with a solid-state H_3PO_4 /poly(vinyl alcohol) gel electrolyte (Fig. 6). The energy-harvesting TENG fabric with an extreme peak power density of approximately 85 mW m^{-2} is entwined with a single energy-harvesting yarn. As a beneficial output, the TENG fabric can light up a minimum of 124 light-emitting diodes (LEDs) while at the highly stretched state also. As well as good capacitance, higher flexibility, tunable adaptability, and reliable quantifiability, the yarn supercapacitors display outstanding long-term cycling and mechanical stability [68]. A graphene-wrapped PANI nanowire array-modified functionalized carbon cloth (fCC) (fCC-PANI array-rGO) is effectively made up and used as a freestanding electrode for the fabrication of flexible solid-state supercapacitors. As a freestanding electrode, it provides 471 mF cm^{-2} at 0.5 mA cm^{-2} and holds up to 75.5% of its initial capacitance even up to 10,000 cycles of charge/discharge. Besides, the flexible solid-state device exhibits a higher areal capacitance of 197 mF cm^{-2} at 0.1 mA cm^{-2} , which sustains at 91.3% after 7000 cycles at 5 mA cm^{-2} [69].

4.3 Miscellaneous architectures of CPs

Because the hybrid form benefits from low cost and high performance, PANI/carbon-based composites are being viewed as better electrode materials for practical supercapacitors. This is because performance increases with the design, fabrication, and composition of its microstructure. Still, there is some confusion in finding the mechanism of action in this kind of hybrid. For instance, Bai and coworkers thoroughly examined the activation of high C_s of PANI/graphene composites. Electrochemical as well as spectral data validate that throughout the electrochemical measurements of PANI, hydroxyl or amino-terminated oligoanilines (HAOANIs) show substantial theoretic capacitance, which are generated as degradation products of PANI. Here, the degraded PANI-based product offers higher $C_s (> 1000 \text{ F g}^{-1})$. The availability of the graphene with a perfect ratio in the composite assists as a conductive matrix intended for electron transport among the low conductive HAOANIs and the current collector.

Nevertheless, it does not easily attain high C_s without the help of graphene due to the low conductivity of the degraded PANI electrode. Based on the

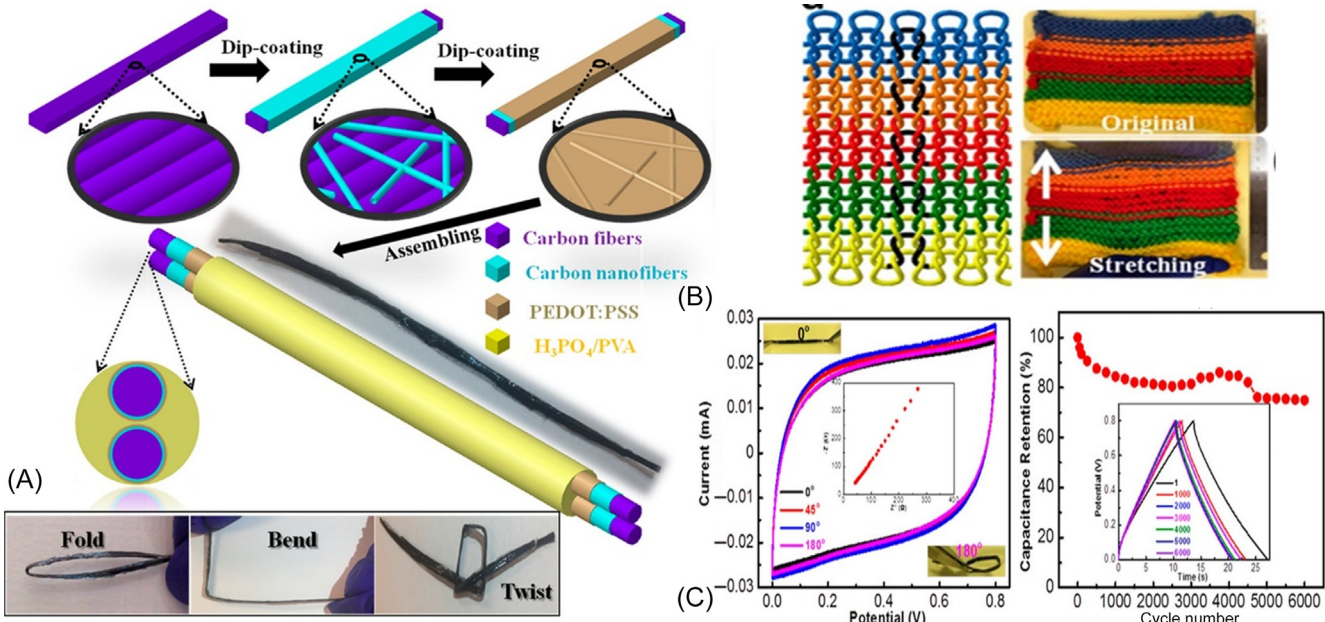


FIG. 6 (A) Schematic design of the yarn supercapacitor fabricated using two PEDOT:PSS-CNF-CF electrodes in parallel. (B) Yarn supercapacitors knitted into the normal weaving fabric material at the initial state (*upper right*) and stretched state (*lower right*). (C) Cyclic voltammetry curves of the supercapacitor (SC) at different bending states (*inset*: electrochemical impedance spectroscopy (EIS) technique of the SC) and long-term stability of the SC for 6000 charging/discharging cycles [68].

results obtained from this work, an approach to raise the overall capacitive performance of PANI-rGO was initiated. Typically, PANI-based electrodes are electrochemically stable only up to 0.7 V, so it exhibits fewer C_s as only the first redox (leucoemeraldine/emeraldine) can be active to store charge. This inconsistency amid the stability and C_s of PANI-rGO can be resolved by familiarizing HAOANIs. Strategies like activation of the PANI-rGO electrode at 0.8 V before use to increase the formation of HAOANI and the working potential of PANI-rGO are restricted below 0.7 V to safeguard the high cycling stability. It is observed that there is about a 16% increase in the C_s of the PANI-rGO composite electrode from 620 to 719 F g^{-1} at 1.4 A g^{-1} after the activation process as a result of the influence of HAOANIs. Besides, in terms of cycling, stability retains 91.3% of its original capacitance after 10,000 cycles [70].

For the fabrication of hierarchical porous structured materials, numerous methods are available, but the greener approach is still a challenge. Recently, a hierarchically porous carbon microsphere (HCM) was prepared through pyrolyzing chitin from a chitin/chitosan blend solution. Here, chitosan acts as a structure-directing agent for the construction of the microspheres, and the result displays a high specific surface area of $1450 \text{ m}^2 \text{ g}^{-1}$. The porous nature of the HCM is utilized for the deposition of PANI nanoclusters (Fig. 7). HCM-PANI composites for a symmetric supercapacitor display extraordinary rate ability and cycling durability of around 90.6% initial capacitance retention subsequently 10,000 cycles. Cycling stability was improved due to an uninterrupted interconnected CNF structure, which allows the fast movement of ions inside the whole electrode, and the homogeneous deposition of PANI nanoclusters proficiently reduced the volume expansion of PANI, which was caused by the doping/dedoping process in cycling. Furthermore, uniformly doped nitrogen and oxygen of HCM presented promising hydrophilicity to benefit the constant deposition of PANI and thus prevent falling off during charge/discharge [71].

Developments of miniature and wearable electronics led to miniaturized, portable, high-energy density, and outstandingly flexible rechargeable power devices. Material exploitation is solely based on the type/nature of the synthesis process and its property. Among other processes, the inkjet printing technique is a simple, noncontact method that has been recommended for the deposition in picoliter volumes of materials in the form of ink in a drop-on-demand style. It significantly decreases the consumption of a widespread selection of substrates such as papers, glasses, polymers, and fabrics, and it may be an ideal technique for simple, low-cost, and rapid fabrication of supercapacitors with specifically intended geometries and patterns. Lu and coworkers prepared an innovative printable ink comprising rGO@PANI composites for high-performance flexible supercapacitors. In this approach, PANI nanoparticles were anchored onto GO nanosheets through covalent attraction toward the formation of GO@PANI composites. The as-prepared material is impressed on flexible substrates, and then reduced using hypophosphorous acid. For the assessment, both

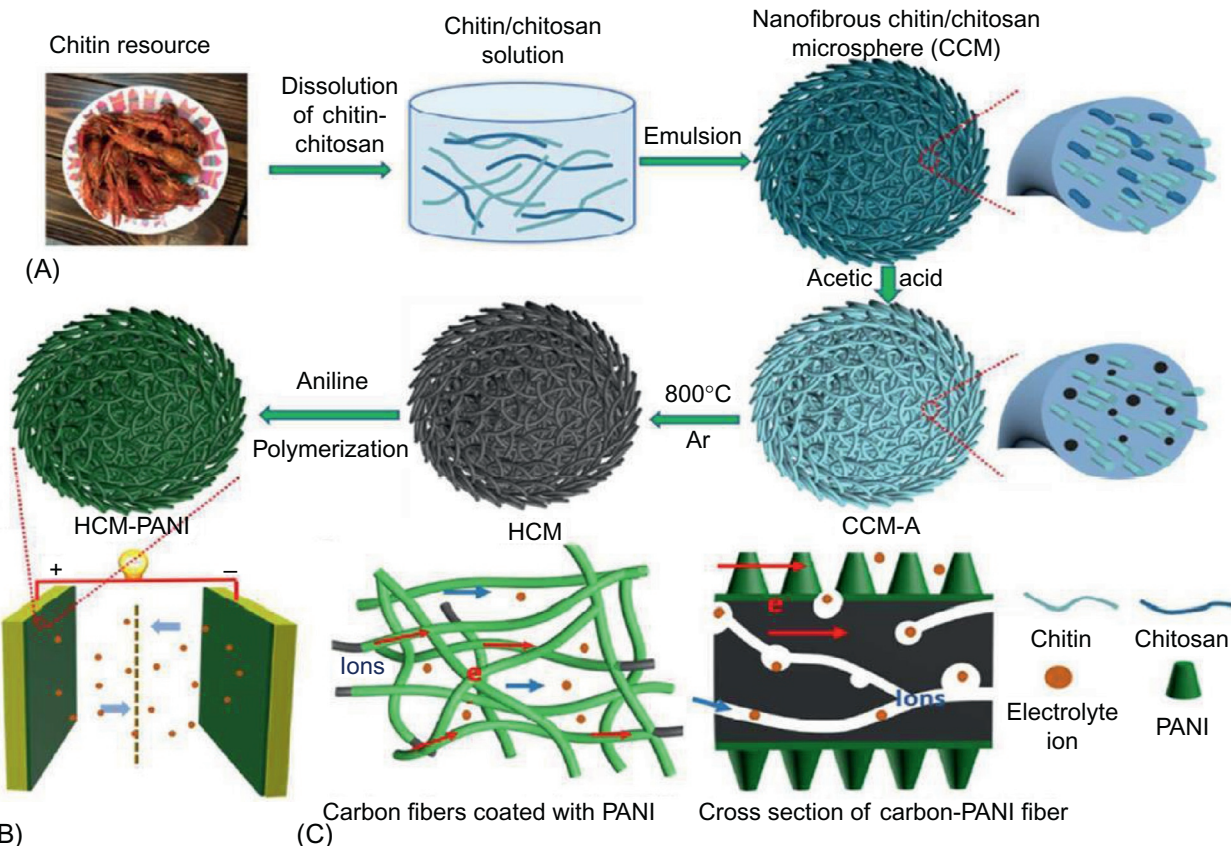


FIG. 7 (A) Graphical illustrations of the formation process. (B) A two-electrode system. (C) Porous structure of nanofibers for HCM-PANI [71].

sandwich-structured and interdigitated supercapacitors were constructed. Both devices exhibited high volumetric capacitances of 258.5 F cm^{-3} at 1 mV s^{-1} for sandwich-structured and 554 F cm^{-3} at 1 mV s^{-1} for interdigitated supercapacitors. These devices afford excellent cycling retention of more than 90% up to 2000 cycles, there are no changes in C_s in the bending stage, and they also have excellent flexibility [72].

Even though CP-based materials (alone or as a hybrid form) play a vital role in supercapacitors it is essential to improve energy density through modifications either in the form of materials or fabrication. Nanoarchitectures are most prominent for further developmental configurations. At the level of device fabrication, energy density (Wh kg^{-1}) and power density (W kg^{-1}) are significant factors. These aspects are not only from the performance of the materials but are also contingent on the precise package parameters like mass of the constituents and cell architecture. By keeping these things in mind, developments are in progress to improve the energy density in the packed cells. The admirable results of CP-based materials and their architectures show great opportunities in emerging energy storage devices with high-energy and power densities for real-world applications. Extraordinary investigation efforts have been devoted to various systems through symmetric/asymmetric configuration to gain higher energy density [48, 73–80] (Fig. 8). The results show the superior or comparable performance of optimum nanoarchitectures developed with PANI fabricated in asymmetric configurations.

5 Summary

Many approaches have been made to fully exploit CPs in supercapacitors. This chapter presented a review of the state-of-the-art of basic and recent advances in supercapacitors, and in the design, synthesis, and applications of nanoarchitected CP-based electrode materials for supercapacitors. Architecturally engineered CPs endorse increased sustainability via their physicochemical properties, which always influence electrochemical characteristics. Even

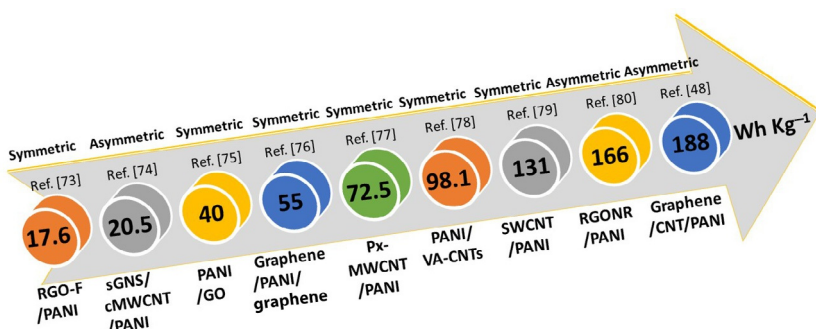


FIG. 8 An increasing strategy of the energy density of various PANI-based supercapacitors.

though high capacitance is a CP's greatest significant benefit, destruction leads to the rapid decrease in capacitance. Flexibility in synthetic methods leads to better conductivity, higher surface area, shorter electronic/ionic path, tolerance to stress/strain, superficial kinetics, and prolonged cyclability. Furthermore, incorporation of CPs in/on other materials will help to achieve the desired properties and fulfill the requirements of supercapacitors. The structure, morphology, designing, and fabrication of CPs are strongly related to their synthesis and hybrid formation. The configurations, designs, architectures, and synergistic exchanges of CP-based materials not only enhance supercapacitance performance but also provide outstanding prolonged cycling stability.

6 Future perspective

Numerous research steps are currently looking at various supercapacitors. It will take a long time to replace batteries in real-time applications. To overcome the obstacles that hinder material and device development, we have to think about designing materials with proper structures. Adequate design configurations of supercapacitor devices with improved performance at every level should be sought in real-world practice. Even though devices are constructed through symmetric or asymmetric configurations there are also some limitations regarding the operational window. For example, utilizing only CPs in the asymmetric configuration is more significant when compared to symmetric configuration. In addition, CPs hybridized with other materials like carbon-based or other pseudocapacitive materials through asymmetric configuration will offer many benefits for future devices. Based on the results, the advantages of CP-based electrodes over conventional electrodes are:

1. Porous and freestanding structure: electrodes, as well as device preparation through porous and freestanding films with utmost transparency of conductive flexible substrates, will give easy fabrication and utilization.
2. Lightweight: preparation of lightweight devices through nanoarchitectural devices will lead to better utilization of printing and patterning technology.
3. Interconnected 3D structure and electrical conductivity: the formation of nanohybrids with diverse materials through interconnected 3D architecture will improve ion facilitation during electrochemical reactions.
4. Structural stability: deviation or deterioration will occur during potential cycling or the charge/discharge process in supercapacitors. To overcome these obstacles, it is important to make the materials and devices with utmost care for long-term utilization.

Furthermore, the electrochromic characteristics of CPs may be beneficial for their prospective use in smart supercapacitors.

With enthusiastic and extraordinary research interest in the growth of CPs, it is predicted that they will perform a primary role in flexible, smart, and economical energy storage.

References

- [1] E.A. Walters, E.M. Wewerka, An overview of the energy crisis. *J. Chem. Educ.* 52 (1975) 282, <https://doi.org/10.1021/ed052p282>.
- [2] J.M. Cullen, J.M. Allwood, E.H. Borgstein, Reducing energy demand: what are the practical limits?. *Environ. Sci. Technol.* 45 (2011) 1711–1718, <https://doi.org/10.1021/es102641n>.
- [3] D.P. Dubal, O. Ayyad, V. Ruiz, P. Gómez-Romero, Hybrid energy storage: the merging of battery and supercapacitor chemistries. *Chem. Soc. Rev.* 44 (2015) 1777–1790, <https://doi.org/10.1039/C4CS00266K>.
- [4] J. Cho, S. Jeong, Y. Kim, Commercial and research battery technologies for electrical energy storage applications. *Prog. Energy Combust. Sci.* 48 (2015) 84–101, <https://doi.org/10.1016/j.pecsc.2015.01.002>.
- [5] J. Libich, J. Máca, J. Vondrák, O. Čech, M. Sedlářková, Supercapacitors: properties and applications. *J. Energy Storage.* 17 (2018) 224–227, <https://doi.org/10.1016/j.est.2018.03.012>.
- [6] M. Winter, R.J. Brodd, What are batteries, fuel cells, and supercapacitors?. *Chem. Rev.* 104 (2004) 4245–4270, <https://doi.org/10.1021/cr020730k>.
- [7] B.E. Conway, Transition from “supercapacitor” to “battery” behavior in electrochemical energy storage. *J. Electrochem. Soc.* 138 (1991) 1539, <https://doi.org/10.1149/1.2085829>.
- [8] B.E. Conway, V. Birss, J. Wojtowicz, The role and utilization of pseudocapacitance for energy storage by supercapacitors, *J. Power Sources* 66 (1997) 1–14.
- [9] B.E. Conway, *Electrochemical Supercapacitors: Scientific Fundamentals and Technological Applications*, Kluwer Academic/Plenum Publishers, New York, 1999.
- [10] J. Wang, S. Dong, B. Ding, Y. Wang, X. Hao, H. Dou, Y. Xia, X. Zhang, Pseudocapacitive materials for electrochemical capacitors: from rational synthesis to capacitance optimization. *Natl. Sci. Rev.* 4 (2017) 71–90, <https://doi.org/10.1093/nsr/nww072>.
- [11] R. McNeill, R. Siudak, J.H. Wardlaw, D.E. Weiss, Electronic conduction in polymers. I. The chemical structure of polypyrrole. *Aust. J. Chem.* 16 (1963) 1056–1075, <https://doi.org/10.1071/CH9631056>.
- [12] C.I. Awuzie, Conducting polymers. *Mater. Today Proc.* 4 (2017) 5721–5726, <https://doi.org/10.1016/j.matpr.2017.06.036>.
- [13] Q. Meng, K. Cai, Y. Chen, L. Chen, Research progress on conducting polymer based supercapacitor electrode materials. *Nano Energy* 36 (2017) 268–285, <https://doi.org/10.1016/j.nanoen.2017.04.040>.
- [14] F. Wolfart, B.M. Hryniwicz, M.S. Góes, C.M. Corrêa, R. Torresi, M.A.O.S. Minadeo, S.I. Córdoba de Torresi, R.D. Oliveira, L.F. Marchesi, M. Vidotti, Conducting polymers revisited: applications in energy, electrochromism and molecular recognition. *J. Solid State Electrochem.* 21 (2017) 2489–2515, <https://doi.org/10.1007/s10008-017-3556-9>.
- [15] A.M. Bryan, L.M. Santino, Y. Lu, S. Acharya, J.M. D’Arcy, Conducting polymers for pseudocapacitive energy storage. *Chem. Mater.* 28 (2016) 5989–5998, <https://doi.org/10.1021/acs.chemmater.6b01762>.
- [16] M.E. Abdelhamid, A.P. O’Mullane, G.A. Snook, Storing energy in plastics: a review on conducting polymers & their role in electrochemical energy storage. *RSC Adv.* 5 (2015) 11611–11626, <https://doi.org/10.1039/c4ra15947k>.
- [17] J. Yang, Y. Liu, S. Liu, L. Li, C. Zhang, T. Liu, Conducting polymer composites: material synthesis and applications in electrochemical capacitive energy storage. *Mater. Chem. Front.* 1 (2017) 251–268, <https://doi.org/10.1039/c6qm00150e>.
- [18] G.A. Snook, P. Kao, A.S. Best, Conducting-polymer-based supercapacitor devices and electrodes. *J. Power Sources* 196 (2011) 1–12, <https://doi.org/10.1016/j.jpowsour.2010.06.084>.

54 PART | I Electrochemical systems and energy storage

- [19] A. Eftekhari, L. Li, Y. Yang, Polyaniline supercapacitors. *J. Power Sources* 347 (2017) 86–107, <https://doi.org/10.1016/j.jpowsour.2017.02.054>.
- [20] Y. Shi, L. Peng, G. Yu, Nanostructured conducting polymer hydrogels for energy storage applications. *Nanoscale* 7 (2015) 12796–12806, <https://doi.org/10.1039/C5NR03403E>.
- [21] S. Ghosh, T. Maiyalagan, R.N. Basu, Nanostructured conducting polymers for energy applications: towards a sustainable platform. *Nanoscale* 8 (2016) 6921–6947, <https://doi.org/10.1039/C5NR08803H>.
- [22] H.D. Tran, D. Li, R.B. Kaner, One-dimensional conducting polymer nanostructures: bulk synthesis and applications. *Adv. Mater.* 21 (2009) 1487–1499, <https://doi.org/10.1002/adma.200802289>.
- [23] Y. Shi, L. Peng, Y. Ding, Y. Zhao, G. Yu, Nanostructured conductive polymers for advanced energy storage. *Chem. Soc. Rev.* 44 (2015) 6684–6696, <https://doi.org/10.1039/c5cs00362h>.
- [24] J. Pecher, S. Mecking, Nanoparticles of conjugated polymers. *Chem. Rev.* 110 (2010) 6260–6279, <https://doi.org/10.1021/cr100132y>.
- [25] K. Wang, H. Wu, Y. Meng, Z. Wei, Conducting polymer nanowire arrays for high performance supercapacitors. *Small* 10 (2014) 14–31, <https://doi.org/10.1002/smll.201301991>.
- [26] E. Frackowiak, V. Khomenko, K. Jurewicz, K. Lota, F. Béguin, Supercapacitors based on conducting polymers/nanotubes composites. *J. Power Sources* 153 (2006) 413–418, <https://doi.org/10.1016/j.jpowsour.2005.05.030>.
- [27] W. Raza, F. Ali, N. Raza, Y. Luo, K.-H. Kim, J. Yang, S. Kumar, A. Mehmood, E.E. Kwon, Recent advancements in supercapacitor technology. *Nano Energy* 52 (2018) 441–473, <https://doi.org/10.1016/j.nanoen.2018.08.013>.
- [28] R. Ramya, R. Sivasubramanian, M.V. Sangaranarayanan, Conducting polymers-based electrochemical supercapacitors—progress and prospects. *Electrochim. Acta* 101 (2013) 109–129, <https://doi.org/10.1016/j.electacta.2012.09.116>.
- [29] S.B. Yoon, E.H. Yoon, K.B. Kim, Electrochemical properties of leucoemeraldine, emeraldine, and pernigraniline forms of polyaniline/multi-wall carbon nanotube nanocomposites for supercapacitor applications. *J. Power Sources* 196 (2011) 10791–10797, <https://doi.org/10.1016/j.jpowsour.2011.08.107>.
- [30] H. Wang, J. Lin, Z.X. Shen, Polyaniline (PANI) based electrode materials for energy storage and conversion. *J. Sci. Adv. Mater. Devices* 1 (2016) 225–255, <https://doi.org/10.1016/j.jsamd.2016.08.001>.
- [31] H. Li, J. Wang, Q. Chu, Z. Wang, F. Zhang, S. Wang, Theoretical and experimental specific capacitance of polyaniline in sulfuric acid. *J. Power Sources* 190 (2009) 578–586, <https://doi.org/10.1016/j.jpowsour.2009.01.052>.
- [32] H.D. Tran, J.M. D'Arcy, Y. Wang, P.J. Beltramo, V.A. Strong, R.B. Kaner, The oxidation of aniline to produce “polyaniline”: a process yielding many different nanoscale structures. *J. Mater. Chem.* 21 (2011) 3534–3550, <https://doi.org/10.1039/C0JM02699A>.
- [33] Y. Ma, C. Hou, H. Zhang, M. Qiao, Y. Chen, H. Zhang, Q. Zhang, Z. Guo, Morphology-dependent electrochemical supercapacitors in multi-dimensional polyaniline nanostructures. *J. Mater. Chem. A* 5 (2017) 14041–14052, <https://doi.org/10.1039/C7TA03279J>.
- [34] X. Zhang, S.K. Manohar, Polyaniline nanofibers: chemical synthesis using surfactants. *Chem. Commun.* 10 (2004) 2360, <https://doi.org/10.1039/b409309g>.
- [35] X. Zhang, H.S. Kolla, X. Wang, K. Raja, S.K. Manohar, Fibrillar growth in polyaniline. *Adv. Funct. Mater.* 16 (2006) 1145–1152, <https://doi.org/10.1002/adfm.200500478>.
- [36] J. Wang, J. Wang, Z. Yang, Z. Wang, F. Zhang, S. Wang, A novel strategy for the synthesis of polyaniline nanostructures with controlled morphology. *React. Funct. Polym.* 68 (2008) 1435–1440, <https://doi.org/10.1016/j.reactfunctpolym.2008.07.002>.

- [37] X. Wang, Y. Li, Y. Zhao, J. Liu, S. Tang, W. Feng, Synthesis of PANI nanostructures with various morphologies from fibers to micromats to disks doped with salicylic acid. *Synth. Met.* 160 (2010) 2008–2014, <https://doi.org/10.1016/j.synthmet.2010.07.030>.
- [38] C. Li, L. Yang, Y. Meng, X. Hu, Z. Wei, P. Chen, S. Zhou, Tuning PANI nanostructure by driving force for diverse capacitance performance. *RSC Adv.* 3 (2013) 21315, <https://doi.org/10.1039/c3ra43696a>.
- [39] S. Grover, S. Goel, R.B. Marichi, V. Sahu, G. Singh, R.K. Sharma, Polyaniline all solid-state pseudocapacitor: role of morphological variations in performance evolution. *Electrochim. Acta* 196 (2016) 131–139, <https://doi.org/10.1016/j.electacta.2016.02.157>.
- [40] J. Lee, H. Jeong, R. Lassarote Lavall, A. Busnaina, Y. Kim, Y.J. Jung, H. Lee, Polypyrrole films with micro/nanosphere shapes for electrodes of high-performance supercapacitors. *ACS Appl. Mater. Interfaces* 9 (2017) 33203–33211, <https://doi.org/10.1021/acsmami.7b11574>.
- [41] S. Nejati, T.E. Minford, Y.Y. Smolin, K.K.S. Lau, Enhanced charge storage of ultrathin Poly-thiophene films within porous nanostructures. *ACS Nano* 8 (2014) 5413–5422, <https://doi.org/10.1021/nn500007c>.
- [42] J.M. D'Arcy, M.F. El-Kady, P.P. Khine, L. Zhang, S.H. Lee, N.R. Davis, D.S. Liu, M.T. Yeung, S.Y. Kim, C.L. Turner, A.T. Lech, P.T. Hammond, R.B. Kaner, Vapor-phase polymerization of nanofibrillar poly(3,4-ethylenedioxythiophene) for supercapacitors. *ACS Nano* 8 (2014) 1500–1510, <https://doi.org/10.1021/nn405595r>.
- [43] H. Zhang, J. Wang, Q. Shan, Z. Wang, S. Wang, Tunable electrode morphology used for high performance supercapacitor: polypyrrole nanomaterials as model materials. *Electrochim. Acta* 90 (2013) 535–541, <https://doi.org/10.1016/j.electacta.2012.12.045>.
- [44] B.H. Patil, A.D. Jagadale, C.D. Lokhande, Synthesis of polythiophene thin films by simple successive ionic layer adsorption and reaction (SILAR) method for supercapacitor application. *Synth. Met.* 162 (2012) 1400–1405, <https://doi.org/10.1016/j.synthmet.2012.05.023>.
- [45] B. Senthilkumar, P. Thenamirtham, R. Kalai Selvan, Structural and electrochemical properties of polythiophene. *Appl. Surf. Sci.* 257 (2011) 9063–9067, <https://doi.org/10.1016/j.apusc.2011.05.100>.
- [46] X.N. Xie, J. Wang, K.K. Lee, K.P. Loh, Supercapacitive energy storage based on ion-conducting channels in hydrophilized organic network. *J. Polym. Sci. Part B Polym. Phys.* 49 (2011) 1234–1240, <https://doi.org/10.1002/polb.22295>.
- [47] M. Rajesh, C.J. Raj, B.C. Kim, R. Manikandan, S.-J. Kim, S.Y. Park, K. Lee, K.H. Yu, Expedited and eco-friendly hydrothermal polymerization of PEDOT nanoparticles for binder-free high performance supercapacitor electrodes. *RSC Adv.* 6 (2016) 110433–110443, <https://doi.org/10.1039/C6RA22958A>.
- [48] Q. Cheng, J. Tang, N. Shinya, L.-C. Qin, Polyaniline modified graphene and carbon nanotube composite electrode for asymmetric supercapacitors of high energy density. *J. Power Sources* 241 (2013) 423–428, <https://doi.org/10.1016/j.jpowsour.2013.04.105>.
- [49] S. Iqbal, S. Ahmad, Recent development in hybrid conducting polymers: synthesis, applications and future prospects. *J. Ind. Eng. Chem.* 60 (2018) 53–84, <https://doi.org/10.1016/j.jiec.2017.09.038>.
- [50] G. Yu, X. Xie, L. Pan, Z. Bao, Y. Cui, Hybrid nanostructured materials for high-performance electrochemical capacitors. *Nano Energy* 2 (2013) 213–234, <https://doi.org/10.1016/j.nanoen.2012.10.006>.
- [51] L. Wang, Y. Ye, X. Lu, Z. Wen, Z. Li, H. Hou, Y. Song, Hierarchical nanocomposites of polyaniline nanowire arrays on reduced graphene oxide sheets for supercapacitors. *Sci. Rep.* 3 (2013) 3568, <https://doi.org/10.1038/srep03568>.

- [52] G. Wang, Y. Zhang, F. Zhou, Z. Sun, F. Huang, Y. Yu, L. Chen, M. Pan, Simple and fast synthesis of polyaniline nanofibers/carbon paper composites as supercapacitor electrodes. *J. Energy Storage.* 7 (2016) 99–103, <https://doi.org/10.1016/j.est.2016.05.011>.
- [53] J. Benson, I. Kovalenko, S. Boukhalfa, D. Lashmore, M. Sanghadasa, G. Yushin, Multi-functional CNT-polymer composites for ultra-tough structural supercapacitors and desalination devices. *Adv. Mater.* 25 (2013) 6625–6632, <https://doi.org/10.1002/adma.201301317>.
- [54] C.-M. Chang, C.-J. Weng, C.-M. Chien, T.-L. Chuang, T.-Y. Lee, J.-M. Yeh, Y. Wei, Polyaniline/carbon nanotube nanocomposite electrodes with biomimetic hierarchical structure for supercapacitors. *J. Mater. Chem. A* 1 (2013) 14719, <https://doi.org/10.1039/c3ta13758a>.
- [55] S. Arulmani, J.J. Wu, S. Anandan, Amphiphilic triblock copolymer guided polyaniline embraced CNT nanohybrid with outcropping whiskers as an energy storage electrode. *Electrochim. Acta* 246 (2017) 737–747, <https://doi.org/10.1016/j.electacta.2017.06.101>.
- [56] M. Yu, Y. Ma, J. Liu, S. Li, Polyaniline nanocone arrays synthesized on three-dimensional graphene network by electrodeposition for supercapacitor electrodes. *Carbon N. Y.* 87 (2015) 98–105, <https://doi.org/10.1016/j.carbon.2015.02.017>.
- [57] J. Zhang, X.S. Zhao, Conducting polymers directly coated on reduced graphene oxide sheets as high-performance supercapacitor electrodes. *J. Phys. Chem. C* 116 (2012) 5420–5426, <https://doi.org/10.1021/jp211474e>.
- [58] N.P.S. Chauhan, M. Singh Solanki, Approaches and Challenges of Polyaniline–Graphene Nanocomposite for Energy Application. Elsevier Inc., 2018<https://doi.org/10.1016/B978-0-12-813574-7.00017-4>
- [59] L. Li, A.-R.O. Raji, H. Fei, Y. Yang, E.L.G. Samuel, J.M. Tour, Nanocomposite of polyaniline nanorods grown on graphene nanoribbons for highly capacitive pseudocapacitors. *ACS Appl. Mater. Interfaces* 5 (2013) 6622–6627, <https://doi.org/10.1021/am4013165>.
- [60] K. Jurewicz, C. Vix-Guterl, E. Frackowiak, S. Saadallah, M. Reda, J. Parmentier, J. Patarin, F. Béguin, Capacitance properties of ordered porous carbon materials prepared by a templating procedure. *J. Phys. Chem. Solid* 65 (2004) 287–293, <https://doi.org/10.1016/j.jpcs.2003.10.024>.
- [61] Z. Zhang, G. Wang, Y. Li, X. Zhang, N. Qiao, J. Wang, J. Zhou, Z. Liu, Z. Hao, A new type of ordered mesoporous carbon/polyaniline composites prepared by a two-step nanocasting method for high performance supercapacitor applications. *J. Mater. Chem. A* 2 (2014) 16715–16722, <https://doi.org/10.1039/C4TA03351E>.
- [62] S. Arulmani, S. Michelraj, C. Suresh, C. Sivakumar, Interconnected porous carbon: unique versatile matrix for the growth of nanostructured polyaniline and its enhanced performance towards electrochemical energy storage. *ChemistrySelect* 2 (2017) 2197–2204, <https://doi.org/10.1002/slct.201602064>.
- [63] X. Pu, L. Li, M. Liu, C. Jiang, C. Du, Z. Zhao, W. Hu, Z.L. Wang, Wearable self-charging power textile based on flexible yarn supercapacitors and fabric nanogenerators. *Adv. Mater.* 28 (2016) 98–105, <https://doi.org/10.1002/adma.201504403>.
- [64] Q. Wu, Y. Xu, Z. Yao, A. Liu, G. Shi, Supercapacitors based on flexible graphene/polyaniline nanofiber composite films. *ACS Nano* 4 (2010) 1963–1970, <https://doi.org/10.1021/nm1000035>.
- [65] M. Moussa, M.F. El-Kady, S. Abdel-Azeim, R.B. Kaner, P. Majewski, J. Ma, Compact, flexible conducting polymer/graphene nanocomposites for supercapacitors of high volumetric energy density. *Compos. Sci. Technol.* 160 (2018) 50–59, <https://doi.org/10.1016/j.compscitech.2018.02.033>.

- [66] B. Li, J. Cheng, Z. Wang, Y. Li, W. Ni, B. Wang, Highly-wrinkled reduced graphene oxide-conductive polymer fibers for flexible fiber-shaped and interdigital-designed supercapacitors. *J. Power Sources* 376 (2018) 117–124, <https://doi.org/10.1016/j.jpowsour.2017.11.076>.
- [67] Y. Lin, H. Zhang, W. Deng, D. Zhang, N. Li, Q. Wu, C. He, In-situ growth of high-performance all-solid-state electrode for flexible supercapacitors based on carbon woven fabric/polyaniline/graphene composite. *J. Power Sources* 384 (2018) 278–286, <https://doi.org/10.1016/j.jpowsour.2018.03.003>.
- [68] K. Dong, Y.C. Wang, J. Deng, Y. Dai, S.L. Zhang, H. Zou, B. Gu, B. Sun, Z.L. Wang, A highly stretchable and washable all-yarn-based self-charging knitting power textile composed of fiber triboelectric nanogenerators and supercapacitors. *ACS Nano* 11 (2017) 9490–9499, <https://doi.org/10.1021/acsnano.7b05317>.
- [69] P. Du, Y. Dong, H. Kang, X. Yang, Q. Wang, J. Niu, S. Wang, P. Liu, Graphene-wrapped polyaniline nanowire array modified functionalized of carbon cloth for high-performance flexible solid-state supercapacitor. *ACS Sustain. Chem. Eng.* 6 (2018) 14723–14733, <https://doi.org/10.1021/acssuschemeng.8b03278>.
- [70] Q. Zhang, A. Zhou, J. Wang, J. Wu, H. Bai, Degradation-induced capacitance: a new insight into the superior capacitive performance of polyaniline/graphene composites. *Energ. Environ. Sci.* 10 (2017) 2372–2382, <https://doi.org/10.1039/C7EE02018J>.
- [71] L. Gao, L. Xiong, D. Xu, J. Cai, L. Huang, J. Zhou, L. Zhang, Distinctive construction of chitin-derived hierarchically porous carbon microspheres/polyaniline for high-rate supercapacitors. *ACS Appl. Mater. Interfaces* 10 (2018) 28918–28927, <https://doi.org/10.1021/acsaami.8b05891>.
- [72] J. Diao, J. Yuan, A. Ding, J. Zheng, Z. Lu, Flexible supercapacitor based on inkjet-printed graphene@polyaniline nanocomposites with ultrahigh capacitance. *Macromol. Mater. Eng.* 303 (2018) 1800092, <https://doi.org/10.1002/mame.201800092>.
- [73] P. Yu, X. Zhao, Z. Huang, Y. Li, Q. Zhang, Free-standing three-dimensional graphene and polyaniline nanowire arrays hybrid foams for high-performance flexible and lightweight supercapacitors. *J. Mater. Chem. A* 2 (2014) 14413–14420, <https://doi.org/10.1039/C4TA02721C>.
- [74] J. Shen, C. Yang, X. Li, G. Wang, High-performance asymmetric supercapacitor based on nanoarchitected polyaniline/graphene/carbon nanotube and activated graphene electrodes. *ACS Appl. Mater. Interfaces* 5 (2013) 8467–8476, <https://doi.org/10.1021/am4028235>.
- [75] A.G. Tabrizi, N. Arsalani, A. Mohammadi, L.S. Ghadimi, I. Ahadzadeh, H. Namazi, A new route for the synthesis of polyaniline nanoarrays on graphene oxide for high-performance supercapacitors. *Electrochim. Acta* 265 (2018) 379–390, <https://doi.org/10.1016/j.electacta.2018.01.166>.
- [76] N. Chen, L. Ni, J. Zhou, G. Zhu, Q. Kang, Y. Zhang, S. Chen, W. Zhou, C. Lu, J. Chen, X. Feng, X. Wang, X. Guo, L. Peng, W. Ding, W. Hou, Sandwich-like holey graphene/PANI/graphene nanohybrid for ultrahigh-rate supercapacitor. *ACS Appl. Energy Mater.* (2018) acsaem.8b00725 <https://doi.org/10.1021/acsaem.8b00725>.
- [77] D.D. Potphode, L. Sinha, P.M. Shirage, Redox additive enhanced capacitance: multi-walled carbon nanotubes/polyaniline nanocomposite based symmetric supercapacitors for rapid charge storage. *Appl. Surf. Sci.* 469 (2019) 162–172, <https://doi.org/10.1016/j.apsusc.2018.10.277>.
- [78] G. Wu, P. Tan, D. Wang, Z. Li, L. Peng, Y. Hu, C. Wang, W. Zhu, S. Chen, W. Chen, High-performance supercapacitors based on electrochemical-induced vertical-aligned carbon nanotubes and polyaniline nanocomposite electrodes. *Sci. Rep.* 7 (2017) <https://doi.org/10.1038/srep43676>.

58 PART | I Electrochemical systems and energy storage

- [79] Z. Niu, P. Luan, Q. Shao, H. Dong, J. Li, J. Chen, D. Zhao, L. Cai, W. Zhou, X. Chen, S. Xie, A “skeleton/skin” strategy for preparing ultrathin free-standing single-walled carbon nanotube/polyaniline films for high performance supercapacitor electrodes. *Energy Environ. Sci.* 5 (2012) 8726, <https://doi.org/10.1039/c2ee22042c>.
- [80] S. Grover, S. Goel, V. Sahu, G. Singh, R.K. Sharma, Asymmetric supercapacitive characteristics of PANI embedded holey graphene nanoribbons. *ACS Sustain. Chem. Eng.* 3 (2015) 1460–1469, <https://doi.org/10.1021/acssuschemeng.5b00184>.

Chapter 3

Current progress in the development of Fe-air batteries and their prospects for next-generation batteries

Wai Kian Tan^a, Go Kawamura^b, Hiroyuki Muto^{a,b}, and Atsunori Matsuda^b

^aInstitute of Liberal Arts and Sciences, Toyohashi University of Technology, Toyohashi, Aichi, Japan, ^bDepartment of Electrical and Electronic Information Engineering, Toyohashi University of Technology, Toyohashi, Aichi, Japan

1 Introduction

The interest in Fe-air batteries began in the 1970s amid the oil crisis. Recent advancement in nanotechnology has enabled the feasibility of nanosized Fe electrode design prompting a renewed interest in Fe-air batteries due to their good potentials [1]. Moreover, the rapid development of electric vehicles and Internet-of-Things (IoT) have increased the demand for batteries with higher energy density without compromising on safety. Although much research is still focusing on Li-ion batteries, new researches seeking for alternative power sources which are more environmental friendly and safe such as metal-air batteries are on-going [2–4]. Besides safety, concerns have also been raised regarding the disposal of used batteries and therefore, recyclability and contamination level control are also crucial. Metal-air batteries are configured with metals such as iron (Fe) [2, 5], zinc (Zn) [4, 6, 7], or aluminum [8–10] as their negative electrode, while oxygen from air is employed as the source of fuel for the reaction at the positive electrode. Metal-air batteries not only possess high specific energy densities but also can be fabricated using materials that are abundant, environmentally friendly, and most importantly, inexpensive [11]. Therefore, the usage of metal-air batteries is aligned with the sustainable development goals set by World Health Organization toward the promotion of a sustainable and affordable energy source. Until now, only limited number of researches have been reported on the fabrication of rechargeable metal-air batteries due to several challenges, such as precise control of chemical reaction and battery

design involving the three core components: anode, cathode, and electrolyte [12]. The synchronization of every component is very important to obtain a highly functional metal-air battery and any weak link in one of the core components would lead to poor battery performance.

Although the electrochemical reactions that occur in rechargeable metal-air batteries differ according to the metal used at the negative electrode and the type of electrolyte used in the system, the basic chemical equations that occur during operation are as follows:



M represents the metallic materials used such as Fe, Zn, Al, etc., while n is the ion charge number of the respective metal. In a common discharge reaction in alkaline aqueous solution, metal ions that are generated after oxidation (Eq. 1) would move within the electrolyte to the positive electrode to react with oxygen to form metal oxides (Eq. 2). Eq. (3) represents the overall reaction that occurs throughout the charge/discharge process in a metal-air battery [3]. Fig. 1 shows a schematic illustration of the overall mechanism in a metal-air battery.

Different types of metal-air batteries have been reported depending on the active metal used in the negative electrode such as Li-air, Fe-air, Zn-air, Mg-air, Sn-air, etc. Each aforementioned metal-air battery system has its own advantages and disadvantages and in this chapter, the focus will be on the progress and development of Fe-air batteries.

Table 1 provides a comparison for various types of metal-air batteries available. From the comparison, although the Mg-air and Al-air batteries possess significantly higher theoretical energy densities, the attainable values are low due to the parasitic corrosion reaction with hydrogen. Another issue faced with both

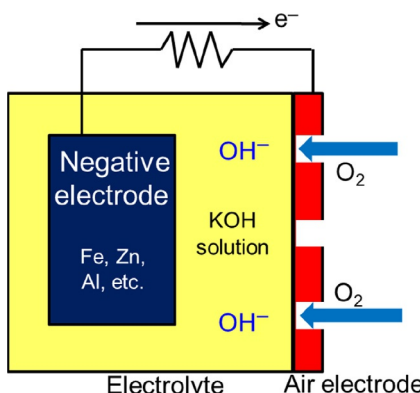


FIG. 1 Schematic illustration of a metal-air battery.

TABLE 1 Metal-air batteries comparison [13].

Battery systems	Fe-air	Zn-air	Al-air	Mg-air	Na-air	K-air	Li-air
Year invented	1968	1878	1962	1966	2012	2013	1996
Cost of metals (\$/kg)	0.40	1.85	1.75	2.75	1.7	~20	68
Theoretical voltage (V)	1.28	1.65	2.71	3.09	2.27	2.48	2.96
Theoretical energy density (Wh kg ⁻¹)	763	1086	2796	2840	1106	935	3458
Electrolyte for practical batteries	Alkaline	Alkaline	Alkaline or saline	Saline	Aprotic	Aprotic	Aprotic
Practical voltage (V)	~1.0	1.0–1.2	1.1–1.4	1.2–1.4	~2.2	~2.4	~2.6
Practical energy density (Wh kg ⁻¹)	60–80	350–500	350–500	400–700	Unclear	Unclear	Unclear
Primary (P) or rechargeable (R)	R	R	P	P	R	R	R

Reproduced by permission of the Royal Society of Chemistry (<https://pubs.rsc.org/en/content/articlelanding/2014/CS/C4CS00015C#!divAbstract>).

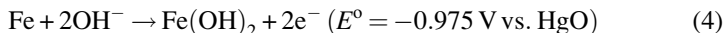
Mg-air and Al-air batteries is the improbability to electrically recharge in aqueous solution thermodynamically. Even though Fe-air batteries possess the lowest theoretical energy density among them, their advantages of long lifecycle and good rechargeability with low production cost have led to increasing research interest. As for Zn-air batteries, high stability as well as good reversibility have seen this system being used in low-rate Zn-air batteries such as watches and hearing aids. However, zinc dendrite formation and shape transformation during the recharge process have huge adverse effects on the battery's capacity retention and lifecycle [6]. Meanwhile, Li-air is the most investigated battery in the metal-air batteries category due to its exceptionally high energy density of 3458 Wh kg^{-1} , which is many times higher than those of Li-ion batteries. However, the high cost of lithium has researchers seeking alternatives such as Na-air and K-air batteries. Nevertheless, the high reactivity of lithium, sodium, and potassium metals continue to raise concerns over safety issues besides incurring higher production cost due to the requirement of sophisticated equipment costs.

As Fe possesses excellent charge/discharge characteristics and inhibits the formation of an undesirable dendritic precipitate upon repetitive charge/discharge cycles, it has good potential in the development of the negative electrode for metal-air batteries [14]. In comparison, other advantages of Fe-air batteries are easier rechargeability, longer lifetime of the negative electrode, and lower susceptibility to corrosion.

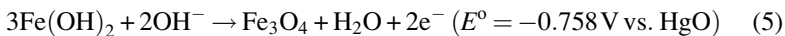
Given the potential practicality of Fe-air batteries, in this chapter the development of Fe-based-air batteries as well as the electrolyte used for this type of battery are discussed. To obtain a good battery performance, the synergy between the negative electrode (anode), electrolyte, and positive electrode (cathode) plays important roles in the overall functionality of the batteries.

2 Fe-air batteries operational principle

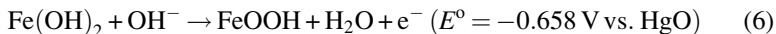
The redox reaction at the surface of the negative electrode during charge/discharge is mainly dependent on the electrochemical reactions of Fe in alkaline aqueous solution. Two steps of chemical reactions are involved, where, the first step is the redox of Fe(OH)_2 and Fe as depicted in Eq. (4):



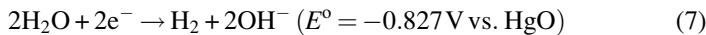
The second step involves the redox reaction of Fe(OH)_2 and FeOOH or Fe_3O_4 as shown in Eqs. (5) and (6):



and/or



As for hydrogen evolution reaction during the charging process, the reaction is shown in Eq. (7):



2.1 Negative electrode (anode)

Commonly, Fe powder or Fe oxide powders, which are supported on a conductive current collector such as carbon or nickel sheets, are used to maximize the effective surface area and conductivity of the working electrode. Although nickel foam is commonly used for many studies, carbon-based conductive electrode is preferred as researchers shift toward the design and fabrication of light-weight portable energy systems for wearable and portable devices.

Although one of the strategies to obtain a large discharge capacity for Fe-air batteries is to increase the amount of active materials such as Fe or Fe oxides in the negative electrode, too high an amount of Fe/Fe oxides loading often leads to specific energy reduction and therefore optimization is very important to achieve a good specific energy density.

Various methods have been investigated to obtain an optimized performance by modifying the negative electrode. From an industrial and practical application viewpoint, fabrication of the battery components should be simplified toward large-scale fabrication with the final goal of enabling low-cost mass production. Methods such as calcination and coprecipitation were reported for the fabrication of Fe-air batteries, which have the potential to meet the market demands for large-scale fabrication [15]. By using calcination and coprecipitation methods, iron sulfide/carbon (FeS/C) composite powder was fabricated and applied as the negative electrode in Ni-Fe batteries. Shangguan et al. obtained a reversible discharge capacity of 331 mAh g^{-1} at a discharge current of 60 mA g^{-1} using a 3 wt.% Bi_2O_3 -added FeS/C, while the faradaic efficiency reported was at 91.9%. Even at a high discharge rate of 1500 mA g^{-1} (5C), a specific capacity of nearly 230 mAh g^{-1} was obtained depicting that 3 wt.% Bi_2O_3 -added FeS/C composite could exhibit a high discharge rate with good cyclic potential [15].

Advancement in IoT has enabled new design and fabrication techniques for the negative electrode. Using 3D printing technology, Figueredo-Rodriguez et al. reported the fabrication of Fe-air battery cell achieving an energy density of 453 Wh kg^{-1} (Fe) using computer numerical control machining [16]. The negative electrode used in their work was fabricated by the molten salt method with the Fe electrode consisting of 95 wt.% Fe-carbon paste (containing 85.7 wt.% Fe_2O_3 corresponding to 60 wt.% Fe, 10 wt.% C, and 4 wt.% Bi_2S_3), which was held together with 5 wt.% polytetrafluoroethylene solution that was hot pressed at 200°C and 12,000 kPa for 1 h. Importantly, they demonstrated the feasibility of rapid modification, cell improvement and new electrode design using 3D printing with high potential to accelerate electrode prototyping in the future.

In another work reported by Hayashi et al., by mixing water-atomized Fe powders (several tens of micrometers in diameter) with polyvinyl alcohol (PVA) as pore former, the authors developed a method to obtain sintered porous Fe negative electrodes for rechargeable Fe-air batteries [17]. Throughout the charge/discharge cycles, the active material in the negative electrode (e.g., Fe and Fe oxides for Fe-air batteries) would undergo significant volume change. Oxidation of Fe to Fe(OH)_2 induces approximately 272% of volume expansion, while further oxidation to Fe_2O_3 causes another 330% of volume increment. Therefore, it is crucial to have a porous design of the Fe electrode to eliminate cavity blockage that would prevent the supply of electrolyte reaching the electrode's active material [11]. In their reported work, the electrodes were fabricated after atomization and sintered under a nitrogen atmosphere at 1120°C for a short time of 20 min to obtain a solidified interconnected electrode structure. With the addition of K_2S , a discharge capacity of 120 mAh g^{-1} was reported. Despite the discharge capacity obtained being lower than those reported in the literature, this method provided an insight into a possible cost-effective fabrication method of Fe electrode for large-scale production. This method is also demonstrated to enable porosity control by changing the size of the incorporated PVA particles during the atomization process [18]. The possible addition of desired elements during the production process can be easily implemented to form desirable metal alloys, which is an added advantage of this method. The steps involved in the formation of the porous Fe electrode with the corresponding surface and cross-sectional microstructural images are shown in Fig. 2. In their subsequent investigation, the effect of the sulfur addition to the atomized Fe powders was also conducted. As for the preparation of sulfur-containing Fe powders, FeS was added to the direct current arc furnace and melted prior to the water atomization process to obtain several tens of micrometers of sulfur-containing Fe powders. The addition of sulfur to the Fe powders improved the charge/discharge characteristics by approximately three times compared to those without sulfur addition for Fe-air batteries [17].

In a different study conducted by Weinrich et al. using a porous-sintered Fe negative electrode without the use of a current collector, the authors reported that the thickness of the pressed carbonyl Fe pellets would affect the performance of the electrode [19]. In their work, the thickness of the electrode was controlled by simply changing the amount of the applied material used in the electrode fabrication. It is also important to note that if a charging capacity is fixed, modification of the electrode thickness does not have an effect on the discharge performance, and in their reported work the steady discharge rate increased with thickness as well as in charge capacities. With a thicker electrode, inactive utilization of the material within the electrode is suggested due to the hydrophobic behavior of added binder.

However, the electrochemical reactions that occur in alkaline aqueous solution (6 M KOH) are reported to activate the initial unreachable electrode material (allowing penetration to access the active material region) through

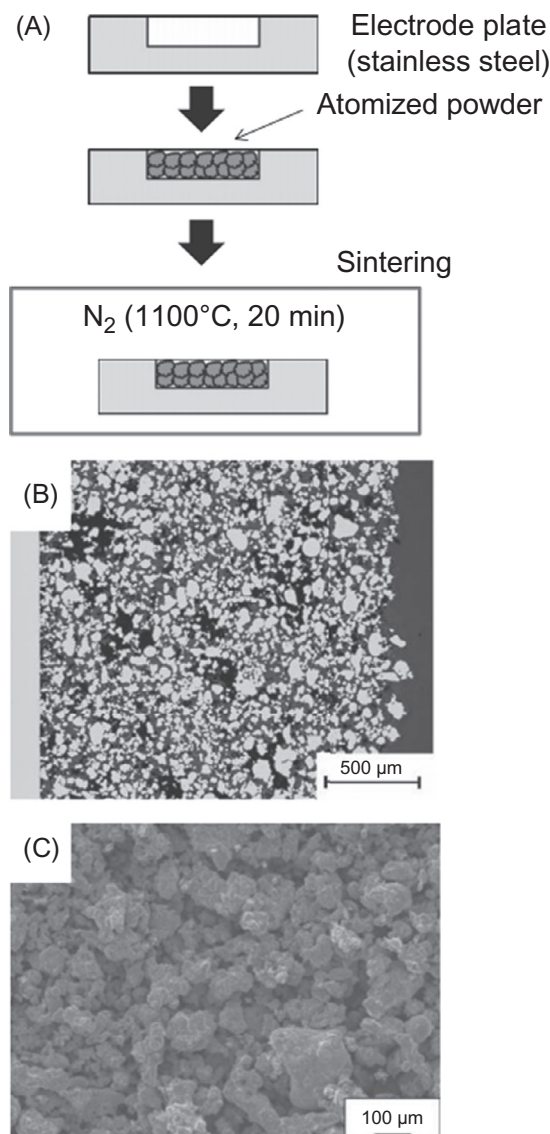


FIG. 2 (A) Fabrication flow of porous-sintered Fe-based negative electrodes. (B) A typical optical microscopy image of the cross-section of the electrode. (C) Surface morphology of the electrodes observed by SEM. Reproduced with copyright permission from K. Hayashi, Y. Wada, Y. Maeda, T. Suzuki, H. Sakamoto, W.K. Tan, G. Kawamura, H. Muto, A. Matsuda, Electrochemical performance of sintered porous negative electrodes fabricated with atomized powders for iron-based alkaline rechargeable batteries, *J. Electrochem. Soc.* 164(9) (2017) A2049–A2055.

progressive wetting of the pores in the inner electrode or partial displacement of the hydrophobic binders. Additionally, the occurrence of particle coarsening due to repeated charge/discharge cycles also overcomes the initial wetting limitation of the inner electrode by the formation of immediate contact between the Fe particles with the electrolyte. A schematic that shows the mechanism proposed in the work of Weinrich et al. is shown in Fig. 3, which demonstrated an enhanced performance of Fe-air batteries using a pressed Fe electrode due to binder displacement as well as improved inner pore volume wettability.

Besides the aforementioned methods, in situ methods for the formation of Fe-based electrodes that are applicable for Fe-air as well as Ni-Fe batteries are also reported. Rajan et al. demonstrated in situ carbon-grafted Fe electrode formation by the decomposition of the $\alpha\text{-FeC}_2\text{O}_4 \cdot 2\text{H}_2\text{O}$ -polyvinyl alcohol

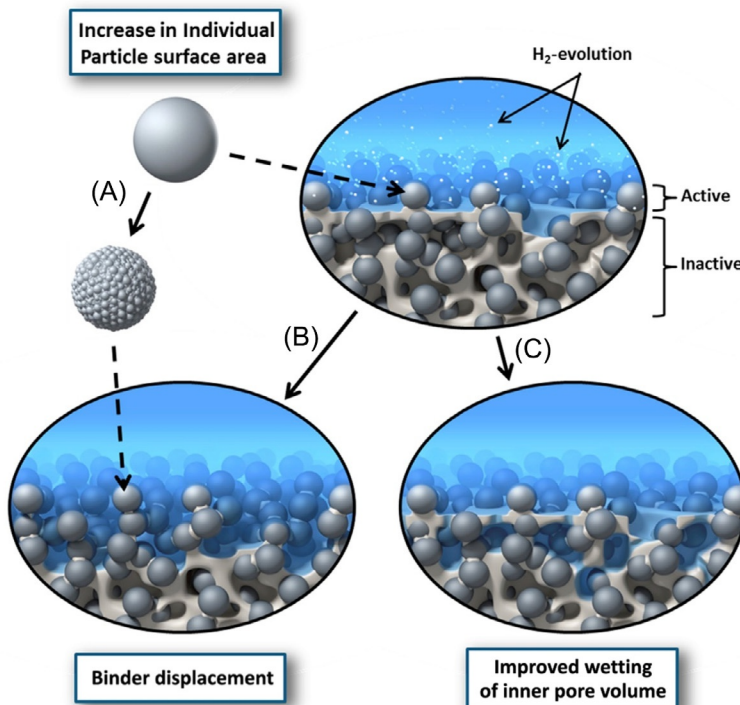


FIG. 3 Schematic representation of the mechanisms behind the electrochemical formation of pressed-plate carbonyl iron electrodes in concentrated alkaline electrolyte. (A) Coarsening of the individual carbonyl iron particles due to repeated charge/discharge. (B and C) Increase in the number of accessible carbonyl iron particles by (B) partial displacement of binder potentially due to hydrogen evolution during the recharge and/or (C) progressive wetting of the inner electrode pore volume. *Reproduced with copyright permission from H. Weinrich, M. Gehring, H. Tempel, H. Kungl, R.-A. Eichel, Electrode thickness-dependent formation of porous iron electrodes for secondary alkaline iron-air batteries, *Electrochim. Acta* 314 (2019) 61–71.*

composite at 600°C in a vacuum environment. The active materials obtained after the in situ reaction consisted of α -Fe and Fe_3O_4 with a prominent presence of α -Fe. In the charge/discharge evaluation, a specific discharge capacity of more than 400 mAh g^{-1} at a current density of 100 mA g^{-1} was achieved demonstrating a faradaic efficiency of 80%. They also managed to demonstrate discharging at both high and low rates while maintaining the achieved faradaic efficiency [20]. The concomitant in situ grafting concept is also investigated by various groups using carbon-based graphitic shell formation (Fe core with an interconnected graphitic network) [33, 40] or intercalation of Fe oxides with reduced graphene oxide (rGO), which can provide a stable structure and platform for longer battery lifecycle.

2.2 Positive electrode (cathode)

The positive electrode (cathode) of metal-air batteries is also one of the core components that plays an important role in battery performance. As this chapter is aimed at the development of the Fe-based negative electrode, only a brief review of the development of the cathode will be mentioned.

At the cathode, the oxidation and reduction of the oxygen from air is converted into OH^- or H_2O and vice versa during oxygen reduction reaction (ORR) and oxygen evolution reaction (OER), respectively. As the positive electrode used is functional for both ORR and OER reactions, it is also known as the bifunctional electrode in the metal-air batteries system. Commonly, noble metals are loaded into the positive electrode due to the requirement for low overpotentials to promote oxygen reduction and evolution. Due to the high cost of noble metals, many researchers are investigating the application of nonnoble metals, that usually involve separate electrocatalyst systems for both ORR and OER under the same electrode configuration [1]. Another important requirement of the positive electrode is strong resistance to the alkaline environments. In an alkaline aqueous Fe-air battery, the common electrolyte used is an aqueous 8 M KOH solution. However, as the interest in all-solid-state metal-air batteries is on the rise, development of solid electrolytes has also attracted attentions.

Recent developments have seen alloys of noble metals being investigated for the ORR and OER of metal-air batteries. The search for new catalysts that can carry out both ORR and OER without the use of noble metals is still ongoing. Perovskite materials are reported to possess the bifunctional properties that are comparable to Pt and Pd, leading to active research and development in these materials [21]. Due to the restricted conductivity of the bifunctional oxygen catalyst, conductive supporting materials are commonly applied or mixed in order to improve the conductivity of the positive electrode.

There are also studies that reported the use of layered double hydroxides (LDHs) such as Ni-Fe LDHs for intercalation with multifunctional inorganic materials, which served multiple roles in the catalyst layer as a mixed conductor

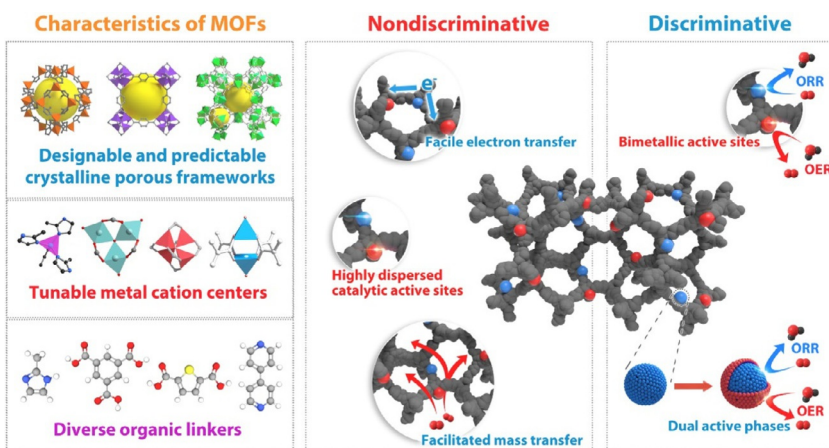


FIG. 4 Schematic showing the prominent characteristics of MOFs and the utilization of these characteristics to improve their bifunctional catalytic performance in metal-air batteries. *Reproduced with copyright permission from B. Zhu, Z. Liang, D. Xia, R. Zou, Metal-organic frameworks and their derivatives for metal-air batteries, Energy Storage Mater 23 (2019) 757–771.*

for hydroxide ions, electrons, as well as electrocatalysts. Kubo et al. demonstrated a superior performance achieved using the Ni-Fe CO_3^{2-} LDH as the air electrode in comparison with several other LDHs. Their findings indicated that Ni-Fe CO_3^{2-} LDH formed a more favorable triple-phase region in the air electrode's catalyst layer [22].

Recent development also involves the usage of metal-organic frameworks (MOFs) and their derivatives as bifunctional cathodes [23]. MOFs, as shown in Fig. 4, possess unique properties such as crystalline porosity with tunable chemical properties. With the controlled design of MOFs, catalysts with a porous network exhibiting a large surface area can promote smooth electron and mass transfer pathways besides providing preferred active sites for different catalytic processes.

2.3 Electrolyte

In the commonly used alkaline aqueous metal-air batteries, aqueous KOH is used as the electrolyte due to its good electrical conductivity, while not being too corrosive to Fe. However, drawbacks such as irreversibility of OH^- ion conduction, fast capacity decay and electrode deformation still remain as challenges, not to mention the occurrence of hydrogen evolution reaction during battery charging.

To inhibit hydrogen evolution reaction (HER), the addition of bismuth sulfide or sulfide compounds into the negative electrode as well as utilization of high-purity Fe have been reported [20, 24–26]. As the suppression of HER still

remains a difficult challenge, another alternative is to modify the negative Fe electrode [5]. Hayashi et al. investigated the suppression of HER by adding different types of additives such as K₂S, LiOH, and Bi₂S₃ to an alkaline 8 M KOH aqueous electrolyte in their evaluation of rechargeable Fe-air batteries. The negative electrode used in their studies consisted of a porous metallic Fe fabricated via Fe powder atomization, while the electrolyte was either added with K₂S, LiOH, or Bi₂S₃. It was reported that K₂S-added electrolyte exhibited two times higher the discharge capacity of those obtained using LiOH- or Bi₂S₃-added electrolyte [17, 18].

In a recent work reported by McKerracher et al., the authors reported the effect of 1-octanethiol addition to the electrolyte. As for the active materials in their negative electrode, a composite was prepared via ball milling of Fe₂O₃ with Ketjenblack carbon. From their results, the ratio of Fe/C to 1-octanethiol in the battery system had a significant impact on the charge/discharge capacity of the electrode. The presence of 1-octanethiol in the electrolyte inhibited electrode passivation during discharge, and during a high discharge rate of 2C, the electrode's specific capacity was reported to improve 10 times from 17 to 171 mAh g⁻¹ (Fe) [11]. Interestingly, they also demonstrated that the crystallinity of Fe₂O₃ nanoparticles remained without much crystal growth observed, underlining the potential for application in Fe-air batteries with long cyclic stability.

Although a relatively higher discharge capacity is obtained using an alkaline aqueous solution system, its bulkiness, heavier weight, as well as leakage risk continue to hamper its application for portable electronic and wearable devices. Besides the possibility of mitigating HER, the usage of solid-state electrolytes can also eliminate the issues linked with electrolyte dissipation and gas crossover. Therefore, in the development of all-solid-state metal-air batteries, the improvement and development of solid-state electrolyte is indispensable to achieve a high energy density for portable and flexible wearable devices. An ideal solid electrolyte should possess good ionic conductivity, a wide potential range, good chemical stability, as well as good interfacial contact with the electrodes and the solid electrolyte. The study and design of the physical and mechanical properties of the solid electrolytes are also vital to obtain a robust structure for accommodating the cyclic expansion and shrinkage that will significantly affect interface connectivity within the all-solid-state Fe-air batteries [2]. The change of particle size during the transition between Fe₂O₃ and Fe₃O₄ throughout the continuous cyclic charge/discharge process will result in volume fluctuation causing interfacial disconnection between the electrode/electrolyte as well as electrode/conductor interface leading to poor electrical conductivity [2, 16]. Research into the development of electrolyte, especially for Zn-air batteries has been actively carried out as Zn electrode is more susceptive toward corrosion and dendrite formation. Besides solid-state electrolytes, the development of other types of non-aqueous electrolytes such as ionic liquid electrolytes

[27], polymer gel electrolytes [28], and solid polymer electrolytes [29] have also gained pace recently.

Not many works have been reported for the development of all-solid-state electrolytes for Fe-air batteries. In a study reported by Matsuda et al., formation of an all-solid-state KOH-ZrO₂ electrolyte using the sol-gel method was investigated. The produced KOH-ZrO₂ solid electrolyte that exhibited a high ionic conductivity (9×10^{-3} S cm⁻¹ at 20°C and 60% relative humidity) as well as moisture resistance. As for the transport mechanism, the hydroxide ions were considered to be the main charge carrier from the potentials of the water vapor concentration cells. The KOH-ZrO₂ solid electrolyte obtained was mixed with Fe powders and carbon black for fabrication of the all-solid-state Fe-air batteries that exhibited charge/discharge characteristics [30].

3 Current progress of Fe-air batteries

In the design of the anode for Fe-air batteries, the three main factors that are taken into consideration are the maximization of Fe/Fe oxides utilization at the negative electrode, inhibition of Fe passivation, and the suppression of the HER during the charging process [19]. There are various methods being implemented to improve the aforementioned factors.

In an effort to improve the utilization of Fe/Fe oxides, submicro or nano-sized Fe/Fe oxide particles are used to increase the effective surface area enabling higher accessibility of the electrolyte to the negative electrode's active materials. In a recently reported work, Tan et al. demonstrated on a fast and facile deposition of submicron-sized Fe₃O₄ particles onto carbon paper in just 10 min. The Fe₃O₄ particles decorated carbon paper was used as the negative electrode for both alkaline solution and all-solid-state rechargeable Fe-air batteries. Although the alkaline-solution-based system exhibited a high initial discharge capacity, the cyclic performance was rather poor due to the detachment of the Fe₃O₄ particles from the surface of the carbon paper throughout the charge/discharge process [2]. The weaved structure of carbon paper provided a good platform with large surface area for the adsorption of Fe₃O₄ particles. The porous-like microstructure of the Fe₃O₄ particle-decorated carbon paper also allowed the penetration and sufficient mass transport of OH⁻ ions from the electrolyte to reach the active materials in the negative electrode.

In an effort to inhibit HER and to improve the charge efficiency of the electrode, investigation using additive compounds such as Bi₂S₃, Bi₂O₃, FeS, and Na₂S were reported. For example, a mixture that consisted of carbonyl Fe with bismuth obtained by in situ electrodeposition, was reported to reduce the hydrogen evolution rate by 10 times with a charge efficiency of 96%. This was due to the suppression of HER by bismuth, while the generated FeS promoted high discharge rates during the charge/discharge cycles. The presence of sulfur promoted the formation of FeS that reduced the passivation effect caused by the formation of the Fe(OH)₂ passive layer on the surface [31].

To provide a detailed insight into the phenomenon that occurs during redox reaction under a concentrated alkaline environment, Weinrich et al. investigated the charge-transfer reactions that occurred at the negative electrode/electrolyte interface using a 0.5 M KOH [12]. Their analysis was carried out using an *in situ* electrochemical atomic force microscopy, which enabled the observation of the formation and growth of the redox layer on Fe surface during charge/discharge cycles. Their findings and revelation are crucial as they provided an in-depth insight for the understanding of the Fe electrochemical reactions that occurred involving the parallel Fe oxides particle growth and the thin passivating layer formation on the Fe metal's surface in an alkaline aqueous solution. Fig. 5 shows the illustration that depicts the mechanism for the redox layer formation in a concentrated alkaline solution under a repeated potentiodynamic redox reaction. In the formation of the redox layer, they reported that both oxidation and reduction processes resulted in the growth of nanoscale Fe particles (Fig. 5A). Simultaneous to the particle growth during the oxidation process, a thin homogeneous passive layer was also formed on the Fe metal's surface inhibiting further oxidation. As the passive layer formed was reversible (Fig. 5B), partial depassivation was achieved during a repeated reduction reaction. The repetitive redox loop led to the particulate growth in size and amount but did not indicate the formation of a dense passivating layer, instead, a thin homogenous surface that was parallel to the Fe electrode was generated (Fig. 5C and D).

From the aforementioned observation, during the discharge process according to Eq. (3), oxidation of the Fe electrode to $\text{Fe}(\text{OH})_2$ is thought to occur via an intermediate dissolved species of HFeO_2^- . The reaction of HFeO_2^- with OH^- ions then forms an $\text{Fe}(\text{OH})_2$ passive layer on the surface of the metal. The presence of passive $\text{Fe}(\text{OH})_2$ would affect the subsequent charge/discharge cycles of the Fe-air batteries due to the insulative behavior. In addition, the occurrence of HER during charging also reduces the cell potential. The addition of aliphatic sulfides such as Bi_2S_3 , K_2S , and Na_2S to the negative electrode or the electrolyte are reported to inhibit the formation of the passivating $\text{Fe}(\text{OH})_2$ layer [17, 18, 24].

For battery application, one of the important parameters is the cyclic performance. To improve on the cyclic performance of metal-air batteries, one of the strategies employed by researchers is to embed the active materials such as Fe or Fe oxides within a framework of highly conductive material such as tubular carbon nanofiber (TCNF) [32], graphitic shell [33], or rGO [34–36]. This design not only provides a stable encapsulating structure to prevent the detachment or desorption of active materials (Fe/Fe oxides), but also provides a conductive pathway for electron transfer besides improving the mechanical robustness of the microstructure. Kim et al. reported the formation of Fe nanoparticle-entrained TCNF by impregnation of Fe precursor ions into the TCNF via the fractures that existed on TCNF. Interestingly, the dissolution and redeposition process that occurred during the prolonged electrochemical process resulted in

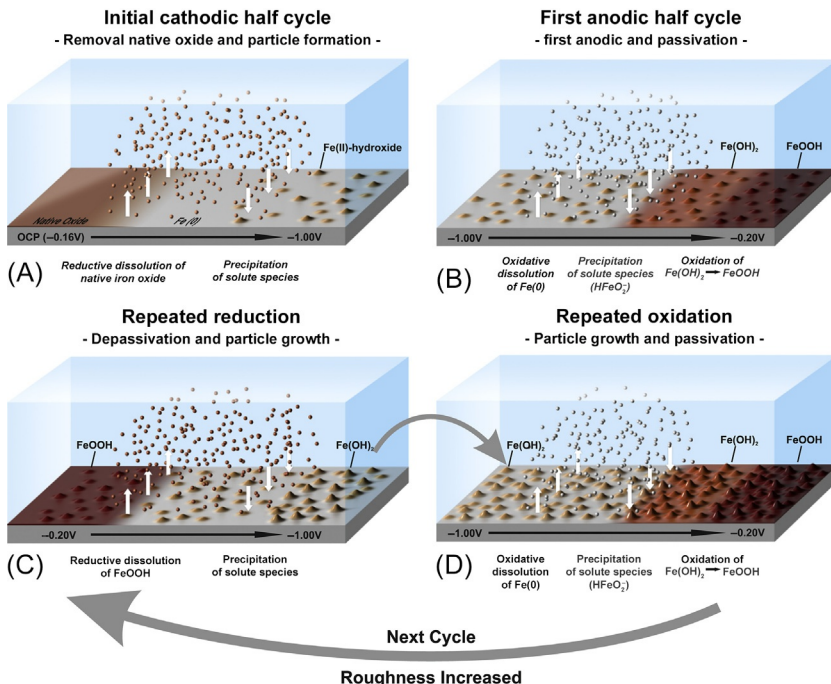


FIG. 5 Schematic representation of the evolution of the redox layer on iron in concentrated alkaline electrolyte due to consecutive electrochemical cycling. Image (A) depicts the evolution of the iron electrode surface for the initial cathodic half cycle during which the native iron oxide layer is reductively dissolved resulting in the formation of hydrated iron(II) oxide particles. Image (B) shows the topographic evolution for the first anodic half cycle during which $\text{Fe}(0)$ is oxidatively dissolved from the iron electrode forming an FeOOH redox layer by the precipitation of HFeO_2^- and the subsequent oxidation of $\text{Fe}(\text{OH})_2$ to FeOOH . Images (C) and (D) represent the evolution of the redox layer over the course of additional electrochemical redox cycles. Similar to the processes in images (A) and (B), first, the iron electrode is depassivated and subsequently oxidized leading to the continuous growth of the particulate surface layer and the increase in electrode roughness. Reproduced with copyright permission from H. Weinrich, J. Come, H. Tempel, H. Kungl, R.-A. Eichel, N. Balke, Understanding the nanoscale redox-behavior of iron-anodes for rechargeable iron-air batteries, *Nano Energy* 41 (2017) 706–716.

the formation of elongated oxygen-lean Fe nanoparticles allowing fast 1D mass transfer of the soluble Fe species within the CNF [32]. However, they only reported on the cyclic electrochemical performance of the negative electrode and did not evaluate its performance for Fe-air batteries. Further investigation and development for a controlled Fe precursor penetration through the fracture, which serves as the “nanogate,” will be beneficial for future design of Fe-confined CNF for stable metal-air batteries.

Meanwhile, Xu et al. reported on the formation of a high-performance Fe anode using a simple chemical precipitation method. The Fe nanoparticles were encapsulated within a graphitic shell demonstrating a good robust structure to retard the growth and structural deterioration of the Fe nanoparticles during

charge/discharge process. After 1000 cycles, an impressive high discharge capacity of 224 mAh g^{-1} at a high current density of 32 A g^{-1} with a high capacity retention of 90% was reported in their work. Recent progress and findings have indicated the importance of 2D structured carbon materials for the design of negative electrodes. The rapid development of 2D rGO has attracted tremendous attention especially in the development of Li-ion batteries, setting up a new platform for further advancement in other battery applications such as metal-air batteries [35, 37].

In a recent study reported using rGO for Ni-Fe batteries, Liu et al. demonstrated the usage of a novel $\text{Fe}_{(1-x)}\text{S}/\text{rGO}$ composite as the active material in the negative electrode achieving a specific capacity of $320\text{--}120 \text{ mAh g}^{-1}$ using a current density ranging from $0.3\text{--}10 \text{ A g}^{-1}$, respectively. The $\text{Fe}_{(1-x)}\text{S}$ -wrapped rGO sheets provided a compact sheet/particle interface and significantly improved the conductivity of the anode electrode. Also, the wrapping of $\text{Fe}_{(1-x)}\text{S}$ particles within the rGO sheets was reported to inhibit the crystal transformation and prevent the aggregation/dissolution of the $\text{Fe}_{(1-x)}\text{S}$ composite. As a result, a long cyclic performance of 100 cycles with capacity retention of 83.3% was obtained at 1 A g^{-1} [36]. The morphologies and charge/discharge curves obtained by Liu et al. are shown in Figs. 6 and 7, respectively.

In a recent investigation aimed at preventing Fe electrode passivation and to inhibit HER, Aremu et al. have reported on the effect of MoS_2 presence in the negative electrode by using a high-purity carbonyl Fe- MoS_2 composite electrode [38]. By varying the amount of MoS_2 added, they obtained good battery performances utilizing carbonyl Fe anodes that comprised of 3, 5, and 10 wt.% MoS_2 additives in the negative electrode. The electrolyte used in their investigation was 2 mM Na_2S -added 6 M KOH electrolyte solution with 1.88 wt.% polyacrylic acid as the gelling agent. Owing to the anodically and cathodically active behavior of MoS_2 , both Fe passivation and HER were reported to be mitigated. Interestingly, the MoS_2 -added electrode was also reported to be able to deliver higher than theoretical initial capacity. Moreover, doping of MoS_2 into the metal electrode was reported to improve conductivity as well as charge/discharge characteristics, while reducing the generated compressive stress [38, 39]. The emergence of MoS_2 as a good additive will be beneficial toward the development of electrode materials for Fe-air and metal-air batteries.

Table 2 summarizes the development of the anode materials as well as the methods used for Fe-air and Ni-Fe batteries.

4 Future outlook and challenges

A battery with reliable performance should possess important characteristics such as long charge/discharge lifecycle up to 5000 cycles with a good efficiency of 80%. Further development in this area is necessary as the current advanced Fe-air batteries only exhibit an efficiency of approximately 50%, up to 2000 lifecycles [1]. Although precise control of the active material formation is deemed to be the key toward further advancement of Fe-air batteries, recent

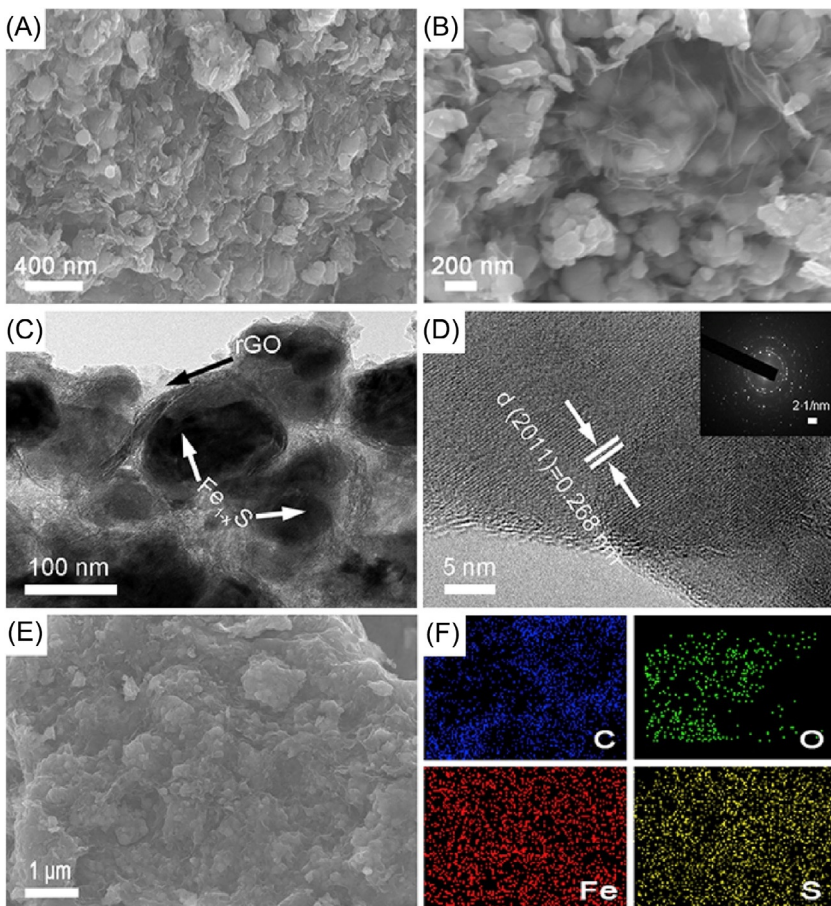


FIG. 6 (A) Normal and (B) enlarged SEM images of the $\text{Fe}_{(1-x)}\text{S}@\text{rGO}$ composite. (C) TEM and (D) HR-TEM images of the $\text{Fe}_{(1-x)}\text{S}@\text{rGO}$ composite along with an inset showing the corresponding SAED pattern. (E) SEM image and (F) corresponding EDS mappings of the $\text{Fe}_{(1-x)}\text{S}@\text{rGO}$ composite. Reproduced with copyright permission from X. Liu, Q. Yang, M. Mi, W. Kong, Y. Ge, J. Ma, J. Hu, *Fe1-S/reduced graphene oxide composite as anode material for aqueous rechargeable Ni/Fe batteries*, *J. Alloys Compd.* 800 (2019) 99–106.

research developments have indicated feasible approaches to achieve an enhanced battery performance. With the aim to gain a breakthrough toward superior battery performance, fundamental investigations involving electrochemical reactions at the interfacial surface have been actively carried out. The indepth understanding allows the modification of the reaction path through materials engineering to achieve better interphase connectivity, inhibition of passive layer formation and hydrogen evolution reduction are vital for further development of Fe-air batteries. The discovery of new electrolyte additives and

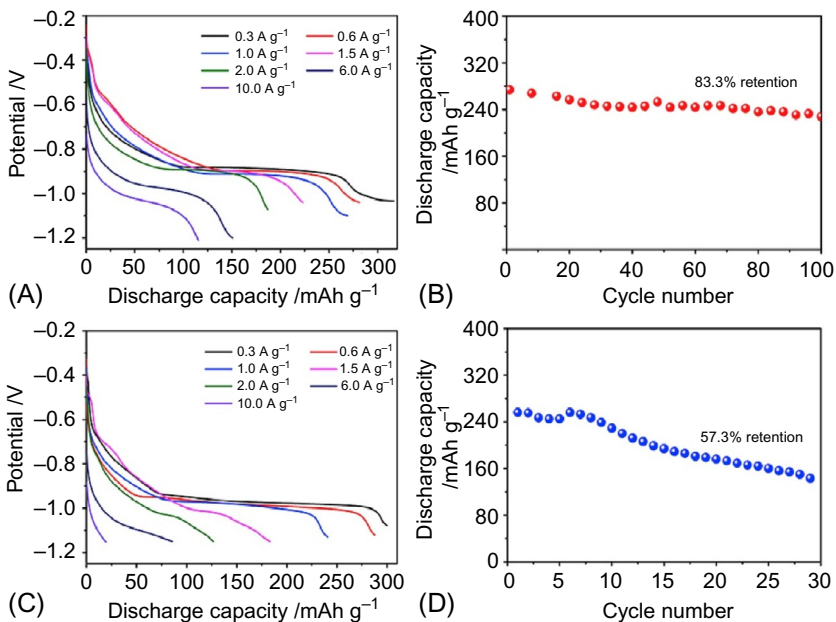


FIG. 7 Discharge curves of (A) the optimized $\text{Fe}_{(1-x)}\text{S}@\text{rGO}$ electrode and (C) the $\text{Fe}_{(1-x)}\text{S}$ electrode at different current densities and cyclic stability tests of (B) the $\text{Fe}_{(1-x)}\text{S}@\text{rGO}$ electrode and (D) the $\text{Fe}_{(1-x)}\text{S}$ electrode at a current density of 1.0 A g^{-1} . Reproduced with copyright permission from X. Liu, Q. Yang, M. Mi, W. Kong, Y. Ge, J. Ma, J. Hu, $\text{FeI-S/reduced graphene oxide composite as anode material for aqueous rechargeable Ni/Fe batteries}$, *J. Alloys Compd.* 800 (2019) 99–106.

timely incorporative techniques may allow the recovery of the initial discharge capacity of the batteries, thus, improving their lifespan [40]. In the age of IoT, the incorporation of a smart replenishment system that allows automated additives refill when a battery's discharge capacity has reached a preset lower limit can be easily implemented. In the overall development of Fe-air batteries, the synergistic improvisation of the active materials, design of the negative electrode, electrolyte's composition (aqueous and solid state) as well as the development of the bifunctional positive electrode are indispensable toward fabrication of robust rechargeable next generation batteries.

The rechargeability of the current metal-air batteries are still insufficient (coulombic efficiency) and suffer from fast capacity decay. Therefore, the design of materials used in the negative electrode as well as the predetermined additives are keys to improving the reversibility and reducing the formation of unfavorable passive layers. In the development of metal-air batteries, most researchers are focused on the development of materials and design of either the electrodes (metal or air), electrolyte, or separator. Several studies have been conducted on the cell configuration, which is one of the alternatives to overcome some of the challenges and limitations faced using current systems

TABLE 2 Recent development of Fe-based anode materials used in Fe-air and Ni-Fe batteries.

No.	Methods	Materials used and the structure of the anodes	Reported characteristics	References
1.	Calcination and coprecipitation	FeS/C composite powder (Ni-Fe batteries)	<ul style="list-style-type: none">• A reversible discharge capacity of 331 mAhg^{-1} at a discharge current density of 60 mA g^{-1} using a 3 wt.% Bi_2O_3-added FeS/C• High faradaic efficiency of 91.9%• Even at a high discharge rate of 1500 mA g^{-1} (5C), a specific capacity of nearly 230 mAhg^{-1} was achieved	[15]
2.	3D printing	Molten salt Fe electrode with 95 wt.% Fe-carbon paste (containing 85.7 wt.% Fe_2O_3 corresponding to 60 wt.% Fe, 10 wt.% C, and 4% wt.% Bi_2S_3)	<ul style="list-style-type: none">• An energy density of 453 Wh kg^{-1} was obtained using the electrode fabricated by computer numerical control machining	[16]
3.	Water atomization	Sintering of water-atomized Fe powders (several tens of micrometers in diameter) with polyvinyl alcohol as pore former	<ul style="list-style-type: none">• Sulfur addition improved the charge/discharge performance• The discharge capacities for the Fe electrodes with sulfur increased gradually and reached 200 mAhg^{-1} at the 15th cycle, and remained consistent up to 25 cycles with the coulombic efficiency of approximately 100%	[17]
4.	Vacuum decomposition	In situ carbon-grafted Fe electrode by decomposition of the $\alpha\text{-FeC}_2\text{O}_4 \cdot 2\text{H}_2\text{O}$ -polyvinyl alcohol composite at 600°C in a vacuum environment	<ul style="list-style-type: none">• A specific discharge capacity $>400 \text{ mAhg}^{-1}$ was obtained at a current density of 100 mA g^{-1} with a faradaic efficiency of 80%• High and low rates discharged were confirmed without losing much of the achieved faradaic efficiency	[20]

5.	Adams and oxalate methods	Hot-pressed Fe-C electrodes made from an Fe_2O_3 mixture, $\text{Fe}_2\text{O}_3/\text{C}$, with 4 wt.% bismuth sulfide hydrogen evolution inhibition	<ul style="list-style-type: none"> The effects of the Fe to C ratio, the use of K_2CO_3 as pore-forming agent, and the addition of 1-octanethiol for HER and passivation inhibition were reported $\text{Fe}_2\text{O}_3/\text{C}$ electrodes with a medium-low Fe to C mass ratio (0.7 or 2.0) provided equally good discharge capacity of approximately 650 mAh g^{-1} The Fe/C ratio of 2.0 was preferred for battery design due to density difference of Fe and C which caused volume increment High ratio of $\text{Fe}/\text{C} = 5.7$ decreased the capacity of the electrode due to the low amount of conductive carbon Addition of 1-octanetiol to the electrolyte improved the electrode performance at high current densities 	[11]
6.	Electrostatic adsorption	Carbon paper decorated with submicron-sized Fe_3O_4 particles	<ul style="list-style-type: none"> A high initial discharge capacity of 460 mAh g^{-1} was achieved using alkaline aqueous solution The discharge capacity reduced drastically at the 15th cycle due to the detachment of the Fe_3O_4 particles Improved cyclic performance in the all-solid-state Fe-air batteries using KOH-ZrO_2 solid electrolyte despite lower discharge capacity was obtained 	[2]

Continued

TABLE 2 Recent development of Fe-based anode materials used in Fe-air and Ni-Fe batteries—cont'd

No.	Methods	Materials used and the structure of the anodes	Reported characteristics	References
7.	Chemical impregnation method	Fe nanoparticle-loaded tubular carbon nanofiber (TCNF) tubes and commercial carbon nanotubes (CCNTs)	<ul style="list-style-type: none">● Observation of Fe precursor ions penetrating into TCNF tubes through the fractures between the structural units, which was absent in CCNTs● During electrochemical dissolution and redeposition processes, Fe nanoparticles evolved into elongated oxygen-lean Fe nanoparticles in the confined space of TCNF tubes and to oxygen-rich Fe oxide dendrites on CCNTs● The dendrites on CCNTs needed a higher overpotential for a dissolution and redeposition process● The mass transfer of soluble Fe species was faster (lower overpotential of elongated oxygen-lean Fe nanoparticles) in the confined space of TCNF tubes than in the open space between CCNTs leading to a higher efficiency of Fe nanoparticles loaded on TCNF for battery application	[32]
8.	Decomposition of homogeneous Fe salt polymeric complexes	Graphitic carbon-coated Fe nanoparticles	<ul style="list-style-type: none">● Robust graphitic carbon-coated Fe particles exhibited good conductivity	[33]

			<ul style="list-style-type: none"> • Retardation of Fe nanoparticle degradation during the cyclic charge/discharge process • A high-energy, power density, and high cyclic performance of Fe anode was reported for Ni-Fe batteries • An impressive high capacity of 224 mAh g^{-1} at a high current density of 32 Ag^{-1} exhibiting a good capacity retention of 90% after 1000 cycles was reported • When the graphitic carbon-coated Fe particles were coupled with a cathode fabricated using composites of Ni(OH)_2 and nitrogen-doped graphene, the battery delivers a high energy density of 136.7 Wh kg^{-1} at a power density of 0.7 kW kg^{-1} or 71.4 Wh kg^{-1} at 11.7 kW kg^{-1} 	
9.	Chemical precipitation of reduced graphene oxide (rGO) (obtained by Hummers' method) using Fe precursor	A highly conductive rGO sheet wrapped in $\text{Fe}_{(1-x)}\text{S}$ particle composites	<ul style="list-style-type: none"> • A compact sheet/particle interface that significantly improved the conductivity of the anode • The $\text{Fe}_{(1-x)}\text{S}$ particle sheets were embedded within the rGO sheets inhibited change in the crystal unit cell as well as the aggregation/dissolution of the $\text{Fe}_{(1-x)}\text{S}$ particle sheets • Aqueous Ni-Fe batteries fabricated using the $\text{Fe}_{(1-x)}\text{S}/\text{rGO}$ composite as the anode achieved specific capacities of $320\text{--}120 \text{ mAh g}^{-1}$ using current densities of $0.3\text{--}10 \text{ Ag}^{-1}$, respectively • A good cyclic performance of 100 cycles with initial capacity retention of 83.3% was obtained at 1 Ag^{-1} 	[36]

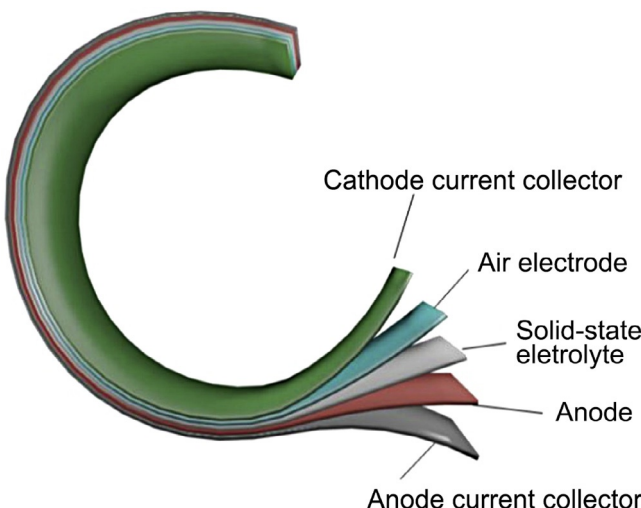


FIG. 8 Schematic showing a plausible, flexible, metal-air battery for wearable devices with the development of an all-solid-state system. Reproduced with copyright permission from Q. Liu, Z. Pan, E. Wang, L. An, G. Sun, *Aqueous metal-air batteries: fundamentals and applications*, *Energy Storage Mater.* 27 (2019) 487–505.

[27]. For example, the circulation of electrolyte in a flow battery system can solve or mitigate the problem related with the passive layer formation as well as eliminate the need for constant monitoring of the electrolyte compared to a stagnant system. Therefore, the design and cell configuration that can fully effectuate the advantages of materials design is also important to in order to maximize the potential of metal-air batteries.

As to power lightweight wearable devices, light and flexible metal-air batteries are envisioned, and therefore, many researchers are focusing on the development of robust all-solid-state metal-air batteries. With the rapid progress in IoT and wearable gadgets, flexible metal-air batteries as shown in Fig. 8 have a promising prospect to be a reliable power source.

5 Conclusions

From the progress and current development of the core components in metal-air batteries, this battery system holds good potentials for next-generation energy storage applications due to its achievable energy densities. The understanding of the active materials' (Fe/Fe oxides) electrochemical redox reactions in the Fe-based negative electrodes is crucial for the micro/nanoarchitectural materials design and optimization process. Integrated detailed studies of the battery's operating system (electrode/electrolyte and electrode/current collector interface) as a whole are also indispensable to achieve a good synergistic performance as any weak link within the core components will hamper the battery's

performance. As the development of metal-air batteries involve interdisciplinary fundamental and comprehensive understanding from various fields, a strong collaboration between researchers with different expertise backgrounds is essential to promote the advancement of metal-air batteries toward a more sustainable and pragmatic manner.

Acknowledgment

This work was partly supported by the Japan Society for the Promotion of Science (JSPS) Grant-in-Aid for Scientific Research JP17K18985 and JSPS KAKENHI Early-Career Scientist JP18K14013.

Technical consultation of Dr. Kazushi Hayashi and Dr. Hisatoshi Sakamoto is acknowledged during research collaboration between TUT and Kobe Steel Ltd.

References

- [1] R.D. McKerracher, C. Ponce de Leon, R.G.A. Wills, A.A. Shah, F.C. Walsh, A review of the iron-air secondary battery for energy storage, *ChemPlusChem* 80 (2) (2015) 323–335.
- [2] W.K. Tan, K. Asami, Y. Maeda, K. Hayashi, G. Kawamura, H. Muto, A. Matsuda, Facile formation of Fe_3O_4 -particles decorated carbon paper and its application for all-solid-state rechargeable Fe-air battery, *Appl. Surf. Sci.* 486 (2019) 257–264.
- [3] N. Chawla, Recent advances in air-battery chemistries, *Mater. Today Chem.* 12 (2019) 324–331.
- [4] Q. Liu, Z. Pan, E. Wang, L. An, G. Sun, Aqueous metal-air batteries: fundamentals and applications, *Energy Storage Mater.* 27 (2019) 487–505.
- [5] S.R. Narayanan, G.K.S. Prakash, A. Manohar, B. Yang, S. Malkhandi, A. Kindler, Materials challenges and technical approaches for realizing inexpensive and robust iron–air batteries for large-scale energy storage, *Solid State Ionics* 216 (2012) 105–109.
- [6] W.K. Tan, Y. Wada, K. Hayashi, G. Kawamura, H. Muto, A. Matsuda, Fabrication of an all-solid-state Zn-air battery using electroplated Zn on carbon paper and KOH-ZrO₂ solid electrolyte, *Appl. Surf. Sci.* 487 (2019) 343–348.
- [7] J.-S. Lee, S. Tai Kim, R. Cao, N.-S. Choi, M. Liu, K.T. Lee, J. Cho, Metal-air batteries with high energy density: Li-air versus Zn-air, *Adv. Energy Mater.* 1 (1) (2011) 34–50.
- [8] M. Nestoridi, D. Pletcher, R.J.K. Wood, S. Wang, R.L. Jones, K.R. Stokes, I. Wilcock, The study of aluminium anodes for high power density Al/air batteries with brine electrolytes, *J. Power Sources* 178 (1) (2008) 445–455.
- [9] Y. Wang, H.Y.H. Kwok, W. Pan, Y. Zhang, H. Zhang, X. Lu, D.Y.C. Leung, Printing Al-air batteries on paper for powering disposable printed electronics, *J. Power Sources* 450 (2020) 227685.
- [10] Y. Wang, W. Pan, H.Y.H. Kwok, H. Zhang, X. Lu, D.Y.C. Leung, Liquid-free Al-air batteries with paper-based gel electrolyte: a green energy technology for portable electronics, *J. Power Sources* 437 (2019) 226896.
- [11] R.D. McKerracher, H.A. Figueiredo-Rodriguez, C. Alegre, A.S. Aricò, V. Baglio, C. Ponce de León, Improving the stability and discharge capacity of nanostructured $\text{Fe}_2\text{O}_3/\text{C}$ anodes for iron-air batteries and investigation of 1-octanethiol as an electrolyte additive, *Electrochim. Acta* 318 (2019) 625–634.

- [12] H. Weinrich, J. Come, H. Tempel, H. Kungl, R.-A. Eichel, N. Balke, Understanding the nano-scale redox-behavior of iron-anodes for rechargeable iron-air batteries, *Nano Energy* 41 (2017) 706–716.
- [13] Y. Li, H. Dai, Recent advances in zinc-air batteries, *Chem. Soc. Rev.* 43 (15) (2014) 5257–5275.
- [14] C. Ding, X. Huang, H. Zhang, W. Zhong, Y. Xia, C. Dai, Y. Qin, J. Zhu, Self-assembled porous $\text{Fe}_3\text{O}_4/\text{C}$ nanoclusters with superior rate capability for advanced lithium-ion batteries, *J. Mater. Sci. Mater. Electron.* 29 (8) (2018) 6491–6500.
- [15] E. Shangguan, F. Li, J. Li, Z. Chang, Q. Li, X.-Z. Yuan, H. Wang, FeS/C composite as high-performance anode material for alkaline nickel–iron rechargeable batteries, *J. Power Sources* 291 (2015) 29–39.
- [16] H.A. Figueredo-Rodríguez, R.D. McKerracher, M. Insausti, A.G. Luis, C.P. de León, C. Alegre, V. Baglio, A.S. Aricò, F.C. Walsh, A rechargeable, aqueous iron air battery with nanostructured electrodes capable of high energy density operation, *J. Electrochem. Soc.* 164 (6) (2017) A1148–A1157.
- [17] K. Hayashi, Y. Wada, Y. Maeda, T. Suzuki, H. Sakamoto, W.K. Tan, G. Kawamura, H. Muto, A. Matsuda, Electrochemical performance of sintered porous negative electrodes fabricated with atomized powders for iron-based alkaline rechargeable batteries, *J. Electrochem. Soc.* 164 (9) (2017) A2049–A2055.
- [18] K. Hayashi, Y. Wada, Y. Maeda, T. Suzuki, H. Sakamoto, W.K. Tan, G. Kawamura, H. Muto, A. Matsuda, Development of iron-based rechargeable batteries with sintered porous Iron electrodes, *ECS Trans.* 75 (18) (2017) 6.
- [19] H. Weinrich, M. Gehring, H. Tempel, H. Kungl, R.-A. Eichel, Electrode thickness-dependent formation of porous iron electrodes for secondary alkaline iron-air batteries, *Electrochim. Acta* 314 (2019) 61–71.
- [20] A.S. Rajan, S. Sampath, A.K. Shukla, An in situ carbon-grafted alkaline iron electrode for iron-based accumulators, *Energy Environ. Sci.* 7 (3) (2014) 1110.
- [21] A. Grimaud, K.J. May, C.E. Carlton, Y.L. Lee, M. Risch, W.T. Hong, J. Zhou, Y. Shao-Horn, Double perovskites as a family of highly active catalysts for oxygen evolution in alkaline solution, *Nat. Commun.* 4 (2013) 2439.
- [22] D. Kubo, K. Tadanaga, A. Hayashi, M. Tatsumisago, Multifunctional inorganic electrode materials for high-performance rechargeable metal–air batteries, *J. Mater. Chem. A* 1 (23) (2013) 6804–6809.
- [23] B. Zhu, Z. Liang, D. Xia, R. Zou, Metal-organic frameworks and their derivatives for metal-air batteries, *Energy Storage Mater* 23 (2019) 757–771.
- [24] B.T. Hang, D.H. Thang, Effect of additives on the electrochemical properties of $\text{Fe}_2\text{O}_3/\text{C}$ nanocomposite for Fe/air battery anode, *J. Electroanal. Chem.* 762 (2016) 59–65.
- [25] B. Tian, J. Świątowska, V. Maurice, S. Zanna, A. Seyeux, P. Marcus, The effect of Na_2S additive in alkaline electrolyte on improved performances of Fe-based air batteries, *Electrochim. Acta* 259 (2018) 196–203.
- [26] A.K. Manohar, C. Yang, S. Malkhandi, G.K.S. Prakash, S.R. Narayanan, Enhancing the performance of the rechargeable iron electrode in alkaline batteries with bismuth oxide and iron sulfide additives, *J. Electrochem. Soc.* 160 (11) (2013) A2078–A2084.
- [27] H.-F. Wang, Q. Xu, Materials design for rechargeable metal-air batteries, *Matter* 1 (3) (2019) 565–595.
- [28] A.A. Mohamad, Zn/gelled 6M KOH/O₂ zinc–air battery, *J. Power Sources* 159 (1) (2006) 752–757.

- [29] A.R. Mainar, E. Iruin, L.C. Colmenares, A. Kvasha, I. de Meatza, M. Bengoechea, O. Leonet, I. Boyano, Z. Zhang, J.A. Blazquez, An overview of progress in electrolytes for secondary zinc-air batteries and other storage systems based on zinc, *J. Energy Storage* 15 (2018) 304–328.
- [30] A. Matsuda, H. Sakamoto, T. Kishimoto, K. Hayashi, T. Kugimiya, H. Muto, Preparation of hydroxide ion conductive KOH-ZrO₂ electrolyte for all-solid state iron/air secondary battery, *Solid State Ionics* 262 (2014) 188–191.
- [31] A.K. Manohar, S. Malkhandi, B. Yang, C. Yang, G.K. Surya Prakash, S.R. Narayanan, A high-performance rechargeable iron electrode for large-scale battery-based energy storage, *J. Electrochem. Soc.* 159 (8) (2012) A1209–A1214.
- [32] T. Kim, Y. Ohata, J. Kim, C.K. Rhee, J. Miyawaki, S.-H. Yoon, Fe nanoparticle entrained in tubular carbon nanofiber as an effective electrode material for metal–air batteries: a fundamental reason, *Carbon* 80 (2014) 698–707.
- [33] X. Wu, H.B. Wu, W. Xiong, Z. Le, F. Sun, F. Liu, J. Chen, Z. Zhu, Y. Lu, Robust iron nanoparticles with graphitic shells for high-performance Ni-Fe battery, *Nano Energy* 30 (2016) 217–224.
- [34] Q. Zhao, J. Liu, X. Li, Z. Xia, Q. Zhang, M. Zhou, W. Tian, M. Wang, H. Hu, Z. Li, W. Wu, H. Ning, M. Wu, Graphene oxide-induced synthesis of button-shaped amorphous Fe₂O₃/rGO/CNFs films as flexible anode for high-performance lithium-ion batteries, *Chem. Eng. J.* 369 (2019) 215–222.
- [35] R. Kumar, S. Sahoo, E. Joanni, R.K. Singh, W.K. Tan, K.K. Kar, A. Matsuda, Recent progress in the synthesis of graphene and derived materials for next generation electrodes of high performance lithium ion batteries, *Prog. Energy Combust. Sci.* 75 (2019) 100786.
- [36] X. Liu, Q. Yang, M. Mi, W. Kong, Y. Ge, J. Ma, J. Hu, Fe1-S/reduced graphene oxide composite as anode material for aqueous rechargeable Ni/Fe batteries, *J. Alloys Compd.* 800 (2019) 99–106.
- [37] R. Kumar, S. Sahoo, E. Joanni, R.K. Singh, R.M. Yadav, R.K. Verma, D.P. Singh, W.K. Tan, A. Pérez del Pino, S.A. Moshkalev, A. Matsuda, A review on synthesis of graphene, -BN and MoS₂ for energy storage applications: recent progress and perspectives, *Nano Res.* 12 (2019) 2655–2694.
- [38] E.O. Aremu, K.-S. Ryu, Performance and degradation behavior of carbonyl Fe–MoS₂ composite as anode material in Fe-air batteries, *Electrochim. Acta* 313 (2019) 468–477.
- [39] Y. Teng, H. Zhao, Z. Zhang, Z. Li, Q. Xia, Y. Zhang, L. Zhao, X. Du, Z. Du, P. Lv, K. Świerczek, MoS₂ nanosheets vertically grown on graphene sheets for lithium-ion battery anodes, *ACS Nano* 10 (9) (2016) 8526–8535.
- [40] W.K. Tan, K. Asami, K. Maegawa, G. Kawamura, H. Muto, A. Matsuda, Formation of Fe-embedded graphitic carbon network composites as anode materials for rechargeable Fe-air batteries, *Energy Storage* (2020) (accepted).

Chapter 4

Functional material developments of fuel cells and the key factors for real commercialization of next-generation energy devices

Dasheng Lee

Department of Energy and Refrigerating Air-Conditioning Engineering, National Taipei University of Technology, Taipei, Taiwan, ROC

1 Introduction

There are a huge number of research publications related to fuel cells. Searching ScienceDirect Online (SDOL) in September 2019, there were a total of 317,056 publications between 1997 and 2018. Statistics of publications for every year are shown in Fig. 1.

In addition to SDOL, the IEEE/IET Electronic Library (IEL) was also investigated. Publications on IEL focus on electronic developments and control techniques. There are 9935 publications between 1976 and 2018. The statistics are shown in Fig. 2.

Publications on SDOL give multidiscipline results. Publication numbers increase year by year until 2018. IEL provides a dedicated area for research into electronics. Publication numbers reached a plateau around 2000–10. This indicates that control and electronic devices of fuel cells have been developed to a mature stage. However, multidisciplinary development is ongoing.

2 Fuel cell technology development

Among publications collected from SDOL and IEL, review papers were picked out to illustrate the technological development of fuel cells. The following sections will briefly illustrate reported results of these publications. Reference numbers are given after the description.

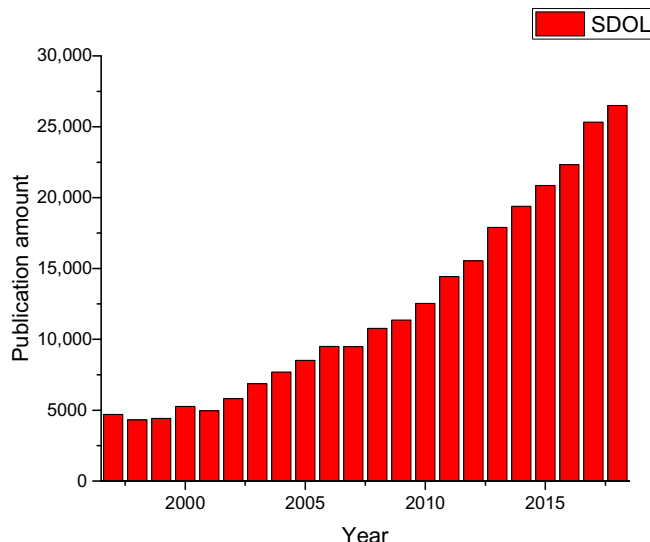


FIG. 1 Fuel cell-related research publications on SDOL.

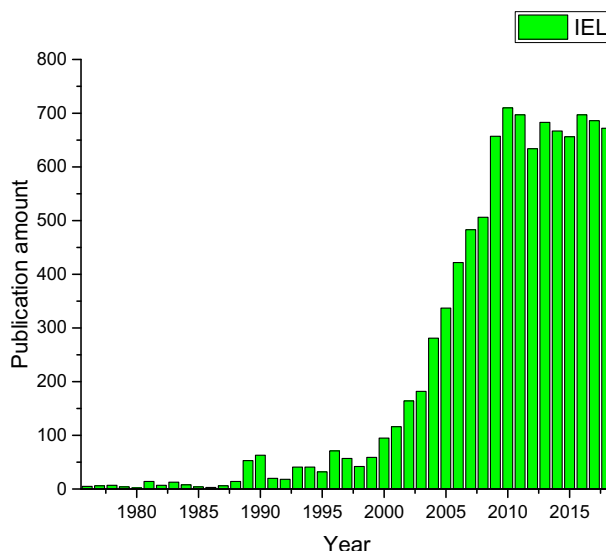


FIG. 2 Fuel cell-related research publications on IEL.

In 1988, Westinghouse Electric Corporation published a paper on SOFC systems and a 24-cell generator prototype. According to this publication, SOFCs—pioneered by Westinghouse in the 1960s—applied stabilized zirconia as an electrolyte; stabilized zirconia can operate as a solid electrolyte at elevated

temperatures. The 24-cell SOFC generator prototype was designed, fabricated, and tested. The generator contained three cells in parallel and eight in series. These cells operated at approximately 1000°C. A design current density of 250 mA/cm², a power of 284 W, and 45% efficiency were achieved [1]. After approximately 500 h of testing, the performance was stable. Commercial products were expected to be offered by the early 1990s. However, Westinghouse experienced a business downturn in the 1990s. In 1997, the company's fuel cell department was acquired by the German company Siemens AG. Despite its unsuccessful business development, Westinghouse was the most active company to invest in SOFC development. In 1968, the company filed a patent application for the aforementioned key component of SOFCs: a zirconium oxide electrode doped in or on an oxide cathode. From 1960 to 1990, Westinghouse led the development of SOFC technology and filed the key patent application for constructing power generators.

In 1992, Japan held a seminar involving 19 participating countries [2]. During this seminar, Mr. Mayfield from the US Department of Energy (DOE) stated that the United States had decided to concentrate on funding molten carbonate fuel cells (MCFCs) and SOFCs—committing approximately US\$30 million and US\$20 million, respectively, for these causes—and considered the near-term commercialization of phosphoric acid fuel cells (PAFCs). The key report of the seminar involved the experiences of a commercialized power plant that adopted SOFCs. Mr. Yokota from Tokyo Electric provided a summary of his operational experiences with an 11-MW Goi power plant. Construction commenced in November 1990, and rated power was achieved in April 1991. By August 1992, 10,200 MWh had been generated with an efficiency of 41%.

A review paper on fuel cell status published in 1994 explained that the development of fuel cells in the 1990s primarily involved three directions: SOFCs, MCFCs, and PAFCs. Among these developmental directions, MCFC-related R&D is crucial (particularly the development of MCFCs with internal reforming) and can solve technical issues pertaining to complex piping in fuel cells for fuel preparation. A review of commercial development trends indicates that by mid-1994, the United States had exported approximately thirty-three 300-kW PAFC plants, twenty 675-kW PAFC stacks, two 25-kW SOFC modules, and one MCFC system. PAFCs were successfully developed in the 1990s, surpassing the development of SOFCs. This is because the operating temperature of PAFCs is in the range of 180–200°C, whereas that of SOFCs is 1000°C [3]. Hence, the lower operating temperature of PAFCs affords greater reliability, which is a major factor influencing the commercialization of a power generation system.

A 1996 review of fuel cell status [4] proposed that proton exchange membrane fuel cells (PEMFCs) constitute the fourth R&D direction regarding fuel cells; the first three R&D directions are SOFCs, MCFCs, and PAFCs. The review revealed that the worldwide commercialization of fuel cells had begun in 1996 and that 200 fuel cell units were operational in 15 countries during that

period. In addition, the review reported the following four fuel cell systems as prominent systems: PEMFC (Ballard Power Systems, Vancouver, British Columbia, Canada), PAFC (ONSI Corporation, South Windsor, Connecticut, United States), MCFC (Energy Research, Inc., Danbury, Connecticut and M-C Power Corp., Burr Ridge, Illinois, United States), and SOFC (Westinghouse Corporation, Pittsburgh, Pennsylvania, United States). Notably, Ballard Power Systems provided 10–250-kW proton exchange membrane (PEM) plants in the 1990s.

According to the 1996 review [4], PEMFCs, PAFCs, MCFCs, and SOFCs have operating temperatures of 80°C, 200°C, 650°C, and 1000°C, respectively. This demonstrates that the development trend of fuel cell technology is toward lower operating temperatures. Apart from their lower operating temperatures, PEMFCs exhibit rapid start-up capabilities. This technological advantage is suitable for vehicle applications.

A 1997 study compiled information on five fuel cell systems, namely alkaline fuel cells (AFCs), PAFCs, PEMFCs, SOFCs, and MCFCs; subsequently, the study proposed a sixth technology: direct methanol fuel cells (DMFCs) [5]. The advantages of DMFCs are that they can directly generate power from methane, have simple storage requirements (unlike hydrogen), and are simple to fabricate and transport. However, DMFCs are associated with greater contamination problems compared with other fuel cells, thus impairing their effective commercialization. Furthermore, the review estimated the capital costs required for constructing power systems of different fuel cells. The 1997 study also reported that the capital cost required for constructing a PAFC, the most commonly constructed power system in the era, was approximately US\$2000 per 5000kW. The report predicted that in 2000, a 200-kW power generation system with a PAFC core would save US\$1500 for every 2000kW generated. If MCFC or SOFC systems achieve a 60%–75% power generation rate, greatly exceeding the 40% power generation rate of PAFC systems, the estimated short-term capital cost would be US\$1600–1800. In the long term, the estimated capital cost would be US\$650–850 for every 1kW. Notably, the study indicated that PEMFC technology was selected by the US DOE for mid-term introduction of fuel cells in light-duty applications (National Programme Plan for Fuel Cell in Transport). DOE studies have indicated that prices in the range of US\$50/kW should be possible for mass production.

Compared with the estimated capital costs proposed in the aforementioned studies, the unicorn start-ups investigated in this study released a 1-kW home-sized energy server priced at US\$3000 in 2010, indicating a capital cost of up to US\$3000/kW. Considering changes in the US consumer price index between 2000 and 2010, the actual capital cost of SOFCs is US\$2180/kW. This statistic indicates that the cost of commercializing fuel cells is considerably greater than that predicted by the aforementioned studies.

In 2000, the Science and Technology Centre of Siemens Westinghouse Power Corporation published an article: *Advances in SOFC technology* [6].

The company combined an SOFC with a microturbine generator to create a 250-kW hybrid pressurized SOFC-GT power generation system that could achieve a 57% power generation rate. Theoretically, the system could achieve a 70% power generation rate (a detailed test report can be referred to in Ref. [5]), thereby meeting the expected power generation rate proposed by the 1997 review.

Numerous scholars have reviewed SOFC technology development between 2001 and 2017. Topics considered in such reviews are outlined as follows: status and design selection of anode materials for SOFCs [7–11]; sealants for SOFCs [12]; vacuum deposition methods for SOFCs [13]; optimization of set-up and operating conditions for single-chamber SOFCs [14]; numerical and mathematical modeling of SOFCs [15–20]; Ni-YSZ cermet anode materials and alternative materials [21]; requirements of power electronics in SOFC systems [22]; power generation by SOFCs [23–25]; mathematical analysis of SOFCs [26]; microelectromechanical system fabrication, machining techniques, and electrospinning for SOFCs [26, 27]; nanostructured anodes for SOFCs [28]; glass-based seals for SOFCs [29]; integration strategies for SOFCs, including pressurized SOFC+Brayton cycle, nonpressurized SOFC+Brayton cycle, pressurized SOFC+Brayton cycle+air reheating, SOFC+PEMFC, SOFC+absorption refrigeration cycle, and SOFC+thermophotovoltaic power generation [30]; metal-supported SOFC design [31]; SOFCs operating under electrolysis mode [18, 32]; cathode-supported tubular SOFC designs [33]; SOFC control [34]; gas transport phenomena in porous electrodes of SOFCs [35]; chromium deposition and poisoning of SOFC cathodes [36]; and biomass as the energy source of ammonia-fed SOFCs [37, 38]. The aforementioned studies involved review papers instead of individual research papers. Therefore their conclusions were based on various other research theories. Compiling and assessing these reviews reveals a changing trend. Most studies conducted before 2000 proposed novel types of fuel cells. After 2000, a substantial body of research has focused on mechanical design, electronic design, and SOFC material selection. In addition, research has proposed adopting numerical-modeling-optimized operating strategies to optimize and adjust established SOFC frameworks.

In addition to SOFCs, other fuel cell systems were massively produced after 2000. However, because R&D processes for SOFCs occurred earlier, research on other types of fuel cells was published at later dates. Therefore research on SOFC applications was published relatively earlier. For example, *A Review of Fuel Cell Systems for Maritime Applications*, published in 2016 [39], reported that between 1980 and 1998, PEMFC systems and hydrogen were used as the power source in submarine air-independent propulsion systems. From 1998 to 2004, an MCFC-PEMFC hybrid power application for naval ships was created. Between 2003 and 2013, an offshore supply vessel adopted MCFC and liquefied natural gas as power sources. Between 2005 and 2008, a mega-yacht from the Fraunhofer Institute combined SOFC and gas turbines for power

generation. Moreover, between 2008 and 2011, the boat BV employed a PEMFC as its power source. Between 2009 and 2016, SOFC and diesel engines were employed for a multipurpose marine system. During the same period, a high-temperature PEMFC was being experimented on for cruise ship applications. As mentioned, PEMFCs are characterized by rapid start-up and are suitable for maritime applications. Therefore this explains why they became the primary fuel cells in mobile vehicles. Studies have also tested the suitability of MCFCs and SOFCs in the aforementioned applications and compared their performance with that of PEMFCs. Notably, low-temperature fuel cells such as PEMFCs can achieve high electrical efficiencies if hydrogen is available as a logistic fuel. However, the efficiency is significantly reduced if hydrocarbon fuels are used; this is mostly due to the need to reform and clean these fuels and subsequent parasitic losses. Therefore heavy-duty internal combustion engine generators are probably more efficient. High-temperature fuel cells such as SOFCs provide better integration with fuel-processing equipment and have higher tolerance levels for fuel impurities; in particular, when combined with gas turbines or reciprocating engines, SOFC systems can attain higher electrical efficiency levels than conventional generators can.

Studies on PEMFC enhancement are currently ongoing. Anion exchange membrane fuel cells (AEMFCs) are enhanced PEMFC models. Research on anion fuel cells first appeared in 2000. A study [40] reported that AEMFCs exhibited improved performance and high stability in 2018. In 2019, numerous reviews of PEMFCs were published, including a review of PEMFC-based microcombined heat and power systems [41], PEMFC applications for electric vehicles and energy management strategies [42, 43], PEMFC poisoning by contaminants and impurities [44], mechanical compression effects and stress effects on PEMFCs [45, 46], humidification strategy for PEMFCs [47], and design optimization for PEMFCs [48]. These reviews are similar to the 2000 reviews of SOFCs. The 2019 reviews of PEMFCs discussed the mechanical design, electric design, and material selection of PEMFCs. Compared with the SOFC reviews, the PEMFC reviews involved greater discussions of PEMFC applications and strategies for combining PEMFCs with heat and power systems. Furthermore, SOFCs were developed in the 1980s, whereas PEMFCs were developed between 1990 and 2000; hence, PEMFC reviews were mostly published later, from 2000 to 2019.

A 2019 review [49] was also included. The article examined 190 research publications on fuel cells integrated into electric grids and discussed the fuel cell-grid interface, interfacing components, and power quality problems. Moreover, the review categorized power ratings into low power (less than 10kW), medium power (between 10 and 100kW), and high power (more than 100kW) and described development trends and optimization strategies. Finally, the review discussed the practicability of fuel cells. The review paper indicated that among numerous fuel cells, only PEMFCs and SOFCs are suitable for connection with power grids. PEMFCs are suitable for small and moderate power

loads between 10W and 10kW and exhibit the advantages of high power density and rapid response. SOFCs are suitable for moderate- and high-power loads from 10kW to 10MW and exhibit the advantage of high conversion efficiency. Additionally, one review conducted energy and exergy analyses on various fuel cell types [50]. A theoretical analysis indicated that PEMFCs constitute a promising electrochemical energy conversion device for light-duty applications and have a maximum temperature of 90°C, thus rendering them suitable for use in applications such as automobiles, buildings, electronics, and rechargeable batteries. However, on the basis of pressure and voltage parameters, the energy and exergy analyses showed energy and exergy efficiencies of 47.6% and 50.4%, respectively. SOFCs are promising and reliable devices with several advantages, including safety, high robustness against fuel contaminants, and suitability for high-temperature production. The efficiency can be increased to more than 50%. If a PEMFC is combined with heat and power systems such as gas turbines, its efficiency can be up to 70%.

With these 50 review papers, the developing history of fuel cell technology was investigated from 1980 to 2019. Details of functional materials are further discussed in the next section.

3 Functional material developments for fuel cells

For SOFC, functional material developments can be divided into five categories: anode, electrolyte, cathode, interconnects, and sealants. Anode material research includes nickel metal; nickel/YSZ cermet; sulfur poisoning and carbon deposition; copper and other noble metal cermets; ceria and other components; perovskite and double-perovskite structure-based material; pyrochlores; etc. Electrolyte material developments focused on fluorite structure oxides with high ionic conductivity and low defect. δ - Bi_2O_3 - and $\text{Bi}_4\text{V}_2\text{O}_{11}$ -based ceramics and perovskite and related intergrowth structures, including LaGaO_3 , Brown-millerites, La-MOX, and apatites, are investigated to increase the performance of fuel cells. Material research for cathodes includes LaSr perovskites with gadolinium-doped ceria; $\text{A}_2\text{BO}_{4+\delta}$ composites; $\text{LnBaCO}_2\text{O}_{5+\delta}$ double perovskite; cobalt-free perovskite; alkaline earth metal-free perovskite, etc. Interconnects has the researched related to ceramic interconnect materials, metallic alloys as interconnect materials and material degradation and protection. Sealants use compressive seals, rigid seals, and sealing glass. SOFC material developments have 5 categories and each category has 3–12 different types of research topics. Within five categories, perovskite material attracted attention due to its performance and special structures. Details of crystal structures and thin film formation, morphology, and processing improvement can be referred to in Ref. [51]. The foregoing discussions and material developments make the material selection of SOFC components elicit extreme complexity, as each of the layers must be designed strictly keeping the adjoining components and fuel purity. So, there is no single material that satisfies the concerns raised

in each of the components of SOFCs. Subsequently, it is also difficult to identify what the key is for commercialization.

With respect to PEMFCs, the membrane is a major research topic for increasing exchange current density. Two commercial membranes, Nafion 115 and Tokuyama A210, are widely employed for real products. Similar to SOFC, PEMFCs have many kinds of anode and cathode selections. Catalyst material research is another point to avoid the problem of contamination. Air contaminants, fuel impurities, cleansers, and some materials from which fuel cell compartments are made have been proven to have negative effects on PEM fuel cell performance. These materials can access the anode and cathode catalyst layers, occupy catalyst sites, and deviate principal electrochemical reaction paths. Diversified research has been conducted to date that illustrates that commercialization of fuel cells is still a state of the art from an academic point of view.

Except SOFCs and PEMFCs, different kinds of fuel cells have special materials such as molten carbonate, phosphoric acid, etc. Among them, the most important research is the application of nanomaterials. Such materials seem to be utilized well in the development and improvement of the performance of SOFCs. The high operating temperature of SOFCs has resulted in serious demerits regarding their overall performance and durability. The application of nanotechnology in fabricating SOFCs has successfully omitted or at least reduced the internal resistance and showed considerable improvement in power density of the SOFCs at reduced temperatures. The recommendations of nanomaterials with integration of carbon or graphene may change the map of fuel cells and will offer more efficient devices with high power and performance in various applications. However, this is still under development.

Briefly summarizing, academic research has provided versatile results. Eight categories of functional material developments can be identified:

- Anode material
- Electrolyte material
- Cathode material
- Interconnect material
- Sealants
- Membrane
- Catalyst material
- Nanomaterial

In the next step, we employ the Derwent Innovation (DI) tool to analyze world-wide patent applications related to fuel cells to identify what the key factors are for commercialization.

4 Key factors for real commercialization

Patent application is the first and fundamental step of commercialization. Thus we use the DI tool to investigate worldwide patents related to fuel cells and try

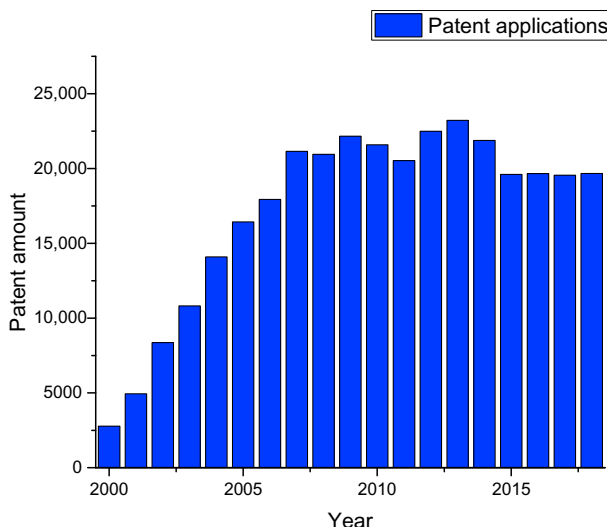


FIG. 3 Fuel cell-related patent applications around the world.

to find key factors. Investigation shows that 363,832 patents were applied for from 1970 to 2018. The statistics of patent applications for every year are shown in Fig. 3.

ThemeScape is the DI tool employed to deal with these patents. ThemeScape creates content maps from full text patent data, enhanced patent data from Derwent World Patent Index (DWPI), and scientific literature content. Common conceptual terms are displayed in a two-dimensional map, with peaks representing a concentration of documents and showing the relative relationship of one record to another. The thematic topographical map enables “at a glance” assessments and is searchable.

When including DWPI data, the consistency of language used in DWPI’s all-English abstracts improves the quality of the resulting analysis and gives a landscape map far superior to the one created from first-level patent data only.

Patent numbers increase each year. The DI tool gives statistical results of patents filed during the past 18 years. Patent numbers reached their plateau from 2007 to 2014. Since 2015, patent applications of fuel cells have been developed to a mature stage. The application number is continuously flat.

A total of 363,832 patents were visualized by ThemeScape. Using visualization, the key factors for successful commercialization can be easily inspected. As mentioned before, patent application is the crucial step of commercialization. Subsequently, the technical topic accumulates more patents indicates it’s more important than other technologies. Using ThemeScape, the patent accumulation status is shown by a contour map. The dense contour lines will induce a white peak. This indicates a lot of patent applications related to this technology. It is the critical technology for the commercialization of fuel cells. The thematic map is shown in Fig. 4.



FIG. 4 The 363,832 patents related to fuel cells worldwide and their distribution on ThemeScape.

Four peaks are shown in Fig. 4. They are fuel cell assembly, fuel cell stack, fuel cell vehicle, and solid oxide system. It goes without saying that commercialization of fuel cells mainly depends on mature assembly technologies. Around 2052 patents have been accumulated on this topic. Among these patents, the functional materials related to sealants are the most often-mentioned keywords. The main function of sealants is summarized from patent review. All patents are listed in Appendix A. How to analyze these patents to generate Fig. 4 and peak formation can be found in Ref. [52].

The second peak is the fuel cell stack. There are 1539 patents related to this topic. Among these patents, the critical material is the interconnect. All patents related to the interconnect are listed in Appendix B.

The fuel cell vehicle is a highly anticipated future product. There are 1124 patents related to the hydrogen car powered by fuel cells. Membrane is the most often-mentioned functional material. New developments of membrane material can be found in patents listed in Appendix C.

The last is the solid oxide fuel cell system. From the detailed inspection of this peak, one can find two peaks and a total of 2357 patents included in the double-peak area. All patents are listed in Appendix D. Appendices A–D can be accessed on our companion site (<https://www.elsevier.com/books-and-journals/book-companion/9780128206287>).

The SOFC product created a unicorn start-up. Unicorn start-ups are privately held start-up companies valued at over US\$1 billion. The term was coined in 2013 by venture capitalist Aileen Lee, choosing the mythical animal to represent the statistical rarity of such successful ventures. At the time of writing (2019), only 391 start-up companies worldwide are listed as unicorn start-ups. This indicates an extremely successful case of commercialization and will be further discussed in the following section. Herein, regarding SOFC, anode and cathode materials are the two most important functional material technology developments.

Combining with the academic literature survey and patent analytics, key factors of commercialization of fuel cells can be concluded as follows:

- Sealant material development for reliable and low-cost fuel cell assembly
- Interconnects of fuel cell systems to provide stable operation and maintain high-power generation efficiency
- Novel membrane material development for fuel cell vehicles
- Anode and cathode material development for stable operation of SOFC at high temperatures up to 900°C

With these key factors, how to enable successful commercialization of next-generation energy devices can be derived and illustrated in the following section.

5 Conclusion

Four factors analyzed before give the following conclusions. Stable operation and low cost is the way to successful commercialization but not those advanced researches. This chapter was completed in September 2019. Currently, a unicorn start-up called Bloom Energy submitted its initial public offering for 1 year. This company commercialized SOFC as its exclusive product.

Bloom Energy received substantial funding in May 2002 within 1 year after its establishment. This funding, referred to as A round funding, involved US\$4.7 million. In February 2003, Company B received US\$12 million. By the end of 2014, the company had accumulated US\$825.7 million worth of funding and received a valuation of US\$2.9 billion. Continual acquisition of venture capital for product development during the inception stage is crucial for companies that have yet to release products. In addition, a high business valuation based on funding is essential for unicorn start-ups.

The core commercial value of Bloom Energy is to increase power generation efficiency from 41%–45% to 52%. By using these fuel cells to generate power with the company's energy servers, Bloom Energy could sell power at a price 5%–15% lower than the price of power grid-supplied power. Therefore the core value for successful commercial development is to promote renewable energy supply with lower prices.

Key factor analysis and a successful commercial case both indicate that lower price is the only way to win business. From the review of fuel cell research and several reports related to commercialization of renewable energy technologies [53–55], the original concept suggests that subsidies from governments are necessary to compensate the price difference up to 40%. Or at least society must increase the level of environmental awareness to make consumers accept the high price of new/renewable energy devices. However, this study has overturned this concept. The only way to commercialize or successfully promote next-generation energy devices is to lower the price. According to an investigating report promoted by McKinsey & Company [56], 70% of consumers would pay an additional 5% for a green product if it met the same performance standards as a nongreen alternative. However, referring to the successful business development of a unicorn start-up, the Bloom Energy experience discussed in this study, a 5%–15% low power price for next-generation energy devices is suggested for practical commercialization.

Fig. 5 shows the real competitiveness of next-generation energy devices.

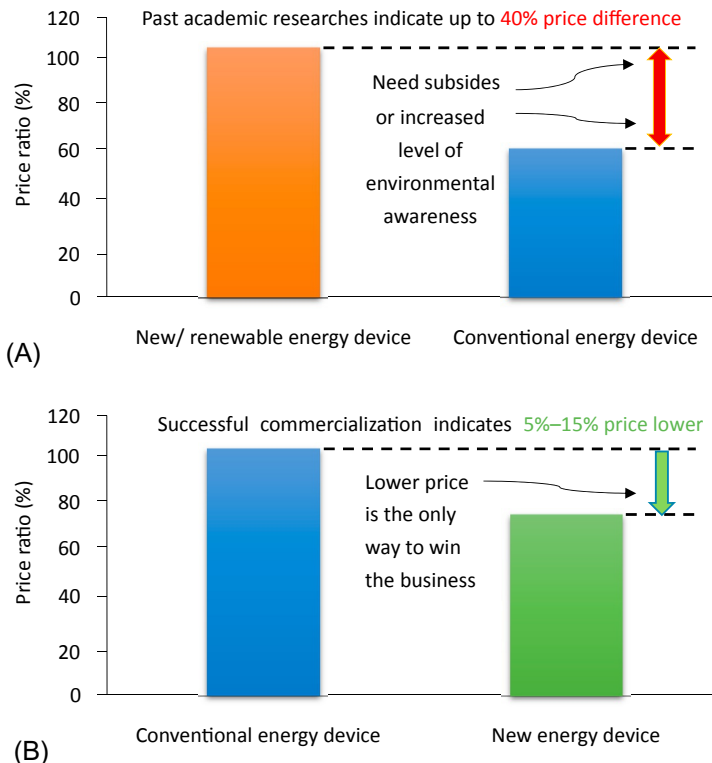


FIG. 5 The original concept suggests that there is a need to raise the level of awareness to a point where there is a willingness to pay for new/renewable energy devices as shown in (A). In this study, key factor analysis and a successful commercial case have proven that lower price is the only way to win business as shown in (B). Surely, it is the only way to build competitiveness for next-generation energy devices.

References

- [1] J.T. Brown, Solid oxide fuel cell technology, *IEEE Trans. Energy Convers.* 3 (2) (1988) 193–198.
- [2] I. Stann, Fuel cells are coming to town, *Power Eng. J.* 6 (May) (1992) 107–110.
- [3] J.H. Hirschenhofer, Fuel cell status, 1994, *IEEE Aerosp. Electron. Syst. Mag.* 9 (November (1994) 10–15.
- [4] J.H. Hirschenhofer, 1996 Fuel Cell Status, Parsons Power Group Inc, Reading, PA, 1996.
- [5] A. T-Raissi, A. Banerjee, K.G. Sheinkopf, Current technology of fuel cell systems, *Proc. Internat. Soc. Energy Convers. Eng. Conf.* 3–4 (1997) 1953–1957.

- [6] S.C. Singhal, Advances in solid oxide fuel cell technology, *Solid State Ionics* 135 (1–4) (2000) 305–313.
- [7] W.Z. Zhu, S.C. Deevi, A review on the status of anode materials for solid oxide fuel cells, *Mater. Sci. Eng. A* 362 (1–2) (2003) 228–239.
- [8] B. Shri Prakash, S. Senthil Kumar, S.T. Aruna, Properties and development of Ni/YSZ as an anode material in solid oxide fuel cell: a review, *Renew. Sust. Energ. Rev.* 36 (2014) 149–179.
- [9] S.P.S. Shaikh, A. Muchtar, M.R. Somalu, A review on the selection of anode materials for solid-oxide fuel cells, *Renew. Sust. Energ. Rev.* 51 (2015) 1–8.
- [10] N. Mahato, A. Banerjee, A. Gupta, S. Omar, K. Balani, Progress in material selection for solid oxide fuel cell technology: a review, *Prog. Mater. Sci.* 72 (2015) 141–337.
- [11] F.S. da Silva, T.M. de Souza, Novel materials for solid oxide fuel cell technologies: a literature review, *Int. J. Hydrog. Energy* 42 (41) (2017) 26020–26036.
- [12] J.W. Fergus, Sealants for solid oxide fuel cells, *J. Power Sources* 147 (1–2) (2005) 46–57.
- [13] L.R. Pederson, P. Singh, X.D. Zhou, Application of vacuum deposition methods to solid oxide fuel cells, *Vacuum* 80 (10) (2006) 1066–1083.
- [14] M. Yano, A. Tomita, M. Sano, T. Hibino, Recent advances in single-chamber solid oxide fuel cells: a review, *Solid State Ionics* 177 (39–40) (2007) 3351–3359.
- [15] S. Kakaç, A. Pramuanjaroenkij, X.Y. Zhou, A review of numerical modeling of solid oxide fuel cells, *Int. J. Hydrog. Energy* 32 (7) (2007) 761–786.
- [16] K. Wang, et al., A review on solid oxide fuel cell models, *Int. J. Hydrog. Energy* 36 (12) (2011) 7212–7228.
- [17] S.A. Hajimolana, M.A. Hussain, W.M.A.W. Daud, M. Soroush, A. Shamiri, Mathematical modeling of solid oxide fuel cells: a review, *Renew. Sust. Energ. Rev.* 15 (4) (2011) 1893–1917.
- [18] M.A. Laguna-Bercero, Recent advances in high temperature electrolysis using solid oxide fuel cells: a review, *J. Power Sources* 203 (2012) 4–16.
- [19] M. Lee, G. Park, V. Radisavljevic-Gajic, Modeling of solid oxide fuel cells (SOFCs): an overview, in: 2013 5th Int. Conf. Model. Simul. Appl. Optim. ICMSAO 2013, vol. 2, no. 1, 2013, pp. 1–6.
- [20] M. Peksen, Numerical thermomechanical modelling of solid oxide fuel cells, *Prog. Energy Combust. Sci.* 48 (2015) 1–20.
- [21] C. Sun, U. Stimming, Recent anode advances in solid oxide fuel cells, *J. Power Sources* 171 (2) (2007) 247–260.
- [22] T. Riipinen, V. Väistönen, M. Kuisma, L. Seppä, P. Mustonen, P. Silventoinen, Requirements for power electronics in solid oxide fuel cell system, in: 2008 13th Int. Power Electron. Motion Control Conf. EPE-PEMC 2008, 2008, pp. 1233–1238.
- [23] A. Kirubakaran, R.K. Nema, S.K. Jain, Distributed generation by solid oxide fuel cell: a review, in: 2008 Jt. Int. Conf. Power Syst. Technol. POWERCON IEEE Power India Conf. POWERCON 2008, 2008, pp. 1–7.
- [24] A. Choudhury, H. Chandra, A. Arora, Application of solid oxide fuel cell technology for power generation - a review, *Renew. Sust. Energ. Rev.* 20 (2013) 430–442.
- [25] S.K. Nayak, D.N. Gaonkar, Fuel cell based hybrid distributed generation systems, ‘a review,’ in: 2013 IEEE 8th Int. Conf. Ind. Inf. Syst. ICIIS 2013 - Conf. Proc., 2013, pp. 525–530.
- [26] A. Pramuanjaroenkij, S. Kakaç, X. Yang Zhou, Mathematical analysis of planar solid oxide fuel cells, *Int. J. Hydrog. Energy* 33 (10) (2008) 2547–2565.
- [27] S.T. Aruna, L.S. Balaji, S.S. Kumar, B.S. Prakash, Electrospinning in solid oxide fuel cells – a review, *Renew. Sust. Energ. Rev.* 67 (2017) 673–682.

- [28] A. Evans, A. Bieberle-Hütter, J.L.M. Rupp, L.J. Gauckler, Review on microfabricated micro-solid oxide fuel cell membranes, *J. Power Sources* 194 (1) (2009) 119–129.
- [29] R.J. Gorte, J.M. Vohs, Nanostructured anodes for solid oxide fuel cells, *Curr. Opin. Colloid Interface Sci.* 14 (4) (2009) 236–244.
- [30] X. Zhang, S.H. Chan, G. Li, H.K. Ho, J. Li, Z. Feng, A review of integration strategies for solid oxide fuel cells, *J. Power Sources* 195 (3) (2010) 685–702.
- [31] M.C. Tucker, Progress in metal-supported solid oxide fuel cells: a review, *J. Power Sources* 195 (15) (2010) 4570–4582.
- [32] S.Y. Gómez, D. Hotza, Current developments in reversible solid oxide fuel cells, *Renew. Sust. Energ. Rev.* 61 (2016) 155–174.
- [33] K. Huang, S.C. Singhal, Cathode-supported tubular solid oxide fuel cell technology: a critical review, *J. Power Sources* 237 (2013) 84–97.
- [34] M. Leung, G. Park, V. Radisavljevic-Gajic, Control of solid oxide fuel cells: an overview, in: 2013 9th Asian Control Conf. ASCC 2013, 2013, pp. 1–6.
- [35] W. He, et al., Gas transport in porous electrodes of solid oxide fuel cells: a review on diffusion and diffusivity measurement, *J. Power Sources* 237 (2013) 64–73.
- [36] S.P. Jiang, X. Chen, Chromium deposition and poisoning of cathodes of solid oxide fuel cells - a review, *Int. J. Hydrol. Energy* 39 (1) (2014) 505–531.
- [37] M. Liu, P.V. Aravind, The fate of tars under solid oxide fuel cell conditions: a review, *Appl. Therm. Eng.* 70 (1) (2014) 687–693.
- [38] A. Afif, N. Radenahmad, Q. Cheok, S. Shams, J.H. Kim, A.K. Azad, Ammonia-fed fuel cells: a comprehensive review, *Renew. Sust. Energ. Rev.* 60 (2016) 822–835.
- [39] L. van Biert, M. Godjevac, K. Visser, P.V. Aravind, A review of fuel cell systems for maritime applications, *J. Power Sources* 327 (2016) 345–364.
- [40] D.R. Dekel, Review of cell performance in anion exchange membrane fuel cells, *J. Power Sources* 375 (2018) 158–169.
- [41] A. Arsalis, A comprehensive review of fuel cell-based micro-combined-heat-and-power systems, *Renew. Sustain. Energy Rev.* 105 (January) (2019) 391–414.
- [42] M. Yue, S. Jemei, R. Gouriveau, ScienceDirect Review on health-conscious energy management strategies for fuel cell hybrid electric vehicles: degradation models and strategies, *Int. J. Hydrol. Energy* 44 (13) (2019) 6844–6861.
- [43] H. Chen, X. Zhao, T. Zhang, P. Pei, The reactant starvation of the proton exchange membrane fuel cells for vehicular applications: a review, *Energy Convers. Manag.* 182 (December) (2019) 282–298.
- [44] B. Shabani, M. Hafttanian, S. Khamani, A. Ramiar, A.A. Ranjbar, Poisoning of proton exchange membrane fuel cells by contaminants and impurities: review of mechanisms, effects, and mitigation strategies, *J. Power Sources* 427 (December) (2019) 21–48.
- [45] E. Mahdi, K. Bouziane, N. Zamel, X. François, Effects of mechanical compression on the performance of polymer electrolyte fuel cells and analysis through in-situ characterisation techniques - a review, *J. Power Sources* 424 (December) (2019) 8–26.
- [46] A. Mohamed, F. Jiang, ScienceDirect Stresses and their impacts on proton exchange membrane fuel cells: a review, *Int. J. Hydrol. Energy* 43 (4) (2017) 2327–2348.
- [47] Y. Chang, Y. Qin, Y. Yin, J. Zhang, X. Li, Humidification strategy for polymer electrolyte membrane fuel cells – a review, *Appl. Energy* 230 (August) (2018) 643–662.
- [48] L. Xing, et al., Membrane electrode assemblies for PEM fuel cells: a review of functional graded design and optimization, *Energy* 177 (2019) 445–464.
- [49] M. Inci, Review of fuel cells to grid interface: configurations, technical challenges and trends, *J. Clean. Prod.* 213 (2019).

- [50] A. Arshad, M. Jabbal, Y. Yan, A. Habib, M.A. Bashir, Energy and exergy analysis of fuel cells: a review, *Therm. Sci. Eng. Prog.* 9 (2019) 308–321.
- [51] N. Ashurov, et al., Current state and perspectives for organo-halide perovskite solar cells. Part 1. Crystal structures and thin film formation, morphology, processing, degradation, stability improvement by carbon nanotubes. A review, *Mod. Electron. Mater.* 3 (1) (2017) 1–25.
- [52] https://support.clarivate.com/Patents/s/article/Derwent-Innovation-Explanation-on-ThemeScape?language=en_US.
- [53] N. Symeonidou, J. Bruneel, E. Autio, Commercialization strategy and internationalization outcomes in technology-based new ventures, *J. Bus. Ventur.* 32 (3) (2017) 302–317.
- [54] S.R. Shakeel, J. Takala, L.D. Zhu, Commercialization of renewable energy technologies: a ladder building approach, *Renew. Sustain. Energy Rev.* 78 (December) (2017) 855–867.
- [55] P. Balachandra, H.S. Kristle Nathan, B.S. Reddy, Commercialization of sustainable energy technologies, *Renew. Energy* 35 (8) (2010) 1842–1851.
- [56] <https://www.mckinsey.com/business-functions/sustainability/our-insights/how-much-will-consumers-pay-to-go-green>.

Chapter 5

Graphene and its derivatives, synthesis route, and mechanism for photovoltaic solar cell applications

Foo Wah Low^a, Chin Wei Lai^b, Nurul Asma Samsudin^a, Yulisa Yusoff^a, Su Mei Goh^c, Chien Fat Chau^c, Mohammad Shakeri^a, Nowshad Amin^a, and Sieh Kiong Tiong^a

^a*Institute of Sustainable Energy, Universiti Tenaga Nasional (@The Energy University), Kajang, Selangor, Malaysia,* ^b*Nanotechnology & Catalysis Research Centre (NANOCAT), University of Malaya (UM), Kuala Lumpur, Malaysia,* ^c*College of Engineering, Universiti Tenaga Nasional (@The Energy University), Kajang, Selangor, Malaysia*

1 Introduction

The conception and appreciation of renewable energy are profoundly crucial in our present-day landscape. Current natural energy resources are fast depleting and this matter is not to be taken lightly. The search for alternative energy, especially clean and sustainable renewable energy, is twofold: the energy needs to serve existing demand and adequate generation for future demands. To have sustainable development in all sectors, sustainable energy systems are required. The availability of renewable energy sources dictates the type of renewable energy supplies for the most appropriate technologies. There are currently many types of renewable energy under intensive research, such as wind energy, solar thermal, supercapacitor, photovoltaic (PV), biomass, hydropower, nuclear fission, geothermal, ocean energy, fuel cells, etc. [1].

Among the renewable energy resources currently available, solar energy is by far the easiest to exploit; it is also inexhaustible, quiet, and adjustable to enormous applications [2]. Efficient solar cells are very much sought after due to their simplicity and inexpensive nature for generating clean energy. Energy conversion (e.g., PVs and fuel cells) and energy storage (e.g., supercapacitors) are technologies reliant on the choice of materials. As such, various emerging nanomaterials with desired nanostructures have been specifically developed for applications in energy-related devices, and

expectedly, carbon-based nanomaterial is an element of interest thanks to its versatility in forming variable allotropes [3].

The World Energy Outlook 2017 reported that solar PV capacity has seen a rapid growth, mainly led by China and India [4]. In fact, the global total installed capacity for solar PVs crossed the 500GW mark in 2018, with China alone contributing to a total installed capacity of 176.1GW [5]. This is mainly attributed to the falling cost of new solar PVs by almost 70% since 2010 [4]. Bloomberg New Energy Finance, in its recently released New Energy Outlook 2019, predicts that by 2030, wind and solar energy will be cheaper than energy generation by coal and gas globally. In fact, it is projected that by 2050, both wind and solar energy will make up to 48% of global energy supply [6]. Solar energy itself will see a close to 10-fold growth from its current 2.6% of world electricity generation today to a predicted 22% by 2050 [6].

Solar cells are generally not that efficient in terms of performance. Various types of solar cells have been fabricated and characterized to increase and achieve higher efficiency. The performance of a PV device mainly depends on the type of solar cell and material used for fabrication. Si-based first-generation PVs still dominate the solar energy market for commercial purposes with 11% efficiency [7]. Second-generation PVs are based on thin film technology and have low efficiency compared to first generation. A more environmentally friendly and cost-effective third-generation solar cell includes dye-sensitized solar cells (DSSCs), quantum dot solar cells (QDSCs), and organic PVs [8–10]. These devices exhibit low power conversion efficiency (PCE), less stability, and strength compared to other generations [11]. Therefore further research is being carried out to enhance the efficiency and stability of PV devices.

Recent advances in graphene-based solar cells have seen their potential efficiency increased. There are currently many different variations of graphene-based solar cells being researched today. Graphene, an atomically thin flat sheet of carbon atoms, has several key features that can address emerging energy needs; in particular it can enhance the energy conversion efficiency of PV devices. An extensive review of energy conversion efficiency of graphene-incorporated solar cell devices can be found in Iqbal and Rehman [12]. In their paper, various structures of solar cell devices were investigated, including organic, inorganic, and hybrid structures. Graphene's potential for PV applications were well noted here. Its stability and flexibility were also addressed. Overall, their results indicate that utilization of graphene in energy devices yields more efficient results and opens new avenues for future applications.

2 Photovoltaic solar cell technologies

The PV effect was first discovered by Alexandre-Edmond Becquerel in 1839 when he observed that an electric current was produced upon shining light on a silver-coated platinum (Pt) electrode immersed in an electrolyte

solution [13]. In 1876, the first solid-state PV devices were produced by William G. Adams and his student Richard E. Day based on the photoconductivity effect of selenium. Later, in 1884, an American inventor, Charles Fritts, demonstrated the feasibility of a large area thin film solar cell consisting of a layer of selenium covered with a thin film of gold, albeit with poor efficiency. In early 1905, Albert Einstein reported a photoelectric effect generated from photon absorption, which later won him a Nobel Prize in 1921. The first practical silicon solar cells, based on the concept of p-n junction photodiodes, were produced by Bell Laboratories in 1954, and were generally known as first-generation solar cells.

The two major materials used in the majority of first-generation solar cells are monocrystalline silicon and polycrystalline silicon doped with other materials. Solar cells made of monocrystalline silicon, which has a continuous lattice with almost no defects, hence a better light absorption efficiency, generally demonstrate better PCE, a ratio of the electrical energy output over the incident solar photon energy. To date, the highest confirmed PCE of a single-junction crystalline silicon nonconcentrator solar cell is 26.7% with a designated illumination area of 79 cm^2 [14, 15]. However, being the highest grade of silicon, monocrystalline silicon solar cells are also the most expensive due to high fabrication and material costs. On the other hand, polycrystalline (also known as multicrystalline) silicon solar cells, which have inherent grain boundaries and dislocations, are easier and cheaper to produce. The polycrystalline silicon solar cells are slightly less efficient with a reported confirmed highest PCE of 22.3% [14].

Second-generation PV solar devices are mainly based on thin film solar cell technology, which offers prospects of cost reduction in the material and fabrication process. Silicon-based thin film solar cells, predominantly known as amorphous silicon solar cells, are produced by the deposition of silicon film onto glass substrates. This process uses less silicon compared to the manufacturing approach in the first-generation solar cells. However, the cost advantage of an amorphous silicon solar cell is traded off with lower efficiency; the highest confirmed PCE of such cells is reported to be 10.2% [14].

Thin film gallium arsenide (GaAs)-based solar cells, with a near-optimum bandgap of 1.42 eV, have thus far achieved the highest performance of all single-junction solar cells with a record of 29.1% [14]. For applications where high performance is more critical than the costs of production, such as in satellite applications, single-crystalline GaAs thin films made by epitaxial lift-off are often used. Other similar generation III–IV materials used as solar cells include single-crystalline indium phosphide (InP) with a reported PCE of 24.2% [16], gallium indium phosphide (GaInP, typically $\text{Ga}_{0.5}\text{In}_{0.5}\text{P}$) with a confirmed PCE of 20.8% [17], and multicrystalline GaAs with a reported PCE of 18.4% [14].

In addition to the generation III–IV group of materials, multicrystalline chalcogenide thin films have also demonstrated great commercial potentials.

Notably, solar cells made of copper indium gallium selenite (CIGS) and cadmium telluride (CdTe) have demonstrated PCEs of 23.35% [18] and 21% [14], respectively. These CIGS and CdTe solar cells each contain one or more rare earth materials, which can be scarce and/or highly sought after for other applications, and therefore are unsustainable for large-scale production. To create a more sustainable option, other more readily available materials such as zinc (Zn) and tin (Sn) have been used. Solar cells using copper zinc tin sulfide (CZTS, typically $\text{Cu}_2\text{ZnSnS}_4$) and copper zinc tin sulfur-selenium alloy (CZTSS, $\text{Cu}_2\text{ZnSnS}_{4-y}\text{Se}_y$) thin films have demonstrated substantial progress in the past 5 years [19, 20].

Third-generation solar cell technology often refers to its emerging organic solar cell technologies that deviate from silicon or similar materials. These solar cells mainly focus on the cost of production and ease of fabrication process. Remarkably, the thickness of an active layer of organic solar cells is relatively 100 times thinner than inorganic thin film solar cells. The low material consumption per solar cell is comparable with simpler ways of processing, because of low cost with a large area solar cell production and low-temperature processing without vacuum medium. However, the PCE performance of organic-based solar cells is far lower, about two or three times lower than conventional Si solar cells. Thus further efficiency improvements are required before stepping into the commercialization stage. According to the National Renewable Energy Laboratory chart, various types of organic solar cells were first discovered in 2001 amounting to 3.8%. Since then, PCE rose to 11.5% in 2015, an amazing three times improvement after 14 years.

Cross-fertilization between technologies is becoming more experimental and some, such as the development of metal halide perovskites, have demonstrated positive results. Future fourth-generation solar cells generally include these hybrid novel PV cells. To date, perovskite solar cells (PSCs) represent a relatively new class of low-cost solar cells with great promise [21]. In PSCs, the electron transporting layer (ETL) is one of the important parts responsible for enhancing overall PCE performance. Hence, the material selection for ETL is a crucial point to study intensively since it is an electron collector that determines PCE performance. In hole transport media (HTM), inorganic p-type materials, CuO is applied for PSCs in this research work instead of organic HTM. In fact, CuO material could reduce the production cost and also improve the resistance to degradation [22]. Furthermore, CuO can provide good carrier mobility, is defect free with an absorbing layer, and minimizes charge carrier recombination. A typical PSC consists of a transparent anode (i.e., fluorine-doped tin oxide [FTO]), a highly porous semiconductor (TiO_2 -graphene nanocomposite) layer as ETL, which is then soaked in a layer of methylammonium lead iodide, MAPI ($\text{CH}_3\text{NH}_3\text{PbI}_3$) as the main perovskite source, a p-type layer (CuO) as HTM, and a counter electrode (i.e., silver). The working principle of PSCs is that perovskite will harvest the high-energy photons from solar irradiation and then photoelectrons will release an excited electron from the

perovskite, inject it into the conduction band of TiO_2 across the graphene layer, and leave a temporary hole in the perovskite region. The electrons will flow through the outer circuit, pass into the counter electrode and through HTM, and then the electron will replace the hole at the perovskite.

3 Graphene material

Graphene, an intriguing material, is a two-dimensional (2D) sheet of carbon atoms arranged in a chicken wire pattern that provides properties like mechanical strength, thermal and electrical conductivity, optical properties, and more. This astonishing material is known as a 2D nanostructure comprised of sp^2 -hybridized single-layer carbon atoms arranged as a basal plane of graphite with superior properties such as electrical conductivity (10^8 S/m), electron conductivity ($20,000 \text{ cm}^2/\text{VS}$), mechanical strength (breaking point of 42 N/m and Young's modulus of 1.0 TPa), thermal conductivity ($\sim 5000 \text{ Wm/K}$), deflecting cracks, etc. [23–26]. For simplicity, it is 10 times stronger than steel but 1000 times lighter than a sheet of paper per unit area. Graphene materials are not necessarily displayed in a monolayer but might be in a few graphitic layers. The restacking carbon network between graphitic structures is one of the main challenges in a specific related field. According to a synthesized graphene sheet count, one graphitic layer is assigned as a single-layer or monoatomic graphene, two or three graphitic layers are bilayer and trilayer graphene, 5–10 graphitic layers are known as few layer graphene, whereas up to 20 layers are categorized as multilayer graphene or nanocrystalline thin graphite. Furthermore, the roughness of the graphene texture is caused by an expanded surface area with 2D geometry. It has great surface bonds, tightly surrounded by polymers, and addresses the efficient interfacial load transfers. A planer sheet of graphene boosts the surface area in contact with the polymers compared to other carbon phases [1].

Currently, graphene-based composite nanomaterials and their derivatives have been extensively researched in the field of renewable energy. Researchers have now discovered that graphene anodes have the capability of sustaining up to 10 times battery charging in electric vehicles compared to graphite. In fact, Liu and coworkers also reported that graphene could combine with boron dopants as an ultrathin flexible anode to facilitate an efficient charge rate for lithium ion battery applications [27]. Also, graphene has the ability to recharge in 20 s and retain more than 90% of its capacity when incorporated with vanadium oxide. Moreover, graphene could also develop in a hydrogen fuel cell with nitrogen, and cobalt will perform effectively as a durable catalyst for hydrogen production from water instead of Pt material [28]. In fact, graphene itself could revolutionize graphene-based transistors, medical devices, display technology, power-generating buildings, salon hair dyes, the potability of seawater, wall illuminations, lightweight protective gear, and fuel from thin air [1].

3.1 Properties of graphene material

Graphene possesses many desirable physical, thermal, electrical, and optical properties that are highly sought after for solar PV applications. In this section, the properties of graphene that prompted it to be dubbed the “wonder material” for PV applications will be discussed in brief.

3.1.1 Physical properties

Being made of a single layer of carbon atoms approximately 0.35 nm thick, graphene is undeniably one of the thinnest materials known to science. However, this single layer of graphene is not 100% flat. Instead, it contains ripples in the form of minute hills and valleys due to the realignment of the carbon atoms for thermodynamic stability ([Fig. 1](#)) [29].

It is also very lightweight at only 0.77 mg/m^2 . To date, graphene has been touted as the toughest 2D material—much stronger than a similar-sized diamond. Lee et al. reported that the tensile strength of graphene is 125 GPa, while its elastic modulus is 1.1 TPa [30]. This means that in addition to its strength, graphene is also highly flexible. This makes it very attractive for use in flexible solar cells.

3.1.2 Thermal properties

Similar to electronic equipment, heat is detrimental to solar cell operations. This is because excess heat increases phonon vibrations in the crystal lattice. In turn, the increased vibrations can interfere with the mobility of photogenerated electrons in the solar PV device. As a result, the PV efficiency of the solar cell reduces. Thus the high thermal conductivity of graphene is highly desirable for PV applications. Thermal conductivity refers to the ability of a material to pass heat from one object to another through physical contact. In the case of graphene, its thermal conductivity was found to be within the range of

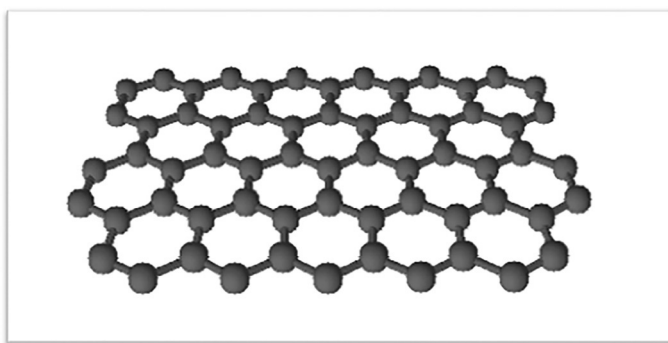


FIG. 1 Ripples in a sheet of graphene.

4.84×10^3 to 5.8×10^3 W/mK at room temperature [25]. These values are 12 times higher than the thermal conductivity of copper at approximately 401 W/mK at room temperature. It is for this reason that graphene is considered to be an excellent heat conductor. In fact, several studies have reported an unlimited potential for heat conduction by graphene [31, 32]. In both computer simulations and experiments, researchers found that the larger the segment of graphene, the more heat it could transfer. Theoretically, graphene could absorb an unlimited amount of heat.

3.1.3 Electrical properties

Zero-overlapped or zero bandgap graphene is remarkably advantageous in related electrical fields, where it is identified that both holes and electrons could be counted as charge carriers and even be directly applied to high-conductivity appliances. Theoretically, a carbon atom has a total of six electrons (two inner shells with four outer shells); the four outer shell electrons are free to bond with other alien chemicals but graphene has extraordinary properties where each atom is connected with three other carbon atoms on the 2D plane, leaving one electron moving around in three-dimensional (3D) electronic conduction. These mobile electrons are defined as pi (π) electrons and are located in between graphene sheets. These π orbitals overlap and facilitate C—C bonds in graphene. In addition, the Dirac point of graphene, mostly categorized as zero effective mass between electron-hole pairs, shows that the excitation is linear for low energies near to the six respective corners of the Brillouin zone. In other words, the Dirac point demonstrates that the Dirac fermions, Graphinos, and six corners of the Brillouin zone are considered to be the electrons and holes. However, zero density of states at the Dirac point actually creates a very low electrical conductivity. As such, the doping approach is one of the few tricks to tune the Fermi level for better electrical conductivity.

3.1.4 Optical properties

A single sheet of graphene has the ability to absorb up to 2.3% of visible light, resulting in rapid charge carrier mobility because of its massless density (see previous paragraph). It is noted that the same value of 2.3% absorbance increases of graphene layer in the moment for light abusability increase purpose. The 2.3% of optical intensity converts into a universal dynamic conductivity expression as shown in the following equation:

$$G = \frac{e^2}{4h} \quad (1)$$

where $\pi\alpha = G = 2.3\%$ over the visible frequency range.

4 Synthesis of graphene and its derivatives for thin film PV cells

Graphene synthesis is based on two types of methodology, namely the “top-down” (destruction) approach and “bottom-up” (construction) approach. By using the “top-down” approach, the starting material, graphite, is usually isolated and delaminated into single, bi-, and a few layers of graphene by using methods such as mechanical exfoliation [33], oxidative exfoliation-reduction [34–36], liquid-phase exfoliation [37, 38], and electrochemical exfoliation [39, 40]. These methods will break the graphite to form nano-sized graphene. Generally, most of the “top-down” method is highly expendable and produces high crystal quality of graphene but the production yield is still low and insufficient for practical application. In the “bottom-up” approach, graphene is synthesized by molecular growth from small molecular carbon precursors using methods such as chemical vapor deposition (CVD) [41, 42], epitaxial growth [43, 44], and the template route [45]. The thickness (number of layers) of graphene can be controlled by using different substrate catalyst and synthesis parameters. Although these methods produce almost defect-free and high-surface area graphene, they often require high-cost production and sophisticated operational setup.

Graphene is a game-changer for conductive transparent devices due to its 2D structures and unique optical and electrical properties. In the past few decades, graphene has been widely explored as a PV material due to properties such as high optical transparency, high carrier mobility, zero bandgap, and high mechanical strength. To date, graphene and graphene nanocomposite have been widely applied as materials for solar cells. They display a significant role as transparent electrodes, photoactive layers, Schottky junctions, and carrier transporters in solar cell devices.

4.1 Deposition technique of graphene and its derivatives of thin film for PV applications

In this section, various deposition techniques and technologies for the fabrication of graphene and its derivatives of thin films for solar cell application will be discussed and emphasized. The deposition techniques are divided into two methods, namely, chemical and physical deposition methods. The chemical deposition method is a reaction wherein the product self-assembles and is deposited on the substrate. It can be further divided into CVD and electrochemical deposition. In the physical deposition method, the graphene precursor, which is in liquid phase or gas phase, is physically deposited onto the substrate by using the spin-coating method, doctor blade method, sputtering technique, or pulse laser deposition technique.

4.1.1 Chemical deposition method

Chemical vapor deposition

CVD is the most popular method and has dominated the deposition of graphene thin films, since it allows good control over synthesis, film thickness, and material properties. During the CVD process, the precursor, which is in a gas, solid, or liquid phase, is injected into/placed in the reaction chamber, where it reacts with a catalyst at elevated temperature. The gas precursor and the assistant gases are usually flowed into the reaction chamber, while solid and liquid precursors are typically added directly onto the substrate by spin coating or other methods. The gas precursor is usually a small hydrocarbon such as methane or ethylene. When the precursor and catalyst come into contact with the substrate within the reaction chamber, material films on the substrate surface will form. A diagram representing the CVD technique is shown in Fig. 2A. By tailoring the experimental conditions, such as substrate material, substrate temperature, composition of the reaction gas mixture, total pressure gas flows, etc., materials with a wide range of physical, tribological, and chemical properties can be grown.

Electrodeposition technique

The electrodeposition technique is an electrochemical deposition method in which the charge particles are directed to an electrode of opposite charge under the influence of an electric field to form a thin film. This technique can be applied to any powdered solid that forms a stable suspension and operates in a wide range of particle sizes from micro- to nanoparticles. Moreover, a variety of target substrates from flat or cylindrical to porous, fibrous or 3D substrate can be applied using this technique, which makes it a versatile and flexible technique to deposit a thin film. It uses simple and cost-effective equipment that requires a short processing time to produce uniform films with high microstructural homogeneity. This technique uses three electrode configurations, which are the working electrode (substrate), counter electrode (Pt), and reference

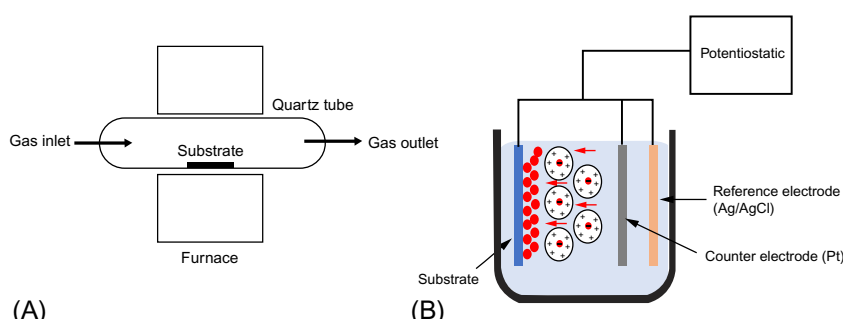


FIG. 2 (A) CVD diagram and (B) electrochemical deposition diagram.

electrode (Ag/AgCl), as shown in Fig. 2B. The thickness of the films deposited via the electrodeposition technique can be easily controlled, thereby making this a suitable technique for upscaling graphene deposition onto conducting substrates. Furthermore, this technique allows a series of parameters such as potential, deposition time, electrolyte, pH, temperature, and state of graphene suspension to vary during the deposition process. It is noteworthy that this technique allows an electrochemical modification of the graphene film to be produced.

4.1.2 *Physical deposition method*

Spin-coating technique

The spin-coating technique is the most common and simple technique for depositing a thin film on a substrate. In this technique, the specific material solution, dispersion, or fluid is dropped cast onto the center of a flat substrate, followed by vigorous spinning of the rotating disk as shown in Fig. 3A. A step-by-step process of spin coating includes the loading of solvent, rotation at high speed, drying, and film formation. The applied solution is distributed on the substrate by centrifugal force during the high-speed rotation. High spinning speed will lead to thinning of the layer, and uniform evaporation (drying process) of the solvent occurs due to the rapid rotation of the disk. The thickness of the films can be controlled by the viscosity of the material solution and the angular velocity of the substrate. The spin-coating method has created the possibility of graphene-coated glass, replacing expensive transparent electrode materials such as indium tin oxide (ITO) or aluminum-doped zinc oxide (AZO). It is a facile and cost-effective method that produces single- to multi-layer films. However, due to the poor adhesion of graphene films to the glass substrate, a few factors such as film roughness, homogeneity, and coverage still need to be addressed for it can be used as an effective method in the future. To overcome these issues, the substrate needs to be pretreated or the graphene needs to be functionalized [46]. Kymakis et al. reported that a systematic spin-coating procedure by the glass substrate has undergone pretreatment by using thermal treatment at 200°C [47]. A series of spin coatings at different rotation speeds were done using graphene powder, which was dissolved in water at a concentration of 15 mg/mL. The graphene films were reduced with hydrazine vapor and further annealed at 400, 800, and 1000°C under argon (Ar) conditions. The thickness of the graphene films varied from 5 to 20 nm depending on the annealing temperature. It was reported that the Ar annealing temperature is directly related to the sheet resistance of the films. As the annealing temperature increased, both transparency and sheet resistance reduced. The spin-coating method was also applied in depositing graphene/metal oxide and graphene/polymer nanocomposites. In DSSCs, graphene/poly(3,4-ethylenedioxythiophene) polystyrene sulfonate (PEDOT:PSS) composites were spin coated onto an ITO substrate, which demonstrated a potential for replacing

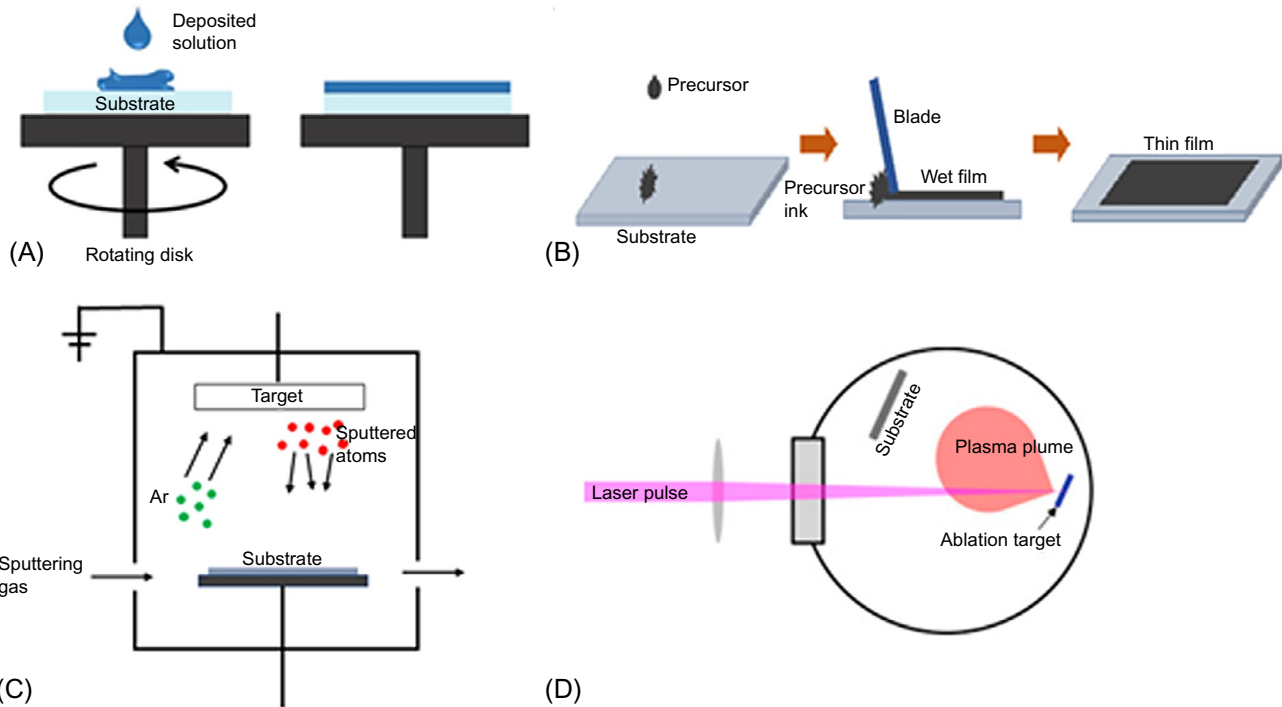


FIG. 3 Schematic diagram of (A) spin coating, (B) doctor blade, (C) sputtering and pulse laser deposition process.

Pt as a counter electrode [48]. It was also reported that the graphene/PEDOT:PSS composites possess a thickness of \sim 60 nm, while a single sheet of graphene had a thickness of only 2.1 nm. These devices show improvement in efficiency from 2.3% to 4.5% by adding 1 wt% of an untreated graphene to PEDOT:PSS. Although applying Pt as counter electrode gave a much higher efficiency, having further improvements in graphene films may lead to an even better efficiency.

4.1.3 Doctor blade technique

The doctor blade technique is one of the widely used methods for producing a large-area thin film. Generally, in the doctor blade technique, a well-mixed slurry consisting of a suspension of specific material along with additives such as binders is placed on a flat substrate. When a constant relative movement is applied between the blade and the substrate, the slurry spreads on the substrate to form a thin film upon drying. A schematic diagram of the doctor blade technique is shown in Fig. 3B. This technique is able to produce a very wide range of film thicknesses ranging from 20 to several hundred microns. Eshaghi et al., Tsai et al., and Shahid et al. intensively used the doctor blade method to deposit graphene in DSSCs. They reported successful deposition of graphene-metal oxide and graphene-polymer nanocomposite as a cathode, replacing the Pt electrode with enhancement of photocurrent efficiency [49–51].

4.1.4 Sputtering technique

Sputtering is a nonthermal vaporization process where surface atoms are physically ejected from a solid surface by momentum transfer from an atomic-sized energetic bombarding particle, which is usually a gaseous ion, accelerated from a plasma. This technique can be performed by energetic ion bombardment of a solid surface (sputtering target) in a vacuum using an ion gun or low-pressure plasma (<5 mTorr), where the sputtered particles suffer few or no gas-phase collisions in the space between the target and the substrate. Sputtering can also be done under higher plasma pressure (5–30 mTorr) where energetic particles sputtered or reflected from the sputtering target are “thermalized” by gas-phase collisions before they reach the substrate surface. The plasma used in sputtering can be confined near the sputtering surface or may fill the region between the source and the substrate. The sputtering source can be an element, alloy, mixture, or compound and the material is vaporized with the bulk composition of the target. The sputtering target provides a long-lived vaporization source that can be mounted to vaporize in any direction. A schematic diagram of the sputtering process is shown in Fig. 3C.

Typically, the sputtering technique has two means of operation: direct current (DC) and radio frequency (RF), which also function in two configurations: magnetron DC (balanced and unbalanced) and magnetron AC (balanced and unbalanced). DC is the most common sputtering operation whereby the target

material is bombarded with ionized gas molecules causing atoms to be “sputtered” off into the plasma. These vaporized atoms are then deposited when they condense as a thin film on the substrate. The DC sputtering technique has been widely used in research and industry as the process is easy to control, low cost, and produces uniform thin film.

In the DC sputtering technique, the target material is placed in a vacuum chamber parallel to the substrate to be deposited. The vacuum chamber is evaluated to the base pressure and high-purity inert gas is backfilled into the chamber. Inert gas like Ar is usually used, due to its relative mass and ability to convey kinetic energy upon impact during high-energy molecular collisions in the plasma, which creates gas ions that are the primary driving force of sputter thin film deposition. The sputtering pressure and DC electrical current are varied to achieve a desired thin film for each material. The electrically neutral Ar gas atoms are first ionized, resulting in forceful collision of these gas atoms onto the surface of the negatively charged target (cathode), which ejects the atom off into the plasma. The ionized Ar gas is then driven to the substrate, which has a positively charged bias (anode), attracting ionized gas ions, electrons, and the vaporized target material atoms, which will condense and form a thin film on the substrate. Another type of DC sputtering is DC magnetron sputtering, which uses a magnet behind the negative cathode to trap electrons over the negatively charged target material. The magnetic field forms a boundary “tunnel” that traps electrons near the surface of the target, and ultimately improves the efficiency of gas ion formation. DC magnetron sputtering allows for higher current at lower gas pressure and achieves an even higher thin film deposition rate. Although this technique is an economical choice for deposition of many types of metal, its primary limitation is for the deposition of dielectric target materials, which are nonconducting and can take on a polarized charge. To overcome this limitation, the RF sputtering technique can be used for depositing nonconducting materials.

RF sputtering is a technique that involves alternating the electrical potential of the current in the vacuum environment at RFs. This is to avoid charge building up on certain types of sputtering target materials, which over time can result in arcing into the plasma, where spew droplets will create quality control issues on the thin films and can even lead to the complete cessation of the sputtering of atoms. The process will then need to be terminated. The basic operations of RF sputtering and RF magnetron sputtering techniques are as same as DC sputtering and DC magnetron sputtering techniques. The only difference is that the electrical potential of this technique uses RF. By alternating the electrical potential with RF sputtering, the surface of the target material can be “cleaned” of a charge buildup with each cycle. The positive cycle electrons are attracted to the target material or cathode giving it a negative bias. On the negative portion of the cycle, which occurs at an RF of 13.56 MHz (used internationally for RF power supply equipment), ion bombardment of the target to be sputtered will continue. The most recent research into the deposition of multilayer graphene

by using RF magnetron sputtering is by Nakajima et al. [52]. The multilayer graphene has been deposited by using carbon (C) as target on the SiO₂ substrate in the presence of Ni, Co, and Fe thin film layer as catalyst at 400°C with a deposition rate of 2.2 nm/min in Ar plasma. High-crystalline multilayer graphene was successfully produced, proving that this technique has great potential for integrating graphene-based devices on various applications, especially solar cells. Zhang et al. reported on the deposition of a graphene/Co₃O₄ nanocomposite by using the RF magnetron sputtering technique [53]. In their study, graphite was used as a target and deposited on Co₃O₄/Ni foam at 600°C in Ar conditions. The thermal treatment at 600°C during the sputtering leads to the transformation of graphite to graphene.

4.1.5 Pulse laser deposition technique

Pulse laser deposition is another reliable technique to produce high-quality thin film. This technique consists of irradiating the surface of a target material with sufficiently intense pulse laser beam inside a vacuum chamber. The irradiated volume will be vaporized and the flux of the material will form and collect onto a substrate to grow a thin film. When a sufficiently intense laser beam is focused on the surface of a target material, different phenomena take place; pure thermal or electronic properties occur, leading to the ejection of material from the target as a form of electrons, atomic species, diatomic species, or aggregates. The ejected material forms a luminous plume directed toward the substrate placed in front of the target, where it will recondense and form a thin film. A schematic diagram of pulse laser deposition is shown in Fig. 3D. The deposition of graphene thin film by the pulse laser deposition technique using pyrolytic graphite as target and pulsed KrF laser was used as the excitation source reported in [53]. The graphene films were grown directly on the single-crystal Cu substrate with the target continuously rotated to ensure each pulse laser could shoot on the fresh surface during the deposition process. High-pulse laser energy offers large incident energy for carbon particles deposited on the surface of the Cu substrate, which is beneficial to the nucleation of graphene. As the incident particles increase, the graphene nuclei are combined and grow together to form a thin film.

5 Mechanism/working operation of graphene/graphene metal oxide for PV cells

With the increasing demands of renewable energy as alternative sustainable resources, PV is acknowledged as low cost with a high-volume return, where it is definitely a free and clean resource under solar harvesting. In PV energy conversion, the main concern is to achieve better PCE. There are four basic generations and integrated types of smart grid solar cell devices such as silicon, thin film, organic, futuristic, artificial intelligence controllers, smart home concepts,

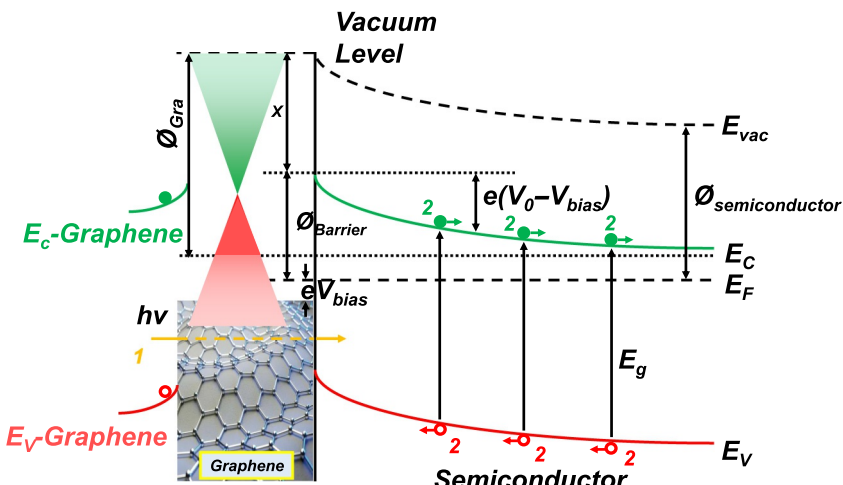
etc. The most influential factor for overall PCE performance is the material used for the renewable solar energy application. There has been a huge improvement after continuous research and it has gained 300 GW over global installation of crystalline silicon PV cells over the past 2 years. This amount was equivalent to ~80% of globally installed PV cells. Next, thin film-based solar technologies were established for CdTe, CIGS, and also amorphous silicon. The aim is to find an alternative cheaper process and a promise of better mechanical properties compared to first-generation solar cells. Furthermore, developments in thin film solar technologies are more focused on the growth of methods, and also the involvement of electrochemistry, not unlike the first generation of microelectronics fabrication. Apart from this, third-generation technologies were categorized as emerging concepts due to their low market demand. Third-generation PV cells basically consist of organic, dye-sensitized, perovskite, tandem, and high-cost with high-efficiency carriers called III–V multijunction PV devices. Commonly, the nanoarchitecture of material plays an essential role in every single PV cell to create efficient charge carrier mobility to reduce the cost of production. 2D materials were also tried in their hard-to-fabricate devices, to be converted into hybrid/polymer to enhance the PCE performance of PV cells. However, stability is still poor and the devices have limited practical applications.

Today, nanocarbon materials find themselves being used in PV solar systems due to their flexibility in tunable electrical and optical properties. Both of these outstanding properties are sufficient to fulfill the criteria of PVs and address improvement of charge carrier mobility and wide bandgap energy, reduction of recombination center, decrease of sheet resistance, reduction in corrosion rate and degradation, and hence increase in the lifespan of PV cell systems. Recently, numerous researchers have intensively explored a variety of carbon nanomaterials, including zero-dimensional (0D) material of fullerene, one-dimensional (1D) material of carbon nanotubes (CNTs), 2D material of graphene, and 3D material of diamond or graphite that is widely used as a catalyst agent in every single PV cell. Surprisingly, carbon nanomaterial incorporated with silicon (Si) can perform a highly efficient heterojunction with a PCE of 29.43% [54]. Eventually, 2D material of graphene will become a flexible graphitic building block for other dimensional patterns. For example, when graphene sheet is cut and folded into a spherical shape, it transforms into 0D fullerene. Also, graphene building blocks can be formed into 1D CNTs when they are rolled up, while graphene sheets that are stacked on top of each other become 3D graphite (1 mm thick graphite contains about 3 million layers of graphene). Nonetheless, 2D graphene could assist PV solar systems for enhancement of conductivity and strengthen light access due to its high transparency. However, graphene itself has poor behavior in electrical current collecting in PV cells. Thus PV-based graphene incorporating metal oxide with wide bandgap energy is required such as ZnO, TiO₂, Cu₂O, Al₂O₃, SnO₂, WO₃, NiO, In₂O₃, etc. Henceforth, this section will briefly explore how the participation

of 2D graphene material with metal oxide as part of solar elements can enhance the overall PCE performance for current solar technologies in terms of mechanism or working principle (i.e., p-n junction, membrane, photoanode, counter electrode, hole transport material, electron transport material, etc.).

5.1 Graphene-based Schottky solar cells

Fig. 4 illustrates an energy diagram of p-n junction theory where a semiconductor is reinforced with graphene-based Schottky solar cells. Specifically, the working solar cell system illustrates that the photons from a light source are converted into useful electricity. However, the phonons will create a different energy, which is then accessed into the solar cell system. Furthermore, charge carrier separation is composed of two main motions. The first is “drifting of carriers” with excited electrons being pushed away and a hole being left at the opposing direction. Another charge carrier motion is called “diffusion of carriers” where $\phi_{carrier}$ is lower than $e(V_0 - V_{bias})$ resulting in a charge recombination incident. As shown in **Fig. 4**, the induced PV is dominated by the Schottky barrier formed at the graphene/semiconductor interface due to the difference in



$\phi_{Gra}, \phi_{semiconductor}$: Work functions of graphene & semiconductor;

eV_0 : Built-in potential;

V_{bias} : Output voltage of the solar cell;

X : Electron affinity of semiconductor;

$E_{vac}, E_c, E_F, E_g, E_V$: Vacuum level; conduction band edge; Fermi level of semiconductor; band gap energy; valence band edge

eV_{bias} : Applied bias voltage potential

FIG. 4 Energy band diagram of a semiconductor/graphene Schottky junction solar cell under illumination.

E_F value level. The complete cycle of Schottky solar cell-based graphene material is as follows:

1. The harvest energy is absorbed into the graphene/semiconductor interface during illumination. Typically, once photon energy is higher than the E_g value of the semiconductor, the photon energy will be absorbed, and electron-hole pairs will be created.
2. An excited electron charge carrier will leave a hole at the valence band and drift into the graphene sheet, while the excited electron will transfer into the conduction band and pull toward the semiconductor/graphene.
3. Driven an induced photogenerated carriers obey the hole-electron pairs concept and generate photocurrent electricity.

Eventually, the graphene layer improves the reduction of photogenerated electrons moving backward from the semiconductor to graphene and also assists in charge carrier recombination at the anode element. However, the $e(V_0 - V_{bias})$ value is a rather low barrier ($\sim 0.6\text{--}0.7\text{ eV}$) and becomes lower in the infrared light region, resulting in a large current leakage (high value of short-circuit current).

5.2 Graphene-based Schottky junction GaAs solar cells

Generally, graphene has been intensively fabricated into Schottky barrier solar cells with various semiconductors in typical p-type, n-type, or even metal oxide compounds such as Si [55], SiC [56], CdS [57], GaAs [58], etc. A strong rectifying behavior could be identified from the current/voltage characteristics. Li and his team fabricated GaAs solar cell-based graphene where SiN_x film acts as a dielectric insulating layer between graphene and GaAs substrate [59]. The major advantage of using GaAs material is when it is n-type doped, which has the flexibility of electron carrier flow into the conduction band of the graphene sheet with very low resistivity of $0.01\text{--}0.1\Omega\text{cm}$. According to the work function of GaAs solar cells, the work function of GaAs substrate is $/Q_{GaAs}$ with $4.07 \pm 0.05\text{ eV}$ (denoted as $/Q_{\text{semiconductor}}$ in Fig. 4). Nonetheless, the energy difference between vacuum level and Dirac point of graphene ($/Q_{ra}$) is slightly higher than $/Q_{GaAs}$ with 4.6 eV . In addition, the Fermi level of graphene can be easily tuned by doping concentration. Once the van der Waals forces of graphene are connected with GaAs, a Schottky junction will be generated between graphene and GaAs, thus forming a depletion region and also a built-in barrier. In GaAs-graphene solar cells, the barrier height of the Schottky junction, $/Q_{\text{barrier}}$, is the difference between $/Q_{GaAs}$ and $/Q_{ra}$. In a GaAs-graphene Schottky junction, there are two conditions for current density: voltage ($J\text{-}V$) evaluations, which are in dark conditions and under light illumination. Under light harvesting conditions, the production of electron-hole pairs in GaAs substrate will be governed by the basic concepts of the Schottky junction and the charge carrier will eventually transport into GaAs and also graphene. On the other hand, the $J\text{-}V$

characteristics will be measured as in the following expressions, especially in dark conditions:

$$\text{Thermionic - emission theory, } J_o = AT^2 \exp\left(-\frac{q\phi_{\text{barrier}}}{KT}\right) \quad (2)$$

$$J = J_o \left(\exp \frac{qV}{N_{IF}KT} - 1 \right) \quad (3)$$

where $A = 8.9 \text{ A/k}^{-1} \text{ cm}^{-2}$, the effective Richardson's constant of GaAs; $K = 1.38 \times 10^{-23} \text{ J/K}$, the Boltzmann constant; N_{IF} = junction ideality factor; and $q = 1.602 \times 10^{-19} \text{ C}$, the electron charge.

5.3 Graphene-based organic solar cells

5.3.1 Graphene-based bulk-heterojunction organic solar cells

The working principle of bulk-heterojunction organic solar cells can be divided into four main processes: (1) photon absorption and exciton production; (2) exciton diffusion and splitting; (3) charge transportation; and (4) charge collection [60]. These processes are summarized as follows:

1. Photon absorption and exciton production: Photon absorption under light harvesting and excited electron transport from the highest occupied molecular orbital (HOMO) to the lowest unoccupied molecular orbital (LUMO) and the offset between LUMO and HOMO should be around 0.1–1.4 eV to produce electron-hole pairs (excitons).
2. Exciton diffusion and splitting: The electron-hole pairs must have sufficient electrostatic force to diffuse the free charge carrier from LUMO to jump into HOMO while preventing recombination occurrence.
3. Charge transportation: After free charge carriers are generated, they will be transported in organic semiconductors based on the Fermi level of the electrode configuration. Normally, these charge transports are mainly driven by carrier diffusion or electric field-induced drift.
4. Charge collection: The charge carriers without recombination are collected and considered as photogenerated charge. These charges are collected at respective electrodes. The charge collection will be measured at the final step and generated into a useful photocurrent source.

5.3.2 Dye-sensitized solar cells

The structure of TiO_2 incorporated with a graphene (graphene- TiO_2) nanocomposite-based photoanode for DSSCs is shown in Fig. 5A. Generally, the entire interface of DSSCs is assembled in a sandwiched configuration, which comprises FTO as a glass slide as photoanode to allow visible light absorption, N-719 dye sensitizer for electrostatic binding with TiO_2 , KI electrolyte for redox pair reaction, and counter electrode for charge carrier

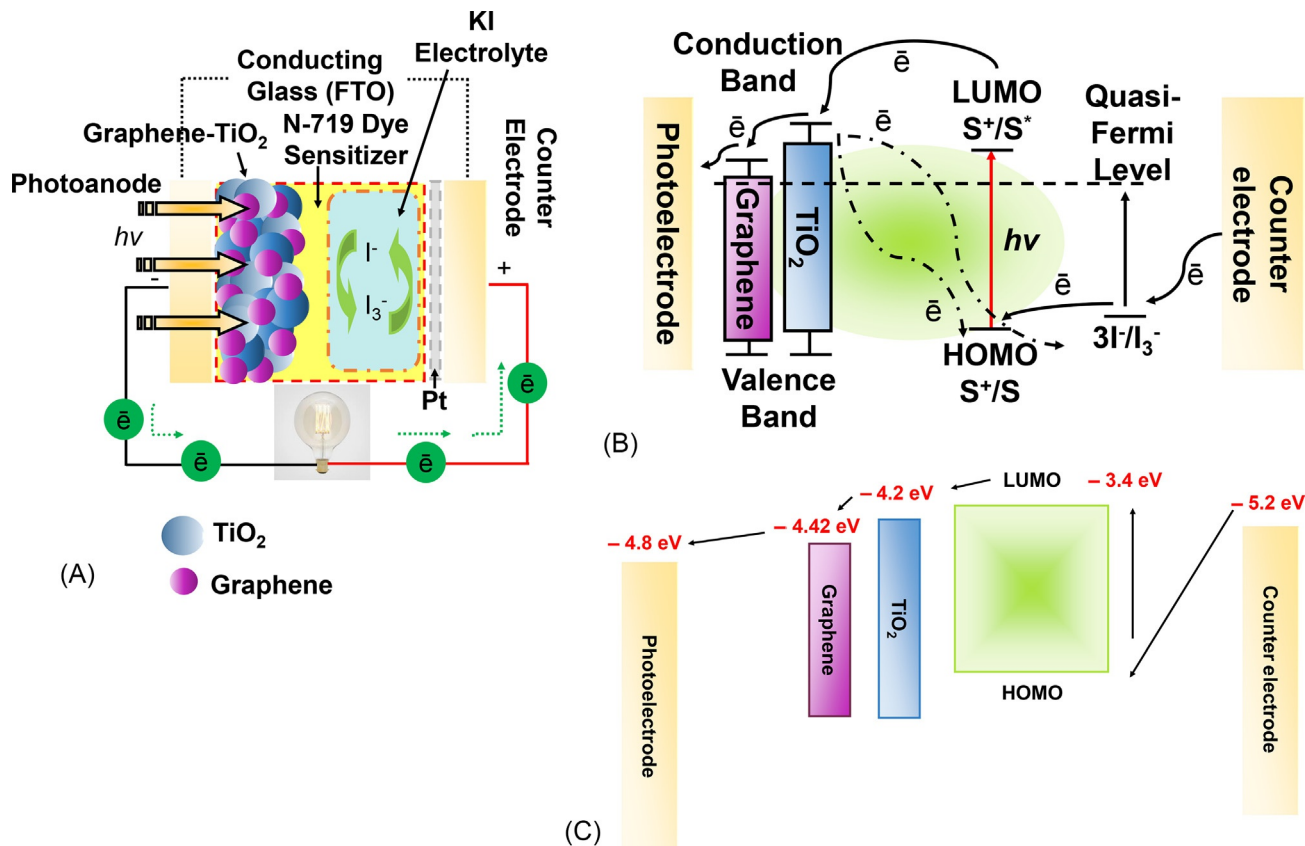


FIG. 5 Schematic diagram of graphene-based DSSCs: (A) working principle, (B) electron transport mechanism, (C) energy diagram.

electron transport from the outer circuit and to regenerate the excitation/oxidation/reduction process.

Basically, a working DSSC device consists of a photoanode coated on a transparent conductive oxide/FTO (TCO/FTO) glass slide deposited with a wide bandgap semiconductor or metal oxide (TiO_2 , ZnO , Fe_3O_4 , SnO_2 , etc.). Some improved DSSC devices will apply superconductor materials like graphene to improve the overall PCE performance, a dye sensitizer anchored to the surface of metal oxide (N-719 dye, N-3, N-749, Z-907, etc.), an electrolyte used for redox-coupled pair reaction (iodide and triiodide ion formation, I^-/I_3^-), and FTO coated with metal thin film (typically Pt, Ag, Zn, etc.) [61]. A complete schematic diagram of a working mechanism of a DSSC device is illustrated in Fig. 5B. When the cell device is irradiated under UV light region, the light photons will anchor with the dye molecules (S) and consequently form excited state S^* after photon absorption. Within a short duration, the electrons will be injected into TiO_2 and the S^* will be oxidized into S^+ (Eq. 3). At the same time, the electrons will be injected into the conduction band of TiO_2 from the valence band and then transport the electron through the graphene. Subsequently, electrons will flow to the external load and reach the counter electrode. At this moment, the oxidized dye molecules S^+ are reduced into the original S by regaining electrons from the organic electrolyte solution. Thus the electrolyte solution contains an I^-/I_3^- redox pair system in which the I^- ions are being oxidized to I_3^- ions resulting in a hole in the dye molecules. To further restore the I^- ions, a free electron is needed from the counter electrode to reduce the I_3^- molecules to an I^- state. This complete loop of the regenerated excitation/oxidation/reduction cycle thereby establishes a continual conversion of solar energy into useful electricity.

Fig. 5C shows the energy level of the entire device configuration with photoanode/graphene/ TiO_2 /LUMO-HOMO energy level and also counter electrode with -4.8 , -4.42 , -4.2 , -3.4 , and -5.2 eV, respectively. Initially, the excited electrons in dye molecules are being introduced into a high-energy state (HOMO) with associated energy level (~ -6.0 eV) and simultaneously creating an electron-deficient low-energy state (LUMO, -3.4 eV). Luckily, LUMO energy level is higher than the conduction band of TiO_2 to facilitate electron injection into graphene thin film before being transported into FTO glass at the photoanode. The graphene was promoted as a catalyst pathway with lower energy level (-4.42 eV) compared with TiO_2 (-4.2 eV), which facilitates and accelerates electron charge carrier mobility, hence resulting in better PCE performance.

5.3.3 Tandem solar cells

You et al. constructed polymer tandem solar cells based on graphene oxide (GO) and successfully obtained an optimized PCE performance with an

impressive result of 10.6% [62]. They fabricated an ITO/PEDOT:PSS/PCDTBT:PCBM/GO-Cs/Al/GO/MoO₃/PCDTBT:PCBM/Ca/Al structure and showed a PCE of 3.91%. Besides, they also measured the ITO/PEDOT:PSS/PCDTBT:PCBM/Ca/Al structure without GO and gained a PCE of 2.92%. However, the interconnecting layer resistance was in the sequence of GO-Cs/Al/GO/MoO₃>GO-Cs/Al/GO>GO-Cs/GO. Furthermore, they also proved that GO played an important role in the GO-Cs/Al/GO/MoO₃ composite for improvement in open-circuit voltage.

5.3.4 Perovskite solar cells

PSCs are typically constructed with ETL/CH₃NH₃PbI₃ recognized as an MAPI/HTM/counter electrode configuration. In PSCs, ETL is one of the main parts that enhances PCE performance. Material selection for ETL is a crucial process to determine light absorption. However, the wide bandgap of TiO₂ (3.2 eV) has light sensitivity limitation below ~380 nm and charge recombination occurs for electron-hole pair formation [63]. Therefore graphene, which is relatively low cost and available in abundance, is used due to its high electric charge carrier mobility. Comprehensively, graphene could be incorporated with TiO₂ and form a nanocomposite to easily inject the excited electrons from TiO₂ into the graphene surface, and thus extend the light absorption cutoff wavelength. As shown in Fig. 6A, PSCs consist of a transparent anode (i.e., FTO), a highly porous semiconductor (graphene-TiO₂ nanocomposite) layer as ETL, MAPI as the main perovskite source, CuO as HTM, and silver as counter electrode. The working principle of PSCs is such that perovskite will harvest the high-energy photons from the solar irradiation and then the photoelectrons will release an excited electron from the perovskite. The excited electron is then injected into the conduction band of TiO₂, and then across graphene layer, hence leaving a temporary hole in the perovskite region. The electrons will flow through the outer circuit, passing through the counter electrode and HTM. Lastly, the electron will replace the hole at the perovskite. Referring to Fig. 6B, the working principle of PSCs is such that the Fermi level of perovskite should be higher than TiO₂ during the extraction of photoelectrons, whereas HTM should be lower than perovskite during the extraction of holes. With the assistance of a graphene layer, the extracted electron will flow faster into FTO glass from TiO₂ [64].

6 Graphene-incorporated PV application

Highly efficient charge carrier mobility is needed to improve the overall PCE performance of solar cells. In fact, the material itself also plays an important factor. Therefore a variety of materials has been explored for fabrication layer devices and their test characterizations [65–69]. Among these novelty materials, the 2D carbon network family has a number of fascinating properties such

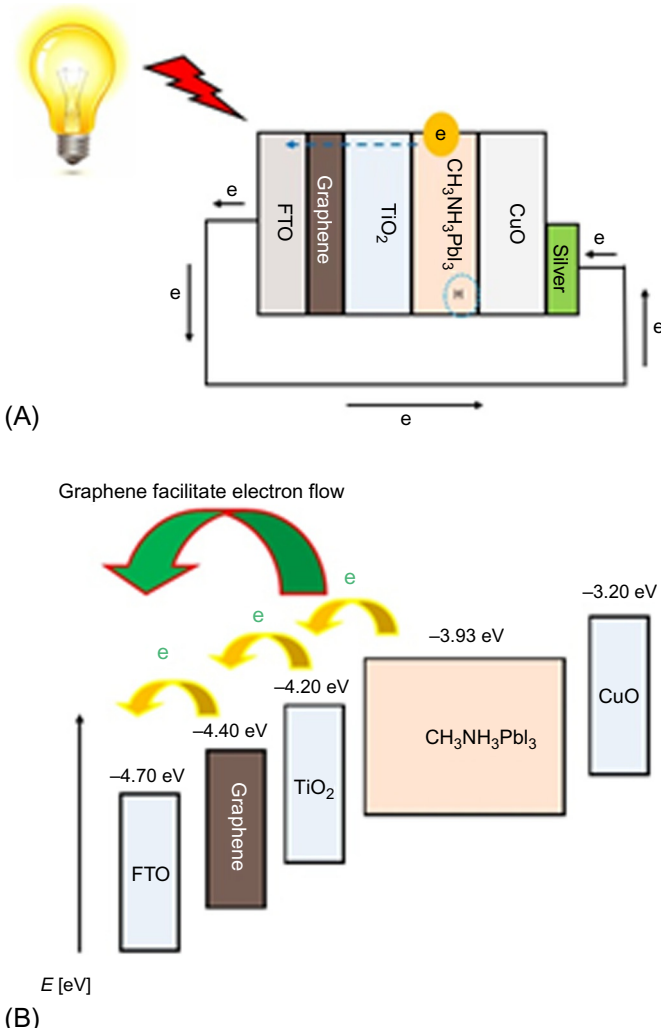


FIG. 6 (A) Schematic diagram of PSCs and (B) energy diagram of a graphene-TiO₂ anode system.

as electronic, optical, and thermal properties, which could trigger PV performance. These outstanding properties will definitely benefit the PV devices with graphene-based material and also its derivative compounds. Thus graphene material has been intensively explored for every PV generation as functional electrodes (i.e., photoanode, counter electrode, ETL, hole transporting material, etc.). Fig. 7 illustrates graphene material applications in various types of PV technologies.

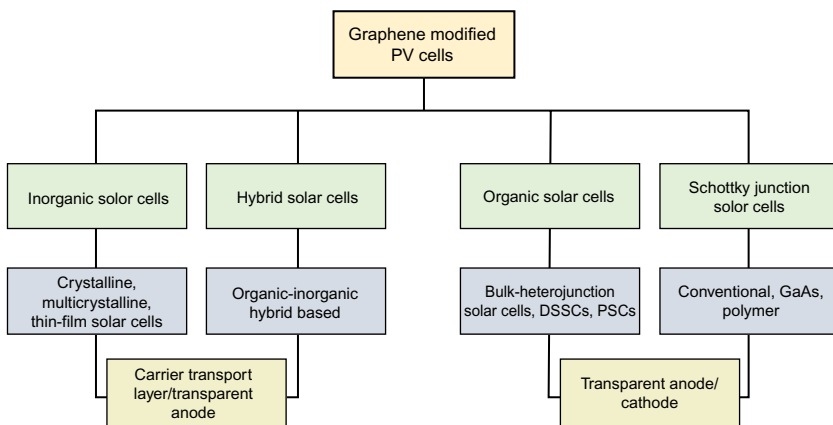


FIG. 7 Schematic diagram of graphene catalytic material incorporation for various types of PV applications.

6.1 Inorganic solar cell technologies

Attempts were made to implement different allotropes of carbon material into silicon PV cells to reduce the overall production cost. Most of the other carbon allotropes obtained poor PCE performance due to the bandgap and thickness of the layers, thus the electronic properties could not be tuned. However, they can still be tuned by adding a doping mixture and analyzing the measurements. This graphene concept is not only applicable for silicon, n-type/p-type heterojunction, crystalline, and thin film, but also for Schottky junction solar cells. Notably, graphene possesses high transparency over a wide absorption spectral range. Lastly, graphene reacts as a substitute not only for ITO conducting glass, but also as a cathode electrode.

6.1.1 Carrier transport layer

In fact, the high aspect ratio and large surface area of graphene materials can be impactful for exciton dissociation as well as charge carrier transport, thus facilitating enhancement of the overall PCE performance. Li and his coworkers established a pioneering work for silicon Schottky junction-incorporated graphene up to 11.5% [70]. Besides, some researchers have also tried to improve PCE performance by varying their doping material, coating parameter, and interfacial layer [71–73]. Graphene doping for silicon solar cells could increase the concentration carrier and thus improve conductivity. On the other hand, the antireflecting coating of graphene could improve the absorption of photons under light trapping and achieve a PCE of 15.6% [74]. It was found that an interfacial layer manages to resist the electrons and transmits holes to reduce the recombination center and eventually enhance the overall PCE performance.

However, there are some critical factors that could impede PCE performance in terms of photocurrent characteristics for a graphene/silicon-based Schottky junction. These factors include recombination, transparency, and short lifetime of excitons provided by the graphene itself. The thickness of the applied graphene is typically thinner than an ordinary p-n junction. However, an optimum thickness of graphene is desired to increase absorption in the photoactive layer. Accordingly, researchers have intensively studied and determined that four layers of graphene are the optimized number of layers resulting in a PCE of 1.48% [75]. Hence, a controlled single layer of graphene is still recommended for further investigation prior to being used in graphene/silicon-based Schottky junction PV cells. The difficulty of thickness control of graphene is therefore another challenge for PV devices.

6.1.2 Graphene as transparent anode

As mentioned previously, graphene exhibits high charge carrier mobility where the charge carriers are delocalized over large surface areas and create a platform for electron-hole transport. High Fermi velocity and the ability to be doped contribute to extremely high in-plane conductivities. Li and his coresearchers developed organic-inorganic hybrid Schottky solar cells with three layers of graphene film as transparent electrode and achieved a PCE of up to 5.48% [76]. They assembled the hybrid solar cells in a sandwiched configuration, including silicon wafer and graphene electrode. Although the graphene-based electrode slightly modifies the structure of silicon solar cells, the concept of traditional PV cells is still maintained. It is believed that lowering the resistance by increasing the thickness of graphene sheet will improve the overall PCE performance. In this context, however, the transparency of the graphene film is needed to allow more light to be transmitted into the PV system. Hence, it is an interesting research challenge to try to increase the thickness of graphene films without compromising the optical transparency of the film. Perhaps this graphene thickness control could be achieved by varying the solution concentration.

6.2 Organic solar cell technologies

To date, graphene electrodes have been applied for different types of solar cells, namely, solid-state solar cells, electrochemical solar cells, QDSCs, and polymer solar cells. The main advantages of applying graphene in different solar cells are: (1) it creates a window for inducing wide ranges (from ultraviolet to far-infrared regions) of photon energy inside the solar cells, (2) it exhibits higher charge transfer kinetics at the interface of electrochemical hybrid cells, (3) it manufactures a flexible device with robust architecture, and (4) it provides greater heat dissipation. On the other hand, electrocatalytic activities of graphene play a key role in enhancing the efficiency of electrochemical solar cells.

6.2.1 *Transparent cathode*

Graphene and graphene-conducting polymer composites could possess excellent electrocatalytic activity and high conductivity for redox electrolytic reduction purposes at the counter electrode for DSSC application. The criteria for an efficient counter electrode in DSSCs are as follows:

- Low charge transfer resistance (R_{CT})
- High reflectance of transmitted light
- High current density
- High surface area with porous nature
- Good adhesivity with TCO film
- Good mechanical stability

So far, Pt is commonly applied as a counter electrode for DSSCs because it is an efficient metal for redox reaction (triiodide/iodide). However, high cost and susceptibility to corrosion are the drawbacks of Pt. To fulfill the criteria as mentioned previously, carbonaceous graphene material is the ideal alternative to Pt as the cathode element because it provides high electrical conductivity, high corrosion resistance against I_2 , high reactivity at triiodide reduction, and a surface area for DSSC devices. There are numerous examples of successful graphene incorporation as a conducting polymer for improving the counter electrode (i.e., polybutylene, poly(γ -butyl-L-glutamate), polyaniline film, poly-pyrrole spongy, etc.). It was also discovered that the thickness of graphene is important for its conductivity. Besides, graphene has the ability to sustain current density up to six orders of magnitude higher than copper in terms of stiffness, robustness, and thermal conductivity. Other than the unique properties of graphene described here, there are other properties that make it crucial and useful for PV cells such as inertness either oxygen or water vapor source and efficient electron mobility than traditional basal plane.

6.2.2 *Transparent anode*

For the photoanode of DSSCs, most researchers commonly use TiO_2 material due to its superior properties like wide bandgap energy ($\sim 3.4\text{ eV}$), active photocatalytic activity, and high stability against corrosion [77]. The TiO_2 particles are often deposited with a size range of $\sim 15\text{--}30\text{ nm}$, whereas the thickness is $\sim 5\text{--}15\text{ }\mu\text{m}$ with porosity between 50% and 70%. The colloidal TiO_2 material is usually prepared via the hydrothermal sol-gel method in acidic or basic aqueous media and screen printing on transparent conducting oxide glass. Subsequently, the deposited TiO_2 layer is further annealed around $450\text{--}550^\circ\text{C}$ after screen printing to remove organic additives such as binders or dispersants. Furthermore, there are some common metal oxides such as ZnO , CuO , NiO_2 , Nb_2O_5 , MgO , and SnO_2 , which are applied as photoanode for DSSCs for achieving higher electron mobilities, while reducing electron transport resistance.

7 Conclusion

In this chapter, the properties of graphene, its synthesis, and working mechanism, as well as its application in various PV solar cell technologies, were presented. It is clear that both the inorganic- and organic-based PV solar cells benefited one way or another from the incorporation of graphene and/or its derivatives into their technologies. One-atom thick layer graphene has shown promising prospects with its flexibility of charge carrier mobility and thus impacts positively the entire PCE performance for PV systems. With its outstanding properties, graphene definitely addresses and points to the development of fourth-generation PV solar cells (multijunction and futuristic). It is much hoped that with improved PCE performance along with the reduced cost of these fourth-generation PV solar cells, solar energy will be a dominant and a sustainable source of renewable energy.

Acknowledgments

This work was financially supported by BOLD2025 Grant (No. 10436494/B/2019008 and No. 10436494/B/2019097) and BOLD2025 Publication (No. RJO10436494) under Universiti Tenaga Nasional Sdn. Bhd., Malaysia. Also, this research work was financially supported by the Impact-Oriented Interdisciplinary Research Grant (No. IIRG018A-2019) and Global Collaborative Programme-SATU Joint Research Scheme (No. ST012-2019) under Universiti Malaya.

References

- [1] F.W. Low, C.W. Lai, S.K. Tiong, N. Amin, *Graphene-Based Nanocomposites for Renewable Energy Application*, Springer Nature, 2019.
- [2] W.L. Chin, et al., An overview: recent development of titanium dioxide loaded graphene nanocomposite film for solar application, *Curr. Org. Chem.* 19 (19) (2015) 1882–1895.
- [3] A. Hirsch, The era of carbon allotropes, *Nat. Mater.* 9 (2010) 868.
- [4] International Energy Agency, *World Energy Outlook 2017*, International Energy Agency, 2017.
- [5] G. Masson, I. Kaizuka, A. Detollenaere, J. Lindahl, Report IEA PVPS T1–35: 2019 Snapshot of Global PV Markets, Vol. 2019, (2019).
- [6] Bloomberg New Energy Finance, New Energy Outlook 2019, Available: <https://about.bnef.com/new-energy-outlook/>, 2019.
- [7] T. Matsui, et al., Development of highly stable and efficient amorphous silicon based solar cells, in: Proceedings of 28th European Photovoltaic Solar Energy Conference, 2013, pp. 2213–2217.
- [8] H. Hoppe, N.S. Sariciftci, Organic solar cells: an overview, *J. Mater. Res.* 19 (7) (2004) 1924–1945.
- [9] B. O’regan, M. Grätzel, A low-cost, high-efficiency solar cell based on dye-sensitized colloidal TiO₂ films, *Nature* 353 (6346) (1991) 737.
- [10] J.G. Radich, R. Dwyer, P.V. Kamat, Cu₂S reduced graphene oxide composite for high-efficiency quantum dot solar cells. Overcoming the redox limitations of S₂–/Sn₂– at the counter electrode, *J. Phys. Chem. Lett.* 2 (19) (2011) 2453–2460.

- [11] S. Mathew, et al., Dye-sensitized solar cells with 13% efficiency achieved through the molecular engineering of porphyrin sensitizers, *Nat. Chem.* 6 (2014) 242.
- [12] M.Z. Iqbal, A.-U. Rehman, Recent progress in graphene incorporated solar cell devices, *Sol. Energy* 169 (2018) 634–647.
- [13] J. Nelson, *The Physics of Solar Cells*, Imperial College Press, 2008.
- [14] M.A. Green, E.D. Dunlop, D.H. Levi, J. Hohl-Ebinger, M. Yoshita, A.W.Y. Ho-Baillie, Solar cell efficiency tables (version 54), *Prog. Photovolt. Res. Appl.* 27 (7) (2019) 565–575.
- [15] K. Yoshikawa, et al., Silicon heterojunction solar cell with interdigitated back contacts for a photoconversion efficiency over 26%, *Nat. Energy* 2 (5) (2017) 17032.
- [16] M. Wanlass, *Systems and Methods for Advanced Ultra-High Performance InP Solar Cells*, USA(2017).
- [17] J.F. Geisz, M.A. Steiner, I. García, S.R. Kurtz, D.J. Friedman, Enhanced external radiative efficiency for 20.8% efficient single-junction GaInP solar cells, *Appl. Phys. Lett.* 103 (4) (2013) 041118.
- [18] M. Nakamura, K. Yamaguchi, Y. Kimoto, Y. Yasaki, T. Kato, H. Sugimoto, Cd-free cu(in, Ga)(se,S)₂ thin-film solar cell with record efficiency of 23.35%, *IEEE J. Photovolt.* 9 (2019) 1–5.
- [19] M.P. Suryawanshi, et al., CZTS based thin film solar cells: a status review, *Mater. Technol.* 28 (1–2) (2013) 98–109.
- [20] C. Yan, et al., Cu₂ZnSnS₄ solar cells with over 10% power conversion efficiency enabled by heterojunction heat treatment, *Nat. Energy* 3 (9) (2018) 764–772.
- [21] T. Adhikari, *Amorphous Organic Molecular Glasses for Photovoltaic Applications*, (2018).
- [22] J. Zhao, et al., Is cu a stable electrode material in hybrid perovskite solar cells for a 30-year lifetime? *Energy Environ. Sci.* 9 (12) (2016) 3650–3656.
- [23] A.H. Castro Neto, F. Guinea, N.M.R. Peres, K.S. Novoselov, A.K. Geim, The electronic properties of graphene, *Rev. Mod. Phys.* 81 (1) (2009) 109–162.
- [24] I.A. Ovid'ko, Mechanical properties of graphene, *Rev. Adv. Mater. Sci.* 34 (2013) 1–11.
- [25] A.A. Balandin, et al., Superior thermal conductivity of single-layer graphene, *Nano Lett.* 8 (3) (2008) 902–907.
- [26] H.S.S.R. Matte, K.S. Subrahmanyam, C.N.R. Rao, Novel magnetic properties of graphene: presence of both ferromagnetic and antiferromagnetic features and other aspects, *J. Phys. Chem. C* 113 (23) (2009) 9982–9985.
- [27] Y. Liu, V.I. Artyukhov, M. Liu, A.R. Harutyunyan, B.I. Yakobson, Feasibility of lithium storage on graphene and its derivatives, *J. Phys. Chem. Lett.* 4 (10) (2013) 1737–1742.
- [28] W. Zhou, et al., N-doped carbon-wrapped cobalt nanoparticles on N-doped graphene nanosheets for high-efficiency hydrogen production, *Chem. Mater.* 27 (6) (2015) 2026–2032.
- [29] G. Pacchioni, Graphene: taming the ripples, *Nat. Rev. Mater.* 1 (2016) 16090.
- [30] C. Lee, X. Wei, J.W. Kysar, J. Hone, Measurement of the elastic properties and intrinsic strength of monolayer graphene, *Science* 321 (5887) (2008) 385–388.
- [31] B. Mortazavi, T. Rabczuk, Multiscale modeling of heat conduction in graphene laminates, *Carbon* 85 (2015) 1–7.
- [32] X. Xu, et al., Length-dependent thermal conductivity in suspended single-layer graphene, *Nat. Commun.* 5 (2014) 3689.
- [33] C. Cheng, P. Jia, L. Xiao, J. Geng, Tandem chemical modification/mechanical exfoliation of graphite: scalable synthesis of high-quality, surface-functionalized graphene, *Carbon* 145 (2019) 668–676.
- [34] K. De Silva, H.-H. Huang, R. Joshi, M. Yoshimura, Chemical reduction of graphene oxide using green reductants, *Carbon* 119 (2017) 190–199.

- [35] I.A. Sahito, K.C. Sun, A.A. Arbab, S.H. Jeong, Synergistic effect of thermal and chemical reduction of graphene oxide at the counter electrode on the performance of dye-sensitized solar cells, *Sol. Energy* 190 (2019) 112–118.
- [36] C.K. Chua, M. Pumera, Chemical reduction of graphene oxide: a synthetic chemistry viewpoint, *Chem. Soc. Rev.* 43 (1) (2014) 291–312.
- [37] Q. Wan, H. Wang, S. Li, J. Wang, Efficient liquid-phase exfoliation of few-layer graphene in aqueous 1, 1, 3, 3-tetramethylurea solution, *J. Colloid Interface Sci.* 526 (2018) 167–173.
- [38] X. Gu, et al., Method of ultrasound-assisted liquid-phase exfoliation to prepare graphene, *Ultrason. Sonochem.* 58 (2019) 104630.
- [39] A. Mir, D.K. Singh, A. Shukla, Size distribution of trilayer graphene flakes obtained by electrochemical exfoliation of graphite: effect of the synthesis parameters, *Mater. Chem. Phys.* 220 (2018) 87–97.
- [40] J. Lee, S. Noh, N.D. Pham, J.H. Shim, Top-down synthesis of S-doped graphene nanosheets by electrochemical exfoliation of graphite: metal-free bifunctional catalysts for oxygen reduction and evolution reactions, *Electrochim. Acta* 313 (2019) 1–9.
- [41] S. Naghdi, K.Y. Rhee, S.J. Park, A catalytic, catalyst-free, and roll-to-roll production of graphene via chemical vapor deposition: low temperature growth, *Carbon* 127 (2018) 1–12.
- [42] M. Son, M.-H. Ham, Low-temperature synthesis of graphene by chemical vapor deposition and its applications, *FlatChem* 5 (2017) 40–49.
- [43] G. Yazdi, T. Iakimov, R. Yakimova, Epitaxial graphene on SiC: a review of growth and characterization, *Crystals* 6 (5) (2016) 53.
- [44] H. Huang, S. Chen, A. Wee, W. Chen, Epitaxial growth of graphene on silicon carbide (SiC), in: *Graphene*, Elsevier, 2014, pp. 3–26.
- [45] Z.-L. Cheng, B.-C. Cao, P.-R. Wu, L. Ma, Z. Liu, Templatized synthesis of graphene nanosheets within curling layered nanostructure of halloysite nanotubes, *Mater. Lett.* 202 (2017) 62–65.
- [46] V.C. Tung, M.J. Allen, Y. Yang, R.B. Kaner, High-throughput solution processing of large-scale graphene, *Nat. Nanotechnol.* 4 (1) (2009) 25.
- [47] E. Kymakis, E. Stratakis, M. Stylianakis, E. Koudoumas, C. Fotakis, Spin coated graphene films as the transparent electrode in organic photovoltaic devices, *Thin Solid Films* 520 (4) (2011) 1238–1241.
- [48] W. Hong, Y. Xu, G. Lu, C. Li, G. Shi, Transparent graphene/PEDOT-PSS composite films as counter electrodes of dye-sensitized solar cells, *Electrochem. Commun.* 10 (10) (2008) 1555–1558.
- [49] A. Eshaghi, A.A. Aghaei, Effect of TiO₂-graphene nanocomposite photoanode on dye-sensitized solar cell performance, *Bull. Mater. Sci.* 38 (5) (2015) 1177–1182.
- [50] C.-H. Tsai, P.-H. Fei, C.-M. Lin, S.-L. Shiu, CuO and CuO/graphene nanostructured thin films as counter electrodes for Pt-free dye-sensitized solar cells, *Coatings* 8 (1) (2018) 21.
- [51] M.U. Shahid, N.M. Mohamed, A.S. Muhsan, R. Bashiri, A.E. Shamsudin, S.N.A. Zaine, Few-layer graphene supported polyaniline (PANI) film as a transparent counter electrode for dye-sensitized solar cells, *Diam. Relat. Mater.* 94 (2019) 242–251.
- [52] Y. Nakajima, H. Murata, N. Saitoh, N. Yoshizawa, T. Suemasu, K. Toko, Low-temperature (400° C) synthesis of multilayer graphene by metal-assisted sputtering deposition, *ACS Omega* 4 (4) (2019) 6677–6680.
- [53] H. Zhang, et al., RF magnetron sputtering synthesis of three-dimensional graphene@ Co₃O₄ nanowire array grown on Ni foam for application in supercapacitors, *J. Alloys Compd.* 740 (2018) 174–179.
- [54] A. Richter, M. Hermle, S.W. Glunz, Reassessment of the limiting efficiency for crystalline silicon solar cells, *IEEE J. Photovolt.* 3 (4) (2013) 1184–1191.

- [55] S. Parui, R. Ruiter, P. Zomer, M. Wojtaszek, B. Van Wees, T. Banerjee, Temperature dependent transport characteristics of graphene/n-Si diodes, *J. Appl. Phys.* 116 (24) (2014) 244505.
- [56] S. Sonde, et al., Electrical properties of the graphene/4 H-SiC (0001) interface probed by scanning current spectroscopy, *Phys. Rev. B* 80 (24) (2009) 241406.
- [57] X. Miao, et al., High efficiency graphene solar cells by chemical doping, *Nano Lett.* 12 (6) (2012) 2745–2750.
- [58] S. Tongay, M. Lemaitre, X. Miao, B. Gila, B. Appleton, A. Hebard, Rectification at graphene-semiconductor interfaces: zero-gap semiconductor-based diodes, *Phys. Rev. X* 2 (1) (2012) 011002.
- [59] X. Li, et al., High performance solar cells based on graphene-GaAs heterostructures, *Nano Energy* 16 (2014) 310arXiv preprint arXiv:1409.3500.
- [60] S. Rafique, S.M. Abdullah, K. Sulaiman, M. Iwamoto, Fundamentals of bulk heterojunction organic solar cells: an overview of stability/degradation issues and strategies for improvement, *Renew. Sust. Energ. Rev.* 84 (2018) 43–53.
- [61] P. Trihutomo, S. Soepartman, D. Widhiyanuriawan, L. Yuliati, Performance improvement of dye-sensitized solar cell-(DSSC-) based natural dyes by Clathrin protein, *Int. J. Photoenergy* 2019 (2019) 4384728.
- [62] J. You, et al., A polymer tandem solar cell with 10.6% power conversion efficiency, *Nat. Commun.* 4 (2013) 1446.
- [63] X. Pan, Y. Zhao, S. Wang, Z. Fan, TiO₂/graphene nanocomposite for photocatalytic application, in: A. Méndez-Vilas (Ed.), *Materials and Processes for Energy: Communicating Current Research and Technological Developments*, 2013, pp. 913–920.
- [64] G.S. Han, et al., Reduced graphene oxide/mesoporous TiO₂ nanocomposite based perovskite solar cells, *ACS Appl. Mater. Interfaces* 7 (42) (2015) 23521–23526.
- [65] A. ur Rehman, S.H. Lee, Crystalline silicon solar cells with nickel/copper contacts, in: *Solar Cells—New Approaches and Reviews*, 2015.
- [66] M.M. Stylianakis, et al., Ternary organic solar cells incorporating zinc phthalocyanine with improved performance exceeding 8.5%, *Dyes Pigments* 146 (2017) 408–413.
- [67] S. Rao, A. Morankar, H. Verma, P. Goswami, Emerging photovoltaics: organic, copper zinc tin sulphide, and perovskite-based solar cells, *J. Appl. Chem.* 2016 (2016) 3971579.
- [68] S.S. Mali, J.V. Patil, H. Kim, C.K. Hong, Gallium cationic incorporated compact TiO₂ as an efficient electron-transporting layer for stable perovskite solar cells, *Matter* 1 (2) (2019) 452–464.
- [69] Q. Chen, et al., Ag-incorporated organic-inorganic perovskite films and planar heterojunction solar cells, *Nano Lett.* 17 (5) (2017) 3231–3237.
- [70] X. Li, et al., Graphene-on-silicon Schottky junction solar cells, *Adv. Mater.* 22 (25) (2010) 2743–2748.
- [71] A. Suhail, G. Pan, D. Jenkins, K. Islam, Improved efficiency of graphene/Si Schottky junction solar cell based on back contact structure and DUV treatment, *Carbon* 129 (2018) 520–526.
- [72] J.M. Kim, et al., Si-quantum-dot heterojunction solar cells with 16.2% efficiency achieved by employing doped-graphene transparent conductive electrodes, *Nano Energy* 43 (2018) 124–129.
- [73] A. Alnuaimi, I. Almansouri, I. Saadat, A. Nayfeh, Interface engineering of graphene–silicon Schottky junction solar cells with an Al₂O₃ interfacial layer grown by atomic layer deposition, *RSC Adv.* 8 (19) (2018) 10593–10597.
- [74] Y. Song, et al., Role of interfacial oxide in high-efficiency graphene–silicon Schottky barrier solar cells, *Nano Lett.* 15 (3) (2015) 2104–2110.

- [75] Y. Li, et al., Schottky junction solar cells based on graphene with different numbers of layers, *Appl. Phys. Lett.* 104 (4) (2014) 043903.
- [76] P. Li, C. Chen, J. Zhang, S. Li, B. Sun, Q. Bao, Graphene-based transparent electrodes for hybrid solar cells, *Front. Mater.* 1 (2014) 26.
- [77] L.-J. Guo, J.-W. Luo, T. He, S.-H. Wei, S.-S. Li, Photocorrosion-limited maximum efficiency of solar photoelectrochemical water splitting, *Phys. Rev. Appl.* 10 (6) (2018) 064059.

Chapter 6

Solution-processed quantum dot-sensitized solar cell based on “green” materials

Hieng Kiat Jun

Department of Mechanical and Material Engineering, Lee Kong Chian Faculty of Engineering and Science, Universiti Tunku Abdul Rahman, Sungai Long Campus, Kajang, Malaysia

1 Introduction and current scenario

According to the report released by the World Energy Council, global energy demand will continue to increase from year to year [1]. In fact, the demand for electricity consumption will double beyond the year 2040 [2]. On the other hand, primary energy demand will peak until 2030. This primary energy source includes energy derived from coal, oil, and gas. The slow growth of primary energy is anticipated due to the disruptive trends of emerging energy sources. Coupled with environmental concern, especially on global warming, the adoption of emerging energy sources has begun to encroach into the dominance of the primary energy source. Generally, these emerging energy sources are referred to as alternative energy or green energy, where electricity generation is not derived from fuel and coal. Some examples of such alternative energy sources are solar energy, hydro energy, and wind energy. The provision of energy power will enable the usage of various equipment, be it portable or stationary, to perform useful work, provide valuable output, and sustain the livelihood of humankind. Therefore it is the goal of inventors and researchers to design an efficient energy device where maximum useful energy can be extracted.

As solar energy is abundant, it makes economic sense to harvest solar energy for energy consumption. Not only is it clean and abundant, the conversion of solar energy to electricity does not emit any harmful or toxic gases. The whole energy conversion process only requires a simple solar photovoltaic (PV) or solar cell setup. Thus it is a safe process with no untoward risks. Due to these attractive features, the PV market has been growing at a rapid rate for the past two decades [3]. Furthermore, with in-depth research and increased adoption of

solar PV, various types of PV systems have been introduced. In general, solar cells can be categorized into three generations of technology, namely, first-, second-, and third-generation solar cells (Fig. 1) [4, 5]. First-generation solar cells are silicon-based solar cells such as monocrystalline and polycrystalline solar cells. They are commercially available and were established a few decades ago. Efficiency of the commercial PV of this category solar cell is around 20%, although the possible maximum efficiency is at 33.3% (Shockley-Queisser's limit) [6]. However, because of their complicated processing requirement and high production cost, second- and third-generation solar cells have been gaining popularity due to their low production cost. Second-generation solar cells are thin film solar cells. Due to their thin and lightweight structure, they continue to be developed to match the efficiency of first-generation solar cells. The highest reported efficiency of thin film solar cells has a value exceeding 20% [7]. Some examples of thin film solar cells are gallium arsenic and cadmium telluride solar cells. Third-generation solar cells were introduced as a result of a better understanding of the physical and chemical properties of nanostructured materials. Some examples are dye-sensitized solar cells (DSSCs), quantum dot-sensitized solar cells (QDSSCs), and perovskite solar cells (PSCs). The development of third-generation solar cells has been fast, especially in PSCs where the highest recorded efficiency to date has reached 25%, which matches the performance of silicon-based solar cells but with lower cost [8].

Among the types of third-generation solar cells, QDSSCs have attracted significant attention from solar cell researchers. QDSSCs are a derivative of DSSCs. Instead of a dye, a semiconductor quantum dot (QD) is used as the sensitizer or light converter material [9]. QDSSCs are deemed attractive due to their tunability of light absorption and multiple exciton generation by the semiconductor QD sensitizers. Semiconductor QDs are the core materials for the functionality of QDSSCs, where they harvest sunlight and convert it into electricity via the generation of electron-hole pairs within the internal structure. In most cases, the type of QD materials used are Pb or Cd based such as PbS, CdS, and CdSe. They are mainly used due to better and stable performance. Unfortunately, such materials pose environmental and health risks when they are

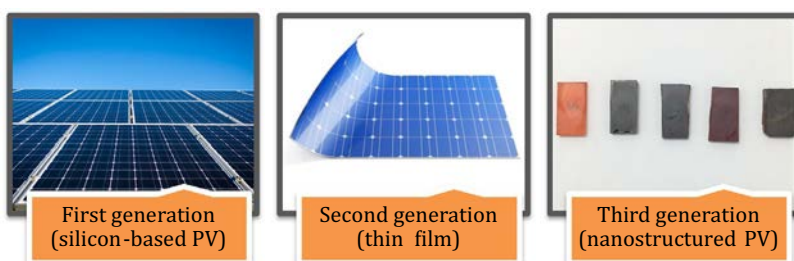


FIG. 1 Classes of solar PV.

exposed or degraded after end-of-life use. Consequently, research has been carried out to analyze the environmental impact of PV devices. The most common analysis carried out is the lifecycle assessment (LCA) of the devices (also known as lifecycle analysis) [10]. Unfortunately, there are not many reports of LCA on QDSSCs. The nearest comparison is on DSSCs and QDPVs [11].

Exposure to heavy metals like Cd and Se has been linked to cancer and degenerative diseases as well as environmentally potential damaging factors [12, 13]. The remedy for this problem is to use “green” materials [14]. The term “green” materials refers to the absence of harmful and toxic heavy metal elements such as mercury (Hg), antimony (Sb), arsenic (As), lead (Pb), cadmium (Cd), and chromium (Cr). In some cases, cobalt (Co) is also included in the heavy metal list. For fully “green” QDSSCs, the entire solar cell structure should not have any of the heavy metal elements mentioned. This applies to the architecture of anode, cathode, and electrolyte (or redox mediator). Thus researchers are left with a few options, which are discussed in [Section 3](#). Before any attempt to upscale QDSSCs, one should understand the fundamental principles and working mechanism behind this PV. Next, a suitable fabrication technique should be reviewed and explored. Finally, challenges and limitations of “green” QDSSCs should be reviewed for future research plans. It is not the intention of this chapter to give a comprehensive and exhaustive review, but rather to provide insight based on notable findings in this niche area.

2 Fundamental principles of QDSSCs

Over the past decade, QDSSCs have seen much improvement particularly in power conversion efficiency. The first few reported QDSSCs had an efficiency of less than 1%. A recent result showed that it has reached 16%, which is quite a good development within a short period of time [15]. The rapid development of QDSSCs is attributed to the simple structure and facile fabrication method. QDSSCs take root in DSSCs where both have similar architecture, that is, a sensitized photoanode attached to a cathode electrode (counter electrode) with electrolyte (redox mediator) in between them (refer [Fig. 2](#)).

In the anode electrode, nanoparticles of a wide bandgap semiconductor like TiO_2 are layered on the surface of the conducting substrate. Semiconductor QDs are then attached to the layer of TiO_2 . This is where the sensitizing effect takes place. Typically, the particle size of TiO_2 is larger than the size of individual QDs (refer to the inset in [Fig. 2](#)). Meanwhile, on the cathode electrode, a layer of catalytic noble metal like platinum or gold is deposited on the conducting substrate surface. The electrolyte consists of a redox couple such as polysulfide electrolyte. It should be noted that polysulfide electrolyte has been proven to be compatible with QDSSCs, particularly Cd-based QDSSCs due to lower charge recombination [9, 16].

In terms of working mechanism, both DSSCs and QDSSCs share a similar mechanism except that semiconductor QDs are involved in QDSSCs instead of

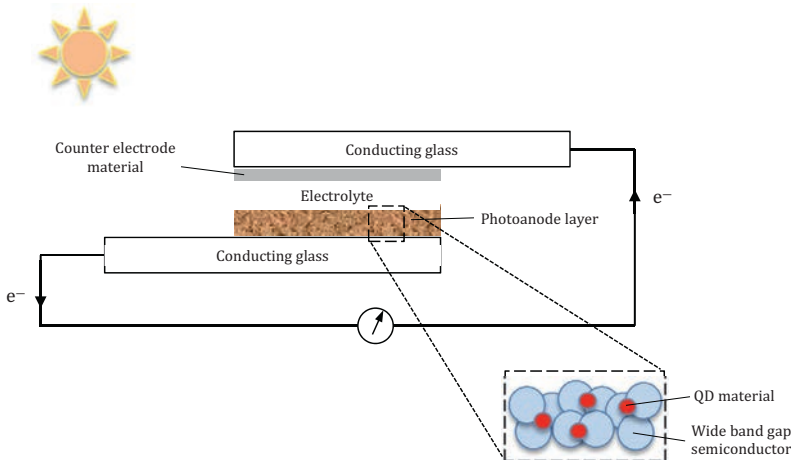


FIG. 2 Schematic of a QDSSC.

dye molecules [17]. When the device is exposed to light, the electrons within QDs will be energized. This will allow the electron to move from the valence band to the conduction band of the QD. However, such action will only be possible if the light spectrum matches the activation stage of the QD since different QD sizes correspond to different wavelengths of light absorbance. As the activated electron moves to the conduction band, an electron-hole pair is created. Electrons will then be injected into the TiO_2 layer and proceed to the external circuit to perform work. At the same time, the hole will oxidize the polysulfide electrolyte to recover the stable state of the QD. At this juncture, the electron that has completed the work will reach the counter electrode where it will be used to reduce the oxidized polysulfide electrolyte. The whole cycle will be repeated as long as there is light and a closed loop external circuit.

The performance of a QDSSC is a measure of percentage of useful work obtained from the conversion of light to electricity. The parameters can be obtained from the plot of current density (J) against voltage (V). Fig. 3 shows the generic J - V plot with its main parameters.

In essence, the important parameters that govern the performance of QDSSCs are short-circuit current density (J_{SC}), open-circuit photovoltage (V_{OC}), fill factor (FF), and efficiency. Efficiency is also expressed as power conversion efficiency (PCE) and is calculated as follows:

$$\text{PCE}, \eta(\%) = \frac{J_{\text{SC}} \times V_{\text{OC}} \times \text{FF}}{P} \times 100$$

where P is the incident solar power applied on the device. This equation depends on the light conversion efficiency and electron-hole pair formation and injection. It also depends on the electron lifetime [18]. For a representative

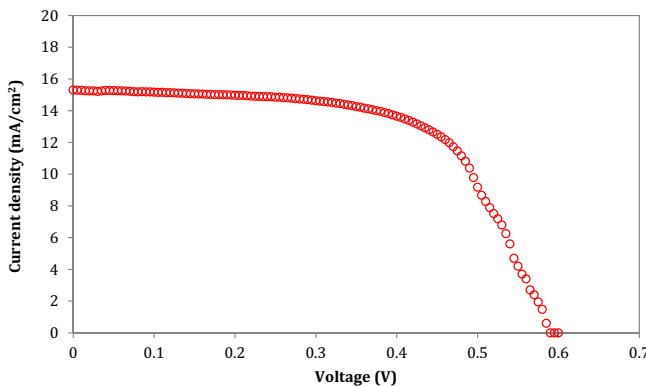


FIG. 3 Generic plot of current density (J) versus voltage (V).

and trustworthy result, the measurement of J - V response should be conducted in a standard manner [19].

To further understand the performance of QDSSCs, electrochemical impedance spectroscopy (EIS) is usually conducted [19, 20]. The EIS result can provide insight into the kinetics of charge collection, transport, and recombination from a single measurement. The notable response used for interpretation is the Nyquist plot. In this plot, a well-defined QDSSC configuration will yield two semicircles that are the manifestation of responses at high and middle-to-low frequency. Series resistance (R_s), charge-transfer resistance (R_{ct}), and recombination resistance (R_{rec}) can be derived from the plot.

Besides the aforementioned characterization methods, other notable approaches include time-resolved photoluminescence, ultrafast transient absorption, open-circuit voltage decay, and charge-extraction measurements.

3 Alternative materials for active layers in QDSSCs

As discussed, a typical QDSSC consists of two electrodes coupled together with an electrolyte intermediately between the two electrodes. The photoanode electrode is formed with a nanostructured layer. The usual material for the nanostructured layer is TiO_2 , a wide bandgap semiconductor. Such a combination is called a TiO_2 -based photoanode. The earlier design had the TiO_2 layer sensitized with dyes, or in other words, attached with dye molecules. To boost the performance of the QDSSC, three-dimensional hierarchically branched TiO_2 nanowires are presented. Such cells can produce higher PCE. The improved performance of these cells is attributed to the increased QD attachment sites where the nanowires consist of long nanowire trunks with short nanorod branches. Besides TiO_2 , ZnO -based photoanodes have also been tested. Although ZnO as the wide bandgap material for QDSSCs is limited by its lower stability compared with TiO_2 , it is relatively easy to crystallize with anisotropic

crystal growth. When the ZnS surface is treated with TiO₂, a decrease in charge recombination at the interface is postulated.

Due to the possible adverse afterlife effect of Cd- and Pb-based QDSSCs, alternative “green” QD sensitizers should be explored as substitutes [14, 21]. The commonly explored “green” QD sensitizers are free of toxic Cd and Pb elements. In some research, other elements like Se, Sb, and Co are also excluded in the “green” QDSSC architecture. Some examples are Ag₂S, SnS, Bi₂S₃, and CuInS₂ [22–25]. Among these options, ternary and quaternary Cu-based compounds have proven to produce better efficiency. An Ag-based QD is deemed to be the best candidate “green” material. Unfortunately, the compound does not produce sufficient efficiency for further upscaling.

Tubtimtae et al. started the investigation on Ag-based QDSSCs by sensitizing TiO₂ film with Ag₂S QDs [22]. Their approach was the investigation of the effect of different successive ionic layer adsorption and reaction (SILAR) cycles to the efficiency of Ag₂S QDSSCs. The best result was obtained in samples prepared from four dipping cycles with ZnS as the QD coating layer. Such a device produced an efficiency of 0.98% with a J_{sc} of 7.3 mA/cm². The group then tried another Ag-based QDSSC, that is, Ag₂Se, which produced better performance than the Ag₂S QDSSC [26]. Their best solar devices yielded a power conversion efficiency of 1.76% under approximately 1 sun.

Bi-based QDs also have the potential to be the substitute sensitizer for QDSSCs. Desale et al. reported their attempt to improve the photosensitivity of Bi₂S₃ synthesized from the SILAR process [24]. When the Bi₂S₃ thin film was annealed at 250 °C, the bandgap energy decreased, coupled with improved photoresponse. Unfortunately, the performance of Bi₂S₃ QDSSCs remained relatively low compared to Cd-based QDSSCs. One of the reasons for low performance is attributed to the formation of NaBiS₂ instead of Bi₂S₃ during the SILAR process [27]. The remedy for this problem is to replace Na₂S solution (precursor for S) with elemental S vapor. The QD synthesized from vapor method has resulted in a better performance at 0.84%, although this value is still low. Cossensitization of the Bi₂S₃ QD with the CdS QD could further improve the power conversion efficiency of the QDSSC [28]. Unfortunately, such QD architecture has defeated the purpose of achieving “green” and sustainable solar cell devices. A better option would be the ternary compound AgBiS₂ [29]. To produce ternary AgBiS₂ QDs, a two-stage SILAR process was introduced. The produced cell exhibited a J_{sc} of 7.61 mA/cm² and efficiency of 0.53%. With such a low efficiency, perhaps the best approach is to redesign the solar cell architecture. Bernechea et al. produced a solution-processed AgBiS₂ solar cell with power conversion efficiency of 6.3% [30]. Such cell had the architecture of ITO/ZnO/AgBiS₂/polymer/MoO₃.

Probably the most widely studied “green” QD material is SnS. Tsukigase et al. demonstrated the feasibility of fabricating SnS nanoparticles for application in solar cells [31, 32]. Although SnS QDs are easy to synthesize (the simplest approach is a solution process with precursors of Sn and S ions), their

performance as a solar energy converter agent still needs much improvement. A thorough study of the compatibility of SnS with other counter electrode and electrolyte materials is very much needed. In one of the reported studies, Guo et al. fabricated an SnS QDSSC with TiC as its counter electrode and organic disulfide/thiolate electrolyte system [33]. An efficiency of 1.03% was reported in that study. This result showed that QDSSCs can function in a redox couple system, which is beyond the usual polysulfide system. Its stable performance is attributed to the catalytic selectivity of TiC counter electrode for a disulfide/thiolate electrolyte system. A systematic study of the solution-processed parameters of SnS QDs has been performed by Deepa and Nagasaki [34]. In their work, SnS QDs were fabricated via the SILAR process. The optimum dipping cycle was determined. The best cell performance was reported at 0.54% with Cu₂S as the counter electrode and polysulfide electrolyte system. Hortikar et al. also did a similar optimization study on SnS QDSSCs [35]. Nevertheless, the performance is still on the low side. This raises a question: Are “green” QDs like SnS suitable for use as a light-to-electricity converter? Perhaps such material performs well in other parts of the active layer of the QDSSC such as the counter electrode. Dai et al. showed that SnS thin film can function as a counter electrode [36]. In addition, the application of noble metals like Pt and Au as cathode electrodes might not be suitable for QDSSCs where a polysulfide electrolyte is used. In such a case, metal chalcogenides and polymer-based materials like Cu₂S and poly(3,4-ethylenedioxythiophene) have proven to be effective counter electrode materials [37]. The efficacy of such counter electrode materials is attributed to their good electrocatalytic activity as well as compatibility with the electrolyte system. Other attempts to produce interesting and value-added QDSSCs include solid-state “green” QDSSCs, although the performance is far from feasible [38]. On the other hand, a comparable performance of solid-state Cd-based QDSSCs has been proven by using gel-type electrolyte instead of the usual solid-state spiro-ometad [39]. A notable list of “green” QDSSCs is given in Table 1. It must be noted that the list of “green” QDSSCs is confined to QD elements that meet the criteria of “green” material as defined in an earlier section.

4 Fabrication of “green” QDs and QDSSCs

A typical QDSSC can be fabricated with various techniques, namely, chemical bath deposition (CBD), SILAR, microwave-assisted CBD, molecular linker attachment, direct adsorption, and electrophoresis. Among these techniques, solution-processed techniques like CBD and SILAR are more frequently used due to their ease of processing method and low cost [45]. In both techniques, photoanode samples usually consist of conducting glass coated with wide band-gap semiconductor particles such as TiO₂ and ZnO.

The CBD fabrication technique was adopted a long time ago, particularly in depositing CdS layers for thin film-based PV devices. This method is also

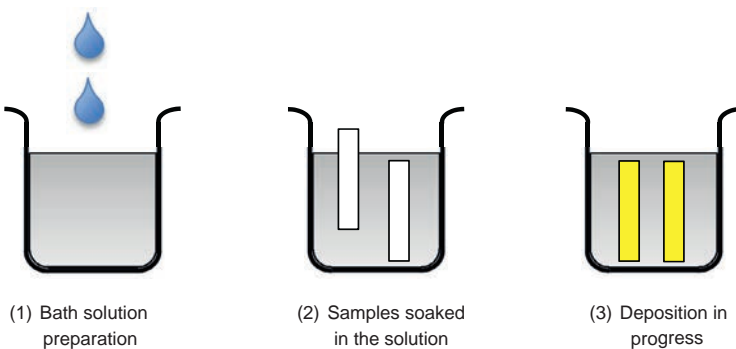
TABLE 1 Performance of some “green” quantum dot-sensitized solar cells.

“Green” QDs	J_{SC} (mA/cm ²)	V_{OC} (V)	PCE (%)	References
Ag ₂ S	9.28	0.509	2.41	[40]
InP	10.58	0.590	3.54	[41]
CuInS ₂	22.82	0.601	8.54	[42]
Zn-Cu-In-S	22.70	0.612	8.55	[43]
Cu ₂ ZnSnS ₄	17.48	0.47	3.29	[44]

PCE, Power conversion efficiency; QDs, quantum dots.

applied in other electronic devices such as sensors, conductive oxide coatings, and catalyst deposition. The widespread adoption of CBD in solar cell devices occurred around 1990 [46]. At the laboratory scale, CBD is performed in a beaker with a metal salts solution. A saturated solution is preferred for ease of nucleation of the QDs. In some cases, complexing agents and buffer solutions may be included. Fig. 4 shows a schematic diagram of a typical CBD process. This technique provides the flexibility for obtaining different sizes of nanostructure particles. The formation of QDs via CBD is preceded with the nucleation of nanostructure seeds. This is followed by particle growth. Liu et al. reported the deposition of CdSe QDs on TiO₂ film with proven photoelectrochemical performance [47]. Lokhande et al. also reported several findings with the CBD technique [48, 49]. For “green” QDs, Deepa et al. showed that SnS QDs can be fabricated with this simple technique as well [23]. In their work, SnS QDs were prepared from a solution of SnCl₂ and thioacetamide with deposition time ranging from 30 to 120 min. The produced QD sizes had a range between 2.6 and 15.5 nm. The longer the deposition time, the bigger the QD size obtained. On the downside, performance of the samples obtained from this work was low. The best efficiency obtained was 0.11%. A study by Adhyapak et al. also showed the fabrication of SnS QDs with the CBD technique [35]. They prepared nanoparticles by ultrasound-assisted CBD, where the bath solution consisted of SnCl₂ with ethanolamine as the capping agent. In addition, ammonia and trisodium citrate solutions were used as buffer and complexing solutions, respectively. Similar to previous work, a low performance value was recorded, where the current density was 60 μA/cm², the open-circuit voltage was 135 mV, and the fill factor was 18%.

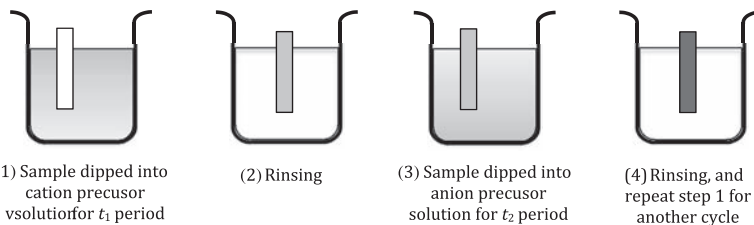
Due to the low performance of samples prepared from the CBD method, an improved solution technique was introduced by Nicolau in 1985 [50]. Since then, the SILAR technique has been widely used for the synthesis of QD nanoparticles. In this technique, the growth of QD nanoparticles depends on ion-by-ion reaction and growth, which involves the adsorption and reaction of cations

**FIG. 4** Schematic of CBD.

and anions from two separate solutions. This is possible when cation precursor solution and anion precursor solution are prepared separately. Samples are then dipped into ionic precursor solutions successively, with rinsing during the interval dipping process. This dipping process is deemed to be one cycle. The dipping process is usually repeated, depending on the number of cycles required for the sample. The control parameters involved here are dipping time, reaction temperature, precursor solution concentration, and number of dipping cycles. Fig. 5 depicts the schematic process of a typical SILAR method. The fabrication of “green” QDs has been demonstrated by a few groups. Notable facile syntheses of QDs are Ag_2S and Bi_2S_3 [22, 27, 51]. Last but not least, hot injection has become an important method of synthesizing high-performing QDs. Unfortunately, this method is seldom reported in the fabrication of “green” QDs. Perhaps a new approach is needed in designing the synthesis route. For more details on the hot-injection method, readers are recommended to refer to the chapter titled “Colloidal Quantum Dot-Based Solar Cells” within this book.

5 Challenges and limitations

The major challenge for achieving good performance with QDSSCs is minimizing the charge recombination. Due to the different properties and behaviors of each component in the QDSSC, charge recombination is an avoidable

**FIG. 5** Schematic of SILAR.

phenomenon. It can occur in a few paths such as between the interface of a wide bandgap semiconductor and QD sensitizer, between the QD sensitizer and the electrolyte, and between the wide bandgap semiconductor and the electrolyte. It can also occur within the QD sensitizer itself where the energized electrons at the conduction band recombine with the hole, which ultimately reduces the number of available free electrons. Besides, for QDSSCs where there is a linker agent between the QDs and the wide bandgap semiconductor, recombination exists within the linkage, which is known as intraparticle recombination [52]. There are two main approaches to minimizing the charge recombination in QDSSCs. These strategies include materials engineering and surface treatment.

To reduce the charge recombination within the photoanode interface layer, treatment of the surface with a passivation layer is the most widely used technique. In such a strategy, ZnS has been employed in QDSSCs as a passivation layer. Such a technique has yielded an efficiency improvement of 10% or more [53, 54]. The improved performance is due to the passivation effect of the ZnS layer. The layer is responsible for hindering the back-electron transfer across the interface. It also increases the rate of electron transfer. For a ZnO-based photoanode, passivation of the surface with TiO₂ proved to be effective in reducing interfacial charge recombination as well [55]. Other metal oxides like MgO and Al₂O₃ have also been used to act as a passivation layer. It should be noted that the application of a passivation layer could only help in improving the performance of QDSSCs to a certain extent.

In recent years, performance improvement in QDSSCs as seen in Cd-based and Se-based QDs has been quite encouraging [5, 9, 14]. Such improvements were attributed to the enhancement in heterointerface engineering and bandgap alignment of QDs. Although the solution process has yielded a high coverage of QDs on the wide bandgap semiconductor surface, the nanoparticle growth process has created numerous trap-state defect sites in the QD layer. The consequence of this phenomenon gives rise to weak optoelectronic properties. As such, a high-performing “green” QD should be the main focus for future study. Unfortunately, the material engineering approach for “green” QDs is the most challenging task since not many “green” material compounds can serve as high-performing QDs. Nevertheless, with proper understanding of the properties and structure of the compounds, we may see better performance from QDSSCs utilizing “green” elements, such as CuInS₂ and Zn-Cu-In-Se, in the near future.

Another alternative is fabrication of the core–shell structure. Unfortunately, there are not many reports of QD core–shell structures based on “green” elements. This could be attributed to the nonsynergistic bandgap alignment among the “green” elements. The commonly reported QDs for such structures consist of CdS- or CdSe-based compounds. Probably the only notable report is by Zhong et al. [25]. In their work, core–shell CuInS₂/ZnS QDSSCs produced an efficiency of 7.04%. As such, perhaps the best approach to date is the fabrication of ternary and quaternary QD compounds. Some examples are CuInS₂, Cu₂ZnSnS₄, and Zn-Cu-In-S (refer to Table 1). The improved performance

delivered by the QD compounds could be attributed to the fast injection of charge as well as lower charge recombination rate within the structure. On the other hand, some researchers suggested that preprepared QDs could provide a better way to control the charge recombination issue [56]. The preprepared QDs are normally synthesized via the solution process as well. The best recorded QDSSC performance was achieved by Pan et al. through dual sensitizers of Zn-Cu-In-Se and Zn-Cu-In-S, although the presence of an Se element could be a concern for toxicity risk [57]. The strategy of cosensitization of two groups of QD sensitizers has yielded improved performance, which was attributed to better light-harvesting capability, fast electron injection, and reduced charge recombination rate. Unfortunately, QDSSCs with pure “green” compounds using the cosensitization technique have not been reported anywhere. The presence of an Se element seems to play an important role in the performance of a QD sensitizer.

6 The way forward

As conventional QDSSCs use Cd- and Pb-based materials as sensitizers, the impact of these substances on the toxicity effect to the environment and human health has become a major concern. Although “green” QDs may pose minimal environmental and health risk effects, the amount of waste that will be produced should be monitored and managed as well. One of the proposals is the implementation of end-of-life management policies [58]. Such policies should be translated into concrete actions or procedures. These include setting up a management body to collect and segregate the unused or expired PV devices for proper disposition. Nevertheless, the most effective approach will be the total elimination of Cd- and Pb-based compounds as materials for QDSSCs. To achieve this, effective “green” QD sensitizers are needed. Thus continuous investigation and research in this area are necessary. Based on the previous work by various groups, research into “green” QDSSCs has been observed to gain traction. As the highest reported performance QDSSC consists of quaternary QD compounds, we may expect that the future trend of QDSSCs will move toward the study of complex compounds. It is expected that the ratio of Cd in compounds will be reduced too. To some extent, Cd-free compounds with high efficiency could be possible. Additionally, the other major factor that needs to be considered is the fabrication technique of “green” QDSSCs. This forms part of the overall LCA of the QDSSC itself. No doubt the current effective fabrication technique will be a solution-based process, combining a number of methods, such as microwave-assisted CBD [59]. Most importantly, the processing technique should be “green,” which means no elements of Cd or Pb are involved throughout the fabrication steps. Since “green” QDs are prepared from their respective precursors, it is very unlikely that Cd- or Pb-based chemicals will be used unless they are needed as a catalyst or precursor for the intermediate process. Therefore based on these observations, adoption and upscaling of

“green” QDSSCs are possible. Researchers should take heed of the call to introduce sustainable and environmentally friendly materials and processes. Finally, governments should encourage participation and research in this field, which have been very encouraging over the last decade.

Acknowledgment

Special thanks to exchange student Mr. Kyohei Yamaguchi from Gifu University for assistance in reference sources.

References

- [1] World Energy Scenarios 2019, World Energy Council, (2019).
- [2] Global Energy Perspective 2019, Reference Case, McKinsey Energy Insights, 2019.
- [3] P. Shah, R. Torres, N. Tscharner, N. Wyrtsch, H. Keppner, Photovoltaic technology: the case for thin-film solar cells, *Science* 285 (1999) 692–698.
- [4] J. Wu, Z. Lan, J. Lin, M. Huang, Y. Huang, L. Fan, G. Lou, Y. Lin, Y. Xie, Y. Wei, Counter electrodes in dye-sensitized solar cells, *Chem. Soc. Rev.* 46 (2017) 5975–6023.
- [5] V.T. Chebrolu, H.-J. Kim, Recent progress in quantum dot sensitized solar cell: an inclusive review of photoanode, sensitizer, electrolyte, and the counter electrode, *J. Mater. Chem. C* 7 (2019) 4911–4933.
- [6] S. Ruhle, Tabulated values of the Shockley-Queisser limit for single junction solar cells, *Sol. Energy* 130 (2016) 139–147.
- [7] M. Powalla, S. Paetel, E. Ahlswede, R. Wuerz, C.D. Wessendorf, T.M. Friedlmeier, Thin-film solar cells exceeding 22% solar cell efficiency: an overview on CdTe-, Cu(In,Ga)Se₂-, and perovskite-based materials, *Appl. Phys. Rev.* 5 (2018) 041602.
- [8] Y. Cheng, F. So, S. Tsang, Progress in air-processed perovskite solar cells: from crystallization to photovoltaic performance, *Mater. Horiz.* 6 (2019) 1611–1624.
- [9] H.K. Jun, M.A. Careem, A.K. Arof, Quantum dot-sensitized solar cells—perspective and recent developments: a review of cd chalcogenide quantum dots as sensitizers, *Renew. Sust. Energ. Rev.* 22 (2013) 148–167.
- [10] S. Gerbenet, S. Belboom, A. Leonard, Life cycle analysis (LCA) of photovoltaic panels: a review, *Renew. Sustain. Energy Rev.* 38 (2014) 747–753.
- [11] H. Sengül, T.L. Theis, An environmental impact assessment of quantum dot photovoltaics (QDPV) from raw material acquisition through use, *J. Clean. Prod.* 19 (2011) 21–31.
- [12] M. Vinceti, I. Bottecchi, A. Fan, Y. Finkelstein, J. Mandrioli, Are environmental exposures to selenium, heavy metals, and pesticides risk factors for amyotrophic lateral sclerosis? *Rev. Environ. Health* 27 (2012) 19–41.
- [13] K. Cai, Y. Yu, M. Zhang, K. Kim, Concentration, source, and total health risks of cadmium in multiple media in densely populated areas, China, *Int. J. Environ. Res. Public Health* 13 (2019) 2269.
- [14] Z. Pan, H. Rao, I. Mora-Sero, J. Bisquert, X. Zhong, Quantun dot-sensitized solar cells, *Chem. Soc. Rev.* 47 (2018) 7659–7702.
- [15] The National Renewable Energy Laboratory, Best research-cell efficiency chart, Available: <https://www.nrel.gov/pv/cell-efficiency.html>, 2019.
- [16] Y. Liao, J. Zhang, W. Liu, W. Que, X. Yin, D. Zhang, L. Tang, W. He, Z. Zhong, H. Zhang, Enhancing the efficiency of CdS quantum dot-sensitized solar cells via electrolyte engineering, *Nano Energy* 11 (2015) 88–95.

- [17] T. Sogabe, Q. Shen, K. Yamaguchi, Recent progress on quantum dot solar cells: a review, *J. Photon. Energy* 6 (2016) 040901.
- [18] B.M. David, Templating and structural engineering in organic-inorganic perovskites, *J. Chem. Soc. Dalton Trans.* (2001) 1–12.
- [19] M. Pazoki, U.B. Cappel, E.M.J. Johansson, A. Hagfeldt, G. Boschloo, Characterization techniques for dye-sensitized solar cells, *Energy Environ. Sci.* 10 (2017) 672–709.
- [20] F. Fabregat-Santiago, G. Garcia-Belmonte, I. Mora-Sero, J. Bisquert, Characterization of nanostructured hybrid and organic solar cells by impedance spectroscopy, *Phys. Chem. Chem. Phys.* 13 (2011) 9083–9118.
- [21] H. Choi, S. Jeong, A review on eco-friendly quantum dot solar cells: materials and manufacturing processes, *Int. J. Precis. Eng. Manuf. Green Technol.* 5 (2018) 349–358.
- [22] A. Tubtimtae, K.-L. Wu, H.-Y. Tung, M.-W. Lee, G.J. Wang, Ag₂S quantum dot-sensitized solar cells, *Electrochem. Commun.* 12 (2010) 1158–1160.
- [23] K.G. Deepa, J. Nagaraju, Growth and photovoltaic performance of SnS quantum dots, *Mater. Sci. Eng. B* 177 (2012) 1023–1028.
- [24] D.J. Desale, S. Shaikh, F. Siddiqui, R. Birajdar, R. Late, A. Ghule, R. Sharma, Enhancement of photosensitivity by annealing in Bi₂S₃ thin films grown using SILAR method, *Compos. Part B* 46 (2013) 1–6.
- [25] Z. Pan, I. Mora-Sero, S. Qing, H. Zhang, Y. Li, K. Zhao, J. Wang, X. Zhong, J. Bisquert, High-efficiency “green” quantum dot solar cells, *J. Am. Chem. Soc.* 136 (2014) 9203–9210.
- [26] A. Tubtimtae, M.-W. Lee, G.-J. Wang, Ag₂Se quantum-dot sensitized solar cells for full solar spectrum light harvesting, *J. Power Sources* 196 (2011) 6603–6608.
- [27] I. Zumeta-Dubè, V.-F. Ruiz-Ruiz, D. Diaz, S. Rodil-Posadas, A. Zeinert, TiO₂ sensitization with Bi₂S₃ quantum dots: the inconvenience of sodium ions in the deposition procedure, *J. Phys. Chem. C* 118 (2014) 11495–11504.
- [28] D. Esparza, I. Zarazúa, T. López-Luke, R. Carriles, A. Torres-Castro, E. De la Rosa, Photovoltaic properties of Bi₂S₃ and CdS quantum dot sensitized TiO₂ solar cells, *Electrochim. Acta* 180 (2015) 486–492.
- [29] P.-C. Huang, W.-C. Yang, M.-W. Lee, AgBiS₂ semiconductor-sensitized solar cells, *J. Phys. Chem. C* 117 (2013) 18308–18314.
- [30] M. Bernechea, N.C. Miller, G. Xercavins, D. So, A. Stavrinadis, G. Konstantatos, Solution-processed solar cells based on environmentally friendly AgBiS₂ nanocrystals, *Nat. Photonics* 10 (2016) 521–525.
- [31] H. Tsukigase, Y. Suzuki, M.-H. Berger, T. Sagawa, S. Yoshikawa, Wet chemical synthesis and self-assembly of SnS₂ nanoparticles on TiO₂ for quantum dot-sensitized solar cells, *J. Nanosci. Nanotechnol.* 11 (2011) 3215–3221.
- [32] H. Tsukigase, Y. Suzuki, M.-H. Berger, T. Sagawa, S. Yoshikawa, Synthesis of SnS nanoparticles by SILAR method for quantum dot-sensitized solar cells, *J. Nanosci. Nanotechnol.* 11 (2011) 1914–1922.
- [33] W. Guo, Y. Shen, M. Wu, L. Wang, L. Wang, T. Ma, SnS-quantum dot solar cells using novel TiC counter electrode and organic redox couples, *Chem. Eur. J.* 18 (2012) 7862–7868.
- [34] K.G. Deepa, J. Nagasaki, Development of SnS quantum dot solar cells by SILAR method, *Mater. Sci. Semicond. Process.* 27 (2014) 649–653.
- [35] S.S. Hortikar, V.S. Kadam, A.B. Raghu, C.V. Jagtap, H.M. Pathan, I.S. Mulla, P.V. Adhyapak, Synthesis and deposition of nanostructured SnS for semiconductor-sensitized solar cell, *J. Solid State Electrochem.* 21 (2017) 2707–2712.
- [36] X. Dai, C. Shi, Y. Zhang, F. Liu, X. Fang, J. Zhu, SnS thin film prepared by pyrolytic synthesis as an efficient counter electrode in quantum dot sensitized solar cells, *J. Nanosci. Nanotechnol.* 15 (2015) 6813–6817.

- [37] P.N. Kumar, A. Kolay, S.K. Kumar, P. Patra, A. Aphale, A.K. Srivastava, M. Deepa, Counter electrode impact on quantum dot solar cell efficiencies, *ACS Appl. Mater. Interfaces* 8 (2016) 27688–27700.
- [38] Y. Oda, H. Shen, L. Zhao, J. Li, M. Iwamoto, H. Lin, Energetic alignment in nontoxic SnS quantum dot-sensitized solar cell employing spiro-OMeTAD as the solid-state electrolyte, *Sci. Technol. Adv. Mater.* 15 (2014) 035006.
- [39] W. Feng, Y. Li, J. Du, W. Wang, X. Zhong, Highly efficient and stable quasi-solid-state quantum dot-sensitized solar cells based on superabsorbent polyelectrolyte, *J. Mater. Chem. A* 4 (2016) 1461–1468.
- [40] R.M. Chava, M. Kang, Ag_2S quantum dot sensitized zinc oxide photoanodes for environment friendly photovoltaic devices, *Mater. Lett.* 199 (2017) 188–191.
- [41] S. Yang, P. Zhao, X. Zhao, L. Qu, X. Lai, InP and Sn:InP based quantum dot sensitized solar cells, *J. Mater. Chem. A* 3 (2015) 21922–21929.
- [42] G. Wang, H. Wei, J. Shi, Y. Xu, H. Wu, Y. Luo, D. Li, Q. Meng, Significantly enhanced energy conversion efficiency of CuInS₂ quantum dot sensitized solar cells by controlling surface defects, *Nano Energy* 35 (2017) 17–25.
- [43] L. Yue, H. Rao, J. Du, Z. Pan, J. Yu, X. Zhong, Comparative advantages of Zn-Cu-In-S alloy QDs in the construction of quantum dot-sensitized solar cells, *RSC Adv.* 8 (2018) 3637–3645.
- [44] B. Bai, D. Kou, W. Zhou, Z. Zhou, S. Wu, Application of quaternary Cu₂ZnSnS₄ quantum dot-sensitized solar cells based on hydrolysis approach, *Green Chem.* 17 (2015) 4377–4382.
- [45] H.K. Jun, M.A. Careem, A.K. Arof, Fabrication, characterization and optimization of CdS and CdSe quantum dot-sensitized solar cells with quantum dots prepared by successive ionic layer adsorption and reaction, *Int. J. Photoenergy* 2014 (2014) 93942314 pages.
- [46] P.K. Nair, V.M. Garcia, A.B. Hernandez, M.T.S. Nair, Photoaccelerated chemical deposition of PbS thin films: novel applications in decorative coatings and imaging techniques, *J. Phys. D Appl. Phys.* 24 (1991) 1466.
- [47] D. Liu, P.V. Kamat, Photoelectrochemical behavior of thin cadmium selenide and coupled titania/cadmium selenide semiconductor films, *J. Phys. Chem.* 7 (1993) 10769–10773.
- [48] C.D. Lokhande, Chemical deposition of metal chalcogenide thin films, *Mater. Chem. Phys.* 27 (1991) 1–43.
- [49] S.M. Pawar, B.S. Pawar, J.H. Kim, O.S. Joo, C.D. Lokhande, Recent status of chemical bath deposited metal chalcogenide and metal oxide thin films, *Curr. Appl. Phys.* 11 (2011) 117–161.
- [50] Y.F. Nicolau, Solution deposition of thin solid compound films by a successive ionic-layer adsorption and reaction process, *Appl. Surf. Sci.* 22–23 (1985) 1061–1074.
- [51] Y.C. Chai, H.K. Jun, Solution processed bi-based sensitized solar cell: effects of post heat treatment, *J. Nanosci. Nanotechnol.* 19 (2019) 3505–3510.
- [52] Y.Q. Bai, J.W. Chen, L. Wang, Z. Li, Z. Yang, J.B. Wen, Y.F. Wang, J.-X. Jiang, F. Shi, Y. Chen, J.H. Zeng, Metal chalcogenide complex as surface exchanger in quantum dot-sensitized solar cells, recombination limited efficiency, *Chem. Phys. Lett.* 723 (2019) 170–174.
- [53] Q. Shen, J. Kobayashi, L. Diguna, T. Toyoda, Effect of ZnS coating on the photovoltaic properties of CdSe quantum dot-sensitized solar cells, *J. Appl. Phys.* 103 (2008) 084304.
- [54] N. Guijarro, J.M. Campina, Q. Shen, T. Toyoda, T. Lana-Villareal, R. Gomez, Uncovering the role of the ZnS treatment in the performance of quantum-dot sensitized cells, *Phys. Chem. Chem. Phys.* 13 (2011) 12024–12032.

- [55] M. Shalom, S. Dor, S. Ruhle, L. Grinis, A. Zaban, Core/CdS quantum dot/shell mesoporous solar cells with improved stability and efficiency using an amorphous TiO₂ coating, *J. Phys. Chem. C* 113 (2009) 3895–3898.
- [56] H.-Y. Wei, G.-S. Wang, H.-J. Wu, Y.-H. Luo, D.-M. Li, Q.-B. Meng, Progress in quantum dot-sensitized solar cells, *Acta Phys. Chim. Sin.* 32 (2016) 201–213.
- [57] Z. Pan, L. Yue, H. Rao, J. Zhang, X. Zhong, Z. Zhu, A.K.-Y. Jen, Boosting the performance of environmentally friendly quantum dot-sensitized solar cells over 13% efficiency by dual sensitizers with cascade energy structure, *Adv. Mater.* 31 (2019) 1903696.
- [58] D. Sica, O. Malandrino, S. Supino, M. Testa, M.C. Lucchetti, Management of end-of-life photovoltaic panels as a step towards circular economy, *Renew. Sust. Energy Rev.* 82 (2018) 2934–2945.
- [59] J.-S. Ma, S. Das, C.-H. Lu, Microwave-assisted chemical bath deposition process to fabricate CdS buffer layers used in Cu(In,Ga)Se₂ solar cells, *RSC Adv.* 6 (2016) 107886–107893.

Chapter 7

Colloidal quantum dots based solar cells

Shengyi Yang^{a,b}, Jinming Hu^{a,b}, and Zhenheng Zhang^{a,b}

^a*Beijing Key Lab of Nanophotonics and Ultrafine Optoelectronic Systems, School of Physics, Beijing Institute of Technology, Beijing, PR China,* ^b*Key Lab of Advanced Optoelectronic Quantum Design and Measurement, Ministry of Education, Beijing Institute of Technology, Beijing, PR China*

1 Introduction

The efficient conversion of solar radiation into electrical or chemical energy is one of humanity's greatest challenges in the twenty-first century, in view of the ever-growing global demand for renewable energy solutions [1]. Current research directions in solar technologies focus on new methods, new materials, and their processing which will result in integrated, more efficient, and lower-cost power harvesters [2]. Materials that can harness and convert energy from the sun are by necessity semiconductors, in which a gap that should absorb a number of photons and then convert them into excited states (excitons), split them into electron-hole pairs, and drive the resulting charges toward electrodes.

Semiconductor quantum dots (QDs) have drawn considerable interest for more than 20 years because of their optoelectronic advantages based on a zero-dimensional system. Basically, these QDs include self-assembled quantum dots (SAQDs, by epitaxial growth) and colloidal quantum dots (CQDs, by chemical methods), and have the potential to enhance the photogeneration of carriers through the QD energy level or band [3–7]. An increase in the maximum attainable thermodynamic conversion efficiency is theoretically predicted by expanding the available spectrum for the photoexcitation. However, the fundamental physics of carriers transport and collection must be considered for the real photovoltaic operation. Understanding of their basic photovoltaic mechanisms in SAQDs and CQDs is essential to design ideal solar cells with high power-conversion efficiency (PCE). In addition, technical progress in the growth of SAQDs and the synthesis of CQDs is most important to construct realistic solar cells, which include appropriate materials with high crystal quality, well-controlled heterointerface, and surface passivation.

The CQDs have the advantages of low-temperature fabrication and solution-based processing, which can make the preparation cost very cheap [8, 9]. Therefore, CQDs have been studied extensively as compared to SAQDs for their excellent optoelectronic properties [8, 10–18] and low cost. Normally, semiconductor CQDs are fluorescent nanocrystals (NCs) with nanoscale dimensions (i.e., smaller than 20 nm in diameter) [10], and they are composed of an inorganic core, made of a few hundred to a few thousand atoms, surrounded by an organic outer layer of surfactant molecules (i.e., ligands). Semiconductor QDs exhibit dramatic quantum effects, defined by an increasing band gap accompanied by quantization of the energy levels in discrete values, similar to atomic energy levels [10, 19]. In most semiconductors, once the size is reduced to a few nanometers, quantum confinement occurs, leading to size-dependent optoelectronic properties of QDs. Such size effects allow us to design and synthesize QDs with controllable size, shape, and chemical composition to precisely tune the optical transitions and the energy of discrete electronic energy states. Over the past two decades, various types of high-quality CQDs, including bare and core-shell CQDs (see Fig. 1), with strong absorption, size-tunable emission and absorption, high photoluminescence quantum yield (PLQY), and good photo-stability have been realized by various well-controlled synthetic approaches [11, 14–16, 20–28]. Recent studies revealed that QDs show great potential in clean and renewable energy applications to address the grand challenges represented by the energy crisis and environmental pollution [29–37].

In this chapter, we focus on the synthesis of CQDs and their applications in solar cells. Therefore, the synthetic routes, structure and property relationships, optoelectronic properties, device architecture, and performance of various kinds of QDs will be described, and the key challenges for energy applications such as size monodispersity, tunable band gap, and high PLQY, including different sizes and structures, are addressed, as well as by controlling either band alignment or structure, and using these QDs in optoelectronic devices to maximize overall solar-device PCE.

2 Synthesis of CQDs

The development of simple, efficient, and environmentally friendly, large-scale synthetic routes for high-performance QDs with controlled size, crystalline phase, and chemical composition is crucial to exploit the relationship between their structure and properties. Synthetic routes for QDs have been explored since 1990s [10, 28] and can be divided into two categories: wet-chemical synthesis and gas (or vapor) phase deposition [28, 38, 39].

Here, solution-based synthetic routes such as hydro- and solvothermal synthesis, thermolysis method, co-precipitation synthesis, sol-gel method, continuous flow approach, etc. [10, 40–44], will be introduced since these methodologies are especially powerful for the convenient and reproducible synthesis of highly monodisperse CQDs, and they allow the size, structure, and

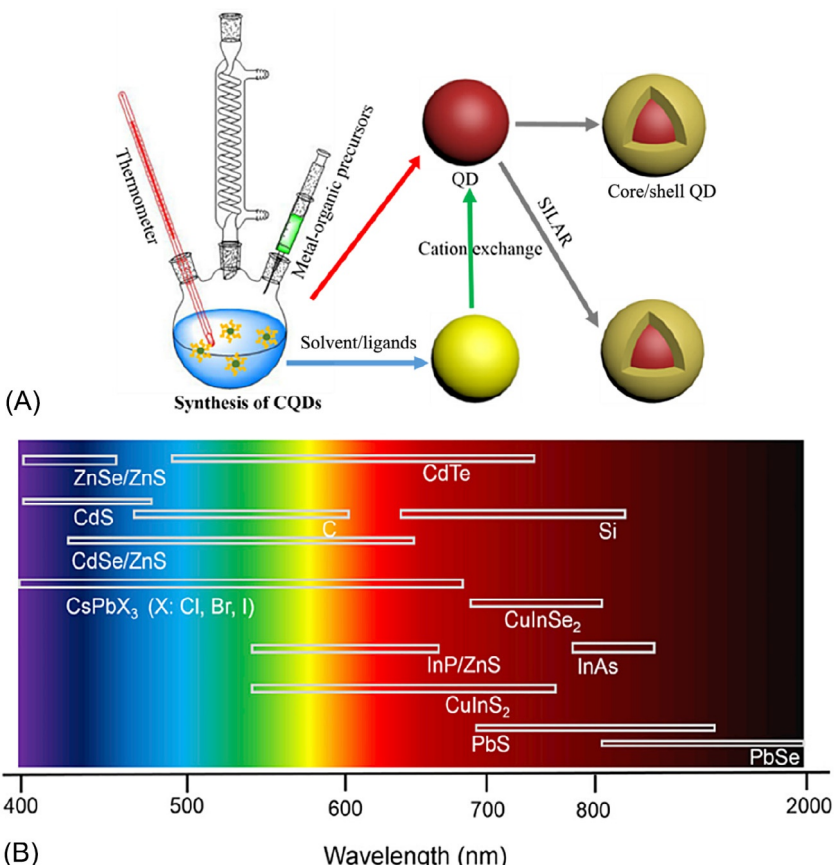


FIG. 1 Schematic diagram of the CQDs synthesis via various approaches and their emission range. (A) A synthetic apparatus used in the preparation of various structured QDs. The bare QDs can be synthesized via a cation exchange approach. The core-shell structure can be obtained via both cation exchange approach and successive ion layer adsorption and reaction [SILAR] approach. (B) The emission range for representative QDs. (Source: Reprinted from Chem, Zhao et al., *Colloidal Quantum Dots for Solar Technologies*, (3) 229–258, Copyright 2017, with permission from Elsevier.)

chemical composition of the resulting NCs to be tuned. The typical reaction setup for the thermolysis method is shown in Fig. 1A.

2.1 Synthesis of bare CQDs

The synthesis of CQDs has been conducted in both organic and aqueous phases [28, 38]. QDs with different elemental composition, including II–VI (e.g., CdX, X = S, Se, Te), III–V (e.g., InP, InAs, GaAs), and IV–VI (e.g., PbX, X = S, Se, Te) semiconductors (Fig. 1B), have been synthesized [10, 40, 43]. Other types

of group IV QDs, such as carbon, silicon, and germanium QDs with size- and chemical-composition dependent emission properties, have also been realized via wet-chemical approaches [45–47]. However, high-quality QDs with narrow size and size distribution, high PLQY, and good photo- and thermal stability have been synthesized almost exclusively via a high-temperature organometallic route by the hot-injection method [40, 43]. The organometallic precursor was mixed with the solvent in the presence of molecular surfactants. The mixture was then heated to a certain temperature in the range of 100–320°C under a gas flow (nitrogen or argon), which can prevent the oxidation of precursors. Subsequently, the non-metallic precursor was injected into the mixture at a much lower temperature (usually at room temperature). Small nuclei were formed at higher temperature and grow further at a lower temperature, leading to separate stages of nucleation and growth of the NCs [48]. The size, shape, and structure of QDs can be further controlled by varying parameters such as the type of precursors and surfactants, reaction temperature, molar ratios of precursors, precursor concentration, reaction time, etc. [40, 43, 49] As an example of visible-emitting II–VI QD synthesis [49], cadmium oxide, hexylphosphonic acid trioctylphosphine oxide, and tetradecylphosphonic acid were loaded in a three-necked flask. At about 300°C, the reddish CdO powder was dissolved and generated a colorless homogeneous solution. After the formation of the complex, an injection of selenium dissolved in tributylphosphine at 250–300°C generated CdSe NCs. Tunable particle sizes of CdSe QDs in the range of 2–8 nm can be synthesized by changing the growth, temperature, and reaction time. The as-produced CdSe QDs exhibit a typical emission in the wavelength range of 450–650 nm.

Another interesting example is the organometallic synthesis of near-infrared (NIR)-emitting PbS QDs with tunable size in the 2–8 nm range [48]. Typically, a certain amount of PbO dissolved in oleic acid (OA) was purged with a nitrogen gas flow and heated in a reaction flask to 150°C. Stock solutions of bis(trimethylsilyl) sulfide and octadecene were then added to the flask and mixed under vigorous stirring. After injection, PbS NCs nucleated quickly. The temperature was maintained at 100°C for the growth of NCs. This synthetic approach is able to produce PbS NCs with a highly crystalline rock-salt structure with a narrow size distribution ($\sigma < 10\%–15\%$). PbS NCs show a peak emission ranging from about 800 to 2000 nm, as well as a narrow emission peak with PLQY up to 20%. The as-produced QDs capped with OA ligands and large-scale synthesis can produce 1 g of NCs in one batch [48]. Because of its effectiveness, the hot-injection method has also been applied for the preparation of binary semiconductor QDs such as CdS, CdTe, ZnSe, HgS, InAs, PbSe, PbTe, and ternary semiconductor QDs such as $\text{CdS}_{x}\text{Se}_{1-x}$, $\text{Zn}_x\text{Cd}_{1-x}\text{S}$, and $\text{CuInS}_x\text{Se}_{2-x}$ [35, 49–52]. The as-produced QDs exhibit high PLQYs in the range of 20%–90% with size distribution $< 10\%$. However, it is critical to control the reaction temperature because both nucleation and the growth rate are highly dependent on temperature. In addition, in this method, the injection temperature is generally higher than 150°C and up to 320°C [49–52].

Quite recently, high-quality perovskite CsPbX_3 ($X = \text{Cl}, \text{Br}, \text{I}$) CQDs were also synthesized via a hot-injection approach in order to control their size and size distribution [53]. Typically, after injecting the Cs precursor into a mixture of PbX and oleylamine, growth occurs within the first 1–3 s. By tuning the reaction temperature (140–200°C), molar ratio of Cl/Br or Br/I, and reaction time, the as obtained QDs exhibit size- and composition-tunable band gap energies covering the entire visible spectral region (410–700 nm) with narrow and bright emission (Fig. 2A–C). The size of CsPbX_3 QDs can be conveniently tuned in the 4–15 nm range with cubic shape and a cubic perovskite crystal structure. The perovskite QDs show narrow emission line widths of 12–42 nm, high PLQYs of 50%–90%, and short radiative lifetimes of 1–29 ns (Fig. 2C and D). However, this type of perovskite QD is very sensitive to moisture, causing the PL signal to decrease gradually over time. After only a day, the PL intensity disappears totally. This is because of the degradation of perovskite materials after reacting with moisture, which causes them to rapidly change color. The product of PbX ($X = \text{Cl}, \text{Br}, \text{I}$) after reaction does not show any optical properties and leads to the disappearance of the PL signal in perovskite materials. Further improvement instability might be achieved by improving our understanding of the degradation mechanism and by optimizing synthetic methods. For example, a new surface technique in which the surface of CsPbBr_3 QDs was capped with an inorganic-organic hybrid ion pair has been found to improve the air stability of perovskite materials [54]. The formation of a protective layer enriched with sulfide endows perovskite QDs with unprecedented stability in air ($60\% \pm 5\%$ humidity) for at least 4 months and under high laser influences, with samples showing no noticeable degradation after 34 h. Other possible approaches to improve the stability of perovskite QDs could use an inorganic shell (e.g., PbS) via an over-coating approach to protect the core material. A clear advantage of the hot-injection method is the simple control of the size and size distribution of QDs, within less than 10% because of the good separation of nucleation and growth at different temperatures by controlling the temperature of the injected precursor solution. As the optical properties of QDs are size dependent, the narrow size distribution leads to very narrow emission spectra with PL width less than 100 meV [48]. In addition, high-temperature growth yields highly crystalline structures, avoiding possible surface traps and defects, and leading to a high PLQY.

This approach can also be applied to a variety of QDs, with emission ranging from UV to visible and the NIR range (400–2000 nm) [48]. This approach can produce high-quality QDs on a large scale with high yield and low cost. The disadvantage of the hot-injection method, similarly to other methods such as solvothermal synthesis and co-precipitation synthesis, is the use of toxic organic solvents and surfactants. In addition, the reaction temperature required to decompose the precursor species is often very high (up to 300°C) [49]. Aqueous colloidal synthesis is considered a “greener” approach for QD production. Because of the low synthetic temperature (<100°C), the as obtained QDs in

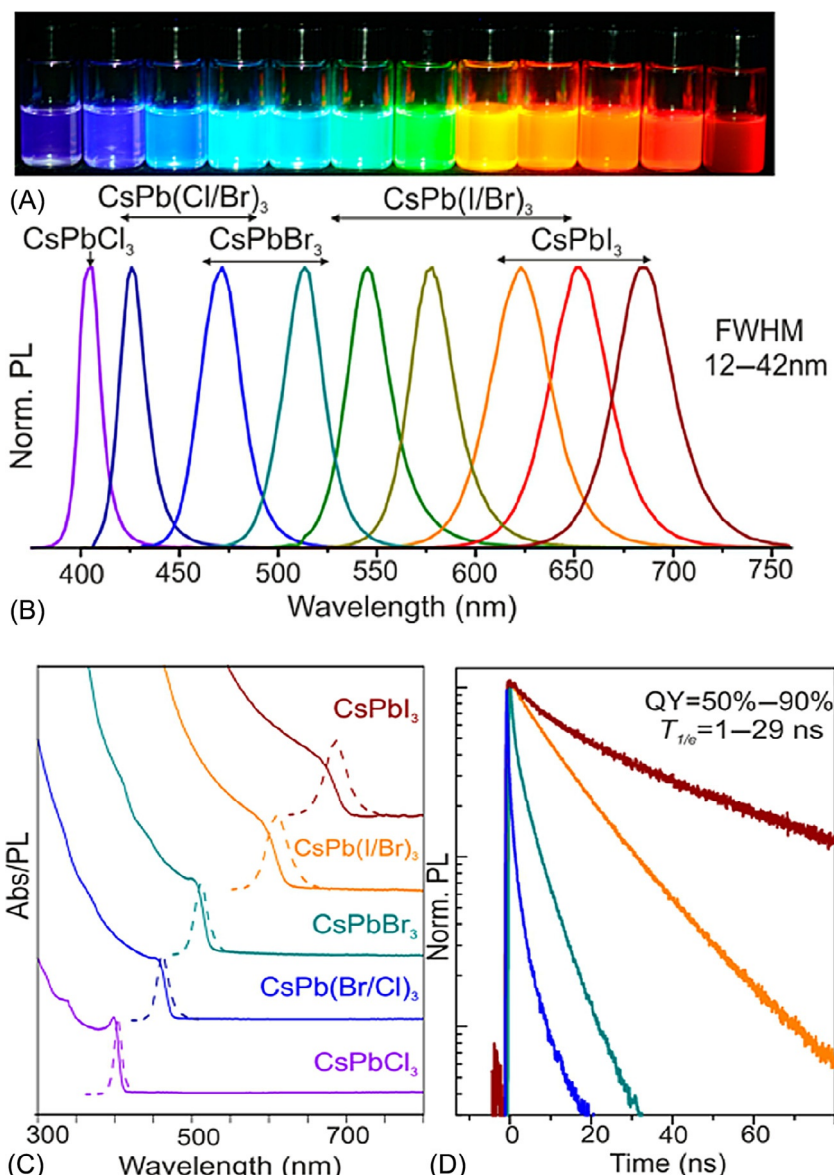


FIG. 2 Colloidal perovskite CsPbX_3 ($X = \text{Cl}, \text{Br}, \text{I}$) NCs exhibit size- and composition-tunable band gap energies covering the entire visible spectral region with narrow and bright emission. [(A) Colloidal solutions in toluene under a UV lamp ($\lambda = 365\text{ nm}$); (B) Representative PL spectra ($\lambda_{\text{exc}} = 400\text{ nm}$ for all but 350 nm for CsPbCl_3 samples); (C) Typical optical absorption and PL spectra; (D) Time-resolved PL decays for all samples shown in (C) except CsPbCl_3 . (Adapted with permission from L. Protesescu, S. Yakunin, M.I. Bodnarchuk, F. Krieg, R. Caputo, C.H. Hendon, R.X. Yang, A. Walsh, M.V. Kovalenko, Nanocrystals of cesium lead halide perovskites (CsPbX_3 , $X = \text{Cl}, \text{Br}$, and I): novel optoelectronic materials showing bright emission with wide color gamut. *Nano Lett.* 15 (2015) 3692–3696. Copyright 2015 American Chemical Society.)

general exhibit low PLQY because of the presence of surface traps or defects. The traps and defects lead to charge trapping, inhibiting efficient charge separation and transfer, and worsen the performance of QD-based optoelectronic devices. It is still very challenging to produce high-quality CQDs with outstanding optoelectronic properties. A further postsurface treatment approach, such as inorganic ligands or inorganic shell coating, might improve the surface passivation of QDs, as well as their optical and electronic properties.

Another well-established approach to synthesize high-quality QDs is through a cation-exchange reaction (Fig. 1A) [26, 54]. Presynthesized QDs with well-defined size and structure, such as CdS and CdSe QDs, can be used as an anion template for the synthesis of compositionally bare and alloyed NC structures [54]. For example, Kim et al. [55] developed a direct, cation-exchange-based procedure that produces PbSe from ZnSe QDs. The Zn cations are replaced by Pb cations and form PbSe QDs capped with both halide anion and zinc cation passivation. The typical reaction procedure consisted of first synthesizing ZnSe QDs via a hot-injection approach. Then PbX_2 ($X = \text{Cl}, \text{Br}, \text{I}$) precursors were mixed with oleylamine and heated to 140°C. Subsequently, the ZnSe QDs dispersed in octadecene at room temperature were injected into the PbX_2 /oleylamine complex at injection temperatures ranging from 80°C to 200°C. Finally, OA was injected into the final solution to exchange the native oleylamine ligands. After injection of the ZnSe QDs, as the reaction proceeds, the PbSe QDs continue to grow. The final size of the PbSe QDs obtained can be effectively controlled by optimizing the QD injection temperature and reaction time. With an initial seed of 3 nm in diameter (first excitonic absorption peak of 3.3 eV) the diameter of the PbSe QDs can be turned over a broad range (1.8–7 nm) [54]. Similar methods have been used to synthesize CuInSe NCs by partial cation exchange in Cu_{2-x}S NCs with the presence of In cations [26]. Generally, the as-prepared PbSe (or PbS) QDs via cation exchange exhibit better air stability than directly synthesized QDs, benefiting from better surface halide passivation [30]. Improving the air stability of cation-exchanged PbSe QDs enables us to fabricate solar energy devices with higher PCE.

On the other hand, the main drawback of this approach is that the reaction process is complicated, involving a seed-based QD synthesis. In addition, during cation exchange, a large amount of precursors was used to facilitate complete exchange (in general, the molar ratio of precursors and cation in QDs is >10) [50]. To address the limitations of this method, chemically active precursors could help to accelerate the degree of cation exchange to obtain completely exchanged QDs with a lower concentration of precursors.

2.2 Synthesis of core-shell QDs

The typical size of a QD is very small (less than 20 nm), leading to a very high surface-to-volume ratio [39]. The co-ordination of surface organic ligands can

stabilize CQDs in solution and at the same time passivate dangling bonds at the QD surface. However, the interaction between the QD and surface organic ligand is weak. Therefore, the properties of bare QDs capped by organic ligands are very sensitive to changes in their surface conditions, especially after exposing the QDs to illumination. The surface-related traps and defects formed act as fast non-radiative de-excitation channels for photogenerated charge carriers, thereby reducing the PLQY and long-term photostability [10, 28]. Recent studies revealed that a core-shell structure is an efficient strategy to improve the surface passivation of QDs [17, 27, 40, 55–64]. As a result, a robust inorganic shell can protect the semiconductor core against surface defect states, trap sites and environmental chemical status, improving both PLQY and stability [65, 66]. Furthermore, by the appropriate choice of core-shell materials, it is possible to tune the band alignment of the core and shell to improve the exciton separation and charge (electron-hole) transfer in the presence of electron or hole scavenger, which is a crucial factor for photovoltaic applications [62, 67].

As shown in Fig. 3, the core-shell heterostructures are typically classified as type-I and type-II depending on the relative alignment of conduction- and valence-band edges of the elements that are combined at the heterointerface [68]. In type-I core-shell QDs, the band gap of the core is smaller than that of the shell, and both band edges of the core are located in the band gap of the shell. Therefore, both electrons and holes are confined in the core region, leading to fewer interactions of core-localized e-h pairs (excitons) with surface traps than with bare QDs and thus enhanced PLQY and photo- and thermal stability over that of pure QDs [28]. In the type-II structure, either the

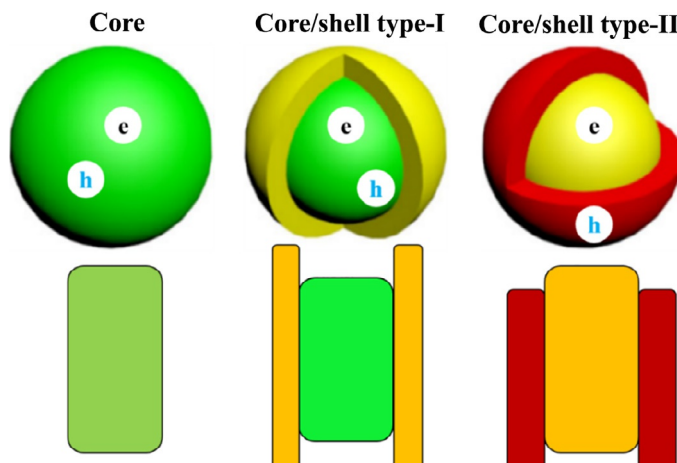


FIG. 3 Schematic diagram of the structure and energy-level alignment in pure QDs and different core-shell QDs systems. Different colors indicate different materials. (*Reprinted from Chem., Zhao et al., Colloidal Quantum Dots for Solar Technologies, (3) 229–258, Copyright 2017, with permission from Elsevier.*)

conduction-band edge or the valence-band edge of the shell is located in the band gap of the core (see Fig. 3). The band alignment causes spatial separation of the electrons and holes into different regions of the core-shell structure [55, 69]. A special case is called quasi type II. In this case, only one type of carrier is delocalized over the entire core-shell structure, whereas the other type of carrier is confined in the core [62, 68, 70]. For example, core-shell PbSe/CdSe QDs [68] present the typical properties of quasi type II band alignment. The electron spreads over the entire core-shell structure, whereas the holes are still confined in the core region.

Core-shell QDs have most commonly been achieved through injection of the shell precursors into the core solution [10, 28, 55, 71]. Several approaches have been reported, including injection of a mixture of cationic and anionic precursors at the growth temperature or alternative injections of cationic and anionic precursors (also named a successive ion layer adsorption and reaction [SILAR] approach), etc. [10, 28, 55, 71, 72] To prevent homogeneous nucleation of the shell material and uncontrolled ripening of the core NCs, the temperature for shell growth (T_2) is generally lower than that used for the core NC synthesis [10]. For example, for the synthesis of CdSe/ZnS core-shell QDs [28], core QDs of CdSe were first synthesized via a hot-injection approach at 300–320°C. After purification, CdSe QDs were dispersed in octadecene and octadecylamine. The mixture was then heated to 240°C in N_2 for shell growth. Equimolar amounts of the Zn/S precursor mixture solution were slowly injected into the core mixture. The optimal thickness of the shell is less than 1.5 nm [28]. Via an overgrowth approach, many core-shell QDs, such as CdSe/ZnS, CdSe/CdS, CdS/HgS, CdSe/ZnTe, InP/ZnS, and PbSe/PbS, have been synthesized with well-controlled shell thickness [55, 61, 71–73].

Core-shell QDs possess significantly enhanced PLQY and largely improved chemical, thermal, and photo-physical stability over pure QDs [28]. For example, the PLQY increases from 5% to 15% for bare CdSe QDs to values ranging from 30% to 50% for CdSe/ZnS QDs [28]; the PLQY of InP QDs increases from around 10%–22% to up to 60% with the deposition of a thin ZnS shell (0.6 nm) [73]. The advantage of the SILAR approach is that the shell thickness can be effectively controlled within one monolayer. The main disadvantage of this method is the high overgrowth temperature of the shell elements, which requires good thermal stability of the core, limiting the selection of suitable materials in the core-shell architecture.

Among various types of core-shell systems, “giant” core-shell QDs (in which the shell is very thick, from several up to 20 nm, and the core exhibits quantum confinement behavior) have been widely studied because of their superior chemical and photostability over both pure QDs and thin-shell QDs [57, 72, 74]. A thicker shell can efficiently protect the core material, insulating it from QD surface chemistry and the surrounding chemical environment. More importantly, for suitably tailored compositions and electronic band structures, the lifetime of excitons generated in the core can be significantly longer than

pure and thin-shell QDs as a result of efficient leakage of the electrons in the shell, forming a quasi type-II band alignment. For instance, in CdSe/CdS “giant” core-shell QDs, the electrons leak into the shell region, and the holes are still confined within the core. The decrease in spatial overlap between electron and hole wave functions leads to a reduced recombination probability, resulting in a prolonged lifetime, up to 50–100 ns [75]. Besides CdSe/CdS, CdSe/ZnSe, ZnSe/CdS, and ZnTe/ZnSe, “giant” core-shell QDs have also been synthesized via the SILAR approach [76]. The type-II (or quasi type-II) band alignment of these “giant” QDs makes them excellent candidates as building blocks for future solar technologies [75].

In the above-mentioned over-coating approach, the core size remains essentially constant during the process. Compared with high-temperature growth of shell materials via a SILAR approach, cation exchange has been reported for the growth of a wider-bandgap material onto lead chalcogenide QDs [27, 63, 66, 77]. The formation of PbSe/CdSe core-shell QDs by cation exchange was first demonstrated by Pietryga et al. [66]. As shown in Fig. 1A, during the shell-coating process, the overall size of the QDs does not change. Only the precursor of the cationic constituent of a shell material is introduced during the shell formation process, and shell growth proceeds through the gradual replacement of core cations by newly introduced cations in solution. For example, core-shell structured lead chalcogenide/cadmium chalcogenide core-shell QDs have been synthesized via a cation-exchange approach. In general, PbX (X = S, Se, Te) QDs were first synthesized. After purification, the PbXQDs were dispersed in toluene and heated to 100°C. In a separate flask, a Cd(OA)₂ mixture was heated to 155°C under N₂ and then injected into the PbX QD dispersion. The core size of PbX QDs can be tuned by varying the reaction temperature and time. The as-synthesized QDs show a typical core-shell structure. By controlling the reaction parameters, such as the starting core size of the QDs, the reaction temperature, the molar ratio of QD/precursor and reaction time, the core size, and structure of the QDs can be controlled, allowing us to study their optical and optoelectronic properties [77]. The as-synthesized PbS/CdS core-shell QDs show PL emission covering the whole NIR region with a quite narrow PL peak width. The shell can largely enhance the PLQY and stability of core QDs. For example, the PLQYs in PbS/CdS core-shell QDs are typically around 60%–70%, which is much higher than 20%–40% for bare QDs [27]. A similar cation-exchange approach was also used to realize core-shell CuInS Se/ZnS QDs with typical PLQY of the order of 40%–50% [34].

The cation-exchange approach can be performed at relatively low temperature (20–150°C), which is in general lower than the seeded overgrowth approach (>200°C). The experimental setup is simple because only one precursor is used in the reaction. In addition, when the shell thickness exceeds a certain value (>1 nm), rather than forming concentric core-shell structures, it also often forms a non-concentric structure, leading to a non-uniform shell thickness distribution. Thicker shells often lead to surface defects as a result of interfacial strain. Thus, the PLQY is very low in thicker-shelled core-shell QDs [27]. On the other hand,

cation exchange is limited to some systems, and accurate control of the interfacial layer between the core and the shell and the thickness of the shell remains challenging. Similar to atomic layer deposition (ALD), which is a powerful technique for deposition of high-quality thin films of dielectric oxides (e.g., Al_2O_3 , HfO_2 , etc), semiconductors (ZnO , ZnS , InGaAs) and metals (Pt, Ir, etc.) on various substrates [78, 79], colloidal ALD is a self-limiting layer-by-layer (LBL) growth method that has been developed to deposit CdS layers on PbS QDs to produce high-quality PbS/CdS core-shell QDs [78]. This method allows for fine control of the CdS thickness, down to the monolayer, combined with room temperature conditions, in principle it can be extended to the synthesis of other QDs system, such as PbSe/CdSe, PbS/CdS/ZnS, HgSe/CdS, etc. [80]

3 Charge dynamics in CQDs

In QD-based solar cells, the PCE is critically related to the ability to generate excitons after photon absorption, electron injection from photo excited QDs to the wide-bandgap semiconductor, as well as carrier lifetime and mobility [81]. In general, charge carriers' recombination is regarded as one of the most significant factors in limiting the performance of solar cells. Efficient charge injection, long lifetime carriers, and high charge mobility can minimize charge recombination processes, thus increasing charge collection efficiency, improving the device performance.

In the solar cell, the valence- and conduction-band energy alignments of the donor and acceptor materials must facilitate charge separation at their interface [81, 82]. For example, in some QD solar cells, anodic charge transport is carried out by a wide bandgap oxide semiconductor. Electrons are injected from the QDs to the oxide, generating a photocurrent. This is why one of the most important challenges to improve device efficiency is to understand and control fast exciton dissociation at the QD-oxide interface and charge injection into the anodic material. Exciton separation and charge injection are regulated by the general band-edge scheme of the whole system, including QDs, hole transporter and metal oxide. It is important to tune the band alignment of the core-shell structure to improve charge separation and transport in the presence of the electron-hole acceptor. The band energy alignment is strongly dependent on the structure of core and shell materials, core and shell size, and the chemical component [82]. In the bare QD system, the charge-transfer rate is strongly dependent on the size of the QDs, the type of carrier acceptor, and the distance between the QD and acceptor [81, 83]. For example, Hines et al. [81] used transient absorption spectroscopy to monitor the electron transfer rate at the interface as a function of the bridge molecules that link QDs to TiO_2 . With the use of mercaptoacetic acid, 3-mercaptopropionic acid (3-MPA), 8-mercaptopoctanoic acid (8-MOA), and 16-mercaptohexadecanoic acid (16-MHA), the distance between the QDs and TiO_2 can be precisely varied (Fig. 4A). The difference in absorption spectrum of CdSe QDs connected by various types of linker

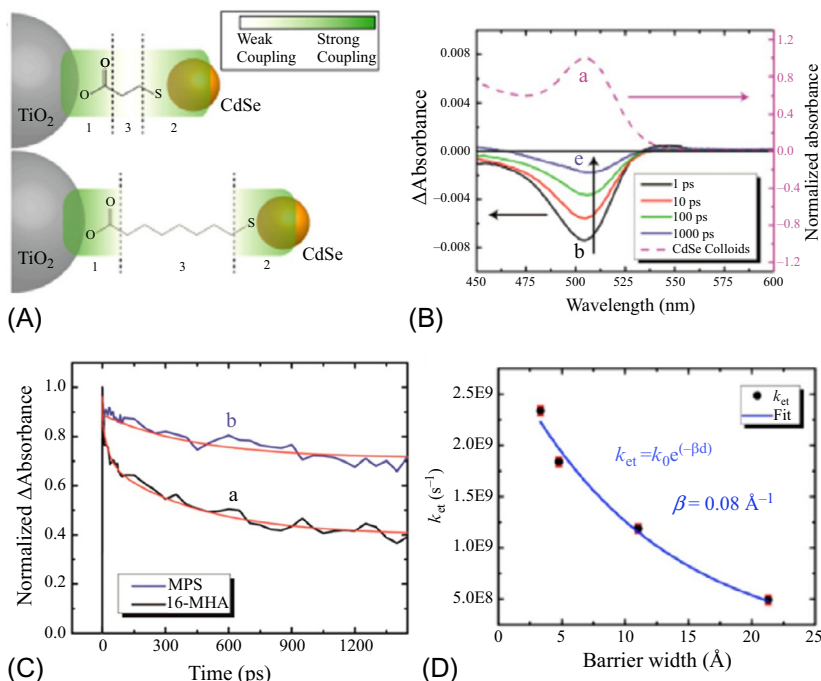


FIG. 4 Electron dynamic in QDs capped with ligands indifferent lengths. (A) Qualitative prediction of electronic coupling in short (represented as 3-MPA) versus long ligands (represented as 8-MOA). (B) The steady-state absorption spectrum of (a) CdSe QDs plotted alongside the difference absorption spectrum of CdSe-(16-MHA)-TiO₂ measured at (b) 1 ps, (c) 10 ps, (d) 100 ps, and (e) 1000 ps via transient absorption spectroscopy. (C) Kinetic traces for (a) CdSe linked to TiO₂ with 16-MHA and (b) CdSe linked to SiO₂ with 3-mercaptop trimethoxysilane (3-MPS). The red traces represent the exponential fitting equation. (D) Experimental values of ket plotted against the barrier width, determined by measuring the length of the extended molecule. Black dots are experimental values, the blue line is the fit, and red represents the error bars determined from four separate measurements. The exponential fit equation is presented on the plot. (Adapted with permission from D.A. Hines, R.P. Forrest, S.A. Corcelli, P.V. Kamat, Predicting the rate constant of electron tunneling reactions at the CdSe/TiO₂ interface, *J. Phys. Chem. B* 119 (2015) 7439–7446. Copyright 2015 American Chemical Society.)

(Fig. 4B, spectra b–e) is monitored over the course of 1.6 ns after excitation with a 387 nm pump pulse. Exponential attenuation of k_t with increasing linker length was observed and was attributed to the tunneling of electrons through the insulating linker molecule (see Figs. 4B and 5C). The observed decrease in lifetime is a consequence of the photoexcited electron transfer from CdSe QDs to TiO₂. k_t was then estimated by the following equation to provide a quantitative description of charge injection:

$$k_t = \frac{1}{\langle \tau \rangle} - \frac{1}{\langle \tau \rangle_{SiO_2}}$$

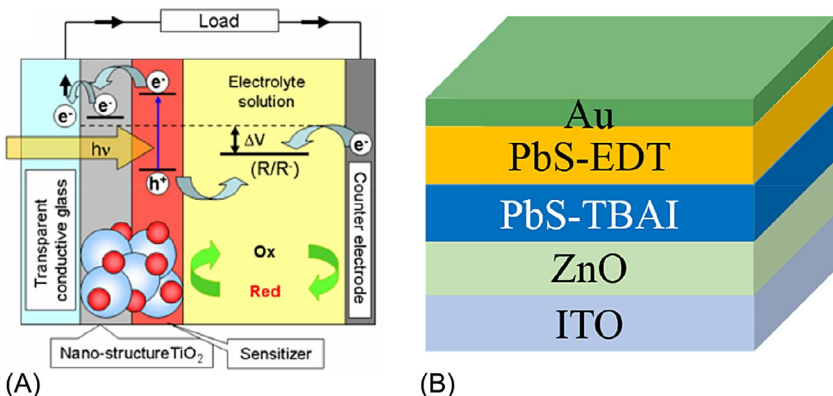


FIG. 5 (A) Schematic illustrations of the working principle and configuration of QD-sensitized solar cells and the possible charge transfer processes occurring at $\text{TiO}_2/\text{QD}/\text{electrolyte}$ interfaces, including injection (I_{nj}), trapping (T_{rp}) and recombination (R_{rc}) of photoexcited carriers. Copyright 2016 Society of Photo-Optical Instrumentation Engineers (SPIE). (B) Schematic diagram of QDHSC ITO/ZnO/PbS-TBAI/PbS-EDT/Au, in which PbS-TBAI represents the PbS QDs treated with tetrabutylammonium iodide (TBAI), and PbS-EDT represents PbS QDs capped with 1,2-ethanedithiol (EDT).

where $\langle \tau \rangle$ and $\langle \tau \rangle_{\text{SiO}_2}$ are the average lifetimes of QDs/ TiO_2 and QDs/ SiO_2 , respectively. With an increase in barrier width, k_t decreases (see Fig. 4D). This demonstrates that electron transfer between CdSe and TiO_2 can be viewed as electron tunneling through a layer of linking molecules and provides a useful method for predicting electron transfer rate constants. In general, k_t is around 5.0×10^8 to $2.2 \times 10^9 \text{ s}^{-1}$ (see Fig. 4D). Without any linker, the direct deposition of CdSe QDs on TiO_2 can yield k_t as high as $1.5 \times 10^{10} \text{ s}^{-1}$ [83].

Because of the small size of QDs, they are very sensitive to environmental conditions, such as light and moisture. A promising solution is to use core-shell QDs as light absorbers. In type-I QDs, both electrons and holes are confined in the core region, which is not suitable for efficient charge transfer. On the other hand, in type-II or quasi type-II QDs, electrons can delocalize into the shell region and improve charge separation and transport in the presence of electron-hole acceptors [54, 70]. These observations provide important insights for the design of efficient core-shell QDs systems in which exciton dynamics can be controlled by means of a core-shell structure, core-shell materials and components, and their relative energy levels for efficient charge transfer.

It was recently shown that the charge-transfer rate in core-shell QDs can be largely improved by carefully engineering the core-shell structure. Zhao et al. [82] synthesized PbS/CdS QDs with tunable core sizes and shell thickness and further investigated the photoelectron-transfer rate from core-shell QDs to wide-bandgap semiconducting mesoporous films by using transit PL spectroscopy. In all the experiments, the same linker (methyl methacrylate [MAA]) was used to connect the QDs with the oxide surface. The different electron affinity

of the oxides (SiO_2 , TiO_2 , and SnO_2), the core size, and the shell thickness allow the electron injection rate to be fine-tuned by determining the width and height of the energy barrier for tunneling from the core to the oxide. Electrons can still transfer into TiO_2 while k_t decreases with the increase in both core size and shell thickness. The results demonstrate the possibility of obtaining fast charge injection in NIR QDs stabilized by an external shell (injection rates as high as $8 \times 10^6 \text{ s}^{-1}$ for TiO_2 films, comparable with that of pure PbS QDs; k_t , $1.2 \times 10^7 \text{ s}^{-1}$), with the aim of providing viable solutions to the stability issues typical of NIR QDs capped with pure organic ligand shells.

Typically, in PbS/CdS core-shell systems, the shell acts as a barrier to be overcome through tunneling for injection to take place, through leakage of electrons from core to shell (quasi type-II band alignment) [82]. In some core-shell systems, such as CdSe/CdS (shell thickness less than 1 nm), the bulk band alignment is type-I [75]. Both electron and hole are confined in the core region. With a further increase in the CdS shell thickness, the electron begins to delocalize into the shell, leading to efficient electron transfer. The leaked electrons are long lived (up to 60 ns), which allows for efficient electron transfer from the QDs to the oxide. However, the hole is still confined mainly in the core region.

In general, with the increase in shell thickness, the physical barrier can slow down or even block hole transfer because the hole density at the QD surface is very low (close to 0). Recently, Alivisatos' group synthesized CdSe QDs (R , 1.95 nm) with tunable CdS shell thickness (H , 0.35–2.45 nm) [84]. They further examined hole transfer from the CdSe core to acceptors covalently linked to the QD surface via the thiolate binding group. As the band energy level of various molecules is favorable for hole transfer, the dominant pathway for quenching PL intensity and the decrease in PL lifetime is attributed to hole transfer from the CdSe core to ferrocene. The PLQYs of core and shell QDs with different shell thickness decrease as a function of N (the average number of hole acceptor molecules). The acceptors are the high driving force (defined as the difference between the oxidation potential of the hole acceptor and the valence band of QDs) for the hole-accepting ferrocene moiety and the low driving force thiol. In summary, it is still possible to achieve a high photostability core-shell system and high charge transfer efficiency concurrently in core-ultra-thick-shell QDs. This finding suggests a promising approach to overcome current challenges in liquid-junction QD-based solar cells (i.e., QD-sensitized solar cells, QDSSCs), by either modifying the surface capping ligands of QDs or adding efficient hole scavengers to the electrolyte to improve the hole transfer rate in “giant” core-thick-shell QDs. However, the combination of the shells and surface long-chain ligands on the QD cores still largely reduces carrier transport in comparison with a pure QD thin-film system. For example, in many optoelectronic devices, such as solid-state solar cells (i.e., QD heterojunction solar cells, QDHSCs), the efficient coupling strength among core-shell QDs can be much less because of the presence of the shell [62]. This situation is favorable for fabricating

high-luminescent solar concentrators but not for transport of electrons and holes between QDs.

In addition, in QDHSCs, without the additional hole acceptor, even one type of carrier in core-thick-shell QDs can be transported efficiently, but another type of carrier is suppressed in the QDs. This occurrence hinders the use of “giant” QDs in QDHSCs. In this framework, engineering the interfacial composition of core-shell QDs could facilitate carrier transfer of both holes and electrons. In view of its significance, the core size, shell thickness, and shell composition need to be controlled at the atomic level.

4 Applications in solar cells

QDs are considered particularly attractive for energy applications, such as photovoltaic devices, photo- and electrochemical catalysts for hydrogen and methanol production, as well as luminescent solar concentrators for their tunable optoelectronic properties [37, 67]. As a result of recent developments in the field, there are increasing efforts to improve their performance [2, 12, 13, 31, 52, 67]. QDSCs are promising devices because of a series of critical properties and performance indicators such as low cost and high PCE, as well as full-spectrum solar harvesting by tuning QD size. In addition, they present a theoretically predicted PCE of 45% in a single-junction QDSC and up to 66% in a multiple-junction QDSC as a result of efficient multiple-exciton generation and hot-electron extraction, with the potential to exceed the Shockley-Queisser limit [16]. In addition, they can be fabricated through low-temperature processes, enabling solar cell fabrication on inexpensive, flexible substrates and large-scale roll-to-roll processing, involving continuous processing of a flexible substrate transferred between two moving rolls of material.

For III–V compounds, such as InAs/GaAs SAQDSCs, Okada et al. [85] have reviewed the latest progress on intermediate band solar cells (IBSCs) focused on the thermodynamics of solar energy conversion, the device physics and the two-step intersub-band absorption/recombination. Zheng et al. [86] reviewed the recent progress in QDSC, especially on the enhanced optical absorption. On the other hand, for CQD-based solar cells, Kramer et al. [87] have thoroughly reviewed the architecture of CQDSCs with special focus on the materials and devices. Duan et al. [88] have reviewed the recent advance in materials for QD-sensitized solar cell application. Wang [89] reviewed the device physics in CQDSC. Zhao et al. [90] have reviewed the CQDs for solar technologies.

Basically, two kinds of CQDSCs have been developed rapidly [8, 9]: QD-sensitized solar cells (QDSSCs) and QD heterojunction solar cells (QDHSCs). Great efforts have been devoted to a fundamental understanding of QDSSCs and QDHSCs; specifically, interface engineering has been carried out systematically, which leads to a significant improvement in the record PCE of these CQDSCs from <1% to as high as 16.6% [15, 91–94]. The breakthrough in

the CQDSCs mostly results from the rapid development of the synthesis technique of high-quality QDs with lower surface trap states and the interface control through various organic and inorganic ligand exchanges on the QDs [8, 9].

4.1 QD-sensitized solar cells (QDSSCs)

Fig. 5A shows the schematic diagram of the working principle and configuration of typical QDSSCs [95]. Similar to dye sensitized solar cell (DSC), QDSSCs consist of a QD sensitized photoelectrode and a counter electrode separated by a liquid electrolyte. In general, wide bandgap metal oxide (TiO_2 , ZnO , and SnO_2 ; in the following TiO_2 is used as an example) nanostructures (such as nanoparticulate, nanorods, nanowires (NWs), nanotubes, and inverseopals) are used as the photoelectrodes in QDSSCs. QDs can be deposited on the photoelectrodes by two kinds of in-situ growth methods, i.e., chemical bath deposition (CBD) and successive SILAR, and by adsorption of presynthesized QDs through direct adsorption or linker-assisted QD deposition method [9, 96–98]. The in-situ deposition methods lead to high loading of QDs, but it is difficult to precisely control the QD size distribution, and surface trap state density in the QDs is high. For the presynthesized QD deposition method, the QDs are size-controlled and high-quality with low surface trap states, but normally the QD loading was low (14%) and thus the PCE was as low as <1% [99]. However, recently, Zhong's group developed a method to increase the QD loading up to 34%, which leads to the highest record PCE of QDSSCs of 16.6% [94]. A number of QDs, such as CdS , CdSe , CdTe , PbS , Sb_2S_3 , CuInS_2 , CdSeTe , $\text{CuInSe}_{1-x}\text{S}_x$, and core-shell structure or double layered QDs, such as CdSe/CdTe , ZnTe/CdSe , CdS/CdSe , PbS/CdS , have been applied as sensitizers in QDSSCs [9]. Aqueous polysulfide solution is most widely used as the electrolyte for QDSSCs. Some solid-state hole-transporting materials (HTMs), such as P3HT, Spiro-OMeTAD and CuSCN, are also used as hole-scavenging and transport layers in QDSSCs [100–102]. For the polysulfide electrolyte, copper sulfide (Cu_2S) is the most used counter electrode. For the solid-state HTMs, gold and silver are commonly used as electrodes.

As shown in **Fig. 5A**, once electron-hole pairs are generated in the QD sensitizer after optical absorption, photoexcited electrons are injected into the metal oxide electrode and then transported to collection electrode (transparent conducting electrode), while the oxidized QDs are regenerated by electrolyte (hole-scavenging medium) and then the oxidized species of redox couple are regenerated at the counter electrode.

Generally, CQD-based solar cells can have much better PCE than SILAR-deposited CQD-based solar cells because the CQDs have better size and structure control [36]. For example, Du et al. [36] synthesized Zn-Cu-In-Se (ZCISe) alloyed CQDs with an absorption onset extending to 1000 nm as effective light harvesters to construct liquid-junction QDSCs. An average PCE of 11.66% and a certified PCE of 11.61% have been demonstrated in QDSCs on the basis of

these ZCISe QDs, which is better than the CISe-based solar cell under identical measurement conditions. The high photocurrent density in ZCISe QDSCs was further confirmed by the incident photon-to-electron efficiency (IPCE) spectra. The improved photovoltaic performance for ZCISe QDSCs over that of CISe QDSCs (11.66% vs 9.54%, respectively, in PCE) is mainly due to the higher conduction-band edge, which leads to a higher photocurrent, and the alloyed structure, which benefits suppression of charge recombination at the photoanode-electrolyte interfaces [36]. The certified PCE was further improved from 11.66% to 12.07% simply by replacing the Cu₂S-based counter electrode with nitrogen-doped mesoporous carbon (N-MC)-based counter electrodes [103]. The N-MC-based counter electrode exhibits much stronger activity in catalyzing the reduction of a polysulfide redox couple (Sn²⁺/S²⁻) with respect to counter electrodes based on Cu₂S.

The advantages of QDHSCs are the simple fabrication procedure and low cost. However, liquid-junction QDSSCs obviously contain a liquid electrolyte and might leak during cell preparation and further use. Initially, CQDs with high extinction coefficients were used instead of dyes in dye-sensitized solar cells (DSSCs). In this case, the CQD absorbs light to form excitons, and electrons and holes separated from the excitons are generally transferred through TiO₂ and the electrolyte, respectively [104]. Consequently, the electric characteristics of the CQDs have relatively low influence on the device in the dye-sensitized solar cell. However, the CQDs with uncontrolled electrical properties can be formed as a monolayer on TiO₂ to absorb only a small amount of light. Therefore, mesoporous TiO₂ is commonly used to overcome this problem. In recent years, new CQDs without heavy metals (such as Zn-Cu-In-Se CQDs) have been employed to produce a dye-sensitized solar cell structure that exhibits a relatively high PCE [35, 105, 106].

Over the last 10 years, QDHSCs have been widely explored to overcome the drawback of QDSSCs.

4.2 QD heterojunction solar cells (QDHSCs)

QDHSCs architectures were developed to overcome the main limitations associated with Schottky CQD solar cells. Taking inspiration from sensitized solar cell architectures, which typically employs a monolayer of molecular absorbers on a wide-band-gap semiconductor matrix, the depleted heterojunction architecture [104] uses a highly doped n-type metal oxide in a p-n heterojunction with a p-type CQD film. However, performance in QDHSCs based on planar films is limited by short carrier transport lengths in the CQD material. Specifically, the absorption lengths for infrared photons at the optimum single-junction band gap energies are longer than the sum of the depletion region width plus the diffusion length in the CQD materials. This trade-off is termed as the “absorption-extraction compromise,” and it limits the thickness of the absorbing CQD material that can be effectively used in solar cells.

Strategies for overcoming the “absorption-extraction compromise” include the use of bulk heterojunction architectures and light-trapping schemes. A typical architecture for a QDHSCs is shown in Fig. 5B, CQDs are deposited on an electrode coated with a metal oxide layer (such as indium-doped tin oxide, ITO), which serves as electron acceptor. As CQDs are often capped with long-chain ligands, which serve as insulator to block efficient charge transfer, a LBL ligand-exchange approach is used to replace the surface long chains with shorter ligands, such as MAA, MPA, etc. [36] An efficient ligand-exchange procedure is important to achieve high-efficiency QDSCs because this process involves surface modification, which leads to the formation of surface traps. Lan et al. [36] used a new surface-ligand-exchange approach that enables increased passivation of QDs with the use of iodide anion. The approach allows the ionic molecule, methyl ammonium iodide (MAI), to access targeted non-polar-dispersed CQDs by tuning the polarity of the dispersion medium. They first used MAI to replace theoleate ligands of PbS QDs in solution, followed by the solid-state ligand-exchange process using tetrabutylammonium iodide (TBAI). The enhanced passivation increases the photovoltaic performance up to a certified efficiency of 10.6%. The improvement comes mainly from the increase in short-circuit current density (J_{sc}) as a result of the improved passivation, which contributes to enhanced diffusion lengths and thus enables thicker devices.

Core-shell QDs have also been used for high-efficiency solid-state solar cells. Benefiting from the improved surface passivation, the QDs are very robust during cell fabrication and in operation [62]. For example, Neo et al. [62] used core-shell PbS/CdS for QDSCs. They fabricated the solar cells in ambient conditions because of the superior air stability of the core-shell QDs. Compared with bare QDs, the core-shell QDs show improved values for open circuit voltage (V_{oc}) and J_{sc} . In particular, V_{oc} can increase from 0.42 to 0.66 V. This is attributed to a decrease in recombination events as a result of the passivating shell. With an optimal shell thickness of 0.1 nm, a PCE of $5.6\% \pm 0.4\%$ has been achieved with a simple heterojunction device architecture. These results indicate that the core-shell strategy has great potential for the realization of air-stable QDSCs. Current research efforts still focus on improving the PCE by addressing the passivation and transport properties of QD films with the aid of organic, inorganic, or hybrid ligands, which have led to the rapid development of high-efficiency solar cells with PCE exceeding 10%, as summarized in Table 1 [35, 36, 103, 107, 108].

The main reason for the poor photovoltaic performance of the QDHSCs, especially the low V_{oc} , is the interfacial recombination. During the last few years, the photovoltaic properties of the two kinds of QDHSCs have been improved rapidly due to the advances of the QD preparation method and device engineering [8, 9]. In particular, some strategies of interface engineering have been explored to reduce the recombination occurring at (1) the QD surface and/or QD-QD interface [30, 109–112]; (2) the QD/metal electrode (usually

TABLE 1 Photovoltaic parameters of QDSCs.

Cell	Type	J_{sc} (mA/cm ²)	V_{oc} (V)	Fill Factor (FF)	PCE (%)	Reference
ZnCuInSe ^a	Liquid	25.25	0.739	0.622	11.6	[35]
ZnCuInSe ^b	Liquid	25.21	0.626	0.765	12.07	[101]
CuInGaSe	Liquid	25.01	0.74	0.621	11.49	[106]
PbS ^c	Solid	24.3	0.61	0.71	10.6	[36]
PbS ^d	Solid	27.23	0.61	0.68	11.28	[107]

^aCounter electrode based on Cu₂S.
^bCounter electrode based on nitrogen-doped mesoporous carbons.
^cQDs were surface treated by MAI.
^dQDs were surface treated by hybrid organic-inorganic ligands (lead halide and ammonium acetate).

Au) interface [113–115]; and (3) the QD/metal oxide (ZnO or TiO₂) interface [116, 117].

For suppressing the recombination (1), QD surface passivation through organic dithiol ligand [109] and inorganic atomic halide ligand [110] exchanging has been proven to be very useful. In addition, a hybrid organic-inorganic ligand approach could effectively decrease the mid gap electronic trap state density of QDs, and an increase in V_{oc} was achieved [111]. Another approach to reduce the mid gap trap state density is to passivate the QD surfaces during the synthesis process. Using this method, Zhang et al. [30] achieved high-performance PbSe QDHSCs with record PCE over 6% by using the Cd and Cl passivation. Recently, the same group prepared air-stable PbSeQDHSCs (over 50 days) with a certified PCE of 5.9% by passivating the PbSe QD surfaces with halide anions and residual Zn cations through cation-exchange reaction of ZnSe QDs with PbX₂ (X = Cl, Br, or I) precursors [112].

For suppressing the recombination (2) at the QDs/metal electrode interface (i.e., electron transfer from QDs to metal electrode), a strategy of band alignment at the interface was proposed. Brown et al. [113] have demonstrated that the absolute energy level of QD film is critically dependent on surface chemistry and can be modified through ligand exchange. Bawendi et al. [114] introduced an EDT-capped PbS QD layer between an tetrabutyl ammonium iodide (TBAI)-treated (i.e., iodine passivated) PbS QD layer and the metal electrode to control the band alignment of the QD layers in ZnO/PbS QDHSCs. This band alignment engineering led to a certified PCE of 8.55% and the device showed a long-term air stability. Cao et al. [115] used the same device structure of ZnO/PbS QDHSCs but replaced TBAI with 1-ethyl-3-methylimidazolium iodide for halide-based ligand exchange, and they achieved a certified PCE of 8.7% and a better long-term photostability was demonstrated.

For suppressing the recombination (3) occurring at the QD/metal oxide interface, surface passivation of the metal oxide nanostructure is very important. Jang et al. [116] effectively reduced the interband trap sites of the ZnO nanoparticles by using simple EDT treatment, which resulted in a great suppression of the interfacial recombination in ZnO/PbS QDHSCs. As a result, a certified PCE of 10.14 was achieved. Kim et al. [117] reported a high performance ZnO/PbS QDHSCs with a certified PCE of 10.7% by depositing robust self-assembled monolayers on ZnO surface to adjust the energy alignment of the interface. To push the PCE of QDSCs to be as high as over 40%, as expected theoretically, fundamental studies on multiple exciton generation (MEG) effect in QDs and its realization in practical QDSC devices are very important and have attracted much interest. The MEG has been observed optically in several kinds of QDs, such as PbS, PbSe, PbTe, CdSe, InAs, Si, carbon nanotube and $\text{Cd}_x\text{Hg}_{1-x}\text{Te}$ [6, 118–122]. It was found that the generation of multiple-exciton state by MEG in the QDs, such as PbS and PbSe, occurred as fast as a few 100 fs and the relaxation to a single-exciton states on a time scale of a few 10 to a few 100 ps through an Auger-like process [6, 121]. The extraction of more than one electron per absorbed photon as electrical current in CQDHSCs has been reported with the internal and external quantum efficiency (EQE) exceeding 100%, such as PbS, PbSe, and CuInSe₂ QDHSCs [123–125]. For improving the efficiencies of both QDSCs and QDHSCs, photoexcited electron and hole transfer from the QDs are essential, especially for designing the devices of MEG-type QDSCs. Dependence of electron transfer from photoexcited QDs to molecular acceptors on the QD sizes has been studied systematically by Zhu et al. [126]. They found that the photoexcited electron transfer rate increased as the QD size decreased, i.e., the driving force increased. The unusual driving force dependence was explained by an Auger-assisted electron transfer model in which the electron transfer could be coupled to the excitation of the hole, circumventing the unfavorable Franck-Condon overlap in the Marcus inverted regime [126]. Olshansky [127] investigated the relationship between driving force and rate for hole transfer from photoexcited QDs systematically by using CdSe/CdS core/shell QDs and different molecular hole acceptors. The experimental relationship between the rate and energetic driving force for hole transfer was not well explained by the standard two-state Marcus model because the inverted Marcus region was not observed. An Auger-assisted photoexcited holes transfer mechanism was proposed in which experimental results were modeled successfully. These relationships between interfacial charge transfer and energetic driving force are very useful for designing CQDSCs to maximize interfacial charge transfer and minimize energetic losses associated with the driving force.

In CQDs, the quantum confinement effect separates the levels of the energy band of bulk semiconductors, resulting in an increase in the energy band gap and a discrete energy level. This discrete energy level decreases the density of state and reduces the amount of absorbed light around the energy band gap. Therefore,

observations of the EQE spectrum of a CQD PV show a markedly decreased efficiency near the energy band gap. This is a unique characteristic of the CQD. To solve this problem, surface plasmons of metal nanoparticles have been used to shift the spectrum of the incident sunlight to the region in which CQDs can absorb large amounts of light, thereby improving the PCE [128].

Also, multiple junctions techniques can improve the PCE because they provide easier control of the light absorption region of the CQDs, thus adjusting the energy band gap. Although relatively few studies have been conducted on multi-junction CQD PVs, they have shown a possibility of maximized efficiency. The LBL process is performed to fabricate the conductive CQD film. In this case, because an organic ligand has a specific acidity and LBL process is performed using a polar solvent and a non-polar solvent alternately, the pre-formed front subcell and intermediate recombination layer (IRL) is damaged and the efficiency is lowered. As an example, Aqoma et al. [129] placed a CQD PV with a smaller band gap in front of the organic PV sub-cell, thereby minimizing the reduction in efficiency. In addition, IRLs have been developed that can induce sufficient electron and hole recombination without damage by using the solution process during the formation of the rear subcells to minimize the efficiency reduction [130]. However, the current efficiency of multi-junction CQD PVs is lower than that of single-junction CQD PVs; therefore, further research is required to address these problems. One possible solution is to minimize the damage of the front sub-cell by using CQDs in which the ligand is exchanged in the liquid phase. Further, the efficiency of organic solar cell can be enhanced by inserting PbS QDs film as the infrared absorption layer [131], or by incorporating PbSe QDs into the active layer [132] and even by incorporating CdSe/ZnS QDs [133] and by functionalized single-walled carbon nanotubes decorated with CdSe/ZnS core-shell CQDs [134].

Great progress in the surface passivation of CQDs, such as by short-chain ligands [135], by organic ligands [113, 136–138] and/or by inorganic ligands [110, 139], particularly by halide ions [140, 141], have led to rapid improvements in PbS CQDs solar cells, and the maximum certified PCE has reached 16.6% [94]. However, there are still some challenges remaining, and the charge carrier conduction mechanism in the CQDs solar cells are still unclear. Much more attention should be paid to the fundamental understanding of the PbS CQDs-based solar cell since this is the basis on how to enhance the performance of CQDs-based solar cells. Usually, current density-voltage (*J-V*) characteristics are used to analyze the cell performance and the V_{OC} , J_{SC} , and fill factor (FF) of the solar cells. However, the full physical mechanism beneath the active layer and solar cells cannot be derived only from its *J-V* characteristics.

As we know, electrochemical impedance spectroscopy (EIS) is applied for current change monitoring as a response of alternating frequency of alternating current (AC) voltage, which permits an investigation of electrical characteristics other than those obtained by direct current (DC) testing equipment.

In order to achieve the better performance of devices, EIS measurement has been applied for the study of carriers' relaxation and transport properties for many types of optoelectronics devices, such as DSSCs [142, 143], perovskite solar cells [144], organic solar cells [145–149] and PbS CQDs-based solar cells [150] to better understand the carriers accumulation and transport mechanism underneath. Also, the influence of post-synthesis annealing on PbS QD solar cells were studied [151].

Currently, QDSCs are still far from commercialization because of the small active area, limited PCE and poor long-term stability. It is still very challenging to obtain high-efficiency QDSCs because of polydispersity, random packing and inhomogeneous aggregation of QDs during the ligand-exchange process [36, 62, 107], leading to the inhomogeneous energy landscape present in QD solids. Various strategies have been developed to enhance the PCE of QDSCs, such as synthesis of high-quality QDs with respect to a trap-free surface, broad light-harvesting range, and narrow size distribution; use of plasmonic nanostructures to enhance the absorption of QD films [152]; and use of a QDSCs tandem structure to improve IR absorption [153].

A most pressing challenge is to improve the long-term stability of QDSCs. Device stability depends on the interface and band alignment between the QDs and anodes, as well as on the QD layer itself [154]. To date, PbS QD-based solid-state QDSCs only retain 90% of their initial PCE (11.28%) after 1000 h of storage in air without encapsulation [107]. This would be even worse if the QDSCs operate under sunlight. A greater understanding of the thermal and photostability of QDs, optoelectronic properties of QDSCs, and further progress in materials development and solar cell structure could potentially lead to a new generation of air-stable QDSCs.

5 Conclusions and outlook

In summary, in this chapter we have highlighted recent research on the design and synthesis of various types of CQDs, their optical and electronic properties, and their use in solar cells. An overview of various strategies developed for the synthesis of CQDs, including bare QDs and core-shell QDs with controlled structure for photovoltaic devices, is provided. Controlling the synthesis and optoelectronic properties of CQDs has emerged as a promising approach to improve the efficiency and stability of next-generation solar cells. Although recent QD research has led to significant advances in synthetic approaches and device efficiency, there are still several key challenges.

The first is to synthesize QDs with well-controlled structure. Depending on the intended application, QDs need to exhibit specific optoelectronic properties. A low-cost and environmentally friendly approach is still urgent for the development of trap-free QDs. For example, current methodologies rely on relatively toxic organometallic precursors in organic solvent at a relatively high

temperature (typically $>100^{\circ}\text{C}$) because of the high decomposition temperature of the precursors. In addition, typically the ligands are long-chain surfactant molecules, which serve as electrical insulator in solar energy devices [10, 24, 28, 49, 50]. Thus, identifying new precursors for the low-temperature synthesis of QDs with short-chain ligands or electroactive ligands is an emerging direction [155]. For instance, atomic layer deposition can be used to produce structurally controllable core-shell QDs at room temperature with active precursors [80]. For core-shell QDs, future directions should focus on developing a simple, lower-temperature synthesis procedure to realize core-shell QDs with a gradient interfacial structure to tune the electronic properties of QDs to facilitate charge separation and transfer. Other approaches to improve optoelectronic properties should focus on treatment after QD synthesis. Novel postsurface passivation strategies, including inorganic ligands and hybrid organic-inorganic ligands, can reduce trap states created during QD synthesis and device fabrication.

The second is to improve the efficiency and stability of solar cells based on QDs. In solid-state QDSCs, even though the certified PCE is over 10%, the active area is still very small ($<1\text{ cm}^2$), and the stability is not competitive with existing commercial technologies. New strategies to improve PCE and stability are still urgently needed. For example, efficiency could be improved by optimization of the QD film thickness, film uniformity, and engineering of the band structure of the QD film, etc. The stability can be addressed with the use of trap-free QDs or posttreatment of the QD film for the removal of traps. Addressing these challenges could lead to a more profound understanding of the structure-property relationships in these materials and to exciting technological opportunities for solar energy.

In the last few years, QDSCs have developed rapidly because of great efforts in interface engineering of these CQDSCs. The certified PCEs of both QDSSCs and QDHSCs have reached as high as over 16.6% through various interface engineering strategies. However, the PCEs are still much lower than the theoretical value of 44%. Therefore, further fundamental studies on the mechanism on how to improve the efficiency of CQDSCs are very necessary and important. The photovoltaic performances of the CQDSCs would be improved further by solving the following issues: (1) deep understanding, precise control, and passivation of the nanointerfaces of CQDSCs, and (2) clarifying the mechanism of MEG in QDs and realization of MEG in CQDSCs.

Acknowledgments

This project was partially funded by the project of State Key Laboratory of Transducer Technology (SKT1404), the project of the Key Laboratory of Photoelectronic Imaging Technology and System (2017OEIOF02), Beijing Institute of Technology, Ministry of Education of China.

References

- [1] J.A. Turner, A realizable renewable energy future, *Science* 285 (1999) 687–689.
- [2] P.V. Kamat, Meeting the clean energy demand: nanostructure architectures for solar energy conversion, *J. Phys. Chem.* 111 (2007) 2834–2860.
- [3] A. Luque, A. Martí, Increasing the efficiency of ideal solar cells by photon induced transitions at intermediate levels, *Phys. Rev. Lett.* 78 (1997) 5014–5017.
- [4] A.J. Nozik, Quantum dot solar cells, *Phys. E* 14 (2002) 115–120.
- [5] M.C. Beard, Multiple exciton generation in semiconductor quantum dots, *Chem. Phys. Lett.* 457 (2008) 3–11.
- [6] R.D. Schaller, V.I. Klimov, High efficiency carrier multiplication in PbSe nanocrystals: implications for solar energy conversion, *Phys. Rev. Lett.* 92 (2004), 186601.
- [7] M.C. Hanna, A.J. Nozik, Solar conversion efficiency of photovoltaic and photoelectrolysis cells with carrier multiplication absorbers, *J. Appl. Phys.* 100 (2006), 074510.
- [8] G.H. Carey, A.L. Abdelhady, Z.J. Ning, S.M. Thon, O.M. Bakr, E.H. Sargent, Colloidal quantum dot solar cells, *Chem. Rev.* 115 (2015) 12732–12763.
- [9] K. Zhao, Z.X. Pan, X.H. Zhong, Charge recombination control for high efficiency quantum dot sensitized solar cells, *J. Phys. Chem. Lett.* 7 (2016) 406–417.
- [10] A.P. Alivisatos, Semiconductor clusters, nanocrystals, and quantum dots, *Science* 271 (1996) 933–937.
- [11] S.A. McDonald, G. Konstantatos, S.G. Zhang, P.W. Cyr, E.J.D. Klem, L. Levina, E.H. Sargent, Solution-processed PbS quantum dot infrared photodetectors and photovoltaics, *Nat. Mater.* 4 (2005) 138–142.
- [12] M.J. Currie, J.K. Mapel, T.D. Heidel, S. Goffri, M.A. Baldo, High-efficiency organic solar concentrators for photovoltaics, *Science* 321 (2008) 226–228.
- [13] P.V. Kamat, Quantum dot solar cells: semiconductor nanocrystals as light harvesters, *J. Phys. Chem. C* 112 (2008) 18737–18753.
- [14] A.J. Nozik, M.C. Beard, J.M. Luther, M. Law, R.J. Ellingson, J.C. Johnson, Semiconductor quantum dots and quantum dot arrays and applications of multiple exciton generation to third-generation photovoltaic solar cells, *Chem. Rev.* 110 (2010) 6873–6890.
- [15] D.V. Talapin, J.S. Lee, M.V. Kovalenko, E.V. Shevchenko, Prospects of colloidal nanocrystals for electronic and optoelectronic applications, *Chem. Rev.* 110 (2010) 389–458.
- [16] M.G. Walter, E.L. Warren, J.R. McKone, S.W. Boettcher, Q. Mi, E.A. Santori, N.S. Lewis, Solar water splitting cells, *Chem. Rev.* 110 (2010) 6446–6473.
- [17] R.G. Chaudhuri, S. Paria, Core/shell nanoparticles: classes, properties, synthesis mechanisms, characterization, and applications, *Chem. Rev.* 112 (2012) 2373–2433.
- [18] L.R. Bradshaw, K.E. Knowles, S. McDowall, D.R. Gamelin, Nanocrystals for luminescent solar concentrators, *Nano Lett.* 15 (2015) 1315–1323.
- [19] I. Moreels, K. Lambert, D. Smeets, D. De Muynck, T. Nollet, J.C. Martins, F. Vanhaecke, A. Vantomme, C. Delerue, G. Allan, Z. Hens, Size-dependent optical properties of colloidal PbS quantum dots, *ACS Nano* 3 (2009) 3023–3030.
- [20] J.B. Rivesta, P.K. Jain, Cation exchange on the nanoscale: an emerging technique for new material synthesis, device fabrication, and chemical sensing, *Chem. Soc. Rev.* 42 (2013) 89–96.
- [21] S. Kim, Y.T. Lim, E.G. Soltesz, A.M. De Grand, J.Y. Lee, A. Nakayama, J.A. Parker, T. Mihaljevic, R.G. Laurence, D.M. Dor, L.H. Cohn, M.G. Bawendi, J.V. Frangioni, Near-infrared fluorescent type II quantum dots for sentinel lymph node mapping, *Nat. Biotechnol.* 22 (2004) 93–97.

- [22] X. Michalet, F.F. Pinaud, L.A. Bentolila, J.M. Tsay, S. Doose, J.J. Li, G. Sundaresan, A.M. Wu, S.S. Gambhir, S. Weiss, Quantum dots for live cells, *in vivo* imaging, and diagnostics, *Science* 307 (2005) 538–544.
- [23] H.G. Zhao, A. Vomiero, F. Rosei, Ultrasensitive, biocompatible, self-calibrating, multiparametric temperature sensors, *Small* 11 (2015) 5741–5746.
- [24] E. H. Sargent, Infrared quantum dots, *Adv. Mater.* 17 (2005) 515–522.
- [25] H.G. Zhao, D.F. Wang, T. Zhang, M. Chaker, D.L. Ma, Two-step synthesis of highquality water-soluble near-infrared emitting quantum dots via amphiphilic polymers, *Chem. Commun.* 46 (2010) 5301–5303.
- [26] W. van der Stam, A.C. Berends, F.T. Rabouw, T. Willhammar, X.X. Ke, J.D. Meeldijk, S. Bals, C. de Mello Donega, Luminescent CuInS₂ quantum dots by partial cation exchange in Cu_{2-x}S nanocrystals, *Chem. Mater.* 27 (2015) 621–628.
- [27] H.G. Zhao, M. Chaker, D.L. Ma, Effect of CdS shell thickness on the optical properties of water-soluble, amphiphilic polymerencapsulated PbS/CdS core/shell quantum dots, *J. Mater. Chem.* 21 (2011) 17483–17491.
- [28] B.O. Dabbousi, J. Rodriguez-Viejo, F.V. Mikulec, J.R. Heine, H. Mattoussi, R. Ober, K.F. Jensen, M.G. Bawendi, (CdSe) ZnS core-shell quantum dots: synthesis and characterization of a size series of highly luminescent nanocrystallites, *J. Phys. Chem. B* 101 (1997) 9463–9475.
- [29] D.K. Ko, P.R. Brown, M.G. Bawendi, V.I. Bulovic, p-i-n Heterojunction solar cells with a colloidal quantum-dot absorber layer, *Adv. Mater.* 26 (2014) 4845–4850.
- [30] J.B. Zhang, J.B. Gao, C.P. Church, E.M. Miller, J.M. Luther, V.I. Klimov, M.C. Beard, PbSe quantum dot solar cells with more than 6% efficiency fabricated in ambient atmosphere, *Nano Lett.* 14 (2014) 6010–6015.
- [31] Y.M. Zhao, G.A. Meek, B.G. Levine, R.R. Lunt, Near-infrared harvesting transparent luminescent solar concentrators, *Adv. Opt. Mater.* 2 (2014) 606–611.
- [32] I. Concina, C. Manzoni, G. Grancini, M. Celikin, A. Soudi, F. Rosei, M. Zavelani-Rossi, G. Cerullo, A. Vomiero, Modulating exciton dynamics in composite nanocrystals for excitonic solar cells, *J. Phys. Chem. Lett.* 6 (2015) 2489–2495.
- [33] X. Tong, Y.F. Zhou, L. Jin, K. Basu, R. Adhikari, G.S. Selopal, X. Tong, H.G. Zhao, S.H. Sun, A. Vomiero, Z.M. Wanga, F. Rosei, Heavy metal-free, near-infrared colloidal quantum dots for efficient photoelectrochemical hydrogen generation, *Nano Energy* 31 (2017) 441–449.
- [34] F. Meinardi, H. McDaniel, F. Carulli, A. Colombo, K.A. Velizhanin, N.S. Makarov, R. Simonutti, V.I. Klimov, S. Brovelli, Highly efficient large-area colourless luminescent solar concentrators using heavymetal-free colloidal quantum dots, *Nat. Nanotechnol.* 10 (2015) 878–885.
- [35] J. Du, Z.L. Du, J.S. Hu, Z.X. Pan, Q. Shen, J.K. Sun, D.H. Long, H. Dong, L.T. Sun, X.H. Zhong, L.J. Wan, Zn-Cu-In-Se quantum dot solar cells with a certified power conversion efficiency of 11.6%, *J. Am. Chem. Soc.* 138 (2016) 4201–4209.
- [36] X.Z. Lan, O. Voznyy, F.P. García de Arquer, M.X. Liu, J.X. Xu, A.H. Proppe, G. Walters, F.J. Fan, H.R. Tan, M. Liu, Z.Y. Yang, S. Hoogland, E.H. Sargent, 10.6% Certified colloidal quantum dot solar cells via solvent polarity-engineered halide passivation, *Nano Lett.* 16 (2016) 4630–4634.
- [37] Y.F. Zhou, D. Benetti, Z.Y. Fan, H.G. Zhao, D.L. Ma, A.O. Govorov, A. Vomiero, F. Rosei, Near infrared, highly efficient luminescent solar concentrators, *Adv. Energy Mater.* 6 (2016) 1501913.

- [38] V. Lesnyak, N. Gaponik, A. Eychmuller, Colloidal semiconductor nanocrystals: the aqueous approach, *Chem. Soc. Rev.* 42 (2013) 2905–2929.
- [39] I. Ka, V. Le Borgne, D. Ma, M.A. El Khakani, Pulsed laser ablation based direct synthesis of single-wall carbon nanotube/PbS quantum dot nanohybrids exhibiting strong, spectrally wide and fast photoresponse, *Adv. Mater.* 24 (2012) 6289–6294.
- [40] P. Reiss, M. Protiere, L. Li, Core/shell semiconductor nanocrystals, *Small* 5 (2009) 154–168.
- [41] I.U. Arachchige, S.L. Brock, Sol-gel methods for the assembly of metal chalcogenide quantum dots, *Acc. Chem. Res.* 40 (2007) 801–809.
- [42] J. Pan, A.O.E. Ballouli, L. Rollny, O. Voznyy, M. Burlakov, A. Goriely, E.H. Sargent, O.M. Bakr, Automated synthesis of photovoltaic-quality colloidal quantum dots using separate nucleation and growth stages, *ACS Nano* 7 (2013) 10158–10166.
- [43] A.L. Rogach, A. Eychmller, S.G. Hickey, S.V. Kershaw, Infrared-emitting colloidal nanocrystals: synthesis, assembly, spectroscopy, and applications, *Small* 3 (2007) 536–557.
- [44] H. Zhang, L. Wang, H. Xiong, L. Hu, B. Yang, W. Li, Hydrothermal synthesis for high-quality CdTe nanocrystals, *Adv. Mater.* 15 (2003) 1712–1717.
- [45] J.R. Heath, J.J. Shiang, A.P. Alivisatos, Germanium quantum dots: optical properties and synthesis, *J. Chem. Phys.* 101 (1994) 1607–1615.
- [46] Z.F. Ding, B.M. Quinn, S.K. Haram, L.E. Pell, B.A. Korgel, A.J. Bard, Electrochemistry and electrogenerated chemiluminescence from silicon nanocrystal quantum dots, *Science* 296 (2002) 1293–1297.
- [47] Y.P. Sun, B. Zhou, Y. Lin, W. Wang, K.A.S. Fernando, P. Pathak, M.J. Meziani, B.A. Harruff, X. Wang, H.F. Wang, P.G. Luo, H. Yang, M.E. Kose, B.L. Chen, L.M. Veca, S.Y. Xie, Quantum-sized carbon dots for bright and colorful photoluminescence, *J. Am. Chem. Soc.* 128 (2006) 7756–7757.
- [48] M.A. Hines, G.D. Scholes, Colloidal PbS nanocrystals with size-tunable nearinfrared emission: observation of postsynthesis self-narrowing of the particle size distribution, *Adv. Mater.* 15 (2003) 1844–1849.
- [49] Z.A. Peng, X.G. Peng, Formation of high-quality CdTe, CdSe, and CdS nanocrystals using CdO as precursor, *J. Am. Chem. Soc.* 123 (2001) 183–184.
- [50] L.A. Swafford, L.A. Weigand, M.J. Bowers II, J.R. McBride, J.L. Rapaport, T.L. Watt, S.K. Dixit, L.C. Feldman, S.J. Rosenthal, Homogeneously alloyed CdS_xSe_{1-x} nanocrystals: synthesis, characterization, and composition/size-dependent band gap, *J. Am. Chem. Soc.* 128 (2006) 12299–12306.
- [51] T. Zhang, H.G. Zhao, D. Riabinina, M. Chaker, D.L. Ma, Concentration-dependent photoinduced photoluminescence enhancement in colloidal PbS quantum dot solution, *J. Phys. Chem. C* 114 (2010) 10153–10159.
- [52] S. Draguta, H. McDaniel, V.I. Klimov, Tuning carrier mobilities and polarity of charge transport in films of CuInSexS_{2-x} quantum dots, *Adv. Mater.* 27 (2015) 1701–1706.
- [53] L. Protesescu, S. Yakunin, M.I. Bodnarchuk, F. Krieg, R. Caputo, C.H. Hendon, R.X. Yang, A. Walsh, M.V. Kovalenko, Nanocrystals of cesium lead halide perovskites (CsPbX₃, X = Cl, Br, and I): novel optoelectronic materials showing bright emission with wide color gamut, *Nano Lett.* 15 (2015) 3692–3696.
- [54] S. Kim, A.R. Marshall, D.M. Kroupa, E.M. Miller, J.M. Luther, S. Jeong, M.C. Beard, Air-stable and efficient PbSe quantumdot solar cells based upon ZnSe to PbSe cation-exchanged quantum dots, *ACS Nano* 9 (2015) 8157–8164.
- [55] S. Kim, B. Fisher, H.-J. Eisler, M. Bawendi, Type-II quantum dots: CdTe/CdSe(core/shell) and CdSe/ZnTe(core/shell) heterostructures, *J. Am. Chem. Soc.* 125 (2003) 11466–11467.

- [56] J.B. Li, L.W. Wang, First principle study of core/shell structure quantum dots, *Appl. Phys. Lett.* 84 (2004) 3648–3650.
- [57] Y.F. Chen, J. Vela, H. Htoon, J.L. Casson, D.J. Werder, D.A. Bussian, I. Klimov, J.A. Hollingsworth, ‘Giant’ multishell CdSe nanocrystal quantum dots with suppressed blinking, *J. Am. Chem. Soc.* 130 (2008) 5026–5027.
- [58] H.G. Zhao, M. Chaker, N.Q. Wu, D.L. Ma, Towards controlled synthesis and better understanding of highly luminescent PbS/CdS core/shell quantum dots, *J. Mater. Chem.* 21 (2011) 8898–8904.
- [59] J.E. Huang, K.L. Mulfort, P.W. Du, L.X. Chen, Photodriven charge separation dynamics in CdSe/ZnS Core/shell quantum dot/cobaloxime hybrid for efficient hydrogen production, *J. Am. Chem. Soc.* 134 (2012) 16472–16475.
- [60] W.K. Bae, L.A. Padilha, Y.S. Park, H. McDaniel, I. R, J.M. Pietryga, V.I. Klimov, Controlled alloying of the core-shell interface in CdSe/CdS quantum dots for suppression of auger recombination, *ACS Nano* 7 (2013) 3411–3419.
- [61] J. Lim, B.G. Jeong, M. Park, J.K. Kim, J.M. Pietryga, Y.S. Park, V.I. Klimov, C. Lee, D.C. Lee, W.K. Bae, Influence of shell thickness on the performance of lightemitting devices based on CdSe/Zn_{1-x}Cd_xS core/shell heterostructured quantum dots, *Adv. Mater.* 26 (2014) 8034–8039.
- [62] D.C.J. Neo, C. Cheng, S.D. Stranks, S.M. Fairclough, J.S. Kim, A.I. Kirkland, J.M. Smith, H.J. Snaith, H.E. Assender, A.A.R. Watt, Influence of shell thickness and surface passivation on PbS/CdS core/shell colloidal quantum dot solar cells, *Chem. Mater.* 26 (2014) 4004–4013.
- [63] A. Christine, A. Silva, S.W. da Silva, P.C. Morais, N.O. Dantas, Shell thickness modulation in ultrasmall CdSe/CdS_xSe_{1-x}/CdS core/shell quantum dots via 1-thioglycerol, *ACS Nano* 8 (2014) 1913–1922.
- [64] H.G. Zhao, H.Y. Liang, F. Vidal, F. Rosei, A. Vomiero, D.L. Ma, Size dependence of temperature-related optical properties of PbS and PbS/CdS core/shell quantum dots, *J. Phys. Chem. C* 118 (2014) 20585–20593.
- [65] L.K. Sagar, W. Walravens, Q. Zhao, A. Vantomme, P. Geiregat, Z. Hens, PbS/CdS core/shell quantum dots by additive, layer-by-layer shell growth, *Chem. Mater.* 28 (2016) 6953–6959.
- [66] J.M. Pietryga, D.J. Werder, D.J. Williams, J.L. Casson, R.D. Schaller, V.I. Klimov, J.A. Hollingsworth, Utilizing the lability of lead selenide to produce heterostructured nanocrystals with bright, stable infrared emission, *J. Am. Chem. Soc.* 130 (2008) 4879–4885.
- [67] L. Etgar, D. Yanover, R.K. Capek, R. Vaxenburg, Z.S. Xue, B. Liu, M. Khaja Nazeeruddin, E. Lifshitz, M. Grätzel, Core/Shell PbSe/PbS QDs TiO₂ heterojunction solar cell, *Adv. Funct. Mater.* 23 (2013) 2736–2741.
- [68] B. De Geyter, Y. Justo, I. Moreels, K. Lambert, P.F. Smet, D.V. Thourout, A.J. Houtepen, D. Grodzinska, C. de Mello Donega, A. Meijerink, D. Vanmaekelbergh, Z. Hens, The different nature of band edge absorption and emission in colloidal PbSe/CdSe core/shell quantum dots, *ACS Nano* 5 (2011) 58–66.
- [69] A. Piryatinski, S.A. Ivanov, S. Tretiak, V.I. Klimov, Effect of quantum and dielectric confinement on the exciton-exciton interaction energy in type II core/shell semiconductor nanocrystals, *Nano Lett.* 7 (2007) 108–115.
- [70] Y.Y. Jia, J.Q. Chen, K.F. Wu, A. Kaledin, D.G. Musaev, Z.X. Xie, T.Q. Lian, Enhancing photo-reduction quantum efficiency using quasi-type II core/shell quantum dots, *Chem. Sci.* 7 (2016) 4125–4133.
- [71] E. Lifshitz, M. Brumer, A. Kigel, A. Sashchiuk, M. Bashouti, M. Sirota, E. Galun, Z. Burshtein, A.Q. Le Quang, I. Ledoux-Rak, J. Zyss, Stable PbSe/PbS and PbSe/PbSe_xS_{1-x},core-shell nanocrystal quantum dots and their applications, *J. Phys. Chem. B* 110 (2006) 25356–25365.

- [72] H.G. Zhao, G. Sirigu, A. Parisini, A. Camellini, G. Nicotra, F. Rosei, V. Morandi, M. Zavelani-Rossi, A. Vomiero, Dual emission in asymmetric ‘giant’ PbS/CdS/CdS core/shell/shell quantum dots, *Nanoscale* 8 (2016) 4217–4226.
- [73] S. Xu, J. Ziegler, T. Nann, Rapid synthesis of highly luminescent InP and InP/ZnS nanocrystals, *J. Mater. Chem.* 18 (2008) 2653–2656.
- [74] Y. Ghosh, B.D. Mangum, J.L. Casson, D.J. Williams, H. Htoon, J.A. Hollingsworth, New insights into the complexities of shell growth and the strong influence of particle volume in nonblinking ‘giant’ core/shell nanocrystal quantum dots, *J. Am. Chem. Soc.* 134 (2012) 9634–9643.
- [75] S. Brovelli, R.D. Schaller, S.A. Crooker, F. García-Santamaría, Y. Chen, R. Viswanatha, J.A. Hollingsworth, H. Htoon, V.I. Klimov, Nano-engineered electron-hole exchange interaction controls exciton dynamics in core-shell semiconductor nanocrystals, *Nat. Commun.* 2 (2011), 280.
- [76] K.P. Acharya, H.M. Nguyen, M. Paulite, A. Piryatinski, J. Zhang, J.L. Casson, H.W. Xu, H. Htoon, J.A. Hollingsworth, Elucidation of two giants: challenges to thickshell synthesis in CdSe/ZnSe and ZnSe/CdS core/shell quantum dots, *J. Am. Chem. Soc.* 137 (2015) 3755–3758.
- [77] H.G. Zhao, L. Jin, Y.F. Zhou, A. Bandar, Z.Y. Fan, A.O. Govorov, Z.T. Mi, S.H. Sun, F. Rosei, A. Vomiero, Green synthesis of near infrared core/shell quantum dots for photocatalytic hydrogen production, *Nanotechnology* 27 (2016), 495405.
- [78] B.-R. Hyun, H. Chen, D.A. Rey, F.W. Wise, C.A. Batt, Near-infrared fluorescence imaging with water-soluble lead salt quantum dots, *J. Phys. Chem. B* 111 (20) (2007) 5726–5730.
- [79] L. Sun, J.J. Choi, D. Stachnik, A.C. Bartnik, B.-R. Hyun, G.G. Malliaras, T. Hanrath, F.W. Wise, Bright infrared quantum-dot light-emitting diodes through inter-dot spacing control, *Nat. Nanotechnol.* 7 (6) (2012) 369–373.
- [80] M. Nasilowski, L. Nienhaus, S.N. Bertram, M.G. Bawendi, Colloidal atomic layer deposition growth of PbS/CdS core/shell quantum dots, *Chem. Commun.* 53 (2017) 869–872.
- [81] D.A. Hines, R.P. Forrest, S.A. Corcelli, P.V. Kamat, Predicting the rate constant of electron tunneling reactions at the CdSe/TiO₂ interface, *J. Phys. Chem. B* 119 (2015) 7439–7446.
- [82] H. Zhao, Z. Fan, H. Liang, G.S. Selopal, B.A. Gonfa, L. Jin, A. Soudi, D. Cui, F. Enrichi, M.M. Natile, I. Concina, D. Ma, A.O. Govorov, F. Rosei, A. Vomiero, Controlling photoinduced electron transfer from PbS@CdS core@shell quantum dots to metal oxide nanostructured thin films, *Nanoscale* 6 (2014) 7004–7011.
- [83] D.R. Pernik, K. Tvrdy, J.G. Radich, P.V. Kamat, Tracking the adsorption and electron injection rates of CdSe quantum dots on TiO₂:linked versus direct attachment, *J. Phys. Chem. C* 115 (2011) 13511–13519.
- [84] T.X. Ding, J.H. Olshansky, S.R. Leone, A.P. Alivisatos, Efficiency of hole transfer from photoexcited quantum dots to covalently linked molecular species, *J. Am. Chem. Soc.* 137 (2015) 2021–2029.
- [85] Y. Okada, N.J. Ekins-Daukes, T. Kita, R. Tamaki, M. Yoshida, A. Pusch, O. Hess, C.C. Phillips, D.J. Farrell, K. Yoshida, N. Ahsan, Y. Shoji, T. Sogabe, J.F. Guillemoles, Intermediate band solar cells: recent progress and future directions, *Appl. Phys. Rev.* 2 (2015), 021302.
- [86] Z.R. Zheng, H.N. Jie, P. Yu, Z.M. Wang, Recent progress towards quantum dot solar cells with enhanced optical absorption, *Nanoscale Res. Lett.* 11 (2016) 266.
- [87] I.J. Kramer, E.H. Sargent, The architecture of colloidal quantum dot solar cells: materials to devices, *Chem. Rev.* 114 (2014) 863–882.

- [88] J.L. Duan, H.H. Zhang, Q.W. Tang, B. Heb, L.M. Yu, Recent advances in critical materials for quantum dot-sensitized solar cells: a review, *J. Mater. Chem. A* 3 (2015) 17497–17510.
- [89] X.H. Wang, Recent progress in colloidal quantum dot photovoltaics, *Front. Optoelectron.* 8 (2015) 241–251.
- [90] H.G. Zhao, F. Rosei, Colloidal quantum dots for solar technologies, *Chem* 3 (2017) 229–258.
- [91] I. Mora-Sero, J. Bisquert, Breakthroughs in the development of semiconductorsensitized solar cells, *J. Phys. Chem. Lett.* 1 (2010) 3046–3052.
- [92] P.V. Kamat, Quantum dot solar cells: the next big thing in photovoltaics, *J. Phys. Chem. Lett.* 4 (2013) 908–918.
- [93] J.W. Yang, J. Wang, K. Zhao, T. Izuishi, Y. Li, Q. Shen, X.H. Zhong, CdSeTe/CdS type-I core/shell quantum dot sensitized solar cells with efficiency over 9%, *J. Phys. Chem. C* 119 (2015) 28800–28808.
- [94] Best Research-Cell Efficiencies, National Renewable Energy Laboratory, <https://www.nrel.gov/pv/assets/pdfs/best-research-cell-efficiencies.pdf>. (accessed: September 2019).
- [95] T. Sogabe, Q. Shen, K. Yamaguchi, Recent progress on quantum dot solar cells: a review, *J. Photon. Energy* 6 (4) (2016), 040901. <https://doi.org/10.1117/1.JPE.6.040901>.
- [96] C.H. Chang, Y.L. Lee, Chemical bath deposition of CdS quantum dots onto mesoscopic TiO₂ films for application in quantum-dot-sensitized solar cells, *Appl. Phys. Lett.* 91 (2007), 053503.
- [97] H.J. Lee, M.K. Wang, P. Chen, D.R. Gamelin, S.M. Zakeeruddin, M. Grätzel, M.K. Nazeeruddin, Efficient CdSe quantum dot-sensitized solar cells prepared by an improved successive ionic layer adsorption and reaction process, *Nano Lett.* 9 (2009) 4221–4227.
- [98] G. Hodes, Comparison of dye- and semiconductor-sensitized porous nanocrystalline liquid junction solar cells, *J. Phys. Chem. C* 112 (2008) 17778–17787.
- [99] N. Guijarro, T. Lana-Villarreal, I. Mora-Sero, J. Bisquert, R. Gomez, CdSe quantum dot-sensitized TiO₂ electrodes: effect of quantum dot coverage and mode of attachment, *J. Phys. Chem. C* 113 (2009) 4208–4214.
- [100] Y.Z. Hao, J. Pei, Y. Wei, Y.H. Cao, S.H. Jiao, F. Zhu, J.J. Li, D.H. Xu, Efficient semiconductor-sensitized solar cells based on poly(3-hexylthiophene) at CdSe at ZnO core-shell nanorod arrays, *J. Phys. Chem. C* 114 (2010) 8622–8625.
- [101] H.S. Kim, J.W. Lee, N. Yantara, P.P. Boix, S.A. Kulkarni, S. Mhaisalkar, M. Grätzel, N.G. Park, High efficiency solid-state sensitized solar cell-based on submicrometer rutile TiO₂ nanorod and CH₃NH₃PbI₃ perovskite sensitizer, *Nano Lett.* 13 (2013) 2412–2417.
- [102] P.P. Boix, G. Laramona, A. Jacob, B. Delatouche, I. Mora-Sero, J. Bisquert, Hole transport and recombination in all-solid Sb₂S₃-sensitized TiO₂ solar cells using CuSCN as hole transporter, *J. Phys. Chem. C* 116 (2012) 1579–1587.
- [103] S. Jiao, J. Du, Z.L. Du, D.H. Long, W.Y. Jiang, Z.X. Pan, Y. Li, X.H. Zhong, Nitrogen-doped mesoporous carbons as counter electrodes in quantum dot sensitized solar cells with a conversion efficiency exceeding 12%, *J. Phys. Chem. Lett.* 8 (2017) 559–564.
- [104] A.G. Pattantyus-Abraham, I.J. Kramer, A.R. Barkhouse, X.H. Wang, G. Konstantatos, R. Debnath, L. Levina, I. Raabe, M.K. Nazeeruddin, M. Grätzel, E.H. Sargent, Depleted-heterojunction colloidal quantum dot solar cells, *ACS Nano* 4 (2010) 3374–3380.
- [105] M. Mousavi-Kamazani, Z. Zarghami, M. Salavati-Niasari, Facile and novel chemical synthesis, characterization, and formation mechanism of copper sulfide (Cu₂S, Cu₂S/CuS, CuS) nanostructures for increasing the efficiency of solar cells, *J. Phys. Chem. C* 120 (2016) 2096–2108.
- [106] J.Y. Kim, J. Yang, J.H. Yu, W. Baek, C.H. Lee, H.J. Son, T. Hyeon, M.J. Ko, Highly efficient copper-indium-selenide quantum dot solar cells: suppression of carrier recombination by controlled ZnS overlayers, *ACS Nano* 5 (2015) 11286–11295.

- [107] W.X. Peng, J. Du, Z.X. Pan, N. Nakazawa, J.K. Sun, Z.L. Du, G.C. Shen, J. Yu, J.S. Hu, Q. Shen, X.H. Zhong, Alloying strategy in Cu-In-Ga-Se quantum dots for high efficiency quantum dot sensitized solar cells, *ACS Appl. Mater. Interfaces* 9 (2017) 5328–5336.
- [108] M.X. Liu, O. Voznyy, R. Sabatini, F.P.G. de Arquer, R. Munir, A.H. Balawi, X.Z. Lan, F.J. Fan, G. Walters, A.R. Kirmani, S. Hoogland, F. Laquai, A. Amassian, E.H. Sargent, Hybrid organic-inorganic inks flatten the energy landscape in colloidal quantum dot solids, *Nat. Mater.* 16 (2017) 258–263.
- [109] J.B. Gao, J.M. Luther, O.E. Semonin, R.J. Ellingson, A.J. Nozik, M.C. Beard, Quantum dot size dependent J-V characteristics in heterojunction ZnO/PbS quantum dot solar cells, *Nano Lett.* 11 (2011) 1002–1008.
- [110] J. Tang, K.W. Kemp, S. Hoogland, K.S. Jeong, H. Liu, L. Levina, M. Furukawa, X.H. Wang, R. Debnath, D. Cha, K.W. Chou, A. Fischer, A. Amassian, J.B. Asbury, E.H. Sargent, Colloidal-quantum-dot photovoltaics using atomic-ligand passivation, *Nat. Mater.* 10 (2011) 765–771.
- [111] A.H. Ip, S.M. Thon, S. Hoogland, O. Voznyy, D. Zhitomirsky, R. Debnath, L. Levina, L.R. Rollny, G.H. Carey, A. Fischer, K.W. Kemp, I.J. Kramer, Z.J. Ning, A.J. Labelle, K.W. Chou, A. Amassian, E.H. Sargent, Hybrid passivated colloidal quantum dot solids, *Nat. Nanotechnol.* 7 (2012) 577–582.
- [112] S. Kim, A.R. Marshall, D.M. Kroupa, E.M. Miller, J.M. Luther, S. Jeong, M.C. Beard, Air-stable and efficient PbSe quantum-dot Solar cells based upon ZnSe to PbSe cation-exchanged quantum dots, *ACS Nano* 9 (2015) 8157–8164.
- [113] P.R. Brown, D. Kim, R.R. Lunt, N. Zhao, M.G. Bawendi, J.C. Grossman, V.I. Bulovic, Energy level modification in lead sulfide quantum dot thin films through ligand exchange, *ACS Nano* 8 (2014) 5863–5872.
- [114] C.H.M. Chuang, P.R. Brown, V. Bulovic, M.G. Bawendi, Improved performance and stability in quantum dot solar cells through band alignment engineering, *Nat. Mater.* 13 (2014) 796–801.
- [115] Y.M. Cao, A. Stavrinadis, T. Lasanta, D. So, G. Konstantatos, The role of surface passivation for efficient and photostable PbS quantum dot solar cells, *Nat. Energy* 1 (2016) 16035.
- [116] R. Azmi, S.H. Oh, S.Y. Jang, High-efficiency colloidal quantum dot photovoltaic devices using chemically modified heterojunctions, *ACS Energy Lett.* 1 (2016) 100–106.
- [117] G.H. Kim, F.P.G. de Arquer, Y.J. Yoon, X.Z. Lan, M.X. Liu, O. Voznyy, L.K. Jagadamma, A.S. Abbas, Z.Y. Yang, F.J. Fan, A.H. Ip, P. Kanjanaboons, S. Hoogland, A. Amassian, J.Y. Kim, E.H. Sargent, Correction to high-efficiency colloidal quantum dot photovoltaics via robust self-assembled monolayers, *Nano Lett.* 16 (2016) 822.
- [118] M.C. Beard, K.P. Knutsen, P.R. Yu, J.M. Luther, Q. Song, W.K. Metzger, R.J. Ellingson, A.J. Nozik, Multiple exciton generation in colloidal silicon nanocrystals, *Nano Lett.* 7 (2007) 2506–2512.
- [119] J.E. Murphy, M.C. Beard, A.G. Norman, S.P. Ahrenkiel, J.C. Johnson, P.R. Yu, O.I. Micic, R.J. Ellingson, A.J. Nozik, PbTe colloidal nanocrystals: synthesis, characterization, and multiple exciton generation, *J. Am. Chem. Soc.* 128 (2006) 3241–3247.
- [120] Z.B. Lin, A. Franceschetti, M.T. Lusk, Size dependence of the multiple exciton generation rate in CdSe quantum dots, *ACS Nano* 5 (2011) 2503–2511.
- [121] Q. Shen, K. Katayama, T. Sawada, S. Hachiya, T. Toyoda, Ultrafast carrier dynamics in PbS quantum dots, *Chem. Phys. Lett.* 542 (2012) 89–93.
- [122] S.V. Kershaw, S. Kalytchuk, O. Zhovtiuk, Q. Shen, T. Oshima, W. Yindeesuk, T. Toyoda, A.L. Rogach, Multiple exciton generation in cluster-free alloy Cd_xHg_{1-x}Te colloidal quantum dots synthesized in water, *Phys. Chem. Chem. Phys.* 16 (2014) 25710–25722.

- [123] O.E. Semonin, J.M. Luther, S. Choi, H.-Y. Chen, J.B. Gao, A.J. Nozik, M.C. Beard, Peak external photocurrent quantum efficiency exceeding 100% via MEG in a quantum dot solar cell, *Science* 334 (2011) 1530–1533.
- [124] C.J. Stolle, T.B. Harvey, D.R. Pernik, J.I. Hibbert, J. Du, D.J. Rhee, V.A. Akhavan, R.D. Schaller, B.A. Korgel, Multiexciton solar cells of CuInSe nanocrystals, *J. Phys. Chem. Lett.* 5 (2014) 304–309.
- [125] N.J.L.K. Davis, M.L. Böhm, M. Tabachnyk, F.W.-R. Rivarola, T.C. Jellicoe, C. Ducati, B. Ehrler, N.C. Greenham, Multiple-exciton generation in lead selenide nanorod solar cells with external quantum efficiencies exceeding 120%, *Nat. Commun.* 6 (2015), 8259.
- [126] H. Zhu, Y. Yang, K.H. Deuk, M. Califano, N. Song, Y.W. Wang, W.Q. Zhang, O.V. Prezhdo, T.Q. Lian, Auger-assisted electron transfer from photoexcited semiconducot quantum dots, *Nano Lett.* 14 (2014) 1263–1269.
- [127] J.H. Olshansky, T.X. Ding, Y.V. Lee, S.R. Leone, A.P. Alivisatos, Hole transfer from photoexcited quantum dots: the relationship between driving force and rate, *J. Am. Chem. Soc.* 137 (2015) 15567–15575.
- [128] C.G. Bailey, D.V. Forbes, S.J. Polly, Z.S. Bittner, Y.S. Dai, C. Mackos, R.P. Raffaelle, S.M. Hubbard, Open-circuit voltage improvement of InAs/GaAs quantum-dot solar cells using reduced InAs coverage, *IEEE J. Photovoltaics* 2 (2012) 269–275.
- [129] A. Marti, L. Cuadra, A. Luque, Quasi-drift diffusion model for the quantum dot intermediate band solar cell, *IEEE Trans. Electron. Dev.* 49 (2002) 1632–1639.
- [130] A.S. Lin, W.M. Wang, J.D. Phillips, Model for intermediate band solar cells incorporating carrier transport and recombination, *J. Appl. Phys.* 105 (2009), 064512.
- [131] H.W. Wang, W.L. Li, Y.L. Huang, Y.S. Wang, S.Y. Yang, B.S. Zou, Efficiency enhancement of organic solar cells by inserting PbS quantum dots film as the infrared absorption layer, *Mater. Lett.* 187 (2017) 136–139.
- [132] Z.X. Li, H.W. Wang, D. Yang, L. Zhang, Y.S. Wang, T.J. Song, C.J. Fu, H.Y. Zhang, S.Y. Yang, B.S. Zou, Enhancement of the power conversion efficiency of polymer solar cells by incorporating PbSe quantum dots, *J. Mater. Sci.* 50 (2) (2015) 840–847.
- [133] T. Ni, F. Zou, Y.Y. Jiang, S.Y. Yang, To improve the efficiency of bulk heterojunction solar cells by incorporating CdSe/ZnS quantum dots, *Acta Phys. -Chim. Sin.* 30 (3) (2014) 453–459.
- [134] T. Ni, J.Y. Yan, Y.R. Jiang, F. Zou, L. Zhang, D. Yang, J.Q. Wei, S.Y. Yang, B.S. Zou, Enhancement of the power conversion efficiency of polymer solar cells by functionalized single-walled carbon nanotubes decorated with CdSe/ZnS core–shell colloidal quantum dots, *J. Mater. Sci.* 49 (2014) 2571–2577.
- [135] A.A. Bakulin, S. Neutzner, H.J. Bakker, L. Ottaviani, D. Barakel, Z.Y. Chen, Charge trapping dynamics in PbS colloidal quantum dot photovoltaic devices, *ACS Nano* 7 (2013) 8771–8779.
- [136] J.M. Luther, M. Law, Q. Song, C.L. Perkins, M.C. Beard, A.J. Nozik, Structural, optical, and electrical properties of self assembled films of PbSe nanocrystals treated with 1,2-ethanedithiol, *ACS Nano* 2 (2008) 271–280.
- [137] D. Zhitomirsky, O. Voznyy, S. Hoogland, E.H. Sargent, Measuring charge carrier diffusion in coupled colloidal quantum dot solids, *ACS Nano* 7 (2013) 5282–5290.
- [138] H.T. Zhang, B. Hu, L.F. Sun, R. Hovden, F.W. Wise, D.A. Muller, R.D. Robinson, Surfactant Ligand Removal and Rational Fabrication of Inorganically Connected Quantum Dots, *Nano Lett.* 11 (2011) 5356–5361.
- [139] A. Nag, M.V. Kovalenko, J.S. Lee, W.Y. Liu, B. Spokoyny, D.V. Talapin, Metal-free inorganic ligands for colloidal nanocrystals: S^{2-} , HS^- , Se^{2-} , HSe^- , Te^{2-} , HTe^- , TeS_3^{2-} , OH^- , and NH_2^- as surface ligands, *J. Am. Chem. Soc.* 133 (2011) 10612–10620.

- [140] J.S. Lee, M.V. Kovalenko, J. Huang, D.S. Chung, D.V. Talapin, Band-like transport, high electron mobility and high photoconductivity in all-inorganic nanocrystal arrays, *Nat. Nanotechnol.* 6 (2011) 348–352.
- [141] X.Z. Lan, O. Voznyy, A. Kiani, F.P.G. de Arquer, A.S. Abbas, G.H. Kim, M.X. Liu, Z.Y. Yang, G. Walters, J.X. Xu, M.J. Yuan, Z.J. Ning, F.J. Fan, P. Kanjanaboons, I. Kramer, D. Zhitomirsky, P. Lee, A. Perelgut, S. Hoogland, E.H. Sargent, Passivation using molecular halides increases quantum dot solar cell performance, *Adv. Mater.* 28 (2016) 299–304.
- [142] Q. Wang, J.E. Moser, M. Grätze, Electrochemical impedance spectroscopic analysis of dye-sensitized solar cells, *J. Phys. Chem. B* 109 (2005) 14945–14953.
- [143] L.Y. Han, N. Koide, Y. Chiba, T. Mitate, Modeling of an equivalent circuit for dye-sensitized solar cells, *Appl. Phys. Lett.* 84 (2004) 2433–2435.
- [144] A. Pockett, G.E. Eperon, T. Peltola, H.J. Snaith, A. Walker, L.M. Peter, P.J. Cameron, Characterization of planar lead halide perovskite solar cells by impedance spectroscopy, open-circuit photovoltage decay, and intensity-modulated photovoltage/photocurrent spectroscopy, *J. Phys. Chem. C* 119 (2015) 3456–3465.
- [145] C.C. Hsiao, A.E. Hsiao, S.A. Chen, Design of hole blocking layer with electron transport channels for high performance polymer light-emitting diodes, *Adv. Mater.* 20 (2008) 1982–1988.
- [146] X.L. Zhang, S.Y. Yang, Z.D. Lou, Y.B. Hou, Dynamic electrical characteristics of organic light-emitting diodes, *Acta Phys. Sin.* 56 (2007) 1632–1636.
- [147] P.P. Boix, A. Guerrero, L.F. Marchesi, G. Garcia-Belmonte, J. Bisquert, Current-voltage characteristics of bulk heterojunction organic solar cells: connection between light and dark curves, *Adv. Energy Mater.* 1 (2011) 1073–1078.
- [148] T. Kuwabara, Y. Kawahara, T. Yamaguchi, K. Takahashi, Characterization of inverted-type organic solar cells with a ZnO layer as the electron collection electrode by AC impedance spectroscopy, *ACS Appl. Mater. Interfaces* 1 (2009) 2107–2110.
- [149] B.J. Leever, C.A. Bailey, T.J. Marks, M.C. Hersam, M.F. Durstock, In situ characterization of lifetime and morphology in operating bulk heterojunction organic photovoltaic devices by impedance spectroscopy, *Adv. Energy Mater.* 2 (2012) 120–128.
- [150] H.W. Wang, Y.S. Wang, B. He, W.L. Li, M. Sulaman, J.F. Xu, S.Y. Yang, Y. Tang, B.S. Zou, Charge carrier conduction mechanism in PbS quantum dot solar cells: electrochemical impedance spectroscopy study, *ACS Appl. Mater. Interfaces* 8 (2016) 18526–18533.
- [151] H.W. Wang, S.Y. Yang, Y.S. Wang, J.F. Xu, Y.L. Huang, W.L. Li, B. He, S. Muhammad, Y.R. Jiang, Y. Tang, B.S. Zou, Influence of post-synthesis annealing on PbS quantum dot solar cells, *Org. Electron.* 42 (2017) 309–315.
- [152] D. Paz-Soldan, A. Lee, S.M. Thon, M.M. Adachi, H.P. Dong, P. Maraghechi, M.J. Yuan, A.J. Labelle, S. Hoogland, K. Liu, E. Kumacheva, E.H. Sargent, Jointly tuned plasmonic-excitonic photovoltaics using nanoshells, *Nano Lett.* 13 (2013) 1502–1508.
- [153] X.H. Wang, G.I. Koleilat, J. Tang, H. Liu, I.J. Kramer, R. Debnath, L. Brzozowski, D. Aaron, R. Barkhouse, L. Levina, S. Hoogland, E.H. Sargent, Tandem colloidal quantum dot solar cells employing a graded recombination layer, *Nat. Photon.* 5 (2011) 480–484.
- [154] C.J. Fu, H.W. Wang, T.J. Song, L. Zhang, W.L. Li, B. He, M. Sulaman, S.Y. Yang, B.S. Zou, Stability enhancement of PbSe quantum dots via post-synthetic ammonium chloride treatment for a high-performance infrared photodetector, *Nanotechnology* 27 (2015), 065201.
- [155] Y.Q. Dong, H.C. Pang, H.B. Yang, C.X. Guo, J.W. Shao, Y.W. Chi, C.M. Li, T. Yu, Carbon-based dots co-doped with nitrogen and sulfur for high quantum yield and excitation-independent emission, *Angew. Chem. Int. Ed.* 52 (2013) 7800–7804.

Chapter 8

Future perspectives of perovskite solar cells: Metal oxide-based inorganic hole-transporting materials

Ismail Cihan Kaya^{a,b}, Seckin Akin^{b,c}, and Savas Sonmezoglu^{b,c}

^aDepartment of Metallurgical & Materials Engineering, Konya Technical University, Konya, Turkey, ^bNanotechnology R&D Laboratory, Karamanoglu Mehmetbey University, Karaman, Turkey, ^cDepartment of Metallurgical & Materials Engineering, Karamanoglu Mehmetbey University, Karaman, Turkey

1 Photovoltaic technologies

Fossil fuels are the main supply for electricity generation in the 21st century. However, burning fossil fuels causes CO₂ emissions, which are the main reason for global warming [1]. Therefore the importance of using renewable energy sources to produce electricity is increasing. Among the renewable energy technologies, direct conversion of solar radiation into electrical energy with photovoltaic devices is one of the most promising green and sustainable approaches [2]. Particularly, perovskite solar cells (PSCs), which have a key role in photovoltaic technology, have gained tremendous attention for commercialization with efficiency values above 25% in less than a decade [3]. In this part of the chapter, a brief overview of photovoltaic devices is discussed, and then historical development, components, and working principles of PSCs are explained in detail.

1.1 Evaluation of photovoltaic solar cells

Photovoltaic devices are mainly classified into three main categories: first-, second-, and third-generation according to their historical development process [4]. The first generation consists of crystalline silicon (Si)- and gallium arsenide (GaAs)-based cells. The first demonstration of these cells goes back to the Bell's Lab in 1954 [5]. The efficiency of the first Si-based devices was around 6%; however, development of these cells has continued and record efficiency has

reached 27.6% at laboratory scale [3]. Despite the considerable impact of Si-based cells in energy markets, the solar industry is still looking for new technologies to reduce the cost and complex manufacturing issues of current devices.

In this manner, second-generation photovoltaic technology, namely thin film solar cells, was developed at the beginning of the 1980s [6]. Amorphous silicon (α -Si), cadmium telluride (CdTe), and copper indium gallium selenide (CIGS) are three leaders of second-generation solar cells and the reported efficiencies of these cells are 14.0%, 22.1%, and 23.4%, respectively [3]. Although thin film solar cells possess a much easier manufacturing process with lower material cost, they could not reach the efficiencies of first-generation solar cells. Another issue to keep in mind about thin film solar cells is the toxicity of cadmium, significantly higher greenhouse gas emissions of α -Si, and complex stoichiometry of CIGS. Although both first- and second-generation solar cells have been commercialized because of their high efficiency and long-term durability, emerging photovoltaic technology of third-generation solar cells has also attracted tremendous attention due to their low cost, easy fabrication, and flexibility [7]. Third-generation solar cells consist of dye-sensitized solar cells (DSSCs), quantum dot-sensitized solar cells (QDSSCs), organic solar cells, and perovskite solar cells (PSCs). The PSC is the newest and most efficient member of this family. Research into these cells started in 2009 and over the last decade the efficiency of these cells has come a long way and reached 25.2% [3, 8]. These cells surpassed the efficiency of second- (α -Si, CdTe, CIGS, etc.) and other third-generation solar cells and almost caught up with silicon-based cells.

1.2 Historical overview of perovskite solar cells

In 2009, organic-inorganic lead halides ($\text{CH}_3\text{NH}_3\text{PbX}_3$ [$\text{X} = \text{Br}, \text{I}$]), which crystallize in the perovskite structure, were used as an absorber material to replace the organic dye in TiO_2 -based DSSCs for the first time [8]. The device was fabricated by depositing thin nanocrystalline perovskite film on the surface of an $\sim 10\text{ }\mu\text{m}$ thick TiO_2 layer. The efficiency of the cell obtained was 3.1% for $\text{X} = \text{Br}$ and 3.8% for $\text{X} = \text{I}$. However, the stability of these cells was too low due to the dissolution of perovskite film in liquid electrolyte. In 2011, Park's group enhanced the efficiency of $\text{CH}_3\text{NH}_3\text{PbI}_3$ perovskite-sensitized solar cells [9]. The series of optimizations showed that photovoltaic performance of current devices strongly depends on the film thickness, solution concentration, and annealing conditions. As a result, an efficiency of 6.54% was achieved. It is worth mentioning that although the performance of perovskite-sensitized cells was improved compared to the first study [8], stability was still a top issue in such cells. In 2012, the utilization of perovskite as an absorber in solid-state mesoscopic solar cell architecture was first reported in the presence of 2,2',7,7'-tetrakis[N,N -di(4-methoxyphenyl)amino]-9,9'-spirobifluorene (spiro-OMeTAD) as a hole transport

layer (HTL). The efficiency of these cells was reported to be ~10%. More importantly, it was found that stability of these cells was higher than that of the cell with liquid electrolyte. In the same year, the study by Snaith's group was one of the milestones in PSC research [10]. In this study, n-type semiconductor TiO_2 was replaced by insulating Al_2O_3 mesoporous film. Although the Al_2O_3 was an insulator, open-circuit voltage (V_{OC}) and efficiency of the cell fabricated with Al_2O_3 were higher than that of the cell with TiO_2 . These results indicated that the electrons can also be transported through the perovskite layer. This observation proved that perovskite was not only an absorber material, but also an n-type component transporting the electrons. The other important study in 2012 was a hole-transporting material (HTM)-free mesoscopic TiO_2 -based PSC [11]. The efficiency of this cell was 5.5% under 1 sun intensity. However, this study was significant because it demonstrated that the perovskite layer also has a hole-transporting feature. In summary, studies up to 2013 showed that perovskite semiconductors were endowed with light absorption, carrier generation, and the capability of transporting both holes and electrons. These were three essential features of active layers in solar cells. To further improve the photovoltaic performance and stability of such devices, various engineering approaches have been developed and employed in PSCs. In 2013, the efficiency of both mesoporous and planar PSCs reached 15% by controlling the morphology of perovskite film [12, 13]. In 2014, Seok's group changed the composition of perovskite film by using mixed anion (I and Br). They fabricated uniform and dense $\text{MAPb}(\text{I}_{1-x}\text{Br}_x)_3$ film and achieved an efficiency of 16.2% [14]. One year later, the same group also used mixed cation to extend the light absorption of perovskite by decreasing its bandgap [15]. The average efficiency of the best-performing cell with $(\text{FAPbI}_3)_{1-x}(\text{MAPbBr}_3)_x$ perovskite reached 18.4%. In 2016, Grätzel's group demonstrated that the addition of a small amount of Cs in mixed cation/halide perovskites ($\text{Cs}_x(\text{MA}_{0.17}\text{FA}_{0.83})_{(100-x)}\text{Pb}(\text{I}_{0.83}\text{Br}_{0.17})_3$) facilitated the fabrication of high-quality perovskite films [16]. Thus a perovskite cell with efficiency exceeding 21% was achieved. More importantly, the Cs-employed devices exhibited considerable operational stability over 250 h (at maximum power point tracking under full-sun illumination). Briefly, over the past decade, the effort of figuring out the morphological, structural, electrical, and optical properties of perovskite semiconductors has ensured further progress in PSCs and, very recently, certified that efficiency could reach 25.2% [3].

The aforementioned progress in perovskite photovoltaics has also pioneered upscaling applications. Globally, well-known photovoltaic companies have set out to manufacture upscaling modules [17]. A power conversion efficiency (PCE) of 17.4% for a rigid perovskite minimodule (with an active area of 17.8 cm^2) was achieved by Microquanta Semiconductor (China). In the same direction, a PCE of 12% was obtained by a module with an active area of 100 cm^2 by Greatcell Solar (Australia) in 2019. With continued efforts from the research laboratories and industrial communities toward the scaling up of PSCs, the efficiency gap between lab-scale cells and industrial modules can

be minimized and such devices can compete with other photovoltaic technologies.

1.3 Components and working principle of perovskite solar cells

A typical PSC consists of an absorbing layer, electron- and hole-transporting layers (ETL and HTL), and electrodes. These cells are produced in two different configurations according to the position of ETL and HTL as shown in Fig. 1A and B. If the ETL was coated on the transparent electrode and the light first passes through the ETL to reach the absorbing perovskite layer, then it is known as n-i-p (normal) configuration. In p-i-n configuration (inverted), HTL is the first layer coated on the transparent conductive electrode. Thus the opposite of n-i-p configuration, the light first passes through the HTL to reach the perovskite layer in this configuration. Both of these configurations can be produced in mesoscopic cells as shown in Fig. 1C and D. The planar structure of n-i-p or p-i-n configuration is produced by depositing the absorbing layer onto compact ETLs or HTLs. In mesoscopic cells, semiconductor or insulator mesoporous film is deposited over the compact blocking layer. As shown in Fig. 1E and F, the selective charge-transporting layers collect the electrons and holes generated in the perovskite layer by photon absorption and subsequently transfer them to the corresponding electrodes. The difference between quasi-Fermi levels of charge-transporting layers limits the performance of perovskite devices [18, 19].

In such devices, the organic-inorganic halides with the formula ABX_3 where A is the organic cation (methylammonium $[\text{MA}^+]$ or formadinium $[\text{FA}^+]$), B is the divalent metal cation (Pb^{2+} or Sn^{2+}), and X is the halide anion (Br^- , I^- , or Cl^-) are used as an absorbing layer [20]. In earlier studies, research focused on single-cation MAPbI_3 -based perovskite material as an absorbing layer [10–13, 21–24]. However, mixed cation and/or mixed halide perovskites have been attracting much attention due to their better performance, higher stability, and reduced hysteresis effect [25].

In addition to the absorbing layer, electrodes and charge-transporting layers also affect the performance of PSCs. The main purpose of the electrodes is to collect electrons and holes from ETLs and HTLs, respectively. Therefore the top electrode requires high electrical conductivity and a suitable work function [26, 27]. In addition to the features of the top electrode, the bottom electrode has to provide transparency to allow light to go through to the absorbing layer of the solar cell [28]. While opaque metals such as gold (Au), silver (Ag), or aluminum (Al) are commonly used as a top electrode, transparent conductive oxides such as fluorine-doped tin oxide (FTO) or indium tin oxide (ITO) are used as a bottom electrode in PSCs [27]. The ETL extracts the photogenerated electrons from perovskite and transfers them to the electrode. In n-i-p configuration, generally n-type semiconductor metal oxides such as TiO_2 , ZnO , SnO_2 , etc. are used as an ETL [26], whereas fullerene derivatives such as C_{60} , PC_{61}BM ,

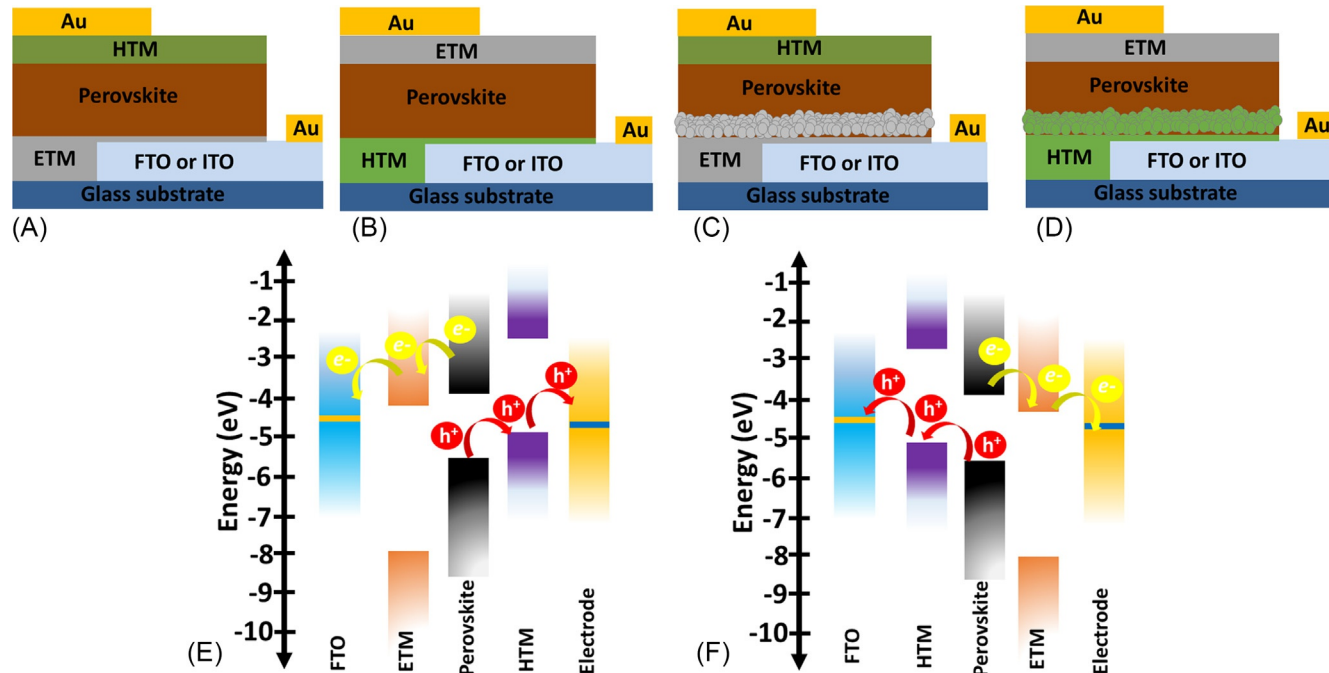


FIG. 1 Device configurations of (A) n-i-p planar, (B) p-i-n planar, (C) n-i-p mesoscopic, (D) p-i-n mesoscopic; schematic energy band diagram of (E) n-i-p-, and (F) p-i-n-structured PSCs.

PC₇₁BM, etc. are preferred in inverted configuration [27]. Highly efficient PSCs in both configurations are fabricated with organic HTLs [28–31], which extract the holes from the absorbing layer. In inverted configuration, poly(3,4-ethylenedioxythiophene):polystyrene sulfonate (PEDOT:PSS) is one of the most frequently used organic HTLs for the fabrication of highly efficient PSCs [29, 30]. However, the hydrophilic nature of this material causes the absorption of water from the environment [26]. In addition, this material reacts with the bottom metal oxide layer due to the highly acidic nature [27]. In n-i-p configuration, $N^2,N^2,N^2,N^2,N^7,N^7,N^7,N^7$ -octakis(4-methoxyphenyl)-9,9'-spirobi[9H-fluorene]-2,2',7,7'-tetramine (spiro-OMeTAD) and poly[bis(4-phenyl)(2,5,6-trimethylphenyl)amine] (PTAA) are the most commonly used HTLs. However, these materials have long-term UV and thermal stability problems [28]. Moreover, hygroscopic additives such as lithium bis(trifluoromethanesulfonyl)imide (LiTFSI) and tert-butylpyridine (tBP), which are used to improve the conductivity of organic HTLs, accelerate the perovskite decomposition [29, 30]. On the other hand, organic HTLs are the most expensive part of PSCs [31]. Therefore these materials are one of the main obstacles to the commercialization of PSCs when considering stability and cost [31, 32].

2 The role of hole-transporting layers

In the last decade, PSCs have attracted outstanding interest because of their perceived benefits over other photovoltaic technologies in terms of tunable absorption range, high absorption coefficient, long diffusion length, high carrier mobility, ambipolar charge transport, and facile fabrication method [33–35]. These fascinating properties facilitate high device efficiencies with remarkable opportunities to realize an industry-scalable technology [36–38]. However, this potential for scalability still requires obstacles to be overcome related to stability and material cost. The stability issue of perovskite materials mainly originated from extrinsic (moisture, oxygen, UV light, and thermal stress) and intrinsic (hygroscopicity and ion migration) factors [39–41]. This is accompanied by a severe decrease in light-harvesting ability, resulting in a deteriorated photovoltaic performance. Hitherto, several attempts have been employed to solve the stability issue of PSCs with regard to the perovskite layer either altering the elemental composition of perovskite or passivating the grain boundary by interlayers [42–45]. Among all the promising techniques, additive/composition engineering has been widely applied as an effective and feasible approach to obtain high-quality perovskite films, thereby leading to significantly enhanced stability of PSCs due to fewer trap states and pinholes. In this context, several additives such as ammonium salts, ionic liquids, and organic-inorganic cations have been introduced [16, 46–50]. Another approach to improve device stability and achieve better performance is the utilization of interfacial layers [42]. Depending on the type of interfacial material and the interface gap, many reports showed higher moisture and UV light stability with significant

performance [42, 51–53]. Recently, the deposition of low-dimensional perovskite materials onto 3D film was reported as one of the most efficient ways to achieve high performance and long-term stability of PSCs [43, 54–56]. Although some degree of recovery in stability has been achieved, further improvements are still required to meet the goal of commercialization. In addition to the aforementioned issues, the diffusion of top metal ions throughout perovskite is another obstacle limiting the long-term stability of perovskite devices. At this point, the protecting function of the HTL comes into question.

HTLs are p-type semiconductors that collect holes from the perovskite layer and transfer them to the electrode. However, all p-type semiconductors cannot be used as HTLs in PSCs. There are some requirements that the ideal HTL has to meet for commercial applications: (i) a favorable band alignment with the perovskite layer is required to guarantee effective transfer of the photoexcited holes from the perovskite to the HTL; (ii) high hole mobility is required to reduce the series resistance and transfer holes from the perovskite layer to the electrode efficiently; (iii) low roughness with controllable surface morphology is required to obtain homogeneous and pinhole-free deposition; (iv) in the case of n-i-p-type PSCs, hydrophobic behavior is quite important against moisture penetration; (v) in the case of p-i-n-type PSCs, the HTL has to exhibit high optical transmittance for incoming light to minimize optical losses; and (vi) HTLs have to show photo and chemical stability to obtain long-term stable PSCs [31, 57–59]. In addition to the aforementioned fascinating requirements, a suitable HTL can be obtained by facile and environmentally friendly methods at low cost.

As mentioned before, an HTL has a subsidiary role in the stability of perovskite material because of its protecting role as an overlayer. The well-known and most frequently used HTL material in highly efficient n-i-p-type PSCs is spiro-OMeTAD. Despite the desirable properties of spiro-OMeTAD such as appropriate ionization potential, low light absorption, and reasonable solubility [60, 61], it is still under debate regarding the high material cost and stability issues [62]. The cost issue of spiro-OMeTAD is mostly associated with the complex synthetic route and purification methods, whereas the stability issue is related to several agents such as its amorphous nature, hygroscopic additives, and mobile ions [61, 63]. As is well known, pristine spiro-OMeTAD suffers from low conductivity ($10^{-6} \text{ S cm}^{-1}$) and moderate hole mobility (μ_h) (10^{-4} – $10^{-5} \text{ cm}^2/\text{Vs}$) as well as the requirement of additives such as LiTFSI and tBP to improve the electrical properties [61]. However, very mobile and hygroscopic Li ions seriously accelerate the degradation of perovskite and even the full device by penetrating through the sublayers. On the other hand, tBP, which helps to increase the polarity of the HTL, unfortunately can dissolve the perovskite layer due to its corrosive effect. In short, while these additives lead to better electrical properties, they accelerate the degradation of the perovskite layer by decomposing the perovskite layer and/or decreasing the glass transition temperature (T_g) (125°C) [64] leading to crystallization of spiro-OMeTAD at elevated temperatures.

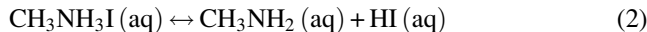
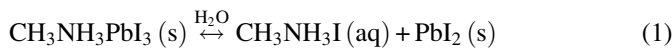
Several approaches based on HTL engineering have also been reported to combat the instability issue of perovskite devices associated with doped HTL materials. New p-type materials were introduced to replace spiro-OMeTAD [61]. These attempts could not change the reality of the presence of such a high-cost HTL material in the device architecture. The HTL-free device architecture is another approach to avoid the negative impacts of HTL; however, a remarkable efficiency could not be achieved in this architecture [65, 66]. Very recently, dopant-free organic molecules (polymers and/or small molecules) have been presented as another promising approach [67–69]. The efficiencies of the PSCs employed with dopant-free HTLs were between 16% and 20% [70]. The efficiency values reported in dopant-free HTL-employed devices were relatively lower than that of PSCs with traditionally doped HTLs.

In contrast to n-i-p-type perovskite devices, the most widely used HTL material in p-i-n-type PSCs is PEDOT:PSS because of its simple, low-temperature processing methods and low roughness [71, 72]. However, HTL PEDOT:PSS has similar challenges to spiro-OMeTAD. For instance, the high acidity of the PEDOT:PSS solution can easily corrode the bottom electrode and perovskite layer. More importantly, the hydrophilic nature of PEDOT:PSS can encourage moisture uptake from the atmosphere, therefore limiting the long-term stability and photovoltaic performance of perovskite devices [73]. In addition, low electrical properties associated with high band-offset between perovskite and PEDOT:PSS layers limit the charge extraction, leading to a poor electron-blocking ability. Although several approaches to mitigate the acidic nature and high band-offset, including surface passivation and doping, have been proposed, its inherent stability issue because of its organic nature has not yet been solved [74]. As a result, in addition to the accelerating effect in perovskite degradation, the fabrication of perovskite devices using such organic HTL materials has faced a number of limitations from a commercialization point of view, that is, high material cost and instability behavior under thermal stress and/or high humidity levels. All these outcomes demonstrate that not only perovskite but also organic-based HTL materials are responsible for long-term device stability. This fact suggests that it is a more appropriate method to develop new alternative materials instead of modifying existing materials. The most important approach in this context is undoubtedly the utilization of inorganic HTL materials.

Various inorganic materials such as metal oxides, chalcogenides, CuSCN, and CuI have been developed instead of expensive and unstable organic-based materials [57, 75–77]. Among inorganic materials, metal oxides have attracted much attention due to their high heat/moisture resistance, promising hole transport properties, and easy production [78]. The most important necessity for developing an alternative material is to determine the specific properties of this material and specify the required parameters to work in harmony with other layers in the architecture. As is well known, the most important role of an effective HTL material is to allow hole transfer from the perovskite layer; however,

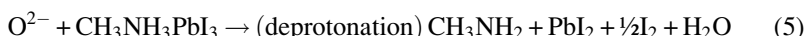
all the desired properties are not limited to this [62, 79]. To obtain a functional HTL, an HTL material ought to present a compatible highest occupied molecular orbital level with the valence band of the perovskite layer. The high mobility and high conductivity of HTL material are also essential for an efficient charge transfer and for minimizing the series resistance in the bulk structure at the perovskite/HTL/contact interfaces. In addition, high mobility and conductivity are advantageous in terms of both overall cost and long-term stability as they can eliminate the doping requirement of the material.

As mentioned earlier, another important aspect of HTL material is the physical barrier role between the perovskite layer and the external environment [62]. In this respect, the potential of a hydrophobic HTL material to contribute the moisture stability of the perovskite layer is quite high. Perovskite materials are naturally unstable and can degrade rapidly due to external factors and organic components in their structure. The perovskite structure is particularly sensitive to water and oxygen, causing irreversible formation of PbI_2 , CH_3NH_2 , and hydrogen iodide (HI). High thermal stress and UV light are also external factors that cause perovskite degradation. Especially, H_2O molecules are known to be the main factor in the degradation of perovskite films. Although different degradation mechanisms are reported by different groups as the final product of different complexes both experimentally and theoretically, the possible degradation reactions of perovskite films are given by the following series of equations [80]:



Basically, $\text{CH}_3\text{NH}_3\text{PbI}_3$ tends to undergo hydrolysis with water molecules to form $\text{CH}_3\text{NH}_3\text{I}$ and PbI_2 . The resulting $\text{CH}_3\text{NH}_3\text{I}$ can easily be separated into CH_3NH_2 and HI solutions. Furthermore, HI can react with oxygen molecules to form I_2 and H_2O . The photochemical reaction of HI will be as in Eq. (4) under radiation.

Oxygen molecules are also one of the main factors causing the degradation of perovskite films. It is known that molecular oxygen, especially under light, leads to the degradation of perovskite. Under dry air and light, photoexcited electrons in the perovskite structure interact with molecular oxygen to form superoxide anions (O^{2-}) [81]. Thus a decay reaction occurs between the superoxide and CH_3NH_3^+ cations, which causes the formation of PbI_2 , iodine, and water molecules. The possible degradation reaction is shown in the following equation:



Apart from the stability issue, the absence of complex synthesis conditions can provide superiority in terms of both applicability and cost for commercial applications of this material. Especially in n-i-p device architecture, the dissolution of HTL material in a low polarity solvent is extremely important to avoid damaging the perovskite layer [77].

The innovative approaches based on oxide-based inorganic HTL materials to overcome the aforementioned challenges will be explained in the following part of this chapter. In this regard, a broad range of metal oxide-based inorganic HTL materials such as NiO_x , CuO , Cu_2O , CuCrO_2 , CuGaO_2 , Co_3O_4 , VO_x , etc. will be discussed and compared in detail. We believe that this chapter will be highly useful for researchers involved in the optoelectronic properties and applications of inorganic HTL materials in PSCs and will provide helpful insights into enhancing state-of-the-art perovskite device stability toward future commercialization.

3 Metal oxide-based inorganic hole-transporting materials

Metal oxide-based p-type materials have long been used in a variety fields such as sensors [82], batteries [83], catalysis [84], and solar cells [28] due to their promising optical and electrical properties as well as superior chemical and thermal stabilities. Utilization of metal oxide as a charge transporting layer in PSCs has attracted major attention due to their advantages, for instance, improving the stability of PSCs [85]. In the following section, metal oxides widely used in PSCs are discussed under different headings: NiO_x , $\text{CuO}/\text{Cu}_2\text{O}$, delafossite oxides, and other transition metal oxides.

3.1 Nickel oxide

Among various inorganic HTLs, earth-abundant p-type semiconductor nickel oxide (NiO_x) has shown great progress because of its high mobility, rapid charge injection, wide bandgap ($E_g > 3.5 \text{ eV}$), and noteworthy stability [86–88]. Although several studies have been reported for the utilization of NiO_x material in n-i-p-type perovskite devices [88, 89], NiO_x HTL is mostly employed in inverted device architecture due to its limited solubility in nonpolar solvents and required high-temperature annealing process. Table 1 summarizes the recent progress of the photovoltaic performance of NiO_x HTL-employing PSCs based on different device configurations. NiO_x has been employed as an alternative to the PEDOT:PSS HTL, which is one of the mostly used HTLs in inverted PSCs. As a result of the limitations of organic-based HTLs, a great deal of progress has been made by using NiO_x as an HTL in inverted PSCs. Although the first study of NiO_x thin film as a transparent semiconductor was reported in 1993 by Sato et al. [120], it was adapted into perovskite devices in 2013. In this study, NiO_x was investigated as an HTL in the structure of FTO/ NiO /perovskite/PC₆₀BM/TiO_x/Al [121]. In the presence of

TABLE 1 Recent progress in photovoltaic performance of NiO_x hole-transporting layers employing perovskite solar cells based on different device configurations.

Device architecture	J_{SC} (mA cm^{-2})	V_{OC} (V)	FF	PCE (%)	References
ITO/ NiO_x (SC)/MAPbI ₃ /PCBM/Al	15.4	1.05	0.48	7.6	[90]
ITO/ NiO_x (SC)/MAPbI _{3-x} Cl _x /PCBM/BCP/Al	12.4	0.92	0.68	7.8	[91]
FTO/ NiO_x (SC)/MAPbI ₃ /PCBM/Au	16.3	0.88	0.64	9.1	[92]
FTO/ NiO_x (SC)/MAPbCl _{3-x} I _x /PCBM:PS/Al	15.6	1.07	0.64	10.7	[93]
FTO/ NiO_x (SC)/MAPbI ₃ /PCBM/Ag	17.9	1.09	0.74	14.4	[94]
ITO/ NiO_x (SC)/MAPbI ₃ /PCBM/Ag	20.5	0.99	0.78	15.7	[87]
ITO/ NiO_x (SC)/MAPbI ₃ /PCBM/Ag	21.3	1.10	0.71	16.7	[95]
ITO/ NiO_x (SC)/MAPbI ₃ /PCBM/Ag	23.5	1.04	0.69	16.9	[96]
ITO/ NiO_x (SP)/MAPbI ₃ /PCBM/BCP/Ag	21.8	1.02	0.78	17.6	[97]
FTO/ NiO_x (SC)/MAPbI ₃ /PCBM/Bis-C ₆₀ /Ag	21.7	1.10	0.75	17.6	[98]
FTO/ NiO_x (SC)/MAPbI ₃ /PCBM/BCP/Ag	22.9	0.99	0.80	18.2	[99]
FTO/ NiO_x (SC) /MAPbI ₃ /C ₆₀ /SnO ₂ /Ag	21.8	1.12	0.77	18.8	[100]
ITO/ NiO_x (SC)/MAPbI ₃ /C ₆₀ /Bis-C ₆₀ /Ag	21.8	1.03	0.78	17.7	[101]
ITO/ NiO_x (SC)/MAPbI _{3-x} Cl _x /PCBM/PDINO/Ag	20.6	1.11	0.76	17.5	[102]
ITO/ NiO_x (SC)/MAPbI ₃ /PCBM/Ag	19.9	1.09	0.77	16.7	[103]
ITO/ NiO_x (SC)/MAPbI ₃ /PCBM/LiF/Al	19.0	1.03	0.69	13.4	[104]

Continued

TABLE 1 Recent progress in photovoltaic performance of NiO_x hole-transporting layers employing perovskite solar cells based on different device configurations—cont'd

Device architecture	J_{SC} (mA cm $^{-2}$)	V_{OC} (V)	FF	PCE (%)	References
ITO/ NiO_x (SC)/CsMAFAPbI _{3-x} Br _x /PCBM/ZnO/Al	22.2	1.02	0.82	18.6	[105]
FTO/ NiO_x (SC)/MA _{1-y} FA _y PbI _{3-x} Cl _x /PCBM/BCP/Ag	23.7	1.12	0.76	20.2	[106]
FTO/ Cs:NiO_x (SC)/MAPbI ₃ /PCBM/ZrAcac/Ag	21.8	1.12	0.79	19.4	[107]
ITO/ Co:NiO_x (SC)//MAPbI ₃ /PCBM/PEI/Ag	22.3	1.05	0.79	18.6	[108]
ITO/ Co:NiO_x (SC)/MAPbI ₃ /PCBM/Bis-C ₆₀ /Ag	22.5	1.04	0.75	17.5	[109]
ITO/ Li:Co:NiO_x (SC)/MA _{1-y} FA _y PbI _{3-x} Cl _x /PCBM/BCP/Ag	23.8	1.09	0.78	20.1	[110]
ITO/ Cu:NiO_x (SC)/MAPbI ₃ /C ₆₀ /BCP/Ag	22.3	1.12	0.81	20.3	[111]
ITO/ F6TCNNQ:NiO_x (SC)/MAPbI ₃ /PCBM/ZrAcac/Ag	23.2	1.12	0.80	20.9	[112]
ITO/ NiO_x:rGO (SC)/MAPbI ₃ /PCBM/BCP/Ag	22.0	1.07	0.81	19.1	[113]
ITO/ KCl@NiO_x (SC)/CsMAFAPbI _{3-x} Br _x /PCBM/ZrAcac/Ag	22.9	1.15	0.80	21.0	[114]
ITO/ c-NiO_x (Spt)/mp-NiO _x /MAPbI ₃ /BCP/Al	19.8	0.96	0.61	11.6	[115]
FTO/ c-Cu:NiO_x /mp-Cu:NiO _x (SC)/MAPbI ₃ /PCBM/bis-C ₆₀ /Ag	21.6	1.11	0.82	19.6	[116]
FTO/ NiO_x (CBD)/CsMAFAPbI _{3-x} Br _x /PCBM/BCP/Ag	21.0	1.02	0.85	16.7	[117]

TABLE 1 Recent progress in photovoltaic performance of NiO_x hole-transporting layers employing perovskite solar cells based on different device configurations—cont'd

Device architecture	J_{SC} (mA cm ⁻²)	V_{OC} (V)	FF	PCE (%)	References
FTO/c-TiO ₂ /mp-TiO ₂ /mp-ZrO ₂ / mp-NiO_x (DB)/carbon-MAPbI ₃	21.4	0.92	0.76	14.9	[89]
FTO/c-TiO ₂ /mp-TiO ₂ /mp-Al ₂ O ₃ / mp-NiO_x (ScP)/carbon-MAPbI ₃	21.6	0.92	0.76	15.0	[118]
FTO/c-TiO ₂ /MAPbI _{3-x} Cl _x / NiO_x/Ni (Spt)	17.9	0.77	0.53	7.3	[119]

CBD, chemical bath deposition; *DB*, doctor blade; *FF*, fill factor; *PCE*, power conversion efficiency; *SC*, spin coating; *ScP*, screen printing; *SP*, spray pyrolysis; *Spt*, sputtering.

$\text{CH}_3\text{NH}_3\text{PbI}_{3-x}\text{Cl}_x$ perovskite absorber, quite a low device performance of only 0.1% was obtained. Such a low efficiency was ascribed to the low coverage of perovskite on the NiO_x surface, leading to direct contact between the NiO and the upper layer of [6,6]-phenyl-C₆₁-butyric acid methyl ester (PCBM). Despite the significant progress in NiO_x -based planar PSCs, further improvement is limited due to the low intrinsic electrical conductivity of pristine NiO material. It is worth noting that pure NiO is an insulator but in its nonstoichiometric state, namely NiO_x , it can exhibit better electrical conductivity because of nickel vacancies caused by the excess of oxygen. However, the large ionization energy associated with Ni vacancies occasion low hole density with energy losses in perovskite devices [88]. Up to now, various methods such as spin coating [92], screen printing [118], magnetron sputter [122], electrochemical deposition [123], and pulsed laser deposition [124] have been used to deposit NiO_x film. Park et al. revealed that the uniform and dense NiO_x film with good optical transparency formed with the pulsed laser deposition technique provided fabrication of efficient p-i-n PSCs (17.3%) [124]. In 2017, uniformly thick and homogeneous NiO_x films were also deposited by electrochemical deposition [123]. It was shown that the rough surface of NiO_x enhanced the fill factor (FF) of PSCs due to the facilitated hole extraction. As a result, a p-i-n PSC with 19.2% efficiency was produced on NiO_x film. However, controlling the oxygen vacancy in NiO_x film is not easy with any kind of deposition method. Therefore most NiO_x -based planar PSCs suffer from low short-circuit current (J_{SC}) and FF, which may have originated from the relatively low conductivity of NiO_x film [125]. A variety of engineering methods such as metal ion doping and

surface modification have been proposed to mitigate such losses and further improve the performance and stability of PSCs. In this respect, several types of metal dopants [125, 126] have been incorporated into NiO_x by using different methods resulting in improved optoelectronic properties. Among them, Cu is one the most frequently used metal dopants because of its similar ionic radius compared to that of nickel (0.69 Å), and subsequently its tendency to substitute the Ni site in the lattice.

For the first time, Kim et al. introduced solution-processed Cu-doped NiO_x film as an efficient HTL in PSCs and demonstrated a significant improvement in device performance [125]. The PCE of the performing FTO/Cu: NiO_x /MAPbI₃/PCBM/Ag device structure was remarkably increased by two orders of magnitude from 8.94% to 15.4%. This improvement was ascribed to the significantly improved electrical conductivity of NiO_x HTL. Moreover, 90% of the initial PCE of the Cu-doped NiO_x -based PSC remained after 240 h of storage in air. This study revealed novel HTL systems for high-performance and decently stable PSCs and provided a new approach for further investigations. Molecular dopants were also introduced to modify the solution-derived NiO_x HTLs by simply spin coating an acetonitrile solution of 2,2'-(perfluoronaphthalene-2,6-diylidene)dimalononitrile (F6TCNNQ) onto the bare NiO_x [127]. This approach helped the molecular dopants to penetrate the grain boundaries of the bare NiO_x film, which guaranteed a strong p-type doping effect, thus leading to a remarkable reduction in contact resistance at the NiO_x /perovskite interface. Moreover, the Fermi level of NiO_x was increased from 4.63 to 5.07 eV after F6TCNNQ doping, while the VBM level was decreased from 5.21 to 5.37 eV, leading to an increase in V_{OC} and overall PCE, because of the minimized thermionic losses (Fig. 2A). As a result of these satisfying properties, the average PCE of inverted CsFAMAPb(I,Br)₃-based devices was boosted by ~8% and the best-performing device achieved a PCE of 20.86% with an outstanding FF of 0.80 (Fig. 2B).

In another study, Li et al. presented a physical oxide composite strategy by uniformly dispersing reduced graphene oxide (rGO) sheets into the NiO_x precursor solution to increase the conductivity of the NiO_x HTL [113]. It is known that rGO has already been used as an HTL in PSCs. The efficiency of the optimized cell with rGO was 16.5% [128]. However, balancing the work function and conductivity of rGO was not easy. In an NiO_x :rGO composite, the rGO sheets acted as conductive binders to connect the NiO_x nanoparticles and hence modify the morphology and increase film conductivity without sacrificing its high work function. Planar PSCs with an ITO/ NiO_x :rGO/perovskite/PCBM/BCP/Ag structure displayed a champion PCE of 19.1% with enhanced J_{SC} (from 20.8 to 22.04 mA cm⁻²) and FF (from 0.73 to 0.81) compared to the device based on pristine NiO_x film. Moreover, PSCs employing NiO_x :rGO HTL showed a negligible hysteresis in the *I-V* characteristics and a long shelf-stability with negligible degradation in device performance over 70 days.

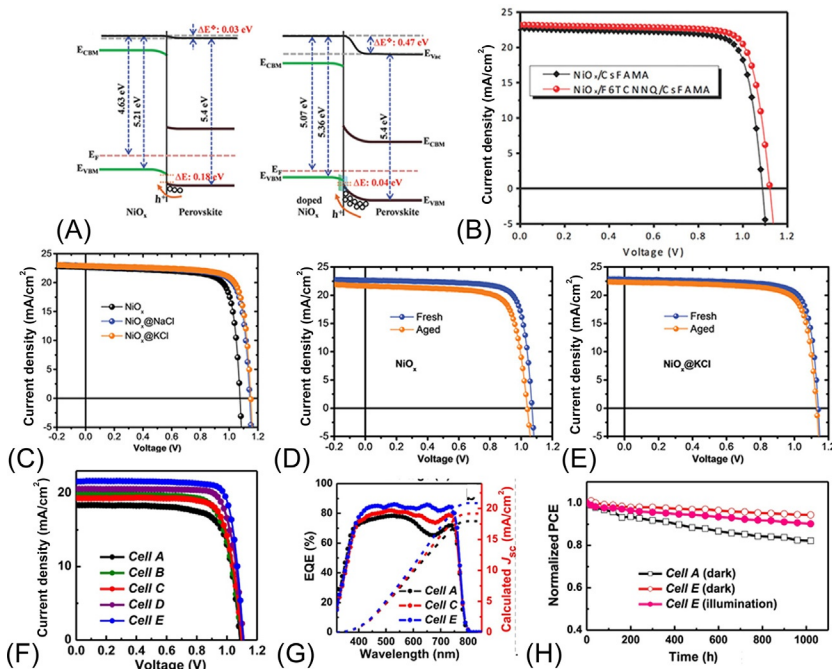


FIG. 2 (A) Effect of molecular doping of F6TCNNQ on the band bending at the $\text{NiO}_x/\text{perovskite}$ interface. (B) $J-V$ curves of PSCs with NiO_x and F6TCNNQ-doped NiO_x HTLs. (C) $J-V$ curves of PSCs with pristine or alkali chloride (MCl)-modified NiO_x HTLs. $J-V$ curves of (D) NiO -based, (E) KCl-modified NiO -based champion cells before and after aging for 150 days. (F) $J-V$ curves for the devices fabricated in different configurations (Cell A: bl- NiO , Cell B: bl-Cu: NiO_x , Cell C: bl- $\text{NiO}_x/\text{mp-NiO}_x$, Cell D: bl-Cu: $\text{NiO}_x/\text{mp-NiO}_x$, Cell E: bl-Cu: $\text{NiO}_x/\text{mp-Cu:NiO}_x$). (G) EQE spectra of the best cells prepared from different NiO_x layers. (H) The stability of Cells A and E in the dark or under constant light irradiation. (Panel (A): Reproduced with permission W. Chen, Y. Zhou, L. Wang, Y. Wu, B. Tu, B. Yu, F. Liu, H. W. Tam, G. Wang, A.B. Djurisic, L. Huang, Z. He, *Molecule-doped nickel oxide: verified charge transfer and planar inverted mixed cation perovskite solar cell*, *Adv. Mater.* 30 (20) (2018) e1800515; Panel (B): Reproduced with permission W. Chen, Y. Zhou, L. Wang, Y. Wu, B. Tu, B. Yu, F. Liu, H.W. Tam, G. Wang, A. B. Djurisic, L. Huang, Z. He, *Molecule-doped nickel oxide: verified charge transfer and planar inverted mixed cation perovskite solar cell*, *Adv. Mater.* 30 (20) (2018) e1800515; Panel (C): Reproduced with permission W. Chen, Y.C. Zhou, G.C. Chen, Y.H. Wu, B. Tu, F.Z. Liu, L. Huang, A.M.C. Ng, A.B. Djurisic, Z.B. He, *Alkali chlorides for the suppression of the interfacial recombination in inverted planar perovskite solar cells*, *Adv. Energy Mater.* 9 (19) (2019) 1803872; Panel (E): Reproduced with permission W. Chen, Y.C. Zhou, G.C. Chen, Y.H. Wu, B. Tu, F.Z. Liu, L. Huang, A.M.C. Ng, A.B. Djurisic, Z.B. He, *Alkali chlorides for the suppression of the interfacial recombination in inverted planar perovskite solar cells*, *Adv. Energy Mater.* 9 (19) (2019) 1803872; Panel (F): Reproduced with permission K. Yao, F. Li, Q.Q. He, X.F. Wang, Y.H. Jiang, H.T. Huang, A.K.Y. Jen, *A copper-doped nickel oxide bilayer for enhancing efficiency and stability of hysteresis-free inverted mesoporous perovskite solar cells*, *Nano Energy* 40 (2017) 155–162; Panel (G): Reproduced with permission K. Yao, F. Li, Q.Q. He, X.F. Wang, Y.H. Jiang, H.T. Huang, A.K.Y. Jen, *A copper-doped nickel oxide bilayer for enhancing efficiency and stability of hysteresis-free inverted mesoporous perovskite solar cells*, *Nano Energy* 40 (2017) 155–162; Panel (H): Reproduced with permission K. Yao, F. Li, Q.Q. He, X.F. Wang, Y.H. Jiang, H.T. Huang, A.K.Y. Jen, *A copper-doped nickel oxide bilayer for enhancing efficiency and stability of hysteresis-free inverted mesoporous perovskite solar cells*, *Nano Energy* 40 (2017) 155–162.)

Besides metal and molecular doping, composition or interface engineering of the NiO_x films is also reported as a simple approach to change the surface properties of HTLs. Very recently, a low-temperature and solution combustion-based method was employed to prepare an NiO_x HTL [106]. The resulting NiO_x indicated a high film quality, slightly larger bandgap, and preferable energy alignment with an $\text{MA}_{1-y}\text{FA}_y\text{PbI}_{3-x}\text{Cl}_x$ perovskite layer compared to high-temperature sol-gel-processed NiO_x . The devices employing combustion-derived NiO_x showed that the perovskite films on corresponding HTLs had larger grain size with fewer defect states, exhibiting a high PCE of 20.2% with a remarkable V_{OC} of 1.12 V. The improved PCE and enhanced ambient air storage stability were ascribed to the high quality of the perovskite/HTL interface resulting in an enhanced charge transport and suppressed charge recombination.

Very recently, interface modification of NiO_x /perovskite by using alkali chlorides (NaCl, KCl) indicated highly efficient and stable p-i-n-type planar PSCs [114]. The alkali halide passivation of the NiO_x HTL reduced the defect density of perovskite film leading to significantly suppressed interfacial recombination. The best-performing device with modified HTL showed an excellent PCE of 21% with a V_{OC} as high as 1.15 V (Fig. 2C). More importantly, KCl-modified devices maintained over 95% of their initial performance after 150 days' storage in a nitrogen-filled dry-box (Fig. 2D and E). This significant enhancement in stability was attributed to decreased defect states in the perovskite layer and suppressed interfacial recombination. Apparently, a PCE of 21% is the highest efficiency reported for NiO_x PSCs so far.

Another milestone in the progress of HTL-based PSCs is the utilization of mesoporous NiO_x in PSCs. Up to now, various methods have been developed to fabricate PSCs where the mesoporous NiO_x film acts as the scaffold of perovskite materials as well as the transport channel for photoexcited holes inferring larger surface area for efficient infiltration of perovskite materials, higher light harvesting efficiency, and improved interface between the perovskite and NiO layer [115, 129]. The first NiO_x -based mesoporous p-i-n-type PSC was introduced by Wang et al. in 2014 [130]. A solution-derived mesoporous NiO_x film was inserted as a host to adsorb more perovskite to improve photon harvesting. Suitable band alignment between mesoporous NiO_x , perovskite, and PCBM conducted to a high-output voltage and minimized energy loss for the charge separation process. As a result, the device employing ITO/c- NiO_x /mp- NiO_x /MAPbI₃/PCBM/BCP/Al structure showed a PCE of 9.51%.

In the same direction, Yao et al. systematically studied mesoporous p-i-n-type PSCs by employing a bilayer structure by blocking the Cu:NiO_x/mp-Cu:NiO_x layer [116]. It is reported that the mesoporous layer increased the light-harvesting efficiency leading to enhanced J_{SC} and improved contact area at the perovskite/HTL interface, and decreased series resistance (Fig. 2F and G). The bilayer HTL-employing devices exhibited a PCE of 19.61% (with FF as high as 0.82) and 18.16% for active areas of 0.0625 and 1.08 cm², respectively. Moreover, the hysteresis effect was significantly eliminated due to the robust

inorganic nature of the bilayer HTL and more than 90% of the initial PCE remained after light soaking for 1000h (Fig. 2H).

Besides p-i-n mesoporous PSCs, mesoporous NiO_x films have also been applied in n-i-p-type PSCs. Xu et al. first fabricated the fully printable n-i-p mesoporous PSCs with a structure of FTO/c-TiO₂/mp-TiO₂/mp-ZrO₂/NiO_x/carbon-MAPbI₃ [131]. This carbon electrode-based device delivered a PCE of 14.2% with excellent stability. In planar n-i-p-type PSCs, direct deposition of NiO_x HTLs on the top of the perovskite layer is limited by potential degradation of the perovskite layer. In addition to the requirement for the postannealing process, the solvents used for the dispersion of NiO_x HTLs are mostly strong polar organic or water. Hence, it is very important to explore a compatible and facile method to fabricate NiO_x HTLs in n-i-p PSCs.

3.2 Copper oxide and cuprous oxide

Copper oxide (CuO) and cuprous oxide (Cu_2O) are widely used inorganic p-type semiconductors because of their high natural abundance, low toxicity, and high ambient stability. Moreover, such materials introduce optimal optoelectronic properties, including sufficient mobility, well-aligned energy level, and minimized energy losses [132–134]. Therefore their utilization as HTLs in various optoelectronic devices has been thoroughly reported [133–135]. The first attempt to use these materials for photovoltaic application was done as a light harvester due to their low bandgap and high absorption coefficient. However, after a while such materials were suggested for potential HTL material in perovskite devices due to their low electron affinity and high hole mobility [136, 137]. Table 2 summarizes the recent progress on photovoltaic performance of $\text{CuO}/\text{Cu}_2\text{O}$ HTLs employing PSCs based on different device configurations.

The photovoltaic performance of Cu_2O HTL employing PSCs was theoretically calculated to deliver a promising efficiency of over 25% by the application of wxAMPS software [147]. In this study, different HTL materials such as NiO_x , CuI , CuSCN , spiro-OMeTAD, and Cu_2O were simulated in n-i-p-type planar PSCs in the architecture of FTO/TiO₂/MAPbI₃/HTL/Au. Among the various HTLs, Cu_2O -based PSCs exhibited the highest efficiency of 25.86% after the optimization of thickness. A similar result was also confirmed in another theoretical simulation calculation, showing the champion efficiency of 25% [148].

$\text{Cu}_2\text{O}/\text{CuO}$ films can be obtained using various techniques, including sputtering, electrodeposition, thermal oxidation, atomic layer deposition, and chemical vapor deposition, which all require advanced equipment and costly and complicated processes [149–151]. A facile and low-temperature method to prepare Cu_2O and CuO films was reported by Zuo and Ding in 2015 [138]. They indicated that Cu_2O can be obtained by in situ conversion of copper iodide (CuI) in an aqueous sodium hydroxide (NaOH) solution, whereas CuO can be formed through high-temperature annealing of Cu_2O in the air (Fig. 3A). As compared to a PEDOT:PSS HTL-based control device, Cu_2O HTL-employed devices showed

TABLE 2 Recent progress in the photovoltaic performance of CuO/Cu₂O hole-transporting layers employing perovskite solar cells based on different device configurations.

Device architecture	J _{SC} (mA cm ⁻²)	V _{OC} (V)	FF	PCE (%)	References
ITO/Cu ₂ O (SC)/MAPbI ₃ /PC ₆₁ BM/Ca/Al	16.5	1.07	0.76	13.4	[138]
ITO/CuO (SC)/MAPbI ₃ /PC ₆₁ BM/Ca/Al	15.8	1.06	0.73	12.2	[138]
ITO/CuO (ED)/MAPbI ₃ /C ₆₀ /Bphen/Ag	18.0	0.88	0.61	9.6	[139]
ITO/CuO (SC)/MAPbI ₃ /PC ₇₀ BM/AZO/Al	18.2	1.09	0.77	15.3	[140]
ITO/Cu ₂ O (Spt)/MAPbI ₃ /PCBM/Ag	17.5	0.95	0.66	11.0	[134]
ITO/Cu ₂ O (DC)/MAPbI ₃ /PCBM/Al	16.5	0.89	0.56	8.2	[135]
ITO/Cu ₂ O (DC)/MAPbI _{3-x} Cl _x /PCBM/Al	15.6	0.92	0.58	8.3	[135]
ITO/CuO _x (SC)/MAPbI ₃ /PCBM/C ₆₀ /BCP/Ag	20.1	1.01	0.71	14.4	[141]
ITO/CuO _x (SC)/MAPbI _{3-x} Cl _x /PCBM/C ₆₀ /BCP/Ag	22.5	1.11	0.76	19.0	[141]
ITO/CuO _x (SC)/MAPbI ₃ /C ₆₀ /BCP/Ag	23.2	0.99	0.74	17.1	[142]
ITO/CuO _x (SC)/MAPbI ₃ /PC ₆₁ BM/ZnO/Al	22.4	1.03	0.76	17.4	[143]
ITO/CuO _x (ES)/MAPbI _{3-x} Cl _x /C ₆₀ /BCP/Al	17.2	0.70	0.48	5.8	[144]
FTO/SnO ₂ /PCBM/MAPbI ₃ /FBT-Th4/Cu _x O (TE)/Au	22.4	1.12	0.75	18.9	[145]
FTO/TiO ₂ /CsFAMAPb(I, Br) ₃ /Cu ₂ O(SC)/Au	22.2	1.15	0.74	18.9	[146]

DC, dip coating; ED, electrodeposition; ES, electrosprayed; FF, fill factor; PCE, power conversion efficiency; SC, spin coating; Spt, sputtering; TE, thermal evaporation.

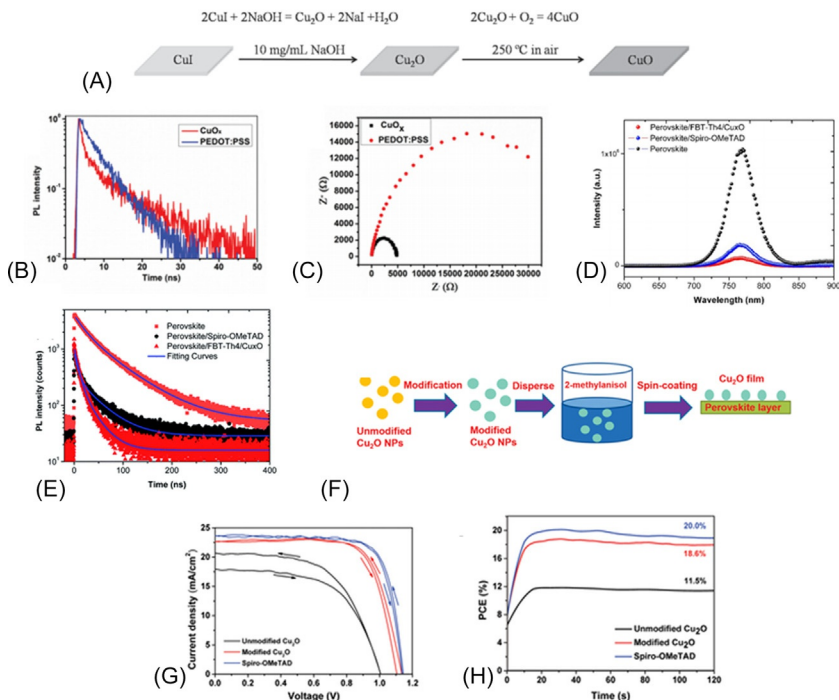


FIG. 3 (A) Preparation process for Cu_2O and CuO films. (B) TRPL and (C) impedance spectra of perovskite films on different HTL films. (D) PL and (E) TRPL spectra of perovskite films on different HTL films. (F) Schematic illustration of the deposition process of the Cu_2O film. (G) J - V curve of the best-performing devices based on Cu_2O and on spiro-OMeTAD HTM. (H) MPP tracking for 120s to yield a stabilized efficiency for unmodified Cu_2O , modified Cu_2O , and spiro-OMeTAD-based devices. (Panel (A): Reproduced with permission C.T. Zuo, L.M. Ding, *Solution-processed Cu_2O and CuO as hole transport materials for efficient perovskite solar cells*, *Small* 11 (41) (2015) 5528–5532; Panel (B and C): Reproduced with permission W.H. Sun, Y.L. Li, S.Y. Ye, H.X. Rao, W.B. Yan, H.T. Peng, Y. Li, Z.W. Liu, S.F. Wang, Z.J. Chen, L.X. Xiao, Z.Q. Bian, C.H. Huang, *High-performance inverted planar heterojunction perovskite solar cells based on a solution-processed Cu_2O layer*, *Nanoscale* 8 (20) (2016) 10806–10813; Panel (D and E): Reproduced with permission Y.X. Guo, H.W. Lei, L.B. Xiong, B.R. Li, G.J. Fang, *An integrated organic-inorganic hole transport layer for efficient and stable perovskite solar cells*, *J. Mater. Chem. A* 6 (5) (2018) 2157–2165; Panel (F): Reproduced with permission C. Liu, X.Y. Zhou, S.M. Chen, X.Z. Zhao, S.Y. Dai, B.M. Xu, *Hydrophobic Cu_2O quantum dots enabled by surfactant modification as top hole-transport materials for efficient perovskite solar cells*, *Adv. Sci.* 6 (7) (2019) 1801169; Panel (G): Reproduced with permission C. Liu, X.Y. Zhou, S.M. Chen, X.Z. Zhao, S.Y. Dai, B.M. Xu, *Hydrophobic Cu_2O quantum dots enabled by surfactant modification as top hole-transport materials for efficient perovskite solar cells*, *Adv. Sci.* 6 (7) (2019) 1801169; Panel (H): Reproduced with permission C. Liu, X.Y. Zhou, S.M. Chen, X.Z. Zhao, S.Y. Dai, B.M. Xu, *Hydrophobic Cu_2O quantum dots enabled by surfactant modification as top hole-transport materials for efficient perovskite solar cells*, *Adv. Sci.* 6 (7) (2019) 1801169.)

a significantly enhanced V_{OC} of 1.07 V and a J_{SC} of 16.52 mA cm^{-2} , leading to a PCE of 13.35%. Similarly, a V_{OC} of 1.06 V, a J_{SC} of 15.82 mA cm^{-2} , and a PCE of 12.16% were obtained in CuO HTL-employed devices. A higher V_{OC} value was attributed to the deep-lying valence bands of Cu_2O and CuO, whereas the improved J_{SC} value was explained on the basis of better crystallinity of the perovskite layer and high transparency of the Cu_2O and CuO layers. A highly crystalline perovskite layer favors light harvesting and charge carrier transport, while high transparency of HTLs facilitates the transmission of incident light.

In the same direction, a facile solution-processed method was applied to simplify the film formation of CuO_x and was employed as an HTL in planar-type inverted PSCs [142]. The solution-processed CuO_x deposited onto the substrate exhibited a smooth surface and high transparency in the visible region. Time-resolved photoluminescence (TRPL) spectra and impedance spectra confirmed the efficient hole transport and low contact resistance at the perovskite/ CuO_x interface, respectively (Fig. 3B and C). The CuO_x HTL-employed device in ITO/ CuO_x /MAPbI₃/C₆₀/BCP/Ag showed a PCE of 17.1% with a high J_{SC} of 23.2 mA cm^{-2} and negligible hysteresis. Considerable air stability was also reported as compared to the PEDOT:PSS counterpart. This study highlighted the importance of interfacial properties at the perovskite/ CuO_x interface for obtaining high device performance.

Guo et al. reported a strategy using an organic-inorganic integrated HTL composed of the solution-processable conjugated polymer FBT-Th4 and Cu_xO [145]. The optimized perovskite devices indicated a significant improvement in performance with a PCE up to 18.85% with negligible hysteresis. FBT-Th4/ Cu_xO devices exhibited slightly improved J_{SC} and higher FF and V_{OC} compared to the spiro-OMeTAD reference devices. To investigate the hole extraction ability of FBT-Th4/ Cu_xO , the steady-state photoluminescence (PL) and TRPL spectra of the corresponding perovskite films were compared. As presented in Fig. 3D, hybrid FBT-Th4/ Cu_xO -based film showed very low PL intensity confirming more efficient reduction in charge recombination. As evidenced by the TRPL spectrum (Fig. 3E), hybrid FBT-Bh4/ Cu_xO in contact with perovskite demonstrated faster extraction rate than the spiro-OMeTAD counterpart. In addition, the mobility of HTL films was measured by the space charge-limited current model and it was found that mobility of the FBT-Th4/ Cu_xO hybrid film was about 1.5 times higher than that of the spiro-OMeTAD film, indicating better charge transport. More importantly, a significant enhancement in long-term stability was observed under a high humidity level (70%–80%). After 500 h of aging, the devices employing the FBT-Th4/ Cu_xO HTL maintained 90% of their initial efficiency.

Liu et al. proposed a simple surface modification strategy for low-cost and stable Cu_2O quantum dots (QDs) [146]. In this interesting study, Cu_2O QDs were modified by silane coupling agent (Fig. 3F) and directly deposited on the perovskite film as an HTL in an n-i-p structure. This approach facilitated an enhancement in the dispersion of Cu_2O QDs in nonpolar solvents, which

led to the formation of a high-quality HTL film without decomposing the perovskite film. As a result, surface-modified Cu₂O HTL-based devices showed an efficiency of 18.9% (stabilized output of 18.6%) (Fig. 3G and H). This PCE was somewhat higher than that of bare Cu₂O (11.9%), meanwhile a dramatic improvement in stability was also reported due to the presence of the functional groups of the silane coupling agent as compared to spiro-OMeTAD HTL-employed devices.

3.3 Delafossite oxides

Copper-based delafossite materials with the formula CuMO₂ (M: Al, Cr, Ga, etc.) are one of the most promising p-type semiconductor oxides with a wide band-gap [152]. The materials belonging to this group have high hole mobility due to their fully filled 3d orbital with an energy close to the O 2p orbital that delocalizes the holes at the valence band edge. Moreover, the layered structure of these materials provides high transparency with decreasing interaction between d¹⁰ electrons of Cu⁺ ions [153]. Apart from these properties, delafossite oxides also exhibit excellent chemical stability and proper energy band alignment with perovskites. Therefore delafossite oxides are considered to be favorable inorganic HTLs for PSCs. Table 3 summarizes the recent progress on photovoltaic performance of delafossite oxide HTL-employed PSCs based on different device configurations. The first use of delafossite oxides in PSCs was as an interfacial layer between the ITO electrode and PEDOT:PSS [154]. In that study, amorphous CuAlO₂ films of different thicknesses were formed on an ITO layer by the magnetron sputtering method. The effects of changing the electrical properties and work function of CuAlO₂ films on the photovoltaic properties of cells were investigated. The optimized cell was fabricated with 15 nm thick CuAlO₂ film and achieved an efficiency of 14.52%. In 2017, Zhang et al. fabricated a perovskite cell with a PCE of 18.51% by employing hydrothermally synthesized CuGaO₂ nanoplates as HTLs [156]. Configuration of the fabricated cell was n-i-p planar as shown in Fig. 4A. CuGaO₂ has been employed as an HTL due to its high hole mobility (10^{-2} – 10^1 cm² V⁻¹ s⁻¹) and suitable valence band maximum to extract holes from the perovskite layer as shown in Fig. 4B. Furthermore, small CuGaO₂ particles formed a dense CuGaO₂ film that completely covered the surface of perovskite film. Thicknesses of the TiO₂, perovskite, and CuGaO₂ films were 20, 320, and 345 nm, respectively. As shown in Fig. 4C and D, by utilizing CuGaO₂ as an HTL, both efficiency and stability of the cell were improved compared to the cell fabricated with spiro-OMeTAD. In 2018, CuGaO₂-based p-i-n perovskite cells were fabricated [94]. A surfactant-assisted hydrothermal method was used to synthesize ultrafine (~5 nm) CuGaO₂ nanoparticles. The efficiency of the CuGaO₂ HTL-based device was 15.3%, which was higher than that of the PEDOT:PSS-based device (9.3%). In 2018, CuGaO₂ was also used as a mesoporous HTL in mesoscopic p-i-n cells [94]. CuGaO₂ mesoporous film was coated on

TABLE 3 Recent progress in the photovoltaic performance of various delafossite oxide hole-transporting layers employing perovskite solar cells based on different device configurations.

Device architecture	J_{SC} (mA cm ⁻²)	V_{OC} (V)	FF	PCE (%)	References
ITO/a: CuAlO₂ (Spt)/PEDOT:PSS/MAPbI _{3-x} Cl _x /PCBM/Ag	22.0	0.88	0.75	14.5	[154]
ITO/ CuAlO₂/Cu-O (FSP)/MAPbI ₃ /PC ₇₀ BM/AZO/Al	19.1	1.07	0.80	16.3	[155]
FTO/TiO ₂ /MAPbI _{3-x} Cl _x / CuGaO₂ (SC)/Au	21.7	1.11	0.77	18.5	[156]
ITO/ CuGaO₂ (SC)/MAPbI ₃ /PC ₇₀ BM/Al	19.5	1.09	0.72	15.3	[157]
FTO/NiO _x / CuGaO₂ (SC)/CsFAPbI _{3-x} Br _x /PC ₆₁ BM /BCP/Ag	22.2	1.13	0.80	20.1	[158]
FTO/NiO _x / Zn:CuGaO₂ (SC)/CsFAPbI _{3-x} Br _x /PC ₆₁ BM/BCP/Ag	23.2	1.11	0.80	20.7	[159]
ITO/ CuCrO₂ (SC)/MAPbI ₃ /C ₆₀ /BCP/Ag	20.0	0.92	0.70	12.8	[160]
ITO/ CuCrO₂ (SC)/MAPbI ₃ /PCBM/BCP/Ag	21.9	1.07	0.81	19.0	[161]
FTO/c-TiO ₂ /mp-TiO ₂ /CsMAFAPbI _{3-x} Br _x / CuCrO₂ (SC)/Au	23.2	1.04	0.69	16.7	[62]
FTO/ Mg:CuCrO₂ (SC)/MAPbI ₃ /PCBM/BCP/Ag	18.4	1.00	0.71	13.1	[162]
ITO/ In:CuCrO₂ (SC)/CsMAFAPbI _{3-x} Br _x /PCBM:C ₆₀ /ZrAcaca/Ag	23.8	1.07	0.81	20.5	[163]
FTO/c-TiO ₂ /mp-TiO ₂ /CsMAFAPbI _{3-x} Br _x / CuFeO₂ (SC)/Au	23.6	1.01	0.65	15.6	[58]

FF, fill factor; *FSP*, flame spray pyrolysis; *PCE*, power conversion efficiency; *SC*, spin coating; *Spt*, sputtering.

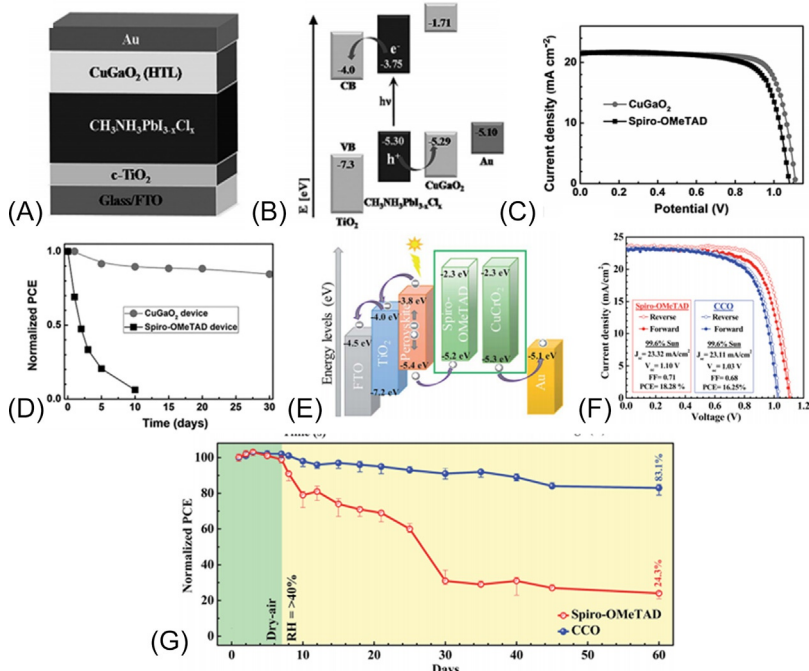


FIG. 4 (A) Schematic illustration. (B) Energy level diagram of CuGaO₂-based PSC. (C) *J-V* curves. (D) Evolution of normalized device performance under ambient environment CuGaO₂-based and reference cells. (E) Energy level diagram of spiro-OMeTAD- and CuCrO₂-based PSCs. (F) Forward and reverse *J-V* curves of CuCrO₂- and spiro-OMeTAD-based cells. (G) Time-dependent normalized PCE of CuCrO₂- and spiro-OMeTAD-based cells under ambient conditions. (Panel (D): Reproduced with permission H. Zhang, H. Wang, W. Chen, A. K. Jen, CuGaO₂: a promising inorganic hole-transporting material for highly efficient and stable perovskite solar cells, *Adv. Mater.* 29 (8) (2017) 1604984; Panel (E): Reproduced with permission S. Akin, Y. Liu, M.I. Dar, S.M. Zakeeruddin, M. Grätzel, S. Turan, S. Sonmezoglu, Hydrothermally processed CuCrO₂ nanoparticles as an inorganic hole transporting material for low-cost perovskite solar cells with superior stability, *J. Mater. Chem. A* 6 (41) (2018) 20327–20337; Panel (F): Reproduced with permission S. Akin, Y. Liu, M.I. Dar, S.M. Zakeeruddin, M. Grätzel, S. Turan, S. Sonmezoglu, Hydrothermally processed CuCrO₂ nanoparticles as an inorganic hole transporting material for low-cost perovskite solar cells with superior stability, *J. Mater. Chem. A* 6 (41) (2018) 20327–20337; Panel (G): Reproduced with permission S. Akin, Y. Liu, M.I. Dar, S.M. Zakeeruddin, M. Grätzel, S. Turan, S. Sonmezoglu, Hydrothermally processed CuCrO₂ nanoparticles as an inorganic hole transporting material for low-cost perovskite solar cells with superior stability, *J. Mater. Chem. A* 6 (41) (2018) 20327–20337.)

the surface of the electron beam-evaporated an NiO compact layer to fabricate an efficient HTL. For comparison, planar CuGaO₂-employing devices were also fabricated. It was observed that the increasing contact area of perovskite and CuGaO₂ using mesoporous film enabled hole injection effectively from the perovskite to CuGaO₂ compared to the planar device. As a result, the

efficiency of the best cell reached 20.13%. Moreover, the cell fabricated with mesoporous CuGaO₂ film retained more than 80% of its initial efficiency after thermal aging at 85°C for 1000 h in a nitrogen atmosphere.

The same research group utilized Zn-doped CuGaO₂ to fabricate p-i-n mesoscopic perovskite cells and reached 20.67% efficiency [95]. The efficiency of the cell fabricated with Zn-doped CuGaO₂ was higher than the cell with pure CuGaO₂ (20%). This improvement was explained by tuning the valence band to maximum, increasing the conductivity of CuGaO₂, and reducing interfacial trap states with Zn doping.

Another important copper-based delafossite is CuCrO₂. In 2018, three different research groups reported the application of hydrothermally synthesized CuCrO₂ nanoparticles as HTLs in p-i-n structure PSCs [160–162]. Among these studies, the highest efficiency was reported as 19% by Zhang et al. [161]. In addition, the efficiency of the NiO-based device that was fabricated for comparison was 17.1%. The improved efficiency was attributed to the superior hole-extraction capability of CuCrO₂, which enhanced the FF of the device. More importantly, the high UV light absorption ability of CuCrO₂ improved the photostability of the CuCrO₂-based device compared to the reference device.

In the same year, hydrothermally synthesized CuCrO₂ nanoparticles were used in n-i-p structure PSCs [62]. In this study, it was revealed that CuCrO₂ was one of the most important HTL candidates to replace spiro-OMeTAD due to its suitable valence band maximum as shown in Fig. 4E. Concentration of CuCrO₂ dispersion solution was optimized and a fully homogeneous film that covered the surface of the perovskite layer was obtained. The efficiency of the best cell with CuCrO₂ was 16.7% with negligible hysteresis. The CuCrO₂-based device also retained ~83% of its initial efficiency, while the spiro-OMeTAD-based reference devices preserved only 24%. Fig. 4F and G shows the J-V curves and the time evolution of normalized PCE for devices based on CuCrO₂ and spiro-OMeTAD, respectively. Moreover, cost estimation results revealed that CuCrO₂ is 180 times cheaper than spiro-OMeTAD.

Indium-doped CuCrO₂ nanoparticles were used as HTL in p-i-n structure perovskite cells [163]. It was found that p-type conductivity and transmittance of CuCrO₂ increased with indium doping due to the formation of more cation vacancies and less d-d transition. Therefore the efficiency of the device fabricated with indium-doped CuCrO₂ reached 20.54%, which was higher than the efficiency of the device constructed with pure sample (18.37%).

3.4 Other transition metal oxides

Except widely used transition metal oxides such as NiO_x, CuO, etc. as HTLs, there are several p-type conductive transition metal oxides such as CrO_x, VO_x, CO₃O₄, MoO_x, and WO_x that are also employed as HTLs in PSCs. Table 4 summarizes the recent progress on photovoltaic performance of some transition

TABLE 4 Recent progress in the photovoltaic performance of other transition metal oxide hole-transporting layers employing perovskite solar cells based on different device configurations.

Device architecture	J_{SC} (mA cm ⁻²)	V_{OC} (V)	FF	PCE (%)	References
FTO/ Cu:CrO_x (Spt)/ MAPbI ₃ /PCBM/Ag	16.0	0.98	0.70	11.0	[164]
ITO/ VO_x (SC)/MAPbI ₃ / PCBM/Al	22.3	0.90	0.71	14.3	[165]
ITO/ VO_x (SC)/MAPbI ₃ / PCBM/C ₆₀ /BCP/Al	20.8	1.02	0.56	11.7	[166]
ITO/ VO_x:0.3Cs (SC)/ MAPbI ₃ /PC ₆₁ BM/BCP/ Ag	20.7	0.92	0.76	14.5	[167]
FTO/ VO_x (SC)/MAPbI ₃ / PCBM/Al	20.3	0.96	0.74	14.5	[168]
FTO/c-TiO ₂ /m-TiO ₂ / MAPbI ₃ /ZrO ₂ / VO_x (DCa)/C	24.2	0.95	0.68	15.8	[66]
FTO/c-TiO ₂ /m-TiO ₂ / MAPbI ₃ /ZrO ₂ / Co₃O₄ (ScP)/C	23.4	0.88	0.64	13.3	[169]
ITO/SnO ₂ /CsPbI ₂ Br/ Co₃O₄ (ScP)/C	13.1	1.18	0.72	11.2	[170]
ITO/ MoO_x (SC)/ MAPbI ₃ /PCBM/C ₆₀ / BCP/Al	16.1	0.94	0.39	5.9	[166]
ITO/ WO_x (TE)/MAPbI ₃ / PCBM/Ag	16.6	0.93	0.64	9.8	[171]
ITO/ MoO_x (TE)/MAPbI ₃ / PCBM/Ag	18.8	0.99	0.71	13.1	[171]
ITO/ MoO_x (SC)/F4-TCNQ/MAPbI ₃ /PCBM/ BCP/Ag	20.1	1.06	0.76	16.3	[172]
ITO/C ₆₀ -SAM/FAMAPb (I,Br) ₃ /PDCBT/ Ta-WO_x (FSP) (SC)/Au	22.7	1.17	0.80	21.2	[173]

DCa, drop casting; FF, fill factor; FSP, flame spray pyrolysis; PCE, power conversion efficiency; SC, spin coating; ScP, screen printing; Spt, sputtering; TE, thermal evaporation.

metal oxide HTLs employing PSCs based on different device configurations. Among them, amorphous CrO_x in which chromium is in the 3+, 4+, and 6+ oxidation states exhibit promising p-type conductivity due to the chromium vacancies. In 2016, Qin et al. reported the fabrication of CrO_x and Cu-doped CrO_x -based p-i-n structure PSCs [164]. Pure and Cu-doped CrO_x films were manufactured by radio frequency sputtering. A cross-sectional scanning electron microscopy image of the fabricated cell is shown in Fig. 5A. It was observed that the Cu doping affected the chromium ion content and formation of surface hydroxylation in the CrO_x film. Therefore work function, electrical conductivity, and carrier mobility of CrO_x film were increased. Hence, the PCE

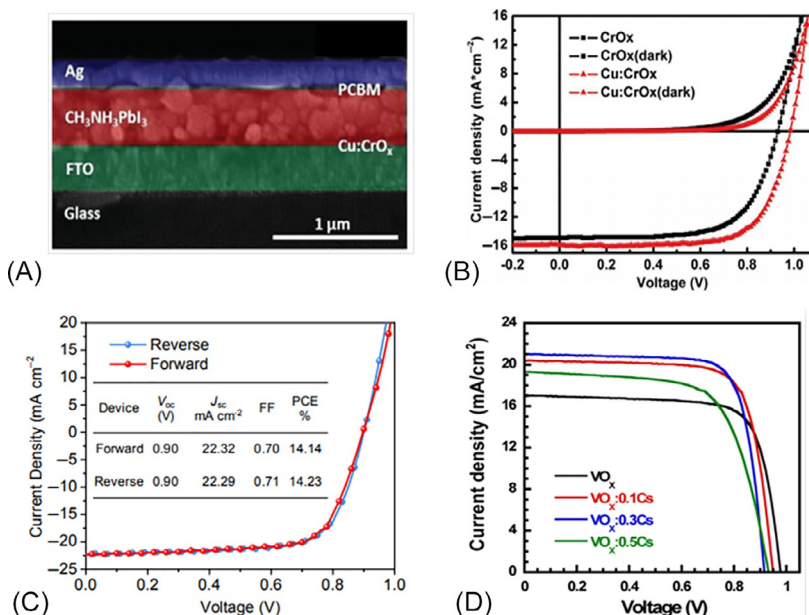


FIG. 5 (A) Cross-sectional SEM image of Cu:CrO_x-based PSC. (B) Dark and illuminated J-V curves of pure and Cu-doped CrO_x-based PSCs. (C) J-V curves of the VO_x-based champion cell. (D) J-V curves of pure and Cs-doped VO_x-based PSCs. (Panel (A): Reproduced with permission P.-L. Qin, H.-W. Lei, X.-L. Zheng, Q. Liu, H. Tao, G. Yang, W.-J. Ke, L.-B. Xiong, M.-C. Qin, X.-Z. Zhao, G.-J. Fang, Copper-doped chromium oxide hole-transporting layer for perovskite solar cells: interface engineering and performance improvement, *Adv. Mater. Interfaces* 3 (14) (2016) 1500799; Panel (B): Reproduced with permission P.-L. Qin, H.-W. Lei, X.-L. Zheng, Q. Liu, H. Tao, G. Yang, W.-J. Ke, L.-B. Xiong, M.-C. Qin, X.-Z. Zhao, G.-J. Fang, Copper-doped chromium oxide hole-transporting layer for perovskite solar cells: interface engineering and performance improvement, *Adv. Mater. Interfaces* 3 (14) (2016) 1500799; Panel (C): Reproduced with permission H. Sun, X. Hou, Q. Wei, H. Liu, K. Yang, W. Wang, Q. An, Y. Rong, Low-temperature solution-processed p-type vanadium oxide for perovskite solar cells, *Chem. Commun. (Camb.)* 52 (52) (2016) 8099–8102; Panel (D): Reproduced with permission X. Yao, J. Qi, W. Xu, X. Jiang, X. Gong, Y. Cao, Cesium-doped vanadium oxide as the hole extraction layer for efficient perovskite solar cells, *ACS Omega* 3 (1) (2018) 1117–1125.)

of the cell employing Cu-doped CrO_x reached 10.99%, which was higher than the cell with pure CrO_x as shown in Fig. 5B (9.27%).

VO_x is another important transition metal oxide with p-type conductivity, which has superior thermal and chemical stability. Application of the solution-processed VO_x thin film as an HTL in a PSC was reported by Snaith's group for the first time [121]. However, the efficiency of the cell was too low due to the poor perovskite film formation on the VO_x . Sun et al. deposited the compact and uniform perovskite film on low-temperature solution-processed VO_x film and obtained a PCE of 14.23% as shown in Fig. 5C [165]. Yao et al. utilized Cs-doped VO_x as an HTL to fabricate a p-i-n-structured PSC [167]. It was found that the cell constructed with $\text{VO}_x:0.3\text{Cs}$ demonstrated the best efficiency of 14.48% with higher J_{SC} and FF compared to the cell with pure VO_x as shown in Fig. 5D. This result was explained by increasing electrical conductivity and the formation of enlarged surface roughness, which enhanced interfacial adhesion between the VO_x layer and the perovskite film. In another study, Guo et al. used amorphous VO_x to replace PEDOT:PSS in p-i-n-structured perovskite cells [168]. The PCE of the fabricated cell with VO_x (14.5%) was lower than the cell with PEDOT:PSS (16.26%). On the other hand, after aging for 500h in an ambient environment, 65.7% of its initial PCE of VO_x -based cell was maintained, while the PEDOT:PSS-based cell retained only 42.2% of its initial PCE. VO_x was also used in printable carbon-based PSCs [66]. In that study, VO_x was employed to posttreat the interface of carbon and perovskite layers. The V_{OC} of the device with treated VO_x was improved from 0.89 to 0.92 V due to the high work function of VO_x ($\sim 5.39 \text{ eV}$) and provided suitable energy level alignment between layers and assisted in the charge transfer between perovskite and the carbon layer. Therefore the PCE of the carbon-based device reached 15.77% with VO_x treatment.

Co_3O_4 was another oxide that was employed as an HTL in carbon-based PSCs. Co_3O_4 has a conventional cubic spinel crystal structure and the valence band position of Co_3O_4 at 5.3 eV below the vacuum level is compatible with the perovskite layer. First, Bashir et al. applied chemical-precipitated Co_3O_4 nanoparticles as an interlayer between $\text{CH}_3\text{NH}_3\text{PbI}_3$ and carbon [169]. It was revealed that the Co_3O_4 interlayer improved the performance of the carbon-based cell from 11.25% to 13.27% by preventing charge recombination. Furthermore, the size of the cell was scaled up from 0.09 to 70 cm^2 and a PCE of 11% was obtained. In 2019, Co_3O_4 was utilized as an HTL in carbon-based CsPbI_2Br PSCs [170]. Similar to the previous works, preventing charge recombination at the CsPbI_2Br and carbon electrode interface with a Co_3O_4 interlayer improved the performance of the cell and a PCE of 11.21% was achieved with negligible hysteresis.

MoO_x and WO_x were also applied as an HTL alternative to PEDOT:PSS in inverted PSCs. Thermally evaporated MoO_x was used as an HTL in PCEs for the first time by Xiao et al. [166]. However, the efficiency of the MoO_x -based PSC was too low due to the high series resistance and mismatched work

function of MoO_x . In 2016, UV ozone-treated MoO_x and WO_x films were employed as an HTL in PSCs [171]. The PCEs of the MoO_x - and WO_x -based devices were 13.1% and 9.8%, respectively. Moreover, the MoO_x -based devices were more stable than the PEDOT:PSS-based devices. The better device performance with MoO_x was attributed to the higher hole-transporting and electron-blocking capability of UV ozone-treated MoO_x due to its suitable band alignment with perovskite. In the case of WO_x HTLs, Hou et al. reported a bilayered HTL structure based on tantalum-doped WO_x (Ta-WO_x) and a poly-thiophene derivative, poly[5,5'-bis(2-butylloctyl)-(2,2'-bithiophene)-4,4'-dicarboxylate-alt-5,5'-2,2'-bithiophene] (PDCBT) polymer [173]. This strategy not only decreased the energy barriers for good selectivity of charges but also reduced the resistivity to form quasi-ohmic contacts. As a result, a PCE over 21% and a considerable light-soaking stability over 1000 h were obtained with a thin coating of highly conductive Ta-WO_x film onto PDCBT.

4 Conclusions and future outlook

PSCs were developed very quickly over the last decade and have started to compete with other photovoltaic technologies. However, the usage of organic materials as HTLs adversely affects the stability of the PSCs. Hence, finding an alternative inorganic material to replace organic ones has received growing attention. Metal oxide semiconductors with p-type conductivity are most favorable candidates to replace organic HTLs in perovskite devices because of their high hole mobility, excellent chemical stability, low cost, and nontoxicity. Up to now, several metal oxides such as NiO_x , CuO , Cu_2O , delafossite oxides (CuAlO_2 , CuCrO_2 , CuGaO_2), CrO_x , VO_x , and Co_3O_4 have been employed. Especially, research has been focused on NiO_x and cells with PCEs of more than 20% have been fabricated by NiO_x . However, there are still drawbacks such as low intrinsic conductivity and/or unmatched energy levels that limit the efficiency of NiO -based PSCs. Recently, delafossite oxides have attracted much attention and been employed as HTLs in both n-i-p- and p-i-n-based PSCs. The PCE of the cells fabricated with metal cation-doped CuCrO_2 and CuGaO_2 -based cells reached 20%. More importantly, cells fabricated with delafossite oxides have been more stable than cells fabricated with organic HTLs. Consequently, replacing organic HTLs that are sensitive to moisture, oxygen, and high temperature with metal oxides will lead to the development of more stable PSCs. Further improving the PCEs of these cells with increasing conductivity of metal oxides and achieving better energy-level matching will pave the way for commercialization.

References

- [1] N. Abas, A. Kalair, N. Khan, Review of fossil fuels and future energy technologies, *Futures* 69 (2015) 31–49.

- [2] S. Yun, Y. Qin, A.R. Uhl, N. Vlachopoulos, M. Yin, D. Li, X. Han, A. Hagfeldt, New-generation integrated devices based on dye-sensitized and perovskite solar cells, *Energ. Environ. Sci.* 11 (3) (2018) 476–526.
- [3] NREL, Best Research Cell Efficiencies, (2019).
- [4] S. Hegedus, A. Luque, Achievements and challenges of solar electricity from photovoltaics, in: A. Luque, S. Hegedus (Eds.), *Handbook of Photovoltaic Science and Engineering*, John Wiley & Sons, Ltd, 2011, pp. 1–38.
- [5] D.M. Chapin, C.S. Fuller, G.L. Pearson, A new silicon p-n junction photocell for converting solar radiation into electrical power, *J. Appl. Phys.* 25 (5) (1954) 676–677.
- [6] W.C. Sinke, Development of photovoltaic technologies for global impact, *Renew. Energy* 138 (2019) 911–914.
- [7] J. Liu, M. Yao, L. Shen, Third generation photovoltaic cells based on photonic crystals, *J. Mater. Chem. C* 7 (11) (2019) 3121–3145.
- [8] A. Kojima, K. Teshima, Y. Shirai, T. Miyasaka, Organometal halide perovskites as visible-light sensitizers for photovoltaic cells, *J. Am. Chem. Soc.* 131 (17) (2009) 6050–6051.
- [9] J.H. Im, C.R. Lee, J.W. Lee, S.W. Park, N.G. Park, 6.5% efficient perovskite quantum-dot-sensitized solar cell, *Nanoscale* 3 (10) (2011) 4088–4093.
- [10] M.M. Lee, J. Teuscher, T. Miyasaka, T.N. Murakami, H.J. Snaith, Efficient hybrid solar cells based on meso-superstructured organometal halide perovskites, *Science* 338 (6107) (2012) 643–647.
- [11] L. Etgar, P. Gao, Z. Xue, Q. Peng, A.K. Chandran, B. Liu, M.K. Nazeeruddin, M. Gratzel, Mesoscopic $\text{CH}_3\text{NH}_3\text{PbI}_3/\text{TiO}_2$ heterojunction solar cells, *J. Am. Chem. Soc.* 134 (42) (2012) 17396–17399.
- [12] M. Liu, M.B. Johnston, H.J. Snaith, Efficient planar heterojunction perovskite solar cells by vapour deposition, *Nature* 501 (7467) (2013) 395–398.
- [13] J. Burschka, N. Pellet, S.J. Moon, R. Humphry-Baker, P. Gao, M.K. Nazeeruddin, M. Gratzel, Sequential deposition as a route to high-performance perovskite-sensitized solar cells, *Nature* 499 (7458) (2013) 316–319.
- [14] N.J. Jeon, J.H. Noh, Y.C. Kim, W.S. Yang, S. Ryu, S.I. Seok, Solvent engineering for high-performance inorganic-organic hybrid perovskite solar cells, *Nat. Mater.* 13 (9) (2014) 897–903.
- [15] N.J. Jeon, J.H. Noh, W.S. Yang, Y.C. Kim, S. Ryu, J. Seo, S.I. Seok, Compositional engineering of perovskite materials for high-performance solar cells, *Nature* 517 (7535) (2015) 476–480.
- [16] M. Saliba, T. Matsui, J.Y. Seo, K. Domanski, J.P. Correa-Baena, M.K. Nazeeruddin, S.M. Zakeeruddin, W. Tress, A. Abate, A. Hagfeldt, M. Gratzel, Cesium-containing triple cation perovskite solar cells: improved stability, reproducibility and high efficiency, *Energ. Environ. Sci.* 9 (6) (2016) 1989–1997.
- [17] Y.G. Rong, Y. Hu, A.Y. Mei, H.R. Tan, M.I. Saidaminov, S.I. Seok, M.D. McGehee, E.H. Sargent, H.W. Han, Challenges for commercializing perovskite solar cells, *Science* 361 (6408) (2018) eaat8235.
- [18] I. Mora-Seró, How do perovskite solar cells work? *Joule* 2 (4) (2018) 585–587.
- [19] A.K. Jena, A. Kulkarni, T. Miyasaka, Halide perovskite photovoltaics: background, status, and future prospects, *Chem. Rev.* 119 (5) (2019) 3036–3103.
- [20] M.I.H. Ansari, A. Qurashi, M.K. Nazeeruddin, Frontiers, opportunities, and challenges in perovskite solar cells: a critical review, *J. Photochem. Photobiol. C Photchem. Rev.* 35 (2018) 1–24.
- [21] M.J. Carnie, C. Charbonneau, M.L. Davies, J. Troughton, T.M. Watson, K. Wojciechowski, H. Snaith, D.A. Worsley, A one-step low temperature processing route for organolead halide perovskite solar cells, *Chem. Commun. (Camb.)* 49 (72) (2013) 7893–7895.

- [22] M.H. Kumar, N. Yantara, S. Dharani, M. Graetzel, S. Mhaisalkar, P.P. Boix, N. Mathews, Flexible, low-temperature, solution processed ZnO-based perovskite solid state solar cells, *Chem. Commun. (Camb.)* 49 (94) (2013) 11089–11091.
- [23] T. Baikie, Y. Fang, J.M. Kadro, M. Schreyer, F. Wei, S.G. Mhaisalkar, M. Graetzel, T.J. White, Synthesis and crystal chemistry of the hybrid perovskite $(\text{CH}_3\text{NH}_3)\text{PbI}_3$ for solid-state sensitised solar cell applications, *J. Mater. Chem. A* 1 (18) (2013) 5628–5641.
- [24] H.S. Kim, C.R. Lee, J.H. Im, K.B. Lee, T. Moehl, A. Marchioro, S.J. Moon, R. Humphry-Baker, J.H. Yum, J.E. Moser, M. Gratzel, N.G. Park, Lead iodide perovskite sensitized all-solid-state submicron thin film mesoscopic solar cell with efficiency exceeding 9%, *Sci. Rep.* 2 (2012) 591.
- [25] L.K. Ono, E.J. Juarez-Perez, Y. Qi, Progress on perovskite materials and solar cells with mixed cations and halide anions, *ACS Appl. Mater. Interfaces* 9 (36) (2017) 30197–30246.
- [26] A.R. Uhl, Metal counter electrodes for perovskite solar cells, in: S. Yun, A. Hagfeldt (Eds.), *Counter Electrodes for Dye-Sensitized and Perovskite Solar Cells*, Wiley-VCH Verlag GmbH & Co., 2018, pp. 421–456
- [27] L. Liang, Y. Cai, X. Li, M.K. Nazeeruddin, P. Gao, All that glitters is not gold: recent progress of alternative counter electrodes for perovskite solar cells, *Nano Energy* 52 (2018) 211–238.
- [28] S. Calnan, A.N. Tiwari, High mobility transparent conducting oxides for thin film solar cells, *Thin Solid Films* 518 (7) (2010) 1839–1849.
- [29] K.M. Reza, A. Gurung, B. Bahrami, S. Mabrouk, H. Elbohy, R. Pathak, K. Chen, A.H. Chowdhury, M.T. Rahman, S. Letourneau, H.-C. Yang, G. Saianand, J.W. Elam, S.B. Darling, Q. Qiao, Tailored PEDOT:PSS hole transport layer for higher performance in perovskite solar cells: enhancement of electrical and optical properties with improved morphology, *J. Energy Chem.* 44 (2020) 41–50.
- [30] K. Jiang, F. Wu, G. Zhang, P.C.Y. Chow, C. Ma, S. Li, K.S. Wong, L. Zhu, H. Yan, Inverted planar perovskite solar cells based on CsI-doped PEDOT:PSS with efficiency beyond 20% and small energy loss, *J. Mater. Chem. A* 7 (38) (2019) 21662–21667.
- [31] N. Arora, M.I. Dar, S. Akin, R. Uchida, T. Baumeler, Y. Liu, S.M. Zakeeruddin, M. Grätzel, Low-cost and highly efficient carbon-based perovskite solar cells exhibiting excellent long-term operational and UV stability, *Small* 15 (49) (2019) e1904746.
- [32] S. Akin, N. Arora, S.M. Zakeeruddin, M. Grätzel, R.H. Friend, M.I. Dar, New strategies for defect passivation in high-efficiency perovskite solar cells, *Adv. Energy Mater.* 10 (2019) 1903090.
- [33] G. Xing, N. Mathews, S. Sun, S.S. Lim, Y.M. Lam, M. Grätzel, S. Mhaisalkar, T.C. Sum, Long-Range Balanced Electron- and Hole-Transport Lengths in Organic-Inorganic $\text{CH}_3\text{NH}_3\text{PbI}_3$, *Science* 342 (6156) (2013) 344–347.
- [34] S.D. Stranks, G.E. Eperon, G. Grancini, C. Menelaou, M.J.P. Alcocer, T. Leijtens, L.M. Herz, A. Petrozza, H.J. Snaith, Electron-hole diffusion lengths exceeding 1 micrometer in an organometal trihalide perovskite absorber, *Science* 342 (6156) (2013) 341–344.
- [35] M.I. Dar, G. Jacopin, S. Meloni, A. Mattoni, N. Arora, A. Boziki, S.M. Zakeeruddin, U. Rothlisberger, M. Grätzel, Origin of unusual bandgap shift and dual emission in organic-inorganic lead halide perovskites, *Sci. Adv.* 2 (10) (2016) e1601156.
- [36] W.H. Ning, F. Wang, B. Wu, J. Lu, Z.B. Yan, X.J. Liu, Y.T. Tao, J.M. Liu, W. Huang, M. Fahlman, L. Hultman, T.C. Sum, F. Gao, Long electron-hole diffusion length in high-quality lead-free double perovskite films, *Adv. Mater.* 30 (20) (2018).
- [37] Q.F. Dong, Y.J. Fang, Y.C. Shao, P. Mulligan, J. Qiu, L. Cao, J.S. Huang, Electron-hole diffusion lengths $>175 \mu\text{m}$ in solution-grown $\text{CH}_3\text{NH}_3\text{PbI}_3$ single crystals, *Science* 347 (6225) (2015) 967–970.

- [38] N.G. Park, Perovskite solar cells: an emerging photovoltaic technology, *Mater. Today* 18 (2) (2015) 65–72.
- [39] L. Meng, J.B. You, Y. Yang, Addressing the stability issue of perovskite solar cells for commercial applications, *Nat. Commun.* 9 (2018) 1–4.
- [40] F.M. Li, M.Z. Liu, Recent efficient strategies for improving the moisture stability of perovskite solar cells, *J. Mater. Chem. A* 5 (30) (2017) 15447–15459.
- [41] B. Conings, J. Drijkoningen, N. Gauquelin, A. Babayigit, J. D'Haen, L. D'Olieslaeger, A. Ethirajan, J. Verbeeck, J. Manca, E. Mosconi, F. De Angelis, H.G. Boyen, Intrinsic thermal instability of methylammonium lead trihalide perovskite, *Adv. Energy Mater.* 5 (15) (2015) 1500477.
- [42] S. Akin, Y. Altintas, E. Mutlugun, S. Sonmezoglu, Cesium-lead based inorganic perovskite quantum-dots as interfacial layer for highly stable perovskite solar cells with exceeding 21% efficiency, *Nano Energy* 60 (2019) 557–566.
- [43] Y. Liu, S. Akin, L. Pan, R. Uchida, N. Arora, J.V. Milić, A. Hinderhofer, F. Schreiber, A.R. Uhl, S.M. Zakeeruddin, A. Hagfeldt, M.I. Dar, M. Grätzel, Ultrahydrophobic 3D/2D fluoroarene bilayer-based water-resistant perovskite solar cells with efficiencies exceeding 22%, *Sci. Adv.* 5 (6) (2019) eaaw2543.
- [44] S. Vidal, M. Izquierdo, S. Filippone, I. Fernandez, S. Akin, J.Y. Seo, S.M. Zakeeruddin, M. Gratzel, N. Martin, Site-selective synthesis of -[70]PCBM-like fullerenes: efficient application in perovskite solar cells, *Chem. A Eur. J.* 25 (13) (2019) 3224–3228.
- [45] W.C. Xiang, Z.W. Wang, D.J. Kubicki, W. Tress, J.S. Luo, D. Prochowicz, S. Akin, L. Emsley, J.T. Zhou, G. Dietler, M. Gratzel, A. Hagfeldt, Europium-doped CsPbI₂Br for stable and highly efficient inorganic perovskite solar cells, *Joule* 3 (1) (2019) 205–214.
- [46] S. Bai, P.M. Da, C. Li, Z.P. Wang, Z.C. Yuan, F. Fu, M. Kawecki, X.J. Liu, N. Sakai, J.T.W. Wang, S. Huettner, S. Buecheler, M. Fahlman, F. Gao, H.J. Snaith, Planar perovskite solar cells with long-term stability using ionic liquid additives, *Nature* 571 (7764) (2019) 245–250.
- [47] W.S. Yang, B.W. Park, E.H. Jung, N.J. Jeon, Y.C. Kim, D.U. Lee, S.S. Shin, J. Seo, E.K. Kim, J.H. Noh, S.I. Seok, Iodide management in formamidinium-lead-halide-based perovskite layers for efficient solar cells, *Science* 356 (6345) (2017) 1376–1379.
- [48] I. Poli, S. Eslava, P. Cameron, Tetrabutylammonium cations for moisture-resistant and semi-transparent perovskite solar cells, *J. Mater. Chem. A* 5 (42) (2017) 22325–22333.
- [49] Z.P. Wang, Q.Q. Lin, F.P. Chmiel, N. Sakai, L.M. Herz, H.J. Snaith, Efficient ambient-air-stable solar cells with 2D-3D heterostructured butylammonium-caesium-formamidinium lead halide perovskites, *Nat. Energy* 2 (9) (2017) 17135.
- [50] X.P. Zheng, B. Chen, J. Dai, Y.J. Fang, Y. Bai, Y.Z. Lin, H.T. Wei, X.C. Zeng, J.S. Huang, Defect passivation in hybrid perovskite solar cells using quaternary ammonium halide anions and cations, *Nat. Energy* 2 (7) (2017) 17102.
- [51] S.H. Wu, R. Chen, S.S. Zhang, B.H. Babu, Y.F. Yue, H.M. Zhu, Z.C. Yang, C.L. Chen, W.T. Chen, Y.Q. Huang, S.Y. Fang, T.L. Liu, L.Y. Han, W. Chen, A chemically inert bismuth interlayer enhances long-term stability of inverted perovskite solar cells, *Nat. Commun.* 10 (2019).
- [52] D. Saranin, P. Gostischev, D. Tatarinov, I. Ermanova, V. Mazov, D. Muratov, A. Tameev, D. Kuznetsov, S. Didenko, A. Di Carlo, Copper iodide interlayer for improved charge extraction and stability of inverted perovskite solar cells, *Materials* 12 (9) (2019).
- [53] D. Wei, H. Huang, P. Cui, J. Ji, S.Y. Dou, E.D. Jia, S. Sajid, M.Q. Cui, L.H. Chu, Y.F. Li, B. Jiang, M.C. Li, Moisture-tolerant supermolecule for the stability enhancement of organic-inorganic perovskite solar cells in ambient air, *Nanoscale* 11 (3) (2019) 1228–1235.

- [54] Y. Bai, S. Xiao, C. Hu, T. Zhang, X.Y. Meng, H. Lin, Y.L. Yang, S.H. Yang, Dimensional engineering of a graded 3D-2D halide perovskite interface enables ultrahigh V_{oc} enhanced stability in the p-i-n photovoltaics, *Adv. Energy Mater.* 7 (20) (2017) 1701038.
- [55] P. Chen, Y. Bai, S.C. Wang, M.Q. Lyu, J.H. Yun, L.Z. Wang, In situ growth of 2D perovskite capping layer for stable and efficient perovskite solar cells, *Adv. Funct. Mater.* 28 (17) (2018).
- [56] G. Grancini, C. Roldan-Carmona, I. Zimmermann, E. Mosconi, X. Lee, D. Martineau, S. Narbey, F. Oswald, F. De Angelis, M. Graetzel, M.K. Zakeeruddin, One-year stable perovskite solar cells by 2D/3D interface engineering, *Nat. Commun.* 8 (2017) 15684.
- [57] J. Chen, N.-G. Park, Inorganic hole transporting materials for stable and high efficiency perovskite solar cells, *J. Phys. Chem. C* 122 (25) (2018) 14039–14063.
- [58] B. Gil, A.J. Yun, Y. Lee, J. Kim, B. Lee, B. Park, Recent progress in inorganic hole transport materials for efficient and stable perovskite solar cells, *Electron. Mater. Lett.* 15 (5) (2019) 505–524.
- [59] S. Akin, F. Sadegh, S. Turan, S. Sonmezoglu, Inorganic CuFeO₂ delafossite nanoparticles as effective hole transport materials for highly efficient and long-term stable perovskite solar cells, *ACS Appl. Mater. Interfaces* 11 (48) (2019) 45142–45149.
- [60] N.H. Tiep, Z.L. Ku, H.J. Fan, Recent advances in improving the stability of perovskite solar cells, *Adv. Energy Mater.* 6 (3) (2016) 1501420.
- [61] J.-Y. Seo, H.-S. Kim, S. Akin, M. Stojanovic, E. Simon, M. Fleischer, A. Hagfeldt, S.M. Zakeeruddin, M. Grätzel, Novel p-dopant toward highly efficient and stable perovskite solar cells, *Energ. Environ. Sci.* 11 (10) (2018) 2985–2992.
- [62] S. Akin, Y. Liu, M.I. Dar, S.M. Zakeeruddin, M. Grätzel, S. Turan, S. Sonmezoglu, Hydrothermally processed CuCrO₂ nanoparticles as an inorganic hole transporting material for low-cost perovskite solar cells with superior stability, *J. Mater. Chem. A* 6 (41) (2018) 20327–20337.
- [63] H.-S. Kim, J.-Y. Seo, S. Akin, E. Simon, M. Fleischer, S.M. Zakeeruddin, M. Graetzel, A. Hagfeldt, Power output stabilizing feature in perovskite solar cells at operating condition: selective contact-dependent charge recombination dynamics, *Nano Energy* 61 (2019) 126–131.
- [64] C.D. Bailie, E.L. Unger, S.M. Zakeeruddin, M. Grätzel, M.D. McGehee, Melt-infiltration of spiro-OMeTAD and thermal instability of solid-state dye-sensitized solar cells, *Phys. Chem. Chem. Phys.* 16 (10) (2014) 4864–4870.
- [65] B. Li, Y.N. Zhang, L.Y. Zhang, L.W. Yin, Graded heterojunction engineering for hole-conductor-free perovskite solar cells with high hole extraction efficiency and conductivity, *Adv. Mater.* 29 (39) (2017) 1701221.
- [66] W.Q. Wu, Q. Wang, Y.J. Fang, Y.C. Shao, S. Tang, Y.H. Deng, H.D. Lu, Y. Liu, T. Li, Z.B. Yang, A. Gruverman, J.S. Huang, Molecular doping enabled scalable blading of efficient hole-transport-layer-free perovskite solar cells, *Nat. Commun.* 9 (2018) 1–8.
- [67] Y.S. Liu, Q. Chen, H.S. Duan, H.P. Zhou, Y. Yang, H.J. Chen, S. Luo, T.B. Song, L.T. Dou, Z.R. Hong, Y. Yang, A dopant-free organic hole transport material for efficient planar heterojunction perovskite solar cells, *J. Mater. Chem. A* 3 (22) (2015) 11940–11947.
- [68] Y. Zhang, C. Kou, J.J. Zhang, Y.H. Liu, W.H. Li, Z.S. Bo, M. Shao, Crosslinked and dopant free hole transport materials for efficient and stable planar perovskite solar cells, *J. Mater. Chem. A* 7 (10) (2019) 5522–5529.
- [69] Y. Li, K.R. Scheel, R.G. Clevenger, W. Shou, H. Pan, K.V. Kilway, Z.H. Peng, Highly efficient and stable perovskite solar cells using a dopant-free inexpensive small molecule as the hole-transporting material, *Adv. Energy Mater.* 8 (23) (2018).

- [70] K. Rakstys, C. Igci, M.K. Nazeeruddin, Efficiency vs. stability: dopant-free hole transporting materials towards stabilized perovskite solar cells, *Chem. Sci.* 10 (28) (2019) 6748–6769.
- [71] Q. Wang, C.C. Chueh, M. Eslamian, A.K.Y. Jen, Modulation of PEDOT:PSS pH for efficient inverted perovskite solar cells with reduced potential loss and enhanced stability, *ACS Appl. Mater. Interfaces* 8 (46) (2016) 32068–32076.
- [72] W. Hu, C.Y. Xu, L.B. Niu, A.M. Elseman, G. Wang, D. Yan, Y.Q. Yao, L. Liao, G.D. Zhou, Q.L. Song, High open-circuit voltage of 1.134 V for inverted planar perovskite solar cells with sodium citrate-doped PEDOT:PSS as a hole transport layer, *ACS Appl. Mater. Interfaces* 11 (24) (2019) 22021–22027.
- [73] L. Biessmann, L.P. Kreuzer, T. Widmann, N. Hohn, J.F. Moulin, P. Muller-Buschbaum, Monitoring the swelling behavior of PEDOT:PSS electrodes under high humidity conditions, *ACS Appl. Mater. Interfaces* 10 (11) (2018) 9865–9872.
- [74] R. Wang, M. Mujahid, Y. Duan, Z.K. Wang, J. Xue, Y. Yang, A review of perovskites solar cell stability, *Adv. Funct. Mater.* 29 (47) (2019) 1808843.
- [75] M. Huangfu, Y. Shen, G. Zhu, K. Xu, M. Cao, F. Gu, L. Wang, Copper iodide as inorganic hole conductor for perovskite solar cells with different thickness of mesoporous layer and hole transport layer, *Appl. Surf. Sci.* 357 (2015) 2234–2240.
- [76] Q. Wu, C. Xue, Y. Li, P. Zhou, W. Liu, J. Zhu, S. Dai, C. Zhu, S. Yang, Kesterite Cu₂ZnSnS₄ as a low-cost inorganic hole-transporting material for high-efficiency perovskite solar cells, *ACS Appl. Mater. Interfaces* 7 (51) (2015) 28466–28473.
- [77] N. Arora, M.I. Dar, A. Hinderhofer, N. Pellet, F. Schreiber, S.M. Zakeeruddin, M. Gratzel, Perovskite solar cells with CuSCN hole extraction layers yield stabilized efficiencies greater than 20%, *Science* 358 (6364) (2017) 768–771.
- [78] P. Qin, Q. He, D. Ouyang, G. Fang, W.C.H. Choy, G. Li, Transition metal oxides as hole-transporting materials in organic semiconductor and hybrid perovskite based solar cells, *Sci. China: Chem.* 60 (4) (2017) 472–489.
- [79] N.J. Jeon, H. Na, E.H. Jung, T.Y. Yang, Y.G. Lee, G. Kim, H.W. Shin, S.I. Seok, J. Lee, J. Seo, A fluorene-terminated hole-transporting material for highly efficient and stable perovskite solar cells, *Nat. Energy* 3 (8) (2018) 682–689.
- [80] G.D. Niu, X.D. Guo, L.D. Wang, Review of recent progress in chemical stability of perovskite solar cells, *J. Mater. Chem. A* 3 (17) (2015) 8970–8980.
- [81] N. Aristidou, I. Sanchez-Molina, T. Chotchuangchutchaval, M. Brown, L. Martinez, T. Rath, S.A. Haque, The role of oxygen in the degradation of methylammonium lead trihalide perovskite photoactive layers, *Angew. Chem. Int. Ed.* 54 (28) (2015) 8208–8212.
- [82] C. Wang, L. Yin, L. Zhang, D. Xiang, R. Gao, Metal oxide gas sensors: sensitivity and influencing factors, *Sensors (Basel)* 10 (3) (2010) 2088–2106.
- [83] M. Zheng, H. Tang, L. Li, Q. Hu, L. Zhang, H. Xue, H. Pang, Hierarchically nanostructured transition metal oxides for lithium-ion batteries, *Adv. Sci.* 5 (3) (2018) 1700592.
- [84] J.C. Védrine, Metal oxides in heterogeneous oxidation catalysis: state of the art and challenges for a more sustainable world, *ChemSusChem* 12 (3) (2019) 577–588.
- [85] S.S. Shin, S.J. Lee, S.I. Seok, Metal oxide charge transport layers for efficient and stable perovskite solar cells, *Adv. Funct. Mater.* 29 (47) (2019) 1900455.
- [86] S. Sajid, A.M. Elseman, H. Huang, J. Ji, S.Y. Dou, H.R. Jiang, X. Liu, D. Wei, P. Cui, M.C. Li, Breakthroughs in NiO_x-HTMs towards stable, low-cost and efficient perovskite solar cells, *Nano Energy* 51 (2018) 408–424.
- [87] X.W. Yin, Z.B. Yao, Q. Luo, X.Z. Dai, Y. Zhou, Y. Zhang, Y.Y. Zhou, S.P. Luo, J.B. Li, N. Wang, H. Lin, High efficiency inverted planar perovskite solar cells with solution-processed NiO_x hole contact, *ACS Appl. Mater. Interfaces* 9 (3) (2017) 2439–2448.

- [88] Z.H. Liu, A.L. Zhu, F.S. Cai, L.M. Tao, Y.H. Zhou, Z.X. Zhao, Q. Chen, Y.B. Cheng, H.P. Zhou, Nickel oxide nanoparticles for efficient hole transport in p-i-n and n-i-p perovskite solar cells, *J. Mater. Chem. A* 5 (14) (2017) 6597–6605.
- [89] X.B. Xu, Z.H. Liu, Z.X. Zuo, M. Zhang, Z.X. Zhao, Y. Shen, H.P. Zhou, Q. Chen, Y. Yang, M.K. Wang, Hole selective NiO contact for efficient perovskite solar cells with carbon electrode, *Nano Lett.* 15 (4) (2015) 2402–2408.
- [90] Z.L. Zhu, Y. Bai, T. Zhang, Z.K. Liu, X. Long, Z.H. Wei, Z.L. Wang, L.X. Zhang, J.N. Wang, F. Yan, S.H. Yang, High-performance hole-extraction layer of sol-gel-processed NiO nanocrystals for inverted planar perovskite solar cells, *Angew. Chem. Int. Ed.* 53 (46) (2014) 12571–12575.
- [91] J.Y. Jeng, K.C. Chen, T.Y. Chiang, P.Y. Lin, T.D. Tsai, Y.C. Chang, T.F. Guo, P. Chen, T.C. Wen, Y.J. Hsu, Nickel oxide electrode interlayer in $\text{CH}_3\text{NH}_3\text{PbI}_3$ perovskite/PCBM planar-heterojunction hybrid solar cells, *Adv. Mater.* 26 (24) (2014) 4107–4113.
- [92] L. Hu, J. Peng, W.W. Wang, Z. Xia, J.Y. Yuan, J.L. Lu, X.D. Huang, W.L. Ma, H.B. Song, W. Chen, Y.B. Cheng, J. Tang, Sequential deposition of $\text{CH}_3\text{NH}_3\text{PbI}_3$ on planar NiO film for efficient planar perovskite solar cells, *ACS Photonics* 1 (7) (2014) 547–553.
- [93] Y. Bai, H. Yu, Z.L. Zhu, K. Jiang, T. Zhang, N. Zhao, S.H. Yang, H. Yan, High performance inverted structure perovskite solar cells based on a PCBM:polystyrene blend electron transport layer, *J. Mater. Chem. A* 3 (17) (2015) 9098–9102.
- [94] X.T. Yin, M.D. Que, Y.L. Xing, W.X. Que, High efficiency hysteresis-less inverted planar heterojunction perovskite solar cells with a solution-derived NiO_x hole contact layer, *J. Mater. Chem. A* 3 (48) (2015) 24495–24503.
- [95] S. Yoon, D.W. Kang, Solution-processed nickel oxide hole transport layer for highly efficient perovskite-based photovoltaics, *Ceram. Int.* 44 (8) (2018) 9347–9352.
- [96] X.W. Guo, G.L. Luo, J. Liu, C. Liao, G. Wang, S.R. Li, A 16.5% efficient perovskite solar cells with inorganic NiO film as hole transport material, *IEEE J. Photovoltaics* 8 (4) (2018) 1039–1043.
- [97] F. Ye, H. Chen, F.X. Xie, W.T. Tang, M.S. Yin, J.J. He, E.B. Bi, Y.B. Wang, X.D. Yang, L.Y. Han, Soft-cover deposition of scaling-up uniform perovskite thin films for high cost-performance solar cells, *Energ. Environ. Sci.* 9 (7) (2016) 2295–2301.
- [98] S. Xiao, Y. Bai, X.Y. Meng, T. Zhang, H.N. Chen, X.L. Zheng, C. Hu, Y.Q. Qu, S.H. Yang, Unveiling a key intermediate in solvent vapor postannealing to enlarge crystalline domains of organometal halide perovskite films, *Adv. Funct. Mater.* 27 (12) (2017) 1604944.
- [99] L.J. Tang, X. Chen, T.Y. Wen, S. Yang, J.J. Zhao, H.W. Qiao, Y. Hou, H.G. Yang, A solution-processed transparent NiO hole-extraction layer for high-performance inverted perovskite solar cells, *Chem. A Eur. J.* 24 (12) (2018) 2845–2849.
- [100] Z.L. Zhu, Y. Bai, X. Liu, C.C. Chueh, S.H. Yang, A.K.Y. Jen, Enhanced efficiency and stability of inverted perovskite solar cells using highly crystalline SnO_2 nanocrystals as the robust electron-transporting layer, *Adv. Mater.* 28 (30) (2016) 6478–6484.
- [101] H. Zhang, J.Q. Cheng, F. Lin, H.X. He, J. Mao, K.S. Wong, A.K.Y. Jen, W.C.H. Choy, Pin-hole-free and surface-nanostructured NiO_x film by room-temperature solution process for high-performance flexible perovskite solar cells with good stability and reproducibility, *ACS Nano* 10 (1) (2016) 1503–1511.
- [102] Y. Hou, W. Chen, D. Baran, T. Stubhan, N.A. Luechinger, B. Hartmeier, M. Richter, J. Min, S. Chen, C.O.R. Quiroz, N. Li, H. Zhang, T. Heumueller, G.J. Matt, A. Osvet, K. Forberich, Z.G. Zhang, Y.F. Li, B. Winter, P. Schweizer, E. Specker, C.J. Brabec, Overcoming the interface losses in planar heterojunction perovskite-based solar cells, *Adv. Mater.* 28 (25) (2016) 5112–5120.

- [103] X.T. Yin, J. Liu, J.Q. Ma, C.X. Zhang, P. Chen, M.D. Que, Y.W. Yang, W.X. Que, C.M. Niu, J.Y. Shao, Solvothermal derived crystalline NiO_x nanoparticles for high performance perovskite solar cells, *J. Power Sources* 329 (2016) 398–405.
- [104] U. Kwon, B.G. Kim, D.C. Nguyen, J.H. Park, N.Y. Ha, S.J. Kim, S.H. Ko, S. Lee, D. Lee, H.J. Park, Solution-processible crystalline NiO nanoparticles for high-performance planar perovskite photovoltaic cells, *Sci. Rep.* 6 (2016) 30759.
- [105] M. Najafi, F. Di Giacomo, D. Zhang, S. Shanmugam, A. Senes, W. Verhees, A. Hadipour, Y. Galagan, T. Aernouts, S. Veenstra, R. Andriessen, Highly efficient and stable flexible perovskite solar cells with metal oxides nanoparticle charge extraction layers, *Small* 14 (12) (2018) 1702775.
- [106] Z.Y. Liu, J.J. Chang, Z.H. Lin, L. Zhou, Z. Yang, D.Z. Chen, C.F. Zhang, S.Z. Liu, Y. Hao, High-performance planar perovskite solar cells using low temperature, solution-combustion-based nickel oxide hole transporting layer with efficiency exceeding 20%, *Adv. Energy Mater.* 8 (19) (2018) 1703432.
- [107] W. Chen, F.Z. Liu, X.Y. Feng, A.B. Djurisic, W.K. Chan, Z.B. He, Cesium doped NiO_x as an efficient hole extraction layer for inverted planar perovskite solar cells, *Adv. Energy Mater.* 7 (19) (2017) 1700722.
- [108] J.B. You, L. Meng, T.B. Song, T.F. Guo, Y. Yang, W.H. Chang, Z.R. Hong, H.J. Chen, H.P. Zhou, Q. Chen, Y.S. Liu, N. De Marco, Y. Yang, Improved air stability of perovskite solar cells via solution-processed metal oxide transport layers, *Nat. Nanotechnol.* 11 (1) (2016) 75–81.
- [109] J.H. Lee, Y.W. Noh, I.S. Jin, S.H. Park, J.W. Jung, A solution-processed cobalt-doped nickel oxide for high efficiency inverted type perovskite solar cells, *J. Power Sources* 412 (2019) 425–432.
- [110] S.X. Wang, B.J. Zhang, D. Feng, Z.H. Lin, J.C. Zhang, Y. Hao, X.Y. Fan, J.J. Chang, Achieving high performance and stable inverted planar perovskite solar cells using lithium and cobalt co-doped nickel oxide as hole transport layers, *J. Mater. Chem. C* 7 (30) (2019) 9270–9277.
- [111] W. Chen, Y.H. Wu, J. Fan, A.B. Djurisic, F.Z. Liu, H.W. Tam, A. Ng, C. Surya, W.K. Chan, D. Wang, Z.B. He, Understanding the doping effect on NiO: toward high-performance inverted perovskite solar cells, *Adv. Energy Mater.* 8 (19) (2018).
- [112] W. Chen, Y.C. Zhou, L.J. Wang, Y.H. Wu, B. Tu, B.B. Yu, F.Z. Liu, H.W. Tam, G. Wang, A.B. Djurisic, L. Huang, Z.B. He, Molecule-doped nickel oxide: verified charge transfer and planar inverted mixed cation perovskite solar cell, *Adv. Mater.* 30 (20) (2018) 1800515.
- [113] M.L. Li, X.W. Xu, Y.M. Xie, H.W. Li, Y.H. Ma, Y.H. Cheng, S.W. Tsang, Improving the conductivity of sol-gel derived NiO_x with a mixed oxide composite to realize over 80% fill factor in inverted planar perovskite solar cells, *J. Mater. Chem. A* 7 (16) (2019) 9578–9586.
- [114] W. Chen, Y.C. Zhou, G.C. Chen, Y.H. Wu, B. Tu, F.Z. Liu, L. Huang, A.M.C. Ng, A.B. Djurisic, Z.B. He, Alkali chlorides for the suppression of the interfacial recombination in inverted planar perovskite solar cells, *Adv. Energy Mater.* 9 (19) (2019) 1803872.
- [115] K.C. Wang, P.S. Shen, M.H. Li, S. Chen, M.W. Lin, P. Chen, T.F. Guo, Low-temperature sputtered nickel oxide compact thin film as effective electron blocking layer for mesoscopic NiO/CH₃NH₃PbI₃ perovskite heterojunction solar cells, *ACS Appl. Mater. Interfaces* 6 (15) (2014) 11851–11858.
- [116] K. Yao, F. Li, Q.Q. He, X.F. Wang, Y.H. Jiang, H.T. Huang, A.K.Y. Jen, A copper-doped nickel oxide bilayer for enhancing efficiency and stability of hysteresis-free inverted mesoporous perovskite solar cells, *Nano Energy* 40 (2017) 155–162.

- [117] J.S. Sun, J.F. Lu, B. Li, L.C. Jiang, A.S.R. Chesman, A.D. Scully, T.R. Gengenbach, Y.B. Cheng, J.J. Jasieniak, Inverted perovskite solar cells with high fill-factors featuring chemical bath deposited mesoporous NiO hole transporting layers, *Nano Energy* 49 (2018) 163–171.
- [118] K. Cao, Z.X. Zuo, J. Cui, Y. Shen, T. Moehl, S.M. Zakeeruddin, M. Grazel, M.K. Wang, Efficient screen printed perovskite solar cells based on mesoscopic $\text{TiO}_2/\text{Al}_2\text{O}_3/\text{NiO}$ /carbon architecture, *Nano Energy* 17 (2015) 171–179.
- [119] B.A. Nejand, V. Ahmadi, H.R. Shahverdi, New physical deposition approach for low cost inorganic hole transport layer in normal architecture of durable perovskite solar cells, *ACS Appl. Mater. Interfaces* 7 (39) (2015) 21807–21818.
- [120] H. Sato, T. Minami, S. Takata, T. Yamada, Transparent conducting p-type NiO thin-films prepared by magnetron sputtering, *Thin Solid Films* 236 (1-2) (1993) 27–31.
- [121] P. Docampo, J.M. Ball, M. Darwich, G.E. Eperon, H.J. Snaith, Efficient organometal trihalide perovskite planar-heterojunction solar cells on flexible polymer substrates, *Nat. Commun.* 4 (2013) 2761.
- [122] B.A. Nejand, V. Ahmadi, H.R. Shahverdi, New physical deposition approach for low cost inorganic hole transport layer in normal architecture of durable perovskite solar cells, *ACS Appl. Mater. Interfaces* 7 (39) (2015) 21807–21818.
- [123] I.J. Park, G. Kang, M.A. Park, J.S. Kim, S.W. Seo, D.H. Kim, K. Zhu, T. Park, J.Y. Kim, Highly efficient and uniform 1 cm^2 perovskite solar cells with an electrochemically deposited NiO_x hole-extraction layer, *ChemSusChem* 10 (12) (2017) 2660–2667.
- [124] J.H. Park, J. Seo, S. Park, S.S. Shin, Y.C. Kim, N.J. Jeon, H.-W. Shin, T.K. Ahn, J.H. Noh, S.C. Yoon, C.S. Hwang, S.I. Seok, Efficient $\text{CH}_3\text{NH}_3\text{PbI}_3$ perovskite solar cells employing nanostructured p-Type NiO electrode formefd by a pulsed laser deposition, *Adv. Mater.* 27 (27) (2015) 4013–4019.
- [125] J.H. Kim, P.W. Liang, S.T. Williams, N. Cho, C.C. Chueh, M.S. Glaz, D.S. Ginger, A.K.Y. Jen, High-performance and environmentally stable planar heterojunction perovskite solar cells based on a solution-processed copper-doped nickel oxide hole-transporting layer, *Adv. Mater.* 27 (4) (2015) 695–701.
- [126] Y. Wei, K. Yao, X.F. Wang, Y.H. Jiang, X.Y. Liu, N.G. Zhou, F. Li, Improving the efficiency and environmental stability of inverted planar perovskite solar cells via silver-doped nickel oxide hole-transporting layer, *Appl. Surf. Sci.* 427 (2018) 782–790.
- [127] W. Chen, Y. Zhou, L. Wang, Y. Wu, B. Tu, B. Yu, F. Liu, H.W. Tam, G. Wang, A.B. Djurisic, L. Huang, Z. He, Molecule-doped nickel oxide: verified charge transfer and planar inverted mixed cation perovskite solar cell, *Adv. Mater.* 30 (20) (2018) e1800515.
- [128] Q.-D. Yang, J. Li, Y. Cheng, H.-W. Li, Z. Guan, B. Yu, S.-W. Tsang, Graphene oxide as an efficient hole-transporting material for high-performance perovskite solar cells with enhanced stability, *J. Mater. Chem. A* 5 (20) (2017) 9852–9858.
- [129] Y.X. Guo, X.T. Yin, W.X. Que, NiO_x mesoporous films derived from $\text{Ni(OH)}_{(2)}$ nanosheets for perovskite solar cells, *J. Alloys Compd.* 722 (2017) 839–845.
- [130] K.C. Wang, J.Y. Jeng, P.S. Shen, Y.C. Chang, E.W.G. Diau, C.H. Tsai, T.Y. Chao, H.C. Hsu, P.Y. Lin, P. Chen, T.F. Guo, T.C. Wen, P-type mesoscopic nickel oxide/organometallic perovskite heterojunction solar cells, *Sci. Rep.* 4 (2014) 4756.
- [131] Z.H. Liu, M. Zhang, X.B. Xu, F.S. Cai, H.L. Yuan, L.L. Bu, W.H. Li, A.L. Zhu, Z.X. Zhao, M.K. Wang, Y.B. Cheng, H.S. He, NiO nanosheets as efficient top hole transporters for carbon counter electrode based perovskite solar cells, *J. Mater. Chem. A* 3 (47) (2015) 24121–24127.

- [132] C.G. Morales-Guio, S.D. Tilley, H. Vrubel, M. Gratzel, X.L. Hu, Hydrogen evolution from a copper(I) oxide photocathode coated with an amorphous molybdenum sulphide catalyst, *Nat. Commun.* 5 (2014) 3059.
- [133] O. Langmar, C.R. Ganivet, G. de la Torre, T. Torres, R.D. Costa, D.M. Guldi, Optimizing CuO p-type dye-sensitized solar cells by using a comprehensive electrochemical impedance spectroscopic study, *Nanoscale* 8 (41) (2016) 17963–17975.
- [134] W.L. Yu, F. Li, H. Wang, E. Alarousu, Y. Chen, B. Lin, L.F. Wang, M.N. Hedhili, Y.Y. Li, K.W. Wu, X.B. Wang, O.F. Mohammed, T. Wu, Ultrathin Cu₂O as an efficient inorganic hole transporting material for perovskite solar cells, *Nanoscale* 8 (11) (2016) 6173–6179.
- [135] S. Chatterjee, A.J. Pal, Introducing Cu₂O thin films as a hole-transport layer in efficient planar perovskite solar cell structures, *J. Phys. Chem. C* 120 (3) (2016) 1428–1437.
- [136] S.S. Jeong, A. Mittiga, E. Salza, A. Masci, S. Passerini, Electrodeposited ZnO/Cu₂O heterojunction solar cells, *Electrochim. Acta* 53 (5) (2008) 2226–2231.
- [137] B.S. Li, K. Akimoto, A. Shen, Growth of Cu₂O thin films with high hole mobility by introducing a low-temperature buffer layer, *J. Cryst. Growth* 311 (4) (2009) 1102–1105.
- [138] C.T. Zuo, L.M. Ding, Solution-processed Cu₂O and CuO as hole transport materials for efficient perovskite solar cells, *Small* 11 (41) (2015) 5528–5532.
- [139] L. Liu, Q.Y. Xi, G. Gao, W. Yang, H. Zhou, Y.X. Zhao, C.Q. Wu, L.D. Wang, J.W. Xu, Cu₂O particles mediated growth of perovskite for high efficient hole-transporting-layer free solar cells in ambient conditions, *Sol. Energy Mater. Sol. Cells* 157 (2016) 937–942.
- [140] A. Savva, I.T. Papadas, D. Tsikritzis, G.S. Armatas, S. Kennou, S.A. Choulis, Room temperature nanoparticulate interfacial layers for perovskite solar cells via solvothermal synthesis, *J. Mater. Chem. A* 5 (38) (2017) 20381–20389.
- [141] H.X. Rao, S.Y. Ye, W.H. Sun, W.B. Yan, Y.L. Li, H.T. Peng, Z.W. Liu, Z.Q. Bian, Y.F. Li, C.H. Huang, A 19.0% efficiency achieved in CuOx-based inverted CH₃NH₃PbI_{3-x}Cl_x solar cells by an effective Cl doping method, *Nano Energy* 27 (2016) 51–57.
- [142] W.H. Sun, Y.L. Li, S.Y. Ye, H.X. Rao, W.B. Yan, H.T. Peng, Y. Li, Z.W. Liu, S.F. Wang, Z.J. Chen, L.X. Xiao, Z.Q. Bian, C.H. Huang, High-performance inverted planar heterojunction perovskite solar cells based on a solution-processed CuO_x, hole transport layer, *Nanoscale* 8 (20) (2016) 10806–10813.
- [143] Z.K. Yu, W.F. Fu, W.Q. Liu, Z.Q. Zhang, Y.J. Liu, J.L. Yan, T. Ye, W.T. Yang, H.Y. Li, H.Z. Chen, Solution-processed CuO_x as an efficient hole-extraction layer for inverted planar heterojunction perovskite solar cells, *Chin. Chem. Lett.* 28 (1) (2017) 13–18.
- [144] I.Y.Y. Bu, Y.S. Fu, J.F. Li, T.F. Guo, Large-area electrospray-deposited nanocrystalline Cu_xO hole transport layer for perovskite solar cells, *RSC Adv.* 7 (74) (2017) 46651–46656.
- [145] Y.X. Guo, H.W. Lei, L.B. Xiong, B.R. Li, G.J. Fang, An integrated organic-inorganic hole transport layer for efficient and stable perovskite solar cells, *J. Mater. Chem. A* 6 (5) (2018) 2157–2165.
- [146] C. Liu, X.Y. Zhou, S.M. Chen, X.Z. Zhao, S.Y. Dai, B.M. Xu, Hydrophobic Cu₂O quantum dots enabled by surfactant modification as top hole-transport materials for efficient perovskite solar cells, *Adv. Sci.* 6 (7) (2019) 1801169.
- [147] M.I. Hossain, F.H. Alharbi, N. Tabet, Copper oxide as inorganic hole transport material for lead halide perovskite based solar cells, *Sol. Energy* 120 (2015) 370–380.
- [148] G.A. Casas, M.A. Cappelletti, A.P. Cedola, B.M. Soucase, E.L.P.Y. Blanca, Analysis of the power conversion efficiency of perovskite solar cells with different materials as hole-transport layer by numerical simulations, *Superlattice. Microst.* 107 (2017) 136–143.

- [149] M. Yurddaskal, T. Dikici, E. Celik, Effect of annealing temperature on the surface properties and photocatalytic efficiencies of Cu₂O/CuO structures obtained by thermal oxidation of Cu layer on titanium substrates, *Ceram. Int.* 42 (15) (2016) 17749–17753.
- [150] D. Dhakal, K. Assim, H. Lang, P. Bruener, T. Grehl, C. Georgi, T. Waechtler, R. Ecke, S.E. Schulz, T. Gessner, Atomic layer deposition of ultrathin Cu₂O and subsequent reduction to Cu studied by *in situ* x-ray photoelectron spectroscopy, *J. Vac. Sci. Technol. A* 34 (1) (2016) 01A111.
- [151] L.C. Chen, Review of preparation and optoelectronic characteristics of Cu₂O-based solar cells with nanostructure, *Mater. Sci. Semicond. Process.* 16 (5) (2013) 1172–1185.
- [152] A.N. Banerjee, K.K. Chattopadhyay, Recent developments in the emerging field of crystalline p-type transparent conducting oxide thin films, *Prog. Cryst. Growth Charact. Mater.* 50 (1-3) (2005) 52–105.
- [153] N. Zhang, J. Sun, H. Gong, Transparent p-type semiconductors: copper-based oxides and oxychalcogenides, *Coatings* 9 (2) (2019) 137.
- [154] F. Igbari, M. Li, Y. Hu, Z.-K. Wang, L.-S. Liao, A room-temperature CuAlO₂ hole interfacial layer for efficient and stable planar perovskite solar cells, *J. Mater. Chem. A* 4 (4) (2016) 1326–1335.
- [155] A. Savva, I.T. Papadas, D. Tsikritzis, A. Ioakeimidis, F. Galatopoulos, K. Kapnisis, R. Fuhrer, B. Hartmeier, M.F. Oszajca, N.A. Luechinger, S. Kennou, G.S. Armatas, S.A. Choulis, Inverted Perovskite photovoltaics using flame spray pyrolysis solution based CuAlO₂/Cu-O hole-selective contact, *ACS Appl. Energy Mater.* 2 (3) (2019) 2276–2287.
- [156] H. Zhang, H. Wang, W. Chen, A.K. Jen, CuGaO₂: a promising inorganic hole-transporting material for highly efficient and stable perovskite solar cells, *Adv. Mater.* 29 (8) (2017) 1604984.
- [157] I.T. Papadas, A. Savva, A. Ioakeimidis, P. Eleftheriou, G.S. Armatas, S.A. Choulis, Employing surfactant-assisted hydrothermal synthesis to control CuGaO₂ nanoparticle formation and improved carrier selectivity of perovskite solar cells, *Mater. Today Energy* 8 (2018) 57–64.
- [158] Y. Chen, Z. Yang, S. Wang, X. Zheng, Y. Wu, N. Yuan, W.H. Zhang, S.F. Liu, Design of an Inorganic mesoporous hole-transporting layer for highly efficient and stable inverted perovskite solar cells, *Adv. Mater.* 30 (52) (2018) e1805660.
- [159] Y. Chen, Z. Yang, X. Jia, Y. Wu, N. Yuan, J. Ding, W.-H. Zhang, S. Liu, Thermally stable methylammonium-free inverted perovskite solar cells with Zn²⁺ doped CuGaO₂ as efficient mesoporous hole-transporting layer, *Nano Energy* 61 (2019) 148–157.
- [160] W.A. Dunlap-Shohl, T.B. Daunis, X. Wang, J. Wang, B. Zhang, D. Barrera, Y. Yan, J.W.P. Hsu, D.B. Mitzi, Room-temperature fabrication of a delafossite CuCrO₂ hole transport layer for perovskite solar cells, *J. Mater. Chem. A* 6 (2) (2018) 469–477.
- [161] H. Zhang, H. Wang, H. Zhu, C.-C. Chueh, W. Chen, S. Yang, A.K.Y. Jen, Low-temperature solution-processed CuCrO₂ hole-transporting layer for efficient and photostable perovskite solar cells, *Adv. Energy Mater.* 8 (13) (2018) 1702762.
- [162] S. Jeong, S. Seo, H. Shin, P-type CuCrO₂ particulate films as the hole transporting layer for CH₃NH₃PbI₃ perovskite solar cells, *RSC Adv.* 8 (49) (2018) 27956–27962.
- [163] B. Yang, D. Ouyang, Z. Huang, X. Ren, H. Zhang, W.C.H. Choy, Multifunctional synthesis approach of In:CuCrO₂ nanoparticles for hole transport layer in high-performance perovskite solar cells, *Adv. Funct. Mater.* 29 (34) (2019) 1902600.
- [164] P.-L. Qin, H.-W. Lei, X.-L. Zheng, Q. Liu, H. Tao, G. Yang, W.-J. Ke, L.-B. Xiong, M.-C. Qin, X.-Z. Zhao, G.-J. Fang, Copper-doped chromium oxide hole-transporting layer for perovskite solar cells: interface engineering and performance improvement, *Adv. Mater. Interfaces* 3 (14) (2016) 1500799.

- [165] H. Sun, X. Hou, Q. Wei, H. Liu, K. Yang, W. Wang, Q. An, Y. Rong, Low-temperature solution-processed p-type vanadium oxide for perovskite solar cells, *Chem. Commun. (Camb.)* 52 (52) (2016) 8099–8102.
- [166] M. Xiao, M. Gao, F. Huang, A.R. Pascoe, T. Qin, Y.-B. Cheng, U. Bach, L. Spiccia, Efficient perovskite solar cells employing inorganic interlayers, *ChemNanoMat* 2 (3) (2016) 182–188.
- [167] X. Yao, J. Qi, W. Xu, X. Jiang, X. Gong, Y. Cao, Cesium-doped vanadium oxide as the hole extraction layer for efficient perovskite solar cells, *ACS Omega* 3 (1) (2018) 1117–1125.
- [168] Q. Guo, C. Wang, J. Li, Y. Bai, F. Wang, L. Liu, B. Zhang, T. Hayat, A. Alsaedi, Z. Tan, Low-temperature solution-processed vanadium oxide as hole transport layer for efficient and stable perovskite solar cells, *Phys. Chem. Chem. Phys.* 20 (33) (2018) 21746–21754.
- [169] A. Bashir, S. Shukla, J.H. Lew, S. Shukla, A. Bruno, D. Gupta, T. Baikie, R. Patidar, Z. Akhter, A. Priyadarshi, N. Mathews, S.G. Mhaisalkar, Spinel Co_3O_4 nanomaterials for efficient and stable large area carbon-based printed perovskite solar cells, *Nanoscale* 10 (5) (2018) 2341–2350.
- [170] Y. Zhou, X. Zhang, X. Lu, X. Gao, J. Gao, L. Shui, S. Wu, J.M. Liu, Promoting the hole extraction with Co_3O_4 nanomaterials for efficient carbon-based CsPbI_2Br perovskite solar cells, *Solar RRL* 3 (4) (2019) 1800315.
- [171] Z.-L. Tseng, L.-C. Chen, C.-H. Chiang, S.-H. Chang, C.-C. Chen, C.-G. Wu, Efficient inverted-type perovskite solar cells using UV-ozone treated MoO_x and WO_x as hole transporting layers, *Sol. Energy* 139 (2016) 484–488.
- [172] L. Chen, Q. Xie, L. Wan, W. Zhang, S. Fu, H. Zhang, X. Ling, J. Yuan, L. Miao, C. Shen, X. Li, W. Zhang, B. Zhu, H.-Q. Wang, Solution-processed MoO_x hole-transport layer with F4-TCNQ modification for efficient and stable inverted perovskite solar cells, *ACS Appl. Energy Mater.* 2 (8) (2019) 5862–5870.
- [173] Y. Hou, X.Y. Du, S. Scheiner, D.P. McMeekin, Z.P. Wang, N. Li, M.S. Killian, H.W. Chen, M. Richter, I. Levcuk, N. Schrenker, E. Specker, T. Stubhan, N.A. Luechinger, A. Hirsch, P. Schmuki, H.P. Steinrück, R.H. Fink, M. Halik, H.J. Snaith, C.J. Brabec, A generic interface to reduce the efficiency-stability-cost gap of perovskite solar cells, *Science* 358 (6367) (2017) 1192–1197.

Chapter 9

Recent advancement in sustainable energy harvesting using piezoelectric materials

Noorhashimah Mohamad Nor^{a,b}, Hairul Hisham Hamzah^c, and Khairunisak Abdul Razak^{a,b}

^aSchool of Materials & Mineral Resources Engineering, Engineering Campus, Universiti Sains Malaysia, Nibong Tebal, Pulau Pinang, Malaysia, ^bNanoBiotechnology Research and Innovation (NanoBRI), Institute for Research in Molecular Medicine, Universiti Sains Malaysia, Gelugor, Pulau Pinang, Malaysia, ^cSchool of Chemical Sciences, Universiti Sains Malaysia, Gelugor, Pulau Pinang, Malaysia

1 Introduction to the piezoelectric effect

A piezoelectric energy harvester converts mechanical energy into electrical power and vice versa, and has attained great interest in powering electronic devices that offer advantages of unlimited lifetime supply of energy, pollution-free energy sources, low maintenance, and easy installation. The word “piezo” is adopted from the Greek word “*piezen*,” which means push/pressure, while “electric” refers to electricity. Generally, kinetic energy harvesting on piezoelectric materials converts movement in the form of vibration into electricity. There are a few types of vibrational energy harvester such as strain from beam elements, ocean waves, human motion, rotating machinery, and fluid flow [1–3].

Piezoelectric materials under mechanical strain or changes of dimension have the capability to produce electric polarization in the form of an electric field or voltage. The direction of field reverses when reversing the sign of the force (e.g., from tension to compression) [4, 5]. Examples of mechanical strain energy harvesters are harvesting energy from muscle extension, compression of vehicles on roadways, and heartbeat pressure. In mechanical strain energy harvesters, performance depends on a material’s electromechanical efficiency conversion and the extension/compression force induced.

Regarding vibration sources such as ocean waves, human motion, and rotating machinery, performance of the mechanical vibration energy harvester depends on the resonant frequency of the generator, frequency of ambient vibration, and a steady vibration source. There is a requirement for resonant

frequency matching between ambient vibration and resonant frequency of the generator. The mismatch causes reduction in output performance [6]. In fluid flow energy harvesting, fluid flow from water and wind induce vibrational energy harvesting. Thus the application of piezoelectric materials with fluid flow in water channels, pipelines, canals, rivers, and creeks is able to harness electrical energy [7].

2 Fundamentals and configurations of the piezoelectric effect

2.1 Piezoelectric transduction principle

The piezoelectric transduction principle is concerned with electric dipole moments in a crystalline solid material, which demonstrate charge separation. When piezoelectric materials are under mechanical stress, polarization is induced on the crystal lattice of the structure materials. Thus the electric field is produced across the piezoelectric material. In electrically neutral conditions (Fig. 1A), piezoelectric materials have balance charges between positive and negative charges. Under external forces (Fig. 1B), the charge balance is disturbed, which deforms the internal structure. Thus the positive and negative charges are separated producing a surface charge density that can be collected using electrodes. This means that the material is polarized [8].

Generally, piezoelectricity is determined based on three factors: the orientation of dipole density, the crystalline orientation, and the applied mechanical stress. In single-crystal materials, the axes of polarity are aligned in one direction and have symmetry charges. In contrast, polycrystalline materials have various regions within the materials in which polarity is not aligned and charges are not symmetrical. Thus polycrystalline materials are required to be heated up to Curie temperature to free the movement of the molecules. When a strong electric field is applied together with heating, all dipoles are forced to be aligned in one direction. These dipoles are permanently locked in the same arrangement and achieve permanent net polarization even after the electric field

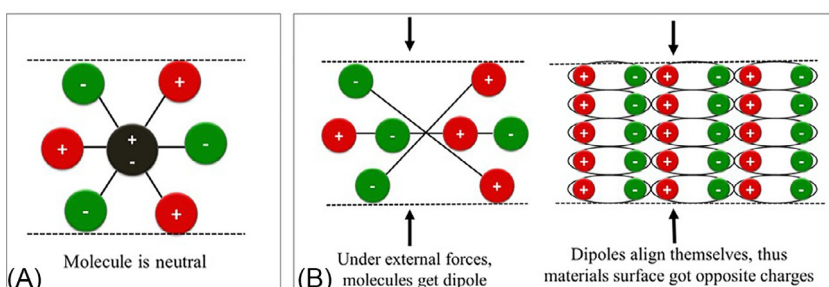


FIG. 1 Piezoelectric effect of the molecule: (A) In neutral condition, balance charges are separated between positive and negative, (B) under external forces, materials become polarized.

is removed [9]. Most energy-harvesting piezoelectric materials display well-defined polar axes. Normally in ferroelectric ceramic and polymeric materials, the polar axis determines the poling direction. For materials like aluminum nitride (AlN) or zinc oxide (ZnO), which are nonferroelectric, the crystal orientation determines the polar axis [10].

2.2 Piezoelectric operation modes

Mainly, there are two operation modes for a piezoelectric energy harvester, which are d_{31} and d_{33} . The d_{31} mode has a polarization direction in “3” and is perpendicular to the direction of applied stress, which is in “1,” as shown in Fig. 2A. d_{31} mode is the most frequent operation mode applied and is most commonly found in bending-beam structures. As for the d_{33} model (Fig. 2B), polarization and applied stress are in a similar direction and most commonly found in direct compressive/tensile harvesters or harvesters with an interdigitated electrode. In both operation modes (d_{31} and d_{33}), the electrodes are placed perpendicular to the poling direction, thus electric fields are aligned with polarization. There is another operation mode for piezoelectric energy harvesters, which is d_{15} . In d_{15} , the piezoelectric working principle is in a shear mode, which requires special treatment because the electrodes are formed on the surfaces that are parallel to the poling direction.

2.3 Structure of a piezoelectric energy harvester

Mainly, the output power generated by a piezoelectric energy harvester is controlled by the properties of the piezoelectric materials and their structure design. Three common structure designs have been reported in piezoelectric energy harvesters, which are cantilever, cymbal, and stack designs. Among these, the cantilever structure design is the most common structure design applied

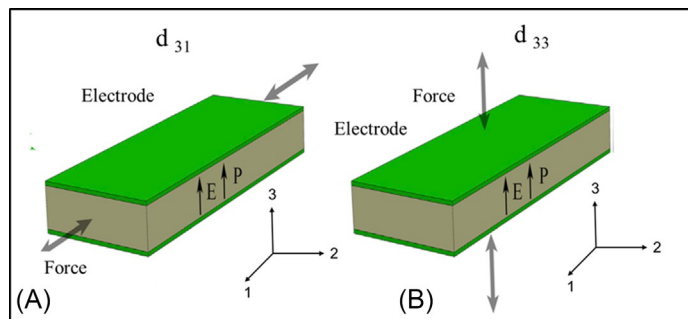


FIG. 2 The illustration of piezoelectric operation mode: (A) d_{31} mode and (B) d_{33} mode. (Reproduced with permission from Z. Yang, et al., High-performance piezoelectric energy harvesters and their applications, Joule 2 (2018) 642–697.)

in piezoelectric energy harvesters. The cantilever design offers simple and easy design, yet is able to generate larger mechanical strain during vibration and exhibit lower resonance frequency of fundamental flexural modes [11].

The unimorph cantilever and bimorph cantilever are the common structure designs used in piezoelectric energy harvesting. The unimorph cantilever consists of a layer of piezoelectric material combined with nonpiezoelectric materials or a substrate as shown in Fig. 3A. The bimorph cantilever consists of two layers of piezoelectric materials combined with the substrate in series or parallel connection (Fig. 3B). The main advantage of the bimorph cantilever design over the unimorph design is higher conversion efficiency of the piezoelectric energy harvester [10].

However, the cantilever structure design of the piezoelectric energy harvester is limited by its narrow resonant frequency band. A lower power conversion efficiency is generated if there is a deviation between the mechanical vibration frequency and natural device frequency. Therefore the higher conversion efficiency of the piezoelectric energy harvester is developed by the cymbal

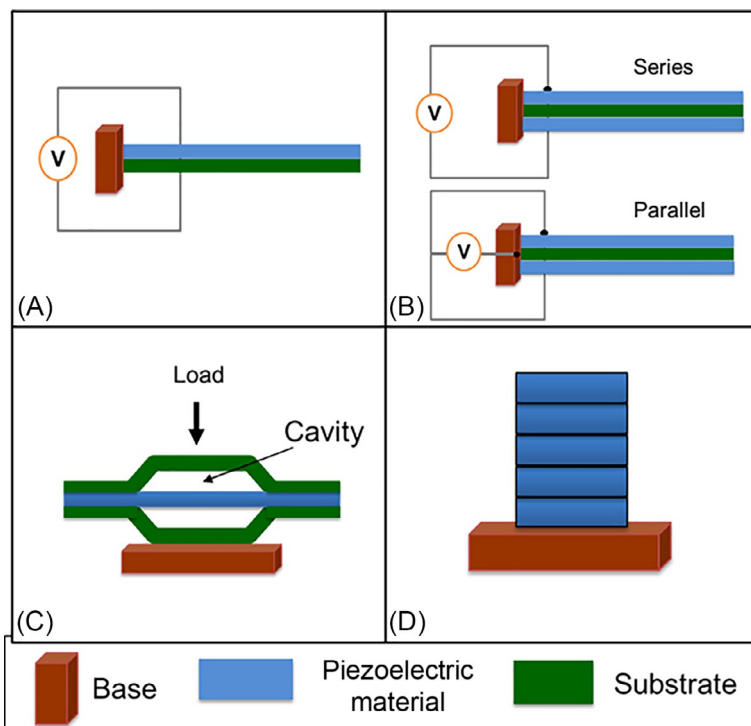


FIG. 3 Piezoelectric structure design: (A) Piezoelectric unimorph cantilever, (B) Piezoelectric bimorph cantilever in series and parallel configuration, (C) Piezoelectric cymbal, (D) Piezoelectric stack.

and stack structure designs. The cymbal structure (Fig. 3C) consists of piezoelectric materials sandwiched between two metal cymbal-shaped endcaps. The metal cap of the cymbal acts to improve the strength of the piezoelectric materials under high load and to amplify the piezoelectric coefficient. For stack piezoelectric energy harvester structure designs, a few layers of piezoelectric materials are stacked along the direction of the electric field (Fig. 3D). Higher output power in a high mechanical load can be obtained. The drawbacks of the cymbal and stack structure design of piezoelectric materials are the high stiffness and low sensitivity to the applied stress, which limit applications in low-amplitude natural environment energy harvesters [12].

3 Materials for a piezoelectric energy harvester

Generally, piezoelectric materials for energy harvesters can be grouped into a few categories [13]:

1. Piezoelectric ceramics: Lead zirconate titanate ($\text{Pb}(\text{Zr},\text{Ti})\text{O}_3$; PZT), lead metaniobate ($\text{Pb}(\text{NbO}_3)_2$), lead titanate (PbTiO_3), barium titanate (BaTiO_3), and potassium niobate (KNbO_3).
2. Piezoelectric polymer: Poly(vinylidene fluoride) (PVDF), poly(vinylidene fluoride-*co*-trifluoroethylene) (PVDF-TrFE), and polymer composite.
3. Piezoelectric green materials: Cellulose and chitosan.
4. Piezoelectric semiconductor materials: Zinc oxide (ZnO), gallium nitride (GaN), indium nitride (InN), molybdenum disulfide (MoS_2), and cadmium selenide (CdS).

Piezoelectric ceramics is the first class of materials explored for piezoelectric properties [14]. Among this class, lead-based piezoelectric ceramic materials are the most common piezoelectric materials explored and applied as energy harvesters due to their excellent properties of large quantities of piezoelectricity, good shaping flexibility, easy phase control, and relative low cost of manufacture. However, lead-based piezoelectric ceramic materials suffer limitations in terms of low tensile strength, high brittleness, and toxicity to the environment. Therefore lead-free piezoelectric materials have been explored to obtain comparable or better performance piezoelectric materials [15]. Piezoelectric polymers, green materials, and semiconductor materials have been studied for application in smart and integrated piezoelectric devices.

Piezoelectric materials for energy harvesting can also be classified based on their morphology such as bulk type, thin film, and nanostructured piezoelectric materials. Mainly, there are a lot of parameters that control the operating performance of piezoelectric materials as energy harvesters such as applied force, vibration frequency, acceleration, impedance matching, mass, environmental condition, materials composition, and structural design. Among all parameters, materials composition and structural design are commonly explored by researchers to improve piezoelectric material performance for energy

harvesting. Several structural designs have been explored, including cantilever type, cymbal type, and stack type [16]. In modifying the composition, doping has become an important strategy to accomplish high-performance piezoelectric ceramics by introducing appropriate donors to acceptors in the piezoelectric ceramic. Improved piezoelectric properties include the newly formed morphotropic phase boundary in the doped ceramics, which have high polarization [17]. Another important factor to maximize output power in piezoelectric energy harvesting is the matching frequency between vibrational frequency and natural frequency of the devices. If the applications of the piezoelectric material require higher frequency ($\sim 100\text{ Hz}$), higher stiffness piezoelectric ceramic materials are most suitable. In contrast, for lower-frequency application, piezoelectric polymers or piezoelectric polymer composites are more suitable. Table 1 summarizes the properties of common piezoelectric materials.

3.1 Lead-based piezoelectric ceramic materials

Among piezoelectric ceramic materials, PZT exhibits excellent properties and applicability as the piezoelectric material for energy harvesting. PZT constitutes a solid solution of PbZrO_3 and PbTiO_3 and has a perovskite crystal structure with ABO_3 compositional formula. The A-site location is filled with Pb ions and the B-site locations are randomly filled with zirconium (Zr) and titanium (Ti) ions. PZT is a polycrystalline material whose polarity is not aligned and whose charges are not symmetrical. A strong direct current electric field is applied together with heating at Curie temperature to align the polarity of PZT materials following the direction of the electric field [9]. The piezoelectric properties of PZT have a polarization value of $26.79\text{ }\mu\text{C/cm}^2$ and a high dielectric constant of 300–3850. PZT could be applied as biointerface mechanical probes, microelectromechanical systems (MEMS), actuators, and energy harvesters.

PZT with improved properties of piezoelectric charge constant (d), voltage constant (g), electromechanical coupling factor (k), and mechanical quality factor (Q_m) was explored by improving the composition, fabrications, and design. The vibration energy from the environment has a lower frequency (lower than 100 Hz), thus developed piezoelectric materials having high transduction coefficient ($d_{33} \times g_{33}$) is the key to improving the power generation capability of the piezoelectric energy harvester. This was achieved by modification of doping composition in piezoelectric ceramic materials.

Yu et al. [22] reported on an improved cantilever energy harvester in piezoelectric ceramic materials for charging an electrolytic capacitor that ignited blue light-emitting diodes (LEDs). A suitable amount of target doping of $(\text{Zn}_{0.1}\text{Ni}_{0.9})\text{TiO}_3$ (ZTN9) was introduced into PZT producing $0.2\text{Pb}(\text{Zn}_{1/3}\text{Nb}_{2/3})\text{O}_3\text{-}0.8\text{Pb}(\text{Zr}_{0.5}\text{Ti}_{0.5})\text{O}_3$ (PZN-PZT). The Ni^{2+} ions have a dual function, which is to replace the Zn^{2+} ions by entering the perovskite matrix and to produce a 0–3 a $\text{ZnO}/\text{perovskite}$ composite structure. This then improves the $d_{33} \times g_{33}$ value due to changes in the domain configuration to be more conducive with

TABLE 1 Summary of the properties of common piezoelectric materials.

Materials	d_{31}	d_{33}	g_{31}	g_{33}	k_{33}	Permittivity	Dielectric constant	Curie temperature	References
	10^{-12} C/N		10^{-3} Vm/N						
PZT	–97 to –274	225–590	–11	26	0.7	1200	1180	328	[9, 18]
BT	–78	149	5	14.1	0.48	1700	–	115	[19]
PVDF	23	–33	216	–330	0.15	12	10–15	100	[20]
Cellulose	1.8–30	5.7	–	–	–	–	–	–	[20]
ZnO	–	12.4	–	–	0.48	–	–	–	[21]

BT, barium titanate; PVDF, poly(vinylidene fluoride); PZT, lead zirconate titanate.

piezoelectricity. A higher $d_{33} \times g_{33}$ value ($12,433 \times 10^{-15} \text{ m}^2/\text{N}$) and high output power ($4.50 \mu\text{W}/\text{mm}^3$) at 1 g acceleration were produced compared to commercial PZT-based ceramic materials. The same group [23] reported on the doping of a PZN-PZT matrix with low dielectric constant (ϵ_r) material of Pb (In_{1/2}Nb_{1/2})O₃ (PIN) for igniting blue LEDs. Introducing PIN, which has a lower ϵ_r , decreased the ϵ_r of the quaternary system, thus stabilizing the d_{33} by domain refinement and consequently increasing the $d_{33} \times g_{33}$ value to $16,081 \times 10^{-15} \text{ m}^2/\text{N}$. The output power was also increased to $3.37 \mu\text{W}/\text{mm}^3$ at 1 g acceleration.

Another interesting work was reported by Lu et al. [24] on a magnetic energy harvester from a low-frequency (50/60 Hz) and low-amplitude magnetic field ($\leq 10 \text{ Oe}$) using a PZT/Ni unimorph cantilever with a permanent Nd magnet (NdFeB) as a tip mass. The output power density produced by the PZT/Ni-NdFeB magnetic harvester was $270 \mu\text{W}/\text{cm}^3$, which was higher than the PZT/Cu piezoelectric magnetic energy harvester ($11.73 \mu\text{W}/\text{cm}^3$) [25] and comparable to an expensive PMN-PZT single-crystal fiber/multilayer fetal bovine serum film cantilever energy harvester ($333 \mu\text{W}/\text{cm}^3$) [26]. The PZT/Ni-NdFeB magnetic harvester can be applied in wireless temperature or humidity sensors. As for application in shoe energy harvesting, Xie and Cai [27] reported on the prototype of 20 PZT-5H bimorphs with dimensions of $30 \times 15 \times 0.2 \text{ mm}^3$ inserted in the heels of shoes as shown in Fig. 4. The user load applied was 68 kg, which resulted in an output power of $0.41 \text{ mW}/\text{cm}^3$. Table 2 summarizes the recent properties of modified lead-based piezoelectric ceramic materials.

3.2 Lead-free piezoelectric ceramic materials

There is increasing research into utilizing lead-free piezoelectric ceramic materials for energy harvesting due to the toxic environmental effect of using lead-based piezoelectric ceramic materials. Examples of lead-free piezoelectric ceramic materials are barium titanate (BaTiO₃; BT) based-, sodium potassium niobate ((K,Na)NbO₃; KNN) based-, sodium bismuth titanate ((Bi_{1/2}Na_{1/2})TiO₃; BNT) based-ceramic systems, and bismuth layer-structured ferroelectrics. The first work on lead-free piezoelectric ceramic material was BT-based ceramic materials [32], which have low dielectric loss and stable electrical properties. The limitation of BT lies in low Curie temperature (120°C) and low d_{33} ($160 \times 10^{-12} \text{ C/N}$). Among all, KNN-based ceramics and BNT-based ceramics exhibit excellent piezoelectric energy-harvesting properties because they have high Curie temperatures (220–440°C) and high polarization.

Recently, lead-free (K_{0.48}Na_{0.52})(Nb_{0.97}Sb_{0.03})O₃-0.05Sr_x(Bi_{0.5}Na_{0.5})_(1-x)ZrO₃-0.15%Fe₂O₃ (KNNSb-Sr_xBNZ) ceramics have exhibited greater piezoelectric performance and stability [33]. This is because of denser microstructures and larger grain sizes obtained when appropriate content of Sr²⁺ induces grain growth. This results in large piezoelectric properties

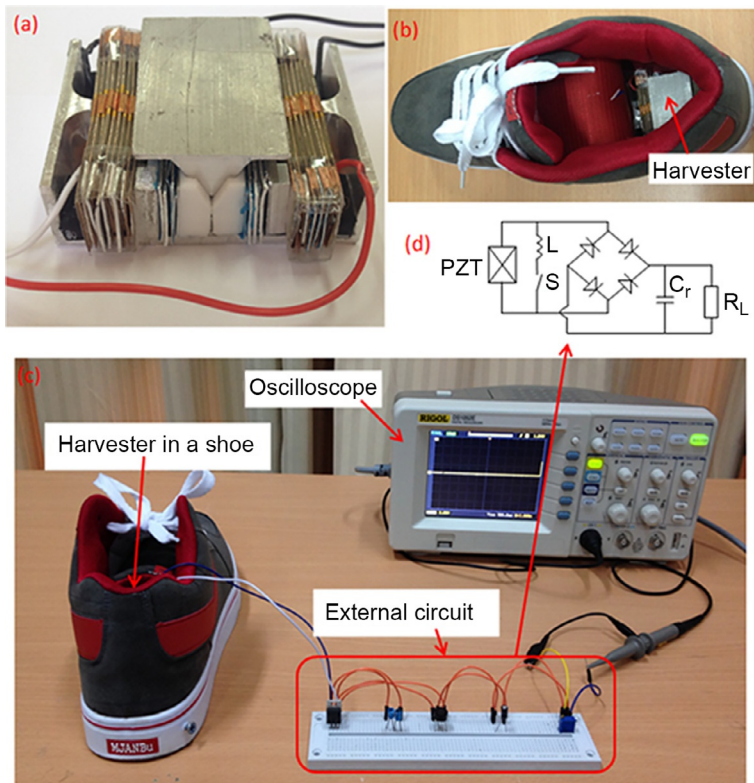


FIG. 4 (A) Prototype harvester used in the experiments. (B) Prototype harvester in a shoe. (C) Experimental setup. (D) Rectifying bridge and external electrical load. (*Reproduced with permission from L. Xie, M. Cai, Increased piezoelectric energy harvesting from human footstep motion by using an amplification mechanism, Appl. Phys. Lett. 105 (2014) 143901.*)

($d_{33}=470\text{ pC/N}$) and high Curie temperature (251°C) of the materials. KNNSb-Sr_xBNZ also has improved thermal stability in a wide temperature range.

Another interesting work was reported by Cheng et al. [34] where mixed balance cations ($\text{Mo}^{6+}/\text{Cr}^{3+}$) were used to modify $\text{CaBi}_2\text{Nb}_2\text{O}_9$ ceramics. The piezoelectric properties of the Mo/Cr-doped CBN-based ceramic exhibits high d_{33} (15 pC/N), high Curie temperature point (939°C), improved electrical resistivity ($3.33 \times 10^5 \Omega\text{ cm}$), decreased dielectric loss of $\tan \delta = 6.5\%$ at 600°C , and high-temperature stability. All the improvements in piezoelectric properties and thermal stability are caused by the replacement of Nb ion with Mo/Cr ion, thus leading to reduced oxygen vacancies and enhanced tetragonality in the lattice structure. Table 3 summarizes the recent properties of modified lead-free piezoelectric ceramic materials.

TABLE 2 Summary of recent properties of modified lead-based piezoelectric ceramic materials.

Materials	$d_{33} \times g_{33}$	Output power	Applications	References
ZTN9-PZN-PZT	$12,433 \times 10^{-15} \text{ m}^2/\text{N}$	$4.50 \mu\text{W/mm}^3$	LED	[22]
PIN-PZN-PZT	$16,081 \times 10^{-15} \text{ m}^2/\text{N}$	$3.37 \mu\text{W/mm}^3$	LED	[23]
PZT/Ni-NdFeB	–	$270 \mu\text{W/cm}^3$	Wireless temperature sensor	[24]
Bulk PZT	–	$1713.58 \mu\text{W/cm}^3$	MEMS	[28]
PEDOT:PSS/PZT	–	1.71 mW	Socks	[29]
20 PZT-5H bimorphs	–	0.41 mW/cm ³	Shoe	[27]
Stacked PZT-8	–	200 mW	Pavement	[30]
PZT	–	41.2 mW	Pavement	[31]

LED, light-emitting diode; *MEMS*, microelectromechanical systems; *PEDOT:PSS*, poly(3,4-ethylenedioxythiophene) polystyrenesulfonate; *PIN*, $\text{Pb}(\text{In}_{1/2}\text{Nb}_{1/2})\text{O}_3$; *PZN*, $2\text{Pb}(\text{Zn}_{1/3}\text{Nb}_{2/3})\text{O}_3$; *ZTN9*, $(\text{Zn}_{0.1}\text{Ni}_{0.9})\text{TiO}_3$.

3.3 Piezoelectric polymeric materials

Piezoelectric polymer materials are also referred to as organic lead-free piezoelectric materials. Piezoelectric polymer materials are commonly grouped based on their topology and dipole moment: bulk polymers, polymer composites, and voided charged polymers. In piezoelectric bulk polymers, the piezoelectric properties are determined based on the molecular structure. For voided charged polymers, the piezoelectric properties are determined by internal dipoles when the gas voids are charged with an electric field. The gas voids are present in its thin polymer layer. For piezoelectric polymer composites, the piezoelectric properties consist of a combination of piezoelectric properties in polymer materials and ceramic nanomaterials or metal oxides [13]. The most commonly explored piezoelectric polymers are poly(vinylidene fluoride) (PVDF) or its copolymer poly(vinylidene fluoride-*co*-trifluoroethylene) (PVDF-TrFE). PVDF has strong polarity, high d_{33} value (20–28 pC/N),

TABLE 3 Summary of the recent properties of modified lead-free piezoelectric ceramic materials.

Materials	d_{33}	Output voltage	Output power	Curie temperature	References
KNN _x Sb-Sr _x BNZ	470 pC/N	–	–	251	[33]
Mo/Cr-CBN	15 pC/N	–	–	939	[34]
Ba _{0.85} Ca _{0.15} Zr _{0.1} Ti _{0.9} O ₃ (BZCT) nanofibers	–	23.5 mV/g	2.95 μW	108	[35]
BT-carbon fiber cloth	–	23.5 mV/g	217 pW/cc	–	[36]
LiSbO ₃ -(Na _{0.5} K _{0.5})NbO ₃	143 pC/N	9.65 V	7.73 μW or 9.63 μW/cm ²	–	[37]

BT, barium titanate; CBN, CaBi₂Nb₂O₉; KNN_xSb-Sr_xBNZ, (K_{0.48}Na_{0.52})(Nb_{0.97}Sb_{0.03})O₃-0.05Sr_x(Bi_{0.5}Na_{0.5})_(1-x)ZrO₃-0.15%Fe₂O₃.

excellent mechanical flexibility, biocompatibility, and low acoustic impedance. However, piezoelectric polymer-based materials suffer limitations such as large leakage and low-temperature stability [38].

By improving the piezoelectric properties and thermal stability of PVDF, various types of nanofillers such as graphene, metal oxide materials, and piezoelectric ceramic materials are added to form piezoelectric composites [39–41]. Shin et al. [42] reported on piezoelectric composites based on hemispherical BT nanoparticles in a poly(vinylidene fluoride-*co*-hexafluoropropylene) (PVDF-HFP) polymer matrix. When a force is applied to the surface, BT-(PVDF-HFP) exhibits high piezoelectric power generation of 75 V and 15 μ A. This happens because the hemispherical BT improves the alignment of dipoles and provides a better structure for mechanical stress harvesting.

In another work [43], a flexible piezoelectric nanogenerator was developed based on a piezoelectric composite of 2D SnO₂ nanosheet/PVDF. The high surface area and uniform distribution of 2D SnO₂ nanosheet enhance the piezoelectric properties of the composite, with a d_{33} value of 36.52 pC/N, and can be applied to charge a 2.2 μ F capacitor. Table 4 summarizes the recent properties of modified piezoelectric polymeric materials.

3.4 Green materials

High concern arises in utilizing green materials for biodegradable piezoelectric energy harvesting. Nanocellulose and chitosan are the main piezoelectric green materials explored in environmentally friendly energy harvesters because of low production cost, good biodegradability, and they are a source of renewable materials. Cellulose is an abundant material and can be found in various sources, including seeds, wood, vegetables, and fruits. Chitosan is produced by the enzymatic reaction of chitin under alkaline conditions. Nowadays, cellulose nanofibrils, cellulose nanocrystals, and cellulose-based electroactive paper are widely explored for biodegradable piezoelectric energy harvesting [48].

Hänninen et al. [49] compared the piezoelectric properties of nanocellulose, microcrystalline chitosan, and their blend films. Plain chitosan showed optimum piezoelectric sensitivity (4 pC/N), while blend films showed the lowest sensitivity compared to the others. Overall, the piezoelectric responses for solvent cast films based on nanocellulose, microcrystalline chitosan, and their blends were in the range of 2–8 pC/N. Later, Zhang et al. [50] reported on a hybrid paper consisting of vanadium-doped ZnO (V-ZnO) microflowers in bacterial cellulose (BC) for application in flexible piezoelectric nanogenerators. The V-ZnO/BC hybrid paper showed ferroelectric property and became polarized when voltage was supplied. An output voltage of 1.5 V, current density of 80 nA/cm², and power density of 60 nW/cm² were obtained. The V-ZnO/BC hybrid paper also exhibited high mechanical strength and excellent flexibility,

TABLE 4 Summary of the recent properties of modified piezoelectric polymeric materials.

Materials	d_{33}	Power generation	Current generation	Output power	References
BT-(PVDF-HFP)	–	75 V	15 μ A	–	[42]
2D SnO ₂ nanosheet/PVDF	36.52 pC/N	–	–	–	[43]
ZnO NWs + paper	–	18 mV	35 nA	51 μ W/cm ²	[44]
PMN-PT+MWCNTs in silicone matrix	–	4 V	500 nA	–	[45]
PVDF fabric	20–30 pC/N	1.5 V	0.04 μ A	–	[46]
PET/EVA/PET	6300 pC/N	–	–	0.444 mW	[47]

BT, BaTiO₃; *HFP*, hexafluoropropylene; *MWCNTs*, multiwalled carbon nanotubes; *NWs*, nanowires; *PET/EVA/PET*, polyethylene terephthalate/ethylene-vinyl acetate; *PMN-PT*, Pb(Mg_{1/3}Nb_{2/3})O₃-PbTiO₃; *PVDF*, poly(vinylidene fluoride).

TABLE 5 Summary of the recent properties of modified piezoelectric green materials.

Materials	Output voltage	Output current	Output power	Applications	References
V-ZnO/BC	1.5V	80 nA/cm ²	60 nW/cm ²	Motion sensors	[50]
PVDF/polyaniline/graphitic-(g-C ₃ N ₄)	30V	3.7 μA	–	LEDs	[51]
P(VDF-TrFE)/ZnO/exfoliated GO	2.5V	0.23 nA	–	Wireless devices	[52]
(rGO)/P(VDF-TrFE)	89.7V	–	0.34 mW/cm ³	Biomedical devices	[53]

PVDF, poly(vinylidene fluoride); P(VDF-TrFE), poly(vinylidene fluoride-*co*-trifluoroethylene); V-ZnO/BC, vanadium-doped ZnO microflowers in bacterial cellulose.

thus is applicable as self-powered motion sensors. Table 5 summarizes the recent properties of modified piezoelectric green materials.

3.5 Semiconductors

Zinc oxide (ZnO), gallium nitride (GaN), indium nitride (InN), molybdenum disulfide (MoS₂), and cadmium selenide (CdS) from the wurzite family are classified as piezoelectric semiconductor materials. The noncentral symmetry of ion polarization in the crystal creates piezoelectric potential (piezopotential) in the crystal structure when stress is applied. The piezopotential created in the crystal is used for controlling or adjusting charge carrier transport behavior across a metal/semiconductor interface or a p-n junction. This process is called the piezotronic effect [54]. The piezotronic effect is commonly applied in the development of innovative devices such as piezoelectric diodes, nanogenerators, field-effect transistors, and piezoelectric chemical sensors.

Meanwhile, the piezophotronic effect is used for controlling and adjusting electrooptical processes by strain-induced piezopotential. The piezophotronic effect involves three combination effects: piezoelectricity, semiconductor transport, and photonic excitation. In the piezophototronic effect, the piezopotential gains from mechanical straining induce photon emission. In phototronic devices, the piezoelectric effect broadens the Schottky height barrier, while photon excitation lowers the Schottky barrier due to the increase in the local

carrier density, resulting in modification of optoelectronic processes. Generally, the piezophototronic effect causes an adjusting process for piezoelectric polarization charges in the p-n junction, thus inducing carrier separation, recombination, and transport to occur. The piezophothronic effect is commonly applied in optoelectronic devices such as solar cells, LEDs, and photon detectors [55].

The sandwich structure of a ZnO nanorod array-patterned textile piezoelectric nanogenerator for energy harvesting (ZnO-T-PET) was studied based on human movement [56]. The developed ZnO-T-PET was able to harvest energy from human movement in hand clapping and finger bending with output voltages of 4 and 0.8 V and output current of 20 and 5 nA. Thus ZnO-T-PET is able to be applied in wearable electronics. Zhao et al. [57] reported on the excellent piezoelectric performance for mechanical energy harvesting based on multiple layers of MoS₂ nanosheets on TiO₂ nanorods (MoS₂@TiO₂ NR). Excellent piezoelectric properties with a maximum power value of 15 μW/cm², output piezoelectric voltage of 34 V, and current density of 1.37 μA/cm² were achieved due to the multiple layers of a heterostructure of MoS₂@TNr due to highly exposed active edge sites of MoS₂ nanosheets. Table 6 summarizes the recent properties of modified piezoelectric semiconductor materials.

4 Recent applications of energy harvesters

Nowadays, the piezoelectric energy harvester is widely explored in sensors, biomedical applications, wearable devices, and wireless sensor networks. Using piezoelectric energy-harvesting technology has eliminated the need for devices to depend on conventional electrochemical batteries. However, the main

TABLE 6 Summary of the recent properties of modified piezoelectric semiconductor materials.

Materials	Output voltages	Output current	Output power	Applications	References
ZnO textiles	4 V, 0.8 V	20 nA, 5 nA	–	Wearable electronic	[56]
MoS ₂ @TiO ₂ NR	34 V	1.37 μA/cm ²	15 μW/cm ²	Nanogenerator	[57]
ZnO ₂ -PDMS	20 V		20 μW	LEDs	[58]
NiO/GaN	30 V	1.43 μA	–	Air flow/vibration energy	[59]

NR, nanorod; *PDMS*, polydimethylsiloxane.

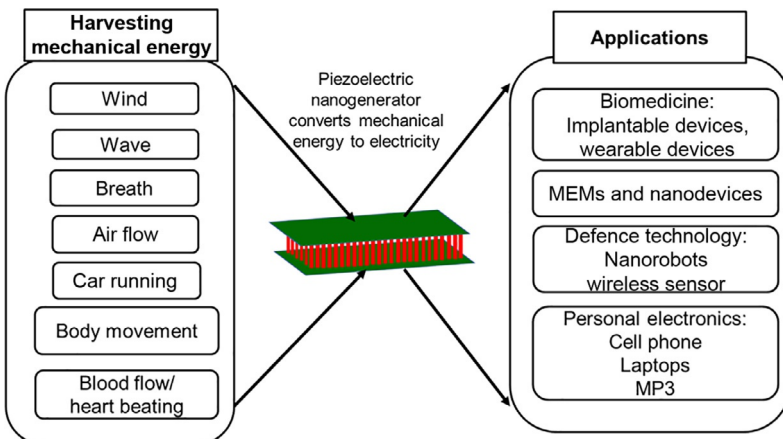


FIG. 5 Possible applications of piezoelectric materials in sensing and energy harvesting.

challenge in piezoelectric energy harvesting is the small amount of energy produced, which is insufficient to directly power electronic devices. Therefore vast research is now aimed at magnifying the energy to self-power electronic devices. Fig. 5 shows the possible applications of piezoelectric materials in sensing and energy harvesting.

4.1 Sensors

The piezoelectric sensor is the device that converts vibrational energy into an electrical signal in the form of voltage under physical strain. Physical strain includes acceleration, pressure, or force. Piezoelectric sensors can be applied in various applications such as biosensors, gas sensors, pressure sensors, and MEMS sensors. Much research has developed applications of piezoelectric material energy harvesters in MEMS sensors due to low power source ($\sim\mu\text{W}$) requirements in MEMS devices [60].

Rashmi et al. [61] reported on a vibration sensor and piezoelectric energy harvester using unimorph d_{33} mode P(VDF-TrFE) microcantilever beams based on novel MEMS Si bulk micromachining. The P(VDF-TrFE) microcantilever beams were developed with $2.5\ \mu\text{m}$ thickness together with a thin film of Cr-Au interdigitated electrodes for power extraction. The P(VDF-TrFE) microcantilever exhibits a lower resonance frequency (477.12Hz and power output of 187.38 pW), and is thus suitable for application in low-frequency energy harvesters and vibration sensors. Previously, Yu et al. [62] reported the application of PVDF film in a flexible piezoelectric tactile sensor array. The device has excellent performance in terms of linearity, low coupling effect, and works under normal and shear loads ranging from 5 to 400Hz.

4.2 Biomedical applications

4.2.1 *Implantable devices*

Implantable medical devices help to improve the quality of human life and prolong patients' lives. The disadvantage of current implantable electronic devices is their lifespan due to the dependency of medical devices on electrochemical batteries. The depletion of electrochemical battery power over time requires the replacement of new implantable electronic devices. Thus the application of piezoelectric materials as energy harvesters from body motions is interesting to improve the lifespan of medical devices and reduce the cost of medical device maintenance. Most of the implantable medical devices need only micro-level energy power (5–10 µW). This can be supplied by harvesting energy from body activity. Mainly, three excitation sources have been studied for energy harvesters in pacemakers: heartbeats, blood pressure gradients, and arterial wall deformation.

In developing implantable medical devices, high flexibility and good biocompatible materials are important criteria. Kim et al. [63] reported on a single-crystal PMN-PZT-Mn thin film *in vivo* tested on a pig heart. The PMN-PZT-Mn thin film exhibits an output voltage of 17.8 V and an output current of 1.75 mA. Zhang et al. [64] conducted theoretical, *in vitro* and *in vivo* studies on feasibility and efficacy of PVDF material to generate electric power using the pulsating energy of an ascending aorta with a flexible and implantable piezoelectric generator. The output power density produced was 170 nW/cm³ in the *in vitro* study.

4.2.2 *Wearable devices*

Commonly, wearable devices harvest energy from human activities: walking, running, breathing, and typing. Thus the amount of energy that can be harvested depends on the amount of energy produced from body movement. Coaxially aligned multiwalled carbon nanotubes (MWCNTs) have improved the performance of P(VDF-TrFE) fibrous membranes for wearable piezoelectric devices [65]. The coaxially aligned MWCNTs have improved the mechanical-to-electrical conversion rate with output voltage and output current of 18.23 V and 2.14 µA, respectively. Fig. 6 shows the schematic structure, appearance, conversion of mechanical to electrical performance, and mechanism of the non-monotonic evolution on the output in an MWCNT/P(VDF-TrFE) piezoelectric nanogenerator device.

4.3 Wireless sensor nodes

Advancement in low-power electronic devices and wireless sensor networks may require the application of piezoelectric materials as the energy harvester. Generally, the components of wireless sensor networks are low-power microcontroller unit, radio-frequency transceiver, and MEMS-based sensor. Each

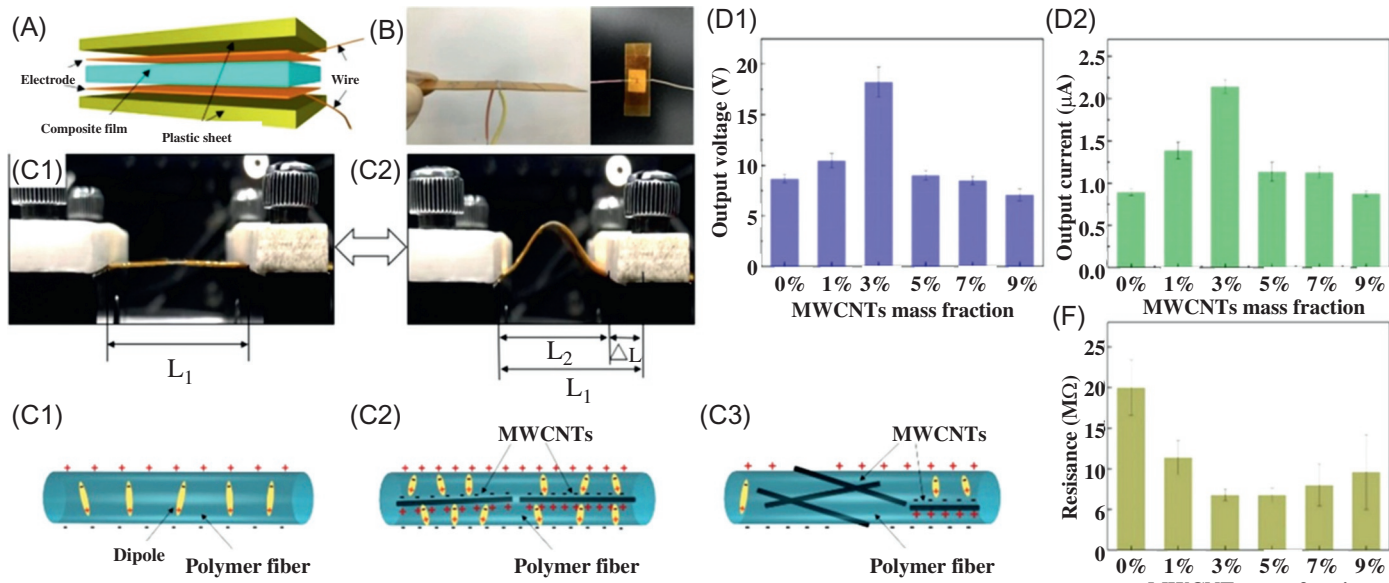


FIG. 6 (A) Schematic drawing of the structure of MWCNT/P(VDF-TrFE) NG devices. Photos of NG devices (B) in appearance, (C1) under releasing mode, (C2) under bending mode in the mechanical-to-electrical conversion measurement. The average peak values of (D1) voltage and (D2) current as a function of MWCNT content. The schematic drawing of dipole and inductive charge distribution inside the nanofibers of (E1) neat P(VDF-TrFE), (E2) low-loading samples, and (E3) high-loading samples. (F) The electric resistance of the MWCNT/P(VDF-TrFE) fibrous membranes. (*Reproduced with permission from C. Zhao, et al., Coaxially aligned MWCNTs improve performance of electrospun P(VDF-TrFE)-based fibrous membrane applied in wearable piezoelectric nanogenerator, Compos. Part B Eng. 178 (2019) 107447.*)

node is responsible for collecting and transmitting data via a radio link. Conventionally, a wireless sensor network is powered by chemical batteries. Therefore utilizing the piezoelectric materials as an energy harvester in a wireless sensor network is interesting to prolong the lifespan of the wireless sensor network. Xu et al. [66] developed a PZT nanowire array as the power source for wireless microelectronics. The PZT nanowire exhibits an output voltage of 0.7 V, a current density of $4\mu\text{A}/\text{cm}^2$, and an average power density of $2.8\text{mW}/\text{cm}^3$. Table 7 summarizes the recent applications of piezoelectric materials.

4.4 Limitation and challenges

Piezoelectric energy harvesters have been widely explored in the applications of sensors, biomedical applications, wearable devices, and wireless sensor networks. However, several limitations need to be resolved for the reliability of these energy harvesters as follows:

1. Maintain the mechanical and geometrical stability of a piezoelectric energy harvester to generate excellent and consistent output power transmission.
2. Ensure excellent biocompatibility of the piezoelectric energy harvester for long-term stability and durability of the materials in biomedical applications.
3. Improve the piezoelectric constant of the organic material and produce high-output power performance.
4. Produce high flexibility of piezoelectric material to fit an organ's shape, therefore excellent device performance for energy harvesting can be produced.
5. Improve dissolution rate of some biodegradable piezoelectric polymers to avoid fast degradation rate.

5 Piezoelectrochemical processes for energy harvesting

Because piezoelectricity can be generated by using various solid materials such as quartz, ceramics, biological matter, and metal oxides through accumulating electric charges at the substrate surfaces, subject to mechanical stress, to date it has received increasing attention to couple this approach to fundamental electrochemistry by using electrode materials for numerous applications. This is because piezoelectrochemical processes at substrate surfaces can also be monitored via surface processes such as adsorption, desorption, and film formation that can induce redox reactions occurring at the electrode/electrolyte interface. Hence, by using a piezoelectric element, the derivative of surface stresses can be complemented with potential [68]. By coupling the piezoelectric method with electrochemistry, various applications can be utilized, including electrochemical sensors [69, 70], corrosion management [71], and harvesting and

TABLE 7 Summary of the recent applications of piezoelectric materials.

Materials	Power generation	Current generation	Output power	Applications	References
20 PZT-5H bimorphs	–	–	0.41 mW/cm ³	Shoe	[27]
Stacked PVDF film	136 V	–	4 mW	Shoe	
Stacked PZT-8	–	–	200 mW	Pavement	[30]
ZnO NWs-carbon paper	18 mV	35 nA	51 µW/cm ²	Wearable and self-powered nanodevices	[44]
P(VDF-TrFE)/MWCNT	18.23 V	2.14 µA	–	Wearable devices	[65]
PVDF fabric	1.5 V	0.04 µA	–	Sensitive impact detectors	[46]
PZT	–	–	5.04 × 10 ⁻⁴ µW/mm ² g ²	MEMS	[67]
Thin PZT ribbons	4–5 V		1.2 mW/cm ²	Pacemaker	
PMN-PZT-Mn thin film	17.8 V	1.75 µA	–	Pacemaker	
PIN-PZN-PZT	–	–	3.37 µW/mm ³	LEDs	[23]

MEMS, microelectromechanical systems; MWCNT, multiwalled carbon nanotube; NW, nanowire; PIN, Pb(In_{1/2}Nb_{1/2})O₃; PMN, Pb(Mg_{1/3}Nb_{2/3})O₃; PVDF, poly(vinylidene fluoride); PZT, lead zirconate titanate.

storing energies [71, 72]. Nevertheless, this section only discusses the fundamental aspects of the coupling of piezoelectric elements with electrochemical processes in harvesting and storing electrochemical energies.

5.1 Piezoelectrochemical processes for water splitting in generating hydrogen (H_2) gas

The first report on piezoelectrochemical energy based on the direct conversion of mechanical energy into electrochemical energy for hydrogen and oxygen generations through the use of piezoelectric materials in water splitting was presented by Hong and coworkers in 2010 [73]. In their work, synthesized piezoelectric materials of ZnO microfibers and BaTiO₃ microdendrites were employed to generate hydrogen and oxygen gases by vibrating the substrate surfaces with ultrasonic waves, leading to the development of a strain-induced electric charge at the surfaces. Then, by sufficient electric potential developed at the substrates, the redox reaction of water occurred by strained piezoelectric ZnO fibers and BaTiO₃ dendrites. As a result, hydrogen and oxygen gases were produced. Since then, their study has provided a simple and cost-effective piezoelectrochemical approach for direct water splitting where the hydrogen fuels could be generated by scavenging energy wastes: noise and stray vibrations from the microenvironment at the electrode interface.

In a different approach, Starr and Wang [2] reported the use piezoelectric material of a Pb(Mg_{1/3}Nb_{2/3})O₃-32PbTiO₃ cantilever based upon mechanical oscillations to experimentally and theoretically study the voltage drop and H₂ production behavior at the substrates in deionized water. The study highlighted that to obtain high electrochemical activity at the electrode interface, a number of factors must be considered in augmenting the efficacy of strain to induce electrochemical reactions such as a high piezoelectric coupling coefficient and low electrical conductivity. Besides, the value of electrical permittivity must be optimized to balance the piezoelectric and capacitive effects of the process. On the contrary, a cell system having a piezoelectric bimorph cantilever and an electrolysis cell to showcase a cost-effective, recyclable, environmentally friendly, and a simple way of piezoelectrochemical process for hydrogen generation at the electrode substrate of PZT-5 ceramics was developed by Zhang and coworkers [74]. In their work, the piezoelectrochemical for water splitting was obtained by employing mechanical vibrations in a bimorph cantilever.

It is to be noted that a single source of energy based on mechanical vibration is commonly used to obtain a piezoelectric strain when generating hydrogen. Nevertheless, Tan et al. [75] reported on the use of multiple energy sources for the development of sustainable operation of dual photocatalytic reactions in developing an energy-harvesting technology. In their work, novel metal

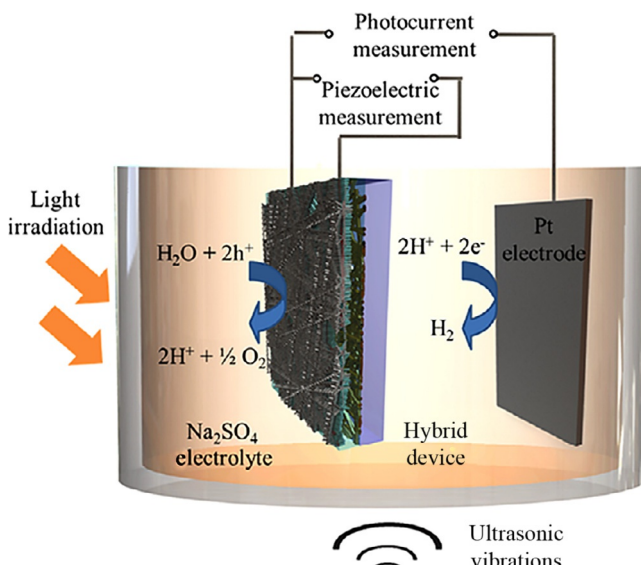


FIG. 7 A hybrid cell for dual operations of piezoelectric photoelectrochemical and photocatalytic processes based on Ag-ZnO BHS and Cu-ZnO BHS substrates by converting energy sources from light irradiation and ultrasonic vibrations to photocatalytic hydrogen (H_2) generation. (Reproduced with permission from C.F. Tan, et al., Self-biased hybrid piezoelectric-photoelectrochemical cell with photocatalytic functionalities, *ACS Nano* 9 (2015) 7661–7670.)

semiconductor-branched heterostructures (BHS), Ag-ZnO BHS and Cu-ZnO BHS, were synthesized and then employed as piezoelectric elements to fabricate a hybrid cell for dual operations of piezoelectric photoelectrochemical and photocatalytic processes as shown in Fig. 7 by coupling energy sources from light irradiation and ultrasonic vibrations.

The synthesized Ag-ZnO BHS and Cu-ZnO BHS offer excellent behavior for visible light absorption, charge separation efficiency, and piezoelectric properties. Moreover, Chuan et al. highlighted that the developed hybrid cell system in their study has high potential for use as H_2 generator and water treatment systems. Meanwhile, in a different research group, Zhao et al. [76] also reported on coupling energy sources of visible light and acoustic energy to generate H_2 by employing wurtzite CdS nanoarrays, where the nanoarrays were in situ assembled on fluorine-doped tin oxide substrate. The study showed that the developed piezoelectrochemical and photocatalyst systems from CdS nanoarrays led to more facile water splitting for H_2 . The findings from this study indicate that the ability of a couple system of piezoelectrochemical and photocatalyst has the ability to simultaneously convert the visible light and acoustic energies into hydrogen energy during the water-splitting process.

5.2 Piezoelectrochemical elements for energy storage

In addition to harvesting hydrogen energy from mechanical vibration and light irradiation in piezoelectrochemical processes, the piezoelectrochemical elements and processes were also employed to store energy. In this instance, a significant work from Ramadoss et al. [77] reported on the conversion of mechanical deformation energy into electrochemical energy by developing a piezoelectrically driven self-charging supercapacitor power cell using MnO_2 nanowires as positive and negative electrodes, where PVDF/ZnO film was used as a separator. Their findings opened up the possibility of making self-powered flexible hybrid electronic devices. Meanwhile, without using any separator, an integrated self-powered charging cell was developed by Xue et al. [78] by employing CuO/PVDF nanoarrays as a piezo anode. They highlighted that the hybrid of PVDF with CuO as a nanocomposite piezo anode offers excellent piezoelectric output where the storage capacity and energy were efficiently charged up from the mechanical deformation. This was attributed to a result of more intimate contact and a larger interface area in the hybrid nanoarray structure of PVDF and CuO.

A different type of PVDF nanostructure film was porously synthesized by Xing and coworkers [79] to explore the piezoelectric behavior of the film and the ability of the film to facilitate the migration of Li-ion by mechanical deformation. Then, the synthesized microporous nanostructure film was used as a piezo-separator in developing a self-charging power cell (SCPC). They showed that the porous nanostructure of PVDF film was able to facilitate the transportation of Li^+ ions, leading to higher energy conversion and storage efficiency. They concluded that such a good performance of the SCPC-based PVDF microporous nanostructure was attributed to the geometrical strain confinement effect and the mesoporous structure of the piezo-separator film.

Development of supercapacitors via the piezoelectrochemical process is also one of the fascinating research topics in energy harvesting and energy storage devices. Song et al. [80] demonstrated that a piezoelectric potential has been developed across the PVDF film where the film is sandwiched between a carbon cloth electrode and a solid-state poly(vinyl alcohol) (PVA) electrolyte. The potential was developed at the film when external mechanical impacts were applied to their device. This makes the developed potential serve as a driving force to transport the ions to the interface of the carbon cloth electrode and then store the electricity in the form of electrochemical energy. Interestingly, they highlighted that the piezosupercapacitor offers high mechanical strength, high capacitance behavior, and stable capacitor performance.

A fast-charging self-powered electric double layer capacitor was developed by Parida and coworkers [81] based on the formation of an electric double layer with fast absorption and desorption of ions at the carbon nanotube electrodes, coupled with piezoelectric porous (PVDF-TrFE) foam (impregnated with poly (methyl methacrylate)-propylene carbonate-lithium perchlorate gel electrolyte)

as the piezoelectric separator upon application of mechanical force. The charging mechanism was proposed by the fast adsorption and desorption ions at the carbon nanotube electrodes, leading the charge to be stored, although a few seconds of slight mechanical perturbation was applied during the charging process. In contrast, a novel high-output nanoenergy cell (NEC) with piezoelectric nanogenerator and supercapacitors was developed by Wang et al. [82]. The NEC was fabricated from vertically aligned piezoelectric ZnO nanowire arrays, a serrated-shaped opposite electrode, and phosphoric acid/poly(vinylalcohol) (H_3PO_4/PVA) as a gel electrolyte. This gives the NEC dual functions of nanogenerator and supercapacitor without increasing device volume and significantly improving the efficiency of mechanical/electrical energy conversion. Essentially, piezoelectric potential and current as the outputs from piezoelectrochemical processes are generated from the mechanical deformation of ZnO nanowires under the pressure of serrated electrodes. From their study, they concluded that NEC has high-density ZnO nanowires that could convert the mechanical energy into electricity as well as store it.

In summary, it is clear that the coupling approach between piezoelectric elements and electrochemical processes at the electrode interface could offer a big advantage in energy harvesting and subsequently the generated energy can be stored within batteries or capacitors.

6 Future outlook

This chapter discussed recent advancements of various piezoelectric materials and their applications in sustainable energy harvesting. The recent combination of piezoelectric materials (composite piezoelectric material) and various material compositions to improve the performance of piezoelectric materials for energy harvesting was discussed. Still, there are vast parameters that control the output performance of piezoelectric materials for energy harvesting, such as the structural design, impedance matching, applied forces, environmental condition, and vibration frequency of piezoelectric material. Thus control and optimization of those parameters are important to turn the research findings of piezoelectric materials in energy harvesting into commercial energy harvesters that benefit our daily lives. Moreover, reliability, stability, and compatibility of piezoelectric materials need further testing in detail.

Moreover, there are many ambient sources that can be utilized as energy harvesters other than mechanical vibrations and human motions, for example, wind flow, rainfall, ocean waves, and roadway loading. However, research into using those ambient energy sources is still not widely explored. It is believed that utilizing the ambient sources will be able to power small electronic devices and place them in many locations, such as urban areas, high wind areas, ventilation outlets, rivers and ocean, ducts of buildings, and lifting components in aircraft structures.

Piezoelectrochemical materials is another interesting area for further exploration. Minute signal generation in electrochemical reaction has great potential in energy harvesting and storage. Moreover, film structure and composition are important in optimizing piezoelectrochemical properties for future applications.

References

- [1] W.S. Hwang, et al., Design of piezoelectric ocean-wave energy harvester using sway movement, *Sensors Actuators A* 260 (2017) 191–197.
- [2] M.B. Starr, X. Wang, Fundamental analysis of piezocatalysis process on the surfaces of strained piezoelectric materials, *Sci. Rep.* 3 (2013) 2160.
- [3] E.M. Nia, et al., A review of walking energy harvesting using piezoelectric materials, *IOP Conf. Ser. Mater. Sci. Eng.* 291 (2017) 012026.
- [4] W.-T. Park, Piezoresistivity, in: B. Bhushan (Ed.), *Encyclopedia of Nanotechnology*, Springer Netherlands, Dordrecht, 2012, pp. 2111–2117.
- [5] K.M. Ok, et al., Bulk characterization methods for non-centrosymmetric materials: second-harmonic generation, piezoelectricity, pyroelectricity, and ferroelectricity, *Chem. Soc. Rev.* 35 (2006) 710–717.
- [6] C. Wei, X. Jing, A comprehensive review on vibration energy harvesting: modelling and realization, *Renew. Sustain. Energy Rev.* 74 (2017) 1–18.
- [7] M. Hamlehdar, et al., Energy harvesting from fluid flow using piezoelectrics: a critical review, *Renew. Energy* 143 (2019) 1826–1838.
- [8] R. Caliò, et al., Piezoelectric energy harvesting solutions, *Sensors* 14 (2014) 4755–4790.
- [9] Z. Yang, et al., High-performance piezoelectric energy harvesters and their applications, *Joule* 2 (2018) 642–697.
- [10] H. Liu, et al., A comprehensive review on piezoelectric energy harvesting technology: materials, mechanisms, and applications, *Appl. Phys. Rev.* 5 (2018) 041306.
- [11] L. Li, et al., Recent progress on piezoelectric energy harvesting: structures and materials, *Adv. Compos. Hybrid Mater.* 1 (2018) 478–505.
- [12] S.R. Platt, et al., The use of piezoelectric ceramics for electric power generation within orthopedic implants, *IEEE/ASME Trans. Mechatron.* 10 (2005) 455–461.
- [13] K.K. Sappati, S. Bhadra, Piezoelectric polymer and paper substrates: a review, *Sensors* 18 (2018) 3605.
- [14] H. Wei, et al., An overview of lead-free piezoelectric materials and devices, *J. Mater. Chem. C* 6 (2018) 12446–12467.
- [15] M. Kimura, et al., 2—Lead zirconate titanate-based piezo-ceramics, in: K. Uchino (Ed.), *Advanced Piezoelectric Materials*, Woodhead Publishing, 2010, pp. 89–110.
- [16] M.-G. Kang, et al., Recent progress on PZT based piezoelectric energy harvesting technologies, *Actuators* 5 (2016) 1–17.
- [17] G. Fan, et al., Morphotropic phase boundary and piezoelectric properties of $(\text{Bi}_{1/2}\text{Na}_{1/2})\text{TiO}_3 - (\text{Bi1/2K1/2})\text{TiO}_3 - \text{KNbO}_3$ lead-free piezoelectric ceramics, *Appl. Phys. Lett.* 91 (2007) 202908.
- [18] A. Jain, et al., Dielectric and piezoelectric properties of PVDF/PZT composites: a review, *Polym. Eng. Sci.* 55 (2015) 1589–1616.
- [19] A. Khan, et al., Piezoelectric thin films: an integrated review of transducers and energy harvesting, *Smart Mater. Struct.* 25 (2016) 053002.

- [20] S. Mishra, et al., Advances in piezoelectric polymer composites for energy harvesting applications: a systematic review, *Macromol. Mater. Eng.* 304 (2019) 1800463.
- [21] C. Wan, C.R. Bowen, Multiscale-structuring of polyvinylidene fluoride for energy harvesting: the impact of molecular-, micro- and macro-structure, *J. Mater. Chem. A* 5 (2017) 3091–3128.
- [22] X. Yu, et al., Targeted doping builds a high energy density composite piezoceramics for energy harvesting, *J. Am. Ceram. Soc.* 102 (2019) 275–284.
- [23] J. Yan, et al., Large enhancement of transduction coefficient in PZN-PZT energy harvesting system through introducing low-*er* PIN relaxor, *J. Eur. Ceram. Soc.* 39 (2019) 2666–2672.
- [24] Y. Lu, et al., The PZT/Ni unimorph magnetoelectric energy harvester for wireless sensing applications, *Energ. Conver. Manage.* 200 (2019) 112084.
- [25] S. Dong, et al., Multimodal system for harvesting magnetic and mechanical energy, *Appl. Phys. Lett.* 93 (2008) 103511.
- [26] M.G. Kang, et al., High power magnetic field energy harvesting through amplified magneto-mechanical vibration, *Adv. Energy Mater.* 8 (2018) 1703313.
- [27] L. Xie, M. Cai, Increased piezoelectric energy harvesting from human footstep motion by using an amplification mechanism, *Appl. Phys. Lett.* 105 (2014) 143901.
- [28] Y. Tian, et al., A low-frequency MEMS piezoelectric energy harvester with a rectangular hole based on bulk PZT film, *J. Phys. Chem. Solid* 117 (2018) 21–27.
- [29] M. Zhu, et al., Self-powered and self-functional cotton sock using piezoelectric and triboelectric hybrid mechanism for healthcare and sports monitoring, *ACS Nano* 13 (2019) 1940–1952.
- [30] X.Z. Jiang, et al., Electromechanical modeling and experimental analysis of a compression-based piezoelectric vibration energy harvester, *Int. J. Smart Nano Mater.* 5 (2014) 152–168.
- [31] Z. Zhang, et al., Modeling on piezoelectric energy harvesting from pavements under traffic loads, *J. Intell. Mater. Syst. Struct.* 27 (2016) 567–578.
- [32] M. Yasseri, et al., Low temperature synthesis of barium titanate powder by a modified sol-gel method, *Adv. Mat. Res.* 829 (2014) 727–731.
- [33] Z. Chen, et al., Enhanced piezoelectric properties and thermal stability in Mo/Cr co-doped CaBi₂Nb₂O₉ high-temperature piezoelectric ceramics, *J. Phys. Chem. Solid* 136 (2020) 109195.
- [34] Y. Cheng, et al., Investigation of high piezoelectric properties of KNNSb-SrxBNZ ceramics, *J. Alloys Compd.* 815 (2020) 152252.
- [35] K.S. Chary, et al., Fabrication of large aspect ratio Ba_{0.85}Ca_{0.15}Zr_{0.1}Ti_{0.9}O₃ superfine fibers-based flexible nanogenerator device: synergistic effect on curie temperature, harvested voltage, and power, *Ind. Eng. Chem. Res.* 56 (2017) 10335–10342.
- [36] C.C. Bowland, et al., Barium titanate film interfaces for hybrid composite energy harvesters, *ACS Appl. Mater. Interfaces* 9 (2017) 4057–4065.
- [37] J. Kim, et al., Improved Li and Sb doped lead-free (Na,K)NbO₃ piezoelectric ceramics for energy harvesting applications, *Ceram. Int.* 44 (2018) 22219–22224.
- [38] R.A. Surmenov, et al., Hybrid lead-free polymer-based nanocomposites with improved piezoelectric response for biomedical energy-harvesting applications: a review, *Nano Energy* 62 (2019) 475–506.
- [39] C.K. Jeong, et al., Lead-free perovskite nanowire-employed piezopolymer for highly efficient flexible nanocomposite energy harvester, *Small* 14 (2018) 1704022.
- [40] M. Choi, et al., Mechanical and electrical characterization of PVDF-ZnO hybrid structure for application to nanogenerator, *Nano Energy* 33 (2017) 462–468.
- [41] H.H. Singh, et al., Design of flexible PVDF/NaNbO₃/RGO nanogenerator and understanding the role of nanofillers in the output voltage signal, *Compos. Sci. Technol.* 149 (2017) 127–133.

- [42] S.-H. Shin, et al., Hemispherically aggregated BaTiO₃ nanoparticle composite thin film for high-performance flexible piezoelectric nanogenerator, *ACS Nano* 8 (2014) 2766–2773.
- [43] E. Kar, et al., 2D SnO₂ nanosheet/PVDF composite based flexible, self-cleaning piezoelectric energy harvester, *Energ. Conver. Manage.* 184 (2019) 600–608.
- [44] C.K. Jeong, et al., A hyper-stretchable elastic-composite energy harvester, *Adv. Mater.* 27 (2015) 2866–2875.
- [45] Q. Liao, et al., Flexible piezoelectric nanogenerators based on a fiber/ZnO nanowires/paper hybrid structure for energy harvesting, *Nano Res.* 7 (2014) 917–928.
- [46] L. Persano, et al., High performance piezoelectric devices based on aligned arrays of nanofibers of poly(vinylidenefluoride-co-trifluoroethylene), *Nat. Commun.* 4 (2013) 1633.
- [47] J. Zhong, et al., Flexible PET/EVA-based piezoelectret generator for energy harvesting in harsh environments, *Nano Energy* 37 (2017) 268–274.
- [48] J. Kim, et al., Discovery of cellulose as a smart material, *Macromolecules* 39 (2006) 4202–4206.
- [49] A. Hänninen, et al., Nanocellulose and chitosan based films as low cost, green piezoelectric materials, *Carbohydr. Polym.* 202 (2018) 418–424.
- [50] G. Zhang, et al., Uniformly assembled vanadium doped ZnO microflowers/bacterial cellulose hybrid paper for flexible piezoelectric nanogenerators and self-powered sensors, *Nano Energy* 52 (2018) 501–509.
- [51] M. Khalifa, S. Anandhan, PVDF nanofibers with embedded polyaniline-graphitic carbon nitride nanosheet composites for piezoelectric energy conversion, *ACS Appl. Nano Mater.* 2 (2019) 7328–7339.
- [52] S. Cherumannil Karumuthil, et al., Electrospun poly(vinylidene fluoride-trifluoroethylene) based polymer nanocomposite fibers for piezoelectric nanogenerators, *ACS Appl. Mater. Interfaces* 11 (2019) 40180–40188.
- [53] R. Bhunia, et al., Milli-watt power harvesting from dual triboelectric and piezoelectric effects of multifunctional green and robust reduced graphene oxide/P(VDF-TrFE) composite flexible films, *ACS Appl. Mater. Interfaces* 11 (2019) 38177–38189.
- [54] Z.L. Wang, Nanopiezotronics, *Adv. Mater.* 19 (2007) 889–892.
- [55] Z.L. Wang, Piezopotential gated nanowire devices: piezotronics and piezo-phototronics, *Nano Today* 5 (2010) 540–552.
- [56] Z. Zhang, et al., ZnO nanorods patterned-textile using a novel hydrothermal method for sandwich structured-piezoelectric nanogenerator for human energy harvesting, *Physica E* 105 (2019) 212–218.
- [57] X. Zhao, et al., Piezotronic effect of single/few-layers MoS₂ nanosheets composite with TiO₂ nanorod heterojunction, *Nano Energy* 66 (2019) 104168.
- [58] W. Rahman, et al., Self-powered piezoelectric nanogenerator based on wurtzite ZnO nanoparticles for energy harvesting application, *Mater. Today* 5 (2018) 9826–9830.
- [59] M.A. Johar, et al., A scalable, flexible and transparent GaN based heterojunction piezoelectric nanogenerator for bending, air-flow and vibration energy harvesting, *Appl. Energy* 222 (2018) 781–789.
- [60] J.J. Dosch, et al., A self-sensing piezoelectric actuator for collocated control, *J. Intell. Mater. Syst. Struct.* 3 (1992) 166–185.
- [61] K.R. Rashmi, et al., Piezoelectric P(VDF-TrFE) micro cantilevers and beams for low frequency vibration sensors and energy harvesters, *Sensors and Actuators A* 295 (2019) 574–585.
- [62] P. Yu, et al., Flexible piezoelectric tactile sensor array for dynamic three-axis force measurement, *Sensors* 16 (2016) 819.

- [63] D.H. Kim, et al., In vivo self-powered wireless transmission using biocompatible flexible energy harvesters, *Adv. Funct. Mater.* 27 (2017) 1700341.
- [64] H. Zhang, et al., A flexible and implantable piezoelectric generator harvesting energy from the pulsation of ascending aorta: in vitro and in vivo studies, *Nano Energy* 12 (2015) 296–304.
- [65] C. Zhao, et al., Coaxially aligned MWCNTs improve performance of electrospun P(VDF-TrFE)-based fibrous membrane applied in wearable piezoelectric nanogenerator, *Compos. Part B Eng.* 178 (2019) 107447.
- [66] S. Xu, et al., Piezoelectric-nanowire-enabled power source for driving wireless microelectronics, *Nat. Commun.* 1 (2010) 93.
- [67] H. Song, et al., Ultra-low resonant piezoelectric MEMS energy harvester with high power density, *J. Microelectromech. Syst.* 26 (2017) 1226–1234.
- [68] R.E. Malpas, et al., The piezoelectric detection of electrode surface processes, *J. Electroanal. Chem. Interfacial Electrochem.* 98 (1979) 171–180.
- [69] M. Stobiecka, et al., Piezoelectric sensor for determination of genetically modified soybean roundup ready^(®) in samples not amplified by PCR, *Sensors* 7 (2007) 1462–1479.
- [70] M. Schweiyer, et al., Electrochemical piezoelectric sensors for trace ionic contaminants, *IEEE Trans. Ultrason. Ferroelectr. Freq. Control* 45 (1998) 1408–1415.
- [71] M.B. Starr, X. Wang, Coupling of piezoelectric effect with electrochemical processes, *Nano Energy* 14 (2015) 296–311.
- [72] E. Jacques, et al., Piezo-electrochemical energy harvesting with lithium-intercalating carbon fibers, *ACS Appl. Mater. Interfaces* 7 (2015) 13898–13904.
- [73] K.-S. Hong, et al., Direct water splitting through vibrating piezoelectric microfibers in water, *J. Phys. Chem. Lett.* 1 (2010) 997–1002.
- [74] J. Zhang, et al., Piezoelectric bimorph cantilever for vibration-producing-hydrogen, *Sensors* 13 (2012) 367–374.
- [75] C.F. Tan, et al., Self-biased hybrid piezoelectric-photoelectrochemical cell with photocatalytic functionalities, *ACS Nano* 9 (2015) 7661–7670.
- [76] Y. Zhao, et al., Hydrogen production from pure water via piezoelectric-assisted visible-light photocatalysis of CdS nanorod arrays, *ChemCatChem* 10 (2018) 3397–3401.
- [77] A. Ramadoss, et al., Piezoelectric-driven self-charging supercapacitor power cell, *ACS Nano* 9 (2015) 4337–4345.
- [78] X. Xue, et al., CuO/PVDF nanocomposite anode for a piezo-driven self-charging lithium battery, *Energ. Environ. Sci.* 6 (2013) 2615–2620.
- [79] L. Xing, et al., PVDF mesoporous nanostructures as the piezo-separator for a self-charging power cell, *Nano Energy* 10 (2014) 44–52.
- [80] R. Song, et al., A rectification-free piezo-supercapacitor with a polyvinylidene fluoride separator and functionalized carbon cloth electrodes, *J. Mater. Chem. 3* (2015) 14963–14970.
- [81] K. Parida, et al., Fast charging self-powered electric double layer capacitor, *J. Power Sources* 342 (2017) 70–78.
- [82] F. Wang, et al., High output nano-energy cell with piezoelectric nanogenerator and porous supercapacitor dual functions—a technique to provide sustaining power by harvesting intermittent mechanical energy from surroundings, *Nano Energy* 21 (2016) 209–216.

Chapter 10

An approach to designing smart future electronics using nature-driven biopiezoelectric/triboelectric nanogenerators

Sumanta Kumar Karan^{a,*†}, Sandip Maiti^{b,†}, Jin Kon Kim^b, and Bhanu Bhushan Khatua^a

^aMaterials Science Centre, Indian Institute of Technology Kharagpur, Kharagpur, India, ^bNational Creative Research Initiative Center for Smart Block Copolymers, Department of Chemical Engineering, Pohang University of Science and Technology, Pohang, Kyungbuk, Republic of Korea

1 Introduction

Development of clean and alternating green energy-harvesting sources is becoming increasingly vital in the modern smart, portable, wearable electronics world [1–3]. However, these smart and flexible electronics should be biocompatible, biodegradable, and easily processable in nature to make them compatible with the environment and all animal bodies [4, 5]. Over the last couple of years, piezoelectric nanogenerators (PNGs) [6–8] and triboelectric nanogenerators (TNGs) [9, 10] have been gaining increased interest in the alternating energy-harvesting family because they convert mechanical energy to green electricity. Mechanical energy is abundant in our surroundings in various forms such as animal/human body motions (dancing, running, walking, wrist/neck/joint movements, kicking, etc.), different vibrations, sound wave frequencies, wind or water flow, and in vivo body motions like blood flow, breathing, and the beating heart. These are all very much responsible for generating electricity using this technology and energy and could be utilized to power up portable and smart electronics, active sensors, and even be used in in vivo e-healthcare monitoring [3, 11, 12]. Furthermore, the energy-harvesting approach is almost a pollution-free approach, where mechanical energy is

* Present address: School of Advanced Materials Science and Engineering, Sungkyunkwan University (SKKU), Suwon 16419, Republic of Korea.

† S. K. K and S. M contributed equally.

the source to generate electricity. Although various piezoelectric and ferroelectric materials are used to develop PNGs like lead zirconate titanate [13], ZnO nanowires [14], BaTiO₃ [15], MoS₂ [16], GaN nanowire [17], organic/inorganic lead halide perovskites [18, 19], Pb-free piezoceramic crystals [20, 21], polyvinylidene fluoride (PVDF) [6, 22], nylon nanowire [23], PVDF composite [24–26], and its copolymer PVDF-TrFE [27], many researchers are studying TNGs with various triboelectric materials [28–30]. However, the use of toxic materials to design smart devices produces a huge amount of electronic waste (e-waste), which is not only a danger to ecosystems, but also threatens human and animal lives. These gigantic amounts of e-waste are spreading pollution in water, soil, and air and creating information security problems as well as exploiting living creatures [3, 31]. The burning of e-wastes creates air pollution and their improper disposal creates soil and water pollution, thus the total ecosystem is increasingly being broken down. More importantly, e-waste recycling is very expensive and \$206 billion have been invested to recycle only 29% of e-wastes in the United States, for example [32], as per a report in 2012. Furthermore, conventional techniques for recycling are not good for the environment. Various dangerous substances like Pd, Ag, Hg, and many others [33] are used to design these devices. As per a report in 2017, smartphones and computer-based e-waste totaled 50 million tons according to the United Nations Environment Program titled “Waste Crimes” [34]. Because of these e-wastes, Third World countries are suffering especially because their land has been used for dumping e-waste since 2015 [35].

To overcome these huge problems, the time has come to design high-performance ultrasmart electronics devices with biodegradable or biocompatible materials. Nature-driven biodegradable piezo/triboelectric materials would be very effective in integrating these portable devices for the development of pollution-free, smart, high-tech generation [36–38]. These bio-based devices harvest sufficient energy from various mechanical and biomechanical activities in our surroundings using these energy-harvesting technologies. Thus we can reuse huge amounts of nature-driven biowaste materials for use as green electricity and develop a pollution-free smart world [39]. Furthermore, it would be economically more beneficial with a continuous energy source. Being biodegradable in nature, these energy-harvesting devices would be used in various *in vivo* biomedical applications such as pacemakers, neural stimulators, brain stimulators, and many more. Then, these advantages of biowaste materials will drive these energy-harvesting technologies in next-generation multifunctional applications through simple and easy fabrication approaches. Different potentialities of bionanogenerators are schematically presented in Fig. 1.

This chapter discusses the potential and smart designs of green energy-harvesting devices inspired by nature-driven biocompatible/biodegradable materials, which are discarded in huge amounts every day, and their effectiveness for flexible PNG/TNG construction. Here, we will discuss the effectiveness of biowaste biodegradable materials in green energy-harvesting

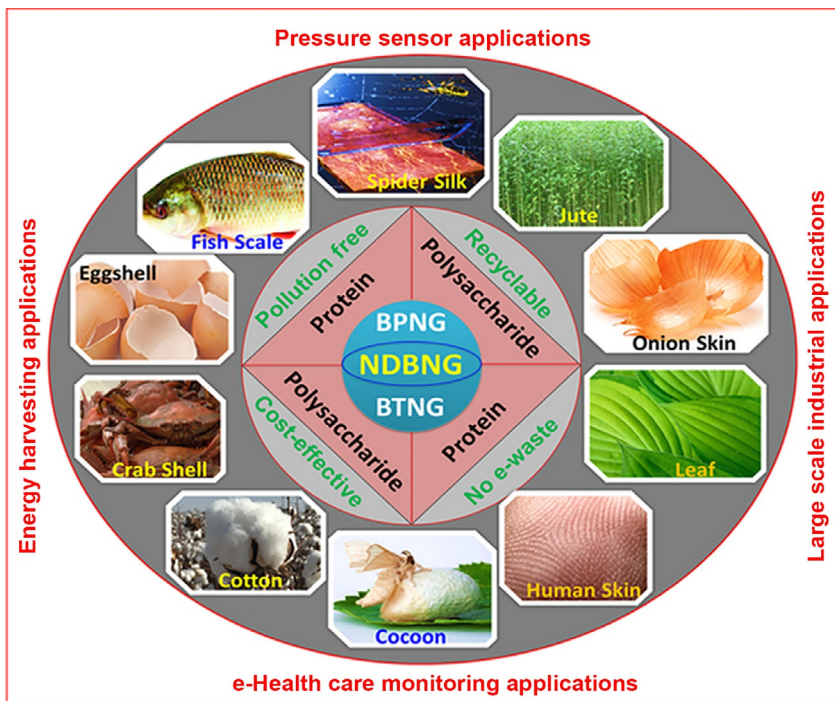


FIG. 1 Schematic of various applications of a nature-driven biowaste materials-based bionano-generator (NDBNG) as an efficient energy scavenger. (Reproduced with permission from S. Maiti, S.K. Karan, J.K. Kim, B.B. Khatua, *Nature driven bio piezoelectric/triboelectric nanogenerator as next generation green energy harvester for smart and pollution free society*, *Adv. Energy Mater.* 9 (9) (2019) 1803027. Copyright 2019, WILEY-VCH Verlag GmbH & Co. KGaA, Weinheim.)

technologies and their possible applications to design a future smart/portable electronics world. Furthermore, using biowaste materials in energy-harvesting technology will definitely help to eradicate huge amounts of biowaste from the environment as well as society.

2 Working principle of piezoelectricity and triboelectricity

Jacques and Pierre Curie first observed in 1880 the development of surface charge through mechanical stress, which they later called piezoelectricity [40]. Due to the linear electromechanical interaction between the mechanical and electrical states in a crystalline substance in the absence of inversion of symmetry, the effect of piezoelectricity is established [41]. During actuation, sensing, and control a piezoelectric material is able to vary its structure under external response. The variation of polarization is directly proportional to applied stress, indicated by the equation $P=d \times \sigma$, where P stands for

polarization, σ represents applied stress, and d signifies piezoelectric coefficient (actually a third rank tensor). Furthermore, the reverse approach is also true, i.e., if an electrical field is applied to the piezoelectric materials, then strain or stress is induced, which is defined by $\epsilon = d \times E$, where ϵ signifies the strain induced, E stands for the applied electric field, and d denotes the piezoelectric coefficient. The working mechanism of piezoelectric crystalline materials under external mechanical stress is shown schematically in Fig. 2A–C.

Fig. 2A displays the piezoelectric material's original shape during poling condition. The dipole moment of piezoelectric materials can change and produce electricity under external force on a particular surface. The direct piezoelectric effect under compression and tensile stress and the converse piezoelectric effect during applied voltage are displayed in Fig. 2B and C. The direct and converse piezoelectric effect of the piezoelectric materials is expressed by two different linearized constitutive equations:

$$\text{Direct piezoelectric effect : } D_i = e_{ij}^{\sigma} E_j + d_{im}^d \sigma_m \quad (1)$$

$$\text{Converse piezoelectric effect : } \epsilon_k = d_{jk}^c E_j + S_{km}^d \sigma_m \quad (2)$$

where the vector D_i signifies the dielectric displacement (unit in N/mV or C/m²), ϵ_k denotes the strain vector, E_j represents the applied electric field vector (unit in V/m), and σ_m stands for the stress vector (unit in N/m²). The piezoelectric constants are the piezoelectric coefficients d_{im}^d and d_{jk}^c in m/V or C/N, the

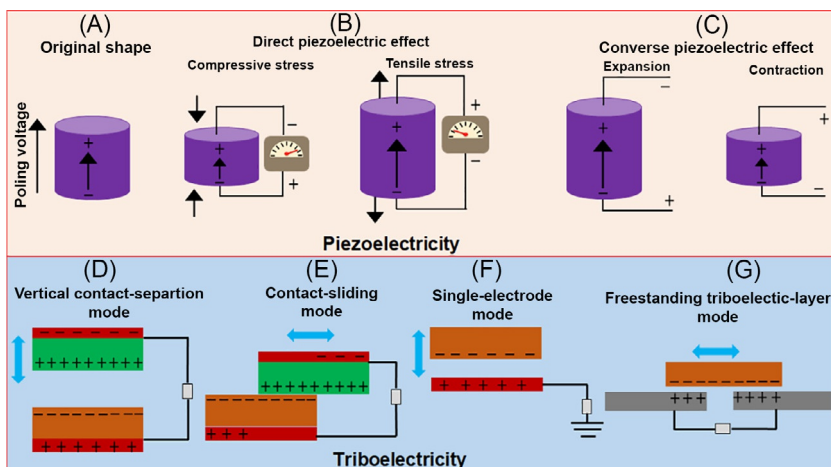


FIG. 2 (A–C) Schematic of the fundamental working mechanism of a piezoelectric material. (D–G) Demonstration of four different types of fundamental working mechanisms of a TNG under external force. (Reproduced with permission from S. Maiti, S.K. Karan, J.K. Kim, B.B. Khatua, *Nature driven bio piezoelectric/trioboelectric nanogenerator as next generation green energy harvester for smart and pollution free society*, *Adv. Energy Mater.* 9 (9) (2019) 1803027 WILEY-VCH Verlag GmbH & Co. KGaA, Weinheim, 2019.)

dielectric permittivity ϵ_{ij}^σ in N/V² or F/m, and S_{km}^d signifies the elastic compliance matrix in m²/N. The superscripts *c* and *d* in the equation represent the converse and direct effects, respectively, and the superscripts *E* and σ in the equation are the quantities measured at constant stress and the electric field, respectively. Common piezoelectric materials with formulas, crystalline structures, and piezoelectric coefficients are shown in [Table 1](#).

Because of contact electrification among the two different materials, the triboelectric effect is usually established. TNGs can generate huge amounts of electricity via a combination of triboelectric effect and electrostatic induction and are considered to be promising technology for harvesting energy. Wang et al. in 2012 introduced the term TNG by which one can harvest green energy [\[42\]](#). There are mainly four types of fundamental mechanism by which a TNG can generate electricity under external force ([Fig. 2D–G](#)) [\[3, 43\]](#), namely vertical contact separation mode TNG, contact sliding mode TNG, single electrode mode TNG, and freestanding mode TNG as shown in [Fig. 2D–G](#), respectively. [Table 2](#) gives some idea of positive and negative triboelectric materials with their loss or gain of electrons.

3 Naturally abundant materials and their piezoelectricity

3.1 Piezoelectricity in protein-based structures

In 1957 Fukada et al. noticed for the first time that a collagen-enriched bone structure can exhibit piezoelectric properties [\[44\]](#). As bone is the combination of various crystalline collagen fibers it is accountable for the origin of piezoelectricity (piezoelectric constant $\sim 6.0 \times 10^{-9}$ CGSesu) in bone. [Fig. 3A](#) shows the pressure-dependent polarization of collagen fibers. [Fig. 3B](#) shows that the strain value improved when an applied electric field was increased. The relation among stress (designated by arrows) and polarization (designated by negative and positive signs) is shown in [Fig. 3C](#). Thus piezoelectric behavior of bone is realized from the linear association among polarization versus stress/or strain versus electric field [\[44\]](#). Later, the direct/converse piezoelectric coefficient was observed in the Achilles' tendon of oxen/horses and due to the alignment of collagen molecules in collagen crystalline fibers, piezoelectricity is obtained [\[45\]](#).

Several biowaste materials like teeth [\[46\]](#), bones [\[45\]](#), fish scales [\[47\]](#), eggshell membranes (ESM) [\[36\]](#), fish bladders (FSBs) [\[48\]](#), viruses [\[49\]](#), and many more have been explored as piezoelectric materials, which generally consist of protein and collagen in their moiety. Fish scale/bladder/skin show high piezoelectric coefficient values: -5 pC/N, 22 pC/N, and -3 pC/N respectively. ESM was explored as an efficient piezoelectric material with a high piezoelectric coefficient of ~ 23.7 pC/N [\[36\]](#). The basic fundamental working mechanisms for these types of materials are still being researched [\[37, 50, 51\]](#). Subsequently, Polonsky [\[52\]](#) and Duchesne [\[53\]](#) first observed piezoelectricity DNA. In 1967

TABLE 1 Some piezoelectric materials with formulas, crystalline structures, and piezoelectric coefficients.

Materials	Formula	Form	Piezoelectric constant (pm/V or pC/N)
Ammonium dihydrogen phosphate	$\text{NH}_4\text{H}_2\text{PO}_4$	Single crystal	$d_{36}=48$
Barium titanate	BaTiO_3	Single crystal	$d_{15}=587$
Barium titanate	BaTiO_3	Polycrystalline ceramic	$d_{15}=270$
Lead zirconate titanate	$\text{PbZr}_{0.6}\text{Ti}_{0.40}\text{O}_3$	Polycrystalline ceramic	$d_{33}=117$
Lead lanthanum zirconate titanate	$\text{Pb}_{0.925}\text{La}_{0.05}\text{Zr}_{0.56}\text{Ti}_{0.44}\text{O}_3$	Polycrystalline ceramic	$d_{33}=545$
Polyvinylidene fluoride	$(\text{CH}_2\text{CF}_2)_n$	Oriented film	$d_{31}=28$
Potassium dihydrogen phosphate	KH_2PO_4	Single crystal	$d_{36}=21$
Quartz	SiO_2	Single crystal	$d_{11}=2.3$
Zinc oxide	ZnO	Single crystal	$d_{33}=12$
Trimethylchloromethyl ammonium trichloromanganese II	$[\text{Me}_3\text{NCH}_2\text{ClMnCl}_3, (\text{TMCMMnCl}_3)]$	Single phase	$d_{33}=185$
Samarium-doped (Sm-PMN-PT)	$\text{Sm-doped Pb}(\text{Mg}_{1/3}\text{Nb}_{2/3})\text{O}_3 \cdot \text{PbTiO}_3$	Single crystal	$d_{33}=3400\text{--}4100$
Cellulose	$(\text{C}_6\text{H}_{10}\text{O}_5)_n$	Crystalline	$d_{33}=4.7\text{--}6.4$
Collagen	—	Crystalline	$d_{33}=5$
Bacteriophage	—	Crystalline	$d_{33}=7.8$
Diphenyl diisopropylamino phosphonium hexafluorophosphate	$[\text{Ph}_2(\text{iPrNH})_2\text{P}] \cdot \text{PF}_6$	Crystalline	$d_{33}=8$

TABLE 2 The triboelectric series that ranks various materials with respect to their tendency to lose (positive) or gain (negative) electrons in the contact charging process.

↑	Polyformaldehyde 1.3-1.4	(continued)	↓
Positive	Etylcellulose	Polyester (Dacron)	Negative
	Polyamide 11	Polyisobutylene	
	Polyamide 6-6	Polyurethane flexible sponge	
	Melanime formal	Polyethyl terephthalate	
	Wool, knitted	Polyvinyl butyral	
	Sil, woven	Polychlorobutadiene	
	Aluminum	Natural rubber	
	Paper	Polyacrilonitrile	
	Cotton, woven	Acrilonitrile-vinyl chloride	
	Steel	Polybisphenol carbonate	
	Wood	Polychloroether	
	Hard rubber	Polyvinylidene chloride (Saran)	
	Nickel, copper	Polystyrene	
	Sulfur	Polyethylene	
	Brass, silver	Polypropylene	
	Acetate, rayon	Polyimide (Kapton)	
	Polymethyl methacrylate (Lucite)	Polyvinyl chloride (PVC)	
	Polyvinyl alcohol	Polydimethylsiloxane (PDMS)	
	(continued)	Polytetrafluoroethylene (Teflon)	

Lavine et al. [53] explored biological soft tissues, which can also show a piezoelectric effect. Later, ribonucleic acid and single-stranded DNA film were found to be efficient piezoelectric materials [54].

In 1978 Ando et al. [55] explored the piezoelectric, dielectric, and elastic nature of silk fibers (Fig. 3D). They observed that elongation of the silk fibers provided higher piezoelectric constant ($d_{14} = -8 \times 10^{-8}$ CGSesu) than the original length at room temperature. Furthermore, uniaxially ordered *Bombyx mori* cocoons' silk fibers has been shown the shear piezoelectricity and proved by Kaplan et al. (Fig. 3E) [56]. They treated the silk fibers using different processing techniques such as the draw ratio, the drawing method, and postdraw treatment to evaluate the piezoelectric coefficient.

In 2018 Karan et al. [51] for the first time realized that spider silk (SS) fiber can show vertical/out-of-plane piezoelectricity ($d_{zz} \sim 0.36 \text{ pm/V}$) under mechanical stress, which they successfully established by piezoresponse force

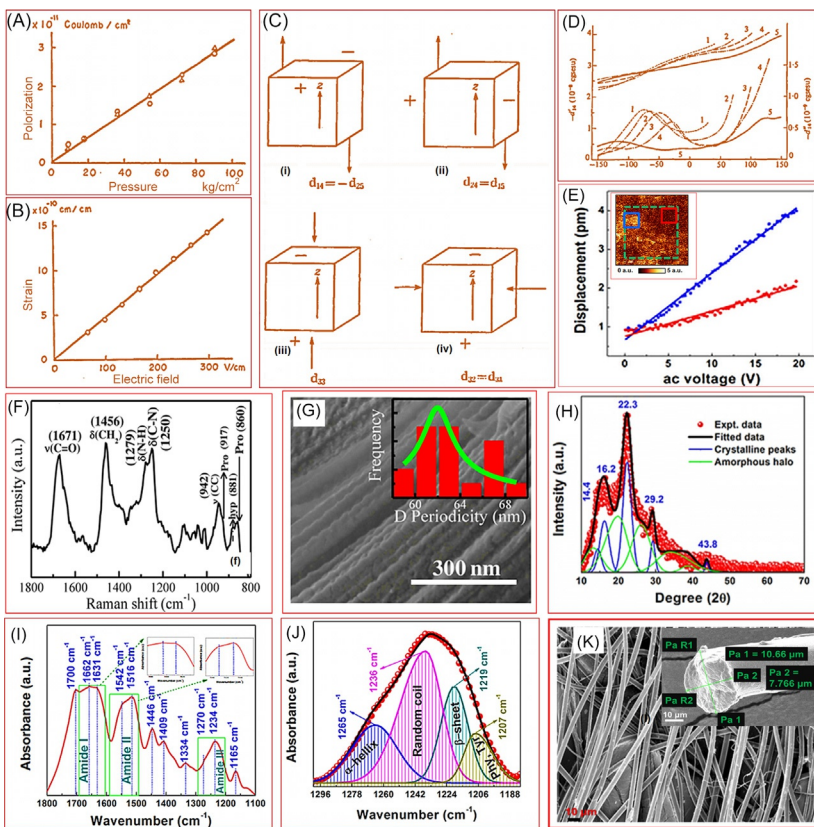


FIG. 3 (A and B) Direct piezoelectric effect and converse piezoelectric effect for bone. (C) Relation among polarization (*negative and positive signs*) and stress (*arrows*). (D) Variation of temperature on piezoelectric strain constant $d_{14} = d'_{14} - id''_{14}$ for oriented silk fibroin (content of water in wt%: 1 → 11%; 2 → 7%; 3 → 5%; 4 → 2%; 5 → 0%). (E) Variation of displacement with AC voltage. Inset of (G) shows the PFM amplitude image (scale bar of 500 nm). (F) Raman spectrum and (G) FESEM image (D-periodicity histogram shown in inset) for fish scale. (H) XRD pattern with deconvolution and (I) FTIR spectra with deconvoluted (J) patterns (amide III region) of SS. (K) FESEM image of SS with enlarged view of a single fiber (inset). ((A and B) Reproduced with permission from E. Fukada, I. Yasuda, *On the piezoelectric effect of bone*, *J. Phys. Soc. Jpn.* 12 (10) (1957) 1158–1162. Copyright 1957, JPS Publishing. (C) Reproduced with permission from E. Fukada, I. Yasuda, *Piezoelectric effects in collagen*, *J. Phys. Soc. Jpn.* 3 (2) (1964) 117. Copyright 1964, IOP Science. (D) Reproduced with permission from E. Fukada, *Piezoelectric properties of biological polymers*, *Q. Rev. Biophys.* 16 (1) (1983) 59–87. Copyright 1983, Cambridge Core terms. (E) Reproduced with permission from S.K. Karan, S. Maiti, O. Kwon, S. Paria, A. Maitra, S.K. Si, Y. Kim, J.K. Kim, B.B. Khatua, *Nature driven spider silk as high energy conversion efficient bio-piezoelectric nanogenerator*, *Nano Energy* 49 (2018) 655–666. Copyright 2018, Elsevier. (F and G) Reproduced with permission from S.K. Ghosh, D. Mandal, *High-performance bio-piezoelectric nanogenerator made with fish scale*, *Appl. Phys. Lett.* 109 (10) (2016) 103701. Copyright 2016, AIP Publishing. (H–K) Reproduced with permission from S.K. Karan, S. Maiti, O. Kwon, S. Paria, A. Maitra, S.K. Si, Y. Kim, J.K. Kim, B.B. Khatua, *Nature driven spider silk as high energy conversion efficient bio-piezoelectric nanogenerator*, *Nano Energy* 49 (2018) 655–666. Copyright 2018, Elsevier.)

microscopy (PFM) analysis (Fig. 3E). This is one of the breakthrough works on out-of-plane piezoelectric effects of SS in the biopiezoelectricity scientific community. The reason behind vertical piezoelectricity was due to α -helix structure, ordered and less ordered β -sheet crystal, various ordered microfibrils, carbonyl groups, and amino and hydroxyl groups in its backbone. The strong interaction between the crystalline domains and the strained elastic semiamorphous regions is responsible for the existence of out-of-plane piezoelectricity of natural SS fiber [51]. Piezoelectricity in supramolecular packing of amino acids in control state has been shown by Thompson et al. recently [57]. They reported high shear piezoelectricity of $\sim 178 \text{ pm/V}$ in amino acid crystal β -glycine, through quantum mechanical calculations. The supramolecular packing effect is responsible for the piezoelectric response in amino acid. Material structure and morphology are very important tools to evaluate the exact property of nature-driven biomaterials. To find out the existence of triple helix amino acid structures in the polypeptide chains of fish scale, Mandal et al. used Raman spectroscopy (Fig. 3F) [47]. The absorption band at $\approx 1671 \text{ cm}^{-1}$ for $\nu(\text{C}=\text{O})$ stretching (amide I band) in Gly-X-Y tripeptide sequences and peaks for $-\text{CH}_2$ deformation ($\delta(\text{CH}_2)$) (at $\approx 1456 \text{ cm}^{-1}$), plane deformation of N—H ($\delta(\text{N}-\text{H})$) (at $\approx 1279 \text{ cm}^{-1}$), and C—N stretching mode ($\nu(\text{C}-\text{N})$) (at $\approx 1250 \text{ cm}^{-1}$) confirmed the presence of a polar triple helix structure in the collagen backbone [58]. They also confirmed the compact crystalline lateral packing triple ($2\theta \approx 31.6$ degrees) and helix (at $2\theta \approx 8.8$ degrees) structure of collagen fibers from X-ray diffraction (XRD) analysis. Aligned collagen fibers with patterned structures of fish scale with D-periodicity ($\approx 62 \pm 4 \text{ nm}$) were seen by field emission scanning electron microscope (FESEM) (Fig. 3G). Furthermore, Mondal et al. also investigated the inherent piezoelectricity of fish swim bladder [48]. To investigate the inner property behind the development of piezoelectricity of SS, structural and morphological analysis is required. XRD patterns (Fig. 3H) confirmed its crystalline nature ($\approx 43\%$) due to alignment of fibers during spraying over the fibers followed by wrapping. The crystalline peaks at ≈ 22.3 degrees (2θ) with various small shoulder peaks at the 2θ region of ≈ 14.4 , ≈ 16.2 , ≈ 29.2 , and ≈ 43.8 degrees, respectively, indicate its crystalline nature. To prove the occurrence of carbonyl groups, hydroxyl, amino/amide linkage (amide I, II, and III), and their stretching and bending vibrations in the fibers' backbone, Fourier transform infrared (FTIR) analysis was studied (Fig. 3I and J). The presence of many adsorption peaks in the regions of ≈ 1700 – 1620 , ≈ 1580 – 1500 , and ≈ 1350 – 1200 cm^{-1} indicated the amide I ($\text{C}=\text{O}$ stretching vibration), amide II (N—H bending ($\delta(\text{N}-\text{H})$) coupled with C—N stretching ($\nu(\text{C}-\text{N})$)), and amide III (N—H-bending ($\delta(\text{N}-\text{H})$ vibration)), respectively [59]. The amide I region is an accumulation of random coil structure, helical conformation structure, or both, the existence of β -sheet arrangements/conformation, and the hairpin-folded antiparallel β -turn conformation. The absorption peaks at ≈ 1631 and $\approx 1662 \text{ cm}^{-1}$ (Fig. 3I and J) indicate the presence of β -sheets and α -helix secondary amino protein in SS fibers.

The four adsorption peaks at ≈ 1265 , ≈ 1236 , ≈ 1219 , and $\approx 1207\text{ cm}^{-1}$ correspond to α -helix structure, random coil structure, and β -sheet, and (Phy, Tyr) arrangement corresponds to the amide III region (Fig. 3J) [60]. The absorption corresponding to the amide III region is much more sensitive with respect to the amide II and I regions. The SS fibers also contain amide A and amide B in the region of $3600\text{--}3000\text{ cm}^{-1}$. The aligned microfibril structure with a diameter of $\approx 8\text{--}11\text{ }\mu\text{m}$ of SS has been confirmed by FESEM image (Fig. 3K).

3.2 Polysaccharide-based materials

Fukuda also predicted the piezoelectricity of polysaccharide-based materials like cellulose together with protein-based materials. He successfully demonstrated for the first time the existence of a converse piezoelectric effect (shear piezoelectric coefficient -0.1 pC/N) in cellulose fibers [61]. Due to mechanical stress or mechanical strain under an electrical field the crystal lattice of wood cellulose experienced piezoelectric polarization. Fig. 3C and D shows the external force-dependent piezoelectric effect on wood fibers. One can easily measure the anisotropy of the piezoelectric effect by altering the position of the rotating disk and clamps. Tuukkanen et al. demonstrated a self-standing native cellulose nanofibril film with a superior piezoelectric sensitivity of $\sim 4.70\text{--}6.40\text{ pC/N}$ [62]. Due to the regular alignment of dipoles inside the crystalline cellulose materials the piezoelectric property can be improved by polarization of the materials. Maiti et al. [37] explored biowaste cellulose-based onion skin (OS) with a superior piezoelectric vertical coefficient of $\sim 2.8\text{ pC/N}$. For the first time OS was reused as a piezoelectric material, which can effectively harvest mechanical energy and convert it into green electricity. In their opinion, plant materials would be very much effective in terms of their availability and handling compared to living creatures. The deformation/displacement/reorientation of crystals inside the OS experienced under external applied mechanical stress or pressure generates a piezoelectric effect as well as green electricity [61]. They also proposed that OS can have an inbuilt self-poled behavior.

Fukuda also found that α -chitin has an inherent piezoelectric property [63]: a wide temperature region from -130°C to 140°C . Chitin contains a long chain polymer of *N*-acetyl glucosamine, which is present in many insects, lobsters, crabs, fungi, shrimps, prawn shells, etc. It has a similar type of structure to cellulose and has three different crystallographic forms: α , β , and γ . Tuukkanen et al. observed that plain chitin has a high piezoelectric sensitivity of $\sim 25\text{ pC/N}$ [64]. Later, Jayakumar et al. [65] stated that the piezoelectric coefficient (d_{33}) may vary with temperature and pressure. They realized a maximum d_{33} value ($\sim 8.4\text{ pC/N}$) at 330 K for chitosan due to noncentrosymmetry. The chitin-based prawn shell nanofibers possess a piezoelectric nature with a vertical piezoelectric coefficient (d_{33}) of -2 pC/N , which may develop because of the effect of the nonlinear electrostriction biased through spontaneous polarization [3]. The chitin nanofibers, extracted from crab shell, can exhibit

piezoelectric properties and have a piezoelectric constant (d_{33}) of $\sim 9.49 \text{ pC/N}$ [3]. Schauer et al. [66] observed the variable piezoelectric effect of electrospun chitin nanofibers. They used the air gap method during electrospinning, which helped to increase the crystallinity as well as piezoelectricity of the chitin nanofibers. They also studied PFM to obtain output voltage from the chitin fibers but achieved only 0.1 peak voltage per applied pressure in kPa. Kang et al. [67] discussed the piezoelectric effect (piezoelectric constant was $\sim 3.986 \text{ pm/V}$) of electroactive nanofiber chitin films effectively used for flexible, sensible, piezoelectric transducers. The cellulose-based OS can exhibit piezoelectric properties under mechanical stress. The FTIR spectrum (Fig. 4E) shows the multiple absorption peaks and the existence of $-\text{OH}$ groups in cellulose chains corresponding to an intense peak at $\approx 3200\text{--}3400 \text{ cm}^{-1}$. Furthermore, FTIR confirms the presence of a $-\text{CH}$ stretching/carbonyl group ($-\text{C=O}$), $-\text{NH}$ bending, a carboxyl group, and $-\text{N}$ -containing bioligands present in the fibers of the OS.

H-bonding (inter/intramolecular) is developed because of the presence of C=O , amino, and $-\text{OH}$ moieties in OS crystalline fibers that ultimately induce the dipole alignments and act as self-poled piezoelectric material. They further investigated the crystallinity ($\approx 39\%$) of the OS by XRD analysis (Fig. 4F). FESEM surface image (Fig. 4G) confirmed that the aligned microfibril cellulose structure developed impulsive electrical dipoles in the OS developing a piezoelectric effect during external force. Fig. 4I shows the crystalline nature of prawn skin in an XRD pattern and exhibits a piezoelectric nature. An FESEM study of the surface and cross-sectional images for chitin fibers containing prawn shell proved its specially organized layer structure (diameter $\approx 25 \text{ nm}$) (Fig. 4J). The orientation of β -crystalline in chitin film analyzed by GIXD showed that it corresponded to planes (010) and (100) [68].

4 Structure and probable interactions

The reasons for the possible chemical/physical interaction for the generation of piezoelectricity in FSB, M13 virus, SS fibers, and chitin are shown schematically in Fig. 5. At the time of applying force we are assuming that the ordered collagen fibers create the rubbing between the crystalline α -helices fibers (on each other) which are connected via H-bonding, resulting in the generation of a piezoelectric charge in fish skin (Fig. 5A) [49]. Because of the triple helical deformation structure, electric dipoles were generated. The rod-like structure of the M13 phage is shown in Fig. 5B. The major coat protein (pVIII) mainly contains the α -helical structure and their interactions with dipole moment directions as displayed in Fig. 5C–E. The residues from 1E to 4E were presented between the first (Ala) and fifth (Asp) amino acids of the wild-type pVIII major coat arrangement, which holds two negative charges within the insert region as shown in Fig. 5F. Shin et al. demonstrated the vertically aligned nanopillars of M13 bacteriophage (phage) and its possible piezoelectricity (Fig. 5G and H) [69]. The probable H-bonding interaction in keratin present in nail is shown

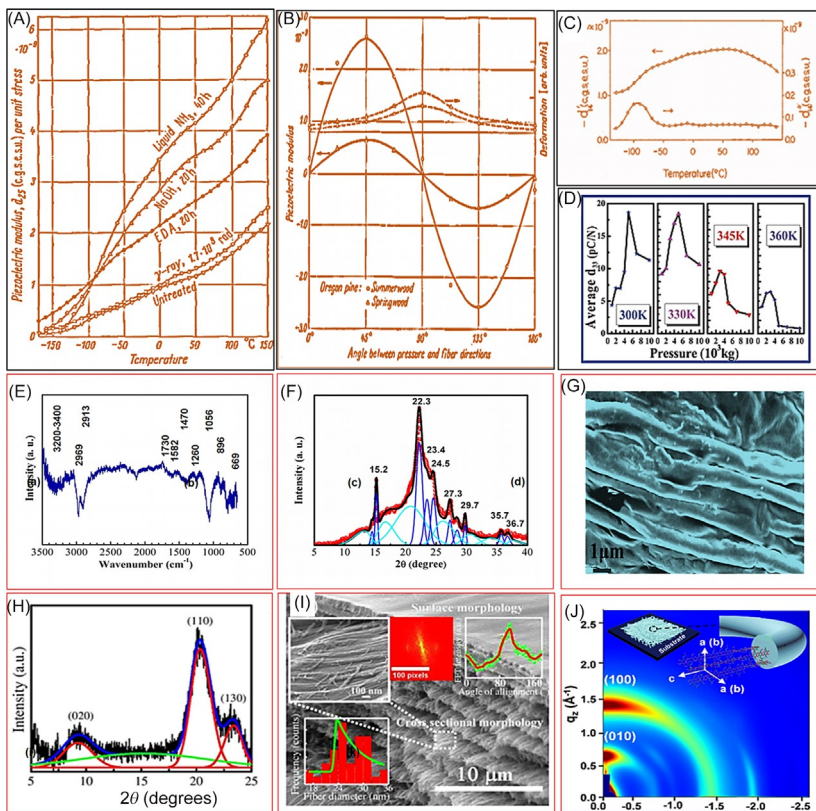


FIG. 4 (A) Piezoelectric modulus and mechanical deformation varies with the angle between pressure and fiber directions for summerwood and springwood (Oregon pine). (B) Polarization generation in piezoelectric wood. (C) Variation of piezoelectric constant $d_{14} = d'_{14} - id''_{14}$ for α -chitin with temperature. (D) Piezoelectric coefficient (d_{33}) of chitosan at different pressures and temperatures. (E) FTIR spectra and (F) XRD and (G) FESEM image of OS, respectively. (H) X-ray diffraction patterns and (I) FESEM of prawn shell. The inset demonstrates the correspondence to 2D FFT, histogram profile, and radial intensity distribution of chitin-aligned fiber. (J) Grazing incidence X-ray (GIXD) pattern of Si substrate containing chitin film (0.2%, w/v). ((A and B) Reproduced with permission from E. Fukada, *Piezoelectricity as a fundamental property of wood*, *Wood Sci. Technol.* 2 (4) (1968) 299–307. Copyright 1968, Springer. (C) Reproduced with permission from E. Fukada, S. Sasaki, *Piezoelectricity of α -chitin*, *J. Polym. Sci. Polym. Phys.* 13 (9) (1975) 1845–1847. Copyright 1975, Wiley-VCH. (D) Reproduced with permission from E. Praveen, S. Murugan, K. Jayakumar, *Investigations on the existence of piezoelectric property of a bio-polymer-chitosan and its application in vibration sensors*, *RSC Adv.* 7 (56) (2017) 35490–35495. Copyright 2017, The Royal Society of Chemistry. (E–G) Reproduced with permission from S. Maiti, S.K. Karan, J. Lee, A.K. Mishra, B.B. Khatua, J.K. Kim, *Bio-waste onion skin as an innovative nature-driven piezoelectric material with high energy conversion efficiency*, *Nano Energy* 42 (2017) 282–293. Copyright 2017, Elsevier. (F–H) Reproduced with permission from S.K. Ghosh, D. Mandal, *Bio-assembled, piezoelectric prawn shell made self-powered wearable sensor for non-invasive physiological signal monitoring*, *Appl. Phys. Lett.* 110 (12) (2017) 123701. Copyright 2017, AIP Publishing. (J) Reproduced with permission from K. Kim, M. Ha, B. Choi, S.H. Joo, H.S. Kang, J.H. Park, B. Gu, C. Park, C. Park, J. Kim, *Biodegradable, electro-active chitin nanofiber films for flexible piezoelectric transducers*, *Nano Energy* 48 (2018) 275–283. Copyright 2018, Elsevier.)

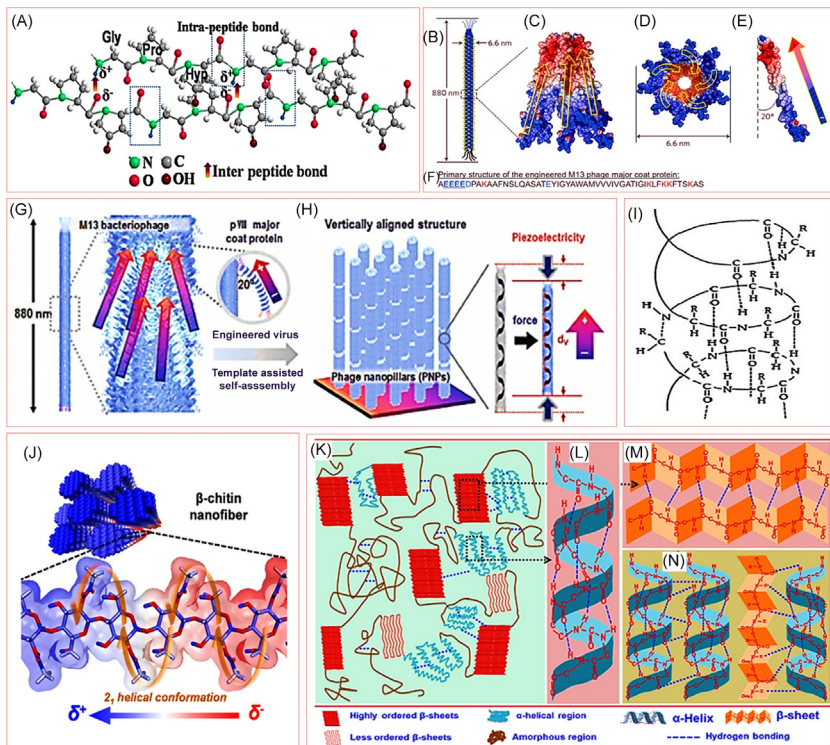


FIG. 5 (A) Origination of polarization in fish skin for intra- and interpeptide collagen chains consisting of a Gly-Pro-Hyp amino acid motif sequence is represented schematically. (B) Schematic representation of the structure of the piezoelectric M13 phage. (C) After bioengineered modification with four glutamate amino acids the side view image shows the electrostatic potential of the M13 phage. (D) Cross-sectional image (vertical) of the electrostatic potential of the M13 phage. (E) Side-view diagram of the electrostatic potential of a single M13-phage pVIII coat protein. (F) Primary structure arrangement of the engineered major coat protein. (G and H) Vertically aligned M13 bacteriophage nanopillars shown schematically. (I) Nail containing α -keratin with a helical structure is shown schematically. (J) Spontaneous polarization present in β -chitin nanofibers shown schematically. (K) Structural presentation in SS fibers shown schematically. The structures for (L) α -helix and (M) β -sheet are shown schematically. (N) Expected interaction from inter/intramolecular H-bonding in β -sheets and α -helices. (Reproduced with permission from S. Maiti, S.K. Karan, J.K. Kim, B.B. Khatua, *Nature driven bio piezoelectric/triboelectric nanogenerator as next generation green energy harvester for smart and pollution free society*, *Adv. Energy Mater.* 9 (9) (2019) 1803027. Copyright 2019, WILEY-VCH Verlag GmbH & Co. KGaA, Weinheim.)

in Fig. 5I. The α -helix and β -sheet structure and their probable H-bonding interaction in SS fibers are represented schematically in Fig. 5K–N.

The SS fibers rub together between the neighboring surfaces of α -helix structures via H-bonding under an external mechanical force (Fig. 5L and M) and develop electrical high-dipole moments [3].

5 Fabrication of biopiezoelectric nanogenerator devices

So far we have discussed the piezoelectric properties of various materials but now we need to know the real application of the materials. Hence, we need to fabricate the device for smart electronic applications.

Previously, researchers did not concentrate on fabrication of the device. Scientists are focusing on bionanogenerators for green energy-harvesting applications from mechanical/biomechanical motions, industrial applications, and even in bioapplications. There are several procedures [3] to construct the device using different piezoelectric materials like virus/OS/SS/fish skin as shown in Fig. 6.

5.1 Protein-based biopiezoelectric nanogenerators

Karan et al. found piezoelectricity in SS fiber [51] and ESM [36] and the fabricated devices achieved outstanding output values using these materials as potential devices. The spider silk biopiezoelectric nanogenerator (SSBPNG) delivered a high voltage of ≈ 21.3 V and a power density of $\approx 3.23 \mu\text{W cm}^{-2}$ with a current value of $\approx 0.68 \mu\text{A}$ (Fig. 7A–I). Even in reverse connection the device has the ability to deliver almost identical output values, confirming its potential dipole reversibility. The enhancement of output voltage was achieved by applying pressure (≈ 5 to ≈ 51 N) because of the gradual increase of crystal deformation with improved pressure on the device [6]. However, crystal deformation became saturated after ≈ 51 N and a negligible change of output voltage was observed. Like pressure, frequency also participates to improve the output voltage and increase slightly with increasing frequency in the range of ≈ 1 to ≈ 3 Hz at ≈ 82.2 kPa. The variation of output voltage with frequency associated with impedance decreased slowly with increasing strain rate [22]. Moreover, a 1D wire-like SSBPNG device was developed to explore its potential applicability in a wide area and it delivered a high-output voltage (≈ 5.7 V) and current (≈ 52 nA) during bending of the wire. For imparting, these values are ≈ 8.0 V and ≈ 77 nA, respectively (Fig. 7G and H), and ≈ 3.2 V was achieved for stretching the 1D SSBPNG device. Again, ESM was shown as an efficient piezoelectric material because of the existence of collagen and protein in its moiety. This designed eggshell membrane biopiezoelectric nanogenerator (ESMBPNG) delivered an output voltage of ≈ 26.4 V and a current of $\approx 1.45 \mu\text{A}$.

Furthermore, variation of output voltage with pressure and frequency was studied, and output values were improved with improving pressure (≈ 8 to ≈ 90 kPa) and frequency up to a certain value for ESMBPNG. Crystal deformation is the main reason behind this characteristic. In addition, fish scale was also introduced as an effective piezoelectric material for green energy harvesting and achieved a current of $\sim 1.5 \mu\text{A}$ and an output voltage of ≈ 4 V with a power density of $\sim 1.14 \mu\text{W cm}^{-2}$. Furthermore, FSB was used as biopiezoelectric material and had the ability to provide a current of ≈ 51 nA and an output

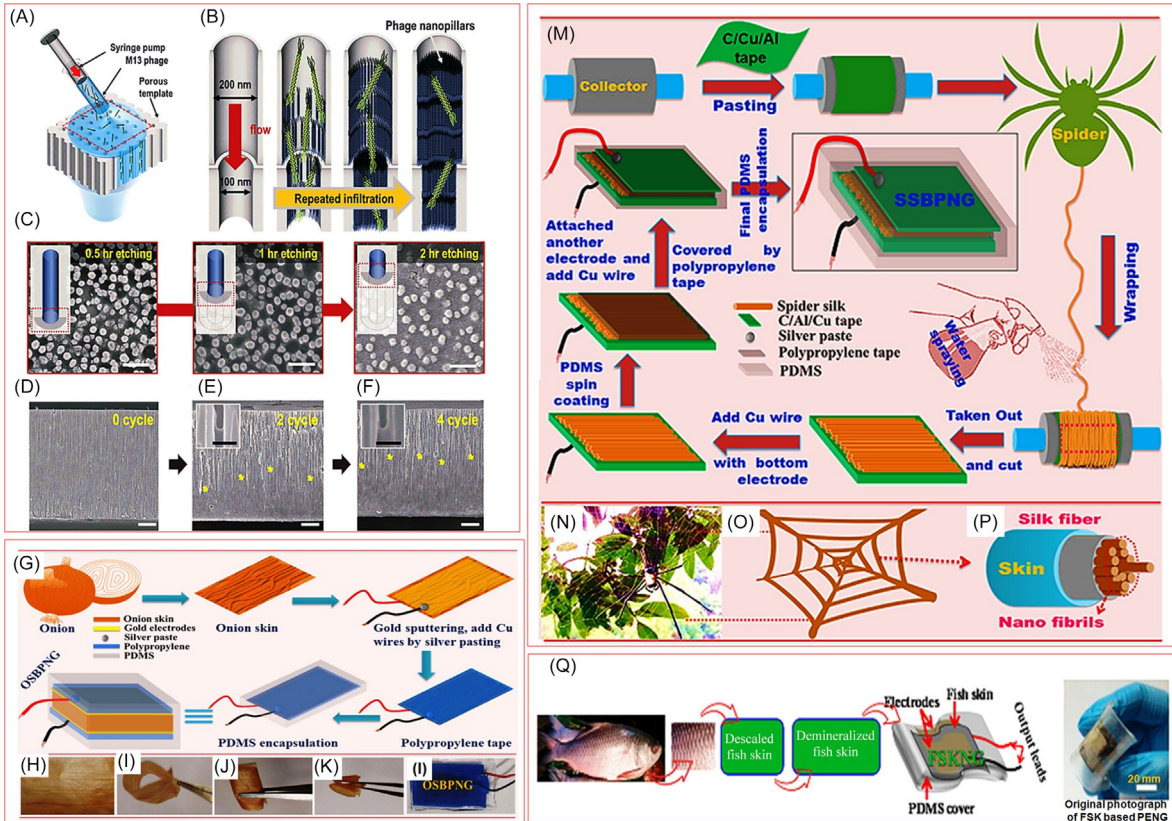


FIG. 6 (A–F) Schematic of the enforced infiltration for the fabrication of vertically aligned phage nanopillars (M13 bacteriophages), demonstration of the phage nanopillar formation controlled through continuous infiltration in the porous template, morphological study, and cross-sectional image of the phage nanpillars in the porous template at different infiltration cycles, respectively. The scale bar for the inset is 500 nm. (G) Schematically shown fabrication procedure of an OS-based bionanogenerator (OSBPNG). (H) Real image of OS, demonstration of flexibility of OS by (I) bending, (J) rolling, and (K) twisting and (L) real picture of OSBPNG, respectively. (M) SS-based bionanogenerator (SSBPNG) fabrication technique. (N) Real image of SS. (O) Schematic view of SS fiber, (P) Single SS fibril structure. (Q) Schematically shown fabrication procedure of fish skin-based nanogenerator. (Reproduced with permission from S. Maiti, S.K. Karan, J.K. Kim, B.B. Khatua, *Nature driven bio piezoelectric/triboelectric nanogenerator as next generation green energy harvester for smart and pollution free society*, *Adv. Energy Mater.* 9 (9) (2019) 1803027. Copyright 2019, WILEY-VCH Verlag GmbH & Co. KGaA, Weinheim.)

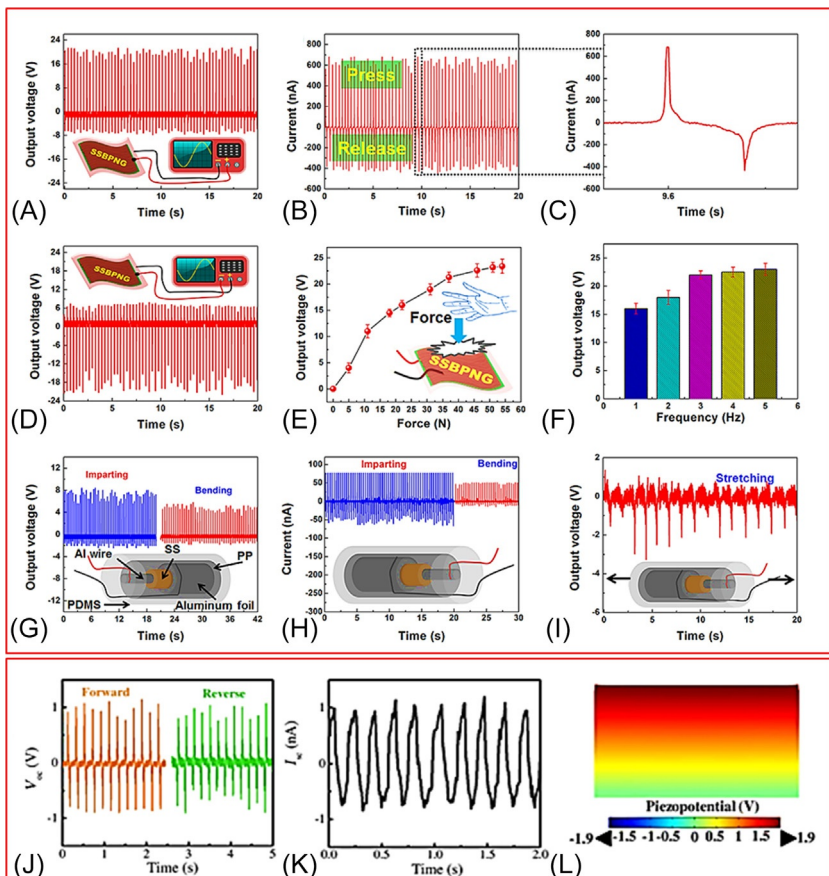


FIG. 7 (A–C) Output performance (voltage and current with enlarged view) for forward connection and (D) during reverse connection from the SSBPNG under mechanical stress. (E) Force and (F) frequency dependence output voltage from an SSBPNG. Output voltage during (G) bending, (H) imparting, and (I) stretching. Inset shows corresponding devices. (J) Developed voltage for forward and reverse connections. (K) Current and (L) simulated curve of prawn skin for piezopotential distribution. (Reproduced with permission from S. Maiti, S.K. Karan, J.K. Kim, B.B. Khatua, *Nature driven bio piezoelectric/triboelectric nanogenerator as next generation green energy harvester for smart and pollution free society*, *Adv. Energy Mater.* 9 (9) (2019) 1803027. Copyright 2019, WILEY-VCH Verlag GmbH & Co. KGaA, Weinheim.)

voltage of ~ 10 V with instantaneous power density ($\approx 4.15 \mu\text{W cm}^{-2}$). This nature-driven bioinspired energy-harvesting device could be used even in large-scale applications. Fish scale-based PNG shows an output voltage (~ 14 V) has been increased by connecting multiple devices (four) in series (Fig. 8A). Also, voltage and current have been monitored for SSBPNG and ESMBPNG by connecting multiple devices in series and parallel, respectively [36, 51]. For SSBPNG, an output voltage of ~ 65 V was achieved for three devices in series connection. For ESMBPNG, an output voltage of ~ 65 V (in

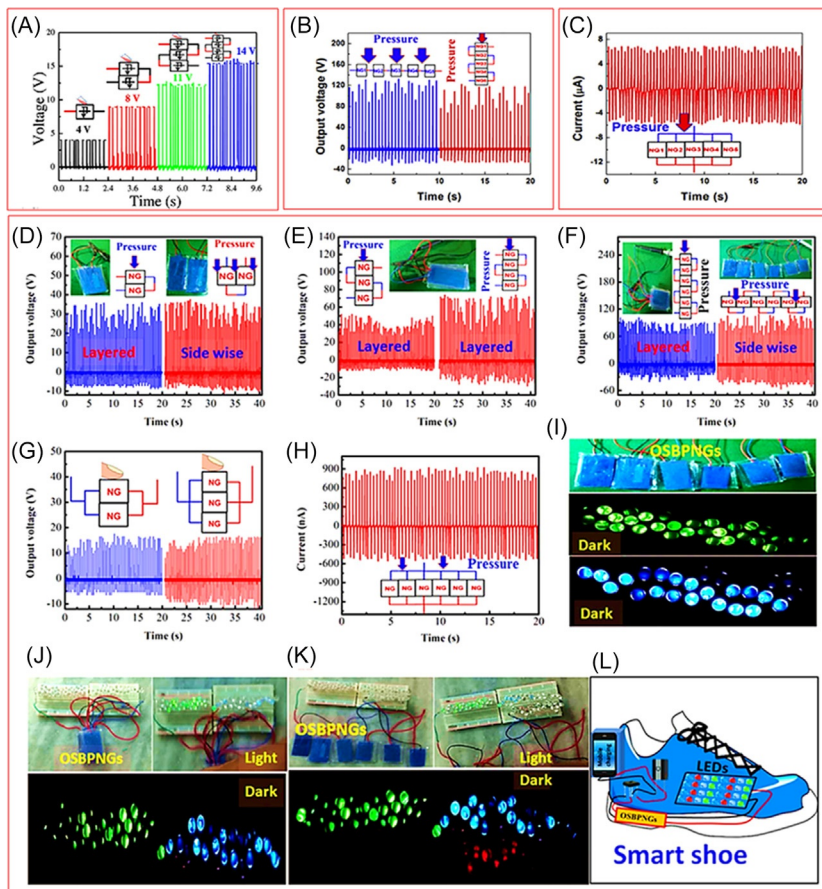


FIG. 8 (A) Generated rectified voltages by assembling four BPNGs (fish skin based) in serial connection. (B, C) Generated output voltage for ESMBPNG when five units are assembled serially and parallelly (inset shows circuit diagrams), and output current (serial connection), respectively. The generated output voltage from OSBPNG during serial assembling (D) two units, (E) three/four units, and (F) six units. (G) Voltage for parallel connection (two/three units). (H) Current for assembling six units parallelly (circuit in inset). Assembling six units lights up (I) blue and green LEDs individually under a dark state, (J) lights up blue/green LEDs during light/dark, and (K) lights up combined blue, red, and green LEDs instantly during light/dark. (L) Probable fabrication of a smart shoe using OSBPNGs is shown schematically. It can light up several commercial LEDs when walking/runnning. (Reproduced with permission from S. Maiti, S.K. Karan, J.K. Kim, B.B. Khatua, *Nature driven bio piezoelectric/triboelectric nanogenerator as next generation green energy harvester for smart and pollution free society*, *Adv. Energy Mater.* 9 (9) (2019) 1803027. Copyright 2019, WILEY-VCH Verlag GmbH & Co. KGaA, Weinheim.)

series) and a current of $\sim 6 \mu\text{A}$ (in parallel) were achieved for five devices, respectively (Fig. 8B and C). Thus these biodegradable Bio-PNGs would be effective for harvesting energy without hampering ecosystems or human/animal health to drive modern, smart, and flexible electronics in new directions. Thus SS fibers, ESM, fish skin, fish swim bladder, or prawn shell could be new

members of the renewable energy-harvesting family to protect our society from huge amounts of e-waste. Also, a genetically modified M13 bacteriophage virus was used to design a Bio-PNG to power up a liquid-crystal display.

5.2 Polysaccharide-based BPNGs

Cellulose-based OS that can generate electricity through the piezoelectric effect has been reported by Maiti et al. [37] They reported that OSBPNG can deliver an output current of $\approx 166\text{ nA}$ and a voltage of $\approx 18\text{ V}$, just by applying mechanical pressure by hand on the device. They also found that these values could be increased by connecting many devices in series or parallel. Thus, as per requirements, output performance can be well monitored for various applications. Interestingly, enhancement of output voltages with increasing number of units in series connection is shown in Fig. 8D (for two units), Fig. 8E (for three and four units), and Fig. 8F (106 V for six units). Hence, this OSBPNG would be very effective to power up many smart devices and could be used for large-scale industrial applications in the near future. Most importantly, it is one of the harvesting approaches that produces the least pollution. Furthermore, they checked that the generated output voltage from six units (in series) showed the same value when devices are arranged in layer-by-layer (stacked vertically) or side-by-side arrangement (Fig. 8F).

This result indicated that devices could be arranged in any format to harvest green energy as per space availability (layer-by-layer arrangement for narrow position and side-by-side arrangement for larger space/high surface areas like a road), which is one more unique characteristic of this energy-harvesting technology. Nevertheless, output voltage multiple units are unchanged in the same parallel connection (Fig. 8G). Moreover, parallel connection of multiple units (six units) increased the current value to $\sim 900\text{ nA}$, which was almost five times higher than a single unit (Fig. 8H). Furthermore, OSBPNGs have the ability to power up instantaneously numerous LEDs separately (Fig. 8I) and collectively (Fig. 8J and K) by connecting six units in series (layer-by-layer or side-by-side). Moreover, proper design of OSBPNGs under shoe rubber (Fig. 8L) was able to power up LEDs in various working conditions like walking, jumping, and running/dancing, confirming its possible potentiality in the future.

6 BPNGs and their applications

Bio-PNGs are very much effective for harvesting green energy from different biomechanical activities, even various ultrasonic vibrations. ESMBPNGs provided $\sim 1.2\text{ V}$ during mouth blowing and $\sim 0.7\text{ V}$ during writing on it (Fig. 9A). Because of the ultrasensitivity of an ESMBPNG, it could be used to design a smart pad and by writing on this pad energy could be harvested. Furthermore, elbow motions ($\approx 5.2\text{ V}$), wrist motions (up/down) ($\approx 6.9\text{ V}$), and neck

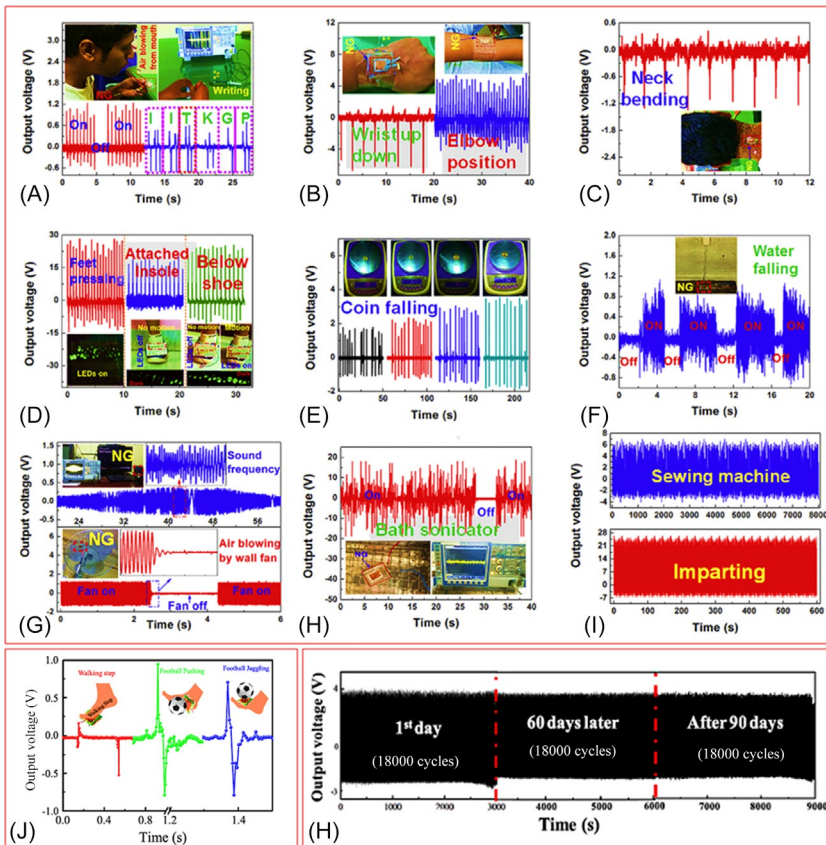


FIG. 9 Generation of output voltage during (A) mouth blowing and writing, (B) wrist and elbow motions, (C) neck movement, (D) feet pressing, walking wearing a shoe, (E) different coins (INR) falling, (F) water flowing, (G) speaker-generated sound frequency and fan air blowing, (H) sonicator vibration. (I) Mechanical durability for an ESMBPNG during sewing machine and hand-punching situations. (A–H) Actual ESMBPNG devices fixed with corresponding specified positions for realizing electric output are shown in the inset. (J) Output voltage generated from walking, juggling, and pushing a football for an FSBPNG. (K) Durability test of BPNG up to 90 days. (Reproduced with permission from S. Maiti, S.K. Karan, J.K. Kim, B.B. Khatua, *Nature driven bio piezoelectric/tri-boelectric nanogenerator as next generation green energy harvester for smart and pollution free society*, *Adv. Energy Mater.* 9 (9) (2019) 1803027. Copyright 2019, WILEY-VCH Verlag GmbH & Co. KGaA, Weinheim.)

movements (≈ 1.3 V) could also generate electricity (Fig. 9B and C) using this device. Additionally, feet pressing/releasing generated an output voltage of ≈ 27.5 V, which has the ability to power up LEDs instantaneously (Fig. 9D). Moreover, an ESMBPNG integrated into the insole and bottom part of a shoe provided output voltages of ~ 19.3 and ~ 25 V, respectively, which powered up 10 LEDs during walking (Fig. 9D). Also, a voltage of ~ 30 V was achieved

during running/jogging on an ESMBPNG-integrated treadmill. Furthermore, ultrasensitivity has been established through various weighted coins (Indian rupee, INR) when allowed to fall and achieved output values in every case ([Fig. 9E](#)). In addition, an ESMBPNG produced ~ 0.9 V during tap water flowing as clearly observed in [Fig. 9F](#) [36]. Sound frequency (20–20,000 Hz), a fan blowing air (~ 1250 rpm), and vibration (bath sonicator: 42 Hz) also effectively play vital roles in delivering output voltages of ~ 1.10 , ~ 0.35 ([Fig. 9G](#)), and ~ 18 V ([Fig. 9H](#)), respectively. A sewing machine provided ~ 6.5 V and this value remained unchanged even after $\sim 48,000$ cycles ([Fig. 9I](#)), confirming the device's high mechanical durability.

Mechanical durability was further confirmed by repeated hand punching over long periods (1600 cycles) ([Fig. 9I](#)). Even after 2.5 months the device produced almost the same output values, indicating that it could be used for long-term potential applications. A biowaste FSB-based NG also delivered output values during walking or soccer playing ([Fig. 9J](#)). The long-term stability of the device was further confirmed ([Fig. 9K](#)). Thus nature-driven biodegradable materials are effectively and widely considered to integrate with bio-devices for harvesting green energy to save society from dangerous e-wastes. Thus it is concluded that nothing is valueless in nature and could be reformatted in another design to serve another valuable purpose.

7 Bio-based triboelectric nanogenerator

7.1 BTNGs based on protein materials

Various naturally abundant bio-based materials are effectively used to design high-performance TNG devices as efficient green energy-harvesting sources. Oh et al. [70] designed a silk fiber (*B. mori* silkworm)-based Bio-TNG through the electrospinning technique. Silk fibers are rich in different amino proteins, peptide chains, β -pleated sheets, and α -helix structures, which are very much responsible for generating electricity. These protein sequences are interlinked through H-bonding ([Fig. 10A](#)). [Fig. 10B–L](#) provides a detailed description of device fabrications and working procedures for this device. Thus a silk-based Bio-TNG delivered a significantly high output voltage of ~ 15 V. Furthermore, this device was mechanically highly durable and delivered continuous identical output values even after long cycles. The charging capability of the device is very fast and provided a high triboelectric surface charge density of $\sim 1.86 \mu\text{C}$ with an instantaneous power density of $\sim 4.3 \text{ mW m}^{-2}$ at a $5 \text{ M}\Omega$ electric load resistance ([Fig. 10C–L](#)). In addition, Yang et al. [71] developed a human skin touch-based TNG for harvesting green energy and its applications as a tactile sensor ([Fig. 10M–T](#)). This device was developed through a contact-separation pathway between a polydimethylsiloxane (PDMS) film micropyramid structure and the human skin touching area. Thus this device delivered a remarkably high output voltage of -1000 V with a significantly high current

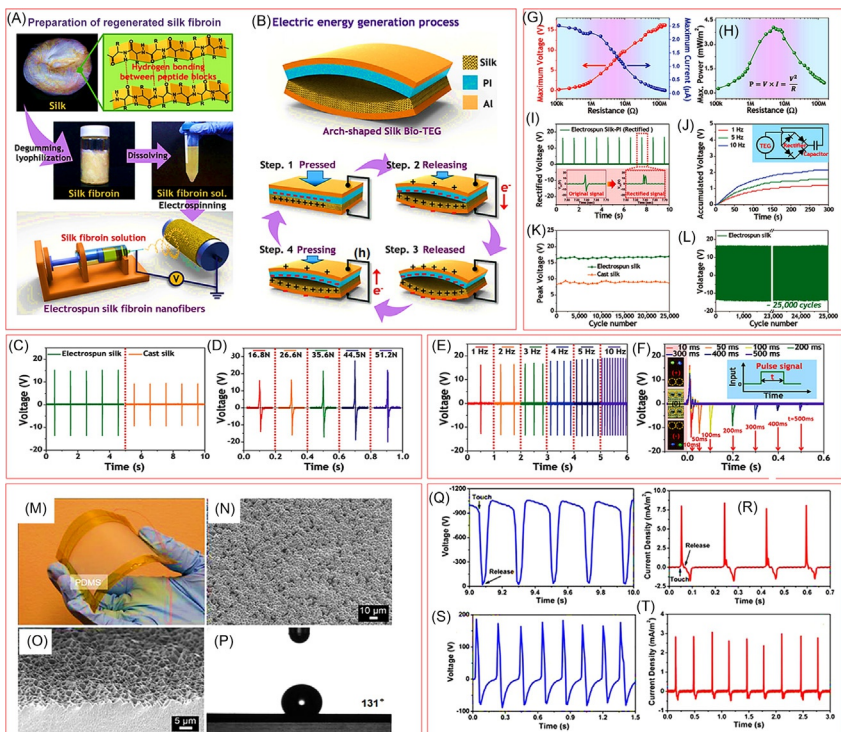


FIG. 10 (A) Schematically shows the preparation of electrospun silk fibroin and electrospun silk fibroin nanofiber-networked film. (B) Working principle of silk fibroin-based TNG. (C) Output voltages generated from electrospun and cast silk. (D) Force, (E) frequency, and (F) pulse width dependence output voltage of the fabricated TNG. Inset of (F) shows the LED turn-on/off at the time of forward or backward signal. (G) Output voltage and (H) output power varying with external load resistance. (I) Generated output rectified voltage. (J) Accumulated output voltage by a $10\ \mu\text{F}$ capacitor charged by the silk Bio-TEG. (K) Stability and durability comparison of electrospun and cast silk under basic output signals. (L) Under long cycle range the stability test and durability were performed for silk Bio-TEG. (M) Micropyramidal structured PDMS film on the ITO electrode shown as an image. (N and O) SEM images of PDMS surface. (P) Contact angle between water and PDMS. (Q) Generated output voltage and (R) current density. The generated (S) output voltage and (T) current density of the fabricated device during the external load resistance of $100\ \text{M}\Omega$. (*Reproduced with permission from S. Maiti, S.K. Karan, J.K. Kim, B.B. Khatua, Nature driven bio piezoelectric/triboelectric nanogenerator as next generation green energy harvester for smart and pollution free society, Adv. Energy Mater. 9 (9) (2019) 1803027. Copyright 2019, WILEY-VCH Verlag GmbH & Co. KGaA, Weinheim.*)

density of $\sim 8\ \text{mA m}^{-2}$. Moreover, this fabricated device provided a power density of $\approx 500\ \text{mW m}^{-2}$ at $100\ \text{M}\Omega$, which could have ability to light up LEDs instantaneously. In general, the working mechanism for designing the TNG was based on the charge transfer between an ITO electrode and ground by modulating the separation distance between the PDMS microstructured film and tribocharged human skin.

7.2 BTNG-based polysaccharide materials

Kim et al. [72] fabricated a TNG using bacterial nanocellulose (BNC) to harvest green energy (Fig. 11A). The energy harvesting principle and fabricated curvature-shaped device are schematically shown in Fig. 11B, which schematically shows that upon imparting and releasing, the electrical charge is generated (Fig. 11B) as well as the possible working mechanism as described earlier [73]. The Bio-TNG delivered a voltage of 13 V under cyclic pressure (Fig. 11C). They achieved a voltage of 7 V while polyimide (PI) film was fixed on the Cu foil (Fig. 11D). Additionally, they plotted comparative plots against different pulse widths from 10 to 500 ms under similar input conditions (Fig. 11E and F). High voltage was obtained for BNC-Bio-TNG because of increased triboelectrification compared to BNC-PI-TNG [72]. They proved that the output signal width was marginally narrower on every side in BNC-Bio-TNG (Fig. 11E and F). This caused quick surface electrification on the conducting material's (Cu) surface compared to PI [74]. Moreover, voltage was checked with applied pressure (Fig. 11G) and frequency (Fig. 11H). With the increasing of applied pressure on the device the output voltage gradually increased. Due to the higher friction speed (from ≈ 16.8 to ≈ 51.2 N) the electrification effect increased, which ultimately increased the output performance of the device. They also found marginal improvement of output performance with increasing frequency for BNC-Bio-TNG (Fig. 11H). They clarified that charge states were not simply neutralized even under high frequency on the friction surface [42], which resulted in higher electrostatic induction. With the help of rectification, they transferred an alternating signal into a direct signal and stored it in a capacitor. The rectified current signal (constant measuring conditions) for BNC-Bio-TNG is shown in Fig. 11I. They checked the storage capacity and the stored charge was $\approx 8.1 \mu\text{Cm}^{-2}$ (Fig. 11J). The load resistance variation with output voltage/current is shown in Fig. 11K. They achieved high instantaneous power density of $\approx 4.8 \text{ mWm}^{-2}$ at 1 MΩ (Fig. 11L). Wang et al. [75] fabricated a Bio-TNG using chitosan biopolymer. They developed many chitosan biopolymers for harvesting energy. Device fabrication is well provided in Fig. 11M. The positive triboelectric charges were accumulated on the chitosan surface (for pure chitosan) due to the tendency to lose electrons from the chitosan film compared to Kapton, which caused electrons to flow in an external circuit. They explored output performance for all chitosan biopolymers as provided in Fig. 11N and O. The statistical output performance data are shown in Fig. 11P. The 10% acetic acid chitosan film provided the highest output values. They also measured the output value for pure chitosan film and gave a power density of $\approx 2.1 \mu\text{Wm}^{-2}$ (Fig. 11Q), and 10% acetic acid chitosan film provided $\approx 17.5 \mu\text{Wm}^{-2}$. Wang et al. [75] for the first time introduced naturally abundant biodegradable leaves for harvesting green energy through TNG. These leaf-based TNGs definitely participated in powering many smart and portable green electronics devices for the next generation through their pollution-free approach. In this device, the leaf itself plays the role of electrode as well as the effective triboelectric layer.

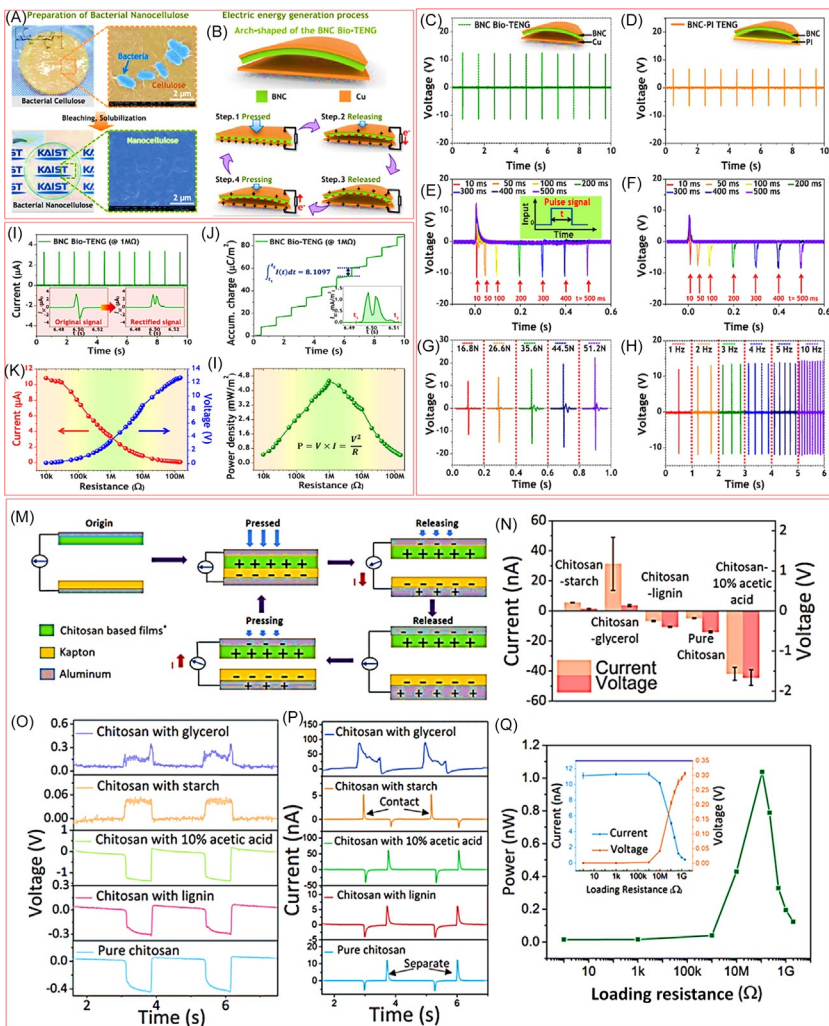


FIG. 11 (A) Optical and SEM images for BNC before and after solubilization. (B) Possible working mechanism and schematic fabrication procedure of Bio-TNG. The voltage for (C) BNC-Bio-TNG and (D) BNC-PI TNG under cyclic applied force. The comparative output voltages under different input pulse widths for (E) BNC-Bio-TNG and (F) BNC-PI-TNG. The output voltages for BNC-Bio-TNG vary under (G) magnitude and (H) frequency. (I) Rectified current and (J) stored charge for BNC-Bio-TNG at 1 MΩ. (K) Load resistance-dependent current and voltage. (L) External load resistance variation instantaneous power density. (M) The working mechanism for the device. (N) Voltage and (O) current value. (P) Average statistical values and standard deviations for device signal. (Q) Load resistance varies with output power for pure chitosan film. (Reproduced with permission from S. Maiti, S.K. Karan, J.K. Kim, B.B. Khatua, *Nature driven bio piezoelectric/triboelectric nanogenerator as next generation green energy harvester for smart and pollution free society*, *Adv. Energy Mater.* 9 (9) (2019) 1803027. Copyright 2019, WILEY-VCH Verlag GmbH & Co. KGaA, Weinheim.)

To fabricate a leaf-based high-performance TNG device, a conducting metal electrode was fixed with an as received leaf to develop an electrical connection, and a polymer sheet of PMMA (poly[methyl methacrylate]) was utilized as contact film, which had a huge electron affinity difference with the green leaf, as schematically displayed in Fig. 12A. *Hosta plantaginea* (*Hosta*) leaf was

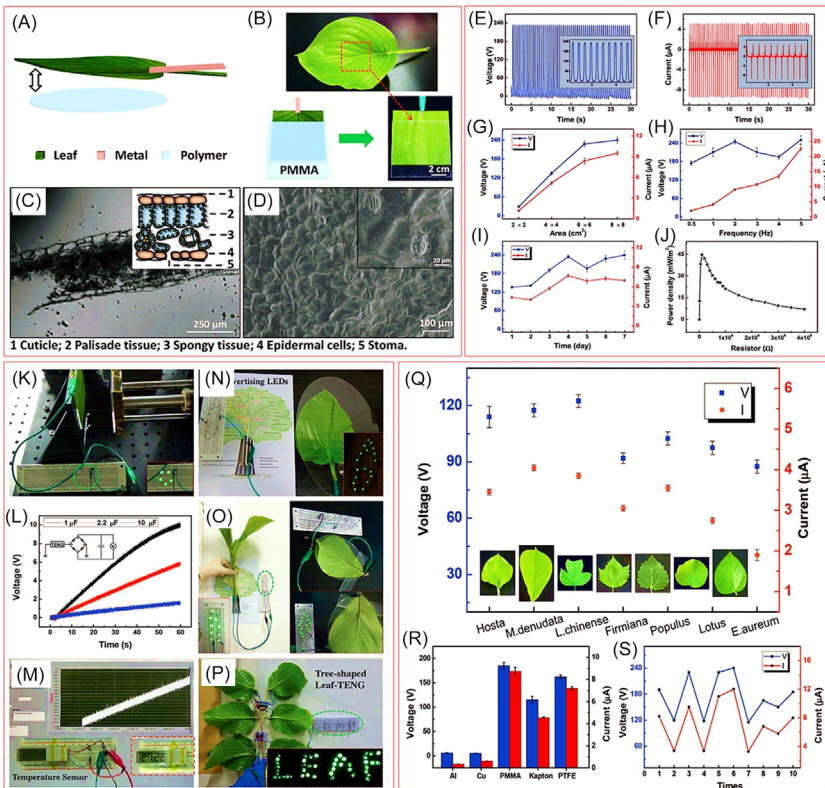


FIG. 12 (A) Schematic presentation of a Leaf-TNG. (B) Image for *Hosta* leaf and Leaf-TNG that are responsible for accumulating the charge with PMMA. (C) *Hosta* leaf cross-section view. Inset shows the cross-section schematic view for leaves. (D) Microscope view of *Hosta* leaf. (E) Voltage and (F) current from a Leaf-TNG. (G) Generated voltage varies with areas for the Leaf-TNG. (H) Variation of voltage with frequency. (I) Voltage with time. (J) Power density variation external load resistance. (K) Linear motor controlling experimental setup and lighting up LEDs. (L) Capacitors' (1, 2.2, and 10 μF) charging voltage. (M) Power-up temperature sensor by a stored capacitor. (N) Lighting up LEDs by hand tapping. (O) Demonstration of two types of natural Leaf-TNGs. (P) Assembly of a tree-shaped-based device (Leaf-TNG) (*M. denudata* leaf) lighting up several LEDs. (Q) Output performance of Leaf-TNG (PMMA) when assembled with leaves. (R) Electrical output values for Leaf-TNG (*Hosta* leaf) with various contact materials. (S) Multiple (when assembling) Leaf-TNG generated output voltage. ((A–J) Reproduced with permission from S. Maiti, S.K. Karan, J.K. Kim, B.B. Khatua, *Nature driven bio piezoelectric/triboelectric nanogenerator as next generation green energy harvester for smart and pollution free society*, *Adv. Energy Mater.* 9 (9) (2019) 1803027. Copyright 2019, WILEY-VCH Verlag GmbH & Co. KGaA, Weinheim.)

chosen to design the Leaf-TNG, which was fixed with a high strength, light-weight PPMA sheet (Fig. 12B). Lastly, a clip was attached to the *Hosta* leaf as an electrode to complete the final TNG (Fig. 12B) to study the output values. Scanning electron microscopy analysis (Fig. 12C) was carried out to check the cross-sectional view of the leaf and porous structures with cells were found. The inset of Fig. 12C provides cross-sectional images for leaves. A layered waxy cuticle and epidermal cells were found on the leaf outer surface. The flat and dense upper leaf surface helps to reduce water evaporation. The back surface of the leaf holds stomata for the exchange of gas. The mesophyll is present in the center position of the leaf as the main component, which consists of spongy tissue and palisade tissue (inset of Fig. 12C). In addition, the electrolyte and water inside the leaf act as a conductive liquid in this designed bio-based Leaf-TNG. The irregular surface structure of the *Hosta* leaf (Fig. 12D) improved the contact area effectively for triboelectrification and increased output values. The external microstructure surface (enlarged view) provided distinctive morphology of the stomata (inset Fig. 12D). Wang et al. [76] found a high output voltage of ≈ 230 V with remarkable current value ($\approx 9.5\ \mu\text{A}$) using a bio-inspired Leaf-TNG (Fig. 12E and F). In addition, the device delivered a maximum power density of $\approx 45\ \text{mW m}^{-2}$ at $10\ \text{M}\Omega$. Moreover, the designed device worked in freestanding mode. For large-scale potential applications, Leaf-TNGs are assembled in a tree shape to store huge amounts of electrical energy and can power up many smart electronic devices. The output values of the designed TNG are strongly dependent on many issues like external resistance, contact area, and mechanical frequency. They achieved best output values (~ 230 V and $\sim 9.5\ \mu\text{A}$) in an area of $8 \times 8\ \text{cm}^2$, frequency of 2 Hz, and peak velocity value of $\approx 0.333\ \text{m s}^{-1}$ as shown in Fig. 12E and F with an enlarged view in the inset figure. These output values improved further by increasing the effective area of the contact surface (Fig. 12G) [77, 78]. Due to the electrostatic shield effect [79], direct scale-up processing is less than ideal for the single electrode mode Leaf-TNG. The output values were checked with frequency (Fig. 12H) and improved [80]. Thus output performance variation at low frequency makes the device potentially more active, as the environmental mechanical energies are in low frequency and are random. The mechanical stability of the designed Leaf-TNG was demonstrated well (Fig. 12I). Normally, leaves continuously evaporate water in open atmosphere and become dry after a certain time, making them mechanically poor. Nevertheless, it was found that the durability of leaves became robust in the laboratory atmosphere even after many days for the designed bio-inspired Leaf-TNG. Moreover, a stability test of the device up to $\approx 10,000$ cycles established its outstanding mechanical stability. The output values depend strongly on the strength and nature of the leaves. A *Populus* leaf-based Leaf-TNG delivered comparatively greater output values than that of the *Hosta* leaf-based TNG because of its low mechanical strength. The voltage of the Leaf-TNG was further checked under different external load resistances to explore its

performance and it showed improvement; nevertheless, current value decreases by improving (0 to $\sim 400\text{ M}\Omega$) the external load resistance. Thus a maximum power density of $\sim 45\text{ mW m}^{-2}$ was obtained at $\sim 10\text{ M}\Omega$ (Fig. 12J), then reduced by $\sim 400\text{ M}\Omega$. Moreover, this self-powered device instantaneously lights many green LEDs (Fig. 12K). Thus, generated electricity can be accumulated into capacitors or batteries for future smart applications [81]. The charging behavior was further studied for this designed self-powered Leaf-TNG through different commercial capacitors (1, 2.2, and $10\text{ }\mu\text{F}$) through a four-probe bridge rectifier unit with their corresponding equivalent circuit model and were fully charged (Fig. 12L and inset). The output voltage achieved up to $\sim 10\text{ V}$ for a $1\text{ }\mu\text{F}$ capacitor and up to $\sim 1.5\text{ V}$ for a $10\text{ }\mu\text{F}$ capacitor within 60 s (Fig. 12L). For realistic potential applications, a Leaf-TNG-charged commercial $100\text{ }\mu\text{F}$ capacitor (after 8 min charging) was utilized to power up an electronic temperature sensor (Fig. 12M) to gauge outside environmental temperature. In addition, this designed Bio-TNG turned on LEDs successfully (Fig. 12N). Therefore a blueprint of a self-powered tree-shaped Leaf-TNG system was developed along with energy science (Fig. 12N) [82]. In addition, a Leaf-TNG also worked in freestanding mode as well as single electrode mode. *Magnolia denudata* and *Hosta* leaves were utilized to develop a freestanding mode Leaf-TNG and powered up green LEDs instantaneously (Fig. 12O). This freestanding mode Leaf-TNG developed electricity without grounding and is suitable for a tree-shaped design.

To improve the output values, several units of devices were connected in parallel [81]. Therefore several numbers of devices (*M. denudata* leaf) were assembled in a tree shape in parallel connection to improve the overall output values, which can turn on many LEDs instantaneously (Fig. 12P). Therefore a biogreen energy scavenger would surely play a key role in modern, smart, green electronics. The output values for various natural leaves were well studied. The different contact surfaces and nature of the leaves strongly influenced the output values of the designed TNGs because of the effect of dissimilar contact electrification of the different leaves. The comparative output values were checked with various leaves while fixed with flexible PMMA film (Fig. 12Q). Every naturally abundant leaf has its own uniqueness to sustain life in nature, and has the implanted venation in the mesophyll structure (insets of Fig. 12Q). In addition, hierarchical micro-/nanopatterns are observed on the leaf surface, which undoubtedly increased the output performance of Leaf-based TNGs. Because of dissimilar surface electron affinity of the different leaf species, output values were not the same (Fig. 12R). Leaf-TNG with a *Hosta*-leaf delivered high output values (voltage and current) when PMMA was used, may be because of their huge difference in electron affinities and effective contact area [83]. In addition, the output values were checked by assembling multiple Leaf-TNGs (*Hosta* leaves) at different times under the same working conditions (Fig. 12S). May be the structure of surface of the leaves is rearranged with times because of their individual or natural diversity.

Thus a leaf-integrated Bio-TNG would be a potential green energy-harvesting source to power up the smart electronics world without adding any pollution to the environment. It could even save society from the huge amounts of e-waste.

8 Summary and future challenges

Since naturally abundant biowaste biodegradable materials are thrown away continuously in huge amounts throughout the world, they could be recycled to design effective green energy harvesters in this energy-deficient world. This chapter discussed the effectiveness of biowaste materials in green energy-harvesting technologies and their possible applications to design future smart/portable electronic devices. Furthermore, using these materials in energy-harvesting technology will definitely help to clean up huge quantities of biowaste from the environment as well as society. In addition, their remarkable high output values and their efficient large-scale potentiality are well discussed in this chapter. These biowaste-based green energy harvesters have many properties like huge abundance, cheap cost, simple fabrication, and most importantly high output values (voltage/current/power density/energy conversion efficiency), which boost these energy-harvesting technologies in new directions. Biowaste materials can not only be used to harvest energy, but can also play an important role in eradicating environmental pollution. Furthermore, being biodegradable in nature, fabricated devices could easily be processed at the end of their life, which means no e-waste. This biowaste is available everywhere (from deserts to seas, forests to mountains, cities to remote areas), therefore anybody can design effective energy harvesting devices using these materials to generate green electricity using cheap and simple techniques. Also, being biodegradable in nature, these devices would play a huge role in improving self-powered medical science, especially *in vivo* or *in vitro* healthcare monitoring without affecting body parts. Because heartbeat, blood pressure, arterial pulse movements, etc. all are kinetic energy, they could be converted to green electricity using these biodevices. Output values are well controlled by connecting multiple devices in series or parallel, which could be good for industrial-scale applications. Although these energy-harvesting technologies have huge facilities, many points need to be explored before future applications can be realized: (1) high-power density is needed to make them potentially active in real life; (2) *in vivo* biomedical applications are needed to ensure their potentiality inside the body; (3) integrated implantable *in vivo* devices should be properly designed to make sure they are compatible with body parts; and (4) tiny devices (micro- or nanosize) with ultrasensitivity are very important so that active sensor networks can detect precisely. Thus these nature-driven biodegradable biowaste-based nanogenerators for harvesting bioenergy would be an encouraging approach to solve e-waste problems and develop a nontoxic future smart and portable world.

Acknowledgments

Department of Science and Technology (DST) Govt. of India provided the INSPIRE fellowship (IF130632) to help carry out this work. The research facilities provided by the Indian Institute of Technology Kharagpur are highly acknowledged. This work was also conducted by the National Creative Research Initiative Program supported by the National Research Foundation of Korea (NRF) grant (no. 2013R1A3A2042196) funded by the Korean government.

Conflict of interest

The authors declare no conflict of interest.

References

- [1] B. Chen, Y. Yang, Z.L. Wang, Scavenging wind energy by triboelectric nanogenerators, *Adv. Energy Mater.* 8 (10) (2018) 1702649.
- [2] G. Zhu, R. Yang, S. Wang, Z.L. Wang, Flexible high-output nanogenerator based on lateral ZnO nanowire array, *Nano Lett.* 10 (8) (2010) 3151–3155.
- [3] S. Maiti, S.K. Karan, J.K. Kim, B.B. Khatua, Nature driven bio piezoelectric/triboelectric nanogenerator as next generation green energy harvester for smart and pollution free society, *Adv. Energy Mater.* 9 (9) (2019) 1803027.
- [4] H. Feng, C. Zhao, P. Tan, R. Liu, X. Chen, Z.J. Li, Nanogenerator for biomedical applications, *Adv. Healthc. Mater.* 7 (10) (2018) 1701298.
- [5] Q. Zheng, Y. Zou, Y. Zhang, Z. Liu, B. Shi, X. Wang, Y. Jin, H. Ouyang, Z. Li, Z.L. Wang, Biodegradable triboelectric nanogenerator as a life-time designed implantable power source, *Sci. Adv.* 2 (3) (2016) e1501478.
- [6] S.K. Karan, R. Bera, S. Paria, A.K. Das, S. Maiti, A. Maitra, B.B. Khatua, An approach to design highly durable piezoelectric nanogenerator based on self poled PVDF/AIO-rGO flexible nanocomposite with high power density and energy conversion efficiency, *Adv. Energy Mater.* 6 (20) (2016) 1601016.
- [7] S. Xu, B.J. Hansen, Z.L. Wang, Piezoelectric-nanowire-enabled power source for driving wireless microelectronics, *Nat. Commun.* 1 (2010) 93.
- [8] S.A. Han, T.H. Kim, S.K. Kim, K.H. Lee, H.J. Park, J.H. Lee, S.W. Kim, Point defect passivated MoS₂ nanosheet-based high performance piezoelectric nanogenerator, *Adv. Mater.* 30 (21) (2018) 1800342.
- [9] Z. Lin, J. Chen, X. Li, Z. Zhou, K. Meng, W. Wei, J. Yang, Z.L. Wang, Triboelectric nanogenerator enabled body sensor network for self-powered human heart-rate monitoring, *ACS Nano* 11 (9) (2017) 8830–8837.
- [10] R. Hinche, H.-J. Yoon, H. Ryu, M.-K. Kim, E.-K. Choi, D.-S. Kim, S.-W. Kim, Transcutaneous ultrasound energy harvesting using capacitive triboelectric technology, *Science* 365 (6452) (2019) 491–494.
- [11] H.S. Lee, J. Chung, G.T. Hwang, C.K. Jeong, Y. Jung, J.H. Kwak, H. Kang, M. Byun, W.D. Kim, S. Hur, Flexible inorganic piezoelectric acoustic nanosensors for biomimetic artificial hair cells, *Adv. Funct. Mater.* 24 (44) (2014) 6914–6921.
- [12] J. Yang, J. Chen, Y. Liu, W. Yang, Y. Su, Z.L. Wang, Triboelectrification-based organic film nanogenerator for acoustic energy harvesting and self-powered active acoustic sensing, *ASC Nano* 8 (3) (2014) 2649–2657.

- [13] K.I. Park, J.H. Son, G.T. Hwang, C.K. Jeong, J. Ryu, M. Koo, I. Choi, S.H. Lee, M. Byun, Z.L. Wang, Highly efficient, flexible piezoelectric PZT thin film nanogenerator on plastic substrates, *Adv. Mater.* 26 (16) (2014) 2514–2520.
- [14] Z.L. Wang, J. Song, Piezoelectric nanogenerators based on zinc oxide nanowire arrays, *Science* 312 (5771) (2006) 242–246.
- [15] A. Koka, H.A. Sodano, A low frequency energy harvester from ultralong, vertically aligned BaTiO₃ nanowire arrays, *Adv. Energy Mater.* 4 (11) (2014) 1301660.
- [16] H. Zhu, Y. Wang, J. Xiao, M. Liu, S. Xiong, Z.J. Wong, Z. Ye, Y. Ye, X. Yin, X. Zhang, Observation of piezoelectricity in free-standing monolayer MoS₂, *Nat. Nanotechnol.* 10 (2) (2015) 151.
- [17] C.-T. Huang, J. Song, W.-F. Lee, Y. Ding, Z. Gao, Y. Hao, L.-J. Chen, Z.L. Wang, GaN nanowire arrays for high-output nanogenerators, *J. Am. Chem. Soc.* 132 (13) (2010) 4766–4771.
- [18] R. Ding, H. Liu, X. Zhang, J. Xiao, R. Kishor, H. Sun, B. Zhu, G. Chen, F. Gao, X. Feng, Flexible piezoelectric nanocomposite generators based on formamidinium lead halide perovskite nanoparticles, *Adv. Funct. Mater.* 26 (42) (2016) 7708–7716.
- [19] Y.B. Lee, J.K. Han, S. Noothongkaew, S.K. Kim, W. Song, S. Myung, S.S. Lee, J. Lim, S.D. Bu, K.S. An, Toward arbitrary direction energy harvesting through flexible piezoelectric nanogenerators using perovskite PbTiO₃ nanotube arrays, *Adv. Mater.* 29 (6) (2017) 1604500.
- [20] S. Paria, S.K. Karan, R. Bera, A.K. Das, A. Maitra, B.B. Khatua, A facile approach to develop a highly stretchable PVC/ZnSnO₃ piezoelectric nanogenerator with high output power generation for powering portable electronic devices, *Ind. Eng. Chem. Res.* 55 (40) (2016) 10671–10680.
- [21] P. Li, J. Zhai, B. Shen, S. Zhang, X. Li, F. Zhu, X. Zhang, Ultrahigh piezoelectric properties in textured (K, Na) NbO₃ based lead free ceramics, *Adv. Mater.* 30 (8) (2018) 1705171.
- [22] S.K. Karan, S. Maiti, A.K. Agrawal, A.K. Das, A. Maitra, S. Paria, A. Bera, R. Bera, L. Halder, A.K. Mishra, Designing high energy conversion efficient bio-inspired vitamin assisted single-structured based self-powered piezoelectric/wind/acoustic multi-energy harvester with remarkable power density, *Nano Energy* 59 (2019) 169–183.
- [23] A. Datta, Y.S. Choi, E. Chalmers, C. Ou, S. Kar-Narayan, Piezoelectric nylon 11 nanowire arrays grown by template wetting for vibrational energy harvesting applications, *Adv. Funct. Mater.* 27 (2) (2017) 1604262.
- [24] S.K. Karan, D. Mandal, B.B. Khatua, Self-powered flexible Fe-doped RGO/PVDF nanocomposite: an excellent material for a piezoelectric energy harvester, *Nanoscale* 7 (24) (2015) 10655–10666.
- [25] S.K. Karan, A.K. Das, R. Bera, S. Paria, A. Maitra, N.K. Shrivastava, B.B. Khatua, Effect of γ -PVDF on enhanced thermal conductivity and dielectric property of Fe-rGO incorporated PVDF based flexible nanocomposite film for efficient thermal management and energy storage applications, *RSC Adv.* 6 (44) (2016) 37773–37783.
- [26] S.K. Si, S.K. Karan, S. Paria, A. Maitra, A.K. Das, R. Bera, A. Bera, L. Halder, B.B. Khatua, A strategy to develop an efficient piezoelectric nanogenerator through ZTO assisted γ -phase nucleation of PVDF in ZTO/PVDF nanocomposite for harvesting bio-mechanical energy and energy storage application, *Mater. Chem. Phys.* 213 (2018) 525–537.
- [27] V. Bhavanasi, D.Y. Kusuma, P.S. Lee, Polarization orientation, piezoelectricity, and energy harvesting performance of ferroelectric PVDF-TrFE nanotubes synthesized by nanoconfinement, *Adv. Energy Mater.* 4 (16) (2014) 1400723.
- [28] S.S. Kwak, S.M. Kim, H. Ryu, J. Kim, U. Khan, H.-J. Yoon, Y.H. Jeong, S.-W. Kim, Butylated melamine formaldehyde as a durable and highly positive friction layer for stable, high output triboelectric nanogenerators, *Energy Environ. Sci.* 12 (10) (2019) 3156–3163.

- [29] S. Paria, S.K. Si, S.K. Karan, A.K. Das, A. Maitra, R. Bera, L. Halder, A. Bera, A. De, B.B. Khatua, A strategy to develop highly efficient TENGs through the dielectric constant, internal resistance optimization, and surface modification, *J. Mater. Chem. A* 7 (8) (2019) 3979–3991.
- [30] S. Paria, R. Bera, S.K. Karan, A. Maitra, A.K. Das, S.K. Si, L. Halder, A. Bera, B.B. Khatua, Insight into cigarette wrapper and electroactive polymer based efficient TENG as biomechanical energy harvester for smart electronic applications, *ACS Appl. Energy Mater.* 1 (9) (2018) 4963–4975.
- [31] G. Zheng, X. Xu, B. Li, K. Wu, T.A. Yekeen, X. Huo, Association between lung function in school children and exposure to three transition metals from an e-waste recycling area, *J. Expo. Sci. Environ. Epidemiol.* 23 (1) (2013) 67.
- [32] D. Lee, D. Offenhuber, F. Duarte, A. Biderman, C. Ratti, Monitour: tracking global routes of electronic waste, *Waste Manag.* 72 (2018) 362–370.
- [33] T.O. Kolawole, A.S. Olatunji, M.T. Jimoh, O.T. Fajemila, Heavy metal contamination and ecological risk assessment in soils and sediments of an industrial area in Southwestern Nigeria, *J. Health Pollut.* 8 (19) (2018) 180906.
- [34] D.J. Rebovich, *Dangerous Ground: The World of Hazardous Waste Crime*, Routledge, 2017.
- [35] M.H. Masud, W. Akram, A. Ahmed, A.A. Ananno, M. Mourshed, M. Hasan, M.U.H. Joardder, Towards the effective E-waste management in Bangladesh: a review, *Environ. Sci. Pollut. Res.* 26 (2) (2019) 1250–1276.
- [36] S.K. Karan, S. Maiti, S. Paria, A. Maitra, S.K. Si, J.K. Kim, B.B. Khatua, A new insight towards eggshell membrane as high energy conversion efficient bio-piezoelectric energy harvester, *Mater. Today Energy* 9 (2018) 114–125.
- [37] S. Maiti, S.K. Karan, J. Lee, A.K. Mishra, B.B. Khatua, J.K. Kim, Bio-waste onion skin as an innovative nature-driven piezoelectric material with high energy conversion efficiency, *Nano Energy* 42 (2017) 282–293.
- [38] A. Ahmed, Z. Saadatnia, I. Hassan, Y. Zi, Y. Xi, X. He, J. Zu, Z.L. Wang, Self-powered wireless sensor node enabled by a duck-shaped triboelectric nanogenerator for harvesting water wave energy, *Adv. Energy Mater.* 7 (7) (2017) 1601705.
- [39] J.M. Wu, C.K. Chang, Y.T. Chang, High-output current density of the triboelectric nanogenerator made from recycling rice husks, *Nano Energy* 19 (2016) 39–47.
- [40] A. Manbachi, R.S. Cobbold, Development and application of piezoelectric materials for ultrasound generation and detection, *Ultrasound* 19 (4) (2011) 187–196.
- [41] G. Gautschi, Piezoelectric sensors, in: *Piezoelectric Sensorics*, Springer, 2002, , pp. 73–91.
- [42] F.-R. Fan, Z.-Q. Tian, Z.L. Wang, Flexible triboelectric generator, *Nano Energy* 1 (2) (2012) 328–334.
- [43] Z.L. Wang, Triboelectric nanogenerators as new energy technology and self-powered sensors—principles, problems and perspectives, *Faraday Discuss.* 176 (2015) 447–458.
- [44] E. Fukada, I. Yasuda, On the piezoelectric effect of bone, *J. Phys. Soc. Jpn.* 12 (10) (1957) 1158–1162.
- [45] E. Fukada, I. Yasuda, Piezoelectric effects in collagen, *J. Phys. Soc. Jpn.* 3 (2) (1964) 117.
- [46] A. Marino, B.D. Gross, Piezoelectricity in cementum, dentine and bone, *Arch. Oral Biol.* 34 (7) (1989) 507–509.
- [47] S.K. Ghosh, D. Mandal, High-performance bio-piezoelectric nanogenerator made with fish scale, *Appl. Phys. Lett.* 109 (10) (2016) 103701.
- [48] S.K. Ghosh, D. Mandal, Efficient natural piezoelectric nanogenerator: electricity generation from fish swim bladder, *Nano Energy* 28 (2016) 356–365.
- [49] B.Y. Lee, J. Zhang, C. Zueger, W.-J. Chung, S.Y. Yoo, E. Wang, J. Meyer, R. Ramesh, S.-W. Lee, Virus-based piezoelectric energy generation, *Nat. Nanotechnol.* 7 (6) (2012) 351.

- [50] N.R. Alluri, S. Selvarajan, A. Chandrasekhar, S. Balasubramaniam, J.H. Jeong, S.-J. Kim, Self-powered pH sensor using piezoelectric composite worm structures derived by ionotropic gelation approach, *Sensors Actuators B* 237 (2016) 534–544.
- [51] S.K. Karan, S. Maiti, O. Kwon, S. Paria, A. Maitra, S.K. Si, Y. Kim, J.K. Kim, B.B. Khatua, Nature driven spider silk as high energy conversion efficient bio-piezoelectric nanogenerator, *Nano Energy* 49 (2018) 655–666.
- [52] J. Polonsky, P. Douzou, C.J. Sadron, Mise en evidence de proprietes ferroelectriques dans l'acide desoxyribonucleique (DNA), *C. R. Acad. Sci.* 250 (1960) 3414.
- [53] J. Duchesne, J. Depireux, A. Bertinchamps, N. Cornet, J.M. Van Der Kaa, Thermal and electrical properties of nucleic acids and proteins, *Nature* 188 (4748) (1960) 405–406.
- [54] N. Zhang, J. Shan, X. Xing, Piezoelectric properties of single-strand DNA molecular brush bilayers, *Acta Mech. Solida Sin.* 20 (3) (2007) 206–210.
- [55] E. Fukada, Piezoelectric properties of biological polymers, *Q. Rev. Biophys.* 16 (1) (1983) 59–87.
- [56] T. Yucel, P. Cebe, D.L. Kaplan, Structural origins of silk piezoelectricity, *Adv. Funct. Mater.* 21 (4) (2011) 779–785.
- [57] S. Guerin, A. Stapleton, D. Chovan, R. Mouras, M. Gleeson, C. McKeown, M.R. Noor, C. Silien, F.M. Rhen, A.L. Khoklin, Control of piezoelectricity in amino acids by supramolecular packing, *Nat. Mater.* 17 (2) (2018) 180.
- [58] B.G. Frushour, J.L. Koenig, Raman scattering of collagen, gelatin, and elastin, *Biopolymers* 14 (2) (1975) 379–391.
- [59] E. Steven, W.R. Saleh, V. Lebedev, S.F. Acquah, V. Laukhin, R.G. Alamo, J.S. Brooks, Carbon nanotubes on a spider silk scaffold, *Nat. Commun.* 4 (2013) 2435.
- [60] S. Ling, Z. Qi, D.P. Knight, Z. Shao, X. Chen, Synchrotron FTIR microspectroscopy of single natural silk fibers, *Biomacromolecules* 12 (9) (2011) 3344–3349.
- [61] M.H. Shamos, L.S. Lavine, Piezoelectricity as a fundamental property of biological tissues, *Nature* 213 (5073) (1967) 267.
- [62] S. Rajala, T. Sipponkoski, E. Sarlin, M. Mettänen, M. Vuoriluoto, A. Pammo, J. Juuti, O.J. Rojas, S. Franssila, S. Tuukkanen, Cellulose nanofibril film as a piezoelectric sensor material, *ACS Appl. Mater. Interfaces* 8 (24) (2016) 15607–15614.
- [63] E. Fukada, S. Sasaki, Piezoelectricity of α -chitin, *J. Polym. Sci. Polym. Phys.* 13 (9) (1975) 1845–1847.
- [64] A. Hänninen, S. Rajala, T. Salpavaara, M. Kellomäki, S. Tuukkanen, Piezoelectric sensitivity of a layered film of chitosan and cellulose nanocrystals, *Procedia Eng.* 168 (2016) 1176–1179.
- [65] E. Praveen, S. Murugan, K. Jayakumar, Investigations on the existence of piezoelectric property of a bio-polymer–chitosan and its application in vibration sensors, *RSC Adv.* 7 (56) (2017) 35490–35495.
- [66] R.M. Street, T. Huseynova, X. Xu, P. Chandrasekaran, L. Han, W.Y. Shih, W.-H. Shih, C.L. Schauer, Variable piezoelectricity of electrospun chitin, *Carbohydr. Polym.* 195 (2018) 218–224.
- [67] K. Kim, M. Ha, B. Choi, S.H. Joo, H.S. Kang, J.H. Park, B. Gu, C. Park, C. Park, J. Kim, Biodegradable, electro-active chitin nanofiber films for flexible piezoelectric transducers, *Nano Energy* 48 (2018) 275–283.
- [68] M. Rinaudo, Chitin and chitosan: properties and applications, *Prog. Polym. Sci.* 31 (7) (2006) 603–632.
- [69] Y. Shi, S. He, J.E. Hearst, Statistical mechanics of the extensible and shearable elastic rod and of DNA, *J. Chem. Phys.* 105 (2) (1996) 714–731.
- [70] H.J. Kim, J.H. Kim, K.W. Jun, J.H. Kim, W.C. Seung, O.H. Kwon, J.Y. Park, S.W. Kim, I.K. Oh, Silk nanofiber networked bio-triobelectric generator: silk Bio-TEG, *Adv. Energy Mater.* 6 (8) (2016) 1502329.

- [71] Y. Yang, H. Zhang, Z.-H. Lin, Y.S. Zhou, Q. Jing, Y. Su, J. Yang, J. Chen, C. Hu, Z.L. Wang, Human skin based triboelectric nanogenerators for harvesting biomechanical energy and as self-powered active tactile sensor system, *ACS Nano* 7 (10) (2013) 9213–9222.
- [72] H.-J. Kim, E.-C. Yim, J.-H. Kim, S.-J. Kim, J.-Y. Park, I.-K. Oh, Bacterial nano-cellulose triboelectric nanogenerator, *Nano Energy* 33 (2017) 130–137.
- [73] K.-E. Byun, Y. Cho, M. Seol, S. Kim, S.-W. Kim, H.-J. Shin, S. Park, S.J. Hwang, Control of triboelectrification by engineering surface dipole and surface electronic state, *ACS Appl. Mater. Interfaces* 8 (28) (2016) 18519–18525.
- [74] S. Niu, S. Wang, L. Lin, Y. Liu, Y.S. Zhou, Y. Hu, Z.L. Wang, Theoretical study of contact-mode triboelectric nanogenerators as an effective power source, *Energy Environ. Sci.* 6 (12) (2013) 3576–3583.
- [75] R. Wang, S. Gao, Z. Yang, Y. Li, W. Chen, B. Wu, W. Wu, Engineered and laser-processed chitosan biopolymers for sustainable and biodegradable triboelectric power generation, *Adv. Mater.* 30 (11) (2018) 1706267.
- [76] Y. Jie, X. Jia, J. Zou, Y. Chen, N. Wang, Z.L. Wang, X. Cao, Natural leaf made triboelectric nanogenerator for harvesting environmental mechanical energy, *Adv. Energy Mater.* 8 (12) (2018) 1703133.
- [77] Q. Zhao, Y. Lu, J. Chen, Advanced organic electrode materials for rechargeable sodium ion batteries, *Adv. Energy Mater.* 7 (8) (2017) 1601792.
- [78] J. Ma, Y. Jie, J. Bian, T. Li, X. Cao, N. Wang, From triboelectric nanogenerator to self-powered smart floor: a minimalist design, *Nano Energy* 39 (2017) 192–199.
- [79] S. Niu, Y. Liu, S. Wang, L. Lin, Y.S. Zhou, Y. Hu, Z.L. Wang, Theoretical investigation and structural optimization of single-electrode triboelectric nanogenerators, *Adv. Funct. Mater.* 24 (22) (2014) 3332–3340.
- [80] F. Xing, Y. Jie, X. Cao, T. Li, N. Wang, Natural triboelectric nanogenerator based on soles for harvesting low-frequency walking energy, *Nano Energy* 42 (2017) 138–142.
- [81] Y. Zi, J. Wang, S. Wang, S. Li, Z. Wen, H. Guo, Z.L. Wang, Effective energy storage from a triboelectric nanogenerator, *Nat. Commun.* 7 (2016) 10987.
- [82] Z.L. Wang, J. Chen, L. Lin, Progress in triboelectric nanogenerators as a new energy technology and self-powered sensors, *Energy Environ. Sci.* 8 (8) (2015) 2250–2282.
- [83] X.Y. Wei, G. Zhu, Z.L. Wang, Surface-charge engineering for high-performance triboelectric nanogenerator based on identical electrification materials, *Nano Energy* 10 (2014) 83–89.

Chapter 11

Polysaccharide-based polymer electrolytes for future renewable energy sources

L.P. Teo, M.H. Buraidah, and A.K. Arof

*Centre for Ionics University of Malaya, Physics Department, Faculty of Science,
University of Malaya, Kuala Lumpur, Malaysia*

1 Introduction

At present, the electric power supply worldwide is mainly dependent on fossil fuels, for example, petroleum, natural gas, and coal. Not only are these resources non-renewable, but pollution also arises from their combustion is harmful to humans and the environment. Renewable energy is the green and eco-friendly option for a sustainable future. Among the renewable energy sources such as hydropower, wind, solar, geothermal, and biomass, solar electricity generation is fast developing since sunlight is free and most bountiful. The solar technology can be categorized into three classes, that is, first-generation photovoltaic based on silicon, second-generation—thin films, and third generation solar cells—polymer and/or nanocrystal based solar cells. The dye-sensitized solar cells (DSSCs) and quantum dot sensitized solar cells (QDSSCs) belong to the third generation solar cells which offer a greener and low cost alternative to the commonly available silicon-based solar cells since they are much cheaper, environmentally friendly and do not require single crystal materials for their operation. Both these cells are photoelectrochemical and have same constituents (i.e., photoanode, electrolyte, and counter electrode) and similar operating principle. The electrolyte can be regarded as the most important component since it plays an important role as medium for charge transport. Conventional electrolyte used is an organic liquid which is favored for its high ionic conductivity. However, liquid electrolyte poses problems such as leakage and electrochemical corrosion that affect the stability of the devices in long run. These have prompted researchers to employ polymer electrolytes. Various polymer electrolytes (GPEs) have been developed including poly(ethylene oxide) (PEO), poly(vinyl alcohol) (PVA), polyacrylonitrile (PAN), and poly

(vinylidene fluoride-hexafluoropropylene) (PVDF-HFP) to name a few as the polymer host. However, these are all synthetic polymers. Synthetic polymers are known as indestructible materials in nature even though they are widely used in the production of plastics. Demolishing these materials will produce harmful gases and cause pollution. Therefore, biopolymer is preferred since it is non-toxic, biocompatible, and biodegradable. Polysaccharides that can be found abundantly in nature have potential as polymer host in polymer electrolytes. Cellulose, chitosan, starch, and agar are some of the polysaccharides which have served as polymer matrix in electrolytes. Generally, they are safe, eco-friendly, biocompatible, cost-effective, biodegradable, and sustainable.

2 Saccharide

The term “saccharide” is derived from the Greek word “*sakkharon*” meaning sugar. It is a biomolecule that consists of carbon, oxygen, and hydrogen atoms with the general formula $(CH_2O)_n$. In other words, each carbon atom in the structure is attached to the hydroxyl group and hydrogen atom. Therefore, the saccharide is also called carbohydrate. The simplest saccharide or carbohydrate is called monosaccharide and the ring structure is very stable. The structure is called a disaccharide if two monosaccharide rings are present. Disaccharide is a sugar such as lactose, which can be found in milk and sucrose in cane and table sugars. The presence of many monosaccharides linked together by glycosidic bonds is called a polysaccharide. Fig. 1 shows the chemical structures of some saccharides.

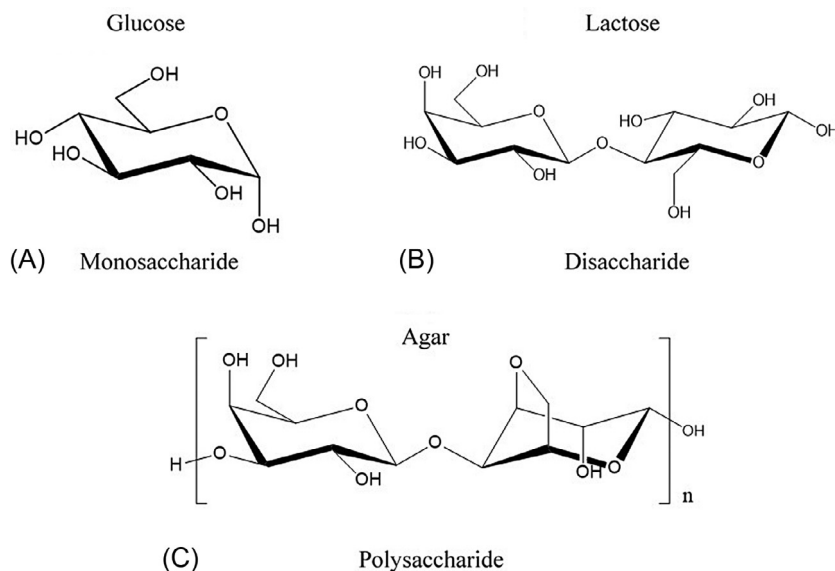


FIG. 1 Chemical structures of (A) monosaccharide, (B) disaccharide and (C) polysaccharide.

3 Polysaccharide

As a biopolymer, polysaccharides (as shown in Fig. 2) are abundant in nature and can be found in living organisms. Their function is either as storage or structural related. Starch, for example, can be found in wheat, rice, and potato that store glucose which then provide energy to the human body. Chitin is the main component of cell wall in crustaceans, insects, exoskeletons, and fungi. Other example of polysaccharide that is important in the structural component of cell wall is cellulose and can be found in wood and cotton. Fig. 2 depicts the chemical structures of chitin, cellulose, and starch.

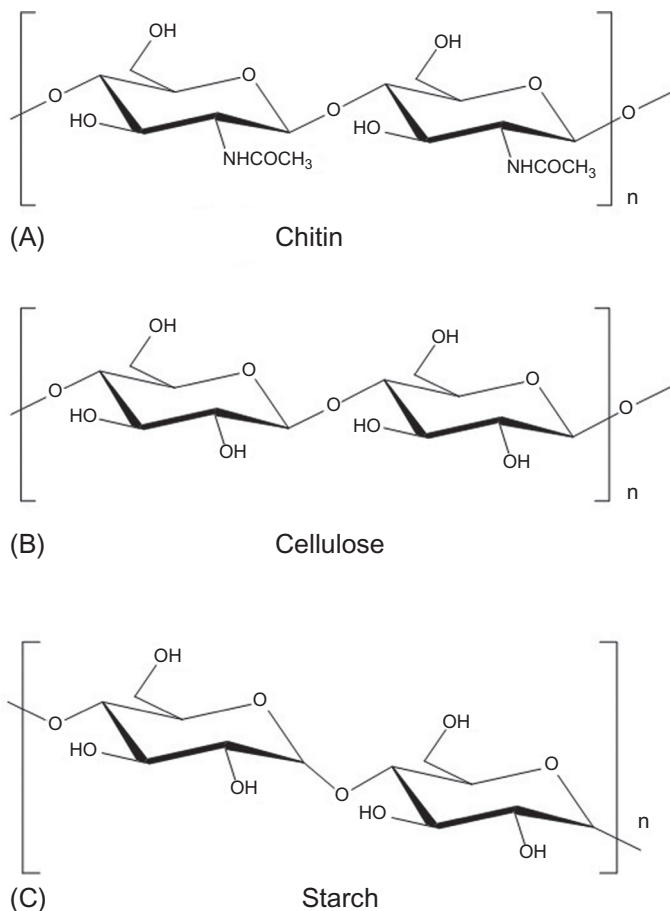


FIG. 2 Chemical structures of (A) chitin, (B) cellulose, and (C) starch.

4 Polysaccharide as electrolyte

Electrolyte is a material that conducts electricity through ions. Polysaccharides are non-conducting. However, polysaccharides can be made conducting by adding free ions into the matrix. The free ions can be obtained by dissolving ionically bonded materials or salts in an appropriate solvent. Thus, by dissolving the polysaccharide into the ionic solution, a solid film can be obtained by casting the polysaccharide-ion solution onto a substrate or gel electrolyte that can be formed on heating the solution appropriately. In gel electrolytes, the ionic solution remains entrapped in the polysaccharides. In solid films, the liquid has evaporated but the ions remain free inside the film due to the presence of functional groups in the polysaccharide structure. The functional group(s) of polysaccharide must contain lone pair electrons in order to coordinate with cation of the salt. Polysaccharides like chitin, cellulose, and chitosan (shown in Fig. 3) that fulfill this criterion to qualify themselves as polymer host in electrolytes have been used for the fabrication of devices, see Table 1. Ionic conductivity being one important characteristic in determining whether the electrolyte is practical and efficient for device applications is provided in Table 1. Also listed in the table are some starch and agar-based electrolytes along with their conductivities.

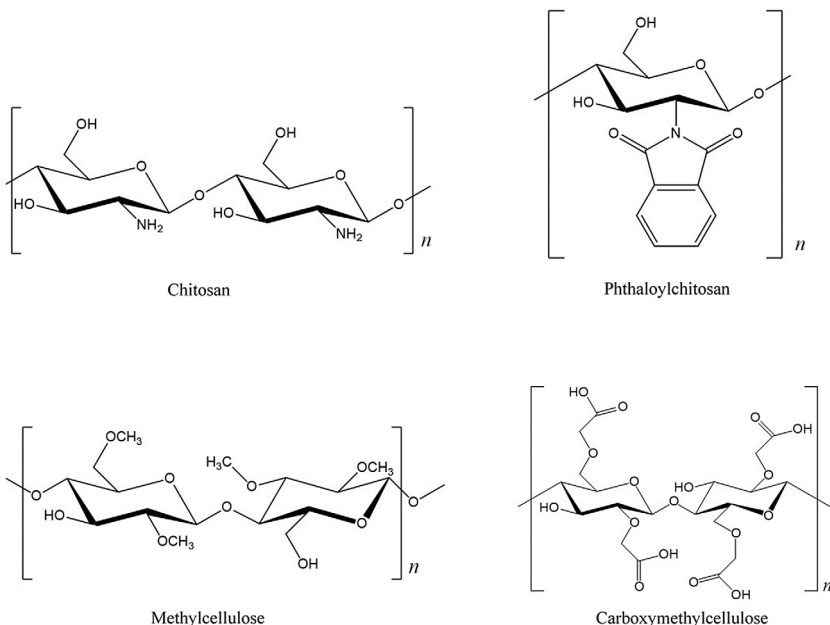


FIG. 3 Structures of chitin and cellulose derivatives.

TABLE 1 Some polysaccharides-based electrolytes reported in the references.

Polysaccharide	Salt	Structure	Conductivity (S cm ⁻¹)	Ref
Sodium carboxymethyl cellulose	NaCl	Hydrogel	1.4×10^{-2}	[1]
Methyl cellulose-chitosan	1-Butyl-3-methylimidazolium bis(trifluoromethylsulfonyl) imide	Solid film	1.5×10^{-6}	[2]
Sodium carboxymethyl cellulose-PEO	NaClO ₄	Solid film	$\sim 10^{-3}$	[3]
Hydroxyethyl cellulose	Nal	Gel	2.16×10^{-2}	[4]
Cellulose acetate	NH ₄ NO ₃	Solid film	1.02×10^{-3}	[5]
Carboxymethyl cellulose-chitosan	NH ₄ NO ₃	Solid film	1.03×10^{-5}	[6]
Starch	NH ₄ NO ₃	Solid film	2.83×10^{-5}	[7]
Corn starch	LiClO ₄	Solid film	1.28×10^{-4}	[8]
Starch	LiTFSI	Solid film	3.39×10^{-4}	[9]
Starch	Lil	Gel	16.1×10^{-1}	[10]
Arrowroot starch	Nal	Solid film	2.81×10^{-2}	[11]
Rice starch	Lil	Solid film	4.68×10^{-5}	[12]
Potato starch	Nal	Solid film	1.22×10^{-5}	[13]
Potato starch	NaClO ₄	Solid film	7.19×10^{-6}	[13]
Potato starch	NaSCN	Solid film	1.12×10^{-4}	[13]
Carboxylated chitosan	Li ₂ SO ₄	Hydrogel	1.74×10^{-2}	[14]
Phthaloyl chitosan	NH ₄ SCN	Solid film	2.42×10^{-5}	[15]
Chitosan/potato starch	LiClO ₄	Solid film	6.50×10^{-4}	[16]
Agar	1-Ethyl-3-methylimidazolium acetate	Solid film	2.35×10^{-5}	[17]

NaCl, sodium chloride; NaClO₄, sodium perchlorate; Nal, sodium iodide; NH₄NO₃, ammonium nitrate; LiClO₄, lithium perchlorate; LiTFSI, lithium bis(trifluoromethanesulfonyl)imide; Lil, lithium iodide; NaSCN, sodium thiocyanate; Li₂SO₄, lithium sulfate.

5 Dye-sensitized solar cells (DSSCs) and quantum dot-sensitized solar cells (QDSSCs)

DSSCs and QDSSCs are electrochemical cells that require an electrolyte for the transfer of charge between two electrodes. The two devices have identical structures where the anode consists of wide bandgap metal oxide (MO) semiconductor and sensitizer, an electrolyte and the cathode consists of catalyst material. The cell with MO sensitized with dye molecules is called DSSC, whereas QDSSC refers to the cell having MO sensitized with quantum dots. The structure is shown in Fig. 4. These sensitized MO are usually deposited on transparent conducting oxide (TCO) glass substrates viz. fluorine-doped tin oxide (FTO) and indium tin oxide (ITO). They can also be coated on plastic substrates (e.g., poly(ethylene terephthalate) (PET)). Usually, the MO which is in nanometer size with its thickness around 10–20 µm can be prepared using doctor blade deposition technique [18]. MO sensitized with dye molecules can be prepared by soaking MO in dye solution whereas MO sensitized with quantum dots can be synthesized via two common methods, that is, successive ionic layer adsorption and reaction (SILAR) and chemical bath deposition methods. Typical MO semiconductors used are titanium dioxide (TiO_2), zinc oxide (ZnO), and tin oxide (SnO_2). On the other hand, the cathode or counter electrode (CE) is made up of TCO coated with a catalyst material such as platinum (Pt), gold (Au), nickel sulfide (NiS), cobalt sulfide (CoS_2), copper sulphide (Cu_2S), molybdenum disulfide (MoS_2), and others. Common techniques employed to deposit the catalyst include spin coating, electrodeposition, doctor blade, and sputtering. Electrolyte (in gel or solid form) is placed between anode and cathode for cell fabrication. In DSSCs, the polysaccharides-based electrolytes usually contain iodide/triiodide (I^-/I_3^-) redox mediator, while electrolytes in QDSSCs use sulfide/polysulfide ($\text{S}^{2-}/\text{S}_x^{2-}$) redox mediator. Most of the single cell of DSSCs and QDSSCs reported in this chapter has the area of not more than 1 cm².

DSSCs and QDSSCs are able to convert light energy into electricity which can be explained by the following mechanism.

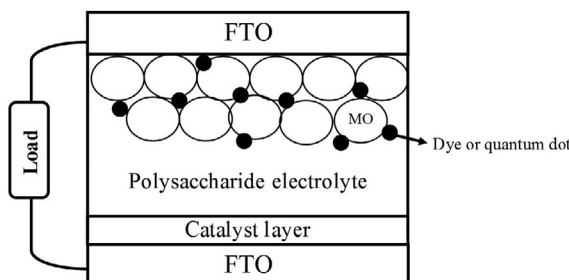


FIG. 4 Structure of electrochemical cell with anode comprises MO sensitized with dye or quantum dot (represented by filled circle).

5.1 Light absorption

Light is absorbed by sensitizer (dye, D in DSSC, and quantum dot, QD in QDSSC). Dyes can be organic or inorganic materials which absorb light energy in the visible spectrum. Inorganic dyes are generally based on ruthenium complexes (e.g., *cis*-bis(isothiocyanato)bis(2,2'-bipyridyl-4,4'-dicarboxylato) ruthenium(II) or simply known as N3, di-tetrabutylammonium *cis*-bis(isothiocyanato)bis(2,2'-bipyridyl-4,4'-dicarboxylato) ruthenium(II) or N719, *cis*-bis(isothiocyanato)(2,2'-bipyridyl-4,4'-dicarboxylato)(4,4'-di-nonyl-2'-bipyridyl) ruthenium(II) or Z907, etc.). Organic dyes, on the other hand, can be natural dyes such as chlorophyll, carotenoid, and anthocyanin or synthetics such as indoline, coumarin, cyanine, and triphenylamine. Quantum dots (QDs) are nanosemiconducting materials with size smaller than 10 nm. By controlling the size of QDs, the energy gap of the semiconductor can be tuned. Therefore, broader light spectrum can be absorbed by the QD. Examples of QDs are zinc selenide (ZnSe), zinc sulfide (ZnS), and the sulfides and selenides of cadmium and lead to name a few.

On absorption of light photons ($h\nu$), electrons in the sensitizer will be excited from the highest occupied molecular orbital (HOMO) of the dye or valence band (VB) of the QD to the lowest unoccupied molecular orbital (LUMO) of the dye or conduction band (CB) of the QD and free electrons are created, Fig. 5.

5.2 Charge separation and transportation

The exciting free electrons have to be transferred out of the dye or QD immediately to prevent the excited free electrons from returning to the HOMO or valence band. This is where the MO semiconductor plays an important role. The MO semiconductor chosen must be environment friendly, chemically stable, and optically transparent [18]. The functions of MO are to facilitate charge transport and charge separation when the sensitizer is excited (D^* or $QD_{(e^-+h)}$) upon illumination. Charge separation occurs when the free electrons in the LUMO or CB of sensitizer are injected into the CB of MO (D^+ or $QD_{(h)}$). This can only occur if the CB edge of the MO is lower than the LUMO of dye or the CB edge of the QD (Fig. 6). In order to maximize the amount of dye loading, nanocrystalline MO with mesoporous structure has been constructed [18].

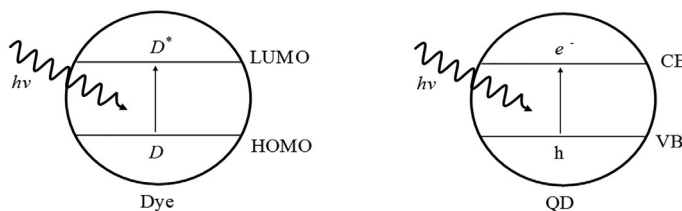


FIG. 5 Absorption of sensitizer.

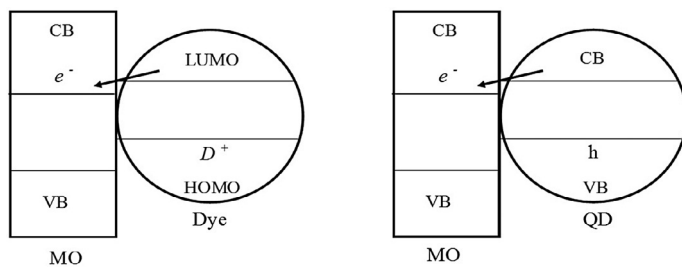
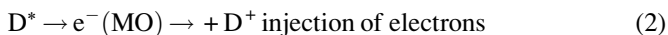


FIG. 6 Injection of electron into MO.

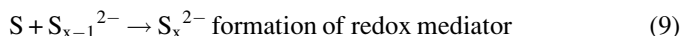
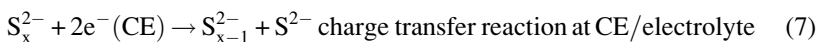
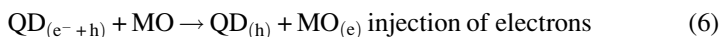
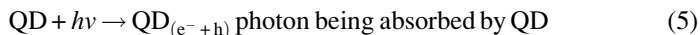
The injected electrons then move toward the external circuit through the MO networks and reach at CE. Charge is then transferred at the boundary or interface between the CE and the electrolyte. The redox mediator in the electrolyte receives electrons from CE and returns them to the oxidized dye to complete the electron circuitry.

5.3 Summary of DSSC and QDSSC mechanisms

DSSC (iodide I^- and triiodide I_3^- redox mediator) [18].



QDSSC (sulfide S^{2-} and polysulfide S_x^{2-} redox mediator) [18].



Four important parameters in DSSCs and QDSSCs are the efficiency (η), short circuit current density (J_{sc}), open circuit voltage (V_{oc}), and fill factor (FF). The efficiency or better known as the light to electricity conversion efficiency (η) of the DSSCs and QDSSCs can be calculated from equation below [19]:

$$\eta = \frac{J_{sc} \times V_{oc} \times FF}{\text{Input power}} \times 100 \quad (10)$$

and FF can be expressed as [19]:

$$FF = \frac{\text{Maximum power output}}{J_{sc} \times V_{oc}} \quad (11)$$

6 Cellulose and its derivatives

Cellulose with chemical formula $(C_6H_{10}O_5)_n$ can be found in plants (in the cell walls), algae, bacteria (e.g., Acetobacter, Agrobacterium, and Sarcina), and fungi. It is a limitless resource and can theoretically produce 1.5×10^{12} tons of biomass per year [20]. Cellulose is a linear homopolymer chain made up of multiple repetitions of D-anhydroglucose units joined by β -1,4 glycosidic bonds and has properties such as cheap, odorless, non-toxic, hydrophilic, and biodegradable. It also has high mechanical strength with glass transition temperature, T_g of 493K [21]. T_g influences the crystallinity of the polymer film. In general, polysaccharides-based films are amorphous in nature and usually have high T_g value. The advantage of such amorphous films is that the polymers can accommodate high salt content within their volume. It is well-known the ionic conductivity occurs in amorphous region. A monomer of cellulose comprises of three hydroxyl (-OH) functional groups in which the oxygen atoms have lone pair electrons to form dative bonding with organic/inorganic salts thereby qualify cellulose as a host for ionic conduction.

Cellulose nanofibers derived from bleached birch wood have been reported by Borghei et al. [22]. The nanofibers were then subjected to multiple treatments (sonication, vacuum filtration, solvent exchange, and freeze-drying) to form aerogels which are well-interconnected, porous yet robust 3-D network arrangements thus enabling it to hold electrolyte solution of sodium sulfide (Na_2S), sulfur (S), potassium chloride (KCl) in water, and methanol mixture [22]. The authors have fabricated a QDSSC based on cadmium sulfide (CdS)/ TiO_2 /FTO photoanode and Pt/FTO CE with the cellulose-based electrolyte membrane and reported the J_{sc} , V_{oc} , FF , and η of 5.20 mA cm^{-2} , 0.558 V , 0.171% , and 0.52% , respectively under 100 mW cm^{-2} irradiance. In the same work [22], bacterial cellulose (BC) has also been produced from *Komagataeibacter medellinensis* bacterium and BC aerogels were formed after solvent exchange and freeze-drying processes. BC is said to possess better fiber composition and higher water absorption competency than cellulose derived from plants although the former has a higher degree of crystallinity as compared to the latter [23]. Nonetheless, comparable performance was obtained using the same configuration of QDSSC but with BC electrolyte membrane with the η of 0.50% and J_{sc} of 4.90 mA cm^{-2} . The V_{oc} was 0.58 V and FF being 0.175 under the same illumination condition. The same group of researchers have also tried using cellulose nanofibers and BC in their cryogel form in Z907 TiO_2 DSSC [24]. The cryogel membranes of cellulose nanofibers and BC served as scaffold to contain electrolyte solution made up of 1-propyl-3-methylimidazolium iodide

(PMII), 1-methylbenzimidazole(NMBI), guanidinium thiocyanate (GuSCN), iodine (I_2), and 3-methoxypropionitrile (MPN). The values of J_{sc} , V_{oc} , FF and η for the cells with BC and cellulose nanofiber membranes were 11.60 mA cm^{-2} , 0.70 V , 0.60 , 4.90% and 10.50 mA cm^{-2} , 0.66 V , 0.51 , 3.60% , respectively. After being exposed to UV light for a period of 216 h , extreme efficiency decrement was observed with efficiencies of 0.80% and 0.20% in the cells containing the former and latter electrolytes [24]. In an unrelated work, nanocellulose hydrogel was freeze-dried to form aerogel before wetted with commercial liquid electrolyte (Dyesol EL-HSE) for DSSC application [25]. Efficiency of 4.70% with $0.70\text{ V }V_{oc}$ and $11.70\text{ mA cm}^{-2} J_{sc}$ were exhibited by the cell with Z907 TiO_2 .

Salvador et al. [26] have recorded an efficiency of 3.33% for N719 TiO_2 DSSC using GPE based on microcrystalline cellulose-containing 1-methyl-3-propylimidazolium iodide (MPII), LiI, 1-ethyl-3-methylimidazolium thiocyanate (EMISCN), 4-tert-butylpyridine (TBP), and iodine (I_2). The values of J_{sc} , V_{oc} , and FF were 8.39 mA cm^{-2} , 0.59 V , and 0.67 , respectively. It must be pointed out that TBP should be incorporated after the gelation process has taken place to avoid it being evaporated since cellulose was dissolved at 363 K and no volatile solvent was used. The ionic liquids, MPII, and EMISCN act as green solvents besides providing additional ions to the electrolyte. A polymer membrane based on microfibrillated cellulose was prepared via solvent-free photo-induced polymerization process as reported by Bella et al. [27]. The microfibrillated cellulose displayed interwoven network of very fine fibrils with high surface area. Electrolyte solution of sodium iodide (NaI), I_2 , TBP, and acetonitrile was used to soak the microfibrillated cellulose membrane before it was sandwiched between N719/ TiO_2 /FTO and Pt/FTO electrodes. At 100 mW cm^{-2} , the DSSC exhibited superior performance with η of 7.03% , V_{oc} of 0.76 V , J_{sc} of 15.20 mA cm^{-2} and FF of 0.61 than a similar cell using liquid electrolyte ($\eta=6.92\%$, $V_{oc}=0.69\text{ V}$, $J_{sc}=16.30\text{ mA cm}^{-2}$, $FF=0.60$) [27]. Improvement in terms of V_{oc} and η is attributable to decreased charge recombination process due to hydrogen bonding formation between cellulose and TiO_2 .

One drawback of cellulose is that it is a rigid, semicrystalline polymer with a high melting temperature of 740 K [28] due to strong hydrogen bonds thus causing it to be water-insoluble and unable to swell in water [29]. Also, cellulose cannot dissolve in unicomponent solvents but it is soluble in multi-component solvents having chelate complexes [30]. Cuprammonium hydroxide, cupriethylene diamine, *N*-methylmorpholine N-oxide, and ionic liquids are some examples of solvents that can dissolve cellulose [31, 32]. This insolubility issue restricts the utilization of cellulose and thus, modification is required to improve its solubility. Cellulose can be altered via etherification and esterification. Examples of cellulose esters are cellulose acetate and cellulose nitrate whereas methyl cellulose (MC), hydroxypropyl cellulose (HPC), sodium carboxymethyl cellulose (NaCMC) to name a few can be grouped together into cellulose ethers category. Cellulose esters are less commonly used than cellulose ethers as polymer host in electrolytes for application in DSSCs and QDSSCs.

Cellulose acetate nanofibers have been produced via electrospinning process by Weerasinghe et al. [33]. A droplet of electrolyte solution prepared from tetrapropylammonium iodide (TPAI), GuSCN, I₂, and ethanol was pipetted on the nanofiber membrane coated on Pt electrode to form nanofiber electrolyte membrane. An efficiency of 4.00% with J_{sc} of 9.83 mA cm⁻², V_{oc} of 0.70 V and FF of 0.58 was delivered by N719 TiO₂ DSSC using this membrane [33]. Kaschuk and co-workers [34] have also electrospun cellulose acetate nanofibers membrane directly on Pt/FTO CE. The cellulose acetate membrane was moistened with electrolyte solution containing NMBI, PMII, GuSCN, I₂, and MPN. A DSSC was fabricated and η of 4.00% was achieved at 1 sun condition. The V_{oc} , J_{sc} , and FF values were 0.78 V, 8.80 mA cm⁻², and 0.58, respectively. The photoanode used was Z907/TiO₂/FTO and no conductivity results were obtained. Lower performance ($\eta=3.50\%$, $J_{sc}=8.70\text{ mA cm}^{-2}$, $V_{oc}=0.771\text{ V}$, $FF=0.52$) was detected in a similar cell but with liquid electrolyte of the same constituents which can be attributed to inhomogeneous distribution of electrolyte upon injecting the liquid electrolyte into the space between two electrodes [34]. However, the cellulose acetate membrane was observed finally to dissolve in MPN and showed lower stability performance as compared to cell using liquid electrolyte.

It is interesting to note that quantum dots of copper indium sulfide/zinc sulfide (CuInS/ZnS) have been employed as fillers in cellulose acetate polymer electrolytes containing ammonium iodide (NH₄I), I₂, ethylene carbonate (EC), and acetone [35]. DSSC with the configuration of ITO/TiO₂/N719/cellulose acetate-based electrolyte/Au/ITO exhibited a remarkably high efficiency of 8.02% with J_{sc} of 11.11 mA cm⁻² and V_{oc} of 1.11 V under illumination of 100 mW cm⁻². For comparison, the cell containing no quantum dots filler showed lower performance ($J_{sc}=6.15\text{ mA cm}^{-2}$, $V_{oc}=0.93\text{ V}$, $\eta=3.83\%$). The authors attributed this to better interfacial contact between electrolyte and electrode due to the smoother surface morphology of electrolyte-containing CuInS/ZnS than electrolyte without CuInS/ZnS, as well as its higher ambient ionic conductivity (0.16 S cm⁻¹) [35]. Phthaloyl cellulose (PhC) was synthesized via phthaloylation by reacting cellulose in *N,N*-dimethylacetamide (DMAc) with phthalic anhydride and pyridine to serve as polymer host in gel polymer electrolyte containing LiI, I₂, and dimethyl sulfoxide (DMSO) [36]. Prior to this, the cellulose was extracted from palm oil empty fruit branch [37]. The X-ray diffractogram of PhC showed reduction in crystallinity as compared to that of cellulose. An optimum conductivity of 9.73 mS cm⁻¹ was exhibited by the electrolyte at room temperature with J_{sc} of 7.89 mA cm⁻², V_{oc} of 0.59 V, FF of 0.71 and η of 3.29% in N719 TiO₂ DSSC [36].

Methyl cellulose (MC) shows almost identical chemical structure to that of cellulose except that some hydrophilic hydroxyl (OH) groups of the latter have been substituted by hydrophobic methoxy (O-CH₃) functional groups. Hence, MC is water-soluble and demonstrates appealing characteristics such as good water retention, high transparency, resistant against grease, and oil, good in

forming film, and decrease in crystallinity [38–40]. The water-soluble MC can also dissolve in DMAc and DMSO. According to literature [21], MC has T_g at around 433–464 K and is thermally stable up to 629 K. How well MC dissolves in various organic solvents depends on how many hydroxyl groups per an hydroglucose unit have been altered. Mingsukang et al. [41] have employed MC as polymer matrix in gel polymer electrolyte comprising Na₂S and S with distilled water as solvent. The gel polymer electrolyte exhibited high ambient conductivity of 0.18 S cm⁻¹ for QDSSC application. A 1.42% efficiency was obtained using SiO₂/ZnS/CdS/TiO₂/FTO photoanode and Pt/FTO CE [41]. In another work of Mingsukang et al. [42], efficiencies of 2.90% and 1.30% were attained by QDSSCs using the same MC-based electrolyte but with Au and lead sulfide (PbS) CEs, respectively. MC-based electrolyte has also been used in DSSC with tetramethylammonium iodide (TMAI) and lithium bis(oxalate) borate (LiBOB) as salts and DMSO solvent [43]. Succinonitrile plastic crystal was also incorporated to enhance the conductivity. Conductivity and efficiency of 1.96 mS cm⁻¹ and 3.46% were achieved. Improvement can be seen upon the inclusion of 1-butyl-3-methylimidazolium iodide (BMII) into the MC gel electrolyte with conductivity of 3.08 mS cm⁻¹ and η of 4.63% [43].

Carboxymethyl cellulose (CMC) is the end product formed after modifying cellulose in sodium hydroxide solution with monochloroacetic acid. Similar to MC, some of the hydroxyl groups have been replaced but by carboxymethyl (-CH₂-COOH) groups instead in CMC. CMC is biocompatible and edible. CMC-based electrolyte in gel form has been prepared with PEO, NaI, MPII, TBP, I₂, and acetonitrile [27]. Using this electrolyte, N719 TiO₂ DSSC exhibited a rather good performance with η of 5.18%. For better solubility, reacting cellulose in organic solution with sodium monochloroacetate salt will yield sodium carboxymethylcellulose (NaCMC). Baharun et al. [44] have prepared solid polymer electrolyte from NaCMC, Na₂S, S, and distilled water via solution cast technique. Using this electrolyte film sandwiched between FTO/TiO₂/CdS/ZnS, and Pt/FTO electrodes, the QDSSC delivered an efficiency of 0.90%. The ambient conductivity of 2.79×10^{-5} S cm⁻¹ was obtained. A QDSSC having configuration of FTO/TiO₂/CdSeTe/SiO₂/NaCMC gel electrolyte/Cu₂S/FTO exhibited η of 9.21% with V_{oc} of 0.67 V and J_{sc} of 21.89 mA cm⁻² [45]. The NaCMC-Na₂S-S gel electrolyte is said to display excellent water retention and superabsorbent properties. The carboxylate (–COO–) group of NaCMC can coordinate with the metal cations of photoanode leading to better interfacial contact. The authors also revealed that the gel electrolyte may act as protective/blocking layer to obstruct electron recombination at photoanode/electrolyte interface [45]. The cell demonstrated steady performance with only 20% efficiency loss after 90 h.

Hydroxypropyl cellulose (HPC) is another derivative of cellulose after reacting with propylene oxide. Its secondary –OH groups can undergo oxidization to yield ketone in order to form cross-linking bonding and thus enhances the properties of HPC-based gel electrolytes [46]. HPC is known to be soluble in water, dichloromethane, dimethylformamide (DMF), ethanol, propanol, EC,

and propylene carbonate (PC) [46–49]. However, it cannot dissolve in acetonitrile and MPN [49]. A GPE comprises of HPC, NaI, MPII, EC, PC, and I₂ with 7.37 mS cm⁻¹ ambient conductivity exhibited an η of 5.79% for N719 TiO₂ DSSC [48]. Another HPC-based GPE but consisting of LiI, tetrabutylammonium iodide (TBAI), MPII, guanine, TBP, I₂, acetonitrile, and valeronitrile exhibited conductivity of 1.78×10^{-2} S cm⁻¹ and produced good performance with J_{sc} , V_{oc} , FF , and η of 15.37 mA cm^{-2} , 0.71 V, 0.68%, and 7.44%, respectively [50]. The N719 TiO₂ DSSC performance was quite stable maintaining 90% of the efficiency after being illuminated for 600 h even though using volatile solvents [50]. Rather than using I⁻/I₃⁻ redox couple, Karthika et al. [51] utilized Co²⁺/Co³⁺ redox mediator from tris(1,10-phenanthroline)cobalt(II)/(III) bis/tris(hexafluorophosphate) and synthesized 1,1'-(3,3',5,5'-tetramethyl-[1,1'-biphenyl]-4,4'-dyl)bis(3-(3,4,5-trimethoxy phenyl)thiourea) to serve as additive in HPC-containing gel polymer electrolyte. The room temperature conductivity was 1.43×10^{-4} S cm⁻¹. Under illumination of 70 mW cm^{-2} , the N719 TiO₂ DSSC achieved an efficiency of 9.10% [51]. Reaction between HPC and acrylonitrile monomer with sodium hydroxide as catalyst produced cyanoethylated HPC as documented by Huang et al. [49]. Such polymer was then used along with LiI, 1-methyl-3-hexylimidazolium iodide (MHII), TBP, I₂, and MPN to prepare polymer gel electrolyte capable of exhibiting ambient conductivity of 2.46 mS cm^{-1} . Huang et al. [49] have also synthesized triphenylamine dye to use as sensitizer in DSSC. The TiO₂ cell with such dye and cyanoethylated HPC electrolyte recorded an efficiency of 7.40%. Employing the same electrolyte but with N719 dye, an efficiency of 7.55% was achieved.

Other than chemical modifications on cellulose itself, there are other means to improve the properties of cellulose and cellulose-based electrolytes such as grafting and blending with another polymer. Improved properties of the electrolytes related to ionic conductivity, flexibility, and mechanical strength will lead to better performance in sensitized solar cells. In grafting, a secondary polymer is bonded covalently at the main polymer chain whereas blending is the process where two polymers are physically mixed together. Li et al. [52] have prepared GPE based on cellulose grafted with acrylic acid that contained BMII, potassium iodide (KI), and I₂ which demonstrated conductivity of 7.33 mS cm^{-1} . Using conventional DSSC architecture comprising GPE sandwiched between N3/TiO₂/FTO photoanode and Pt/FTO counter electrode, an efficiency of 5.51% was obtained under illumination of 1 sun. In the work of Bella et al. [53], CMC has been blended with synthetic PEO to serve as polymer matrix in GPE having NaI, MPII, TBP, I₂, and acetonitrile. Experimental outcome from J-V characterization revealed an efficiency of 5.18%. GPE based on PVdF-HFP blended with hydroxypropyl methyl cellulose (HPMC) and contained NaI, BMII, TBP, I₂, and acetonitrile gave higher conductivity of 8.80×10^{-4} S cm⁻¹ and efficiency of 5.34% than GPE containing only PVdF-HFP as polymer host with conductivity of 8.20×10^{-4} S cm⁻¹ and 3.97% efficiency [54]. Instead of grafting and blending techniques, Or et al. [55] have taken another approach by cross-linking cellulose nanocrystals with

poly(oligoethylene glycol methacrylate) (POEGMA) which was then deposited on Pt/ITO/PET CE before commercial liquid electrolyte (Dyesol EL-HSE) was drop-cast on it to form GPE. With Z907/TiO₂/FTO photoanode, the DSSC exhibited an efficiency of 4.98% [55].

Cellulose and its derivatives are versatile in the sense that they can be used as electrolyte host and in the photoanode. Bella et al. [56] have fabricated a DSSC using nanoscale microfibrillated cellulose membrane as electrolyte and photoanode of configuration N719/TiO₂-cellulose fibers-carboxymethyl cellulose (CMC)/FTO. The CE used was the usual Pt/FTO. The cellulose-based membrane had three dimensional fiber networks entrapping the liquid solution of NaI, I₂, TBP, and MPN. At 1 sun illumination, efficiency of 3.55% was obtained. Stability test showed that the cell was stable with decreased efficiency percentage of only 4% after 1000 h [56]. Nanocrystalline cellulose template has been used to synthesize TiO₂ film [57]. The TiO₂ porosity and surface area can be varied by controlling by the weight ratio of TiO₂ and cellulose. It has also been reported that ethyl cellulose played an important role in modifying the crystal growth favorably in the synthesis of ZnO for QDSSC application [58]. Electrolytes for DSSCs have been added with cellulose-based materials as filler according to Refs. [59, 60].

7 Chitin, chitosan, and their derivatives

Chitin having chemical formula of (C₈H₁₃O₅N)_n is present in sea creatures (crustacean shells of crabs, shrimps, lobsters, and cephalopod beaks of octopuses and squids), insects (cuticles of beetles, ants, and butterflies), as well as in some fungi (Zygomycetes) and algae. It is a well-known fact that cellulose and chitin take the number one and two spots for being the most bountiful natural polymer on earth. In fact, their chemical structures are quite identical except that the former has hydroxyl groups whereas the latter having acetamide (NHCH₃CO) groups. Like the former, the latter is a semicrystalline linear polymer and cannot dissolve in water. In contrast, chitin is insoluble in cuprammonium hydroxide and cupriethylene diamine although cellulose does [31]. Instead, chitin is soluble in formic acid (HCOOH), dichloroacetic acid (Cl₂CHCOOH), trichloroacetic acid (Cl₃CCOOH), hexafluoroacetone sesquihydrate (C₃F₆O·1.5H₂O), hexafluoroisopropanol ((CF₃)₂CHOH), and concentrated acids, i.e., hydrochloric acid (HCl), phosphoric acid (H₃PO₄), and sulfuric acid (H₂SO₄), as well as ionic liquid (1-allyl-3-methylimidazolium bromide) [31, 61, 62]. Kurita et al. [63] reported that chitin is unable to dissolve in dichloroacetic acid. T_g of chitin is 509 K [64].

Chitin was used as precursor to produce carbon quantum dots which were then used as sensitizing agent in ZnO QDSSC with solid-state hole conductor [65]. In another work, chitin-derived carbon was utilized as catalyst in the CE for DSSC [66]. Kawabata and Matsuo [67] have prepared films containing chitin derived from crab shells using an uncommon method, that is, suction

filtration. The chitin sheet functioned as electrolyte which exhibited proton conductivity at around 1mScm^{-1} and power density of 1.35mWcm^{-2} when applied in fuel cell under high humidity (100% relative humidity). Gel electrolyte based on chitin and cellulose blended at weight ratio 1:3 containing ionic liquids and H_2SO_4 delivered a specific capacitance of 162Fg^{-1} in electrical double layer capacitor (EDLC) application [62]. Chitin nanofibers from shrimp shells have been prepared in both aerogel and cryogel forms [22, 24]. The nano-chitin aerogel electrolyte membrane containing $\text{Na}_2\text{S-S-KCl}$ solution for CdS QDSSC exhibited an efficiency of 0.46% [22] whereas an efficiency of 4.30% was attained for Z907 DSSC using the nanochitin cryogel membrane encompassing PMII-GuSCN-NMBI-I₂-MPN solution [24]. Although a rather good performance was obtained by the chitin-based electrolyte in DSSC but its stability could not withstand for long period. After 216h aging under UV light, degradation in performance was detected when the η and J_{sc} decreased drastically. To the best of our knowledge, there are very limited studies on chitin-containing electrolyte for DSSC and QDSSC applications except the aforementioned cases. Apart from the fast degradation factor, another plausible reason is due to the restricted solubility of chitin. Moreover, those unconventional solvents that can dissolve chitin as stated earlier are not suitable to serve as solvent in polymer electrolytes.

Fortunately, the structure of chitin can be modified to reduce its crystallinity and improve the solubility. Chitosan comprising β -(1,4)-2-amino-deoxy-D-glucopyranose repeating unit is the product obtained after chitin undergoes deacetylation process in which the hydrophobic acetyl (CH_3CO) functional group is mostly removed and substituted by hydrophilic amino (NH_2) group. Chitosan (Ch) is soluble in dilute acid solutions (1%) such as acetic, lactic, malic, maleic, formic, succinic, butyric, and phosphorus acids [68, 69]. In addition, Ch can also dissolve in 1% acid media, that is, hydrochloric, L-ascorbic, and L-glutamic acids at elevated temperature of 333K [68]. Praveen et al. [70] have prepared Ch thin films by solvating Ch in acid at different concentrations via solution cast technique. It is found that 1.5% acid was the optimum value whereas films prepared from 0.1%, 0.25%, 0.5%, 0.75%, 1.00%, and 1.25% concentration were unable to be peeled off from Petri glass dishes. Four different acids viz. formic, adipic, succinic, and acetic acids have also been employed to solvate Ch and it was reported that Ch thin film using formic acid as solvent was flexible and easy to use whereas films from the other three solvents were brittle and unstable [70]. Recent work done by Mohan et al. [71] revealed that fractal growth was seen in Ch film utilizing adipic acid while films of acetic and formic acids showed none. T_g of Ch has been reported by different groups of researchers with varying values ranging between 413K and 476K [72–75]. Ch can serve as polymer matrix in electrolytes due to the oxygen atom of OH group and the nitrogen atom of NH₂ group present in its structure that have unused electron pairs that can interact with the doping salt. Table 2 lists the Ch-based polymer electrolytes employed in DSSCs and QDSSCs available in

TABLE 2 DSSCs and QDSSCs performance using chitosan-based electrolytes with respective electrodes and their ambient conductivities. The existence form of electrolytes used is presented in parentheses.

Electrolyte	Photoanode	CE	σ (S cm $^{-1}$)	J_{sc} (mA cm $^{-2}$)	V_{oc} (V)	FF	η (%)	Ref.
Ch-NH ₄ I-I ₂ -BMII (solid)	Black rice/TiO ₂ /ITO	ITO	3.43×10^{-5}	0.065	0.230	0.220	0.003	[76]
Ch-NH ₄ I-I ₂ -BMII (solid)	Callus of <i>Celosia plumosa</i> /TiO ₂ /ITO	ITO	3.43×10^{-5}	0.029	0.140	0.220	0.001	[76]
Ch-NaI-EMISCN-I ₂ (solid)	N719/ TiO ₂ /FTO	Pt/FTO	2.60×10^{-4}	2.62	0.53	0.52	0.73	[77]
Ch-LiI-EC-TiO ₂ -I ₂ (solid)	Pomegranate seeds/TiO ₂ /ITO	Pt/ITO	10^{-5}	6.40	0.53	0.53	1.80	[78]
Ch-NH ₄ I-I ₂ -BMII (solid)	Black rice/TiO ₂ /ITO	Pt/ITO	3.43×10^{-5}	0.288	0.270	0.440	0.030	[79]
Ch-NH ₄ I-I ₂ -BMII (gel)	Black rice/TiO ₂ /ITO	Pt/ITO	3.02×10^{-4}	0.90	0.37	0.45	0.15	[79]
Ch-NH ₄ I-I ₂ -BMII (gel)	Red cabbage/TiO ₂ /ITO	Pt/ITO	3.02×10^{-4}	2.09	0.61	0.30	0.38	[79]
Ch-HCOOH-KI-PEG-I ₂ (gel)	N719/ZnS/FTO	Pt/FTO	–	0.12	0.70	0.54	0.11	[80]
Ch-HCOOH-KI-PEG-I ₂ (gel)	N719/ZnO/FTO	Pt/FTO	–	0.33	0.30	0.65	0.16	[80]
Ch-HCOOH-KI-PEG-I ₂ (gel)	N719/ZnS/ZnO/FTO	Pt/FTO	–	1.69	0.80	0.45	1.58	[80]
Ch (CH ₃ COOH+H ₂ O)-KI-I ₂ -ACN (gel)	N719/TiO ₂ /FTO	Pt/FTO	–	1.29	0.62	0.82	0.66	[81]
Ch (CH ₃ COOH+H ₂ O)-NH ₄ I-I ₂ -ACN (gel)	N719/TiO ₂ /FTO	Pt/FTO	–	0.97	0.64	0.73	0.45	[81]
Ch NP (CH ₃ COOH+H ₂ O)-NH ₄ I-I ₂ -ACN (gel)	N719/TiO ₂ /FTO	Pt/FTO	–	3.66	0.55	0.61	1.23	[81]

Ch-PVA-NH ₄ I-I ₂ (solid)	Blueberries/TiO ₂ /ITO	Pt/ITO	1.77×10^{-6}	0.190	0.300	0.430	0.020	[82]
Ch-PEO-NH ₄ I-I ₂ (solid)	Blueberries/TiO ₂ /ITO	Pt/ITO	3.66×10^{-6}	0.270	0.340	0.400	0.040	[82]
Ch-PEO-NH ₄ I-I ₂ (solid)	Red cabbage/TiO ₂ /ITO	Pt/ITO	3.66×10^{-6}	0.310	0.390	0.480	0.060	[83]
Ch-PEO-NH ₄ I-I ₂ (solid)	N3/TiO ₂ /ITO	Pt/ITO	3.66×10^{-6}	2.710	0.580	0.500	0.780	[83]
Ch-PEO-NH ₄ I-I ₂ (solid)	N3/Ag NP/TiO ₂ /ITO	Pt/ITO	3.66×10^{-6}	2.840	0.580	0.690	1.130	[83]
Ch-PEO-NH ₄ I-I ₂ (solid)	<i>Curcuma longa</i> (turmeric)/TiO ₂ /ITO	Graphite/ITO	1.18×10^{-5}	0.20	0.28	0.32	0.18	[84]
Ch-PEO-NH ₄ I-I ₂ (solid)	<i>Lawsonia inermis</i> (henna)/TiO ₂ /ITO	Graphite/ITO	1.18×10^{-5}	0.38	0.34	0.38	0.49	[84]
Ch-PEO-NH ₄ I-I ₂ (solid)	Sumac/TiO ₂ /ITO	Graphite/ITO	1.18×10^{-5}	0.93	0.39	0.48	1.75	[84]
Ch-PEO-NH ₄ I-I ₂ -BMII (gel)	Black rice/TiO ₂ /ITO	Pt/ITO	5.52×10^{-4}	1.21	0.40	0.47	0.23	[79]
Ch-PEO-NH ₄ I-I ₂ -BMII (gel)	Red cabbage/TiO ₂ /ITO	Pt/ITO	5.52×10^{-4}	2.52	0.40	0.39	0.39	[79]
Ch-PVdF-HFP-KI-PMII-I ₂ (gel)	N719/TiO ₂ /FTO	Pt/FTO	5.36×10^{-4}	6.59	0.53	0.35	1.23	[85]
Ch (CH ₃ COOH+H ₂ O)-PEG-KI-I ₂ (gel)	CdS/ITO	ITO	6.20	$\sim 6 \mu\text{A}^{\text{a}}$	$\sim 0.23^{\text{a}}$	—	—	[86]

PEG, poly(ethylene glycol); HCOOH, formic acid; CH₃COOH, acetic acid; ACN, acetonitrile.

^a14.5 mW cm⁻².

literature. The photovoltaic parameters and electrodes components used along with their ambient conductivity (σ) values (if provided) are presented in the Table 2. The reported performance is obtained at 100 mW cm^{-2} unless indicated otherwise. It is to be noted that 1% acetic and formic acids were used to dissolve Ch in the preparation of the electrolytes listed in the table.

From Table 2, it is obvious that the efficiencies of less than 0.010% have been obtained from the DSSCs that employed the solid polymer electrolytes containing Ch-NH₄I-BMII-I₂ [76, 79]. It is also noticeable that these DSSCs have only ITO as counter electrode without any catalytic material which could be one of the reasons for the low efficiencies. As stated earlier, the reduction process in the case of iodide/triiodide redox mediator is when the triiodide ion is reduced to iodide ion at the CE. Without a catalytic coating on the TCO glass substrate (in this case ITO), the reduction reaction will occur at a much slower rate. Increment in efficiency can be seen for the cell having anthocyanin extracted from black rice after the platinum catalyst has been coated on the ITO glass substrate [79]. It is evident in the table that the Ch-NH₄I-BMII-I₂ electrolyte that exists in gel state has higher ambient conductivity of $1.51 \times 10^{-4}\text{ S cm}^{-1}$ than the electrolyte in thin film form at same composition ($\sigma = 3.43 \times 10^{-5}\text{ S cm}^{-1}$) [79]. The electrolyte in gel form was prepared in the same procedure except reducing the amount of solvent [79]. Gel polymer electrolytes usually possess better interfacial contact other than higher conductivity as compared to solid polymer electrolytes. Nonetheless, the former shows poor mechanical strength than the latter. As expected, improvement in conductivity and performance in cells with Ch blended electrolytes can be observed in the table as compared to that of electrolytes having Ch only regardless whether they are in gel or solid form [76, 79].

Following the work of Khalili et al. [81], Ch in 1% acetic acid solution was added with sodium tripolyphosphate (Na₅P₃O₁₀) and subjected to sonication and centrifugation to obtain Ch nanoparticles (NP) and comparison was made with the chitosan used as received. Both Ch and Ch NP were then used as polymer host in GPE for DSSCs where the latter showed boosted performance in terms of J_{sc} and η by 183.72% and 86.36%. This may be due to fast diffusion rate of triiodide ions to TiO₂ owing to the nanoparticles size. The cell with Ch NP also displayed better efficiency after 14 days with 78% loss as compared to cell with Ch (89% efficiency loss) [81]. This indirectly implied that chitosan showed poor stability in performance for prolonged use. Chitosan, in general, is known to degrade upon exposure to UV radiation and resulting in chain scission, formation of free radicals and additional crosslinking [80, 87]. As anticipated, poor performances can also be observed in those cells sensitized with natural dyes [76, 79, 82–84] since natural dyes are prone to degradation and thus have weak interaction with the MOin the photoanode. Despite this, their inexpensive, readily availability, sustainability, and eco-friendly features making them potential sensitizers for next generation energy devices if we can tackle the photoinstability issue.

It is praiseworthy that Maddu et al. [86] have tried to construct small solar module using four identical solar cells in three different ways, that is, (i) all four cells connected in series, (ii) four cells linked in parallel configuration, and (iii) a parallel pair of two cells connected in series even though one single cell exhibited very low short circuit current in the order of μA , as can be seen in [Table 2](#). Nevertheless, the solar module prepared by method (i) attained the short circuit current, I_{sc} of $1.58\,\mu\text{A}$ and V_{oc} of $1.09\,\text{V}$ under light illumination of $14.5\,\text{mW cm}^{-2}$ whereas I_{sc} of $3.21\,\mu\text{A}$ and $2.31\,\mu\text{A}$ with V_{oc} of $0.40\,\text{V}$ and $0.45\,\text{V}$ were obtained for (ii) and (iii), respectively. In another words, maximum output power of $0.78\,\mu\text{W}$ has been achieved by (i) followed by (ii) ($P_{max}=0.42\,\mu\text{W}$) and (iii) ($P_{max}=0.25\,\mu\text{W}$) [86]. Based on [Table 2](#), it can be concluded that most works focused on Ch-based electrolytes in DSSCs rather than QDSSCs. As aforesaid, QDSSCs usually use $\text{S}_2^-/\text{S}_n^{2-}$ redox mediator and thus water is the solvent employed since sodium sulfide can only dissolve in it whereas if using alcohols, they can react with sodium sulfide due to acid-base interaction [88]. However, Ch is insoluble in water. Neither alkali (e.g., NaOH, KOH, etc.) nor organic (e.g., DMF, DMSO, tetrahydrofuran (THF), pyridine, *m*-cresol, etc.) solvents can be used to solvate Ch [63, 89].

One disadvantage of using dilute formic and acetic acids to dissolve Ch for DSSCs with I^-/I_3^- redox couple in [Table 2](#) is that the water present can cause the creation of iodate (IO_3^-) ions with the help of oxygen [90]. This leads to reduced formation of I_3^- ions to facilitate electron transport from CE to photoanode which can impose negative effect in performance. Therefore, Ch needs to be modified chemically to improve its solubility and for better device performance. One way to modify it is via N-phthaloylation in which mixture containing Ch and phthalic anhydride in DMF undergoes reflux in nitrogen surroundings at elevated temperature (373–393 K) to obtain N-phthaloylchitosan (PhCh). The NH_2 functional group of Ch has been substituted by N-phthalimido functional group. PhCh is soluble in DMSO, DMAc, DMF, *m*-cresol, dichloroacetic acid, and pyridine [63, 91]. In addition, solvent mixture of saturated methanol and calcium chloride dehydrate, as well as DMAc solution with 8% lithium chloride are said to dissolve PhCh [63]. Meanwhile, PhCh-based film showed T_g of $260\,\text{K}$ [15]. [Table 3](#) summarizes the works done on PhCh-based polymer electrolytes employed in DSSCs under illumination of $100\,\text{mW cm}^{-2}$ unless indicated otherwise.

As can be observed in [Table 3](#), an impressive performance with high efficiency of 9.61% was achieved by DSSC using PhCh-PEO blended gel electrolyte [101]. The PhCh/PEO ratio was 4:1. It is also noted that the PhCh-based electrolytes have been used along with various materials for CE other than Pt [100, 102]. Again, there is no report on QDSSC using electrolyte based on PhCh. Besides PhCh, chitosan can be modified into hexanoyl chitosan [89, 104], lauroyl chitosan [89], carboxymethyl chitosan [105], o-nitrochitosan [106], and decanoyl chitosan [89] to name a few which are yet to be exploited for DSSCs.

TABLE 3 Photovoltaic performance of DSSCs with PhCh-based electrolytes with their ambient conductivities. The state of the electrolytes is presented in parentheses.

Electrolyte	Photoanode	CE	σ (S cm^{-1})	J_{sc} (mA cm^{-2})	V_{oc} (V)	FF	η (%)	Ref.
PhCh-NaI-I ₂ (solid)	N719/TiO ₂ /ITO	Pt/ITO	3.25×10^{-4}	0.820	0.530	0.650	0.290	[92]
PhCh-LiI-BMII-I ₂ (solid)	Anthocyanin (red cabbage)/TiO ₂ /ITO	Pt/ITO	6.94×10^{-4}	2.200	0.350	0.260	0.200	[93]
PhCh-LiI-BMII-I ₂ (solid)	Anthocyanin (black rice)/TiO ₂ /ITO	Pt/ITO	6.94×10^{-4}	2.310	0.300	0.300	0.210	[93]
PhCh-NH ₄ I-BMII-I ₂ (gel)	Anthocyanin (red cabbage)/TiO ₂ /ITO	Pt/ITO	5.86×10^{-4}	3.472	0.365	0.340	0.430	[79]
PhCh-PEO-NH ₄ I-BMII-I ₂ (gel)	Anthocyanin (red cabbage)/TiO ₂ /ITO	ITO	6.24×10^{-4}	3.503	0.340	0.390	0.460	[79]
PhCh-EC-PC-TPAI-I ₂ (gel)	N719/TiO ₂ /FTO	Pt/FTO	5.27×10^{-3}	7.380	0.720	0.660	3.500	[94]
PhCh-EC-PC-TPAI-LiI-I ₂ (gel)	N719/TiO ₂ /FTO	Pt/FTO	4.14×10^{-3}	7.250	0.770	0.670	3.710	[94]
PhCh-EC-PC-KI-I ₂ (gel)	N3/TiO ₂ /FTO	Pt/FTO	1.37×10^{-2}	7.710	0.670	0.630	3.230	[95]
PhCh-EC-PC-TBAI-I ₂ (gel)	N3/TiO ₂ /FTO	Pt/FTO	8.45×10^{-3}	8.720	0.800	0.630	4.370	[95]
PhCh-EC-PC-TBAI-I ₂ (gel)	N3/TiO ₂ /FTO	Pt/FTO	4.45×10^{-3}	5.580	0.650	0.630	2.290	[95]

PhCh-EC-PC-KI-TBAI-I ₂ (gel)	N3/TiO ₂ /FTO	Pt/FTO	6.71×10^{-3}	8.700	0.800	0.630	4.360	[95]
PhCh-EC-DMF-TPAI-I ₂ (gel)	N3/TiO ₂ /FTO	Pt/FTO	5.46×10^{-3}	12.720	0.600	0.660	5.000	[96]
PhCh-EC-DMF-TPAI-LiI-I ₂ (gel)	N3/TiO ₂ /FTO	Pt/FTO	6.09×10^{-3}	17.290	0.590	0.620	6.360	[97]
PhCh-PEO-DMF-TPAI-I ₂ (gel)	Anthocyanin (black rice)/TiO ₂ /FTO	Pt/FTO	7.36×10^{-3}	2.240	0.410	0.580	0.530	[98]
PhCh-PEO-DMF-TPAI-I ₂ (gel)	Anthocyanin (black rice)/TiO ₂ + Ag NP/FTO	Pt/FTO	7.36×10^{-3}	2.710	0.400	0.680	0.740	[98]
PhCh-PEO-DMF-TPAI-I ₂ (gel)	N3/TiO ₂ /FTO	Pt/FTO	7.36×10^{-3}	13.040	0.580	0.610	4.610	[98]
PhCh-PEO-DMF-TPAI-I ₂ (gel)	N3/TiO ₂ + Ag NP/FTO	Pt/FTO	7.36×10^{-3}	15.240	0.600	0.570	5.210	[98]
PhCh-PEO-EC-DMF-TPAI-I ₂ (gel)	Anthocyanin (black rice)/TiO ₂ /FTO	Pt/FTO	1.11×10^{-2}	1.830	0.500	0.650	0.590	[99]
PhCh-PEO-EC-DMF-TPAI-I ₂ (gel)	Chlorophyll (screwpine leaves)/TiO ₂ /FTO	Pt/FTO	1.11×10^{-2}	1.190	0.490	0.630	0.390	[99]
PhCh-PEO-EC-DMF-TPAI-I ₂ (gel)	Anthocyanin (black rice) + Chlorophyll (screwpine leaves)/TiO ₂ /FTO	Pt/FTO	1.11×10^{-2}	2.640	0.460	0.630	0.810	[99]
PhCh-PEO-EC-DMF-TPAI-I ₂ (gel)	N3/TiO ₂ /FTO	NiS/FTO	–	12.710	0.680	0.690	5.960	[100]
PhCh-PEO-EC-DMF-TPAI-I ₂ (gel)	N3/TiO ₂ /FTO	Ni _{0.95} Mo _{0.05} S/FTO	–	17.210	0.650	0.640	7.150	[100]

Continued

TABLE 3 Photovoltaic performance of DSSCs with PhCh-based electrolytes with their ambient conductivities. The state of the electrolytes is presented in parentheses—cont'd

Electrolyte	Photoanode	CE	σ (S cm^{-1})	J_{sc} (mA cm^{-2})	V_{oc} (V)	FF	η (%)	Ref.
PhCh-PEO-EC-DMF-TPAI-I ₂ (gel)	N3/TiO ₂ /FTO	Pt/ FTO	—	17.320	0.660	0.630	7.200	[100]
PhCh-PEO-EC-DMF-TPAI-I ₂ (gel)	N3/TiO ₂ /FTO	Pt/ FTO	1.11×10^{-2}	16.560	0.660	0.670	7.100	[101]
PhCh-PEO-EC-DMF-TPAI-BMII-I ₂ (gel)	N3/TiO ₂ /FTO	Pt/ FTO	1.35×10^{-2}	19.680	0.710	0.690	9.610	[101]
PhCh-PEO-EC-DMF-TPAI-I ₂ (gel)	N3/TiO ₂ /FTO	Pt/ FTO	—	17.81	0.69	0.63	7.82	[102]
PhCh-PEO-EC-DMF-TPAI-I ₂ (gel)	N3/TiO ₂ /FTO	CoS ₂ / FTO	—	17.51	0.65	0.64	7.29	[102]
PhCh-EC-DMF-TPAI-LiI-BMII-I ₂ (gel)	N3/TiO ₂ /FTO	Pt/ FTO	5.46×10^{-3}	16.53	0.62	0.65	6.69	[103]

8 Starch

Starch with the chemical formula of $(C_6H_{10}O_5)_n$ can be found in potatoes, tapioca, wheats, oats, rice, corns, peas, sorghum, barley, sweet potatoes, and so on. Unlike chitin and cellulose, starch is made up of two homopolymers, that is, amylopectin and amylose. The former is a branched-chain polymer of repetitive glucose units with primary α -1,4 glycosidic bonds and occasional α -1,6 glycosidic links, whereas the latter is a linear macromolecule consisting of similar units but without the α -1,6 glycosidic linkage. Starch has hydroxyl groups that can interact with the cation of salt. It is semicrystalline and has T_g of 333–353 K [107]. Starch cannot solvate in cold water but it can do so in hot water [108]. Khanmirzaei et al. [109] have dissolved starch in distilled water at 353 K for 15 min. Solid polymer electrolyte containing starch from rice, NaI, and I₂ exhibited ambient ionic conductivity of $4.79 \times 10^{-4} \text{ S cm}^{-1}$. The N719 DSSC using such electrolyte gave an efficiency of 0.78% under 1 sun irradiation [109]. Recent work of Khanmirzaei et al. [110] has showed that the incorporation of 1-hexyl-3-methylimidazolium iodide into the rice starch-NaI-I₂ solid polymer electrolyte increased the conductivity to $1.83 \times 10^{-3} \text{ S cm}^{-1}$. The DSSC performance was also enhanced with efficiency of 3.42% [110]. Aqueous gel electrolyte based on rice starch with LiI and I₂ has been tested in N719 TiO₂DSSC [111]. An efficiency of 0.35% was achieved. Potato starch has been dissolved in DMSO and incorporated with NaI and I₂ to form gel electrolyte which yielded the ambient conductivity of $0.29 \times 10^{-8} \text{ S cm}^{-1}$ [112]. Despite the low conductivity, the electrolyte with N719 TiO₂ and Pt electrodes delivered a rather good DSSC with efficiency of 2.94% under 100 mW cm^{-2} illumination. Improvement in conductivity ($0.38 \times 10^{-8} \text{ S cm}^{-1}$), J_{sc} (8.08 mA cm⁻²) and η (3.33%) were achieved by transforming potato starch into potato starch nanocrystals via acid hydrolysis [112].

One drawback of starch is that it will interact with iodine and form complexes making iodine unavailable to perform its function and subsequently affects the DSSC performance [10]. In order to avoid this, potato starch was cross-linked with citric acid before adding to a mixture containing LiI, DMF, glycerol, and I₂ to form gel electrolyte [10]. Efficiency of 1.40% was attained by such electrolyte in N719 TiO₂ DSSC under illumination of 85 mW cm^{-2} . On comparison, the DSSC using gel electrolyte based on potato starch without cross-linking presented an efficiency of 1.20% under similar condition. The potato starch-based gel electrolyte had higher ambient conductivity of 1.61 S cm^{-1} than the potato starch-citric acid cross-linked electrolyte ($\sigma=0.59 \text{ S cm}^{-1}$) since cross-linking restricted the segmental motion and caused decreased ionic mobility [10].

Another approach is to graft potato starch with ionic liquid (1-glycidyl-3-methylimidazolium chloride) to form positively charged starch [113]. The cationic starch showed improved solubility in DMF and DMSO besides water. The gel electrolyte containing cationic starch, KI, 1-glycidyl-3-methylimidazolium

chloride, I_2 , and DMSO exhibited the ambient conductivity of 0.286 mS cm^{-1} . Using such electrolyte, the N719 TiO_2 DSSC exhibited an efficiency of 0.63% at light intensity of 60 mW cm^{-2} [113]. Starch can also undergo chemical modification to form sodium carboxymethyl starch which dissolves in water at room temperature. Some hydroxyl groups of starch have been swapped with carboxymethyl groups. Sodium carboxymethyl starch is hygroscopic, adhesive, and highly water-absorbent with good water uptake. A gel polymer electrolyte consisting of sodium carboxymethyl starch, Na_2S , and S was prepared for QDSSC [114]. Cu_2S/FTO was used as CE whereas the photoanode was $SiO_2/ZnS/CdSe/TiO_2/FTO$. At 1 sun illumination, the QDSSC displayed J_{sc} of 15.63 mA cm^{-2} , V_{oc} of 0.62 V, and η of 6.32% [114].

9 Agar and agarose

Agar or also known as “agar-agar” is a jelly-like material that is commonly used in food from Southeast Asian countries. Basically, agar is a macromolecule made up of repeating sugar galactose units. It is extracted from certain species of red seaweed (*Rhodophyceae* class) and can also be found in the cell wall of marine algae. To be exact, agar contains two polymers, that is, agarose and agaropectin. The former is a major component made up of alternating D-galactose and 3,6-anhydro-L-galactose units whereas agaropectin has similar polymer chain of D-galactose and L-galactose units with side groups of pyruvates and sulfates [115]. The latter is acidic due to the side groups but the former has neutral charge [115]. Agar is a semi-crystalline polymer and possesses excellent gel-making ability [17, 116]. Similar to starch, agar is insoluble in cold water and can only swell. Nevertheless, it can dissolve in water at elevated temperatures (363–373 K) [116]. Other than water, glycerol can also solvate agar upon heating [117, 118]. Agar has T_g of 317.5 K [119].

Alias and Mohamad [117] have prepared agar-based gel electrolyte containing NH_4I with I_2 and sandwiched between N719/ ZnO/ITO photoanode and $Au-Pd/ITO$ CE. The DSSC exhibited poor performance with photocurrent density in the order of microamperes under 1 sun illumination although the electrolyte had conductivity of 2.64 mS cm^{-1} . It is to be noted that the agar was dissolved in glycerol upon heating at 353 K for 15 min [117]. Nadia et al. [118] have recorded an efficiency of 2.16% for N719 TiO_2 DSSC employing agar-based gel electrolyte with KI , glycerol, I_2 , and 1-methyl-3-propylimidazolium iodide at 1 sun condition. The photocurrent density was 9.28 mA cm^{-2} . The agar-based electrolyte exhibited room temperature conductivity of 1.48 mS cm^{-1} [118]. Another group of researchers have tried to apply agar-based electrolyte in QDSSC having two types of quantum dots (CdS and copper indium sulfide ($CuInS_2$)) and CE of copper sulfide-reduced graphene oxide (Cu_2S-RGO) [120]. The gel electrolyte based on agar comprised of Na_2S , S, glycerol, and formaldehyde displayed optimal conductivity of 1.81 mS cm^{-1} and superior thermal stability up to 523 K. Better performance was achieved by the CdS

QDSSC using the agar-based gel electrolyte ($J_{sc} = 13.51 \text{ mA cm}^{-2}$, $\eta = 2.98\%$) as compared to CuInS₂ cell with the same electrolyte ($J_{sc} = 10.75 \text{ mA cm}^{-2}$, $\eta = 2.97\%$) at 1 sun intensity [120].

Agarose, which exists predominantly in agar, can dissolve in certain ionic liquids such as 1-ethyl-3-methylimidazolium dicyanamide, 1-methyl-3-propylimidazolium iodide, and 1-methyl-3-propylimidazolium hexafluorophosphate under stirring and heating at 423 K [121]. At elevated temperatures (368–373 K), agarose is soluble in DMAc, DMSO, DMF, N-methyl-2-pyrrolidone (NMP), glycol, and orthophosphoric acid [122, 123]. Singh and co-workers [124] have heated agarose in double distilled water at 333 K under constant stirring before adding KI and I₂. Room temperature conductivity of the electrolyte was 9.02 mS cm⁻¹ and efficiency of 0.54% was obtained for N719 DSSC at 1 sun condition [124]. Interaction has occurred between the hydroxyl groups of agarose with the K⁺ ion [124].

In the work by Kaneko et al. [125], agarose in pure water solvent was heated inside microwave oven before pouring the hot solution on N3 photoanode for penetration into the nanoporous TiO₂. Electrolyte solution containing TPAI, I₂, acetonitrile, and 3-methyl-2-oxazolidinone was used to immerse the agarose/N3/TiO₂/FTO electrode before attaching onto Pt/ITO CE to form solid state DSSC. Under 1 sun irradiation, an efficiency of 7.06% was attained. Conductivity of 3.67 mS cm⁻¹ was obtained for the agarose solid containing the electrolyte solution [125]. A N719 TiO₂ DSSC with agarose-based gel electrolyte that contained 1-methyl-3-propylimidazolium iodide, LiI, TBP, and I₂ reported by Suzuki et al. [121] delivered an efficiency of 2.46% at 1 sun condition. It was found that there was a slight increment in efficiency (2.93%) upon aging for 310 h which may be due to the slow diffusion of electrolyte into the TiO₂ nanopores. The same work also showed 3.89% efficiency using ionic gel electrolyte made up of agarose, 1,2-dimethyl-3-propylimidazolium iodide, LiI, 1-ethyl-3-methylimidazolium dicyanamide, TBP, and I₂ [121].

Another agarose-based gel electrolyte that comprised LiI, TiO₂ nanoparticles, and I₂ was prepared after dissolving agarose in NMP at 353 K [126]. Conductivity of 3.98 mS cm⁻¹ was obtained at 303 K. No photovoltaic results were given even though N719 TiO₂ DSSC has been fabricated [126]. Coincidentally, Yang and co-authors [127] have also prepared gel polymer electrolyte having agarose, LiI, I₂, NMP, and TiO₂ nanofiller for application in N3 TiO₂DSSC. Under illumination 73 mW cm⁻², efficiency of 4.74% was obtained. As a comparison, the cell using agarose electrolyte without the nanofiller only exhibited an efficiency of 3.77%. The electrolyte conductivity without nanofiller (2.98 mS cm⁻¹) was lower than that having the filler (4.40 mS cm⁻¹) [127]. A rather similar work has also been published by the same group of researchers in Ref. [128].

In order to improve conductivity and DSSC performance, four different additives viz. MnCo₂O₄, ZnCo₂O₄, (CH₂)₂O₂Ni, and (CH₂)₃O₂Ni were incorporated in agarose-based gel electrolyte containing LiI, I₂, and NMP

[129]. The conductivity decreased in the order of $(\text{CH}_2)_3\text{O}_2\text{Ni}$ (4.29 mS cm^{-1}) - $> (\text{CH}_2)_2\text{O}_2\text{Ni}$ (2.88 mS cm^{-1}) $> \text{ZnCo}_2\text{O}_4$ (2.44 mS cm^{-1}) $> \text{MnCo}_2\text{O}_4$ (1.64 mS cm^{-1}). Electrolyte without the presence of any additive showed lowest conductivity at 1.08 mS cm^{-1} . The efficiency trend followed the conductivity pattern with highest efficiency of 4.59% obtained for cell having $(\text{CH}_2)_3\text{O}_2\text{Ni}$ -containing agarose electrolyte at 1 sun intensity. DSSC with MnCo_2O_4 added electrolyte exhibited the η of 3.97% and the cell having electrolyte without additive presented η of 2.73% [129]. Metal-organic fillers such as $(\text{CH}_2)_2\text{O}_2\text{Ni}$ and $(\text{CH}_2)_3\text{O}_2\text{Ni}$ are superior cross-linking agent than the inorganic oxides (ZnCo_2O_4 and MnCo_2O_4) in enhancing the conductivity and improving the electrolyte/electrode contact, as well as increasing the cell performance.

10 Summary and outlook

As a summary, polysaccharides namely cellulose, chitin/chitosan, starch, agar, and their derivatives have showed promising prospective as polymer host in electrolytes. Nonetheless, there are comparatively less studies on polysaccharide-based electrolytes for application in DSSCs and QDSSCs than synthetic polymer electrolytes in such devices. Hence, there are many aspects of research awaiting to be explored to fully utilize their potential as green electrolytes for new breed of photovoltaic cells. Nevertheless, it is anticipated that such polysaccharide electrolytes will be put into practical use for the next generation renewable energy sources particularly DSSCs and QDSSCs.

Acknowledgments

Authors thank the Universiti Malaya and Malaysian Ministry of Higher Education (MOHE) for the grant no. GPF045B-2018 and FRGS grant no. FRGS/1/2019/STG07/UM/02/3.

References

- [1] M.M. Pérez-Madrigal, M.G. Edo, M.G. Saborío, F. Estrany, C. Alemán, Pastes and hydrogels from carboxymethyl cellulose sodium salt as supporting electrolyte of solid electrochemical supercapacitors, *Carbohydr. Polym.* 200 (2018) 456–467.
- [2] M.S.M. Misenan, M.I.N. Isa, A.S.A. Khar, Electrical and structural studies of polymer electrolyte based on chitosan/methyl cellulose blend doped with BMIMTFSI, *Mater. Res. Express* 5 (2018) 055304.
- [3] F. Colò, F. Bella, J.R. Nair, M. Destro, C. Gerbaldi, Cellulose-based novel hybrid polymer electrolytes for green and efficient Na-ion batteries, *Electrochim. Acta* 174 (2015) 185–190.
- [4] V. Selvanathan, M.N.A. Halim, A.D. Azzahari, M. Rizwan, N. Shahabudin, R. Yahya, Effect of polar aprotic solvents on hydroxyethyl cellulose-based gel polymer electrolyte, *Ionics* 24 (2018) 1955–1964.
- [5] S. Monisha, T. Mathavan, S. Selvasekarapandian, A. Milton Franklin Benial, G. Aristatil, N. Mani, M. Premalatha, D. Vinoth Pandi, Investigation of bio polymer electrolyte based

- on cellulose acetate-ammonium nitrate for potential use in electrochemical devices, *Carbo-hydr. Polym.* 157 (2017) 38–47.
- [6] M.S.A. Rani, N.S. Mohamed, M.I.N. Isa, Characterization of proton conducting carboxy-methyl cellulose/chitosan dual-blend based biopolymer electrolytes, *Mater. Sci. Forum* 846 (2016) 539–544.
 - [7] A.S. Ahmad Khiar, A.K. Arof, Conductivity studies of starch-based polymer electrolytes, *Ionics* 16 (2010) 123–129.
 - [8] K.H. Teoh, C.-S. Lim, S. Ramesh, Lithium ion conduction in corn starch based solid polymer electrolytes, *Measurement* 48 (2014) 87–95.
 - [9] Y. Lin, J. Li, K. Liu, Y. Liu, J. Liu, X. Wang, Unique starch polymer electrolyte for high capacity all-solid-state lithium sulfur battery, *Green Chem.* 18 (2016) 3796–3803.
 - [10] P. Nagaraj, A. Sasidharan, V. David, A. Sambandam, Effect of cross-linking on the performances of starch-based biopolymer as gel electrolyte for dye-sensitized solar cell applications, *Polymers* 6 (2017) 667.
 - [11] T. Tiwari, M. Kumar, M. Yadav, N. Srivastava, Study of arrowroot starch-based polymer electrolytes and its application in MFC, *Star* 71 (2019) 1800313.
 - [12] M.H. Khammirzaei, S. Ramesh, Ionic transport and FTIR properties of lithium iodide doped biodegradable rice starch based polymer electrolytes, *Int. J. Electrochem. Sci.* 8 (2013) 9977–9991.
 - [13] T. Tiwari, N. Srivastava, P.C. Srivastava, Ion dynamics study of potato starch + Sodium salts electrolyte system, *Int. J. Electrochem.* 2013 (2013) Article ID 670914.
 - [14] H. Yang, X. Ji, Y. Tan, Y. Liu, F. Ran, Modified supramolecular carboxylated chitosan as hydrogel electrolyte for quasi-solid-state supercapacitors, *J. Power Sources* 441 (2019) 227174.
 - [15] N.A. Aziz, S.R. Majid, A.K. Arof, Synthesis and characterizations of phthaloyl chitosan-based polymer electrolytes, *J. Non Cryst. Solids* 358 (2012) 1581–1590.
 - [16] S. Majumdar, P. Sen, R. Ray, Ionic interactions and transport properties in chitosan-starch based blend solid biopolymer electrolytes, *Mater. Today Proc.* 18 (2019) 4913–4920.
 - [17] R. Leones, F. Sentanin, L.C. Rodrigues, I.M. Marrucho, J.M.S.S. Esperança, A. Pawlicka, M.M. Silva, Investigation of polymer electrolytes based on agar and ionic liquids, *Express Polym. Lett.* 6 (2012) 1007–1016.
 - [18] M.H. Buraidah, S.N.F. Yusuf, I.M. Noor, A.K. Arof, Optical properties of semiconductor nanoparticles in photoelectrochemical cells, in: T. Chen, Y. Liu (Eds.), *Semiconductor Nano-crystals and Metal Nanoparticles: Physical Properties and Device Applications*, CRC Press, USA, 2017, pp. 283–306.
 - [19] H.K. Jun, M.A. Careem, A.K. Arof, Quantum dot-sensitized solar cells—perspective and recent developments: a review of cd chalcogenide quantum dots as sensitizers, *Renew. Sustain. Energy Rev.* 22 (2013) 148–167.
 - [20] D.T. Reis, A.K.S. Pereira, G.N. Scheidt, D.H. Pereira, Plant and bacterial cellulose: production, chemical structure, derivatives and applications, *Orbital: Electron. J. Chem.* 11 (2019) 321–329.
 - [21] A. Gómez-Carracedo, C. Alvarez-Lorenzo, J.L. Gómez-Amoza, A. Concheiro, Chemical structure and glass transition temperature of non-ionic cellulose ethers DSC, TMDSC® Oscillatory rheometry study, *J. Therm. Anal. Calorim.* 73 (2003) 587–596.
 - [22] M. Borghei, K. Miettunen, L.G. Greca, A. Poskela, J. Lehtonen, S. Lepikko, B.L. Tardy, P. Lund, V.R. Subramanian, O.J. Rojas, Biobased aerogels with different surface charge as electrolyte carrier membranes in quantum dot-sensitized solar cell, *Cellul.* 25 (2018) 3363–3375.

- [23] A.W. Indrianingsih, V.T. Rosyida, T.H. Jatmiko, D.J. Prasetyo, C.D. Poeloengasih, W. Apriyana, K. Nisa, S. Nurhayati, M. Hernawan, C. Darsih, D. Pratiwi, A. Suwanto, D. Ratih, Preliminary study on biosynthesis and characterization of bacteria cellulose films from coconut water, *IOP Conf. Ser. Earth Environ. Sci.* 101 (2017) 012010.
- [24] A. Poskela, K. Miettunen, M. Borghei, J. Vapaavuori, L.G. Greca, J. Lehtonen, K. Solin, M. Ago, P.D. Lund, O.J. Rojas, Nanocellulose and nanochitin cryogels improve the efficiency of dye solar cells, *ACS Sustain. Chem. Eng.* 7 (2019) 10257–10265.
- [25] K. Miettunen, J. Vapaavuori, A. Tiihonen, A. Poskela, P. Lahtinen, J. Halme, P. Lund, Nano-cellulose aerogel membranes for optimal electrolyte filling in dye solar cells, *Nano Energy* 8 (2014) 95–102.
- [26] G.P. Salvador, D. Pugliese, F. Bella, A. Chiappone, A. Sacco, S. Bianco, M. Quaglio, New insights in long-term photovoltaic performance characterization of cellulose-based gel electrolytes for stable dye-sensitized solar cells, *Electrochim. Acta* 146 (2014) 44–51.
- [27] F. Bella, A. Chiappone, J. Nair, G. Meligrana, C. Gerbaldi, Effect of different green cellulosic matrices on the performance of polymeric dye-sensitized solar cells, *Chem. Eng. Trans.* 41 (2014) 211–216.
- [28] C. Krumm, J. Pfaendtner, P.J. Dauenhauer, Millisecond pulsed films unify the mechanisms of cellulose fragmentation, *Chem. Mater.* 28 (2016) 3108–3114.
- [29] J.S. Park, E. Ruckenstein, Viscoelastic properties of plasticized methylcellulose and chemically crosslinked methylcellulose, *Carbohydr. Polym.* 46 (2001) 373–381.
- [30] G.M. Pavlov, G.F. Kolbina, I.N. Shtennikova, N.A. Michailova, E.V. Korneeva, Dynamooptical properties of methylcellulose solutions and the optical anisotropy of glucopyranose ring, *Eur. Polym. J.* 37 (2001) 1219–1225.
- [31] G.A.F. Roberts, Solubility and solution behaviour of chitin and chitosan, in: *Chitin Chemistry*, Palgrave, London, 1992, pp. 274–329.
- [32] B. Lindman, G. Karlström, L. Stigsson, On the mechanism of dissolution of cellulose, *J. Mol. Liq.* 156 (2010) 76–81.
- [33] A.M.J.S. Weerasinghe, M.A.K.L. Dissanayake, G.K.R. Senadeera, V.A. Senaviratne, C.A. Thotawaththage, J.M.K.W. Kumari, Application of electrospun cellulose acetate nano-fibre membrane based quasi-solid state electrolyte for dye sensitized solar cells, *Ceylon J. Sci.* 46 (2017) 93–98.
- [34] J.J. Kaschuk, K. Miettunen, M. Borghei, E. Frollini, O.J. Rojas, Electrolyte membranes based on ultrafine fibers of acetylated cellulose for improved and long-lasting dye-sensitized solar cells, *Cellul.* 26 (2019) 6151–6163.
- [35] N.S. Samsi, N.A.S. Effendi, R. Zakaria, A.M.M. Ali, Efficiency enhancement of dye-sensitized solar cell utilizing copper indium sulphide/zinc sulphide quantum dot plasticized cellulose acetate polymer electrolyte, *Mater. Res. Express* 4 (2017) 1–10.
- [36] C.N. Abouloula, M. Rizwan, V. Selvanathan, A. Hassan, R. Yahya, A. Oueragli, Oil palm waste based phthaloyl cellulose: A product of photosynthesis as an electrolyte of photovoltaics, *Cellul.* 26 (2019) 1605–1617.
- [37] C.N. Abouloula, M. Rizwan, V. Selvanathan, C.I. Abdullah, A. Hassan, R. Yahya, A. Oueragli, A novel application for oil palm empty fruit bunch: extraction and modification of cellulose for solid polymer electrolyte, *Ionics* 24 (2018) 3827–3836.
- [38] N. Sarkar, L.C. Walker, Hydration-dehydration properties of methylcellulose and hydroxypropylmethylcellulose, *Carbohydr. Polym.* 27 (1995) 177–185.
- [39] M.A. Garcia, A. Pinotti, M. Martino, N. Zaritzky, Electrically treated composite FILMS based on chitosan and methylcellulose blends, *Food Hydrocoll.* 23 (2009) 722–728.

- [40] A.M.S. Nurhaqiqah, I.Q. Afiqah, M.F.H. Abd Aziz, N.A. ANik Aziz, S. Hasiah, Optical, structural and electrical studies of biopolymer electrolytes based on methylcellulose doped with $\text{Ca}(\text{NO}_3)_2$, IOP Conf. Ser. Mater. Sci. Eng. 440 (2018) 012034.
- [41] M.A. Mingsukang, M.H. Buraidah, M.A. Careem, Development of gel polymer electrolytes for application in quantum dot-sensitized solar cells, *Ionics* 23 (2017) 347–355.
- [42] M.A. Mingsukang, M.H. Buraidah, M.A. Careem, I. Albinsson, B.E. Mellander, A.K. Arof, Investigation of counter electrode materials for gel polymer electrolyte based quantum dot sensitized solar cells, *Electrochim. Acta* 241 (2017) 487–496.
- [43] S.Z. Yusof, H.J. Woo, M.A. Careem, A.K. Arof, Gel electrolytes with I^-/I_3^- redox mediator based on methylcellulose for dye-sensitized solar cells, *Opt. Mater.* 79 (2018) 381–389.
- [44] N.N.S. Baharun, M.A. Mingsukang, M.H. Buraidah, H.J. Woo, L.P. Teo, A.K. Arof, Development of solid polymer electrolytes basedon sodium-carboxymethylcellulose (NaCMC)-polysulphide for quantum dot-sensitized solar cells (QDSSCs), *Ionics* 26 (2020) 1365–1378.
- [45] W. Feng, L. Zhao, J. Du, Y. Li, X. Zhong, Quasi-solid-state quantum dot sensitized solar cells with power conversion efficiency over 9% and high stability, *J. Mater. Chem. A* 4 (2016) 14849–14856.
- [46] P. Ledwon, J.R. Andrade, M. Lapkowski, A. Pawlicka, Hydroxypropyl cellulose-based gel electrolyte for electrochromic devices, *Electrochim. Acta* 159 (2015) 227–233.
- [47] D. Ishii, K. Ueda, P. Stroeve, T. Nakaoiki, H. Hayashi, Transport properties of chemically crosslinked hydroxypropyl cellulose in solvated state, *Cellul. Chem. Technol.* 50 (2016) 755–760.
- [48] M.H. Khanmirzaei, S. Ramesh, K. Ramesh, Hydroxypropyl cellulose based non-volatile gel polymer electrolytes for dye-sensitized solar cell applications using 1-methyl-3-propylimidazolium iodide ionic liquid. *Sci. Rep.* 5 (2015) 18056, <https://doi.org/10.1038/srep18056>.
- [49] X. Huang, Y. Liu, J. Deng, B. Yi, X. Yu, P. Shen, S. Tan, A novel polymer gel electrolyte based on cyanoethylated cellulose for dye-sensitized solar cells, *Electrochim. Acta* 80 (2012) 219–226.
- [50] A. Ma’alinia, H. Asgari Moghaddam, E. Nouri, M.R. Mohammadi, Long-term stability of dye-sensitized solar cells using a facile gel polymer electrolyte, *New J. Chem.* 42 (2018) 13256–13262.
- [51] P. Karthika, S. Ganesan, A. Thomas, T.M.S. Rani, M. Prakash, Influence of synthesized thiourea derivatives as a prolific additive with tris(1,10-phenanthroline)cobalt(II/III)bis/tris(hexafluorophosphate)/hydroxypropyl cellulose gel polymer electrolytes on dye-sensitized solar cells, *Electrochim. Acta* 298 (2019) 237–247.
- [52] P. Li, Y. Zhang, W. Fa, Y. Zhang, B. Huang, Synthesis of a grafted cellulose gel electrolyte in an ionic liquid ([Bmim]I) for dye-sensitized solar cells, *Carbohydr. Polym.* 86 (2011) 1216–1220.
- [53] F. Bella, J.R. Nair, C. Gerbaldi, Towards green, efficient and durable quasi-solid dye-sensitized solar cells integrated with a cellulose-based gel-polymer electrolyte optimized by a chemometric DoE approach, *RSC Adv.* 3 (2013) 15993–16001.
- [54] L. J. Won, J. H. Kim, S. Thogiti, “A polymer electrolyte for dye-sensitized solar cells based on a poly(polyvinylidenefluoride-co-hexafluoropropylene)/hydroxypropyl methyl cellulose blend,” *Electron. Mater. Lett.*, vol. 14, pp. 342–347, 2018.
- [55] T. Or, K. Miettunen, E.D. Cranston, J.M. Moran-Mirabal, J. Vapaavuori, Cellulose nanocrystalline aerogels as electrolyte scaffolds for glass and plastic dye-sensitized solar cells, *ACS Appl. Energy Mater.* 2 (2019) 5635–5642.

- [56] F. Bella, D. Pugliese, L. Zolin, C. Gerbaldi, Paper-based quasi-solid dye-sensitized solar cells, *Electrochim. Acta* 237 (2017) 87–93.
- [57] A. Ivanova, D. Fattakhova-Rohlfing, B.E. Kayaalp, J. Rathouský, T. Bein, Tailoring the morphology of mesoporous titania thin films through biotemplating with nanocrystalline cellulose, *J. Am. Chem. Soc.* 136 (2014) 5930–5937.
- [58] T.R. Chetia, M.S. Ansari, M. Qureshi, Ethyl cellulose and cetrimonium bromide assisted synthesis of mesoporous, hexagon shaped ZnO nanodisks with exposed $\pm\{0001\}$ polar facets for enhanced photovoltaic performance in quantum dot sensitized solar cells, *ACS Appl. Mater. Interfaces* 7 (2015) 13266–13279.
- [59] M. Willgert, A. Boujemaoui, E. Malmström, E.C. Constable, C.E. Housecroft, Copper-based dye-sensitized solar cells with quasi-solid nano cellulose composite electrolytes, *RSC Adv.* 6 (2016) 56571–56579.
- [60] A. Chiappone, F. Bella, J.R. Nair, G. Meligrana, R. Bongiovanni, C. Gerbaldi, Structure–performance correlation of nanocellulose-based polymer electrolytes for efficient quasi-solid DSSCs, *ChemElectroChem* 1 (2014) 1350–1358.
- [61] R.A.A. Muzzarelli, Stereochemistry and physical characterization, in: Chitin, first ed., Pergamon Press, Oxford, United Kingdom, 1977, pp. 45–86 (Chapter 2).
- [62] S. Yamazaki, A. Takegawa, Y. Kaneko, J. Kadokawa, M. Yamagata, M. Ishikawa, An acidic cellulose–chitin hybrid gel as novel electrolyte for an electric double layer capacitor, *Elec-trochim. Commun.* 11 (2009) 68–70.
- [63] K. Kurita, H. Ikeda, M. Shimojoh, J. Yang, N-Phthaloylated chitosan as an essential precursor for controlled chemical modifications of chitosan: synthesis and evaluation, *Polym. J.* 39 (2007) 945–952.
- [64] S.S. Kim, S.J. Kim, Y.D. Moon, Y.M. Lee, Thermal characteristics of chitin and hydroxy-propyl chitin, *Polymer* 35 (1994) 3212–3216.
- [65] J. Briscoe, A. Marinovic, M. Sevilla, S. Dunn, M. Titirici, Biomass-derived carbon quantum dot sensitizers for solid-state nanostructured solar cells, *Angew. Chem. Int. Ed.* 54 (2015) 4463–4468.
- [66] Y. Di, Z. Xiao, X. Yan, G. Ru, B. Chen, J. Feng, Nitrogen and sulfur dual-doped chitin-derived carbon/graphene composites as effective metal-free electrocatalysts for dye sensitized solar cells, *Appl. Surf. Sci.* 441 (2018) 807–815.
- [67] T. Kawabata, Y. Matsuo, Chitin based fuel cell and its proton conductivity, *Mater. Sci. Appl.* 9 (2018) 779–789.
- [68] G. Romanazzi, F.M. Gabler, D. Margosan, B.E. Mackey, J.L. Smilanick, Effect of chitosan dissolved in different acids on its ability to control postharvest gray mold of table grape, *Phy-topathology* 99 (2009) 1028–1036.
- [69] S. Demarger-Andre, A. Domard, Chitosan carboxylic acid salts in solution and in the solid state, *Carbohydr. Polym.* 23 (1994) 211–219.
- [70] E. Praveen, S. Murugan, K. Jayakumar, Investigations on the existence of piezoelectric property of a bio-polymer–chitosan and its application in vibration sensors, *RSC Adv.* 7 (2017) 35490–35495.
- [71] C.R. Mohan, A. Gowrisankar, R. Uthayakumar, K. Jayakumar, Morphology dependent electrical property of chitosan film and modeling by fractal theory, *Eur. Phys. J. Spec. Top.* 228 (2019) 233–243.
- [72] K. Ogura, T. Kanamoto, M. Itoh, H. Miyashiro, K. Tanaka, Dynamic mechanical behavior of chitin and chitosan, *Polym. Bull.* 2 (1980) 301–304.
- [73] J.S. Ahn, H.K. Choi, C.S. Cho, A novel mucoadhesive polymer prepared by template polymerization of acrylic acid in the presence of chitosan, *Biomaterials* 22 (2001) 923–928.

- [74] K. Sakurai, T. Maegawa, T. Takahashi, Glass transition temperature of chitosan and miscibility of chitosan/poly(N-vinyl pyrrolidone) blends, *Polymer* 41 (2000) 7051–7056.
- [75] Y. Dong, Y. Ruan, H. Wang, Y. Zhao, D. Bi, Studies on glass transition temperature of chitosan with four techniques, *J. Appl. Polym. Sci.* 93 (2004) 1553–1558.
- [76] M.H. Buraidah, L.P. Teo, S.R. Majid, R. Yahya, R.M. Taha, A.K. Arof, Characterizations of chitosan-based polymer electrolyte photovoltaic cells, *Int. J. Photoenergy* 2010 (2010) 7 pages, Article ID 805836.
- [77] P.K. Singh, B. Bhattacharya, R.K. Nagarale, K.-W. Kim, H.-W. Rhee, Synthesis, characterization and application of biopolymer-ionic liquid composite membranes, *Synth. Met.* 160 (2010) 139–142.
- [78] P. Chawla, A. Srivastava, M. Tripathi, Performance of chitosan based polymer electrolyte for natural dye sensitized solar cell, *Environ. Prog. Sustain. Energy* 38 (2019) 630–634.
- [79] M.H. Buraidah, L.P. Teo, S.N.F. Yusuf, M.M. Noor, M.Z. Kufian, M.A. Careem, S.R. Majid, R.M. Taha, A.K. Arof, $\text{TiO}_2/\text{chitosan}-\text{NH}_4\text{I}(\text{I}_2)$ -BMII-based dye-sensitized solar cells with anthocyanin dyes extracted from black rice and red cabbage, *Int. J. Photoenergy* 2011 (2011) Article ID 273683, 11 pages.
- [80] E. Praveen, I. John Peter, A.M. Kumar, K. Ramachandran, K. Jayakumar, Performance of ZnO/ZnS nanocomposite based dye-sensitized solar cell with chitosan-polymer electrolyte, *Mater. Today Proc.* (2019). <https://doi.org/10.1016/j.matpr.2019.05.382> (in Press).
- [81] M. Khalili, M. Abedi, H.S. Amoli, S.A. Mozaffari, Comparison of chitosan and chitosan nanoparticles on the performance and charge recombination of water-based gel electrolyte in dye sensitized solar cells, *Carbohydr. Polym.* 175 (2017) 1–6.
- [82] M.H. Buraidah, L.P. Teo, S.R. Majid, A.K. Arof, Chitosan-based polymer electrolyte for dye-sensitized solar cell, in: M.A.K.L. Dissanayake, I.M. Dharmadasa, R. Weerasooriya, G.K.R. Senadeera, J.M.S. Bandara (Eds.), *Proceedings of the International Conference on Solar Energy Materials, Solar Cells and Solar Energy Applications* Sanduni Offset Printers (Pvt.) Ltd, Sri Lanka, 2011, pp. 200–205.
- [83] M.H. Buraidah, L.P. Teo, C.M.A. Yong, S. Shah, A.K. Arof, Performance of polymer electrolyte based on chitosan blended with poly(ethylene oxide) for plasmonic dye-sensitized solar cell, *Opt. Mater.* 57 (2016) 202–211.
- [84] S.A.M. Al-Bat’hi, I. Alaei, I. Sopyan, Natural dye photosensitizers/solid state electrolyte junction for DSSC application, in: *The European Workshop & Conference on Renewable Energy Systems*, Antalya, Turkey, 17–28 September, 2012, pp. 1–7.
- [85] W.Z.N. Yahya, T.M. Wong, M. Khatani, A.E. Samsudin, N.M. Mohamed, Bio-based chitosan/PVdF-HFP polymer-blend for quasi-solid state electrolyte dye-sensitized solar cells, *e-Polymers* 175 (2017) 355–361.
- [86] A. Maddu, H. Gusra, M.N. Indro, Development of solid-state Photoelectrochemical solar cell circuits based on chitosan-PEG blend electrolyte, *Int. J. Renew. Energy* 7 (2017) 1919–1925.
- [87] K. Makuuchi, Critical review of radiation processing of hydrogel and polysaccharide, *Radiat. Phys. Chem.* 79 (2010) 267–271.
- [88] A.V. Kurzin, A.N. Evdokimov, V.S. Golikova, O.S. Pavlova, Solubility of sodium sulfide in alcohols, *J. Chem. Eng. Data* 55 (2010) 4080–4081.
- [89] Z. Zong, Y. Kimura, M. Takahashi, H. Yamane, Characterization of chemical and solid state structures of acylated chitosans, *Polymer* 41 (2000) 899–906.
- [90] H. Tributsch, Dye sensitization solar cells: a critical assessment of the learning curve, *Coord. Chem. Rev.* 248 (2004) 1511–1530.
- [91] R. Yoksan, M. Akashi, S. Biramontri, S. Chirachanchai, Hydrophobic chain conjugation at hydroxyl group onto γ -ray irradiated chitosan, *Biomacromolecules* 2 (2001) 1038–1044.

- [92] S.N.F. Yusuf, S.R. Majid, R. Yahya, A.K. Arof, Synthesis and characterization of phthaloylchitosan based polymer electrolytes for dye sensitized solar cells, in: A.K. Arof, M.A. Careem, M.H. Buraidah (Eds.), Proceedings of the 2nd International Conference on Solar Energy Materials, Solar Cells and Solar Energy Applications, 22–24 August, Centre for Ionics University of Malaya Publisher, 2013, pp. 193–198 ISBN 978-967-12067-0-6.
- [93] S.N.F. Yusuf, M.M. Noor, M.H. Buraidah, M.A. Careem, R. Yahya, S.R. Majid, A.K. Arof, Synthesis and characterization of N-phthaloylchitosan based polymer electrolytes for dye-sensitized solar cell, in: M.A.K.L. Dissanayake, I.M. Dharmadasa, R. Weerasooriya, G.K.R. Senadeera, J.M.S. Bandara (Eds.), Proceedings of the International Conference on Solar Energy Materials, Solar Cells and Solar Energy Applications, Sanduni Offset Printers (Pvt.) Ltd, Sri Lanka, 2011, pp. 213–220.
- [94] S.N.F. Yusuf, M.F. Aziz, H.C. Hassan, T.M.W.J. Bandara, B.-E. Mellander, M.A. Careem, A.K. Arof, Phthaloylchitosan-based gel polymer electrolytes for efficient dye-sensitized solar cells, *J. Chem.* 2014 (2014) Article ID 783023, 8 pages.
- [95] M.H. Buraidah, S. Shah, L.P. Teo, M.A. Careem, A.K. Arof, Dye-sensitized solar cells utilizing phthaloylchitosan based gel polymer electrolytes containing binary salts, in: A.K. Arof, M.A. Careem, M.H. Buraidah (Eds.), Proceedings of the 2nd International Conference on Solar Energy Materials, Solar Cells and Solar Energy Applications, 22–24 August, Centre for Ionics University of Malaya Publisher, 2013, pp. 217–222 ISBN 978-967-12067-0-6.
- [96] S.N.F. Yusuf, A.D. Azzahari, R. Yahya, S.R. Majid, M.A. Careem, A.K. Arof, From crab shell to solar cell: a gel polymer electrolyte based on N-phthaloylchitosan and its application in dye-sensitized solar cells, *RSC Adv.* 6 (2016) 27714–27724.
- [97] S.N.F. Yusuf, A.D. Azzahari, V. Selvanathan, R. Yahya, M.A. Careem, A.K. Arof, Improvement of N-phthaloylchitosan based gel polymer electrolyte in dye-sensitized solar cells using a binary salt system, *Carbohydr. Polym.* 157 (2017) 938–944.
- [98] S. Shah, I.M. Noor, J. Pitawala, I. Albinson, T.M.W.J. Bandara, B.-E. Mellander, A.K. Arof, Plasmonic effects of quantum size metal nanoparticles on dye-sensitized solar cell, *Opt. Mater. Express* 7 (2017) 2069–2083.
- [99] S. Shah, M.H. Buraidah, L.P. Teo, M.A. Careem, A.K. Arof, Dye-sensitized solar cells with sequentially deposited anthocyanin and chlorophyll dye as sensitizers, *Opt. Quantum Electron.* 48 (2016) 219.
- [100] J. Theerthagiri, R.A. Senthil, M.H. Buraidah, J. Madhavan, A.K. Arof, M. Ashokkumar, One-step electrochemical deposition of $\text{Ni}_{1-x}\text{Mo}_x\text{S}$ ternary sulfides as an efficient counter electrode for dye-sensitized solar cells, *J. Mater. Chem. A* 4 (2016) 16119–16127.
- [101] M.H. Buraidah, S. Shah, L.P. Teo, F.I. Chowdhury, M.A. Careem, I. Albinsson, B.-E. Mellander, A.K. Arof, High efficient dye sensitized solar cells using phthaloylchitosan based gel polymer electrolytes, *Electrochim. Acta* 245 (2017) 846–853.
- [102] S. Prasad, D. Durairaj, M.S. AlSalhi, J. Theerthagiri, P. Arunachalam, G. Durai, Fabrication of cost-effective dye-sensitized solar cells using sheet-like CoS_2 films and phthaloylchitosan-based gel-polymer electrolyte, *Energies* 11 (2018) 281.
- [103] S.N.F. Yusuf, S.R. Majid, R. Yahya, Addition of 1-butyl-3-methylimidazolium iodide to the N-phthaloylchitosan based gel polymer electrolyte, *Mater. Today Proc.* 17 (2019) 416–423.
- [104] T. Winie, A.K. Arof, Transport properties of hexanoyl chitosan-based gel electrolyte, *Ionics* 12 (2006) 149–152.
- [105] N.N. Mobarak, F.N. Jantan, N.A. Dzulkurnain, A. Ahmad, M.P. Abdullah, The effect of lithium nitrate towards electrochemical properties of carboxymethyl chitosan, *Sains Malays.* 47 (2018) 2091–2098.

- [106] N.A. Rahman, S. Abu Hanifah, N.N. Mobarak, M.S. Su'ait, A. Ahmad, L.K. Shyuan, Synthesis and characterizations of o-nitrochitosan based biopolymer electrolyte for electrochemical devices, *PLoS One* 14 (2019) e0212066.
- [107] D.R. Lu, C.M. Xiao, S.J. Xu, Starch-based completely biodegradable polymer materials, *Express Polym. Lett.* 3 (2009) 366–375.
- [108] M.Q. Guo, X. Hu, C. Wang, L. Ai, Polysaccharides: Structure and solubility, in: Z. Xu (Ed.), *Solubility of Polysaccharides*, InTech, Croatia, 2017, pp. 7–21 (Chapter 2).
- [109] M.H. Khanmirzaei, S. Ramesh, K. Ramesh, Effect of different iodide salts on ionic conductivity and structural and thermal behavior of rice-starch-based polymer electrolytes for dye-sensitized solar cell application, *Ionics* 21 (2015) 2383–2391.
- [110] M.H. Khanmirzaei, S. Ramesh, K. Ramesh, Effect of 1-hexyl-3-methylimidazolium iodide ionic liquid on ionic conductivity and energy conversion efficiency of solid polymer electrolyte-based nano-crystalline dye-sensitized solar cells, *J. Nanosci. Nanotechnol.* 20 (2020) 2423–2429.
- [111] K.C. Yogananda, E. Ramasamy, S. Kumar, S.V. Kumar, M. Navya Rani, D. Rangappa, Novel rice starch based aqueous gel electrolyte for dye sensitized solar cell application, *Mater. Today Proc.* 4 (2017) 12238–12244.
- [112] K.C. Yogananda, E. Ramasamy, S. Vasantha Kumar, D. Rangappa, Synthesis, characterization, and dye-sensitized solar cell fabrication using potato starch- and potato starch nanocrystal-based gel electrolytes, *Ionics* 25 (2019) 6035–6042.
- [113] M.O.S. Lobregas, D.H. Camacho, Gel polymer electrolyte system based on starch grafted with ionic liquid: Synthesis, characterization and its application in dye-sensitized solar cell, *Electrochim. Acta* 298 (2019) 219–228.
- [114] X. Wang, W. Feng, W. Wang, W. Wang, L. Zhao, Y. Li, Sodium carboxymethyl starch-based highly conductivegel electrolyte for quasi-solid-state quantum dot-sensitized solar cells, *Res. Chem. Intermed.* 44 (2018) 1161–1172.
- [115] E. Raphael, C.O. Avellaneda, B. Manzolli, A. Pawlicka, Agar-based films for application as polymer electrolytes, *Electrochim. Acta* 55 (2010) 1455–1459.
- [116] M. Osinska-Broniarz, A. Martyla, R. Manczak, A. Sierczynska, Agar as a compound of alkaline solid polymer electrolyte, *WSEAS Trans. Environ. Dev.* 14 (2018) 474–480.
- [117] S.S. Alias, A.A. Mohamad, Effect of NH₄I and I₂ concentration on agar gel polymer electrolyte properties for a dye-sensitized solar cell, *Ionics* 19 (2013) 1185–1194.
- [118] S.R. Nadia, M.H. Khanmirzaei, S. Ramesh, K. Ramesh, Quasi-solid-state agar-based polymer electrolytes for dye-sensitized solar cell applications using imidazolium-based ionic liquid, *Ionics* 23 (2017) 1585–1590.
- [119] R. Mujaheddin, L. Jagadish, R.K. Sheshappa, G.S. Guru, Miscibility studies of agar-agar/starch blends using various techniques, *Int. J. Res. Pharm. Chem.* 2 (2012) 1049–1056.
- [120] E. Raphael, D.H. Jara, M.A. Schiavon, Optimizing photovoltaic performance in CuInS₂ and CdS quantum dot-sensitized solar cells byusing an agar-based gel polymer electrolyte, *RSC Adv.* 7 (2017) 6492–6500.
- [121] K. Suzuki, M. Yamaguchi, M. Kumagai, N. Tanabe, S. Yanagida, Dye-sensitized solar cells with ionic gel electrolytes prepared from imidazolium salts and agarose, *C. R. Chim.* 9 (2006) 611–616.
- [122] R.B. Garcia, R.L. Rosangela Vidal, M. Rinaudo, Preparation and structural characterization of O-acetyl agarose with low degree of substitution, *Polímeros* 10 (2000) 155–161.
- [123] R. Singh, A.R. Polu, B. Bhattacharya, H.-W. Rhee, C. Varlikli, P.K. Singh, Perspectives for solid biopolymer electrolytes in dye sensitized solar cell and battery application, *Renew. Sustain. Energy Rev.* 65 (2016) 1098–1117.

- [124] R. Singh, N.A. Jadhav, S. Majumder, B. Bhattacharya, P.K. Singh, Novel biopolymer gel electrolyte for dye-sensitized solar cell application, *Carbohydr. Polym.* 91 (2013) 682–685.
- [125] M. Kaneko, T. Hoshi, Y. Kaburagi, H. Ueno, Solid type dye-sensitized solar cell using polysaccharidecontaining redox electrolyte solution, *J. Electroanal. Chem.* 572 (2004) 21–27.
- [126] W. Wang, X. Guo, Y. Yang, Lithium iodide effect on the electrochemical behavior of agarose based polymer electrolyte for dye-sensitized solar cell, *Electrochim. Acta* 56 (2011) 7347–7351.
- [127] Y. Yang, H. Hu, C.-H. Zhou, S. Xu, B. Sebo, X.-Z. Zhao, Novel agarose polymer electrolyte for quasi-solid state dye-sensitized solar cell, *J. Power Sources* 196 (2011) 2410–2415.
- [128] Y. Yang, X.-y. Guo, X.-Z. Zhao, A novel composite polysaccharide/inorganic oxide electrolyte for high efficiency quasi-solid-state dye-sensitized solar cell, *Procedia Eng.* 36 (2012) 13–18.
- [129] Y. Yang, Z. Zhang, J. Gao, D. Pan, B. Yuan, X. Guo, G. Huang, Metal-organic materials as efficient additives in polymer electrolytesfor quasi-solid-state dye-sensitized solar cells, *J. Alloys Compd.* 726 (2017) 1286–1294.

Chapter 12

Biomass-derived functional carbon nanomaterials for the development of futuristic energy devices

Navneet Kumar Gupta^{a,*}, Sanjeev Kumar Gupta^b, and Ajai Kumar Garg^b

^a*CSIR-Central Institute of Mining and Fuel Research, Dhanbad, Jharkhand, India,* ^b*Ministry of Electronics and Information Technology (MeitY), New Delhi, India*

1 Introduction

Current energy sources are largely based on fossil-based resources [1, 2]. However, depleting petroleum reserves, rising energy demand, and increasing greenhouse gas emissions urgently demand the discovery of sustainable zero-emission energy solutions [3, 4]. Hence, great attention has been paid to the potential development of processes based on the utilization of biomass, wind, solar, and geothermal energy for renewable and clean energy production [5–7].

Fuel cells, which provide clean and sustainable power, have attracted great attention due to their environmental friendliness and high-energy efficiency and reliability [8, 9]. Fuel cells generate electricity by the electrochemical reduction of oxygen and oxidation of fuel (often H₂) into water as the only by-product [10, 11]. In typical fuel cells, oxidation takes place at the anode and reduction at the cathode, and electrolyte ions transport the current between the electrodes [12, 13]. An oxygen reduction reaction (ORR) at the cathode is considered an important parameter to evaluate the overall performance of fuel cells because an H₂ oxidation reaction at the anode is several orders of magnitude faster than ORR and its reactivity largely depends on the activity of Pt-based electrocatalysts [14–16]. However, the high price of Pt, limited availability, and declining activity due to CO poisoning hamper the development of Pt-based catalysts and commercialization [17–19]. Thus great

* Current address: Centre for Surface Science and Catalysis, KU Leuven, Leuven, Belgium.

effort is required to identify and develop alternative noble metal-free, cost-effective, and widely available catalytic material.

After extensive research on the development of a noble metal-free catalyst, a metal-free catalyst based on carbon material has been identified as an alternative to Pt-based catalysts for ORR [20, 21]. The use of metal-free carbon-based catalysts can drastically reduce the cost and increase the overall performance of fuel cells because of wide availability, greater resistance under experimental conditions, and their environmentally benign nature [22–24]. In particular, heteroatom modification (especially, N, S, B, and P atom functionalization) of carbon materials shows promise as electrocatalysts for ORR due to structural diversity and ease of functionalization [25–27]. Especially, N-modified carbon nanomaterials show superior activity, excellent operation stability, and high efficiency [25]. However, early research suggested that catalytic ORR activity of the metal-free catalyst was induced by transition metal impurities [28–30]. Conversely, this was resolved by control experiments by synthesizing metal-free carbon materials and performing deactivation experiments by passivating active sites of N-doped graphene [31–34].

A much deeper understanding of the design of carbon materials has been developed by structural features in different dimensions/porosity modifications, and tuning electronic features by functionalization degrees, doping configurations, etc. By combining experimental findings and theoretical calculations the improved catalytic performance of N-modified carbon materials was attributed to the positive charge or spin density created on the neighboring carbon of doped N for the activation of O₂ molecules to readily attract anodic electrons for facilitating ORR [35–38]. Further mechanistic studies not only confirmed the critical role of the heteroatom doping-induced charge transfer phenomenon in ORR but also the synthesis of noble metal-free materials such as heteroatom-doped carbon nanotubes, graphene, and graphite, etc. These have different structural and electronic features combined with CO resistance ability in fuel cells and many other gases involving electrocatalytic reactions, including hydrogen evaluation reaction, oxygen evaluation reaction, etc. [39, 40]. The 3D structure of carbon nanomaterial shows the extra advantages of metal-free catalysis in fuel cells [36, 41].

To synthesize metal-free catalysts for ORR, biomass as a starting material has attracted increasing attention due to its low cost, wide availability, and rich diverse functionalities [42–45]. Depending on the source, besides carbon, biomass contains oxygen, nitrogen, sulfur, phosphorus, etc. [46, 47]. Three strategies are broadly adapted for the synthesis of functionalized carbon-nanostructured materials based on the starting precursor either by taking the heteroatom-containing biomass or carbon-containing biomass. In the first strategy, the heteroatoms in final carbon nanomaterials can be controlled in materials synthesized from the heteroatom-containing biomass; however, in the second approach, posttreatment with heteroatom-containing molecules is required for the synthesis of heteroatoms lacking carbon nanomaterials.

In the third approach, the biomass precursor is premixed with different heteroatom-containing molecules for the synthesis of final heteroatom-doped carbon materials [48]. Several synthesis procedures are available, including hard/soft templating methods, chemical vapor deposition, pyrolysis, and hydrothermal carbonization for the synthesis of carbon nanostructures [49–52]. Among these, hydrothermal carbonization is considered the most sustainable and inexpensive approach to utilize lignocellulosic biomass [53]. Lignocellulose is the most abundant organic biomass and represents the largest portion of renewable biomass [54]. N-modified carbon nanomaterial has received special attention due to excellent ORR activity. Therefore herein special attention will be paid to the design and development of N-modified carbon nanostructures especially from biomass for ORR.

In this chapter, the contents are systematized as follows. In the first part, we will discuss ORR in fuel cells, including a reaction mechanism based on experimental and theoretical assumptions. In the second part, we systematically discuss biomass resources, structure, and conversion methods. Afterward, the structure and physicochemical properties of carbon-nanostructured materials and their synthesis from biomass will be presented. Finally, the role of heteroatom-modified carbon material and ORR application will be discussed in detail.

2 Oxygen reduction reaction in fuel cells

Fuel cells convert O_2 and fuel into electricity through electrochemical reactions. H_2 is the main choice as a fuel as it gives only water as a by-product [25]. In fuel cells, H_2 undergoes dissociation at the anode and ORR occurs at the cathode, which is considered the most important reaction in the overall process. Many elementary reactions are involved in the overall ORR process as shown in Table 1.

O_2 can be reduced either in aqueous or nonaqueous aprotic electrolytes following different reaction routes and leads to different products [25]. In aqueous electrolytes, O_2 is reduced by the $4e^-$ route to H_2O and OH^- in acidic electrolytes and basic electrolytes, respectively. Similarly, it can also be reduced by the $2e^-$ route to H_2O_2 (acidic electrolyte) and HO_2^- (alkaline electrolyte) intermediates. With nonaqueous aprotic electrolytes along with the $4e^-$ and $2e^-$ oxidation process, O_2 can be reduced by one-electron transfer to the superoxide (O_2^-). Depending on electrolytes and catalysts, the probable reaction route involving ORR is quite complex, involving several intermediates and elementary steps by electron transfer phenomenon. It is quite obvious that $4e^- O_2$ reaction indicates higher efficacy of ORR.

Park et al. reported high selectivity (90%) of H_2O_2 in acidic electrolyte using well-ordered mesoporous N-doped carbon material and the exceptional catalytic behavior of the catalyst was ascribed to the mesoporous ordered structure [56]. This means that under an acidic electrolyte the main reaction

TABLE 1 Elementary reactions in the oxygen reduction reaction process.

Electrolyte	Reaction	Process	References
Aqueous alkaline	$O_2 + 2H_2O + 4e^- \rightarrow 4OH^-$	$4e^-$	[55]
	$O_2 + 2H_2O + 2e^- \rightarrow HO_2^- + OH^-$	$2e^-$	[55]
	$H_2O + HO_2^- + 2e^- \rightarrow 3OH^-$		[55]
Aqueous acidic	$O_2 + 4H^+ + 4e^- \rightarrow 2H_2O$	$4e^-$	[55]
	$O_2 + 2H^+ + 2e^- \rightarrow H_2O_2$	$2e^-$	[55]
	$H_2O_2 + 2H^+ + 2e^- \rightarrow 2H_2O$		[55]
Nonaqueous aprotic (Alk=Li ⁺ or Na ⁺)	$O_2 + Alk^+ + e^- \rightarrow Alk_2O$	$1e^-$	[25]
	$O_2 + 2Alk^+ + 2e^- \rightarrow Alk_2O_2$	$2e^-$	[25]
	$O_2 + 4Alk^+ + 4e^- \rightarrow 2Alk_2O$	$4e^-$	[25]

proceeds by the $2e^-$ route leading to H_2O_2 . Extremely high selectivity of H_2O_2 was associated with the short contact time in the mesoporous structure, which is supported by low H_2O_2 selectivity using a micropore catalyst. The longer residence time of H_2O_2 into the pores led to further reduction or decomposition over multisite complex sites on carbon catalysts [57–59]. In contrast, N-doped carbon material favors the $4e^-$ route in the presence of alkaline electrolyte [28]. Based on theoretical study the reason for pH-dependent selectivity was suggested due to surface hydrophobicity [60]. The presence of hydrophobic functionalities around the ORR active sites restricts water molecules to access the sites for reactions and results in high catalyst stability. Artyushkova and coworkers studied the catalytic activity of different types of N-modified carbon material for ORR in 0.5 M H_2SO_4 [57, 58, 60]. They proposed the involvement of pyrrolic-N as an active site for H_2O_2 formation and pyridinic-N for H_2O formation. Further extension of the study using a rotating ring disk electrode and X-ray photoelectron spectroscopy characterization catalyst revealed the involvement of a graphitic type of N also for H_2O_2 formation.

The results of these studies indicate that product selectivity via the $2e^-$ or $4e^-$ ORR process depends highly on the electronic intrinsic properties of N-atoms on carbon catalysts, solvation condition over the local structure of the active domain, and textural properties. Therefore a metal-free carbon-nanostructured catalyst needs to be designed considering the foregoing factors.

3 Carbon-nanostructured material

Nanostructured carbon materials are an important class of material that offer a wide range of structural possibilities for creating advanced materials of

different networks from 0D to 3D by fascinating structural and hybridization assembly [61, 62]. The unique flexibility of the C-C bond in material results in exceptional electronic properties for different applications [63–66]. Therefore new carbon-derived nanomaterials, fullerenes, carbon nanotubes, and graphene are used extensively in many areas from catalysis to materials for energy applications [64, 66]. Three different generations of carbon nanomaterials are defined based on their tailoring properties [67], as shown in Fig. 1. The first generation of material comprises the basic structure of carbons such as fullerenes, carbon nanotubes, and graphene. These carbons have well-defined structures with low structural dimensionalities. Other simple carbon materials (nanocages, nanofibers, nanocapsules, nanohorns, and carbon quantum dots) with different morphologies can also be derived. The second generation of carbon materials is derived from the introduction of heteroatoms to the basic structural carbon materials. The structural and electronic properties of carbon atoms can be tailored/modified/altered by the introduction of heteroatoms (N, O, B, S, P, etc.) into the basal plane or edges [68]. The third generation of materials are mainly hybrid and hierarchical composite materials prepared by nanoscale architectural engineering [69].

The synthesis of simple carbon materials could be achieved by well-defined molecular carbon sources. To make them active for ORR, further functionalization with heteroatoms is required, which is achieved by posttreatment in the

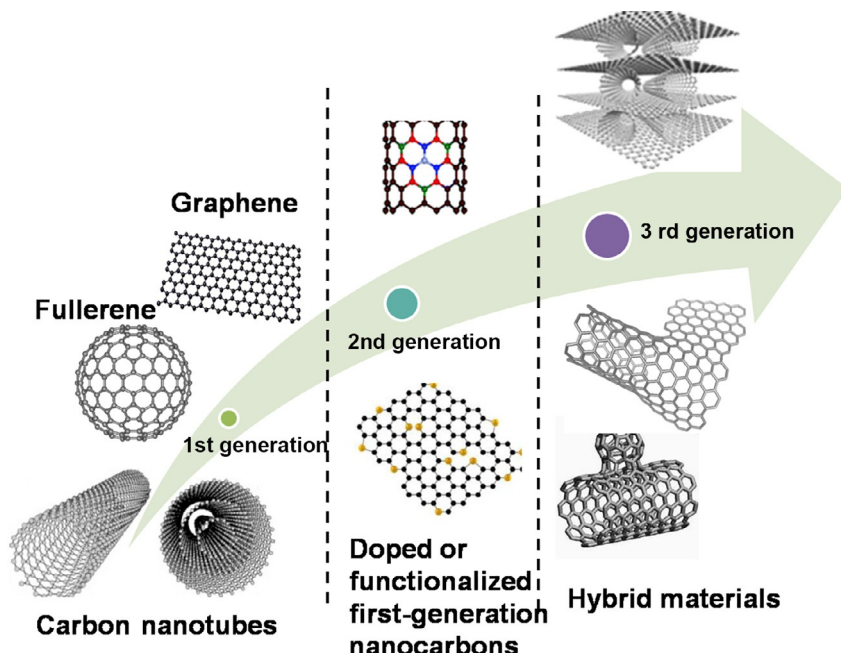


FIG. 1 Different generation of carbon materials.

presence of heteroatom-containing molecules. However, these processes often require complex synthesis procedures, high temperatures, and catalysts. Therefore the development of nanostructured carbon materials from biomass has attracted increasing attention due to many advantages as follows:

- Biomass is abundant, cheap, and sustainable.
- Biomass naturally contains heteroatoms such as N, O, P, etc.
- The synthesis of carbon material from biomass requires simple experimental conditions and setups.
- The carbon materials synthesized from biomass show high surface area and superior thermal and chemical properties.

These special benefits using biomass as a source and exception properties of biomass-derived carbon-nanostructured material make the process highly suitable for industrial commercialization.

4 Biomass and carbon material synthesis methods

4.1 Resources of biomass

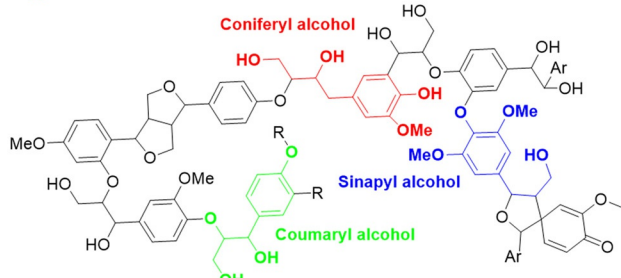
The major section of biomass includes lignocellulose, triglycerides derived from fats of animals, microalgae, and turpentine [70]. Among these, lignocellulosic biomass is most abundant, and has the basic components cellulose, hemicellulose, and lignin [70, 71]. There is also a protein-based portion derived from animals and vegetables [72, 73]. The structural building blocks for biomass components are given in Fig. 2.

Cellulose is a polysaccharide containing a linear chain of glucose units linked by β -1,4-glycosidic linkages [74–76]. The degree of polymerization of cellulose depends highly on the source and origin [76]. Intramolecular hydrogen bonding in cellulose scaffold forms microfibrils with very stable coordination. The degree of crystallinity of cellulose is derived from the extent of structural organization. Hemicellulose is a plant-derived heteropolysaccharide having different compositions subject to their origin [76, 77]. Common hemicelluloses are xylan, xyloglucan, arabinoxylan, glucuronoxylan, and glucomannan [77]. For example, angiosperm hemicellulose mainly contains xylans and gymnosperm hemicelluloses are composed of glucomannans [78]. In contrast to cellulose, the degree of polymerization of hemicellulose is usually lower than 200 units, which mainly constitutes an amorphous structure [79]. Lignin is a complex cross-linked aromatic polymer composed of three types of units: hydroxyl phenyl, guaiacyl, and syringyl in an irregular manner connected by etheric and C-C linkages. The lignin units contain a phenolic ring containing an alkyl chain at the para position and the degree of methoxylation is different at the *o*-position.

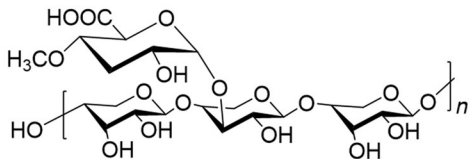
Currently, biomass is utilized in several ways in industries. The pulp and paper industry is one of the largest users of biomass [80]. Green nanocomposites are also made by naturally occurring biopolymers [81]. Biomass can be utilized

Lignocellulose

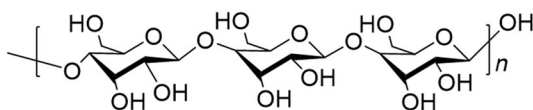
Lignin: 10%–25%



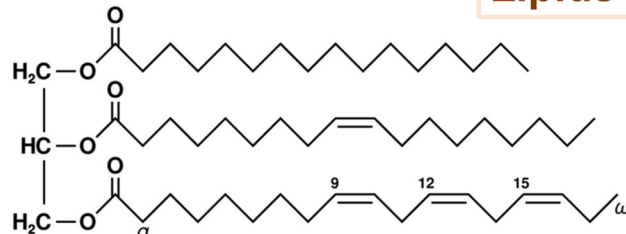
Hemicellulose: 20%–35%



Cellulose: 35%–50%



Lipids



Triglycerides

Proteins

Amino acids:

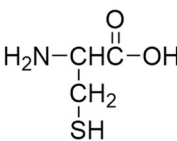
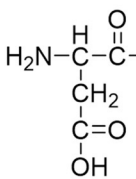
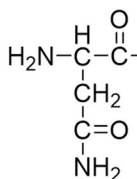
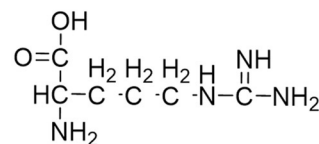
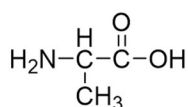


FIG. 2 Major components of biomass feedstock.

by combustion to produce heat and power [82]. However, due to high efficiency and low CO₂ emission, pyrolysis and gasification are other attractive areas for the production of chemicals and high-energy fuels [82, 83]. The gasification process is still not commercialized for the utilization of biomass as feedstocks. Biofuel production from biomass is one of the largest rapidly growing areas and receives a lot of attention, although this process has faced criticism [84]. It is believed that the process may have adverse effects on food availability, biodiversity, etc. [85]. Another area of interest is biomass utilization via the synthesis of high-performance material for energy applications [85, 86]. This is why biomass is currently applied to the synthesis of carbon-based materials and successfully applied in fuel cells and supercapacitors.

4.2 Carbon material synthesis methods from biomass

Biomass as a feedstock for porous carbon has been used for a long time [87, 88]. Under the pyrolysis process, the biomass is converted to carbonaceous materials that are further activated by the thermal treatment of acid, base, or steam to achieve activated carbon material for adsorption and catalysis. The textural design of carbon material via uncontrolled processes using biomass is highly challenging. Therefore the synthesis of well-ordered carbon nanomaterial from biomass is highly desirable for commercial applications [89]. In the last few decades the hydrothermal carbonization (HTC) process has been widely studied regarding the transformation of biomass feedstocks to carbon materials [52]. Template-assisted porous carbon material synthesis has emerged in energy and catalysis applications [89, 90]. These materials have high surfaces (more than 1000 m²/g) with controlled porosity and high pore volumes [91, 92]. The tunable porosity of material is beneficial to control mass transfer to achieve better selectivity toward desired products. Carbon materials are classified by three types based on porosity [93]. A pore size less than 2 nm is known as micro-porous, 2–50 nm is mesoporous, and more than 50 nm is macroporous. Detailed synthesis procedures are summarized in the next section.

4.2.1 Hydrothermal carbonization

HTC is the most widely used method for the synthesis of carbon-nanostructured materials from biomass. A variety of starting materials, including agricultural waste, by-products from forests, isolated carbohydrates, crude plant materials, etc., can be used in this process [93, 94]. Using isolated carbohydrates such as glucose or an amorphous cellulose matrix results in carbon spheres having interstitial porosity, while hard biomass containing crystalline cellulose gives carbon materials with original structure of the starting precursor [95, 96]. Based on the temperature employed, HTC is classified in two types. (1) High-temperature HTC; a high temperature between 300°C and 800°C and high pressure are applied in the thermal treatment step [97, 98]. These processes are beneficial

for the synthesis of high surface area, porous carbon material. Textural properties and chemical composition of the resulting carbon materials depend on the reaction conditions and starting precursors. (2) Low-temperature HTC involves an environmentally friendly pathway and thermal treatment up to 250°C [99]. Under low-temperature HTC, simple chemistry such as polymerization, dehydration, aromatization, etc. results in a carbon material with high surface area.

Details on the synthesis and characterization of biomass-derived materials by the HTC process are well documented by Titirici et al. [95]. N-modified carbon material synthesis has been successfully achieved by the reaction between reducing sugar and amines using the Millard reaction [100]. Hydrothermal carbonization of glucosamine undergoes several reaction steps, including dehydration and deamination, and results in 5-hydroxymethylfurfural (HMF) and amine. Amine reacts further with HMF and results in pyrrole- and pyridine-like compounds [100, 101]. HTC can also be used for the synthesis of hybrid materials using nanostructured carbon and further functionalization with biomass-derived precursors [102–104].

4.2.2 *Template-directed synthesis*

Template-directed synthesis of carbon nanomaterials has received great attention for the synthesis of well-ordered, uniform, and narrow pore size distribution of materials [104, 105]. In this synthesis process, the material architectures are controlled by the template, which serves as a scaffold for carbon material synthesis. A template provides stability for destruction during the synthesis procedure and helps the resulting material to achieve a high degree of structural ordering. The pores are highly preserved during the carbonization process. Mainly, three types of template synthesis are known for carbon material synthesis.

Hard template synthesis

Inorganic porous solids such as zeolites, silicas, metal-organic frameworks, etc. are used as hard templates for the synthesis of ordered carbon material [106]. Depending on the porosity and structure of the template, final material architecture and porosity can be tuned. The hard-templated synthesis approach includes (1) selection, design, and synthesis of template material with uniform porosity; (2) carbon precursor introduction into the pores of the mesoporous template; (3) polymerization of carbon precursor and carbonization to achieve a high degree of graphitization; and (4) removal of inorganic solids. The resulting materials are highly porous, as the template is converted into the pores.

A wide range of starting precursors can be used for the synthesis of porous carbon materials. Ryoo and coworkers synthesized highly ordered mesoporous carbon material using mesoporous silicas (SBA-15) and aluminosilicates (MCM-48) as hard templates [107]. In a typical synthesis process, an aqueous solution of sugars (glucose, sucrose, etc.) and H₂SO₄ was introduced into the

porous inorganic structures. After acid-catalyzed polymerization at 160–200°C, the carbonaceous materials were subjected to carbonization up to 600–1000°C. In the next step, removal of the silica framework using hot EtOH/NaOH solution resulted in ordered mesoporous carbon with a pore size of 3 nm. However, with MCM-41 as a template, carbon showed hexagonally arranged 1D cylindrical pores [108]. Titirici et al. synthesized hierarchical carbon materials such as hollow spheres, carbon nanoparticles, microspheres, etc. by surface modification and polarity/hydrophobicity of nanostructured silica templates [109]. Highly hydrophobic silica gives carbon casts due to the poor interaction with template and hydrophilic carbon precursors, while moderate hydrophobic silica resulted in hollow spheres. Loading of the precursor also had an impact on the structure of the final material—60 wt% furfural as the carbon source gives mesoporous carbon spheres; however, 30 wt% loading gives segregated carbon nanoparticles.

The hard-templated synthesis approach is beneficial to synthesize carbon-nanostructured materials; however, it has drawbacks concerning carbon structure collapse. In this process, inorganic, solid templates are removed by the concentrated solution of NaOH/EtOH or hydrogen fluoride (HF) at high temperature. Since NaOH and HF are highly corrosive, from an environmental point of view extra attention is required on handling and waste disposal.

Soft template synthesis

The soft template synthesis method involves surfactants and block copolymers, etc. as structure-directing templates [109, 110]. The formation of an organic-organic assembly between structure-directing agents and carbon precursor is key to the synthesis procedure. Many parameters such as solvent, temperature, ionic strength, etc. affect the formation of carbon material structure [111]. Since hydrogen-bonding abilities between carbon precursors and surfactants are important parameters to achieve the synthesis of porous carbon material, the selection of a soft template is crucial. For example, hierarchical carbon material was synthesized using sugarcane bagasse as scaffold [112]. In the synthesis procedure, triblock copolymer (F127) was used as the soft template and phenol-formaldehyde as the carbon source. Synthesis of thermally stable material and high surface area material was achieved due to the hydroxyl group interaction between sugarcane bagasse and phenol-formaldehyde.

The soft templating approach is still at the development stage. Although this method is useful to avoid the use of NaOH and HF, the high degree of graphitization is still a big issue because surfactants are unstable at high temperatures.

Dual template method

The dual template synthesis method is interesting to synthesize carbon materials with both macro- and mesoporous structures [112, 113]. The hard template is

used to create microporous structures, while the soft template is used to create mesoporous structures in carbon materials.

N-doped hierarchical carbon material was synthesized using hard template Al composites and soft template pluronic F127 [114]. Banana peel from waste biomass was used as a carbon precursor. Banana peel contains carbon-rich material with carboxylic, hydroxyl, and amine functional groups that favor great interaction with Al composites and pluronic F127. Carbonization at high temperature (800°C) and subsequent template removal give a high surface area hierarchical porous carbon material.

4.2.3 Pyrolysis

Pyrolysis is a thermochemical process involving degradation of small fragments at high temperatures in the absence of oxygen [115]. This method was used for many years for the synthesis of convention carbon materials such as carbon black and activated carbon with wide pore size distribution. A variety of starting materials such as coal, wood, fruit shell, or polymers can be used [116]. Pyrolysis of biomass results in char, bio-oil, and gas. Char is a solid material that can be further utilized as a source for the synthesis of highly porous carbon material [117].

5 Heteroatom modification of biomass-derived carbon materials

Direct synthesis of heteroatom-functionalized carbon: This method is applicable to biomass materials having heteroatom elements. Simple pyrolysis methods using heteroatom-containing biomass are generally applied under different conditions to achieve heteroatom-doped carbon-nanostructured materials. Biomass materials like crab shells and pig bones can be efficiently utilized by this method [118, 119].

Indirect synthesis of heteroatom-functionalized carbon: This method is used for the synthesis of heteroatom-modified carbon material when the precursor does not contain a particular heteroatom [120–122]. In the first step the scaffold is synthesized by the hydrothermal preparation method, the template-assisted method, or pyrolysis. In the second step the resulting material needs to be treated with heteroatom-containing molecules. Depending on the decomposition temperature of N-containing molecules the carbonization temperature can be optimized to synthesize a control N-modified carbon material [122].

5.1 Heteroatom-doped porous biomass-derived carbon catalysts for ORR

A Pt-based catalyst is considered the most efficient catalyst for ORR. However, due to the high cost and necessity for increasing the need for energy devices the

development of efficient and cheap electrocatalysts is highly desirable. In this regard, surface modification of a carbon catalyst has drawn significant attention because of its high activity and CO tolerance ability [123]. Several heteroatom modifications of carbon material have shown improved activity compared to the pristine material. Here, we focus only on the functional cooperativity of N with other heteroatom functionalities for ORR in fuel cells.

5.2 N-modified carbon material

N-modified carbon materials are promising catalysts for the cathodes of fuel cells for low-temperature applications. N-modified carbon materials are also considered efficient support for Pt for enhanced ORR selectivity due to the better metal-support interaction, dispersion, and electron donor properties of N-atoms [124–127]. Largely, four types of N-containing functional groups are formed on the surface of carbon materials, including pyrrolic, pyridinic, graphitic, and nitrogen oxides [128]. The role of different N-functionalities under ORR is still the topic of debate; however, based on density functional theory, calculation of graphitic-N and pyridinic-N is mainly considered to contribute to ORR [121, 123]. Kim et al. showed the importance of quaternary-N on the edges of carbon in ORR, which can create active sites on neighboring carbon atoms for the activation of O₂ [129]. The transfer of an electron from the neighboring carbon atom of the N-functional group contributes to antibonding of O₂, weakens the O-O bond, and improves ORR activity.

Due to high resistance toward CO poisoning of N-modified carbon materials in alkaline fuel cells the selection of cathode based on metal-free material, especially N-based carbon, has been widely investigated. It was believed that the transfer of an electron from the N-modified carbon material to O₂ depends on the N to C atomic ratio. For example, the 4e⁻ route has been favored in high N-content carbon material [130, 131]. N-modified carbon material containing high pyridinic-N also proceeded via the 4e⁻ route [127, 128].

5.2.1 Nonfood biomass precursors

N-doped carbon materials with fullerene-like carbon shells were synthesized by the thermal treatment of Ginkgo leaves at 900°C [132]. Ginkgo leaves contain 10.9–15.5 wt% proteins and can serve as a source of carbon and nitrogen. Gingko leaf-derived material showed 100% selectivity toward the 4e⁻ pathway. This showed methanol tolerance and long-term stability compared to commercial Pt/C. Similarly, chitin-, a most abundant N-containing natural compound, derived carbon nanosheet was found to be an excellent catalyst for ORR in alkaline medium [133]. Extraordinary activity toward ORR of the biomass-derived N-functionalized materials was derived due to the presence of N-functionality, especially pyridinic-N in material and unique porous structures. It was important to note that the N-content, specific N-functional

groups and textural properties, and structure of carbon materials depended on the temperature used for pyrolysis. For instance, carbon materials from honey can be synthesized at a carbonization temperature of 800°C; however, for natural silk as a starting precursor to achieve higher ORR selectively the temperature was 900°C [129, 130]. When N-doped carbon material was synthesized from water hyacinth the optimal pyrolysis temperature was identified at 700°C [123].

The hydrothermal approach was applied for the synthesis of N-modified carbon nanosheet using accessible plant *Typha orientalis* at 180°C followed by annealing in an NH₃ atmosphere [123]. The material showed a high surface area of 898 m²/g with a considerable amount of microporous structures and N-content (9.1 atom %). The resulting material exhibited high ORR activity, stability, and MeOH tolerance in alkaline and acidic media.

Codoping is an attractive approach to enhance ORR performance by the synergy of different heteroatoms. N- and S-codoped carbon material was synthesized using glucose and ovalbumin protein [134]. Glucose acts as a carbon source; however, protein was used as a structure-directing agent as well as a source of N-functional groups. The effect of S-content in material was studied by 2-thienyl-carboxaldehyde precursor by simple addition during hydrothermal carbonization followed by drying using supercritical CO₂ and pyrolysis at 900°C. Catalytic performance of material in acidic and alkaline conditions showed the clear advantages of N- and S-functionalization. The material showed high stability in acidic medium but was unstable in basic conditions due to the poor stability of S. Furthermore, N-doped carbon aerogel materials were prepared using glucose and borax in HTC [135]. Various N-containing aerogels were achieved by varying borax and N-source (2-pyrrol-carboxaldehyde). A good trend between activity versus surface area and N-content was established. In another study, N- and S-codoped carbon materials were prepared by chitosan as a starting N-precursor by the HTC method followed by pyrolysis at 900°C [136]. In the material, N content was 3.4 at% and S was 1.4 at% with a similar surface area of 533–579 m²/g. Both materials were exceptionally active for ORR in alkaline with a similar onset potential to Pt.

5.2.2 Food-based biomass

Several food-based biomass items such as soymilk, soy, mushroom, fermented rice, bamboo fungus, etc. were also applied as a feedstock for the synthesis of carbon material for metal-free ORR in fuel cells. Bifunctional carbon nanodots were prepared to form homemade soymilk, which showed not only photoluminescent properties but was also beneficial as a catalyst for ORR [137]. The material contains C (65.49%), N (10.39%), O (23.43%), and P (0.7%). N-functionalization was found to be responsible for ORR; however, catalytic activity was lower than conventional Pt/C. Both 2e⁻ and 4e⁻ routes were favored over carbon nanodots, confirmed by the calculated e transfer number

of 3.15 at -1.20 V . The lower catalytic activity of material was attributed to the absence of graphitic N, which is mainly introduced by high-temperature thermal treatment. Furthermore, N-doped carbon with a $1072\text{ m}^2/\text{g}$ surface area was prepared from soy chunks as a starting precursor. Typically, the material was prepared by thermal treatment of soy chunks at 300°C under an inert atmosphere followed by high-temperature (600°C) NaOH treatment for 1 h. The removal of NaOH with 1 M HCl washing followed by pyrolysis at $800\text{--}1000^\circ\text{C}$ for 2 h resulted in N-doped carbon material. ORR activity of the catalyst pyrolyzed at 1000°C in alkaline showed half-wave potential of -0.211 V (vs saturated calomel electrode). It was interesting that an 800°C pyrolysis temperature favored mostly the 2e^- pathway (electron transfer numbers = 2.5); however, 1000°C pyrolysis favored the 4e^- pathway (electron transfer numbers = 3.7).

Protein-rich enoki mushroom as a starting material was utilized for the synthesis of N-doped composite material [138]. Low-cost carbon nanoparticles were also used as a matrix in composite material preparation. Different materials were prepared by ball milling for starting precursor and matrix following pyrolysis at different temperatures. Pyrolysis at 900°C resulted in the best composite catalyst for ORR in alkaline medium with onset potential and peak potential of 0.94 and 0.79 V , respectively. Alkaline conditions mainly favor the 4e^- pathway and both 2e^- and 4e^- pathways favor in acidic condition. It was tentatively proposed that both pyridinic-N and graphitic-N have important roles during ORR, and pyridinic-N may be responsible for ORR activity; however, graphitic-N just enhanced the activity.

The HTC method was employed for the synthesis of N-doped carbon spheres from fermented rice [139]. Fermented rice was first prepared by mixing steamed rice with yeast for 2–4 days at 30°C . In the next step, fermented rice was treated hydrothermally at 180°C for 24 h followed by carbonization in the presence of ZnCl_2 at 700°C , and 2 h in an N_2 atmosphere. The ZnCl_2 was finally washed in the presence of dilute HCl to achieve the synthesis of high surface area ($2105.0\text{ m}^2/\text{g}$) carbon nanospheres having N-functionalization. This material showed high selectivity toward the 4e^- pathway in ORR and high stability compared to the reference Pt/C catalyst. A similar approach was again applied for the synthesis of high surface area ($1895.5\text{ m}^2/\text{g}$) N-doped carbon catalyst from bamboo fungus [140]. High electrocatalytic activity by the 4e^- pathway was achieved over material carbonized at 800°C . It was concluded that the high catalytic activity was due to the different types of N-functionalization in material.

N-doped carbon material was synthesized from nori biomass as feedstock in combination with melamine [141]. Nori is an alga consisting of carbohydrates, proteins, and traces of Fe. At first, nori and melamine powders were treated hydrothermally at 190°C for 8 h followed by the stepwise carbonization process at a final temperature of 1000°C . The final material contains C, N, O, and S. The alkaline ORR activity of material was similar to the Pt/C catalyst with excellent stability and tolerance toward MeOH.

Food-based biomass has always conflicted with utilization as a feedstock for sustainable energy applications. While great potential for the application of N-modified carbon material has been shown as a metal-free catalyst in the ORR of fuel cells, upscaling and further commercialization should be considered with care by keeping in mind food shortages and rising prices.

6 Conclusions and perspectives

Here, recent progress in carbon material synthesis by different approaches from a variety of biomass (from food based to nonfood based) has been reviewed for application as electrocatalysts in ORR in fuel cells. The development of cathode material for ORR in fuel cells is critical due to slow reaction compared to anodic reaction and requires highly expensive Pt-based catalysts. Therefore the significant advancement of efficient, more sustainable and economical material is highly desirable. The synthesis and selection of appropriate methods leading to material with different physicochemical properties and subsequently different ORR activities can be a guideline for the selection of proper biomass precursors and methods for given conditions. Porous N-functionalized carbon materials can be synthesized either by taking N-containing biomass precursors such as proteins, algae, chitin, etc. in one-step pyrolysis or by hydrothermal carbonization. The structure-directing agents are beneficial for the synthesis of N-functionalized carbon materials by controlling the well-ordered porous structure of carbon. These N-modified carbon materials play an important role in the efficient activation of O₂ in ORR and show better catalytic performance than that of conventional Pt-based catalysts (namely Pt/C). No doubt a higher catalytic activity was observed on biomass-derived N-modified carbon material; however, its activity was further enhanced by the cooperation of other heteroatoms such as S, O, P, etc. The major benefits of metal-free catalysts are not limited by lower cost; however, these materials are highly stable during reaction as they show very good tolerance toward CO and methanol. There are still challenges to developing metal-free efficient catalysts for acidic medium of fuel cells and material for anode electrodes. Development of metal-free catalysts for application as anodic material is still not fully developed; however, noble metal is reduced by designing supported carbon nanostructures. Moreover, biomass-derived heteroatom-modified carbon materials have proved to be an efficient material for other futuristic materials such as supercapacitors, batteries, CO₂ capture, and catalytic reactions.

References

- [1] L. He, F. Lin, X. Li, H. Sui, Z. Xu, Interfacial sciences in unconventional petroleum production: from fundamentals to applications. *Chem. Soc. Rev.* 44 (15) (2015) 5446–5494, <https://doi.org/10.1039/C5CS00102A>.

- [2] J.E. Naber, K.P. de Jong, W.H.J. Stork, H.P.C.E. Kuipers, M.F.M. Post, Industrial applications of zeolite catalysis, in: *Studies in Surface Science and Catalysis*, vol. 84, Elsevier, 1994, pp. 2197–2219.
- [3] M. Höök, S. Davidsson, S. Johansson, X. Tang, Decline and depletion rates of oil production: a comprehensive investigation. *Proc. R. Soc. A* 372 (2006) (2014) 20120448, <https://doi.org/10.1098/rsta.2012.0448>.
- [4] A. Mardani, D. Streimikiene, F. Cavallaro, N. Loganathan, M. Khoshnoudi, Carbon dioxide (CO_2) emissions and economic growth: a systematic review of two decades of research from 1995 to 2017. *Sci. Total Environ.* 649 (2019) 31–49, <https://doi.org/10.1016/j.scitotenv.2018.08.229>.
- [5] J. Mohtasham, Review article-renewable energies. *Energy Procedia* 74 (2015) 1289–1297, <https://doi.org/10.1016/j.egypro.2015.07.774>.
- [6] O. Edenhofer, K. Seyboth, F. Creutzig, S. Schlömer, On the sustainability of renewable energy sources. *Annu. Rev. Environ. Resour.* 38 (1) (2013) 169–200, <https://doi.org/10.1146/annurev-environ-051012-145344>.
- [7] P.A. Owusu, S. Asumadu-Sarkodie, A review of renewable energy sources, sustainability issues and climate change mitigation. *Cogent Eng.* 3 (1) (2016), <https://doi.org/10.1080/23311916.2016.1167990>.
- [8] I. Staffell, et al., The role of hydrogen and fuel cells in the global energy system. *Energy Environ. Sci.* 12 (2) (2019) 463–491, <https://doi.org/10.1039/C8EE01157E>.
- [9] C. Jiang, J. Ma, G. Corre, S.L. Jain, J.T.S. Irvine, Challenges in developing direct carbon fuel cells. *Chem. Soc. Rev.* 46 (10) (2017) 2889–2912, <https://doi.org/10.1039/C6CS00784H>.
- [10] A. Kirubakaran, S. Jain, R.K. Nema, A review on fuel cell technologies and power electronic interface. *Renew. Sust. Energ. Rev.* 13 (9) (2009) 2430–2440, <https://doi.org/10.1016/j.rser.2009.04.004>.
- [11] S. Wang, S.P. Jiang, Prospects of fuel cell technologies. *Natl. Sci. Rev.* (2017), <https://doi.org/10.1093/nsr/nww099>.
- [12] L. Khotseng, Oxygen reduction reaction, in: A. Ray, I. Mukhopadhyay, R.K. Pati (Eds.), *Electrocatalysts for Fuel Cells and Hydrogen Evolution—Theory to Design*, IntechOpen, 2018.
- [13] H. Erikson, A. Sarapuu, K. Tammeveski, Oxygen reduction reaction on silver catalysts in alkaline media: a mini review. *ChemElectroChem* 6 (1) (2019) 73–86, <https://doi.org/10.1002/celec.201800913>.
- [14] M. Shao, Q. Chang, J.-P. Dodelet, R. Chemitz, Recent advances in electrocatalysts for oxygen reduction reaction. *Chem. Rev.* 116 (6) (2016) 3594–3657, <https://doi.org/10.1021/acs.chemrev.5b00462>.
- [15] Y. Shao, G. Yin, Y. Gao, Understanding and approaches for the durability issues of Pt-based catalysts for PEM fuel cell. *J. Power Sources* 171 (2) (2007) 558–566, <https://doi.org/10.1016/j.jpowsour.2007.07.004>.
- [16] J. Greeley, et al., Alloys of platinum and early transition metals as oxygen reduction electrocatalysts. *Nat. Chem.* 1 (7) (2009) 552–556, <https://doi.org/10.1038/nchem.367>.
- [17] D.Y. Chung, et al., Inhibition of CO poisoning on Pt catalyst coupled with the reduction of toxic hexavalent chromium in a dual-functional fuel cell. *Sci. Rep.* 4 (1) (2015) 7450, <https://doi.org/10.1038/srep07450>.
- [18] C.A. Schiller, F. Richter, E. Gülow, N. Wagner, Relaxation impedance as a model for the deactivation mechanism of fuel cells due to carbon monoxide poisoning. *Phys. Chem. Chem. Phys.* 3 (11) (2001) 2113–2116, <https://doi.org/10.1039/b007674k>.
- [19] J.A. Varnell, et al., Identification of carbon-encapsulated iron nanoparticles as active species in non-precious metal oxygen reduction catalysts. *Nat. Commun.* 7 (1) (2016) 12582, <https://doi.org/10.1038/ncomms12582>.

- [20] J. Zhang, Z. Zhao, Z. Xia, L. Dai, A metal-free bifunctional electrocatalyst for oxygen reduction and oxygen evolution reactions. *Nat. Nanotechnol.* 10 (5) (2015) 444–452, <https://doi.org/10.1038/nnano.2015.48>.
- [21] B. Wang, Recent development of non-platinum catalysts for oxygen reduction reaction. *J. Power Sources* 152 (2005) 1–15, <https://doi.org/10.1016/j.jpowsour.2005.05.098>.
- [22] T. Najam, et al., An efficient anti-poisoning catalyst against SO_x , NO_x , and PO_x : P, N-doped carbon for oxygen reduction in acidic media. *Angew. Chem. Int. Ed.* 57 (46) (2018) 15101–15106, <https://doi.org/10.1002/anie.201808383>.
- [23] A. Morozan, B. Jousselme, S. Palacin, Low-platinum and platinum-free catalysts for the oxygen reduction reaction at fuel cell cathodes. *Energy Environ. Sci.* 4 (4) (2011) 1238, <https://doi.org/10.1039/c0ee00601g>.
- [24] S. Kundu, et al., Electrocatalytic activity and stability of nitrogen-containing carbon nanotubes in the oxygen reduction reaction. *J. Phys. Chem. C* 113 (32) (2009) 14302–14310, <https://doi.org/10.1021/jp811320d>.
- [25] D.-W. Wang, D. Su, Heterogeneous nanocarbon materials for oxygen reduction reaction. *Energy Environ. Sci.* 7 (2) (2014) 576, <https://doi.org/10.1039/c3ee43463j>.
- [26] S. Yang, L. Zhi, K. Tang, X. Feng, J. Maier, K. Müllen, Efficient synthesis of heteroatom (N or S)-doped graphene based on ultrathin graphene oxide-porous silica sheets for oxygen reduction reactions. *Adv. Funct. Mater.* 22 (17) (2012) 3634–3640, <https://doi.org/10.1002/adfm.201200186>.
- [27] L. Yang, et al., Boron-doped carbon nanotubes as metal-free electrocatalysts for the oxygen reduction reaction. *Angew. Chem. Int. Ed.* 50 (31) (2011) 7132–7135, <https://doi.org/10.1002/anie.201101287>.
- [28] J. Masa, W. Xia, M. Muhler, W. Schuhmann, On the role of metals in nitrogen-doped carbon electrocatalysts for oxygen reduction. *Angew. Chem. Int. Ed.* 54 (35) (2015) 10102–10120, <https://doi.org/10.1002/anie.201500569>.
- [29] R. Ye, et al., Manganese deception on graphene and implications in catalysis. *Carbon* 132 (2018) 623–631, <https://doi.org/10.1016/j.carbon.2018.02.082>.
- [30] L. Wang, A. Ambrosi, M. Pumera, ‘Metal-free’ catalytic oxygen reduction reaction on heteroatom-doped graphene is caused by trace metal impurities. *Angew. Chem. Int. Ed.* 52 (51) (2013) 13818–13821, <https://doi.org/10.1002/anie.201309171>.
- [31] J. Zhang, L. Dai, Heteroatom-doped graphitic carbon catalysts for efficient electrocatalysis of oxygen reduction reaction. *ACS Catal.* 5 (12) (2015) 7244–7253, <https://doi.org/10.1021/acscatal.5b01563>.
- [32] S. Chen, et al., Nitrogen-doped carbon nanocages as efficient metal-free electrocatalysts for oxygen reduction reaction. *Adv. Mater.* 24 (41) (2012) 5593–5597, <https://doi.org/10.1002/adma.201202424>.
- [33] W. Xiong, et al., 3-D carbon nanotube structures used as high performance catalyst for oxygen reduction reaction. *J. Am. Chem. Soc.* 132 (45) (2010) 15839–15841, <https://doi.org/10.1021/ja104425h>.
- [34] L. Zhang, Z. Xia, Mechanisms of oxygen reduction reaction on nitrogen-doped graphene for fuel cells. *J. Phys. Chem. C* 115 (22) (2011) 11170–11176, <https://doi.org/10.1021/jp201991j>.
- [35] K. Gong, F. Du, Z. Xia, M. Durstock, L. Dai, Nitrogen-doped carbon nanotube arrays with high electrocatalytic activity for oxygen reduction. *Science* 323 (5915) (2009) 760–764, <https://doi.org/10.1126/science.1168049>.
- [36] M. Borghei, et al., Porous N,P-doped carbon from coconut shells with high electrocatalytic activity for oxygen reduction: alternative to Pt-C for alkaline fuel cells. *Appl. Catal. B Environ.* 204 (2017) 394–402, <https://doi.org/10.1016/j.apcatb.2016.11.029>.

- [37] C. Tang, Q. Zhang, Nanocarbon for oxygen reduction electrocatalysis: dopants, edges, and defects. *Adv. Mater.* 29 (13) (2017) 1604103, <https://doi.org/10.1002/adma.201604103>.
- [38] S.K. Singh, K. Takeyasu, J. Nakamura, Active sites and mechanism of oxygen reduction reaction electrocatalysis on nitrogen-doped carbon materials. *Adv. Mater.* 31 (13) (2019) 1804297, <https://doi.org/10.1002/adma.201804297>.
- [39] C.H. Choi, M.W. Chung, H.C. Kwon, J.H. Chung, S.I. Woo, Nitrogen-doped graphene/carbon nanotube self-assembly for efficient oxygen reduction reaction in acid media. *Appl. Catal. B Environ.* 144 (2014) 760–766, <https://doi.org/10.1016/j.apcatb.2013.08.021>.
- [40] H.-S. Oh, J.-G. Oh, W.H. Lee, H.-J. Kim, H. Kim, The influence of the structural properties of carbon on the oxygen reduction reaction of nitrogen modified carbon based catalysts. *Int. J. Hydrog. Energy* 36 (14) (2011) 8181–8186, <https://doi.org/10.1016/j.ijhydene.2011.04.139>.
- [41] K. Sun, et al., Biomass-derived 3D hierarchical N-doped porous carbon anchoring cobalt-iron phosphide nanodots as bifunctional electrocatalysts for Li O₂ batteries. *J. Power Sources* 412 (2019) 433–441, <https://doi.org/10.1016/j.jpowsour.2018.11.079>.
- [42] S. Gao, X. Li, L. Li, X. Wei, A versatile biomass derived carbon material for oxygen reduction reaction, supercapacitors and oil/water separation. *Nano Energy* 33 (2017) 334–342, <https://doi.org/10.1016/j.nanoen.2017.01.045>.
- [43] D.M. Fernandes, A.S. Mestre, A. Martins, N. Nunes, A.P. Carvalho, C. Freire, Biomass-derived nanoporous carbons as electrocatalysts for oxygen reduction reaction. *Catal. Today* (2019), <https://doi.org/10.1016/j.cattod.2019.02.048>p. S0920586118313737.
- [44] D. He, et al., Bifunctional biomass-derived 3D nitrogen-doped porous carbon for oxygen reduction reaction and solid-state supercapacitor. *Appl. Surf. Sci.* 465 (2019) 303–312, <https://doi.org/10.1016/j.apsusc.2018.09.185>.
- [45] P. Rupa Kasturi, A. Arunchander, D. Kalpana, R. Kalai Selvan, Bio-derived carbon as an efficient supporting electrocatalyst for the oxygen reduction reaction. *J. Phys. Chem. Solids* 124 (2019) 305–311, <https://doi.org/10.1016/j.jpcs.2018.08.019>.
- [46] S.V. Vassilev, D. Baxter, L.K. Andersen, C.G. Vassileva, An overview of the chemical composition of biomass. *Fuel* 89 (5) (2010) 913–933, <https://doi.org/10.1016/j.fuel.2009.10.022>.
- [47] J. Shen, S. Zhu, X. Liu, H. Zhang, J. Tan, The prediction of elemental composition of biomass based on proximate analysis. *Energy Convers. Manag.* 51 (5) (2010) 983–987, <https://doi.org/10.1016/j.enconman.2009.11.039>.
- [48] L.J. Konwar, P. Mäki-Arvela, J.-P. Mikkola, SO₃ H-containing functional carbon materials: synthesis, structure, and acid catalysis. *Chem. Rev.* (2019), <https://doi.org/10.1021/acs.chemrev.9b00199>.
- [49] J. Lee, J. Kim, T. Hyeon, Recent progress in the synthesis of porous carbon materials. *Adv. Mater.* 18 (16) (2006) 2073–2094, <https://doi.org/10.1002/adma.200501576>.
- [50] Y.Z. Jin, et al., Large-scale synthesis and characterization of carbon spheres prepared by direct pyrolysis of hydrocarbons. *Carbon* 43 (9) (2005) 1944–1953, <https://doi.org/10.1016/j.carbon.2005.03.002>.
- [51] J. Kong, A.M. Cassell, H. Dai, Chemical vapor deposition of methane for single-walled carbon nanotubes. *Chem. Phys. Lett.* 292 (4–6) (1998) 567–574, [https://doi.org/10.1016/S0009-2614\(98\)00745-3](https://doi.org/10.1016/S0009-2614(98)00745-3).
- [52] M.-M. Titirici, M. Antonietti, Chemistry and materials options of sustainable carbon materials made by hydrothermal carbonization. *Chem. Soc. Rev.* 39 (1) (2010) 103–116, <https://doi.org/10.1039/B819318P>.
- [53] B. Hu, K. Wang, L. Wu, S.-H. Yu, M. Antonietti, M.-M. Titirici, Engineering carbon materials from the hydrothermal carbonization process of biomass. *Adv. Mater.* 22 (7) (2010) 813–828, <https://doi.org/10.1002/adma.200902812>.

- [54] J.K. Saini, R. Saini, L. Tewari, Lignocellulosic agriculture wastes as biomass feedstocks for second-generation bioethanol production: concepts and recent developments. *3 Biotech* 5 (4) (2015) 337–353, <https://doi.org/10.1007/s13205-014-0246-5>.
- [55] D. Yu, E. Nagelli, F. Du, L. Dai, Metal-free carbon nanomaterials become more active than metal catalysts and last longer. *J. Phys. Chem. Lett.* 1 (14) (2010) 2165–2173, <https://doi.org/10.1021/jz100533t>.
- [56] J. Park, Y. Nabae, T. Hayakawa, M. Kakimoto, Highly selective two-electron oxygen reduction catalyzed by mesoporous nitrogen-doped carbon. *ACS Catal.* 4 (10) (2014) 3749–3754, <https://doi.org/10.1021/cs5008206>.
- [57] G.-L. Chai, M. Boero, Z. Hou, K. Terakura, W. Cheng, Indirect four-electron oxygen reduction reaction on carbon materials catalysts in acidic solutions. *ACS Catal.* 7 (11) (2017) 7908–7916, <https://doi.org/10.1021/acscatal.7b02548>.
- [58] K. Artyushkova, A. Serov, S. Rojas-Carbonell, P. Atanassov, Chemistry of multitudinous active sites for oxygen reduction reaction in transition metal–nitrogen–carbon electrocatalysts. *J. Phys. Chem. C* 119 (46) (2015) 25917–25928, <https://doi.org/10.1021/acs.jpcc.5b07653>.
- [59] I. Matanovic, K. Artyushkova, P. Atanassov, Understanding PGM-free catalysts by linking density functional theory calculations and structural analysis: perspectives and challenges. *Curr. Opin. Electrochem.* 9 (2018) 137–144, <https://doi.org/10.1016/j.colelec.2018.03.009>.
- [60] B.W. Noffke, Q. Li, K. Raghavachari, L. Li, A model for the pH-dependent selectivity of the oxygen reduction reaction electrocatalyzed by N-doped graphitic carbon. *J. Am. Chem. Soc.* 138 (42) (2016) 13923–13929, <https://doi.org/10.1021/jacs.6b06778>.
- [61] S. Kabir, K. Artyushkova, A. Serov, B. Kiefer, P. Atanassov, Binding energy shifts for nitrogen-containing graphene-based electrocatalysts—experiments and DFT calculations: analyzing structure-property relationships of functionalized materials. *Surf. Interface Anal.* 48 (5) (2016) 293–300, <https://doi.org/10.1002/sia.5935>.
- [62] Y. Cai, L. Liang, P. Gao, Promise of commercialization: carbon materials for low-cost perovskite solar cells. *Chinese Phys. B* 27 (1) (2018) 018805, <https://doi.org/10.1088/1674-1056/27/1/018805>.
- [63] H. Badenhorst, A review of the application of carbon materials in solar thermal energy storage. *Sol. Energy* (2018), <https://doi.org/10.1016/j.solener.2018.01.062>p. S0038092X18300835.
- [64] G. Centi, K. Barbera, S. Perathoner, N.K. Gupta, E.E. Ember, J.A. Lercher, Onion-like graphene carbon nanospheres as stable catalysts for carbon monoxide and methane chlorination. *ChemCatChem* 7 (18) (2015) 3036–3046, <https://doi.org/10.1002/cctc.201500662>.
- [65] N.K. Gupta, et al., Bent carbon surface moieties as active sites on carbon catalysts for phosgene synthesis. *Angew. Chem. Int. Ed.* 55 (5) (2016) 1728–1732, <https://doi.org/10.1002/anie.201508922>.
- [66] M. Endo, C. Kim, K. Nishimura, T. Fujino, K. Miyashita, Recent development of carbon materials for Li ion batteries. *Carbon* 38 (2) (2000) 183–197, [https://doi.org/10.1016/S0008-6223\(99\)00141-4](https://doi.org/10.1016/S0008-6223(99)00141-4).
- [67] S. Perathoner, G. Centi, Advanced nanocarbon materials for future energy applications, in: *Emerging Materials for Energy Conversion and Storage*, Elsevier, 2018, pp. 305–325.
- [68] N.K. Gupta, B. Peng, G.L. Haller, E.E. Ember, J.A. Lercher, Nitrogen modified carbon nanomaterials as stable catalysts for phosgene synthesis. *ACS Catal.* 6 (9) (2016) 5843–5855, <https://doi.org/10.1021/acscatal.6b01424>.
- [69] G. Centi, S. Perathoner, Creating and mastering nano-objects to design advanced catalytic materials. *Coord. Chem. Rev.* 255 (13–14) (2011) 1480–1498, <https://doi.org/10.1016/j.ccr.2011.01.021>.

- [70] T. Ennaert, et al., Potential and challenges of zeolite chemistry in the catalytic conversion of biomass. *Chem. Soc. Rev.* 45 (3) (2016) 584–611, <https://doi.org/10.1039/C5CS00859J>.
- [71] N.K. Gupta, A. Fukuoka, K. Nakajima, Amorphous Nb₂O₅ as a selective and reusable catalyst for furfural production from xylose in biphasic water and toluene. *ACS Catal.* 7 (4) (2017) 2430–2436, <https://doi.org/10.1021/acscatal.6b03682>.
- [72] N.K. Gupta, A. Fukuoka, K. Nakajima, Metal-free and selective oxidation of furfural to furoic acid with an N-heterocyclic carbene catalyst. *ACS Sustain. Chem. Eng.* 6 (3) (2018) 3434–3442, <https://doi.org/10.1021/acssuschemeng.7b03681>.
- [73] M. Dusselier, B.F. Sels, Selective catalysis for cellulose conversion to lactic acid and other α -hydroxy acids, in: K.M. Nicholas (Ed.), *Selective Catalysis for Renewable Feedstocks and Chemicals*, 353 Springer International Publishing, Cham, 2014, pp. 85–125.
- [74] L.H. Thomas, et al., Structure of cellulose microfibrils in primary cell walls from collenchyma. *Plant Physiol.* 161 (1) (2013) 465–476, <https://doi.org/10.1104/pp.112.206359>.
- [75] A. Shrotri, H. Kobayashi, A. Fukuoka, Cellulose depolymerization over heterogeneous catalysts. *Acc. Chem. Res.* 51 (3) (2018) 761–768, <https://doi.org/10.1021/acs.accounts.7b00614>.
- [76] P. Kumar Gupta, et al., An update on overview of cellulose, its structure and applications, in: *Cellulose* [Working Title], IntechOpen, 2019.
- [77] N. Ahmad, M.R. Zakaria, Oligosaccharide from hemicellulose, in: *Lignocellulose for Future Bioeconomy*, Elsevier, 2019, pp. 135–152.
- [78] M. Pauly, et al., Hemicellulose biosynthesis. *Planta* 238 (4) (2013) 627–642, <https://doi.org/10.1007/s00425-013-1921-1>.
- [79] J. Ralph, C. Lapierre, W. Boerjan, Lignin structure and its engineering. *Curr. Opin. Biotechnol.* 56 (2019) 240–249, <https://doi.org/10.1016/j.copbio.2019.02.019>.
- [80] Y. Dong, H. Yu, Research progress on biorefinery of lignocellulosic biomass. *IOP Conf. Ser.: Earth Environ. Sci.* 295 (2019) 012078, <https://doi.org/10.1088/1755-1315/295/2/012078>.
- [81] A. Kaushik, M. Singh, G. Verma, Green nanocomposites based on thermoplastic starch and steam exploded cellulose nanofibrils from wheat straw. *Carbohydr. Polym.* 82 (2) (2010) 337–345, <https://doi.org/10.1016/j.carbpol.2010.04.063>.
- [82] A. Dhahak, R. Bounaceur, C. Le Dreff-Lorimier, G. Schmidt, G. Trouve, F. Battin-Leclerc, Development of a detailed kinetic model for the combustion of biomass. *Fuel* 242 (2019) 756–774, <https://doi.org/10.1016/j.fuel.2019.01.093>.
- [83] M. Hervy, et al., Evolution of dolomite composition and reactivity during biomass gasification. *Appl. Catal. A Gen.* 572 (2019) 97–106, <https://doi.org/10.1016/j.apcata.2018.12.014>.
- [84] A.A. Verts, N. Qureshi, H.P. Blaschek, H. Yukawa (Eds.), *Biomass to Biofuels*, Blackwell Publishing Ltd., Oxford, 2010
- [85] A. Anca-Couce, Reaction mechanisms and multi-scale modelling of lignocellulosic biomass pyrolysis. *Prog. Energy Combust. Sci.* 53 (2016) 41–79, <https://doi.org/10.1016/j.pecs.2015.10.002>.
- [86] Z. Bi, et al., Biomass-derived porous carbon materials with different dimensions for supercapacitor electrodes: a review. *J. Mater. Chem. A* 7 (27) (2019) 16028–16045, <https://doi.org/10.1039/C9TA04436A>.
- [87] H. Yang, S. Ye, J. Zhou, T. Liang, Biomass-derived porous carbon materials for supercapacitor. *Front. Chem.* 7 (2019) 274, <https://doi.org/10.3389/fchem.2019.00274>.
- [88] E. Schröder, K. Thomauske, C. Weber, A. Hornung, V. Tumiatti, Experiments on the generation of activated carbon from biomass. *J. Anal. Appl. Pyrolysis* 79 (1–2) (2007) 106–111, <https://doi.org/10.1016/j.jaap.2006.10.015>.
- [89] T.-W. Kim, I.-S. Park, R. Ryoo, A synthetic route to ordered mesoporous carbon materials with graphitic pore walls. *Angew. Chem. Int. Ed.* 42 (36) (2003) 4375–4379, <https://doi.org/10.1002/anie.200352224>.

- [90] K. Jurewicz, et al., Capacitance properties of ordered porous carbon materials prepared by a templating procedure. *J. Phys. Chem. Solids* 65 (2–3) (2004) 287–293, <https://doi.org/10.1016/j.jpcs.2003.10.024>.
- [91] C. Vix-Guterl, et al., Supercapacitor electrodes from new ordered porous carbon materials obtained by a templating procedure. *Mater. Sci. Eng. B* 108 (1–2) (2004) 148–155, <https://doi.org/10.1016/j.mseb.2003.10.096>.
- [92] Y. Yürüm, A. Taralp, T.N. Veziroglu, Storage of hydrogen in nanostructured carbon materials. *Int. J. Hydrog. Energy* 34 (9) (2009) 3784–3798, <https://doi.org/10.1016/j.ijhydene.2009.03.001>.
- [93] Y. Nishi, M. Inagaki, Gas adsorption/desorption isotherm for pore structure characterization, in: *Materials Science and Engineering of Carbon*, Elsevier, 2016, pp. 227–247.
- [94] M.-M. Titirici, A. Thomas, M. Antonietti, Back in the black: hydrothermal carbonization of plant material as an efficient chemical process to treat the CO₂ problem?. *New J. Chem.* 31 (6) (2007) 787, <https://doi.org/10.1039/b616045j>.
- [95] M.-M. Titirici, et al., Sustainable carbon materials. *Chem. Soc. Rev.* 44 (1) (2015) 250–290, <https://doi.org/10.1039/C4CS00232F>.
- [96] M. Sevilla, A.B. Fuertes, The production of carbon materials by hydrothermal carbonization of cellulose. *Carbon* 47 (9) (2009) 2281–2289, <https://doi.org/10.1016/j.carbon.2009.04.026>.
- [97] Z. Liu, F.-S. Zhang, J. Wu, Characterization and application of chars produced from pine-wood pyrolysis and hydrothermal treatment. *Fuel* 89 (2) (2010) 510–514, <https://doi.org/10.1016/j.fuel.2009.08.042>.
- [98] F. Jin (Ed.), *Application of Hydrothermal Reactions to Biomass Conversion*, Springer, Berlin, Heidelberg, 2014.
- [99] S. Karagöz, T. Bhaskar, A. Muto, Y. Sakata, M.A. Uddin, Low-temperature hydrothermal treatment of biomass: effect of reaction parameters on products and boiling point distributions. *Energy Fuel* 18 (1) (2004) 234–241, <https://doi.org/10.1021/ef030133g>.
- [100] R.J. White, N. Yoshizawa, M. Antonietti, M.-M. Titirici, A sustainable synthesis of nitrogen-doped carbon aerogels. *Green Chem.* 13 (9) (2011) 2428, <https://doi.org/10.1039/c1gc15349h>.
- [101] M.-M. Titirici (Ed.), *Sustainable Carbon Materials from Hydrothermal Processes: Titirici/Sustainable*, John Wiley & Sons, Ltd, Oxford, 2013.
- [102] J. Wu, D. Zhang, Y. Wang, B. Hou, Electrocatalytic activity of nitrogen-doped graphene synthesized via a one-pot hydrothermal process towards oxygen reduction reaction. *J. Power Sources* 227 (2013) 185–190, <https://doi.org/10.1016/j.jpowsour.2012.11.074>.
- [103] M. Qiao, et al., Graphene/nitrogen-doped porous carbon sandwiches for the metal-free oxygen reduction reaction: conductivity versus active sites. *J. Mater. Chem. A* 4 (32) (2016) 12658–12666, <https://doi.org/10.1039/C6TA04578B>.
- [104] W.-J. Niu, et al., One-pot synthesis of nitrogen-rich carbon dots decorated graphene oxide as metal-free electrocatalyst for oxygen reduction reaction. *Carbon* 109 (2016) 402–410, <https://doi.org/10.1016/j.carbon.2016.08.002>.
- [105] C.-M. Yang, C. Weidenthaler, B. Spliethoff, M. Mayanna, F. Schüth, Facile template synthesis of ordered mesoporous carbon with polypyrrole as carbon precursor. *Chem. Mater.* 17 (2) (2005) 355–358, <https://doi.org/10.1021/cm049164v>.
- [106] H. Darmstadt, C. Roy, S. Kaliaguine, T.-W. Kim, R. Ryoo, Surface and pore structures of CMK-5 ordered mesoporous carbons by adsorption and surface spectroscopy. *Chem. Mater.* 15 (17) (2003) 3300–3307, <https://doi.org/10.1021/cm020673b>.
- [107] S. Jun, et al., Synthesis of new, nanoporous carbon with hexagonally ordered mesostructure. *J. Am. Chem. Soc.* 122 (43) (2000) 10712–10713, <https://doi.org/10.1021/ja002261e>.

- [108] J. Lee, S. Yoon, S.M. Oh, C.-H. Shin, T. Hyeon, Development of a new mesoporous carbon using an HMS aluminosilicate template, *Adv. Mater.* 12 (2002) 359–362.
- [109] M.-M. Titirici, A. Thomas, M. Antonietti, Replication and coating of silica templates by hydrothermal carbonization. *Adv. Funct. Mater.* 17 (6) (2007) 1010–1018, <https://doi.org/10.1002/adfm.200600501>.
- [110] S. Tanaka, N. Nakatani, A. Doi, Y. Miyake, Preparation of ordered mesoporous carbon membranes by a soft-templating method. *Carbon* 49 (10) (2011) 3184–3189, <https://doi.org/10.1016/j.carbon.2011.03.042>.
- [111] R.J. White, V. Budarin, R. Luque, J.H. Clark, D.J. Macquarrie, Tuneable porous carbonaceous materials from renewable resources. *Chem. Soc. Rev.* 38 (12) (2009) 3401, <https://doi.org/10.1039/b822668g>.
- [112] C.-H. Huang, R.-A. Doong, Sugarcane bagasse as the scaffold for mass production of hierarchically porous carbon monoliths by surface self-assembly. *Microporous Mesoporous Mater.* 147 (1) (2012) 47–52, <https://doi.org/10.1016/j.micromeso.2011.05.027>.
- [113] C. Huang, R. Doong, D. Gu, D. Zhao, Dual-template synthesis of magnetically-separable hierarchically-ordered porous carbons by catalytic graphitization. *Carbon* 49 (9) (2011) 3055–3064, <https://doi.org/10.1016/j.carbon.2011.03.026>.
- [114] R.-L. Liu, W.-J. Ji, T. He, Z.-Q. Zhang, J. Zhang, F.-Q. Dang, Fabrication of nitrogen-doped hierarchically porous carbons through a hybrid dual-template route for CO₂ capture and haemoperfusion. *Carbon* 76 (2014) 84–95, <https://doi.org/10.1016/j.carbon.2014.04.052>.
- [115] A.-H. Lu, W.-C. Li, E.-L. Salabas, B. Spliethoff, F. Schüth, Low temperature catalytic pyrolysis for the synthesis of high surface area, nanostructured graphitic carbon. *Chem. Mater.* 18 (8) (2006) 2086–2094, <https://doi.org/10.1021/cm060135p>.
- [116] S.-W. Han, D.-W. Jung, J.-H. Jeong, E.-S. Oh, Effect of pyrolysis temperature on carbon obtained from green tea biomass for superior lithium ion battery anodes. *Chem. Eng. J.* 254 (2014) 597–604, <https://doi.org/10.1016/j.cej.2014.06.021>.
- [117] N.B. Klinghoffer, M.J. Castaldi, A. Nzihou, Catalyst properties and catalytic performance of char from biomass gasification. *Ind. Eng. Chem. Res.* 51 (40) (2012) 13113–13122, <https://doi.org/10.1021/ie3014082>.
- [118] W. Huang, H. Zhang, Y. Huang, W. Wang, S. Wei, Hierarchical porous carbon obtained from animal bone and evaluation in electric double-layer capacitors. *Carbon* 49 (3) (2011) 838–843, <https://doi.org/10.1016/j.carbon.2010.10.025>.
- [119] H.-J. Liu, X.-M. Wang, W.-J. Cui, Y.-Q. Dou, D.-Y. Zhao, Y.-Y. Xia, Highly ordered mesoporous carbon nanofiber arrays from a crab shell biological template and its application in supercapacitors and fuel cells. *J. Mater. Chem.* 20 (20) (2010) 4223, <https://doi.org/10.1039/b925776d>.
- [120] T. Horikawa, N. Sakao, T. Sekida, J. Hayashi, D.D. Do, M. Katoh, Preparation of nitrogen-doped porous carbon by ammonia gas treatment and the effects of N-doping on water adsorption. *Carbon* 50 (5) (2012) 1833–1842, <https://doi.org/10.1016/j.carbon.2011.12.033>.
- [121] X. Wang, J.S. Lee, Q. Zhu, J. Liu, Y. Wang, S. Dai, Ammonia-treated ordered mesoporous carbons as catalytic materials for oxygen reduction reaction. *Chem. Mater.* 22 (7) (2010) 2178–2180, <https://doi.org/10.1021/cm100139d>.
- [122] T. Granzier-Nakajima, K. Fujisawa, V. Anil, M. Terrones, Y.-T. Yeh, Controlling nitrogen doping in graphene with atomic precision: synthesis and characterization. *Nanomaterials* 9 (3) (2019) 425, <https://doi.org/10.3390/nano9030425>.

- [123] P. Chen, et al., Nitrogen-doped nanoporous carbon nanosheets derived from plant biomass: an efficient catalyst for oxygen reduction reaction. *Energy Environ. Sci.* 7 (12) (2014) 4095–4103, <https://doi.org/10.1039/C4EE02531H>.
- [124] R. Imran Jafri, N. Rajalakshmi, S. Ramaprabhu, Nitrogen doped graphene nanoplatelets as catalyst support for oxygen reduction reaction in proton exchange membrane fuel cell. *J. Mater. Chem.* 20 (34) (2010) 7114, <https://doi.org/10.1039/c0jm00467g>.
- [125] F. Su, et al., Pt nanoparticles supported on nitrogen-doped porous carbon nanospheres as an electrocatalyst for fuel cells. *Chem. Mater.* 22 (3) (2010) 832–839, <https://doi.org/10.1021/cm901542w>.
- [126] Y. Chen, et al., Enhanced stability of Pt electrocatalysts by nitrogen doping in CNTs for PEM fuel cells. *Electrochim. Commun.* 11 (10) (2009) 2071–2076, <https://doi.org/10.1016/j.elecom.2009.09.008>.
- [127] Y. Chen, et al., Nitrogen doping effects on carbon nanotubes and the origin of the enhanced electrocatalytic activity of supported Pt for proton-exchange membrane fuel cells. *J. Phys. Chem. C* 115 (9) (2011) 3769–3776, <https://doi.org/10.1021/jp108864y>.
- [128] H. Li, Y. Gao, C. Wang, G. Yang, A simple electrochemical route to access amorphous mixed-metal hydroxides for supercapacitor electrode materials. *Adv. Energy Mater.* 5 (6) (2015) 1401767, <https://doi.org/10.1002/aenm.201401767>.
- [129] H. Kim, K. Lee, S.I. Woo, Y. Jung, On the mechanism of enhanced oxygen reduction reaction in nitrogen-doped graphene nanoribbons. *Phys. Chem. Chem. Phys.* 13 (39) (2011) 17505, <https://doi.org/10.1039/c1cp21665a>.
- [130] Z. Chen, D. Higgins, Z. Chen, Nitrogen doped carbon nanotubes and their impact on the oxygen reduction reaction in fuel cells. *Carbon* 48 (11) (2010) 3057–3065, <https://doi.org/10.1016/j.carbon.2010.04.038>.
- [131] L. Lai, et al., Exploration of the active center structure of nitrogen-doped graphene-based catalysts for oxygen reduction reaction. *Energy Environ. Sci.* 5 (7) (2012) 7936, <https://doi.org/10.1039/c2ee21802j>.
- [132] S. Gao, X. Wei, H. Fan, L. Li, K. Geng, J. Wang, Nitrogen-doped carbon shell structure derived from natural leaves as a potential catalyst for oxygen reduction reaction. *Nano Energy* 13 (2015) 518–526, <https://doi.org/10.1016/j.nanoen.2015.02.031>.
- [133] H. Yuan, L. Deng, X. Cai, S. Zhou, Y. Chen, Y. Yuan, Nitrogen-doped carbon sheets derived from chitin as non-metal bifunctional electrocatalysts for oxygen reduction and evolution. *RSC Adv.* 5 (69) (2015) 56121–56129, <https://doi.org/10.1039/C5RA05461C>.
- [134] S.-A. Wohlgemuth, R.J. White, M.-G. Willinger, M.-M. Titirici, M. Antonietti, A one-pot hydrothermal synthesis of sulfur and nitrogen doped carbon aerogels with enhanced electrocatalytic activity in the oxygen reduction reaction. *Green Chem.* 14 (5) (2012) 1515, <https://doi.org/10.1039/c2gc35309a>.
- [135] S.-A. Wohlgemuth, T.-P. Fellinger, P. Jäker, M. Antonietti, Tunable nitrogen-doped carbon aerogels as sustainable electrocatalysts in the oxygen reduction reaction. *J. Mater. Chem. A* 1 (12) (2013) 4002, <https://doi.org/10.1039/c3ta10352h>.
- [136] L. Yan, J. Yu, J. Houston, N. Flores, H. Luo, Biomass derived porous nitrogen doped carbon for electrochemical devices. *Green Energy Environ.* 2 (2) (2017) 84–99, <https://doi.org/10.1016/j.gee.2017.03.002>.
- [137] C. Zhu, J. Zhai, S. Dong, Bifunctional fluorescent carbon nanodots: green synthesis via soy milk and application as metal-free electrocatalysts for oxygen reduction. *Chem. Commun.* 48 (75) (2012) 9367, <https://doi.org/10.1039/c2cc33844k>.

- [138] C. Guo, L. Sun, W. Liao, Z. Li, The use of an edible mushroom-derived renewable carbon material as a highly stable electrocatalyst towards four-electron oxygen reduction. *Materials* 9 (1) (2015) 1, <https://doi.org/10.3390/ma9010001>.
- [139] S. Gao, et al., Large scale production of biomass-derived N-doped porous carbon spheres for oxygen reduction and supercapacitors. *J. Mater. Chem. A* 2 (10) (2014) 3317, <https://doi.org/10.1039/c3ta14281g>.
- [140] S. Gao, H. Fan, S. Zhang, Nitrogen-enriched carbon from bamboo fungus with superior oxygen reduction reaction activity. *J. Mater. Chem. A* 2 (43) (2014) 18263–18270, <https://doi.org/10.1039/C4TA03558E>.
- [141] F. Liu, et al., High-performance doped carbon catalyst derived from nori biomass with melamine promoter. *Electrochim. Acta* 138 (2014) 353–359, <https://doi.org/10.1016/j.electacta.2014.06.098>.

Further reading

- Z. Zhao, et al., A 3D organically synthesized porous carbon material for lithium-ion batteries. *Angew. Chem. Int. Ed.* 57 (37) (2018) 11952–11956, <https://doi.org/10.1002/anie.201805924>.
- W. Lu, J.-B. Baek, L. Dai (Eds.), *Carbon Nanomaterials for Advanced Energy Systems: Advances in Materials Synthesis and Device Applications*, John Wiley & Sons, Inc, Hoboken, NJ, 2015.
- G. Centi, *Catalysis for renewables: from feedstock to energy production*, Wiley-VCH, Weinheim, 2007.
- V. Dhyani, T. Bhaskar, Pyrolysis of biomass, in: *Biofuels: Alternative Feedstocks and Conversion Processes for the Production of Liquid and Gaseous Biofuels*, Elsevier, 2019, pp. 217–244.
- A. Nzhihou, B. Stanmore, N. Lyczko, D.P. Minh, The catalytic effect of inherent and adsorbed metals on the fast/flash pyrolysis of biomass: a review. *Energy* 170 (2019) 326–337, <https://doi.org/10.1016/j.energy.2018.12.174>.
- T. Tay, S. Ucar, S. Karagöz, Preparation and characterization of activated carbon from waste biomass. *J. Hazard. Mater.* 165 (1–3) (2009) 481–485, <https://doi.org/10.1016/j.jhazmat.2008.10.011>.
- C. Falco, N. Baccile, M.-M. Titirici, Morphological and structural differences between glucose, cellulose and lignocellulosic biomass derived hydrothermal carbons. *Green Chem.* 13 (11) (2011) 3273, <https://doi.org/10.1039/c1gc15742f>.
- J.W. Baynes, The Maillard reaction: chemistry, biochemistry and implications By Harry Nursten (The University of Reading, Reading, U.K.) Royal Society of Chemistry: Cambridge. 2005. xii + 214 pp. \$199.00. ISBN 0-85404-964-9. *J. Am. Chem. Soc.* 127 (41) (2005) 14527–14528, <https://doi.org/10.1021/ja059794d>.
- J. Lee, S. Han, T. Hyeon, Synthesis of new nanoporous carbon materials using nanostructured silica materials as templates. *J. Mater. Chem.* 14 (4) (2004) 478, <https://doi.org/10.1039/b311541k>.
- W. Li, D. Zhao, An overview of the synthesis of ordered mesoporous materials. *Chem. Commun.* 49 (10) (2013) 943–946, <https://doi.org/10.1039/C2CC36964H>.
- H.I. Lee, et al., Rational design of ordered mesoporous carbon with controlled bimodal porosity via dual silica templating route. *Chem. Commun.* 48 (2005) 6035, <https://doi.org/10.1039/b511423c>.
- D. Guo, R. Shibuya, C. Akiba, S. Saji, T. Kondo, J. Nakamura, Active sites of nitrogen-doped carbon materials for oxygen reduction reaction clarified using model catalysts. *Science* 351 (6271) (2016) 361–365, <https://doi.org/10.1126/science.aad0832>.

- Y. Cui, Z. Wen, Y. Liu, A free-standing-type design for cathodes of rechargeable Li–O₂ batteries. *Energy Environ. Sci.* 4 (11) (2011) 4727, <https://doi.org/10.1039/c1ee02365a>.
- J. Lu, X. Bo, H. Wang, L. Guo, Nitrogen-doped ordered mesoporous carbons synthesized from honey as metal-free catalyst for oxygen reduction reaction. *Electrochim. Acta* 108 (2013) 10–16, <https://doi.org/10.1016/j.electacta.2013.06.066>.
- J. Hou, C. Cao, F. Idrees, X. Ma, Hierarchical porous nitrogen-doped carbon nanosheets derived from silk for ultrahigh-capacity battery anodes and supercapacitors. *ACS Nano* 9 (3) (2015) 2556–2564, <https://doi.org/10.1021/nn506394r>.

Chapter 13

First-principles materials design for graphene-based sensor applications

Yoshitaka Fujimoto

Department of Physics, Tokyo Institute of Technology, Oh-okayama, Meguro-ku, Tokyo, Japan

1 Introduction

Since its discovery, graphene, which is an atomically single layer consisting of two-dimensional hexagonal carbon network, has received much attention from both basic nanoscience and applicable nanotechnology due to various unique and outstanding properties such as massless Dirac fermion behavior near the Fermi energy, Klein tunneling effects, and anomalous quantum Hall effects [1–7]. Especially, graphene is expected to become promising device materials to be used in nanoelectronics including gas sensors since it shows extremely high carrier mobility.

Graphene as well as carbon nanotubes (CNTs) are reported to be sensitive to adsorbates. For example, it is demonstrated experimentally that graphene can detect individual molecules [8]. It is also shown that CNTs can detect NH₃ and NO₂ molecules with fast response time and high sensitivity at room temperatures [9, 10]. Therefore, graphene and CNTs are good candidate materials for promising sensing applications owing to their high carrier mobility and high sensitivity to adsorbates. On the other hand, NO₂ molecules are reported to be not chemisorbed but rather physisorbed to the pristine graphene [11–13] and it is, therefore, surmised that the high sensitivity to gas adsorptions at room temperatures may be caused by the existence of impurities in graphene [11–13].

Substitutionally, doping with impurities is one of the efficient ways to tune the electronic properties of graphene layers and it can also improve the sensitivity to adsorbates. There are so far several experimental and theoretical reports on boron (B) and nitrogen (N) doped graphenes and CNTs since their elements show similar structural properties [14–21]. It is shown that the existence of impurity dopants can improve the adsorption energies

of hydrogens on graphene and CNTs [22, 23]. Therefore, the high sensitivity to adsorbates of doped graphene as well as the high carrier mobility are expected to lead to further developments of high-performance sensing devices [24–32].

This chapter provides a review of a first-principles density-functional study to reveal atomic structures, stabilities, and electronic properties of environmentally polluting gas or “toxic gas” molecules (NO, NO₂, CO, and CO₂) and abundant gas molecules in the air (O₂ and N₂) adsorbed on doped graphene to discuss the possibilities of low power consuming sensing applications of graphene layers for detecting toxic molecules [33, 34].

2 Methodology

2.1 Computational details

First-principles total-energy calculations are performed within the framework of the density-functional theory (DFT) [35]. The interactions between the ions and the valence electrons are described by the norm-conserving Troullier-Martins pseudopotentials [36], and exchange-correlation effects are treated using the local density approximation (LDA) parameterized by Perdew and Zunger [37–39].

To calculate energetics and electronic structures of B(N)-doped graphene, a 4 × 4 supercell is used along with the directions parallel to the graphene sheet. This supercell size has been confirmed to be large enough to discuss quantitative details of the electronic properties of the B(N)-doped graphene [40, 41] and is expected to be large enough for the B(N)-doped graphene as well. Wavefunctions in the Kohn-Sham equations are expanded in terms of the plane-wave basis set with the cutoff energy of 50 Ry [42]. The supercell lattice constant along the direction perpendicular to graphene is set to be 20 Å. The Brillouin-zone integration (BZ) is performed with 6 × 6 × 1 k -points sampling. Upon the geometry optimization, atomic configurations are updated until Hellmann-Feynman forces acting on all atoms are less than 0.05 eV/Å.

2.2 Adsorption energy

To discuss the energetics regarding gas adsorptions on B- and N-doped graphenes, the adsorption energy is defined by

$$E_a = E_{\text{tot}} - E_{\text{gra}} - E_{\text{mol}} \quad (1)$$

where E_{tot} and E_{gra} are the total energies of B(N)-doped graphene with and without the adsorption of gas molecules, respectively, E_{mol} is also the total energy of an isolated gas molecule.

2.3 Charge transfer

To discuss the charge transfer between the graphene sheets and adsorbed molecules, the spatial distribution of the total electron density difference is calculated, which is given by

$$\rho_{\text{diff}}(r) = \rho_{\text{tot}}(r) - \rho_{\text{gra}}(r) - \rho_{\text{mol}}(r) \quad (2)$$

where $\rho_{\text{tot}}(r)$, $\rho_{\text{gra}}(r)$, and $\rho_{\text{mol}}(r)$ are total electron densities of the molecule-adsorbed doped graphene, the doped graphene without adsorbates, and the isolated gas molecule calculated at the same atomic positions, respectively, and r is a three-dimensional coordinate. Note that the atomic configurations, as well as the supercell size used to calculate $\rho_{\text{gra}}(r)$ for the doped graphene without adsorbates and to calculate $\rho_{\text{mol}}(r)$ for the isolated gas molecule, are the same as corresponding parts of the atomic configurations of the molecule-adsorbed doped graphene, and therefore, the total electron densities of $\rho_{\text{gra}}(r)$ and $\rho_{\text{mol}}(r)$ have been calculated independently.

2.4 Scanning tunneling microscopy

The scanning tunneling microscopy (STM) images are calculated using the Tersoff-Hamann approximation [43]. This method is known to be valid for many systems despite its simplicity [44–48]. In this approach, the tunneling current $I(r)$ is assumed to be proportional to the local density of states $\rho(r, \varepsilon)$ (LDOS) of the surface at the tip position integrated over a range of an energy ε restricted by the applied bias voltage V , that is,

$$I(r) \sim \int_{E_F}^{E_F + eV} \rho(r, \varepsilon) d\varepsilon \quad (3)$$

where E_F is the Fermi energy. Images obtained with negative and positive voltages can reflect the occupied and unoccupied electronic states, respectively.

2.5 Electron transport

To calculate electronic transport properties of various graphene systems, a periodic boundary condition is assumed along a zigzag direction of graphene with a period of $L_x = 3a$, where $a = \sqrt{3}a_0$ and $a_0 (= 1.41 \text{ \AA})$ is the C—C bond length of the pristine graphene. For the calculations of the electrical conductances, the scattering wave functions of B-doped graphenes with and without NO and NO_2 molecules between two semiinfinite graphene sheets are constructed from the overbridging boundary-matching (OBM) method [49–52] using the real-space finite-difference approach [53–55]. In this approach, the grid spacing is taken to be 0.21 \AA , which corresponds to the cutoff energy of 61.6 Ry .

We calculated the conductance $G(E)$ associated with the transmission coefficient $T(E, k_x)$ by the Landauer-Büttiker formula [56]:

$$G(E) = \frac{2e^2}{h} \int_{-\pi/L_x}^{\pi/L_x} \frac{dk_x}{2\pi/L_x} T(E, k_x) \quad (4)$$

where e and h denote the electron charge and Planck's constant, respectively.

3 Adsorption energy and optimized structures

Firstly, we begin by discussing the atomic structures of B-doped and N-doped graphenes before gas adsorptions. For the B-doped graphene, the calculated B—C bond length is 1.47 Å, whereas the C—N bond length is 1.40 Å for the N-doped case. The B—C bond length is considerably longer than the C—C bond length of 1.41 Å in pristine graphene, and the C—N bond length is slightly shorter than the C—C bond length in pristine graphene. These are in agreement with the bond lengths reported previously [14, 41]. The B atom in the B-doped graphene as well as the N atom in the N-doped graphene resides in a planar graphene sheet.

We here discuss the energetics on the adsorption of various gas molecules on B- and N-doped graphenes. Table 1 lists the adsorption energies (E_a) and the distances (d) between the single-molecule and the dopant atom for the adsorption of NO, NO₂, CO, CO₂, O₂, and N₂ molecules on B-doped and N-doped graphenes. For the N-doped graphene, all six types of molecules are found not to be chemically but to be physically adsorbed at the N site with relatively small adsorption energies as well as long distances between the molecule and the dopant atom ($d > 2.6$ Å). For the B-doped graphene, CO, CO₂, O₂, and N₂ molecules are also not adsorbed chemically as in the case of the N-doped case. On the other hand, NO and NO₂ molecules can bind chemically with the large adsorption energies ($|E_a| > 1.1$ eV) as well as the short distances ($d < 2$ Å). It is reported that B-doped and N-doped bilayer graphenes show similar results [33].

TABLE 1 Adsorption energy E_a (eV) and distance d (Å) between molecule and B(N) atom for each gas molecules adsorbed on B(N)-doped graphene.

		NO ₂	NO	CO ₂	CO	O ₂	N ₂
Boron	E_a	-1.16	-1.23	-0.03	-0.12	-0.20	-0.27
	d	1.59	2.15	2.84	2.89	1.83	2.93
Nitrogen	E_a	-0.74	-0.35	-0.11	-0.14	-0.32	-0.30
	d	2.66	2.62	2.73	2.94	2.69	2.87

Data from Y. Fujimoto, S. Saito, Effects of gas adsorption on the stabilities, electronic structures, and scanning tunneling microscopy of graphene monolayers doped with B or N, Jpn. J. Appl. Phys. 58 (2019) 015005.

Therefore, NO and NO_2 molecules are expected to bind chemically on B-doped graphene layers without depending on the number of layers below the doped surface layer.

As mentioned previously, the adsorption energy of NO molecule on B-doped graphene is found to be somewhat larger than that of the NO_2 molecule. The difference between the adsorption energies of NO and NO_2 molecules would be mainly attributed to the electronegativity. For the NO_2 -molecule adsorption case, the electronegativity of the O atom is much larger than that of the B atom, and thereby the B atom in the graphene approaches to the O atom in the NO_2 molecule (Fig. 1B). As a result, the B atom moves away from the planar graphene layer by about 0.64 Å. The total energy of this deformed B-doped graphene without the NO_2 molecule is found to be higher by ~0.70 eV, compared with that of the B-doped graphene before the adsorption of the NO_2 molecule. Besides, the N—O bond near the B atom in the NO_2 molecule is stretched by ~0.12 Å after the adsorption although the remaining N—O bond length of 1.19 Å is almost unchanged compared with that of the isolated NO_2 molecule. Thus, the interactions between the B atom and the NO_2 molecule give rise to sizable energy gains. On the other hand, structural deformations of the B-doped graphene and the NO_2 molecule cause energy costs. As a result, the total energy gain upon the adsorption becomes 1.16 eV ($|E_a|$ in Table 1). For the NO-molecule adsorption case, the N atom in the NO molecule just approaches the B atom without noticeable structural modification neither in the B-doped graphene layer nor in the NO molecule (Fig. 1A). The B—N distance, in this case, is much longer than that in the NO_2 case and the energy gain due to the adsorption becomes smaller. In the case of the adsorption of the NO molecule, however, there exists no energy cost due to the structural deformation and the total energy gain ($|E_a| = 1.23$ eV) becomes larger than that of the NO_2 case. A similar discussion has been reported in the case of the B-doped bilayer graphene [33].

It has been reported that the adsorption energy of the H atom to the neighbor C atom is larger than that to the dopant N atom itself [23]. Herein, we discuss the adsorptions of the NO and NO_2 gas molecules at the C atom sites next to the dopant atoms. For the B-doped case, the adsorption energies for NO and

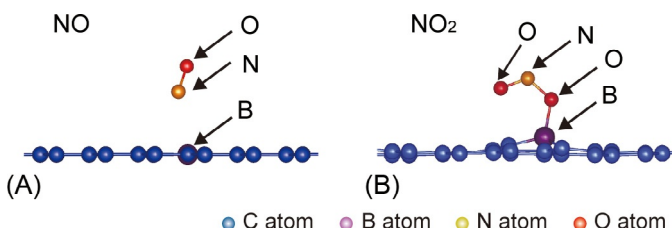


FIG. 1 Side views of optimized atomic structures of (A) NO and (B) NO_2 molecules adsorbed on B-doped graphene.

NO_2 molecules are found to be -1.18 and -1.03 eV , respectively, and the distances between the molecules and the C atoms are 2.15 and 1.61 \AA for NO and NO_2 molecule adsorptions, respectively. For the N-doped case, the adsorption energies for NO and NO_2 molecules are -0.63 eV and -0.92 eV with the distances of 2.25 and 2.49 \AA , respectively. Therefore, for the B-doped graphene, the adsorptions of the NO and NO_2 molecules at the B atom site are favored energetically than those at neighboring C atoms around the B atom. On the other hand, for the N-doped graphene, the adsorptions of the NO and NO_2 molecules at the C atom site next to the N atom become favorable in energy rather than those at the N atom. For the N-doped case, besides, the curvature effects of the nanotubes could enhance the adsorption energies [16, 22]. Therefore, the N-doped CNTs might be useful as a sensor device material to detect the NO_2 molecule than N-doped graphene. In the following, we will focus on the B-doped graphene which is found to show the largest adsorption energy gain for NO and NO_2 molecules.

In the earlier discussion, the three C atom sites next to the B atom in the B-doped graphene are shown to be reactive for the adsorptions of NO and NO_2 molecules. Herein, we discuss the energetics for the adsorptions of four NO and NO_2 molecules on the B-doped graphene. As many as four NO and NO_2 molecules can bind on the B atom and the three neighboring C atoms next to the B atom with the adsorption energies of -1.12 eV/molecule and -0.54 eV/molecule , respectively. Interestingly, the adsorption energy for the NO molecule is found to be much larger than that for the NO_2 molecule. The difference in energy gain between the adsorption of NO and NO_2 molecules would be caused by the size of the molecules: the NO_2 molecule is considerably larger than the NO molecule. Thereby, the electrostatic repulsion for the NO molecules is smaller than those for the NO_2 molecules. Accordingly, the B-doped graphene would be useful as not only highly sensitive sensor applications but also adsorbents for environmentally polluting NO and NO_2 gases (Fig. 1).

4 Energy band structures

As discussed earlier, only NO and NO_2 molecules can be shown to chemically bind to B-doped graphene. We, hereby discuss the adsorption effects of NO and NO_2 gas molecules on the electronic properties of B-doped graphene. Fig. 2 shows the energy band structure and the electronic density of the valence-band maximum (VBM) at the Γ point for B-doped graphene before the adsorption of the molecules. The B-doped graphene gives rise to an acceptor-like state near the Fermi energy. Therefore, it should possess a p-type doping property. The electronic density of the acceptor-like state is distributed in a bright triangular area around the B atom (Fig. 2(a)). This spatial distribution of the electronic state is also seen in B-doped bilayer graphene [33].

Fig. 3 shows the energy band structure and the electronic states near the Fermi energy at the Γ point for B-doped graphene with adsorbed NO molecule.

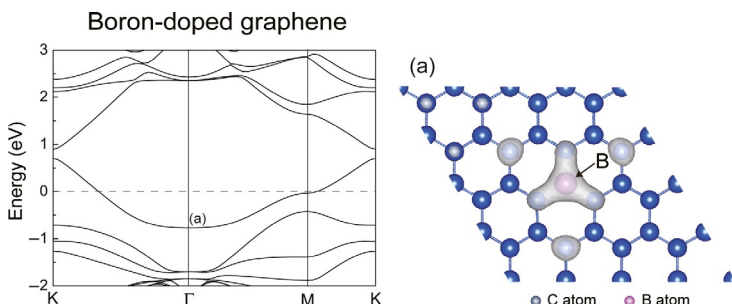


FIG. 2 Energy-band structure and (a) isosurfaces of squared wavefunctions of B-doped graphene. The Fermi energy is set to zero. The isosurface value of the electron density is set to 0.02 electron/ \AA^3 . Data from Y. Fujimoto, S. Saito, Effects of gas adsorption on the stabilities, electronic structures, and scanning tunneling microscopy of graphene monolayers doped with B or N, *Jpn. J. Appl. Phys.* 58 (2019) 015005.

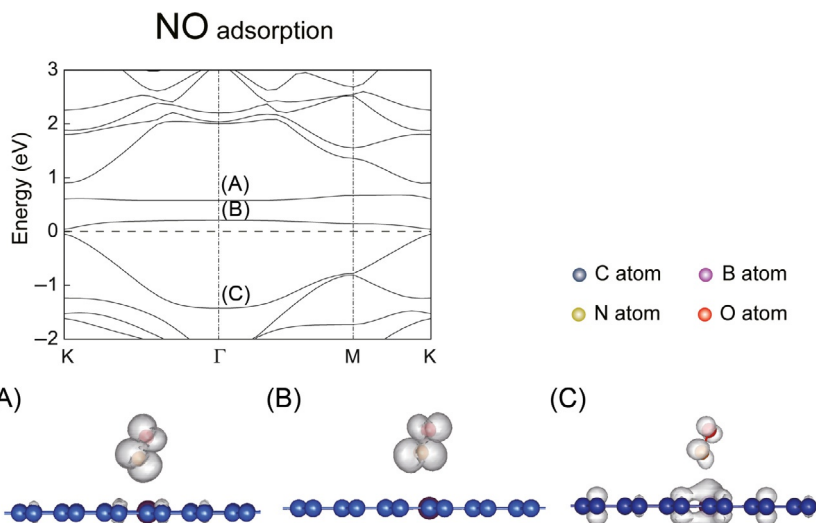


FIG. 3 Energy-band structure and (A–C) isosurfaces of squared wavefunctions of B-doped graphene with adsorbed NO molecule. The Fermi energy is set to zero. The isosurface value of the electron density is set to 0.02 electron/ \AA^3 . Data from Y. Fujimoto, S. Saito, Effects of gas adsorption on the stabilities, electronic structures, and scanning tunneling microscopy of graphene monolayers doped with B or N, *Jpn. J. Appl. Phys.* 58 (2019) 015005.

For the adsorption of the NO molecule, two unoccupied flat NO-molecule-related states emerge above the Fermi energy (Fig. 3A and B) and should become acceptor states as shown in the energy-band structure of Fig. 3. In Fig. 3C, the original acceptor state of the B-doped graphene is shown and is fully occupied by hybridizing with the NO-molecule related orbital.

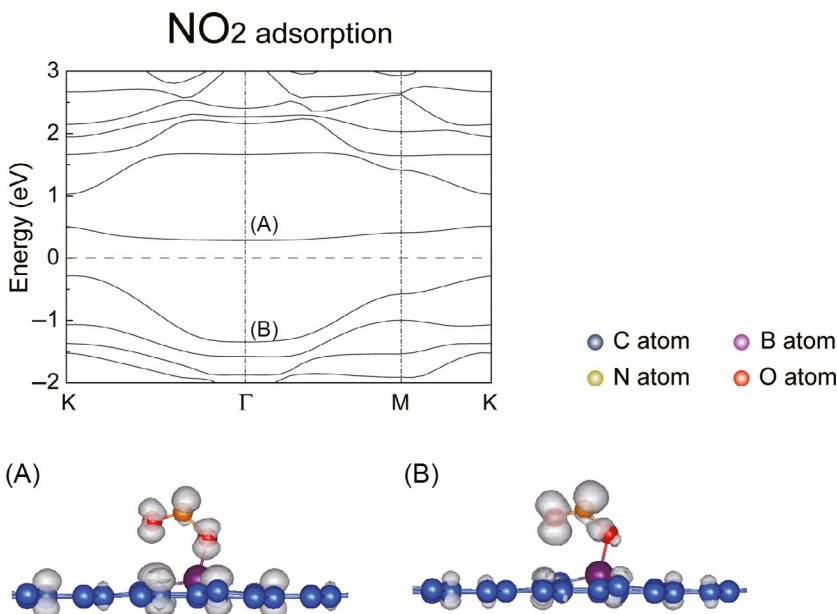


FIG. 4 Energy-band structure and (A and B) isosurfaces of squared wavefunctions of B-doped graphene with adsorbed NO molecule. The Fermi energy is set to zero. The isosurface value of the electron density is set to 0.02 electron/ \AA^3 . Data from Y. Fujimoto, S. Saito, Effects of gas adsorption on the stabilities, electronic structures, and scanning tunneling microscopy of graphene monolayers doped with B or N, *Jpn. J. Appl. Phys.* 58 (2019) 015005.

Thus, the adsorption of the NO molecule on the B-doped graphene would induce p-type polarity.

For the adsorption of a NO_2 molecule, the electronic state at the VBM consists of a hybridized orbital between the B-related state and the state of the NO_2 molecule (Fig. 4). An unoccupied NO_2 -related state emerges above the Fermi energy (Fig. 4A). Thus, the adsorption of a NO_2 molecule should induce an acceptor state (Fig. 4B). It is reported that B-doped bilayer graphene also shows similar results [33].

As mentioned previously, the impurity-related states induced by the adsorption of the molecules could thus dramatically change the electron transport properties of B-doped graphene, depending on the type of adsorbate. Furthermore, their impurity-related states reside near the Fermi energy, which would affect the conductivity of graphene under low bias voltages. Therefore, the variation of the electron transport properties such as the electrical conductance and the current-voltage characteristics could be detected and would be used for low power consuming sensor devices such as field-effect transistors and so on [24, 26, 49, 50].

We now discuss the origin of the impurity-related states near the Fermi energy induced by the adsorption of NO and NO_2 molecules on B-doped graphene.

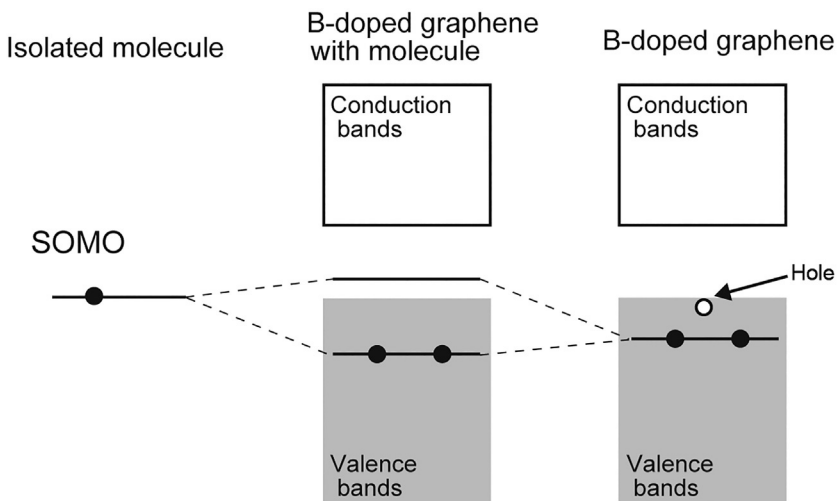


FIG. 5 Schematic representation of energy diagrams near the Fermi energy for B-doped graphenes with and without a molecule. The gray shaded area and blank box denote the occupied and unoccupied states, respectively.

Fig. 5 shows the energy diagram near the Fermi energy for the adsorption of a gas molecule on B-doped graphene. The NO molecule as well as the NO_2 molecule has a SOMO state near the Fermi energy. We, therefore, consider that the isolated molecule possesses a singly occupied molecular orbital (SOMO) near the Fermi energy. On the other hand, the B-doped graphene possesses a hole state induced by the B-atom impurity at the top of the valence band which is composed of a dispersive π -orbital state, while a fully occupied B-related state (“acceptor state”) is located below the Fermi energy (Fig. 2(a)). When the isolated molecule is adsorbed on the B-doped graphene, the SOMO state of the isolated molecule and the fully occupied B-related state of the B-doped graphene are hybridized with each other, resulting in an unoccupied state above the Fermi energy and a lower B-related state hybridized with the isolated molecule state, and the original hole state of the B-doped graphene is now occupied by one electron transferred from the molecular SOMO state. Thus, the interaction between the molecule and the B-doped graphene produces a sizable energy gain with a stabilized fully occupied B-related state and an electron transferred from the higher energy SOMO state to the lower-energy hole state.

For the adsorption of a NO_2 molecule, it is confirmed that one unoccupied state appears above the Fermi energy, the original acceptor state of the B-doped graphene is occupied by an electron, and the B-related state around the Γ point in the valence bands is stabilized [Fig. 4A and B]. On the other hand, the NO molecule has almost doubly degenerated states and one of them is singly occupied. However, similar orbital hybridization takes place via the adsorption of a

NO molecule. Therefore, the adsorption of a NO molecule induces two unoccupied states above the Fermi energy (Fig. 3A–C).

5 Charge transfer

When the NO and NO_2 molecules are adsorbed on the B-doped graphene, the charge transfers should take place between the molecules and the B-doped graphene. Fig. 6 shows the isosurfaces of the total electron density difference obtained by Eq. (2). When the NO molecule is adsorbed, electrons move from the NO molecule to the B-doped graphene with ~ 0.03 electrons. In the case of the adsorption of a NO_2 molecule, electrons move from the B-doped graphene to the NO_2 molecule with ~ 0.18 electrons. It is reported that charge transfers occur between the adsorbed molecules and the B-doped graphene layer for B-doped bilayer graphene [33]. Such charge transfers between the adsorbates and the graphene layers should lead to shifts of the Fermi energy, which could further modify the electron transport properties. Besides, the work functions are also expected to be changed for the adsorption of molecules, as will be discussed in the following section [24].

6 Work function

Fig. 7 shows the work functions of B-doped graphenes with and without NO and NO_2 molecules. Here, the work function is calculated as $V_\infty - E_F$, where V_∞ is the vacuum level. The calculated work function of the pristine graphene is 4.44 eV, which is in good agreement with the experimental results [57, 58]. Since the number of valence electrons of a B atom is one less than that of a C atom, the work function of the B-doped graphene increases by ~ 0.6 eV than that of the pristine graphene. When a NO molecule is adsorbed on the B-doped graphene, the work function decreases by about 0.5 eV, while for NO_2 adsorption, the work function of the B-doped graphene increases to approximately 5.4 eV. Thus, the work functions vary depending on the type and number of adsorbates owing to the charge transfer between the adsorbate and the B-doped graphene, and the variation of the work function induced by the adsorption of

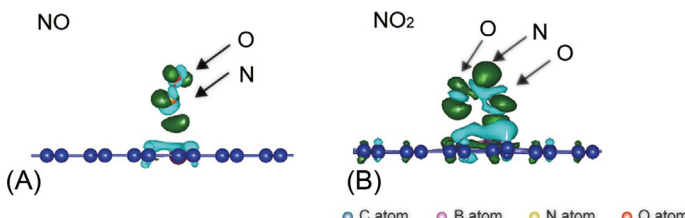


FIG. 6 Isosurfaces of total charge density difference for (A) NO and (B) NO_2 molecules adsorbed on B-doped graphenes. The isosurface values of the electron density are set to $+0.02$ (dark green) $\text{electron}/\text{\AA}^3$ and -0.02 (sky blue) $\text{electron}/\text{\AA}^3$.

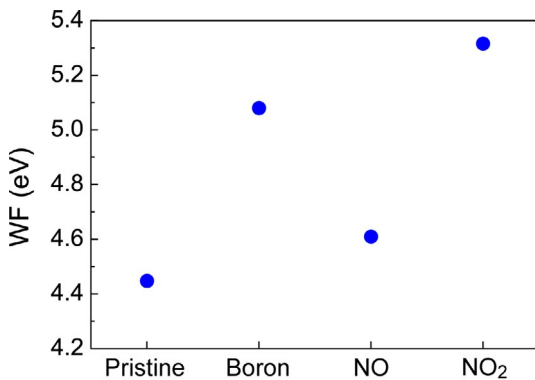


FIG. 7 Work functions (WFs) of pristine graphene and B-doped graphenes with and without NO and NO₂ molecules.

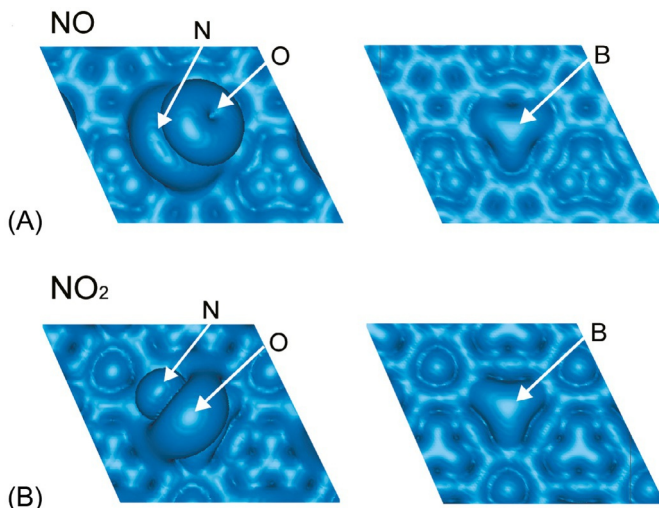


FIG. 8 Simulated STM images of B-doped graphene surfaces with (A) NO and (B) NO₂ molecules. The left and right panels denote the STM images of the upper and lower sides of the graphene layer, respectively. The STM images are generated at a bias voltage of +0.5 eV.

these molecules could be detected by using surface-work-function-change transistors [27, 28].

7 Scanning tunneling microscopy images

STM is a powerful tool to observe electronic structures of surfaces of semiconductors and metals at atomic levels. In Fig. 8, the STM images of B-doped graphenes with NO and NO₂ molecules are exhibited. The theoretical

triangle-shaped STM image of the B-doped graphene agrees well with the experimentally observed images [59, 60]. There are two ring-like corrugations above the NO molecule in the STM image of the graphene surface with the NO molecule, while the STM image at the lower side of the B-doped graphene, that is, the graphene surface without the NO molecule has a triangular-shape hillock around the B atom (Fig. 8A). When the NO_2 -molecule is adsorbed, large, and small spherical-shaped protrusions above the NO_2 molecule appear in the STM image of the graphene surface with the NO_2 molecule. On the other hand, in the STM image of the surface without the NO_2 molecule, there exists a triangular form (Fig. 8B). Thus, the B atom and the NO molecule as well as the NO_2 molecule should be identified in the STM images of the B-doped graphene when these molecules are adsorbed.

8 Electron transport properties

The adsorptions of the NO and NO_2 molecules would change the conductivity of the graphene, and it is of great importance to detect the variation of the conductivity for sensor applications. Herein, we discuss how the adsorption of molecules affects the electronic transport properties of graphene. Fig. 9 shows the conductances of pristine graphene and B-doped graphenes with and without NO and NO_2 molecules calculated by using Eq. (4). The conductance of the pristine graphene exhibits a linear dispersion, which agrees well with experimentally observed results [1]. When a B atom is doped into graphene, electrons are scattered by the B-atom impurity, which reduces the conductance by $\sim 30\%$, compared with that of the pristine graphene at the energy $E = 0.5\text{ eV}$. This reduction rate seems to be mostly independent of the energy studied, which is important for sensor applications. When a NO_2 molecule is adsorbed on the B-atom

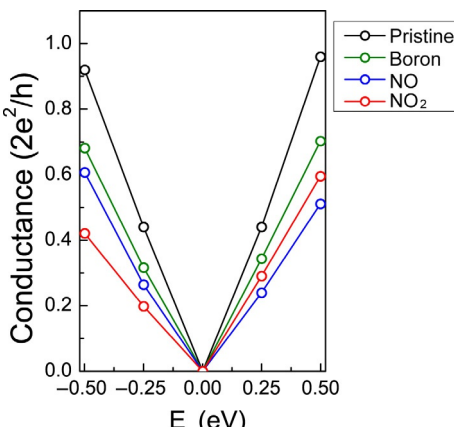


FIG. 9 Conductances of pristine graphene and B-doped graphenes with and without NO and NO_2 molecules as a function of energy E . The Fermi energy is set to zero.

impurity in graphene, the conductance of the graphene diminishes by $\sim 40\%$. Furthermore, the adsorption of a NO molecule on the B-atom impurity reduces the conductance considerably (about 50%). In the case, if the energy $E = -0.5$ eV, the conductance of the B-doped graphene without an adsorbate is less by $\sim 30\%$ than that of the pristine graphene, which shows an almost the same reduction rate as that at $E = 0.5$ eV. The adsorption of a NO_2 molecule diminishes the conductance of the graphene by over 50%. For the adsorption of a NO molecule, the conductance decreases by $\sim 35\%$. The adsorption of molecules thus could dramatically reduce the electrical conductance of graphene, depending on the type of adsorbate. Besides, the variation of the conductance could depend on the impurity concentration and gate voltage as for field-effect transistors. Accordingly, the variation of the electrical conductance induced by the adsorption of NO and NO_2 molecules could be utilized for sensor applications such as field-effect transistors. Furthermore, a large variation upon the adsorption of molecules in the conductance under low bias voltage (below 0.5 eV) would be achieved. Therefore, the low power consuming sensor devices could be realized by using graphene-based field-effect transistors.

9 Conclusions

Based on the first-principles density-functional study, we have reviewed the adsorption effects of environmentally polluting/toxic and abundant molecules in the air (NO, NO_2 , CO, CO_2 , O_2 , and N_2) on the atomic structures, the energetics, and the electronic properties of B-doped and N-doped graphenes. Only the NO and NO_2 molecules are adsorbed chemically on the B-doped graphene in air. Therefore, the B-doped graphene could behave as a sensitive device material for detecting only the NO and NO_2 molecules in the air. Moreover, the charge transfers and the sizable modifications of the energy bands could dramatically change the work functions as well as the electrical conductances of graphene upon the molecular adsorption, and the variation of such electrical signals induced by these molecular adsorptions could be detected by using sensor devices such as field-effect transistors and surface-work-function-change transistors [24, 27]. Thus, the B-doped graphene could act as useful low-power-consuming sensing device materials for detecting individually the types of the NO and NO_2 molecules in air. The NO and NO_2 molecules adsorbed on the B-doped graphene can be identified by STM experiments at the atomic level.

Acknowledgment

This work was partly supported by the MEXT Elements Strategy Initiative to Form Core Research Center through Tokodai Institute for Element Strategy (Grant Number JPMX0112101001), JSPS KAKENHI Grant Numbers JP17K05053, and JP26390062. Computations were partly done at the Institute for Solid State Physics, the University of Tokyo.

References

- [1] K.S. Novoselov, A.K. Geim, S.V. Morozov, D. Jiang, Y. Zhang, S.V. Dubonos, I.V. Grigorieva, A.A. Firsov, Electric field effect in atomically thin carbon films, *Science* 306 (2004) 666.
- [2] C. Berger, Z. Song, X. Li, X. Wu, N. Brown, C. Naud, D. Mayou, T. Li, J. Hass, A.N. Marchenkov, E.H. Conrad, P.N. First, W.A. de Heer, Electronic confinement and coherence in patterned epitaxial graphene, *Science* 312 (2006) 1191.
- [3] E.V. Castro, K.S. Novoselov, S.V. Morozov, N.M. Peres, J. Santos, J. Nilsson, F. Guinea, A.K. Geim, A.H. Neto, Biased bilayer graphene: semiconductor with a gap tunable by the electric field effect, *Phys. Rev. Lett.* 99 (2007) 016802.
- [4] Y. Zhang, Y.W. Tan, H.L. Stormer, P. Kim, Experimental observation of the quantum hall effect and Berry's phase in graphene, *Nature (London)* 438 (2005) 201.
- [5] Y. Zhang, T.-T. Tang, C. Girit, Z. Hao, M.C. Martin, A. Zettl, M.F. Crommie, Y.R. Shen, F. Wang, Direct observation of a widely tunable bandgap in bilayer graphene, *Nature (London)* 459 (2009) 820.
- [6] J.R. Williams, L. DiCarlo, C.M. Marcus, Quantum hall effect in a gate-controlled p-n junction of graphene, *Science* 317 (2007) 638.
- [7] A.F. Young, P. Kim, Quantum interference and Klein tunnelling in graphene heterojunctions, *Nat. Phys.* 5 (2009) 222.
- [8] F. Schedin, A.K. Geim, S.V. Morozov, E.W. Hill, P. Blake, M.I. Katsnelson, K.S. Novoselov, Detection of individual gas molecules adsorbed on graphene, *Nat. Mater.* 6 (2007) 652.
- [9] J. Kong, N. Franklin, C. Zhou, M. Chapline, S. Peng, K. Cho, H. Dai, Nanotube molecular wires as chemical sensors, *Science* 287 (2000) 622.
- [10] P.G. Collins, K. Bradley, M. Ishigami, A. Zettl, Extreme oxygen sensitivity of electronic properties of carbon nanotubes, *Science* 287 (2000) 1801.
- [11] A. Goldoni, R. Larciprete, L. Petaccia, S. Lizzit, Single-wall carbon nanotube interaction with gases: sample contaminants and environmental monitoring, *J. Am. Chem. Soc.* 125 (2003) 11329.
- [12] B. Sanyal, O. Eriksson, U. Jansson, H. Grennberg, Molecular adsorption in graphene with divacancy defects, *Phys. Rev. B* 79 (2009) 113409.
- [13] S. Peng, K. Cho, Ab initio study of doped carbon nanotube sensors, *Nano Lett.* 3 (2003) 513.
- [14] J. Dai, J. Yuan, P. Giannozzi, Gas adsorption on graphene doped with B, N, Al, and S: a theoretical study, *Appl. Phys. Lett.* 95 (2009) 232105.
- [15] D. Wei, Y. Liu, Y. Wang, H. Zhang, L. Huang, G. Yu, Synthesis of N-doped graphene by chemical vapor deposition and its electrical properties, *Nano Lett.* 9 (2009) 1752.
- [16] Y. Fujimoto, S. Saito, Energetics and electronic structures of pyridine-type defects in nitrogen-doped carbon nanotubes, *Phys. E* 43 (2011) 677.
- [17] Y. Fujimoto, S. Saito, Effects of strain on carbon donors and acceptors in hexagonal boron nitride monolayers, *Phys. Rev. B* 93 (2016) 045402.
- [18] Y. Fujimoto, T. Koretsune, S. Saito, Electronic structures of hexagonal boron-nitride monolayer: strain-induced effects, *J. Ceram. Soc. Jpn.* 122 (2014) 346.
- [19] Y. Fujimoto, S. Saito, Atomic geometries and electronic structures of hexagonal boron-nitride bilayers under strain, *J. Ceram. Soc. Jpn.* 123 (2015) 576.
- [20] Y. Fujimoto, S. Saito, Band engineering and relative stabilities of hexagonal boron nitride bilayers under biaxial strains, *Phys. Rev. B* 94 (2016) 245427.
- [21] Y. Fujimoto, S. Saito, Interlayer distances and band-gap tuning of hexagonal boron-nitride bilayers, *J. Ceram. Soc. Jpn.* 124 (2016) 584.

- [22] Y. Fujimoto, S. Saito, Structure and stability of hydrogen atom adsorbed on nitrogen-doped carbon nanotubes, *J. Phys. Conf. Ser.* 302 (2011) 012006.
- [23] Y. Fujimoto, S. Saito, Hydrogen adsorption and anomalous electronic properties of nitrogen-doped graphene, *J. Appl. Phys.* 115 (2014) 153701.
- [24] G. Lu, S. Park, K. Yu, R.S. Ruoff, L.E. Ocola, D. Rosenmann, J. Chen, Toward practical gas sensing with highly reduced graphene oxide: a new signal processing method to circumvent run-to-run and device-to-device variations, *ACS Nano* 5 (2011) 1154.
- [25] H. Yang, J. Heo, S. Park, H.J. Song, D.H. Seo, K. Byun, P. Kim, I. Yoo, H. Chung, K. Kim, Graphene barristor, a triode device with a gate-controlled Schottky barrier, *Science* 336 (2012) 1140.
- [26] S. Wu, G. Wang, Z. Xue, F. Ge, G. Zhang, H. Lu, L. Qiu, Organic field-effect transistors with macroporous semiconductor films as high-performance humidity sensors, *ACS Appl. Mater. Interfaces* 9 (2017) 14974.
- [27] M.W.K. Nomani, V. Shields, G. Tompa, N. Sbrockey, M.G. Spencer, R.A. Webb, G. Koley, Correlated conductivity and work function changes in epitaxial graphene, *Appl. Phys. Lett.* 100 (2012) 092113.
- [28] M. Qazi, T. Vogt, G. Koley, Trace gas detection using nanostructured graphite layers, *Appl. Phys. Lett.* 91 (2007) 233101.
- [29] W. Xuan, M. He, N. Meng, X. He, W. Wang, J. Chen, T. Shi, T. Hasan, Z. Xu, Y. Xu, J.K. Luo, Fast response and high sensitivity ZnO/glass surface acoustic wave humidity sensors using graphene oxide sensing layer, *Sci. Rep.* 4 (2014) 7206.
- [30] H. Zhang, L. Fan, H. Dong, P. Zhang, K. Nie, J. Zhong, Y. Li, J. Guo, X. Sun, Spectroscopic investigation of plasma-fluorinated monolayer graphene and application for gas sensing, *ACS Appl. Mater. Interfaces* 8 (2016) 8652.
- [31] M.G. Chung, D.H. Kim, H.M. Lee, T. Kim, J.H. Choi, D.K. Seo, J. Yoo, S. Hong, T.J. Kang, Y.H. Kim, Highly sensitive NO₂ gas sensor based on ozone treated graphene, *Sens. Actuators B Chem.* 166–167 (2012) 172.
- [32] S. Yang, C. Jiang, S.H. Wei, Gas sensing in 2D materials, *Appl. Phys. Rev.* 4 (2017) 021304.
- [33] Y. Fujimoto, S. Saito, Gas adsorption, energetics and electronic properties of boron- and nitrogen-doped bilayer graphenes, *Chem. Phys.* 478 (2016) 55.
- [34] Y. Fujimoto, S. Saito, Effects of gas adsorption on the stabilities, electronic structures, and scanning tunneling microscopy of graphene monolayers doped with B or N, *Jpn. J. Appl. Phys.* 58 (2019) 015005.
- [35] P. Hohenberg, W. Kohn, Inhomogeneous electron gas, *Phys. Rev.* 136 (1964) B864.
- [36] N. Troullier, J.L. Martins, Efficient pseudopotentials for plane-wave calculations, *Phys. Rev. B* 43 (1991) 1993.
- [37] W. Kohn, L.J. Sham, Self-consistent equations including exchange and correlation effects, *Phys. Rev.* 140 (1965) A1133.
- [38] D.M. Ceperley, B.J. Alder, Ground state of the electron gas by a stochastic method, *Phys. Rev. Lett.* 45 (1980) 566.
- [39] J.P. Perdew, A. Zunger, Self-interaction correction to density-functional approximations for many-electron systems, *Phys. Rev. B* 23 (1981) 5048.
- [40] Y. Fujimoto, S. Saito, Formation, stabilities, and electronic properties of nitrogen defects in graphene, *Phys. Rev. B* 84 (2011) 245446.
- [41] Y. Fujimoto, S. Saito, Electronic structures and stabilities of bilayer graphene doped with boron and nitrogen, *Surf. Sci.* 634 (2015) 57.
- [42] J. Yamauchi, M. Tsukada, S. Watanabe, O. Sugino, Computations have been performed using Tokyo Ab-initio Program Package (TAPP) which is developed by a consortium initiated at University of Tokyo, *Phys. Rev. B* 54 (1996) 5586.

- [43] J. Tersoff, D.R. Hamann, Theory of scanning tunneling microscopy, *Phys. Rev. B* 31 (1985) 805.
- [44] H. Okada, Y. Fujimoto, K. Endo, K. Hirose, Y. Mori, Detailed analysis of scanning tunneling microscopy images of the Si (001) reconstructed surface with buckled dimers, *Phys. Rev. B* 63 (2001) 195324.
- [45] Y. Fujimoto, H. Okada, K. Endo, T. Ono, S. Tsukamoto, K. Hirose, Images of scanning tunneling microscopy on the Si(001)-*p*(2×2) reconstructed surface, *Mater. Trans.* 42 (2001) 2247.
- [46] Y. Fujimoto, A. Oshiyama, Atomic structures and energetics of 90° dislocation cores in Ge films on Si (001), *Phys. Rev. B* 81 (2010) 205309.
- [47] Y. Fujimoto, H. Okada, K. Inagaki, H. Goto, K. Endo, K. Hirose, Theoretical study on the scanning tunneling microscopy image of Cl-adsorbed Si (001), *Jpn. J. Appl. Phys.* 42 (2003) 5267.
- [48] Y. Fujimoto, A. Oshiyama, Structural stability and scanning tunneling microscopy images of strained Ge films on Si (001), *Phys. Rev. B* 87 (2013) 075323.
- [49] Y. Fujimoto, K. Hirose, First-principles treatments of electron transport properties for nanoscale junctions, *Phys. Rev. B* 67 (2003) 195315.
- [50] Y. Fujimoto, K. Hirose, First-principles calculation method of electron-transport properties of metallic nanowires, *Nanotechnology* 14 (2003) 147.
- [51] Y. Fujimoto, Y. Asari, H. Kondo, J. Nara, T. Ohno, First-principles study of transport properties of Al wires: comparison between crystalline and jellium electrodes, *Phys. Rev. B* 72 (2005) 113407.
- [52] Y. Fujimoto, K. Hirose, T. Ohno, Calculation of surface electronic structures by the overbridging boundary-matching method, *Surf. Sci.* 586 (2005) 74.
- [53] J.R. Chelikowsky, N. Troullier, Y. Saad, Finite-difference-pseudopotential method: electronic structure calculations without a basis, *Phys. Rev. Lett.* 72 (1994) 1240.
- [54] K. Hirose, T. Ono, Y. Fujimoto, S. Tsukamoto, First Principles Calculations in Real-Space Formalism, Electronic Configurations and Transport Properties of Nanostructures, Imperial College Press, London, 2005.
- [55] S. Tsukamoto, T. Ono, Y. Fujimoto, K. Inagaki, H. Goto, K. Hirose, Geometry and conduction of an infinite single-row gole wire, *Mater. Trans.* 42 (2001) 2257.
- [56] M. Büttiker, Y. Imry, R. Landauer, S. Pinhas, Generalized many-channel conductance formula with application to small rings, *Phys. Rev. B* 31 (1985) 6207.
- [57] H. Kim, O. Renault, A. Tyurnina, J. Dijion, Doping efficiency of single and randomly stacked bilayer graphene by iodine adsorption, *Appl. Phys. Lett.* 105 (2014) 011605.
- [58] Y.J. Yu, Y. Zhao, S. Ryu, L.E. Brus, K.S. Kim, P. Kim, Tuning the graphene work function by electric field effect, *Nano Lett.* 9 (2009) 3430.
- [59] L. Zhao, M. Levendorf, S. Goncher, T. Schiros, L. Pálová, A. Zabet-Khosousi, K.T. Rim, C. Gutiérrez, D. Nordlund, C. Jaye, M. Hybertsen, D. Reichman, G.W. Flynn, J. Park, A.N. Pasupathy, Local atomic and electronic structure of boron chemical doping in monolayer graphene, *Nano Lett.* 13 (2013) 4659.
- [60] Y. Fujimoto, S. Saito, Energetics and scanning tunneling microscopy images of B and N defects in graphene bilayer, *Springer Proc. Phys.* 186 (2017) 107.

Chapter 14

Recycled silicon waste as a sustainable energy material

Roberto Baca-Arroyo

Department of Electronics, School of Mechanical and Electrical Engineering, National Polytechnic Institute, Mexico City, Mexico

1 Introduction

Silicon is the second most abundant element on earth after oxygen, in the form of silica (SiO_2) and silicates, and is extracted from silica-rich sands. It has been studied for over 60 years and has a large impact on the modern world economy. A small portion (<10%) of very highly purified elemental silicon used in semiconductor electronics is now used in a wide range of products, such as integrated circuits, cell phones, and modern technology. Being a monocrystalline polysilicon, it is usually justified only in the production of integrated circuits and in some high-cost and high-efficiency photovoltaic applications [1]. Pure silicon is made by reducing quartzite or sand with highly pure coke. Reduction is carried out in an electric arc furnace at high temperatures (>1000°C), with an excess of SiO_2 to stop silicon carbide (SiC) from accumulating. This reaction, known as carbon thermal reduction of SiO_2 , is usually conducted in the presence of scrap iron with low amounts of phosphorus and sulfur, producing ferrosilicon alloy. However, only approximately 20% is refined to metallurgical-grade purity (a total of 1.3–1.5 million metric tons/year) through the reduction of SiO_2 by mixing it with carbon and heating, typically in an electric arc furnace to over 1900°C. Here, impurities like Fe, Cr, Mn, Ni, and Ti are removed by various hydrometallurgical processes such as acid leaching, where intermediate volatile compounds such as trichlorosilane (SiHCl_3) and silane (SiH_4) are reduced [2].

Although other materials may exceed the performance of silicon for transistor-dimensional scaling and its specific parameters, silicon has become the most optimum material for speed, power dissipation, as well as integration of new materials and device structures into the silicon-based device platform. In terms of performance it can withstand the highest of temperatures and extreme electrical activity to sustain performance scaling within constraints of

performance versus power tradeoffs [3]. However, today, silicon manufacturing for microelectronics is subdivided into three phases: (1) production of crystalline silicon wafers, (2) integration of electric functions in planar wafer processing, and (3) packaging of integrated circuits. Such phases have been well studied using a scientific tool called lifecycle assessment (LCA), which takes into account several typical manufacturing scenarios, including energy, water, and chemical consumptions, releasing of toxic emissions into the atmosphere, use phase (customer electronics), and end-of-life as electronic waste (e-waste) [4]. Hence, researching uncommon physical behavior of silicon waste as an important breakthrough for next-generation sustainable devices will provide fundamental knowledge about reusing silicon semiconductors for suitable energy-conversion devices.

This chapter is organized as follows. After introducing silicon manufacturing, open-loop recycling applied to out-of-date silicon components from switching mode power supplies (SMPS) is presented. The following section focuses on the study of the uncommon conduction mechanism in silicon semiconductors to understand their technological opportunities. Finally, an electronic module and its experimental validation as a sensing circuit in modern technologies for sustainable energy conversion is described.

2 Open-loop recycling in silicon waste

Concern regarding modern technologies focused on marketing trends has been based on optimized silicon architectures whose operating performance is dependent on advanced digital processing because of its accessible cost, which makes electronic devices obsolete and encourages both nonpolluting (e.g., silicon, copper, Mn-Zn ferrites, and so forth) and highly polluting materials (e.g., glass fiber treated with phenolic resins in printed circuit boards) [5, 6]. Hence, e-waste increases, and negative environmental impact at all stages of silicon semiconductor manufacturing makes it crucial to rethink in silicon waste recycling from outdated customer electronics (e.g., Mn-Zn ferrite-based SMPS). Mn-Zn ferrites in bulk shape with E-core geometry, which are used to build inductors and transformers, are being replaced with air-gap components [7, 8]. Mn-Zn ferrite-based SMPS are nowadays a source of pollutants when they are not correctly handled as waste.

Recent studies using LCA applied to silicon semiconductor manufacturing show that negative environmental damage is dominated by energy consumption followed by upstream production of chemicals. Energy consumption is needed first for production processes and second for service processes such as the production of cooling power, ultrapure water generation, climate control, etc. Although chemicals and gases of high purity are used, chemical composition of solid waste generated during wafer processing and direct emissions in the atmosphere can be measured indirectly via input chemicals, which have been dumped in residual landfills. In accordance with silicon purity processing, toxic

emissions into the atmosphere can include carbon dioxide and methane, with carbon dioxide coming from oxidation and other processes. Also, damage to human health, fauna, and flora in the case of wastewater treatment can be due to assumptions regarding heavy metal content [4, 9]. Consequently, to understand open-loop recycling as applied to the silicon waste management of Mn-Zn ferrite-based SMPS, all the stages included in Fig. 1 in accordance with a systematic process are explaining below.

2.1 E-waste and physical separation

Before going to landfill disposal, typical Mn-Zn ferrite-based SPMS, whose building blocks include input rectifiers and filters, switching power transistors, isolating power transformers, output rectifiers and filters, as well as feedback and control circuits, can be recovered. However, reliability problems have occurred when an Mn-Zn ferrite-based SPMS is operating under switch-on and switch-off cycling for prolonged periods of time, because the combination of core losses, winding losses, and failures in the building blocks under extreme switching conditions produce enough energy to increase the temperature resulting in thermal runaway at high frequencies [10–12]. In addition to the selection of the number of electronic devices useful as silicon waste, availability and

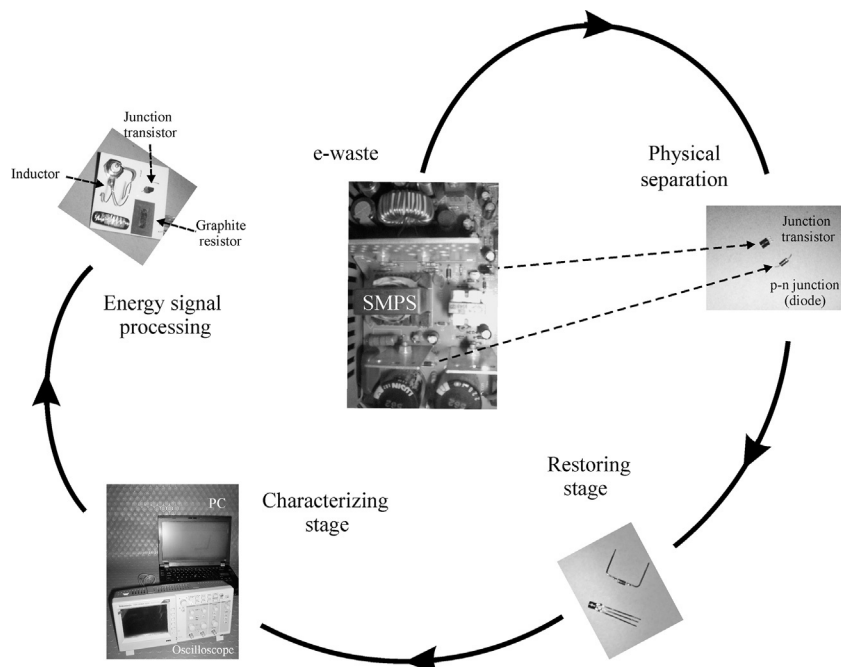


FIG. 1 Schematic for open-loop recycling as applied to the recovery of silicon waste.

recycling are important factors focusing on material attributes, including mechanical, thermal, and electrical properties, which must be evaluated in view of cost effectiveness and resource efficiency [13].

2.2 Restoring and characterizing

Because isolation is provided by a high-frequency power transformer in the Mn-Zn ferrite-based SMPS, several building blocks (output circuits, feedback control, and control circuit based on pulse width modulation as well as a protection network (well known as a resistor-capacitor snubber)) can be recuperated, which includes silicon semiconductors such as fast recovery diodes and small signal transistors [10, 14, 15]. Thus to give an example of the reliability of recycled silicon waste, a fast recovery IN4937 diode and small-signal 2N2222 transistor have been removed from Mn-Zn ferrite-based SMPS. These devices in their first life as electronic components survive thermal and electrical stress under switching conditions; hence, they are a valuable waste resource whose restoring stage involves the soldering of copper leads of 2 cm in length as depicted in Fig. 1.

Additionally, from manufacturer's datasheets of semiconductor devices, certain operating parameters must be taken into account in selecting e-waste useful for energy conversion. These parameters are summarized in Table 1, which includes average forward current, I_F , peak repetitive reverse voltage, V_{RRM} , operating junction temperature, T_J , forward voltage, V_F , reverse recovery time, t_{rr} , collector-emitter breakdown voltage, $V_{BR(CEO)}$, collector current at saturation condition, I_C , frequency at unitary small-signal current gain, f_T , as well as rise t_r and fall t_f times [10, 12].

Accordingly, before using silicon waste to design modules for energy conversion, it is necessary to know the technological capabilities of the recycled devices using a practical alternative approach. This is known as transfer function, which has been defined as the ratio of the output variable to the input variable to the analysis of the linear systems in the control theory [16]. In this study,

TABLE 1 Applied parameters in recycled silicon semiconductors for energy conversion.

	I_F	V_{RRM}	V_F	t_{rr}	T_J
Fast recovery diode	1–3 A	400–600 V	~1.2 V	100–300 ns	50–150 °C
	$V_{BR(CEO)}$	I_C	f_T	t_r	t_f
Small-signal transistor	40–60 V	200–800 mA	200–650 MHz	~25 ns	~60 ns

the transfer function represents the relationship describing a correlation between the physical behavior and the corresponding current/voltage characteristics to reveal uncommon conduction mechanisms under specific operating conditions.

To characterize the recycled silicon devices as a function of the transform function, generation of voltage signals, extraction of the current/voltage curves, and their evaluation in accordance with the electrical parameters of [Table 1](#) are attained using a function generator (Matrix, MFG-8250A), a digital storage oscilloscope (Tektronix, TDS1012C), and mathematical software, respectively.

2.3 Energy signal processing

The advancement of optimized signal processing to the next generation of energy conversion is shown in [Fig. 1](#). This focuses on analyzing, modifying, and synthesizing signals using uncommon conduction mechanisms and novel operating modes, where modules for energy conversion must be anticipated under negligible thermal and electrical stress of the materials. Furthermore, to avoid final disposal of e-waste in landfills, green engineering-inspired recycled materials, such as graphite, copper wire, and silicon semiconductors, are suggested to build modules for sustainable energy conversion, where graphite-based resistors dependent on their distributed resistance assembled on SiC sheets as substrate [\[17\]](#), single winding inductors with recycled magnetic wire AWG #20 from out-of-date magnetic components of iron powder previously manufactured for Mn-Zn ferrite-based SMPS, as well as fast recovery diodes (p-n junctions) and small-signal junction transistors, have been chosen as electronic pieces.

The following sections discuss in detail the uncommon conduction mechanism and sustainable energy conversion of waste-based electronics.

3 Uncommon conduction mechanism in silicon semiconductors

This section discusses uncommon conduction in p-n junctions of silicon junction transistors. Study of their physical behavior is carried out by using small-signal 2N2222 transistors labeled Q_1 , Q_2 , and Q_3 whose schematic circuits are shown in [Figs. 2 and 4](#), respectively. An electrical power supply $+V=5$ V is needed for biasing voltage in all test circuits.

3.1 Regenerative conduction in p-n junctions

The physical behavior of the p-n junction in [Fig. 2A](#) is dependent on biasing conditions in each p⁺-n junction at the conduction regenerative state. At forward bias, each p⁺-n junction begins to conduct through the depletion region at threshold voltages of 1.6, 2.2, and 2.4 V as shown in [Fig. 2B](#). At low-level

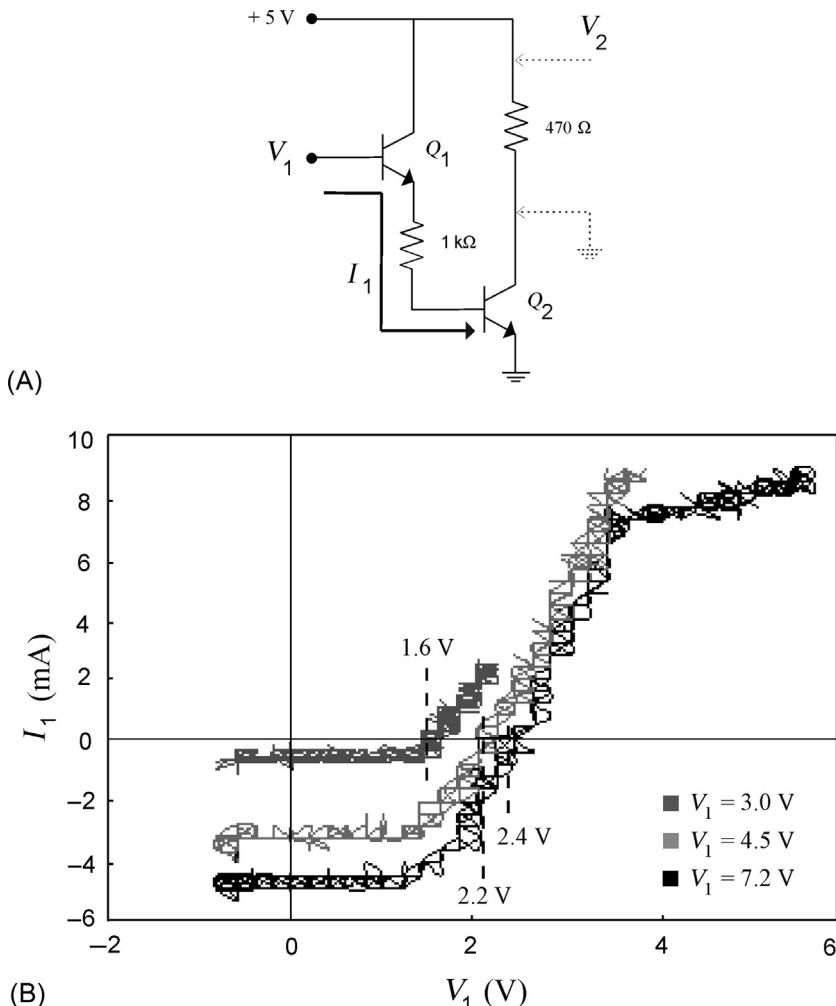


FIG. 2 (A) Schematic circuit to study regenerative conduction. (B) Current/voltage curves at low-level injection under three forward-bias voltages.

injection in the p^+ -n junction, both Q_1 and Q_2 are regeneratively biased when a half-rectified signal is applied as shown in Fig. 3A–C. Hence, an electrical field results in the vicinity of the p^+ -n junction after a certain number of electrons and holes have flowed, which is equivalent to a depleting region of carriers transported at the collector-emitter junction of both Q_1 and Q_2 occurring under forward-bias conditions where the variation of electrostatic potential through each p^+ -n junction is smaller in contrast to the equilibrium, narrowing the space charge region [18]. In this condition, current flow, I_1 , and voltage, V_2 , across the

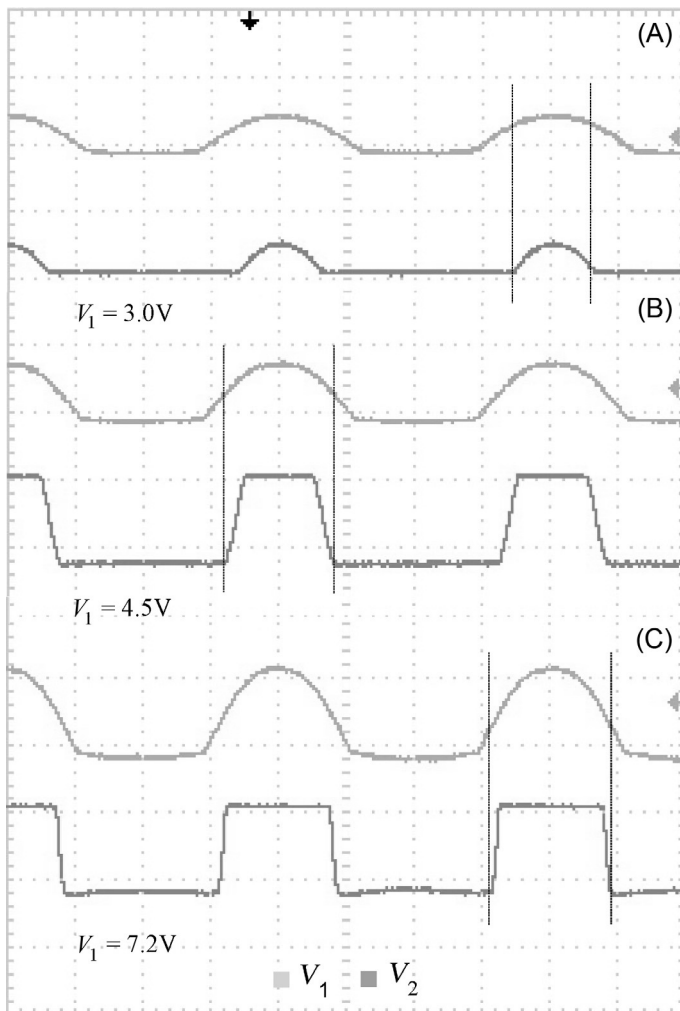


FIG. 3 Waveforms collected from the schematic circuit of Fig. 2A driven at 100 Hz and average voltages: (A) 3 V. (B) 4.5 V. (C) 7.2 V. The input and output signals are shown.

resistor of 470Ω is detected in the circuit of Fig. 2A, because a current begins to flow at applied voltage $V_1 > e^{-1}kT$, where the electrostatic potential variation will decrease the width of the depletion region on both the p-side and n-side in the p⁺-n junction.

A considerable charge due to the mobile carriers occurs everywhere within the p⁺-n junction; therefore a distribution of minority carriers in the lowly doped n-region is located, whose rearrangement will contribute additionally to the conduction-regenerative state [19]. A conduction-regenerative state is

explained as follows. When V_1 begins to decrease below the threshold voltage, a certain current flowing in the reverse direction is observed because the presence of excess minority carriers in the n-region promotes the generation of electron-hole pairs along the depletion region where the probability of recombination is diminished (Fig. 2B); this occurs until the concentration of minority carriers in the n-region is negligible. Simultaneously, such minority carriers are removed from the depletion region, where holes at the p⁺-region and electrons at the n-region are sweeping along p⁺-n junction; hence, a turn-off state of Q_2 is demonstrated in Fig. 3. The current/voltage curves in Fig. 2B demonstrate that both generation current and diffusion current are the conduction mechanism at forward bias under low-level injection [20].

3.2 Transient conduction in junction transistors

The junction transistor remains a competitive technology for multiple operation functions in comparison to the widely used metal-oxide-semiconductor technology [21]. Hence, with low impedance at the base region, high transconductance, and lower output resistance, the junction transistor is useful in computing non-linear functions by their logarithm dependence between base-emitter voltage, collector current, and temperature. It is also based on a combination of its junctions, with the two built-in capacitances continuing to be dependent on biasing conditions, charge densities, and temperature [22, 23]. Hereafter, the impurities-controlled electrical properties at both base-emitter and base-collector junctions demonstrate how a silicon junction transistor can add new functionalities inspired by transient behavior of passive components, such as inductors, when they are operating under switching conditions. Therefore designing novel electronic circuits by combining both active devices and passive components can be a trend for optimizing electronic devices.

To show that a junction transistor can operate under uncommon-biasing operation, the proposed circuit of Fig. 4 was built using a small-signal 2N2222 transistor labeled Q_3 . To understand the important role of the inductor, two inductors were chosen and built as specified in Fig. 4. Taking into account inductor action and junction transistor capacitances, the proposed circuit shown in Fig. 4 is inspired by switching the response of the inductor and the physical behavior of the junction transistor as a function of both conductive and susceptive components. In this case, susceptive parameters are dependent on space charge capacitances and diffusion phenomena, both being controlled by collector current during a transit time, which is used to specify the valid frequency range needed for incremental change of diffusion from minority carriers across the base width [24, 25]. Accordingly, transient current paths at each junction are used here to give a qualitative idea of the physics involved to operate the proposed circuit. Initially, electrons are injected from emitter region into base region, and holes are injected from base region into emitter region with current flow, I_B . Thus the transition

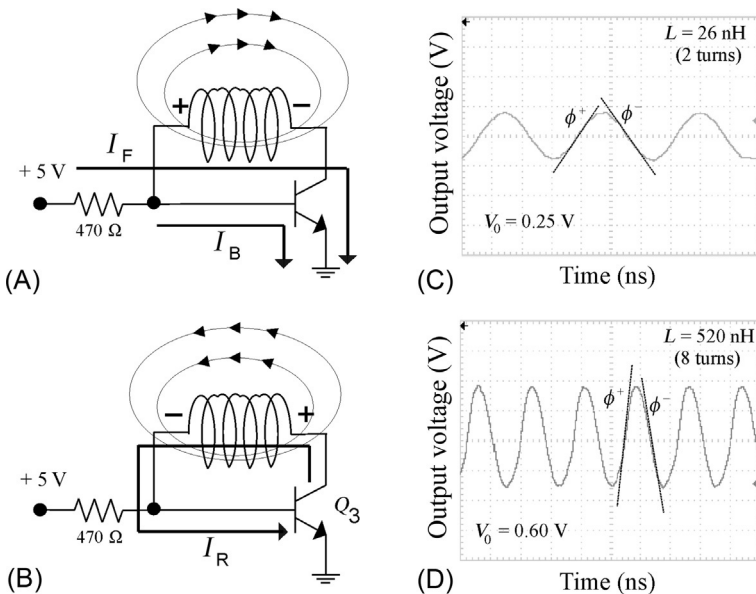


FIG. 4 Schematic circuit of a junction transistor under transient conduction. (A) At forward inductor polarity. (B) At reverse inductor polarity. (C) Output voltage waveform across the collector-emitter junction at 30 MHz. (D) Output voltage waveform across the collector-emitter junction at 25 MHz.

junction capacitance of the base-emitter junction will be loaded, and when the base-collector junction is reverse biased after a time delay there will be current flow, I_F , through the inductor at the polarity shown in Fig. 4A. Hence, electrons from the emitter-base junction are swept away by an electric field into the base-collector junction, and holes are drifted at the base-emitter junction. As a result, transition junction capacitance at the base-collector junction begins to be loaded. A potential ϕ^+ equivalent to the output voltage V_0 is built up at the collector-emitter junction, as shown in Fig. 4C and D, respectively.

After a certain time delay, the inductor polarity changes as shown in Fig. 4B, where the current flow, I_R , across the transition junction capacitance of the base-collector junction is negligible because space charge width is increased. Consequently, as the base-collector junction is equivalent to the reverse-biased junction, the potential ϕ^- proportional at the output voltage V_0 reduces as displayed in Fig. 4C and D, respectively. The waveforms at the collector-emitter junction of the small-signal 2N2222 transistor correspond with the RF signals measured at an operating frequency of 30 MHz in Fig. 4C and 25 MHz in Fig. 4D. In addition, displacement of the near-field magnetic lines as a function of inductor polarity is exhibited in Fig. 4A and B, respectively.

4 Sustainable energy conversion

This section discusses the feasibility of building architectures for short-range RF energy conversion when recycled materials are connected as shown in Fig. 5. To demonstrate operability in the proposed configuration under two novel operating modes, waveforms are collected by using a digital storage oscilloscope (Tektronix, TDS1012C), and a function generator (Matrix, MFG-8250A) was used to emulate voltages or electric currents as sensing signals useful for emergent processing in sensing technologies [6]. Hereafter, the operating modes of the proposed configuration are described.

4.1 Pulse width-assisted sensing

Alternative powering methods, such as solar, heat, vibration, and electromagnetic waves, as well as energy storage components such as auxiliary batteries and capacitors are currently under study; hence, unclaimed energy from environmental sources that can eliminate physical connection with wires from ac lines and overcome their short operation time by batteries is an urgent challenge [26]. Therefore due to the lack of a sustainable power supply that could enable the operation of electronic pieces autonomously in the circuit of Fig. 5, an electrical power supply $+V=5$ V will provide the energy to demonstrate their performance.

A square signal with a magnitude of 5 V was injected on input IN_3 at an operating frequency of 100 Hz. Both inputs IN_1 and IN_2 are injecting 0 V to avoid reinjection of noisy signals from external environmental sources.

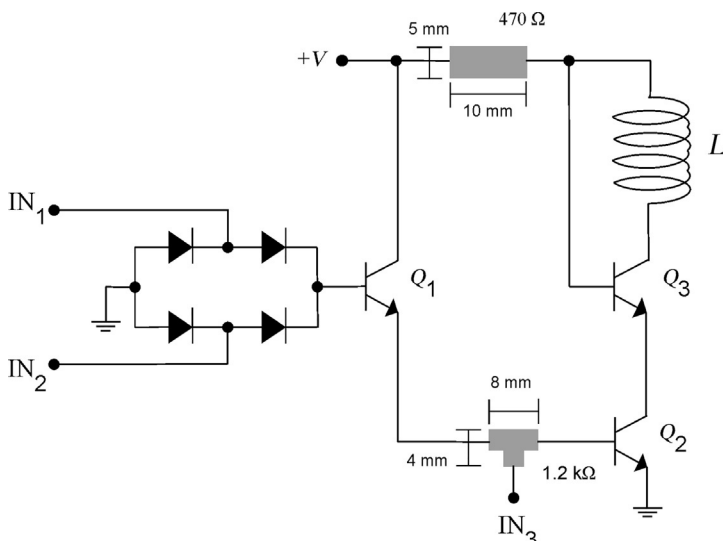


FIG. 5 Circuit configuration useful as an electronic module for sustainable energy conversion.

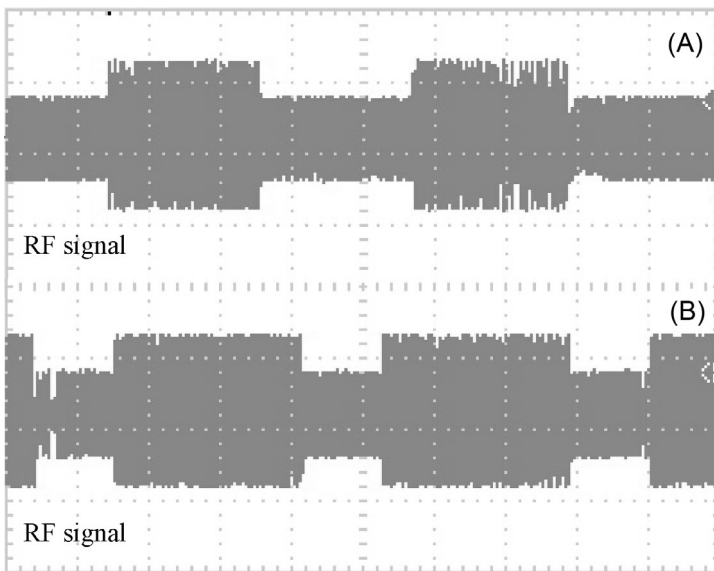


FIG. 6 Radiofrequency signals extracted from the electronic module of Fig. 5 driven at two square signal types: (A) duty cycle equal at 50% and (B) duty cycle above 50%.

Hence, the RF signals extracted on the collector-emitter junction of Q_3 are shown in Fig. 6 for two cases. First, a square signal with a duty cycle of 50% injected on IN_3 (Fig. 6A). Second, a duty cycle in the square signal above 50% injected on IN_3 (Fig. 6B). The latter confirms that data acquisition in digital format can be enabled for wireless sensing [27].

4.2 Phase detection-assisted sensing

Because the conduction-regenerative state in p-n junctions can be a reliable solution to adjust the magnitude of sensing signals at different values, four fast recovery 1N4937 diodes are connected in Fig. 7. A voltage source $+V = 5$ V was connected to power the electronic module under such test conditions. Due to the operating parameters of a small-signal 2N2222 transistor in accordance with Table 1 (see Section 2), the proposed circuit of Fig. 5 is powered under negligible thermal and electrical stress at voltages below 40 V.

To simulate phase difference among two sinusoidal signals of different magnitude, two function generators were connected at the inputs IN_1 and IN_2 , respectively. Signals of 2 V at an operating frequency of 30 kHz were injected at IN_1 and IN_2 with a phase angle of 10.6 degrees (Fig. 7A). In contrast, a phase angle of 55.4 degrees between sinusoidal signals of 2.5 and 1.25 V, respectively, at an operating frequency of 4 kHz were injected at IN_1 and IN_2 (Fig. 7B).

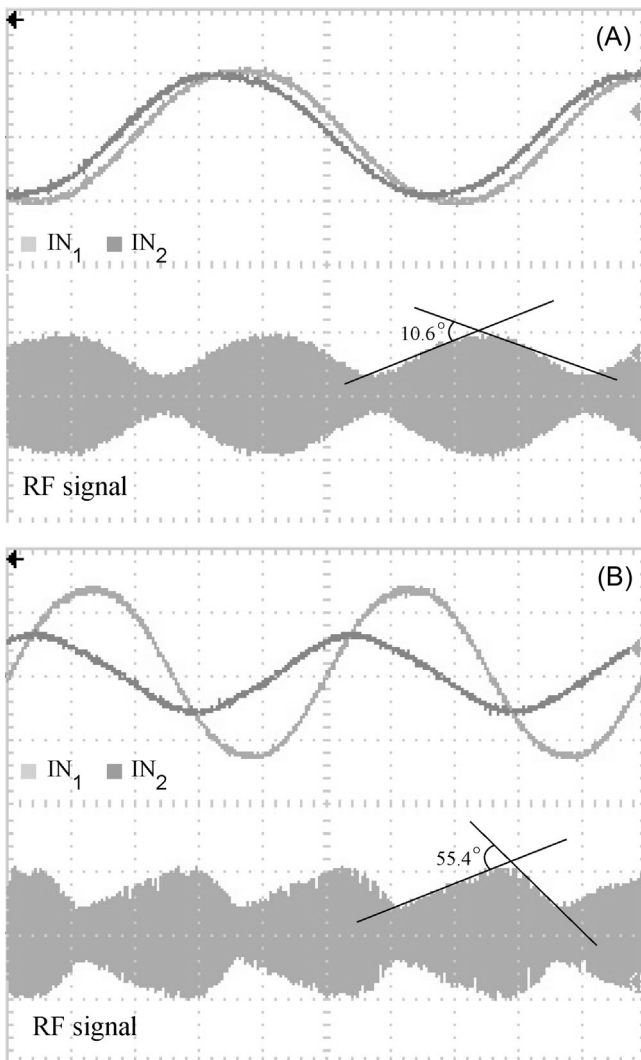


FIG. 7 Radiofrequency signals extracted from the electronic module of Fig. 5 driven at two phase differences. (A) Phase angle of 10.6 degrees. (B) Phase angle of 55.4 degrees.

The RF signals measured at the collector-emitter junction of Q_3 are shown in Fig. 7, where amplitude modulation is observed. The slope changes on each RF signal as revealed in Fig. 7 demonstrate how modulating signals are perturbing as a function in the electrical response of sensing physical variables. Furthermore, correlation among RF signals and sensing signals provides the opportunity to build near-field RF energy sources as modules for electronic instrumentation in radio systems [6, 26].

4.3 Validation of the operating modes

To provide insight into how obsolescence would affect the lifetime of the silicon wastes in the electronic module of Fig. 5, one must consider that the previous electrical performance of the recycled silicon components from three Mn-Zn ferrite-based SMPS used for energy conversion, being previously manufactured by Delta Electronics, have survived cycles of transient temperatures and continuous switching during a realistic profile to sustain performance for several years. Hence, due to the different test conditions for p-n junctions of the small-signal 2N2222 junction transistors (see Section 3), where there was damage to their microstructure at the interface, such a thermal degradation is very insignificant [28]. It is interesting to note that this degradation at the interface in p-n junctions is small under low-injection conduction, which indicates that the electronic module of Fig. 5 will operate under reliable conditions during long-term electrical performance for energy conversion. Nevertheless, its reliability can be limited when electrical power supply $+V$ is perturbed by high-peak inrush currents during turn-on and high-voltage spikes of short duration caused by inductive switching or by natural causes of the environmental sources, such as solar, heat, vibration, ac lines, etc. Consequently, the electronic module shown in Fig. 5 must be redesigned, taking into account the connection of a protective network to reduce electrical breakdown phenomena diverting anomalous current flow during turn-on to enhance reliable operation for periods of several years in accordance with the electrical parameters of Table 1 (see Section 2).

5 Summary

To manufacture waste-based electronics within desired operation characteristics, the selection of materials must be dependent on availability, recycling opportunities, and environmental consequences of use. Hence, to ensure the availability of raw materials for future generations, the recovery of silicon waste into useful applications was discussed, which implies that the modern semiconductor industry must assume other practices for technological innovation to avoid dependence on specific software to support device operation updates and as a consequence early obsolescence.

Mitigation of negative environmental impact resulting from emission of toxic gases and land pollution by e-waste from customers has motivated the recycling of silicon semiconductors from Mn-Zn ferrite-based SMPS, because they provide suitable physical properties when they are driven under unusual test conditions. An open-loop recycling strategy was suggested here as a methodology to study all stages of the second life of recycled electronic devices. Hence, electrical conduction studies have been done on fast recovery diodes and small-signal transistors to understand their operating limits and when they would be useful as functional blocks. As a result, studies on the regenerative

conduction in p-n junctions and transient conduction in junction transistors have confirmed that data acquisition would be enabled by both pulse width-assisted sensing and phase detection-assisted sensing to build architectures of near-field RF energy sources under negligible thermal and electrical degradation.

Although the amount of recycled silicon waste mentioned in this chapter is currently only 20%, which is so far negligible for future regulation requirements, finding innovative properties from silicon waste is the inspiration to continue to find optimum signal processing using fundamental tools such as recycling practices of e-waste and novel characterization routes. The latter must be a philosophy for scientists, engineers, and students responsible for the current state of natural resources to advance the technological challenge to design sustainable devices inspired by e-waste management.

Acknowledgment

I would like to thank the book editors Lung-Chien Chen and Kuan Yew Cheong for giving me the opportunity to write this chapter and expand knowledge of the recovery of e-waste for future sustainable technologies.

References

- [1] M.M. Lunardi, et al., Comparative life cycle assessment of end-of-life silicon solar photovoltaic modules. *Appl. Sci.* 8 (1396) (2018). <https://doi.org/10.3390/app8081396>.
- [2] G. Fisher, M.R. Seacrist, R.W. Standley, Silicon crystal growth and wafer technologies, *Proc. IEEE* 100 (2012) 1454–1474.
- [3] M. Bohr, The evolution of scaling from the homogeneous era to the heterogeneous era. *Tech. Digest IEEE Int. Electron Devices Meeting* (2011). <https://doi.org/10.1109/IEDM.2011.6131469>.
- [4] M. Schmidt, et al., Life cycle assessment of silicon wafer processing for microelectronic chips and solar cells. *Int. J. Life Cycle Assess.* 17 (2012) 126–144, <https://doi.org/10.1007/s11367-011-0351-1>.
- [5] K. Leahy, G. Oster, The evolution of electronic systems technology and its impact on methods of innovation, *Regent Global Bus. Rev.* 5 (2) (2012) 8–15.
- [6] F. Alimenti, et al., Smart hardware for smart objects, *IEEE Microw.* 19 (6) (2018) 48–68.
- [7] Y. Han, et al., Evaluation of magnetic materials for very high frequency power applications, *IEEE Trans. Power Electron.* 27 (1) (2012) 425–435.
- [8] J.A. Garcia, Z. Popovic, Class-E rectifiers and power converters, *IEEE Microw.* 19 (5) (2018) 67–78.
- [9] O.A. Ogunseitan, J.M. Schoenung, Human health and ecotoxicological considerations in materials selection for sustainable development. *MRS Bull.* 37 (4) (2012) 356–363, <https://doi.org/10.1557/mrs.2012.8>.
- [10] G. Chryssis, *High-Frequency Switching Power Supplies: Theory and Design*, second ed., McGraw-Hill, New York, 1989.
- [11] B. Maurice, L. Wuidart, Drive Circuits for Power MOSFETs and IGBTs, Available: <http://datasheet/SGSThomsonMicroelectronics/mxyzws.pdf>, 1999.

- [12] H.O. Granberg, Power MOSFETs Versus BIPOLAR Transistors, Available: http://k5tra.net/tech_library/Motorola_app_notes/AN860_FETvsBipolar.pdf, 1993.
- [13] L. Gaines, To recycle, or not to recycle, that is the question: insights from life-cycle-analysis. MRS Bull. 37 (4) (2012) 333–338, <https://doi.org/10.1557/mrs.2012.40>.
- [14] K. Taniguchi, H. Irie, PWM technique for power MOSFET inverter, IEEE Trans. Power Electron. PE3 (3) (1988) 328–334.
- [15] C.G. Steyn, J.D.V. Wyk, Study and application of the non-linear turn-off snubber for power electronics switches, IEEE Trans. Ind. Appl. IA22 (3) (1986) 471–477.
- [16] H.K. Khalil, Nonlinear Systems, first ed., Macmillan Publishing, New York, 1992.
- [17] R. Baca-Arroyo, Graphite intended for green engineering developed by noncontaminant reverse abrasion. Adv. Mater. Sci. Eng. (2016) 1–6, <https://doi.org/10.1155/2016/7016457>.
- [18] A.S. Grove, Physics and Technology of Semiconductor Devices, first ed., John Wiley & Sons, New York, 1967.
- [19] B.J. Baliga, Modern Power Devices, John Wiley & Sons, New York, 1992.
- [20] S.M. Sze, Physics of Semiconductors Devices, third ed., John Wiley & Sons, New York, 2007.
- [21] G. Wang, et al., An accurate BJT-based CMOS temperature sensor with duty-cycle-modulated output, IEEE Trans. Ind. Electron. 64 (2) (2017) 1572–1580.
- [22] A. Elwakil, et al., A four-quadrant current multiplier/divider cell with four transistors, Analog Integr. Circuits Signal Process. 95 (1) (2018) 173–179.
- [23] B. Yi, et al., Physics-based compact model of parasitic bipolar transistor for single-event transients in FinFETs, IEEE Trans. Nucl. Sci. 65 (3) (2018) 866–870.
- [24] L.J. Giacoletto, Study of P-N-P alloy junction transistor from D-C through medium frequencies, RCA Rev. 15 (1954) 506–562.
- [25] R. Baca-Arroyo, Unusual operation of the junction transistor based on dynamical behavior of impurities. Adv. Cond. Matter Phys. (2018) 1–10, <https://doi.org/10.1155/2018/4237686>.
- [26] J.G.D. Hester, J. Kimionis, M.M. Tentzeris, Printed motes for IoT wireless networks: State of the art, challenges, and outlooks, IEEE Trans. Microw. Theory. Tech. (2017) 1–12. Available: <http://ieeexplore.ieee.org/document/7839226/>.
- [27] S. Kim, et al., Ambient RF energy-harvesting technologies for self-sustainable standalone wireless sensor platforms, Proc. IEEE 102 (11) (2014) 1649–1666.
- [28] R. Skuriat, et al., Degradation of thermal interface materials for high-temperature power electronics applications, Microelectron. Reliab. 53 (2013) 1933–1942.

Index

Note: Page numbers followed by *f* indicate figures and *t* indicate tables.

A

- Absorption-extraction compromise, 165–166
- Activated carbon (AC), 10
- Active materials, supercapacitors, 9–10, 15–16
 - carbon materials, 10
 - conducting polymers, 10–11, 17
 - metal compounds, 11–17
- Adsorption energy
 - B-doped graphene, 344, 346*t*
 - N-doped graphene, 344, 346*t*
- Agar
 - and agarose, 306–308
 - description, 306
- Agar-based gel electrolyte, 306–307
- Agarose, 307
- Agarose-based gel electrolyte, 307–308
- Ag-ZnO branched heterostructures, 241–242
- Al-air batteries, 60–62
- Alkaline fuel cells (AFCs), 88
- Anion exchange membrane fuel cells (AEMFCs), 90
- Aqueous electrolyte, 7
- Atomic layer deposition (ALD), 158–159

B

- Bacterial cellulose (BC), 291–292
- Bacterial nanocellulose (BNC)-Bio-TNG (BNC-Bio-TNG), 272, 273*f*
- Bare colloidal quantum dots, 151–155
- B-doped graphene
 - adsorption energy, 344, 346*t*
 - atomic structures of gas molecules, 347*f*
 - charge transfer, 345, 352
 - electronic transport properties, 345–346, 354–355, 354*f*
 - energetic and electronic structure calculations, 344
 - energy-band structure and isosurfaces, 348–350, 349–350*f*
 - energy diagram near Fermi energy, 350–351, 351*f*

gas molecule adsorption, 346–348
in low power consuming sensor devices, 350, 354–355

scanning tunneling microscopy (STM) images, 345, 353–354, 353*f*

singly occupied molecular orbital (SOMO) state, 350–351

work function, 352–353, 353*f*

Bio-based triboelectric nanogenerator (BTNG)
based on protein materials, 270–271
BTNG-based polysaccharide materials, 272–277

Biodegradable piezo/triboelectric materials, 252

Biomass

- advantages, 321–322
- biofuel production from, 322–324
- carbon nanomaterial synthesis from hydrothermal carbonization (HTC), 324–325
- pyrolysis, 327
 - template-directed synthesis, 325–327
- feedstock components, 322, 323*f*
- food-based, 329–331
- heteroatom modification of carbon materials, 327–331
- industrial utilization, 322–324
- nonfood biomass precursors, 328–329
- resources of, 322–324

Biopiezoelectric nanogenerator (BPNG) device

- fabrication
- applications, 268–270
- polysaccharide-based, 268
- protein-based, 264–268

Biowaste-based green energy harvesters, 277

Bone, piezoelectric effect for, 258*f*

Brillouin zone, 109

Bulk-heterojunction organic solar cells, 120

C

Cadmium telluride (CdTe), 105–106

Cantilever structure design, of piezoelectric energy harvester, 224–225

- Carbon-based perovskite solar cells
 CO_3O_4 hole-transporting layers in, 207
 VO_x hole-transporting layers in, 207
- Carbon cloth, 5–6, 6*f*
- Carbon materials, 10, 15–16*t*
- Carbon-nanostructured material, 320–322
 from biomass
 hydrothermal carbonization (HTC), 324–325
 pyrolysis, 327
 template-directed synthesis, 325–327
- Carbon nanotubes (CNTs), 10, 39
 and graphene, 343
- Carbon thermal reduction, of SiO_2 , 359
- Carbon woven fabric (CWF), 46
- Carboxymethyl cellulose (CMC), 294
- Carrier transport layer, 125–126
- Cellulose, 232, 322
 bacterial, 291–292
 carboxymethyl cellulose, 294
 cellulose acetate nanofibers, 293
 description, 291
 drawback, 292
 esters, 292
 hydroxypropyl cellulose, 294–295
 methyl cellulose, 293–294
 microfibrillated, 292
 nanofibers, 291–292
- Charge transfer
 B-doped graphene, 345, 352
 N-doped graphene, 345
- Chemical bath deposition (CBD), 139–141
- Chemically converted graphene (CCG), 43–44
- Chemical vapor deposition (CVD), 111, 111*f*
- Chitin, 285, 285*f*
 description, 296
 nanofibers, 260–261, 296–297
 in ZnO QDSSC, 296–297
- Chitosan, 232
 nanoparticles, 300
- Chitosan (Ch)-based polymer electrolytes, 297–300, 298–299*t*
- Collagen-enriched bone structure, 255
- Colloidal quantum dot-based solar cells, 140–141
- Colloidal quantum dots (CQDs)
 charge dynamics in, 159–163, 160*f*
 solar cell applications
 QD heterojunction solar cells, 165–170
 QD-sensitized solar cells, 164–165
 synthesis of, 151*f*
 bare colloidal quantum dot, 151–155
 core-shell quantum dot, 155–159
- Conducting plastics. *See* Conducting polymers (CP)
- Conducting polymers (CP), 10–11, 15–16*t*
 chemistry of
 electrochemical efficacy of, 31–34
 types of, 31
 composites, 17
 design and development
 miscellaneous architectures, 47–51
 stretchable, flexible supercapacitors, 43–46
 wearable supercapacitors, 46–47
 electroactive materials, 34
 supercapacitors
 nanohybrids, 38–42
 PANI, 34–37
- Copper-based delafossite materials, 201–204
- Copper indium gallium selenite (CIGS), 105–106
- Core-shell colloidal quantum dots, 155–159, 156*f*
- CQDs. *See* Colloidal quantum dots (CQDs)
- CuO/PVDF nanocomposite piezo anode, 243
- Current collectors, 5–6, 6*f*
- Cu-ZnO branched heterostructures, 241–242
- D**
- Derwent Innovation (DI), 92–93
- Derwent World Patent Index (DWPI), 93
- Direct current (DC) sputtering, 114–115
- Direct methanol fuel cells (DMFCs), 88
- Disaccharides, 284, 284*f*
- Doctor blade technique, 114
- Dopants, 34
- DSSCs. *See* Dye-sensitized solar cells (DSSCs)
- Dual template synthesis, of carbon nanomaterials, 326–327
- Dye-sensitized solar cells (DSSCs), 120–122, 121*f*
 agarose-based gel electrolyte, 307–308
 charge separation and transportation, 289–290
 counter electrode, 127
 description, 288
 light absorption, 289
 light to electricity conversion efficiency, 290–291
 performance
 PhCh-based electrolytes, 302–304*t*
 using chitosan-based electrolytes, 298–299*t*
 photoanode for, 127

triphenylamine dye sensitizer, 294–295
using nanoscale microfibrillated cellulose membrane, 296

E

Eggshell membrane biopiezoelectric nanogenerator (ESMBPNG), 264–268, 267*f*
Egg-shell membranes (ESM), 255–257
Electrical double-layer capacitance (EDLC), 4–5, 9–10, 28
Electrochemical capacitor.
See Supercapacitors
Electrochemical cell structure, 288/*f*
Electrochemical energy storage devices (EESDs), 27–28
Electrochemical impedance spectroscopy (EIS), 137, 169
Electrodeposition technique, 111–112, 111*f*
Electrolytes, 68–70
 agar-based gel, 306–307
 agarose-based gel, 307–308
 alkaline electrolyte, 66/*f*
 aqueous electrolyte, 7
 liquid electrolyte, 7
 quasi-solid-state electrolyte, 7–8
 redox additives, 8–9, 9*f*
Electronic module, for sustainable energy conversion
 circuit configuration, 368/*f*
 operating modes, validation of, 371
 phase detection-assisted sensing, 369–370
 pulse width-assisted sensing, 368–369
Electronic transport properties
 B-doped graphene, 345–346, 354–355, 354*f*
 N-doped graphene, 345–346
Electron-transporting layers (ETL), 106–107
 perovskite solar cells (PSCs), 184–186
Energy conversion
 recycled silicon semiconductors for, 362*t*
 sustainable
 operating modes, validation of, 371
 phase detection-assisted sensing, 369–370
 pulse width-assisted sensing, 368–369
Energy diagram, B-doped graphene, 350–351, 351*f*
Energy signal processing, in open-loop silicon waste recycling, 363
E-waste
 and physical separation, 361–362
 recycling, 251–252
External quantum efficiency (EQE), 168–169

F

Fast-charging self-powered electric double layer capacitor, 243–244
Fe-air batteries
 all-solid-state battery, 70
 chemical reactions, 62
 current progress of, 70–73, 72*f*
 development, 73–80, 76–79*t*
 electrolyte, 68–70
 negative electrode (anode), 63–67, 65–66/*f*
 positive electrode (cathode), 67–68, 68*f*
 rechargeable, 68–70

First-principles density-functional theory (DFT)
 adsorption energy, 344, 346–348
 charge transfer, 345, 352
 computational details, 344
 electron transport properties, 345–346, 354–355
 scanning tunneling microscopy (STM) images, 345, 353–354

Fish skin-based nanogenerator fabrication, 265/*f*
Flexible supercapacitors, 43–46
Food-based biomass, 329–331
Fossil fuels, 181
Fuel cells, 317–318
 functional material developments, 91–92
 metal-free carbon-based catalysts, 318
 N-modified carbon materials, 328–331
 oxygen reduction reaction (ORR), 317–320, 320*t*, 331
 real commercialization, 92–95
 technology development, 85–91

G

Gallium arsenide (GaAs) solar cells, 105
 graphene-based Schottky junction, 119–120
Gas molecule adsorption
 B-doped graphene, 346–348
 N-doped graphene, 346–347
Ginkgo leaf-derived material, 328–329
Graphene
 and carbon nanotubes (CNTs), 343
 composite nanomaterials, 107
 doping with impurities, 343–344
 electrical properties, 109
 optical properties, 109
 physical properties, 108, 108/*f*
 thermal properties, 108–109
 transparent anode, 126
Graphene-based organic solar cells
 bulk-heterojunction organic solar cells, 120
 dye-sensitized solar cells, 120–122, 121*f*

- Graphene-based organic solar cells (*Continued*)
 perovskite solar cells, 123
 tandem solar cells, 122–123
- Graphene-based Schottky junction GaAs solar cells, 119–120
- Graphene-based Schottky solar cells, 118–119, 118*f*
- Graphene-based sensor, first-principles material design for. *See* B-doped graphene
- Graphene metal oxide
 organic solar cells, 120–123
 Schottky junction GaAs solar cells, 119–120
 Schottky solar cells, 118–119
- Graphene nanoribbons (GNRs), 41
- Graphene oxide (GO), 45–46
- Graphene thin film PV cells
 chemical deposition method, 111–112
 doctor blade technique, 114
 physical deposition method, 112–114
 pulse laser deposition technique, 116
 sputtering technique, 114–116
- Green materials, 232–234, 234*f*
- Green quantum dot, 139–141
- H**
- Hard template synthesis, of carbon nanomaterials, 325–326
- Hemicellulose, 322
- Heteroatom-doped porous biomass-derived carbon catalysts, 327–328
- Heteroatom-functionalized carbon
 direct synthesis of, 327
 indirect synthesis of, 327
- Hierarchically porous carbon microsphere (HCM), 49
- High photoluminescence quantum yield (PLQY), 149–150, 152, 157
- High-temperature hydrothermal carbonization, 324–325
- Hole-transporting layers (HTL)
 CuCrO₂ nanoparticles, 204
 perovskite solar cells (PSCs), 184–186
 metal oxide materials, 188–189
 PEDOT:PSS, 188
 requirements, 187
 role of, 186–190
 spiro-OMeTAD, 187
 solution-processed Cu-doped NiO_x films, 194
- Hole transport media (HTM), 106–107, 123
- Hosta* leaf-based TNG, 274–276
- Human skin touch-based triboelectric nanogenerator, 270–271
- Hybrid FBT-Th4/Cu_xO-based film, 200
- Hybrid supercapacitor, 4–5
- Hydro-and solvothermal synthesis, 150–151
- Hydrogen evolution reaction (HER), 68–69
- Hydroquinone (HQ), 8–9
- Hydrothermal carbonization (HTC), 318–319
 of carbon nanomaterials, 324–325
 N-doped carbon sphere synthesis, 330
- Hydroxyl or amino-terminated oligoanilines (HAOANIs), 47
- Hydroxypropyl cellulose (HPC), 294–295
- I**
- IEEE/IET Electronic Library (IEL), 85, 86*f*
- Implantable medical devices, 237
- Indium-doped CuCrO₂ nanoparticles, 204
- Inorganic dyes, 289
- Inorganic solar cell technologies, 125–126
- Interconnected porous carbon (ICPC), 42
- Intermediate recombination layer (IRL), 169
- Ionic electrolyte, 7
- J**
- Junction transistors, transient conduction in, 366–367
- L**
- Landauer-Büttiker formula, 345–346
- Layered double hydroxides (LDHs), 67–68
- Leaf-based TNG device, 274–276, 274*f*
- Lifecycle assessment (LCA), 359–360
- Ligand-exchange, 165–166, 170
- Lignocellulosic biomass, 318–319, 322
- Li-ion battery, 3–4
- Liquid electrolyte, 7
- Low power consuming sensor devices, B-doped graphene in, 350, 354–355
- Low-temperature hydrothermal carbonization, 324–325
- M**
- Mechanical energy, 251–252
- Mechanical strain energy harvesters, 221
- Mechanical vibration energy harvester performance, 221–222
- Metal-air batteries, 59–60, 60*f*
 all-solid-state, 69–70
 anode electrode, 63–67, 80*f*
 cathode electrode, 67–68, 68*f*, 80*f*

- rechargeable, 59–60
types of, 60–62, 61*f*
- Metal compounds, 11–16, 15–16
composites, 17
- Metal-free carbon-based catalysts, 318
- Metal hydroxide, 11
- Metal-organic frameworks (MOFs), 68, 68/*f*
- Metal oxide, 11–13
- Metal oxide-based inorganic hole-transporting materials, for PSCs
copper-based delafossite materials, 201–204
copper oxide and cuprous oxide, 197–201
nickel oxide, 190–197
transition metal oxides, 204–208
- Metal semiconductor-branched heterostructures, 241–242
- Metal sulfides, 14–15
- Methyl ammonium iodide (MAI), 165–166
- Methyl cellulose (MC), 293–294
- Methyl methacrylate (MAA), 161–162
- Mg-air batteries, 60–62
- Microelectronics, silicon manufacturing, 359–360
- Mn-Zn ferrite-based switching mode power supplies (SMPS), 360–361
silicon waste management of (*see* Open-loop silicon waste recycling)
- Mobile electrons, 109
- Modified piezoelectric semiconductor materials, 235/*f*
- Molten carbonate fuel cells (MCFCs), 87
- Monosaccharides, 284, 284*f*
- MoO_x-based perovskite solar cells, 207–208
- Multiple exciton generation (MEG), 168
- Multiwalled carbon nanotubes (MWCNTs), 39–40
- MWCNT/P(VDF-TrFE) piezoelectric nanogenerator device, 237, 238/*f*
- N**
- Nanocellulose, 232
- Nanoenergy cell (NEC), 243–244
- Nanohybrids, 38–42
- Nanostructured carbon materials
from biomass, 321–322
generations of, 320–321, 321*f*
- Nature-driven biowaste materials-based bionanogenerator (NDBNG), 253/*f*
- N*-cetyl-*N,N,N*-trimethyl ammonium bromide (CTAB), 35–37
- N*-doped graphene
adsorption energy, 344
and distance, 346*t*
atomic structures of gas molecules, 347*f*
charge transfer, 345
electronic transport properties, 345–346
energetic and electronic structure calculations, 344
gas molecule adsorption, 346–347
scanning tunneling microscopy (STM) images, 345
- Ni-Fe batteries, 76–79*t*
- Ni foam, 5–6, 6*f*
- N-modified carbon nanomaterials, 318
- Nonfood biomass precursors, 328–329
- Nori biomass, 330
- N-phthaloylchitosan (PhCh)-based electrolytes, 301, 302–304*t*
- N719 TiO₂ DSSC, 292–295, 305
- O**
- Onion skin-based biopiezoelectric nanogenerator (OSBPNG), 265*f*, 267*f*
- Open-loop silicon waste recycling
energy signal processing, 363
e-waste and physical separation, 361–362
restoring and characterizing stage, 362–363
schematic illustration, 361*f*
- Ordered mesoporous carbon (OMCx), 41–42
- Organic dyes, 289
- Organic electrolyte, 7
- Organic solar cell technologies, 126–127
- Overbridging boundary-matching (OBM) method, 345–346
- Oxygen evolution reaction (OER), 67
- Oxygen reduction reaction (ORR), 67
codoping approach, 329
elementary reactions in, 319, 320*t*
in fuel cells, 317–320, 320*t*, 331
heteroatom-doped porous biomass-derived carbon catalysts, 327–328
- P**
- Perovskite films
degradation reactions of, 189
impedance spectra, 199*f*
oxygen molecules, 189
time-resolved photoluminescence (TRPL) spectra, 199*f*, 200
- Perovskite solar cells (PSCs), 106–107, 123
additive/composition engineering, 186–187
components and working principle of, 184–186

- Perovskite solar cells (PSCs) (*Continued*)
 CuCrO₂-based device, 204
 CuGaO₂-based device, 201–204, 203*f*
 device configurations of, 185*f*
 electron-transporting layers (ETL), 184–186
 historical overview of, 182–184
 hole-transporting layers (HTL), 184–186
 metal oxide materials, 188–208
 PEDOT:PSS, 188
 requirements, 187
 role of, 186–190
 spiro-OMeTAD, 187
 Phase detection-assisted sensing, 369–370
 Phosphoric acid fuel cells (PAFCs), 87
 Photoluminescence quantum yield (PLQY), 157–159, 162–163
 Photovoltaic performance
 of CuO/Cu₂O hole-transporting layers, 197, 198*t*
 of delafossite oxide hole-transporting layers, 201–204, 202*t*
 of NiO_x hole-transporting layers, 190–194, 191–193*t*
 of transition metal oxide hole-transporting layers, 204–207, 205*t*
 Photovoltaic solar cells
 classes of, 133–134, 134*f*
 evaluation of, 181–182
 graphene-incorporated application
 inorganic solar cell technologies, 125–126
 organic solar cell technologies, 126–127
 graphene material, 107–109
 graphene metal oxide
 organic solar cells, 120–123
 Schottky junction GaAs solar cells, 119–120
 Schottky solar cells, 118–119
 technologies, 104–107
 thin film
 chemical deposition method, 111–112
 doctor blade technique, 114
 physical deposition method, 112–114
 pulse laser deposition technique, 116
 sputtering technique, 114–116
 Photovoltaic technology, 181.
 See also Perovskite solar cells (PSCs)
 first generation, 181–182
 second-generation, 182
 third-generation, 182
 Physical deposition method, 112–114
 Piezoelectric ceramics, 225
 lead-based materials, 226–228, 230*t*
 lead-free materials, 228–229, 231*t*
- Piezoelectric effect, 221–222
 fundamentals and configurations of, 222–225
 of molecule, 222*f*
- Piezoelectric energy harvester
 bimorph cantilever, 224
 biomedical applications
 implantable medical devices, 237
 wearable devices, 237
 future research, 244–245
 limitation and challenges, 239
 materials for, 225–235
 sensor applications, 236
 structure of, 223–225
 unimorph cantilever, 224
 wireless sensor nodes, 237–239
- Piezoelectricity, 253–255
 of polysaccharide-based materials, 260–261
 in protein-based structures, 255–260
- Piezoelectric materials, 256*t*
 applications, 240*t*
 ceramics (*see* Piezoelectric ceramics)
 dipole moment of, 254–255
 direct and converse piezoelectric effect of, 254–255
 green materials, 232–234, 234*t*
 polymeric materials, 230–232, 233*t*
 properties, 227*t*
 semiconductors, 234–235, 235*t*
 working mechanism of, 253–254, 254*f*
- Piezoelectric operation modes, 223, 223*f*
- Piezoelectric transduction principle, 222–223
- Piezoelectrochemical process, 239–241
 elements for energy storage, 243–244
 supercapacitors development, 243
 for water splitting in hydrogen (H₂ gas) generation, 241–242
- Piezophototronic effect, 234–235
- Piezotronic effect, 234
- Plypyrrole (PPY), 10–11
- PMN-PZT-Mn thin film, 237
- p-n junctions, regenerative conduction in, 363–366
- Poly(3,4-ethylene dioxythiophene) (PEDOT), 31, 37–38, 42–43
- Poly(acetylene) (PAC), 31
- Poly(*p*-phenylene sulfide), 31
- Poly(*p*-phenylene vinylene) (PPV), 31
- Polyaniline (PANI), 10–11, 31, 32*f*
 miscellaneous architectures, 47–51
 nanofibers, 43–44
 nanohybrids, 39–40
- Polymeric materials, piezoelectric, 230–232, 233*t*

- Poly(3,4-ethylenedioxythiophene):poly(styrene sulfonate) (PEDOT:PSS), 46
- Poly(pyrrole)s (PPy), 37
- Poly(thiophene)s (PTh), 31
- Polysaccharide-based biopiezoelectric nanogenerators, 268
- Polysaccharides
- cellulose, 285, 285*f*
 - chitin, 285, 285*f*
 - as electrolytes, 286–287, 287*t*
 - function, 285
 - starch, 285, 285*f*
- Polythiophene (PT), 10–11
- Polyvinyl alcohol (PVA), 64
- Populus* leaf-based TNG, 274–276
- Power-conversion efficiency (PCE), 136–137, 149–150, 159, 163, 183–184
- p-phenylenediamine (PPD), 8–9
- Protein-based biopiezoelectric nanogenerators, 264–268
- Proton exchange membrane fuel cells (PEMFCs)
- functional material developments, 92
 - technology development, 87–88, 90–91
- Pseudocapacitor, 4–5
- Pulse laser deposition technique, 116
- Pulse width-assisted sensing, 368–369
- Pyrolysis, 327, 330
- PZT nanowire, 237–239
- Q**
- QD heterojunction solar cells (QDHSCs), 165–170
- QD-sensitized solar cells (QDSSCs), 164–165
- QDSSCs. *See* Quantum dot-sensitized solar cells (QDSSCs)
- Quantum dots (QDs), 289
- colloidal quantum dots, 151–155
 - of copper indium sulfide/zinc sulfide (CuInS/ZnS), 293
 - core-shell, 155–159
 - Cu₂O, 200–201
 - semiconductor, 134–135
- Quantum dot-sensitized solar cells (QDSSCs)
- active layers in, 137–139
 - agar-based electrolyte, 306–307
 - Ag₂S, 138
 - Bi₂S₃, 138
 - challenges and limitations, 141–143
 - charge separation and transportation, 289–290
 - description, 288
 - fundamental principles, 135–137, 136*f*
- green fabrication, 139–141
- light absorption, 289
- light to electricity conversion efficiency, 290–291
- methyl cellulose-based electrolyte, 293–294
- third-generation solar cells, 134–135
- Quasi-solid-state electrolyte, 7–8
- R**
- Radio frequency (RF) sputtering, 114–116
- Recycled silicon semiconductors, for energy conversion, 362*t*
- Redox additives, 8–9, 9*f*
- Redox reaction, Fe-air batteries, 62
- Reduced graphene oxide (rGO), 10, 17
- Regenerative conduction, in p-n junctions, 363–366
- Renewable energy sources, 283–284
- S**
- Saccharides, 284
- Scanning tunneling microscopy (STM) images
- B-doped graphene, 345, 353–354, 353*f*
 - N-doped graphene, 345
- Schottky solar cells, 118–119, 118*f*
- Searching Science Direct Online (SDOL), 85, 86*f*
- Second-generation photovoltaic technology, 182
- Self-assembled quantum dots (SAQDs), 149–150
- Self-charging power cell (SCPC)-based PVDF microporous nanostructure, 243
- Self-powered Leaf-TNG, 274–276
- Semiconductor materials, piezoelectric, 234–235, 235*t*
- Short-range radiofrequency energy conversion circuit configuration, 368*f*
- operating modes, validation of, 371
 - phase detection-assisted sensing, 369–370
 - pulse width-assisted sensing, 368–369
- Silicon (Si), 359
- performance, 359–360
 - silicon-based cells, 181–182
 - waste management of Mn-Zn ferrite-based SMPS (*see* Open-loop silicon waste recycling)
- Silicon semiconductors
- recycled, for energy conversion, 362*t*
 - uncommon conduction mechanism
 - regenerative conduction in p-n junction, 363–366

- Silicon semiconductors (*Continued*)
 transient conduction in junction transistors, 366–367
- Silk-based Bio-triboelectric nanogenerator, 270–271
- Sodium carboxymethylcellulose (NaCMC), 294
- Sodium carboxymethyl starch, 305–306
- Soft template synthesis, of carbon nanomaterials, 326
- Solar cells, 104
 colloidal quantum dots
 QD heterojunction solar cells, 165–170
 QD-sensitized solar cells, 164–165
- GaAs thin films, 105
 materials, 105
- Solar technology, 283–284
- Solid oxide fuel cells (SOFCs)
 functional material developments, 91–92
 technology development, 86–87, 89
- Spider silk biopiezoelectric nanogenerator (SSBPNG), 264–268, 265^f
- Spider silk (SS) fiber
 α-helix and β-sheet structure and H-bonding interaction in, 261–263, 263^f
 out-of-plane piezoelectricity of, 257–260
- Spin-coating technique, 112–114, 113^f
- Sputtering technique, 114–116
- Standard Oil of Ohio (SOHIO), 28
- Starch, 285, 285^f
 cationic, 305–306
 description, 305
 drawback, 305
 sodium carboxymethyl starch, 305–306
- Successive ionic layer adsorption and reaction (SILAR), 138, 141^f
- Supercapabattery, 4–5
- Supercapacitors
 active materials
 carbon materials, 10
 conducting polymers, 10–11, 17
 metal compounds, 11–17
- application of, 5^t
- components of
 active materials, 9–10
 current collectors, 5–6, 6^f
 electrolyte, 6–9
- CP-based wearable, 46–47
- defined, 3–4
- energy storage devices, 3–4, 4^f
- flexible substrates, 5–6, 11–13
- nanohybrids, 38–42
- PANI, 34–37
- poly(pyrrole)s, 37
- Sustainable energy conversion, short-range RF operating modes, validation of, 371
- phase detection-assisted sensing, 369–370
- pulse width-assisted sensing, 368–369
- T**
- Tandem solar cells, 122–123
- Template-directed synthesis, of carbon nanomaterials
 dual template approach, 326–327
 hard template approach, 325–326
 soft template approach, 326
- Tersoff–Hamann approximation, 345
- Tetrabutyl ammonium iodide (TBAI), 167
- ThemeScape, 93, 94^f
- Thin film photovoltaic solar cell
 chemical deposition method, 111–112
 doctor blade technique, 114
 physical deposition method, 112–114
 pulse laser deposition technique, 116
 sputtering technique, 114–116
- Thin film solar cells, 182
- Third-generation solar cells, 182
- Transfer function, 362–363
- Transient conduction, in junction transistors, 366–367
- Transparent anode, 127
- Transparent cathode, 127
- Triboelectricity, 255
- Triboelectric materials, 257^t
- Triboelectric nanogenerators (TNGs), 47, 255
- Tubular carbon nanofiber (TCNF), 71–72
- V**
- Vanadium-doped ZnO/bacterial cellulose hybrid paper, 232–234
- Vibrational energy harvester, 221
- W**
- Water-soluble methyl cellulose, 293–294
- Wearable devices, 237
- Work function, for B-doped graphene, 352–353, 353^f
- WO_x-based perovskite solar cells, 207–208
- Z**
- Zn-air batteries, 60–62
- ZnO nanorod array-patterned textile piezoelectric nanogenerator (ZnO-T-PET), 235

Companion Website

Appendices A–D can be accessed on our companion site
(<https://www.elsevier.com/books-and-journals/book-companion/9780128206287>).